June 1974

PROCEEDINGS

THIRD SPACE PROCESSING SYMPOSIUM

SKYLAB RESULTS

VOLUME II

APRIL 30-MAY 1-1974
MORRIS AUDITORIUM BLDG. 4200
MARSHALL SPACE FLIGHT CENTER
ALABAMA 35812

TABLE OF CONTENTS

TABLE OF CONTENTS (Continued)

TABLE OF CONTENTS (Continued)

TABLE OF CONTENTS (Continued)

SPACE PROCESSING PAYLOADS FOR SPACELAB

By

N74 [illegible]

K. R. Taylor*
National Aeronautics and Space Administration
Marshall Space Flight Center
Huntsville, Alabama 35812

and

R. L. Hammel, A. G. Smith, P. R. Mock, R. D. Stevenson
TRW Systems Group
Redondo Beach, California 90278

SUMMARY

This paper discusses the definition of facilities which will serve the research needs of a large group of users. These facilities (payloads) are derived by several combinations of items from a large inventory of modular, reusable, research equipment which enables ready response to many flight opportunities. Workable concepts have been prepared and submitted to the Spacelab design activity These designs permit the flying of either partial or dedicated payloads. The technical integrity of the modular approach to payload design/integration and the utility of commercial-equipment technology are also addressed in this paper.

INTRODUCTION

NASA's Space Processing Program [1] has generated six objectives and their related phases for the 1980-1990 time period, as shown in Table I. In total the objectives encompass the required course of product research and development from the initiation of SPA Shuttle/ Spacelab operations to the end-item goal of engaging in commercial manufacturing operations in earth orbit.

This paper discusses the necessary concepts and requirements for Space Processing payloads to accommodate the performance of the Shuttle-supported research phase. Since the purpose of the early activity is to identify those processes and materials having technical merits warranting exploitation, ample opportunities to examine many candidates will be needed. The product(s) and associated payload(s) for prototype or manufacturing activities will be identifiable only after successful accomplishment of the initial R&D efforts.

Consistent with the performance of a research program, frequent, short-term, sortie-mission modes are especially suited[2] to verifying space processing hardware performance and refining experiment protocols. Furthermore, return of space processed samples to earth represents a fundamental difference between this discipline and remote, sensor-type missions such as earth observations or astronomy.

*Paper presented by - K. P. Taylor

While perhaps not so obvious, an equally important feature will be the routine retrieval of the payload equipment via Shuttle. This will open a new era of testing in which reuse, reconfiguration and modifications of the payloads can systematically occur. This latter feature dictates the use of a reusable, reconfigurable, payload design and portends a modular approach to payload design and integration.

Table I. SPA Objectives and Their Related Time Phasing

Objectives	Program Phases
1. Make space easily accessible to the international scientific and industrial community for research and development work in materials science and technology.	Initiation Phase (Manned Missions—Apollo, Skylab, ASTP—in the 1970's and start of Spacelab flights in early 1980's)
2. Develop techniques that take full advantage of the characteristics of space flight to achieve experimental and process conditions that are not obtainable at competitive costs on earth.	
3. Employ the novel materials research and development techniques that are possible in space to advance knowledge in technological [illegible] areas of materials science and technology.	[illegible] (Early to mid-1980's)
4. Apply R&D results obtained in space to advance materials technology generally and in particular, to invent processes to manufacture products in space for use on earth.	
5. When appropriate, reduce selected space manufacturing processes to practice and conduct pilot production operations to demonstrate their practicality.	Reduction to Practice Phase (Mid to late 1980's)
6. When capabilities to manufacture economically viable products are achieved, initiate commercial production operations in space.	Commercial Production Phase [illegible] and beyond

It is believed that the practice of learning how to conduct space processing activities using multi-purpose, reusable and reconfigurable payloads aboard Shuttle will be an active process. This learning process must be aided by establishing simplified hardware/host vehicle and operational interfaces. Design approaches must be fostered that will allow the scientists to have rapid, convenient and repeated access to Space Shuttle facilities in a cost effective manner.

SALIENT REQUIREMENTS ANTICIPATED

Keeping in mind that the ultimate objective of Space Processing is the achievement of product commercialization, the following anticipated requirements[3] describe the nature of the payload equipment capabilities that are necessary to engage in a Shuttle-implemented, R&D phase.

- *Wide Ranging - Broad Experimental Activities*

  The benefits of performing materials processing experiments under a near-weightless condition in

space is projected to have applicability to numerous and various types of materials. These range from electronic materials, crystals and glasses, metals, alloys and compounds to biological specimens. While specific product-oriented activities are yet to be established, initial investigations have uncovered potential space processing in the following areas: crystal growth, purification/separation, mixing, solidification, and chemical and physical processes in fluids.

- *Evolutionary, Ongoing R&D Efforts*

  An initial period spanning many years will be necessary to establish and conduct an ongoing research and development program which will lead to the ultimate discipline goals of identifying and implementing the production of economically viable space products. The in-space R&D efforts will be highly evolutionary, building heavily upon an experimental learning process as the technical community determines methods and evaluates results through the aggressive performance of an in-space R&D program.

- *Process Development Emphasis*

  Due to a lack of prior art, much of the experimental activities will necessarily involve emphasis on identifying and characterizing those process methods and controls which are necessary in the use of the payload equipment.

- *Identification of Sufficient Equipment Capability To Engage the Interest of the Technical Community*

  To best serve the space processing community, provisions must be made for providing an inventory of equipment which is responsive to its R&D needs and which can readily be configured into research payloads. Fortunately, many experimental areas in materials science and technology have common equipment requirements, therefore, the laboratory approach which provides a complement of apparatus and instruments appears feasible. This approach would serve a large number of potential investigators, yet would maintain economical equipment and apparatus development costs. A rational, initial inventory of equipment has been established and must be updated as the program develops in order to meet the wide spectrum of potential research needs.

- *Identification of Equipment Required for Achieving R&D Endeavors and Objectives*

  As stated in the introduction, perhaps the greatest challenges

facing both the Space Shuttle and Spacelab development are those concerned with system usage, not with the vehicles themselves. A new era is beginning, the era of space exploration which requires participation by a very broad cross section of the scientific community. The emphasis is no longer upon simply overcoming phenomena due to a weightless environment but upon exploiting and using these phenomena to achieve economic benefits. In the exploitation phase, the problem is to take advantage of the physical and chemical changes caused by the in-space environment. The behavior of fluids in space is a good example. The implementation of this phase requires thorough understanding and characterization of phenomena which can only result from detailed scientific analysis. To achieve these results the payload design engineer and the research scientist must work closely together so that requirements are continually matched with capabilities.

Workable system level concepts must be based on;

- o real requirements
- o simplified operational procedures
- o minimum interfaces with the flight vehicle

The participation of the international scientific community is vital to the establishment of this system. Only in this way can the design of space processing payloads provide rapid, convenient and repeated access to space in a cost-effective manner.

A review of six R&D categories (as listed below) was conducted using exemplary experimental activities in each R&D area to establish the following:

- Experiment functional requirements
- Required types of apparatus and instruments

The Space Processing R&D categories considered include:

- Biological Processes
- Chemical Process in Fluids
- Crystal Growth
- Glass Preparation
- Metallurgical Processes
- Physical Processes in Fluids

In this process, over 40 separate experiment classes were reviewed. Each individual experiment class considered represents a potential area of study

conceivably of interest to many principal investigators. The resulting equipment and instrumentation identified to support the experimental efforts exceeded 90 items. Both the number of exemplary experiment classes and required associated payload equipment reflect the wide ranging diversity of anticipated space processing activities.

- [illegible]

  The nature of contemplated space processing R&D studies will require frequent and repetitive flight opportunities by most investigators to satisfy their experimental objectives. For this reason planned research studies rather than single-point or random opportunities are needed.

A very active learning process will occur, particularly during the initial years. Thus, progress in Space Processing as a discipline will be closely paced by how repetitively the multitude of investigators can obtain a sufficient number of short-duration, fast-reaction flight opportunities. Shuttle-supported, 7- to 30-day-long, earth orbital, sortie missions afford an excellent means provided that the payload equipment configurations can match available resources. This is particularly necessary when considering shared payload opportunities. Furthermore, quick reaction alternatives must be possible, to allow a constant rematch of continuously evolving scientific requirements with ongoing flight opportunities.

CONCEPTS FOR MEETING ANTICIPATED REQUIREMENTS

The nature of the equipment concepts to meet the experimental needs and usage requirements for both the user and operator are considered here. The establishment of an initial equipment inventory which would be made available to support multiple experimenters is a paramount issue to Space Processing. In addition to the samples, other minor experiment-unique hardware may occasionally be required by an individual investigator; but, primarily the payloads would be formed from a NASA inventory of equipment. Evolutionary changes in both the apparatus designs and equipment inventories would naturally occur as in-space experimentation progresses. The following paragraphs describe[3] activities or approaches directed toward planning ahead for the occurrence of the discussed concepts.

[illegible]

An initial inventory of equipment and instruments has been identified, based upon the examination of a cross section of experiment functional requirements. A listing of this inventory is included in Table II. Equipment functional specifications were then prepared which describe the anticipated areas of usage, functional requirements/rationale and specifications or criteria. Thirty-six specifications were prepared

TABLE II. SPA EXPERIMENT REQUIREMENT SUMMARY

SPA EXPERIMENT REQUIREMENT SUMMARY

EQUIPMENT CATAGORY	EQUIPMENT ITEM	COMMONALITY	SUMMARY DATA: NO. REQ'D.	DIMENSIONS X (M)	Y (M)	Z (M)	WT. KG	VOL. M³	POWER W AVG	PEAK	DATA BPS
ATMOSPHERIC COMPOSITION	FLUID SUPPLY SYSTEM L13E		1	61	.61	1.2	34.0	44?	-	-	-
	GAS CHROMATOGRAPH [illegible], L34E		1	91	.91	.30	22.7	23+	300	3??	32
	HIGH VACUUM PUMP [illegible]25E, L45E		2	30	30	.46	22.7	24?	1000	5??	40
	MOLECULAR SIEVE B27E, F28E, [illegible], 46E		2	.15	.15	.30	4.5	337	-	-	-
	RESIDUAL GAS ANALYZER F12E, L35E		1	74	49	52	34.0	.06?	260	5??	02
	VACUUM/PRESSURE MEASUREMENT UNIT F26E, G17E, L36E		1	24	.49	52	6.8	36?	100	5??	02
	VACUUM/PRESSURE REGULATOR F24E, [illegible]5E, L37E		1	24	49	52	9.1	36?	100	5??	32
BIOLOGICAL PROCESS EQUIPMENT	CONTINUOUS FLOW ELECTROPHORETIC [illegible] PM B11E		1	37	1.22	.10	4.53	345	*	*	-
	DIALYSIS UNIT B3E		1	.30	.30	.30	4.5	037	100	3??	01
	DISSOLVED OXYGEN ANALYZER B14E		2	23	.21	.34	7.7	016	15	15	10
	FLOW METER B12E		4	.03	03	.09	.45	000	10	10	10
	FRACTION COLLECTION SYSTEM B16E		1	37	09	.45	9.0	015	50	50	01
	ISOELECTRIC FOCUSING UNIT B[illegible]		1	.27	03	03	1.36	000	*	*	-
	GAS ELIMINATION SYSTEM B13E		2	15	15	24	2.3	005	50	50	10
	LYOPHILIZATION UNIT B18E		1	76	55	.37	30.6	155	600	90	01
	PH MONITOR B15E, [illegible]3E		1	37	46	.30	13.0	051	20	2??	01
	PUMPS (METERING) B12E		2	18	18	.45	10.?	015	-	30	10
	RECIRCULATING FLUID INCUBATOR B4E		1	90	60	.60	9.0	1.8	200		01
	REGULAR BUFFER SUPPLY & ELECTROLYTE SUPPLY TANK B14E		4	15	15	.15	1.36	003	-		-
	STATIONARY ELECTROPHORETIC CO[illegible] H12E		5	37	03	03	1.36	000	*	*	-
CONTAINERLESS POSITION CONTROL EQUIPMENT	CONTAINERLESS POSITION CONTROL SYSTEM										
	ACOUSTIC TRANSDUCER & DETECTOR L16E		1	.30	30	.30	11.3	027	-		10K
	ELECTROMAGNETIC POSITIONING COILS & DETECTOR L14E		1	30	30	.30	11.3	027	-	33?	10K
	ELECTROSTATIC POSITIONING PLATES & DETECTOR L15E		1	30	.30	30	11.3	027	-	33?	10K
	GAS JET PROBES & DETECTOR L17E		1	30	30	.30	11.3	027	-	33?	10K
COOLING EQUIPMENT	COOLANT SUPPLY TANK B29E			21	42	.42	4.5	037	-	-	-
	DIRECTIONAL SOLIDIFICATION UNIT F3E		1	30	46	.30	18.1	041	-	-	02
	FLUID COOLING/REFRIGERATION UNIT B1E		1	1.34	87	94	140.0	1.033	1592	146	02
	SAMPLE COOLING CHAMBER F5E		1	10	46	.30	18.1	041	-		40
	SAMPLE STORAGE AND PRESERVATION OF BIOLOGICALS										
	DEWAR B25E		1	54	.84	30	22.7	136	-	-	-
	FREEZER B24E		1	54	64	.30	80.0	136	500	30	-
	REFRIGERATOR B23E		1	54	84	61	57.0	277	250	50	-

TABLE II. (CONTINUED)

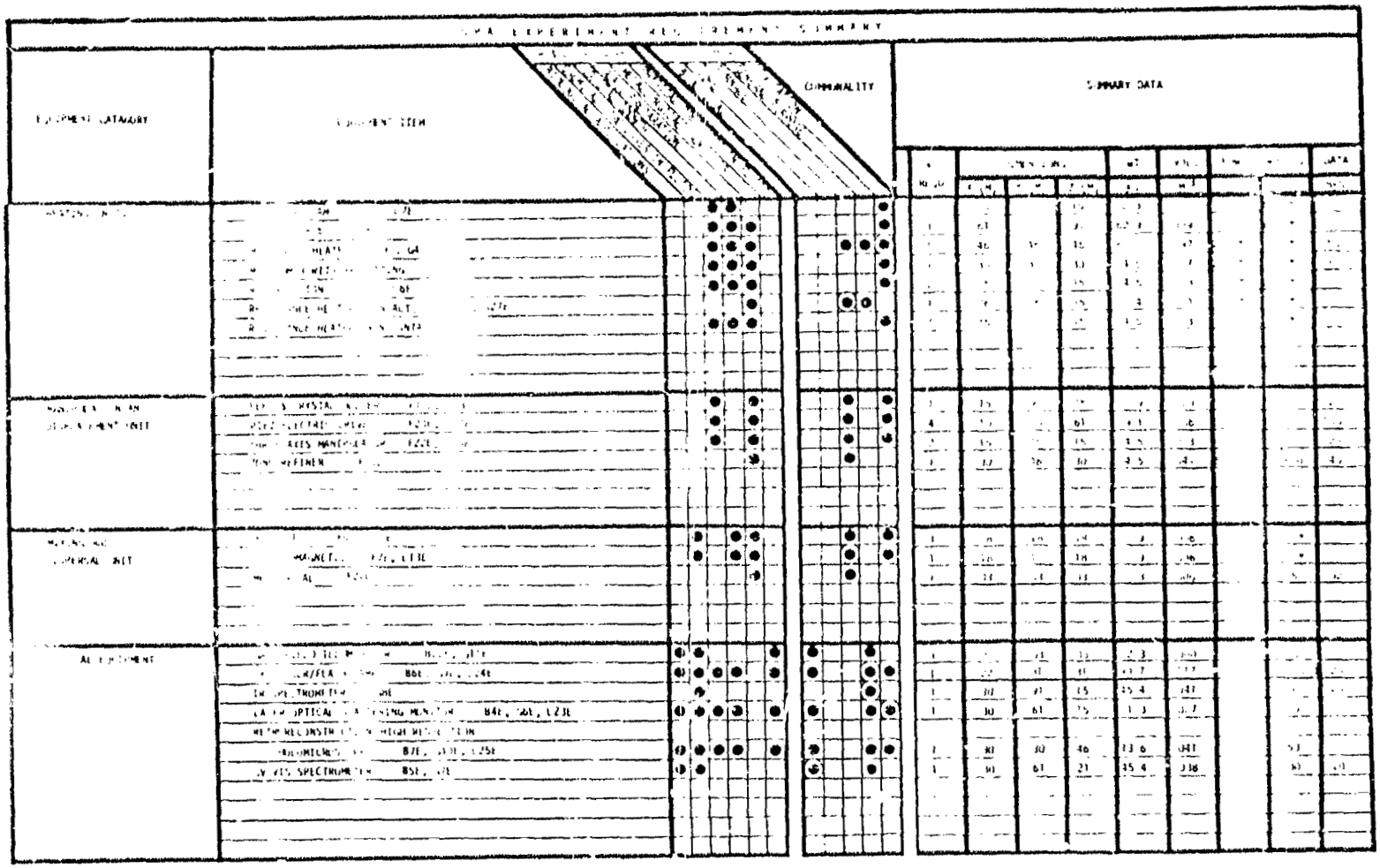

TABLE II. (CONTINUED)

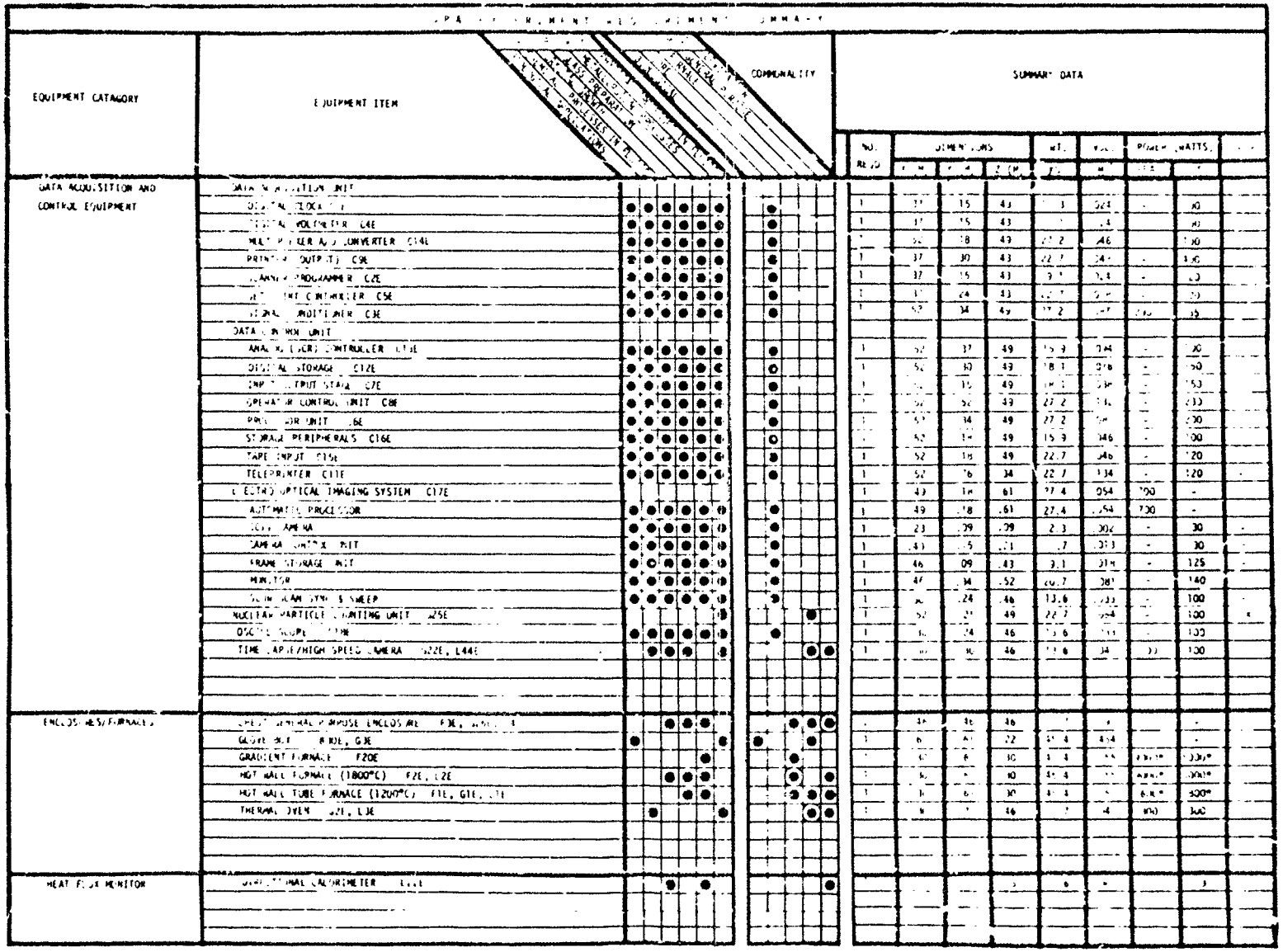

TABLE II. (CONTINUED)

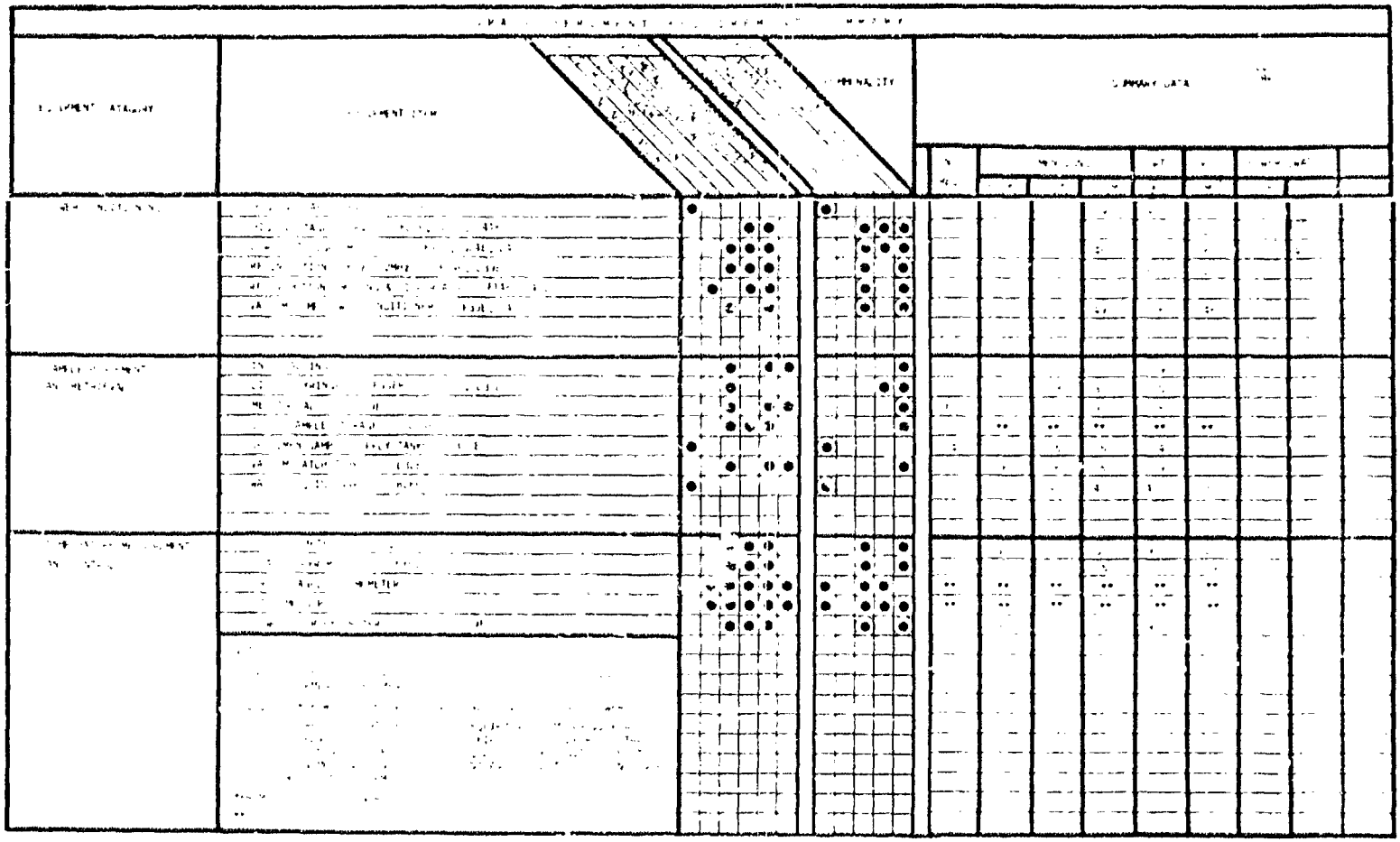

TABLE II. (CONTINUED)

REQUIREMENTS FOR COMBINATIONS OF MAXIMUM MINIMUM EQUIPMENT SUBELEMENTS														
SUBELEMENT COMBINATION (MINIMUM SUBELEMENT COMBINATIONS GIVEN IN PARENTHESES)	WEIGHT [4]		VOLUME [9]		POWER			DURATION PER CYCLE		AVERAGE ENERGY PER CYCLE	CYCLES PER MISSION	TOTAL EXPERIMENT ELAPSED TIME	TOTAL HOURS PER MISSION	TOTAL ENERGY PER MISSION
	(KG)	(LB)	(M^3)	(FT^3)	SUS (KW) [8]	AVERAGE (KW) [7]	PEAK (KW) [6]	AT AVERAGE POWER (HR) [5]	AT PEAK POWER (HR)	(KWH) [4]		(HR) [3]	(HR) [2]	(KWH) [1]
BIOLOGICAL (B)	369	1780	4.3	150	1.8	0.95	2.75	1.68	0.15	1.6	13	21.8	23.3	22
(MINIMUM B)	(434)	(896)	(3.0)	(106)	(1.8)	(1.34)	(1.71)	(4.1)	(0.10)	(5.5)	(1)	(4.1)	(4.9)	(5.5)
FURNACE (F)	529	1160	2.8	100	5.0	4.22	11.3	3.75	0.20	15.8	16	60.0	61.8	254
(MINIMUM F)	(341)	(401)	(1.1)	(39)	(3.9)	(2.84)	(10.7)	(4.5)	(0.5)	(12.8)	(1)	(4.5)	(5.2)	(12.8)
GENERAL PURPOSE (G)	596	1290	3.4	120	1.7	2.56	1.44	4.45	2.00	11.4	9	40.0	41.1	103
(MINIMUM G)	(230)	(510)	(2.3)	(81)	(0.56)	(0.47)	(1.33)	(1.8)	(0.1)	(0.85)	(1)	(1.8)	(2.4)	(0.85)
LEVITATION (L)	1180	2600	4.8	169	6.0	5.05	14.0	3.68	0.30	18.6	12	44.2	47.0	224
(MINIMUM L)	(282)	(627)	(1.9)	(67)	(2.12)	(3.16)	(4.56)	(3.8)	(1.0)	(12.0)	(1)	(3.8)	(4.4)	(12.0)
CORE (C)	518	1140	3.1	110	1.8	1.8	0.7	[10]	0.25	[11]	[11]	[11]	[11]	[11]
B+C	1330	2920	7.4	260	3.6	2.76	2.74	1.68	0.15	4.95	13	21.8	24.3	64.4
(b+c)	(922)	(2040)	(6.1)	(215)	(3.6)	(3.15)	(1.70)	(4.1)	(0.1)	(12.9)	(1)	(4.1)	(5.9)	(12.9)
F+C	1050	2300	5.9	210	6.8	6.03	11.3	3.75	0.20	22.6	16	60.0	62.8	362
(f+c)	(699)	(1540)	(4.2)	(148)	(3.7)	(4.64)	(10.7)	(4.5)	(0.5)	(20.9)	(1)	(4.5)	(6.2)	(20.9)
G+C	1110	2430	6.5	230	3.5	4.36	1.44	4.45	2.00	19.4	9	40.0	42.1	175
(g+c)	(748)	(1650)	(5.4)	(191)	(2.36)	(2.27)	(1.33)	(1.8)	(0.1)	(4.09)	(1)	(1.8)	(3.4)	(4.09)
L+C	1700	3740	7.9	279	7.8	7.20	13.6	3.68	0.30	25.2	12	44.2	48.0	303
(l+c)	(900)	(1770)	(5.0)	(177)	(3.92)	(4.95)	(4.56)	(3.8)	(1.0)	(18.8)	(1)	(3.8)	(5.4)	(18.8)
B+F+C	1860	4090	10.2	360	6.2	5.18	12.1	2.82	0.20	14.6	23	81.8	86.1	424
(b+f+c)	(1190)	(2440)	(7.2)	(254)	(3.7)	(3.93)	(11.4)	(4.3)	(0.5)	(16.9)	(2)	(8.6)	(11.1)	(33.8)
B+G+C	1910	4220	10.8	380	3.5	3.85	1.45	2.81	2.00	10.8	22	61.8	65.4	238
(b+g+c)	(1150)	(2450)	(8.4)	(297)	(3.3)	(2.83)	(2.02)	(3.0)	(0.1)	(8.5)	(2)	(5.9)	(8.3)	(17.0)
B+L+C	2510	5530	12.2	429	6.8	5.54	15.3	2.64	0.30	14.6	25	66.0	71.3	365
(b+l+c)	(1200)	(2670)	(8.2)	(290)	(3.8)	(3.98)	(5.54)	(4.0)	(1.0)	(15.9)	(2)	(7.9)	(10.3)	(31.7)
F+G+C	1650	3600	9.3	330	5.3	5.35	12.0	4.00	0.20	21.4	25	100	104	535
(f+g+c)	(929)	(2050)	(6.5)	(229)	(3.3)	(3.94)	(11.4)	(3.2)	(0.5)	(12.6)	(2)	(6.3)	(8.6)	(25.1)
F+L+C	2230	4900	10.7	379	7.2	6.36	14.4	3.73	0.30	23.7	28	104	110	664
(f+l+c)	(981)	(2170)	(6.3)	(215)	(3.3)	(4.74)	(10.6)	(4.2)	(0.5)	(19.9)	(2)	(8.3)	(10.6)	(39.8)
G+L+C	2280	5040	11.3	399	5.5	5.66	15.1	4.01	0.30	22.7	25	84.2	89.1	47
(g+l+c)	(1030)	(2280)	(7.3)	(258)	(3.5)	(4.11)	(5.41)	(2.8)	(1.0)	(11.5)	(2)	(5.6)	(7.8)	(23.0)

TABLE II. (CONTINUED)

REQUIREMENTS FOR COMBINATIONS OF MAXIMUM/MINIMUM EQUIPMENT SUBELEMENTS

SUBELEMENT COMBINATION (MINIMUM SUBELEMENT COMBINATIONS GIVEN IN PARENTHESES)	WEIGHT [9] (KG)	(LB)	VOLUME [9] (M^3)	(FT^3)	POWER SUS. (KW) [8]	POWER AVERAGE (KW) [7]	POWER PEAK (KW) [6]	DURATION PER CYCLE AT AVERAGE POWER (HR) [5]	DURATION PER CYCLE AT PEAK POWER (HR)	AVERAGE ENERGY PER CYCLE (KWH) [4]	CYCLES PER MISSION	TOTAL EXPER'T ELAPSED TIME (HR) [3]	TOTAL HOURS PER MISSION (HR) [2]	TOTAL ENERGY PER MISSION (KWH) [1]
B+F+J+C	2440	5380	13.6	480	5.1	4.92	12.4	3.13	0.20	15.7	38	122	127	598
(F+J+C)	(13	5550)	(9.5)	(335)	(3.5)	(3.60)	(11.7)	(3.5)	(0.5)	(12.6)	(3)	(10.4)	(13.5)	(37.8)
B+G+L+C	3090	6820	15.6	549	5.3	5.08	15.7	3.11	0.30	15.8	34	106	112	538
(B+J+L+C)	(1430)	3180)	(10.3)	(364)	(3.5)	(3.72)	(5.80)	(3.2)	(1.0)	(11.9)	(3)	(9.7)	(12.7)	(35.8)
B+F+L+C	3040	6700	14.0	529	6.8	5.77	15.0	3.08	0.30	17.8	41	126	133	729
(B+F+J+C)	(1390)	(3070)	(9.3)	(321)	(3.8)	(4.27)	(11.0)	(4.1)	(0.5)	(17.5)	(3)	(12.4)	(15.5)	(52.6)
F+G+L+C	2810	6210	14.1	499	6.0	5.79	15.0	3.91	0.30	22.7	37	144	151	840
(F+ [illegible]	(1210,	3180)	(8.4)	(297)	(3.6)	(4.29)	(11.0)	(3.4)	(0.5)	(14.6)	(3)	(10.1)	(13.0)	(43.8)

REMARKS

[1] ADD THE 'TOTAL ENERGY PER MISSION' FOR EACH INDIVIDUAL SUBELEMENT TO THE ENERGY NEEDED BY THE CORE. THE CORE ENERGY IS DETERMINED BY ADDING 1HR. (FOR INITIAL AND TERMINAL OPERATIONS) TO THE RESPECTIVE 'TOTAL EXPERIMENT ELAPSED TIME' [3] AND MULTIPLYING THIS BY THE POWER LEVEL OF THE CORE (1.8KW).

[2] INCLUDES THE TIME REQUIRED FOR EXPERIMENT PREPARATIONS, OPERATIONS AND POST ACTIVITY PLUS INITIAL AND TERMINAL OPERATIONS.

[3] INCLUDES THE TIME REQUIRED FOR EXPERIMENT PREPARATIONS, OPERATIONS AND POST ACTIVITY.

[4] CALCULATED BY DIVIDING THE 'TOTAL ENERGY PER MISSION' [1] BY THE 'CYCLES PER MISSION'.

[5] CALCULATED BY DIVIDING THE 'TOTAL EXPERIMENT ELAPSED TIME' [3] BY THE 'CYCLES PER MISSION'.

[6] PEAK POWER IS THE DIFFERENCE BETWEEN THE 'AVERAGE POWER' [7] AND THE HIGHEST POWER LEVEL THAT OCCURS WITHIN THE PAYLOAD COMBINATION.

[7] CALCULATED BY DIVIDING THE 'AVERAGE ENERGY PER CYCLE' [4] BY THE 'DURATION PER CYCLE AT AVERAGE POWER' [5].

[8] SUSTAINED POWER IS THE TYPICAL POWER LEVEL THAT OCCURS DURING THE EXPERIMENT OPERATIONS AND EXCLUDES EXPERIMENT PREPARATIONS AND POST ACTIVITY TIMES. IT IS CALCULATED BY ADDING THE SUSTAINED ENERGIES OF THE RESPECTIVE SUBELEMENTS AND CORE AND DIVIDING BY THE SUM OF THE EXPERIMENT OPERATIONS TIMES OF THE SUBELEMENTS.

[9] CONSISTS OF THE TOTAL FOR THE EQUIPMENT ITEMS PLUS AN APPROPRIATE FACTOR TO ALLOW FOR SUPPORTING STRUCTURES OR EXTRA SPACE.

[10] CONTINUOUS.

[11] DEPENDENT UPON PAYLOAD COMBINATION BEING CONSIDERED.

MINIMUM SUBELEMENT DEFINITIONS

b : SEPARATION OF BIOLOGICALS EXPERIMENT
f : IMMISCIBLE SOLIDIFICATION EXPERIMENT
g : RADICAL LIFETIMES EXPERIMENT
l : GLASS PREPARATION EXPERIMENT

TABLE II. (CONCLUDED)

COMPARATIVE ANALYSIS OF SELECTED
SPA EQUIPMENT SUBELEMENTS

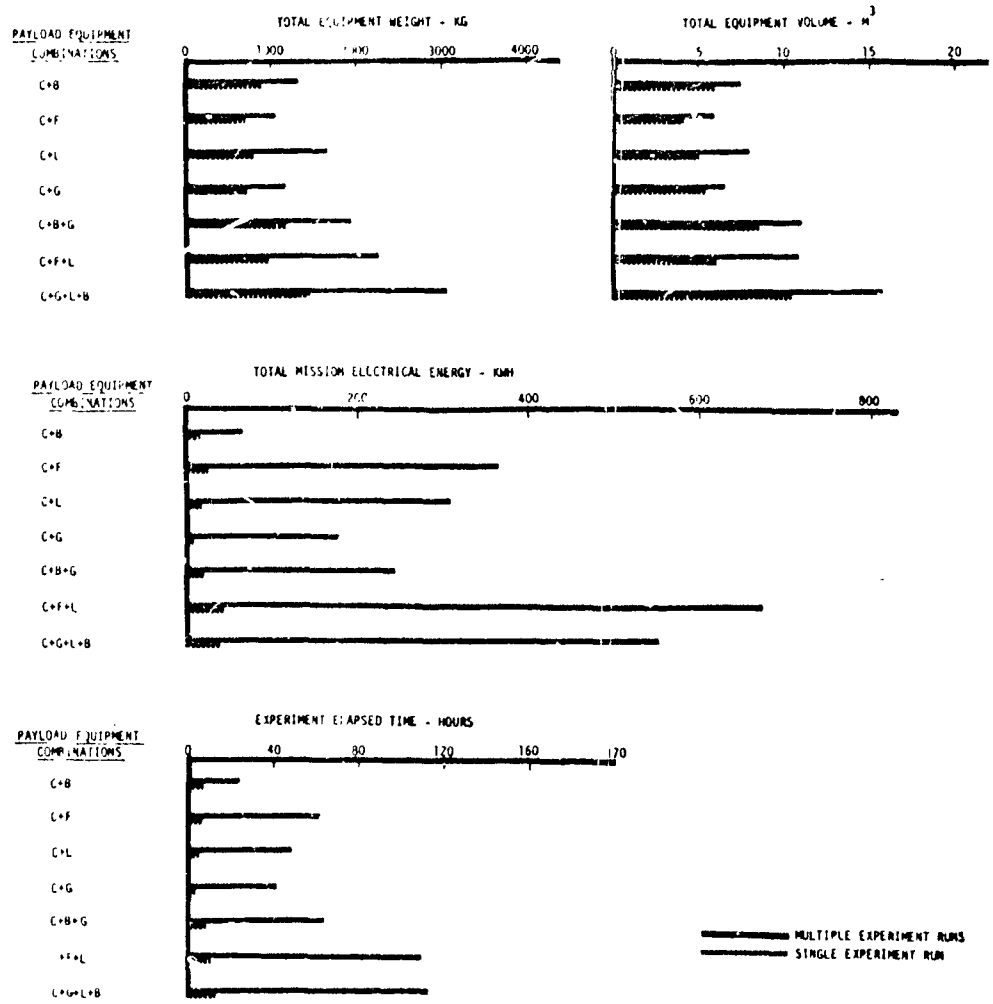

which cover 55 items. These documents quantify the equipment and instrumentation and provide a reference baseline description for record keeping. This inventory of apparatus can then be formed into payload groupings to serve a host of experiments. Large, custom-made facilities must be avoided in order to remain flexible and versatile in the grouping concept.

Derivation of Equipment from Commercial Technologies to the Greatest Degree Possible

Examination of commercial equipment technologies revealed that the functional performance requirements of space processing equipment could generally be met by state-of-the-art design practices. Thus, an apparatus could be evolved from a standard item or derived by custom design using present technologies. About 15 percent of the equipment needed has no analogous commercial base of derivation and requires special development. This equipment is involved primarily with contactless heating and position control.

The derivation of payloads using commercial equipment sources provides a broad and potentially cost-effective base upon which to draw. Since the derivation of payload equipment from commercial technologies poses other issues beyond that of the identifiable functional performance, additional comment is provided in a later section; but preliminary results on selected equipment testing of out-gassing characteristics performed by Beckman Instruments under Contract NAS 8-29776 appear quite favorable.

Modular Payload Equipment Groupings

Concepts for structurally grouping inter-related apparatus and instruments have been based upon modular approaches. On this basis, the following benefits occur:

- Payload equipment groupings can readily be assembled for a variety of possible mission opportunities ranging from austere to dedicated.
- Reconfiguration and refurbishment can be a practical, routine occurrence.
- It is possible to adapt to many possible host-vehicle, interface schemes.
- Equipment and apparatus interface management is effected prior to host vehicle integration.
- Standard interfaces can be defined and maintained between the payload equipment and the host vehicle.

Major payload equipment groupings have been organized around the following five payload subelements:

Furnace: A grouping of furnaces and associative apparatus for

performing activities in which physical contact with the specimen is permissible.

Levitation: Apparatus providing contactless positioning and heating of specimens with associated process control and characterization.

Biological: Equipment which produces separation of biological samples with associated preservation and storage capacity.

General Purpose: Provides services with associated characterization equipment supporting the accommodation of a variety of modest temperature research - physical or chemical fluid studies.

Core: Consists of centralized data acquisition, processing and equipment control functions.

By example, the Furnace subelement equipment listing and interfaces are shown in Figures 1 and 2.

In all cases each of the first four individual experiment subelements, or portions thereof, would be capable of being used independently of other payload equipment when combined with the core subelement. Such autonomous groupings are particularly attractive for participation in shared payload opportunities and to accommodate shifts in functional emphasis.

The subelement concept further lends itself to identifying and establishing Spacelab accommodation modes and operational requirements. Engineering descriptions of these payload groupings have been prepared and are available in Reference 3. Ongoing efforts are also addressing self-contained automated payload concepts which would be used either with or without a Spacelab as part of a Shuttle payload complement.

Out of five Spacelab accommodation concepts which were considered, two were selected for further study. Figure 3 illustrates various payload subelement accommodations for a single floor, two-aisle configuration. Alternately, the same payload subelements are shown in the arch configuration in Figure 4.

SPA power and heat rejection kit (PHRK) concepts which have been identified are shown in Figure 5. The SPA kit is visualized as an augmenting power and heat rejection capability when used in conjunction with Spacelab. By being capable of containing automated furnace and levitation equipment the kit also provides the payload basis for experimentation in an automated mission mode.

MISSION PLANNING

In the foregoing section, the requirements imposed on the payload design by both the space processing goals and the space shuttle flight system were discussed. This section will discuss the current Space Shuttle mission model and its implications on payload design.

Examination of the Space Shuttle System's mission traffic model provides a basis of identifying the degree to which frequent and repetitive access to space might occur for the purpose of conducting Space Processing activities. Furthermore, this enables the structuring of the complement of payload types that are required in order to effect the projected incorporations into the various Shuttle mission modes. Ultimately, the number of sets of payload equipment of each of the defined types can be derived in conjunction with other planning and scheduling constraints.

NASA Mission Model

The most recent mission model contains 727 flights over the period from 1980 to 1991. Currently, payloads are assigned to 488 of these flights and 239 remain unassigned. Figure 6 presents a division of flights by type: Dedicated, Assigned and other opportunities.

Space Processing Payload Flight Requirements

Space processing, both for reasons of operating economy and achieving program goals, must take advantage of every flight opportunity. In fact, an effective space processing experiment program will require a logical iterative sequence of flight experiments. A true evaluation of some processes may require a series of flight experiments in which one parameter at a time is varied. Considering this and the very large number of materials that must be evaluated, it appears that a space processing payload could be effectively utilized on nearly every flight.

In light of the mission model and the desire to maximize the number of SPA flight opportunities, six Shuttle System accommodation mission mode types are summarized in Figure 7. Of the six modes listed, Spacelab-dedicated, Spacelab-shared and automated modes appear to represent the concepts that will require major anticipatory payload planning and will afford maximum SPA flight opportunities within the mission model.

To undertake this many flight opportunities and to utilize fully the Space Shuttle's payload capability will require an inventory of payloads designed to match the capacities and restrictions imposed by each type of mission. In order to accomplish the above objectives, an inventory of payload equipment has been defined which can be combined to form complements of payloads. Specific details are outlined in the following sections.

Equipment Inventory

An initial listing of equipment items was derived as a result of an analysis of generic classes of representative Space Processing experiments. Subsequently, review and updating of the equipment inventory has and is expected to be a continuing effort due to the development of the experimental areas within the international technical community. It is to be emphasized that a continuing active participation of the technical community with regard to the equipment functions will control the prolificacy of the experimental program to a great degree. Use of this preplanned complement of apparatus will occasionally be supplemented by individual, experiment-

unique fixtures supplied by the investigator to further enhance the equipment utility.

Equipment Functional Specifications

A summary of this inventory of equipment is presented in the attachment. Expanding upon the summary data of the attachment has been the preparation of Equipment Functional Specifications. The equipment functional specifications which have been drafted serve as a starting point in the quantification of the equipment and instrumentation. They provide both a reference baseline description and the basis for record keeping. The initial specification performance requirements, design approach and descriptions must be treated as tentative at this time and will require updating as further definition progresses. It is essential to document this continuous learning process.

Three major sections of each Equipment Functional Specification were prepared:

> Anticipated Usage. This is a narrative functional description of application(s) in which the apparatus is to be used. This description may be applicable to several experimental activities and relates to the functional requirements derived from an examination of the generic SPA experiment classes in various R&D categories.
>
> Functional Requirements/Rationale. This is an explicit functional description of the apparatus under consideration. Particular descriptive content may include control functions, data output, power input, interface requirements and safety considerations.
>
> Specifications/Criteria. Where applicable and available, quantitative and qualitative information is included such as temperature ranges of interest, required accuracy of performance/control/measurement.

The collection of these functional specifications are planned to ultimately result in the issuance of an "Experimenter's Handbook" which in conjunction with other activities would assist the Principal Investigators in the planning and execution of their experimental programs.

The next issues at hand require that the equipment inventory be capable of being formed into payload configurations, which must be consistent with both the experimental objectives and the host-vehicle's accommodation modes. Additional issues have been examined and concepts have been developed for this to occur.

Mission Planning

Illustrating another important aspect of the payload accommodation requirement is the necessity of identifying and planning the range of values of interface requirements between the host-vehicle and payload equipment. Since the SPA discipline's objectives require a need to respond to ever-changing equipment complements as both experimental objectives and mission opportunities evolve, an initial system has been established to conveniently allow numerous permutations of experiments and apparatus groupings to be characterized.

For each mission mode selected, overall layouts must be prepared which illustrate the payload equipment/host vehicle accommodation. Due to the enormous number of distinct combinations of experiments that may be performed in the various anticipated mission modes, a detailed analysis of the data requirements involved in each case is mandatory. By using the results of this program in the planning of the experiment timelines, better usage of the facilities available may be made.

After developing this plethora of data, a means must be found by which an effective display may be prepared. A successful method of doing this has been found and involves the computer generation of three-dimensional bar graphs.

A TRW Systems computer program named BG3D makes a graphical display of a set of positive numerical values that are assigned to the separate grid squares of a rectangular grid. This procedure provides a highly effective method of visualizing a vast set of data - much better than by reading a matrix. By using the BG3D program and also by making use of some two-dimensional displays, a comprehensive study may be made of the many data requirements. Those singled out and analyzed initially are power, energy, weight and volume. Others will be completed later, such as heat rejection, source power requirements, electromagnetic compatibility and data management.

Several files must be established from which data may be drawn in order to initiate the plots. These are:

o Equipment Files

For each piece of equipment in the SPA inventory a separate data record is established which includes weight, volume and power profile. If the equipment has both a sustained and peak power level, both are specified.

o Experiment Files

For each experiment to be performed a separate data record is established which includes a list of each piece of equipment used and its start-up and shut-down times.

o Mission Files

For each mission considered, a separate data record is established which includes the experiments being performed and their start times.

Illustrating a power profile display for twelve (12) SPA experiments is the BG3D presentation shown in Figure 8.

INTEGRATION & INTERFACES

There are other aspects which are required in anticipating the payload designs and which compliment the concepts described in the prior paragraphs. The issues of not "what", but "how" must be addressed through early systems engineering and subsystems design analysis in order to

ascertain the technical viability of the concepts. The major interfaces to the payload equipment that must be considered in these analyses are shown in Figure 9. Some of the main issues are summarized below.

Engineering Analysis of Modular Payload

Subsystem interface analysis was performed to establish the integrity of the modular approach to the equipment design and integration. Salient areas that were selected for analysis were power and power conditioning, heat rejection and electromagnetic capability (EMC).

Power and Power Conditioning

Earlier studies indicated that virtually all equipment requires special conditioning of the input power (high volt, low volt, regulation, etc). An examination of the input power available from the Spacelab indicated a possible mismatch in special equipment requirements for a majority of cases (including commercial equipment). Maximum flexibility in integrating subelements into the Spacelab is achieved if the power conditioners are not centralized, but are part of the equipment.

Based upon these conclusions, and in close correlation with the thermal and other aspects of payload design, efforts were directed at examining the power requirements that follow:

Power-Load Requirements

The number of possible SPA experiments are diverse. For the purpose of narrowing the scope of this study, the equipment and load profiles for twelve representative experiments were identified. These twelve SPA experiments are listed in Table II. Throughout this paper, the twelve experiments will be identified by the numbers one through twelve. Two of the twelve experiments were chosen as being representative of the group and are described in greater detail to illustrate the evaluations used in the analysis. They are Experiment #1, Metallurgical-Furnace, Encapsulated Immiscible Combination, and Experiment #8, Biology Applications-Continuous Flow Electrophoretic Separation of Proteins. The profiles of the power-source loads for these two representative experiments are presented in Figure 10.

Power Availability

The Shuttle Orbiter will provide electrical power from its three fuel cells in support of the Orbiter and the Spacelab operations. One of the three Shuttle Orbiter fuel cells is dedicated to the Spacelab electrical power requirements during normal Shuttle operation. This power supplies the Spacelab subsystems and the excess is available to the payload. The current Spacelab subsystem requirements result in a payload allocation of 4.0 to 4.8 KW average (24 hour/day) and 9.0 KW peak for 15 minutes.

TABLE II

SPA EXPERIMENT IDENTIFICATION

1. METALLURGICAL-FURNACE
   ENCAPSULATED IMMISCIBLE COMBINATION
2. METALLURGICAL-LEVITATION
   PREPARATION OF PURE ALLOYS-CONTAINERLESS MELTING
3. CRYSTAL GROWTH-FURNACE
   MOLTEN ZONE CRYSTAL GROWTH
4. CRYSTAL GROWTH - LEVITATION
   CRYSTAL GROWTH BY PULLING FROM CONTAINERLESS MELT
5. GLASS TECHNOLOGY-FURNACE
   PREPARATION OF MULTIPHASE, SILICATE BASED GLASS
6. GLASS TECHNOLOGY-LEVITATION
   CONTAINERLESS PREPARATION OF La_2O_3 BASED GLASS
7. BIOLOGY APPLICATIONS-STATIONARY COLUMN
   ELECTROPHORETIC SEPARATION OF PROTEINS
8. BIOLOGY APPLICATIONS-CONTINUOUS FLOW
   ELECTROPHORETIC SEPARATION OF PROTEINS
9. PHYSICAL PROCESSES IN FLUIDS-LEVITATION
   CONTAINERLESS POSITION CONTROL OF LIQUIDS BY ELECTRO-MAGNETICS
10. PHYSICAL PROCESSES IN FLUIDS-GENERAL
    THERMAL GRADIENT CONVECTION IN LIQUIDS
11. CHEMICAL PROCESSES-LEVITATION
    CHAIN REACTIONS AFFECTED BY CONVECTION
12. CHEMICAL PROCESSES-GENERAL
    RADICAL LIFETIMES

Additional power sources must be provided to fulfill electrical power requirements that exceed the allocation of electrical power from the Orbiter. The power sources considered were supplemental and/or peaking battery kits and the use of a Power-Heat Rejection Kit. This Kit will contain up to two Shuttle-type fuel cells and the necessary plumbing, controls, reactants and tankage to satisfy the SPA experiment requirements. The Power-Heat Rejection Kit would provide up to 14 KW of continuous power and peaks of up to 24 KW for 15 minutes.

The use of the experiment payload allocation from the Orbiter and the Power-Heat Rejection Kit will provide electrical power to the SPA experiments of from 4.0 to 18.8 KW continuously and peaks of up to 33 KW for 15 minutes.

For the purpose of assessing the capability of the electrical power allocations to satisfy the SPA experiment requirements, Figures 11 and 12 summarize the sustaining and peak experiment electrical power requirements at the source for each of the 12 identified experiments. These were used to provide a comparison with the power allocations from the Spacelab and the Power-Heat Rejection Kit which is shown in Figure 13. These figures also compare the average and peak electrical power capabilities of one and two fuel cell systems.

Power Conditioning-Distribution

The electrical power conditioning and distribution subsystem must distribute power to the experimental equipment from the power source, in a safe, efficient manner. A number of concepts were considered and compared relative to:

1) Impact on subelement payloads
2) Impact on host vehicle (Spacelab)
3) Modularity/flexibility
4) Efficiency, weight and size
5) Safety
6) Electromagnetic Compatibility (EMC)

This comparison resulted in the following recommendations: A 115 VAC-400 Hz, single-phase system for the low power experiment bus, and a 115 VAC-1600/1800 Hz, 3-phase, 4-wire system for the high power experiment bus. A block diagram showing the power distribution system is shown in Figure 14. Power conversion from 28 VDC to 400 Hz and 1800 Hz AC is accomplished by static DC to AC inverters, which are frequency and phase synchronized to prevent dynamic interactions and system instability. The inverters are self-protecting for overvoltage on input and overload and short circuit on output. Further consideration will be given to the modularization of both the input and output junction boxes into several separate modules so that in case of a major fault some bus protection will be provided by the physical separation of the switching elements.

Of course, throughout this activity a continuous trade study of power conditioning and distribution equipment efficiencies on the thermal control requirements was made. Several thermal interfaces between the electrical power and thermal control subsystems were evaluated. The primary interface is the dissipation of all electrical energy consumed by the experiments, i.e., the energy under the experiment power source profiles must be dissipated by the thermal control subsystem. The dissipation of this energy requires additional electrical energy for operation of the thermal control equipment resulting in an increase in electrical energy that must be dissipated. Other thermal interfaces considered were the dissipation of heat from the fuel cells and the resultant by-product (water) produced by the fuel cells for potential use by the thermal control subsystem. Based upon the experiment load requirements and assuming the use of the Power-Heat Rejection Kit, a thermal control pump system electrical power requirement of 470 watts continuous was determined to satisfy the thermal control subsystem requirements.

Thermal Performance Requirements

The thermal interface analysis was addressed in the following way:

Identification of Waste Heat Requirements:

The thermal control subsystem provides the required thermal protection to maintain all subsystems within thermal limits for all mission phases for the experimental equipment. Waste heat dissipation timelines were developed for the equipment selected in the subelements. The timelines were necessary to establish magnitude and duration of peak loads. Items of equipment that have waste heat requirements were separated into two groups: (1) those that can be met by the Spacelab capability, and (2) those items that require supplemental capability.

Identification of Special Interface Problems:

In addition to the amount of heat, some items of equipment were identified that have specific temperature requirements such as component touch or condensation temperature limits.

Thermal Control Cooling Concepts:

For the purpose of assessing the magnitude of the thermal control problem, three different thermal control system concepts were investigated to determine their capability to provide the necessary thermal control. Although the assessment was of a preliminary nature, the concept analyses did indicate a number of areas where modifications to SPA timelines and/or equipment would be necessary.

The air cooling system concept depends upon the Spacelab supplied air flow for cooling of rack mounted electronic equipment. In the analysis of this concept, a simplified thermal model of a typical cabin thermal control system and the SPA air cooling loop were generated, based upon the studies conducted at MSFC on the Sortie Lab. Based on the analyses to date, it appears that air cooling is feasible providing the

necessary P/UA* can be provided on the commercial equipment.

The liquid cooling system is similar to the air cooling concept except that the equipment mounting rails in the rack are cooled by coolant lines. A parametric analysis was conducted to assess the feasibility of using a water cooling loop with cold plate mounted electronics. The liquid cooling concept's feasibility depends, to a large extent, on the design of the liquid distribution system. A properly designed system must be capable of providing the required flow rate at a low enough pressure drop to result in a reasonable pump power requirement. A complete assessment of the coolant loop characteristics would require a detailed thermal analysis for a specific configuration, however, it appears that a liquid cooling loop would be feasible.

A heat pipe system employed as a cooling concept for Spacelab was also investigated. Such a system would provide the capability of a thermal energy transport without an attendant expenditure of power for an electromotive device (fans, pumps, etc.). It was determined that the heat transport requirements on the heat pipe system that results from a typical rack power dissipation distribution are too severe. The number of pipes required were considered impractical in relation to air or pumped liquid cooling. Heat pipes can be used, however, for dumping heat from the various components into the air ducts.

Thermal Control Subsystem of Power/Heat Rejection Kit:

The Power/Heat Rejection Kit (PHRK) thermal control subsystem (TCS) consists of a pumped liquid loop which rejects thermal energy to space via a thermal radiator located on the exterior of the PHRK structure. The system is a liquid loop using two radiators to reject the thermal energy absorbed from the fuel cells, electronic equipment and furnaces. The primary radiator is a high temperature radiator for high heat rejection and the secondary radiator is to provide temperature drop in approximately ten percent of the flow for cooling room-temperature operating, electronic equipment. A thermal capacitor is included in the system downstream of the primary radiator to store the thermal energy that exceeds radiator capacity until such a time as the thermal load falls within radiator capability.

---

*P = Component Power

UA = Effective Thermal Conductance From Component to Coolant

Figure 15 shows the PHRK heat dissipation system for those missions where the kit is in support of SPA payloads within the Spacelab. The heat rejection subsystem was baselined on a 7 ft. body mounted radiator length. The useable experiment duty cycle was then defined for this system versus the average experiment power involved. Subsequently, study of the heat rejection system designs required to operate at 7 kW and 14 kW electrical steady-state has been initiated. At the fuel cell sources, the previous electrical values reflect a steady-state heat rejection problem of 11.3 kW and 22.3 kW respectively. The steady-state approach to defining the use of a supplemental power and rejection kit represents an extreme usage limit. On the other hand, examination of possible duty cycle usages based upon average experiment power illustrates usage options with this approach. While the SPA experiment activities revolve around both power and energy availabilities, it can be conclusively shown that heat rejection will always pose the primary limitation in achieving the associated subsystem support. This is particularly true in light of the limitations affecting the thermal subsystem design of radiator size, fuel cell temperatures and use of capacitors.

Electromagnetic Compatibility

A similar activity was performed for the analysis of the electromagnetic compatibility (EMC) interface. Historically, EMC has been approached by testing engineering models per a military specification. In contrast, modeled payload analysis could be used to predict, characterize and provide trade solutions in the design activity. Most of the data required for detailed EMC study was not readily available. A beginning was necessary for two important reasons: one is that the problem area had to be opened up to establish the approach to EMC control, the other was that in order to exploit every mission opportunity, SPA payloads must be capable of operating in close proximity to almost any other experiment. An EMC evaluation of commercial equipment was one of the most important things to emerge from this effort, since commercial equipment of the kind envisioned by SPA had not considered EMC in the broad sense as necessary with space systems. This showed up in component design, component assembly techniques, and lack of measured or analytical EMC data. The EMC problem is further aggravated by the high currents and voltages required by SPA. The initial efforts have been aimed at various levels of categorization of the payloads and interfacing equipment and at the establishment of initial estimates for the EMC environment for the representative payload configurations. A test program was started to measure some of the pertinent EMC characteristics of R&D prototypes of equipment similar to that under consideration as potential SPA payloads.

One of the most prominent sources of steady-state radiated interference among the SPA candidate payloads is the induction heater. The induction heater's radiated interference can be expected to be a major consideration for the design of the Spacelab data handling and communication equipment.

Figure 16 illustrates the levels of magnetic field radiation measured at a 1 meter distance from one of the two induction heaters tested.

Performance of an Analysis Regarding the Subject of Commercial Equipment Utility

An initial review of numerous payload equipment items showed that the functional requirements required of most of the apparatus are available from commercial sources. While the functional aspects are satisfied, other required usage factors that needed to be considered included outgassing or flammability of the materials, packaging and material substitution options, power conditioning, EMC and heat transfer. The ultimate host vehicle criteria imposed will profoundly influence the amount of modification necessary item by item, however, the commercial equipment design technology base remains the primary source of apparatus development. Even though, at the outset, the use of commercial equipment appeared potentially promising, a number of usage factors remained to be resolved. Specific factors that were examined included the following:

- Safety
- Packaging
- Structural
- Power Conditioning
- Thermal Control
- Materials of Construction

The list of commercial utility aspects were broken into three categories. The first category included the areas of packaging, structure, power conditioning and thermal. This group was concerned with questions related to the operational characteristics of the individual equipment item. In this sense judgements and assessments concerning the utility of a commercial piece of gear could be made, to a reasonable extent, by considering several typical equipment items. By example, the operational characteristics of a tube furnace produced by any one of several manufacturers could be used to assess such factors as the thermal, power and structural impacts upon the SPA payload. Certain aspects of the materials of construction such as the susceptibility to contamination deposits or shatterability also fall into this category.

In contrast, the second major category concerned questions relating to materials of construction, such as outgassing and flammability, which are to a much greater degree subject to variations from one manufacturer to another. These questions, in most cases, had to be considered on an individual item basis with respect to each specific equipment item and each specific manufacturer.

The third category was concerned with questions of safety. When an issue within the first two categories presented a potentially hazardous situation which had to be readily accepted, the problem was treated from the point of view of safety. Thus, where high voltage equipment was

considered necessary for performance of SPA missions requirements, suitable steps were determined to be required to assure crew and vehicle safety.

Specific equipment items analyzed were selected from the equipment inventory list using the following criteria:

- o The equipment was representative of a type important to the success of future SPA missions
- o Possible problem areas existed for Spacelab utilization
- o Data availability

A number of specific items were selected for a detailed assessment. These items are as follows: Gas Chromatograph, Continuous Flow Electrophoresis Column, PH Monitor, Freezer/Refrigerator, Data Acquisition System, Chest-General Purpose Enclosure, Hot Wall Furnace, Zone Refiner, Dye Laser/Flash Lamp, High Voltage Power Conditioner, IR Pyrometer, Temperature Controller and Programmer. Because an officially approved NASA specification for equipment and material utilization in the Spacelab did not exist, a set of study criteria, drawn largely from existing NASA documents, were collected for use in bench-marking the utility assessment.

Any assessment of commercial utility considerations must be, in many instances, closely associated with a subsystem interface analysis activity. Coordination of the commercial utility assessment and the interface trade studies was thus required to optimize the information and results of the two efforts. Whenever possible, ongoing equipment considerations and interface studies[3] considered the same equipment items.

CONCLUSIONS

The basic approach to establishing SPA payloads is predicated upon the formulation of pregrouped modular subelements of equipment. A preplanned inventory of equipment, when coupled with modular integration concepts with an ability to readily reconfigure, can then serve the ongoing research needs of a world-wide group of investigators. As such, the typical flow of events expected are identified in Figure 17. The following overriding highlights summarize the SPA payload equipment requirements:

1) A multifacet/evolutionary program must be anticipated in space processing, spanning many years and numerous missions.

2) A comprehensive complement of equipment is required to support the projected ranges of R&D activities.

3) Grouping of equipment to form several self-contained payload subelements allows support of specific experimental classes either alone or in conjunction with each other.

4) Modular subelement approaches allow the R&D technical program to range from austere to comprehensive in modular increments.

5) It is essential to take advantage of every Shuttle flight opportunity and mandatory to have a continuous rematch of scientific interests, instrument capabilities and mission requirements.

6) It is necessary and desirable to derive the space processing equipment from within an existing multibillion dollar commercial technology industry, wherever possible.

Shuttle-supported space endeavors are visualized as portending a new era of equipment and capability development - an era in which the means and the methods used in prior times will be vastly modified through use of this new capability. Implementation of Shuttle-supported experimentation will certainly involve the continued identification and refinement of the methods. It is expected that the in-space activity will be largely concerned with development of experiment technique and equipment optimization, particularly in endeavors which are supported by shared-sortie payload concepts. Hand in hand with Shuttle system versatilities must be an associated implementation of simpler user interfaces.

The use of commercial equipment source derivations for many of the contemplated space activities provides not only for familiar user equipment interfaces, but reinforces the opportunity of achieving selective cost effectiveness through development of space payload equipment via a resource which to date has not been possible.

Many factors will undoubtedly impact the support available for establishing future space processing endeavors. Whatever these resources may be, it is expected that the process of learning how to use the Shuttle System and exploiting the evolution of Space Processing to be an active process for many years.

REFERENCES

1. Final Report of the Space Shuttle Payload Planning Working Groups - Vol. 9, "Materials Processing and Space Manufacturing", May 1973.

2. R. L. Hammel, "Use of Shuttle for Test of Experimental Hardware in Space". Presented AAAS-72 Annual Meeting, Washington, D.C.

3. Requirements and Concepts for Materials Science and Manufacturing in Space Payload Equipment Study. Vols. I, II and III. DCN No. 1-2-21-00172. S2, July 1973.

4. The October 1973 Space Shuttle Traffic Model, NASA/MSFC TMX-64751, January 1974.

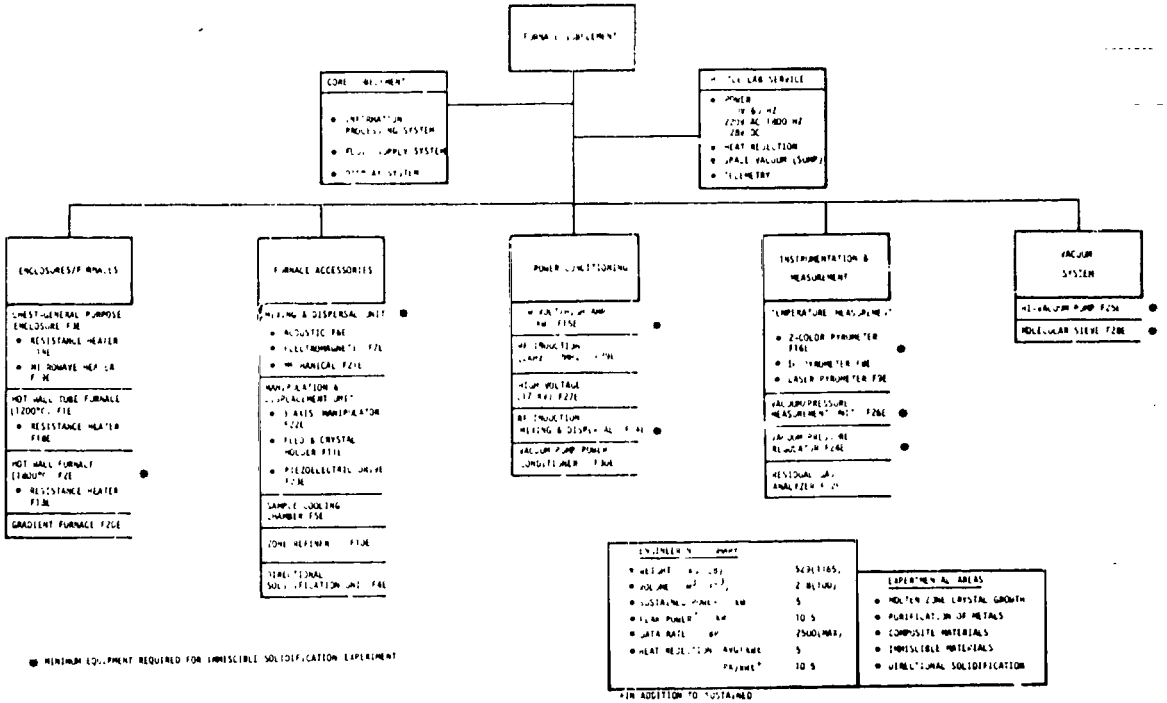

FIGURE 1. FURNACE SUBELEMENT ORGANIZATION OF EQUIPMENT.

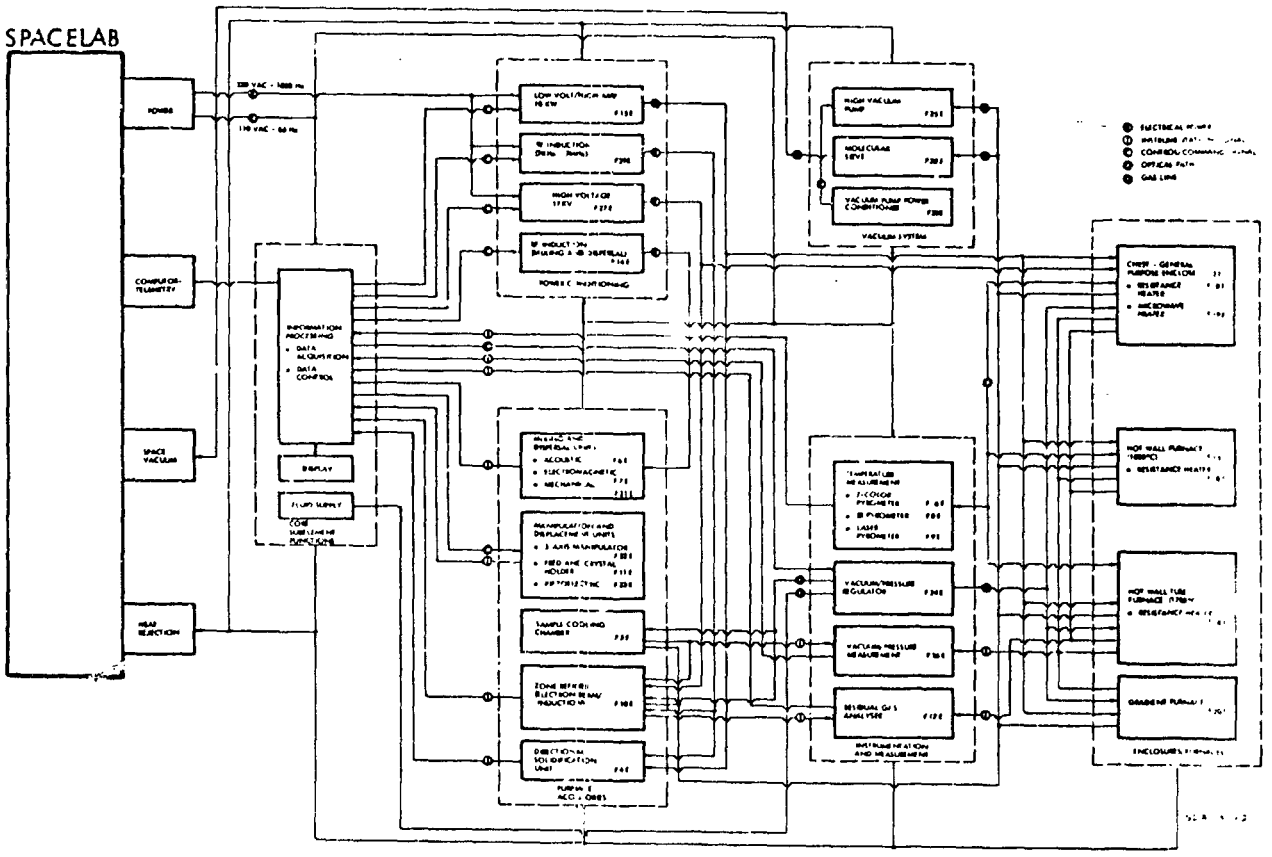

FIGURE 2. FURNACE SUBELEMENT INTERFACES.

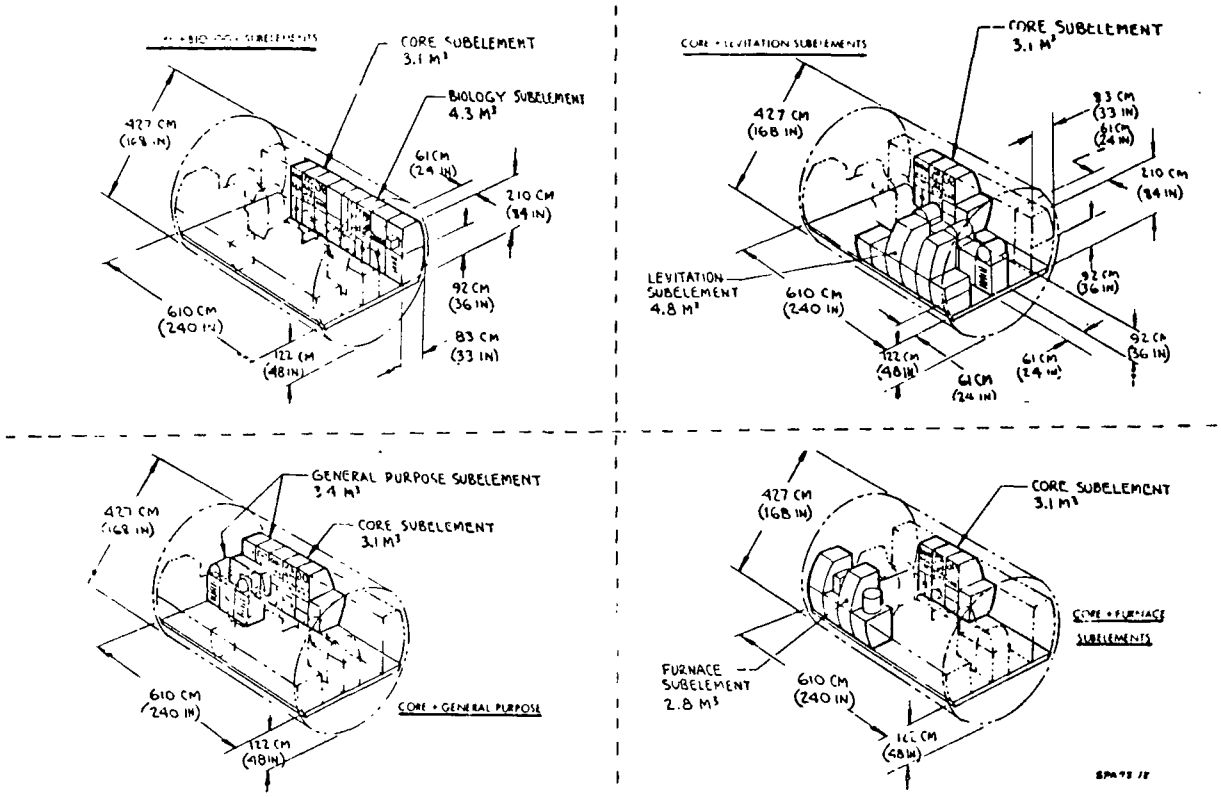

FIGURE 3. SPA PAYLOAD CONFIGURATION - SINGLE FLOOR - TWO AISLE CONCEPT.

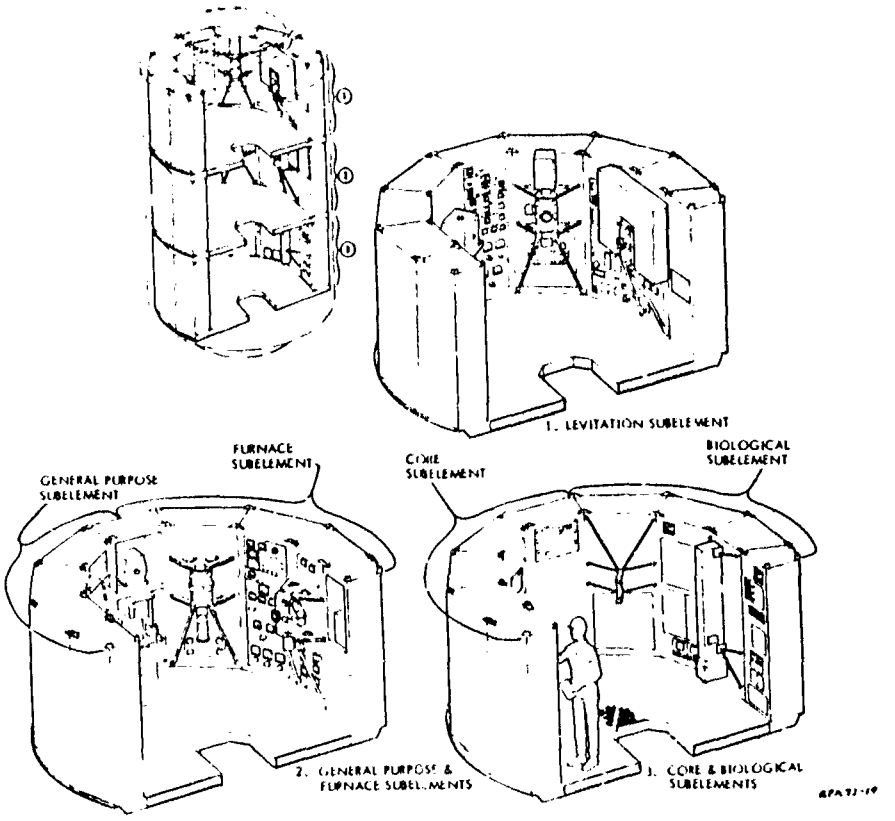

FIGURE 4. SPA PAYLOAD CONFIGURATION - SPACELAB ARCH CONCEPT.

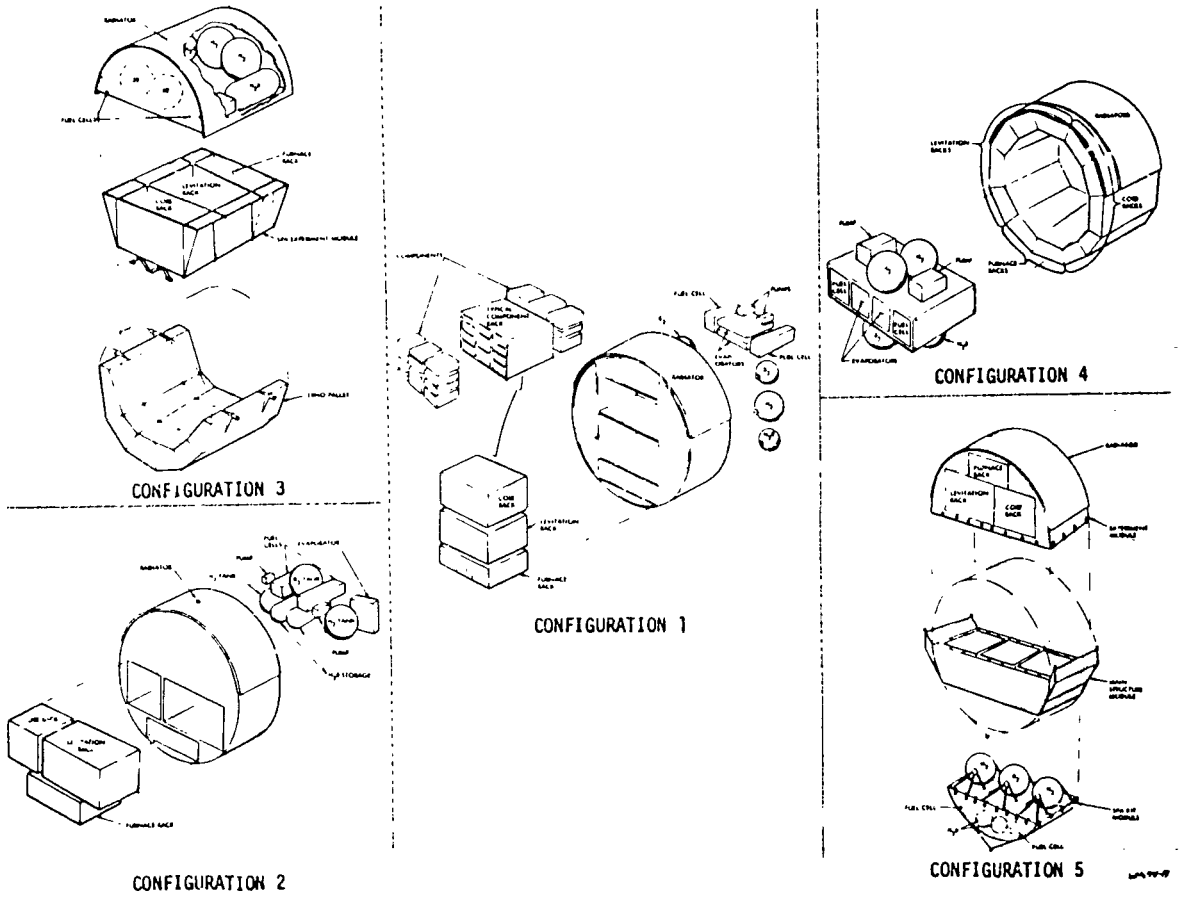

FIGURE 5. CONFIGURATION CONCEPTS FOR SPA POWER/ HEAT REJECTION KIT AND EXPERIMENT EQUIPMENT MODULE.

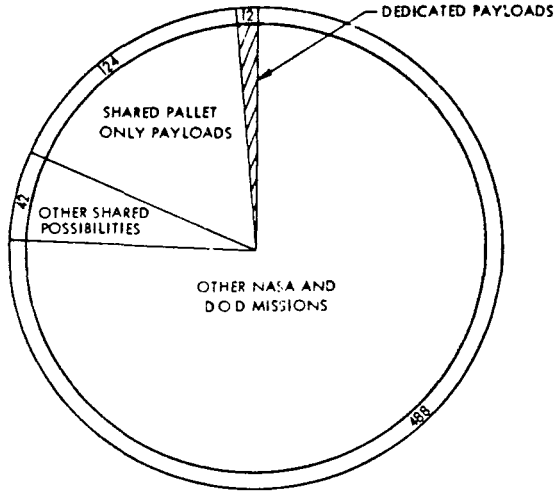

SPA PAYLOAD CATEGORY \ CY	80	81	82	83	84	85	86	87	88	89	90	91	TOTAL SPA PAYLOADS
SPA DEDICATED SPACELAB SORTIE FLIGHTS	1	1	1	1	1	1	1	1	1	1	1	1	12
SPA SHARED MISSIONS PALLET ONLY FLIGHTS	0	4	12	12	12	12	12	12	12	12	12	12	124
TOTAL ASSIGNED SPA PAYLOADS ON SHUTTLE/SPACELAB FLIGHTS	1	5	13	13	13	13	13	13	13	13	13	13	136
SPACE AVAILABLE FLIGHTS WHERE SPA PAYLOADS COULD BE ACCOMMODATED*	2	6	0	2	7	7	2	7	3	1	3	2	42
TOTAL SPA PAYLOAD FLIGHT OPPORTUNITIES	3	11	13	15	20	20	15	20	16	14	16	15	178

SPA 74 - 81

*CRITERIA FOR SELECTING "SPACE AVAILABLE FLIGHTS WHERE SPA PAYLOADS COULD BE ACCOMMODATED":

1) TEN FEET OF RUNNING LENGTH IS AVAILABLE IN SHUTTLE CARGO BAY.
2) SHUTTLE PAYLOAD UP WEIGHT DOES NOT PRESENTLY EXCEED 53,000 LBS.
3) SHUTTLE PAYLOAD LANDING WEIGHT DOES NOT PRESENTLY EXCEED 23,000 LBS.

FIGURE 6. SUMMARY OF PLANNED AND POTENTIAL SPA SPACE MISSIONS FROM 1980 THROUGH 1991

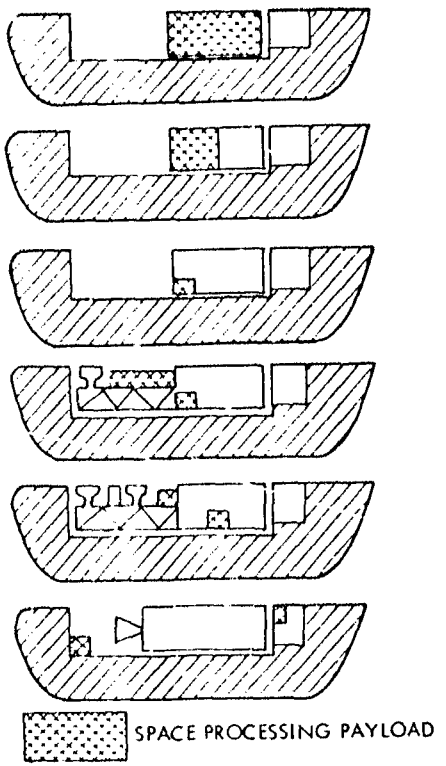

1. DEDICATED SPACELAB MISSION
2. SHARED SPACELAB MISSION
3. MINIMUM IMPACT CARRY-ON (LIKE APOLLO FLYBACK)
4. SHARED AUTOMATED PAYLOAD ATTACHED TO PALLET WITH NECESSARY CONTROL AND DISPLAY EQUIPMENT IN SPACELAB OR SHUTTLE
5. MINIMUM IMPACT CARRY-ON AUTOMATED PAYLOAD ATTACHED TO PALLET WITH NECESSARY CONTROL AND DISPLAY EQUIPMENT IN SPACELAB OR SHUTTLE
6. MINIMUM IMPACT CARRY-ON AUTOMATED PAYLOAD LOCATED IN CARGO BAY WITH NECESSARY CONTROL AND DISPLAY EQUIPMENT IN SHUTTLE

SPACE PROCESSING PAYLOAD

*DELIVERY/RETRIEVAL OF AUTOMATED SATELLITES NOT INCLUDED

FIGURE 7. POTENTIAL MISSION MODES FOR ACCOMMODATING SPACE PROCESSING PAYLOADS*.

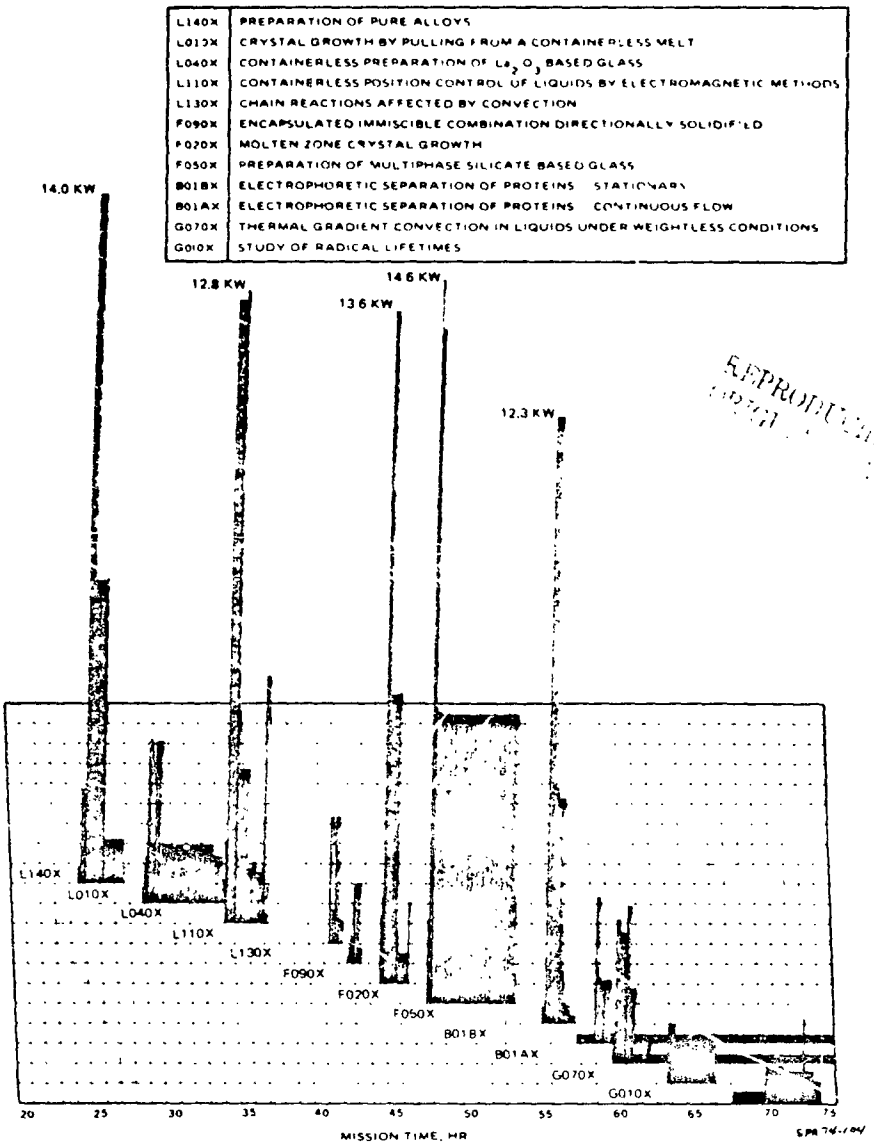

FIGURE 8. TYPICAL MISSION POWER PROFILE FOR TWELVE EXEMPLARY SPA EXPERIMENTS.

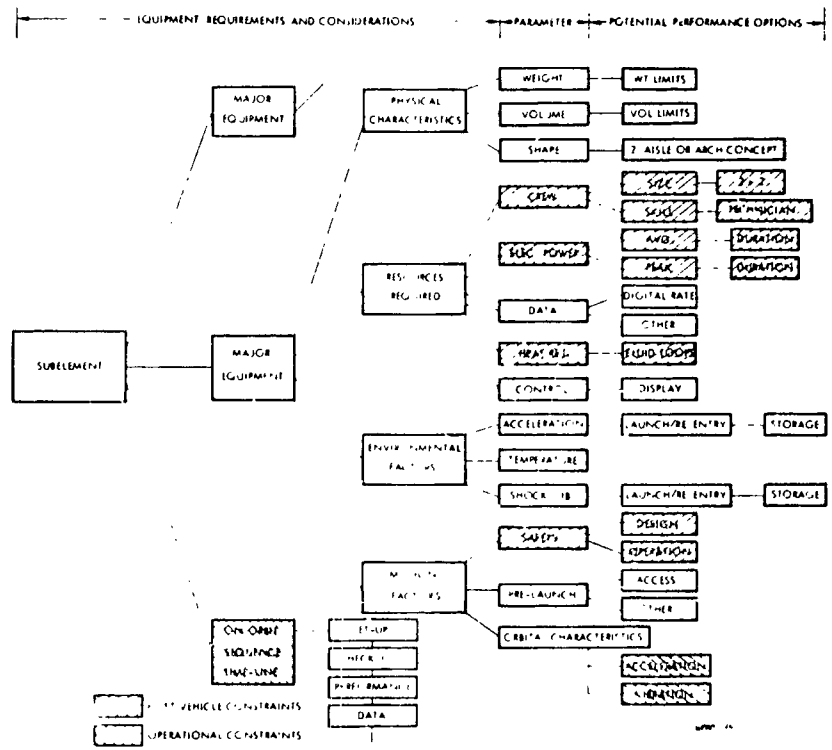

FIGURE 9. SPA EXPERIMENT MODULE/HOST VEHICLE INTERFACE CONSIDERATIONS.

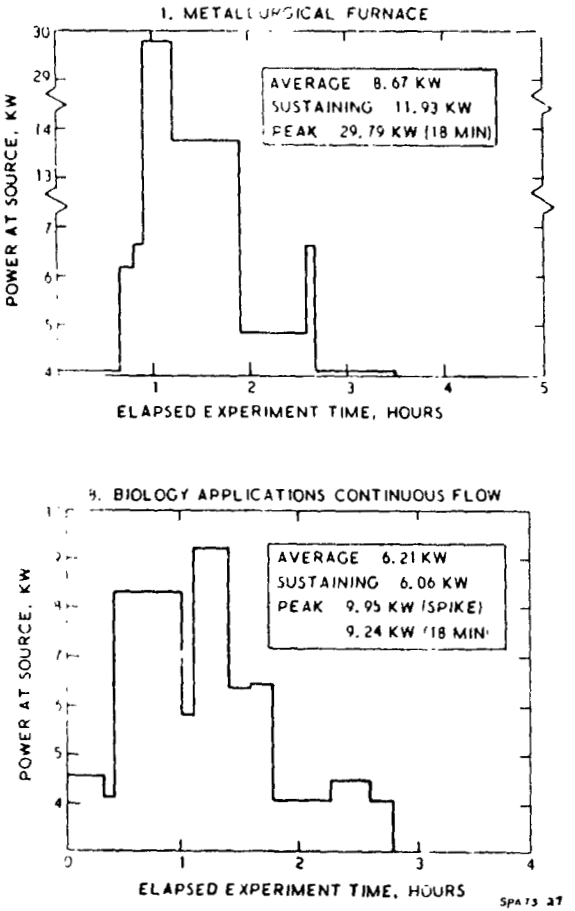

FIGURE 10. SPA EXPERIMENT POWER SOURCE LOAD PROFILES.

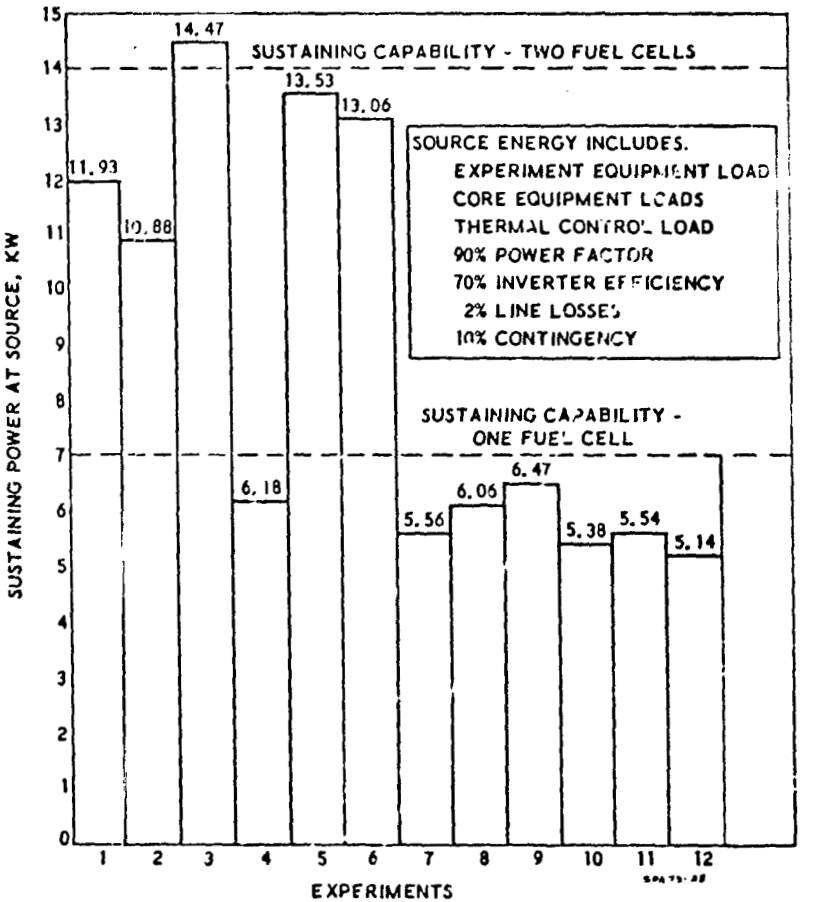

FIGURE 11. SUSTAINING EXPERIMENT POWER (AT POWER SOURCE).

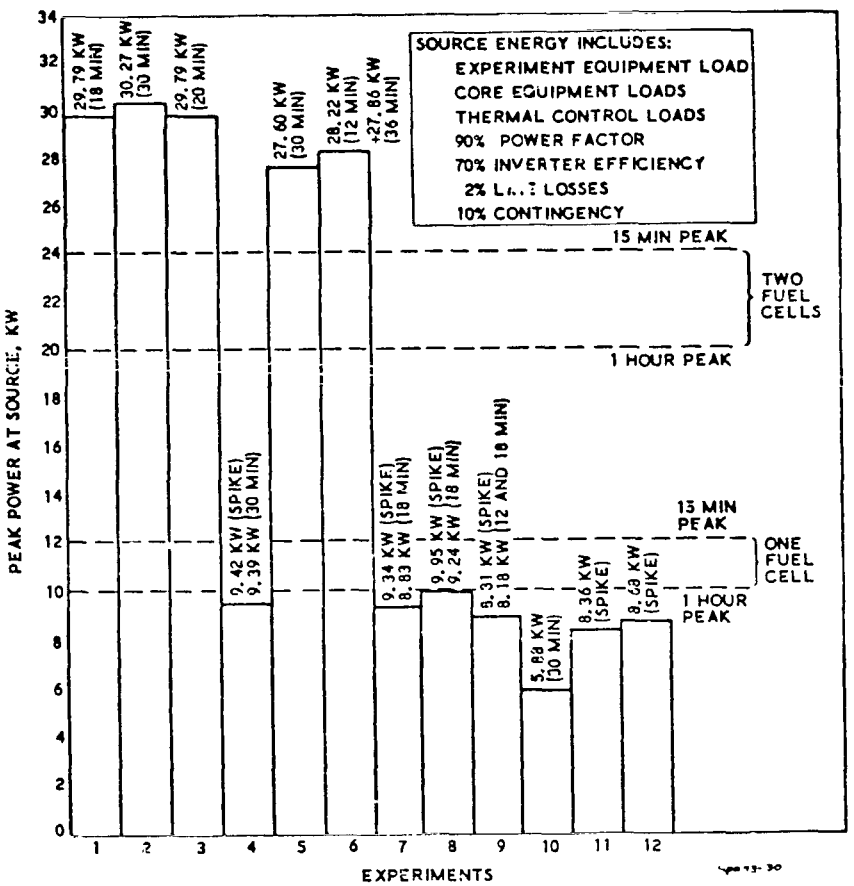

FIGURE 12. PEAK EXPERIMENT POWER (AT POWER SOURCE).

EXPERIMENT NO	EXPERIMENT NAME	POWER SOURCE CONCEPTS									
		1 SPACE LAB ALLOCATION ONLY[1]		2 POWER HEAT REJECTION KIT ONE FUEL CELL		3 SPACE LAB ALLOCATION PLUS POWER HEAT REJECTION KIT ONE FUEL CELL		4 POWER HEAT REJECTION KIT TWO FUEL CELLS		5 SPACE LAB ALLOCATION PLUS POWER HEAT REJECTION KIT TWO FUEL CELLS	
		AVERAGE 4 TO 4.5 KW	PEAK 9 KW	AVERAGE 7 KW	PEAK 12 KW[2]	AVERAGE 11 TO 11.5 KW	PEAK 21 KW	AVERAGE 14 KW	PEAK 24 KW	AVERAGE 10 TO 10.5 KW	PEAK 33 KW
1	METALLURGICAL - FURNACE							X		X	X
2	METALLURGICAL - LEVITATION					X		X		X	X
3	CRYSTAL GROWTH - FURNACE									X	X
4	CRYSTAL GROWTH - LEVITATION			X	X	X	X	X	X	X	X
5	GLASS TECHNOLOGY - FURNACE							X		X	X
6	GLASS TECHNOLOGY - LEVITATION							X		X	X
7	BIOLOGY APPLICATIONS - STATIONARY COLUMN		X	X	X	X	X	X	X	X	X
8	BIOLOGY APPLICATIONS - CONTINUOUS FLOW			X	X	X	X	X	X	X	X
9	PHYSICAL PROCESSES IN FLUIDS - LEVITATION		X	X	X	X	X	X	X	X	X
10	PHYSICAL PROCESSES IN FLUIDS - GENERAL		X	X	X	X	X	X	X	X	X
11	CHEMICAL PROCESSES - LEVITATION		X	X	X	X	X	X	X	X	X
12	CHEMICAL PROCESSES - GENERAL		X	X	X	X	X	X	X	X	X

NOTE
1. SPACELAB, SUBSYSTEM SPECIFICATION, ISSUE 1, REVISION 2, ESRO, 1973 OCTOBER 15.
2. FUEL CELL POWERPLANT, PROCURELIENT SPECIFICATION, MC404-0115, SPACE DIVISION, NAR, 1973 MAY 16.
3. PEAK POWER CAPABILITY IS 12 KW for 15 MIN AND 10 KW FOR ONE HOUR PER FUEL CELL.

X-INDICATES THAT THE ALLOCATION CONCEPTS AVERAGE OR PEAK POWER CAPABILITIES SATISFY THE SUSTAINING PEAK POWER REQUIREMENTS, RESPECTIVELY, OF THE EXPERIMENT.

FIGURE 13. SPA EXPERIMENT POWER SOURCE ACCOMMODATION.

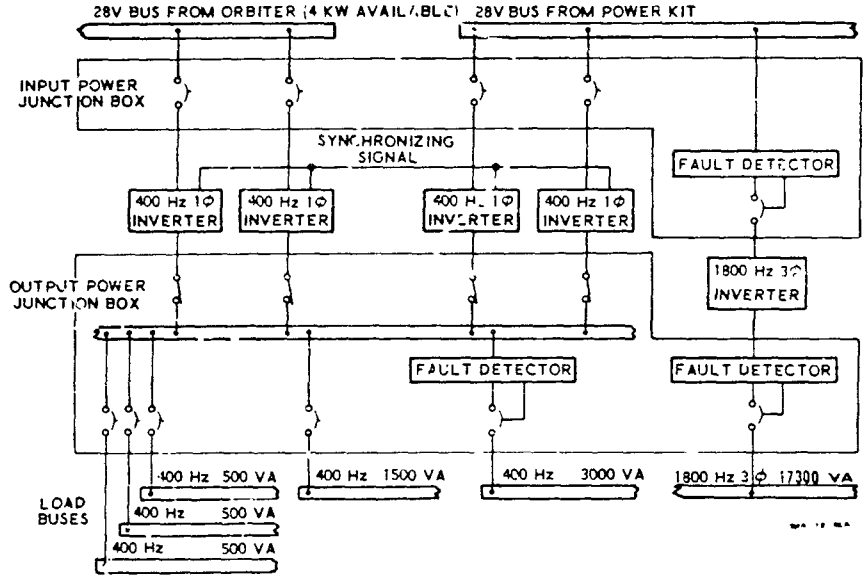

FIGURE 14. SPACE LAB POWER DISTRIBUTION.

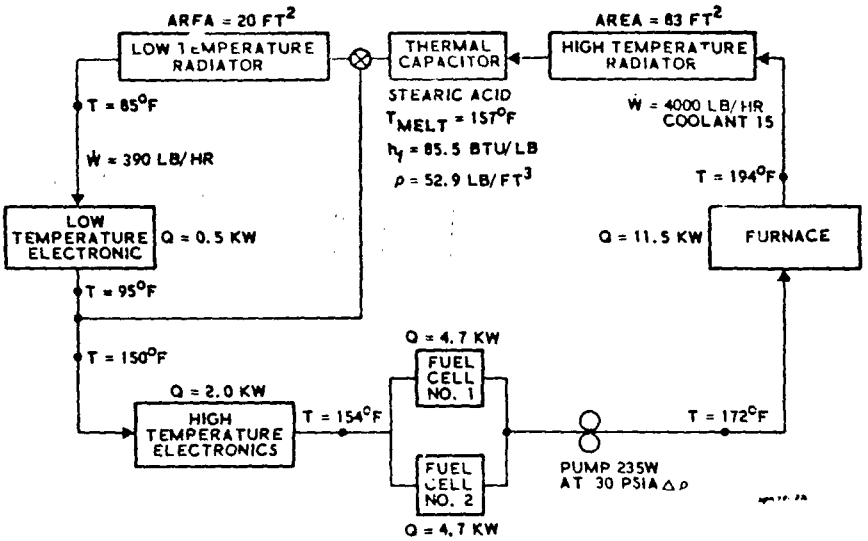

FIGURE 15. POWER/HEAT REJECTION KIT HEAT DISSIPATION SYSTEM.

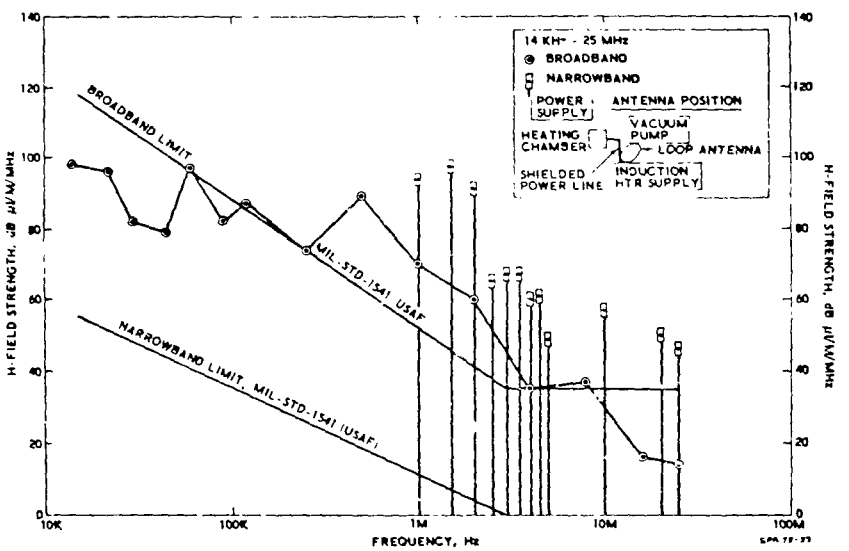

FIGURE 16. HELMHOLTZ TYPE ELECTRON BEAM POWER SUPPLY (H-FIELD NARROWBAND AND BROADBAND RADIATED EMISSIONS, INDUCTION HTR 2).

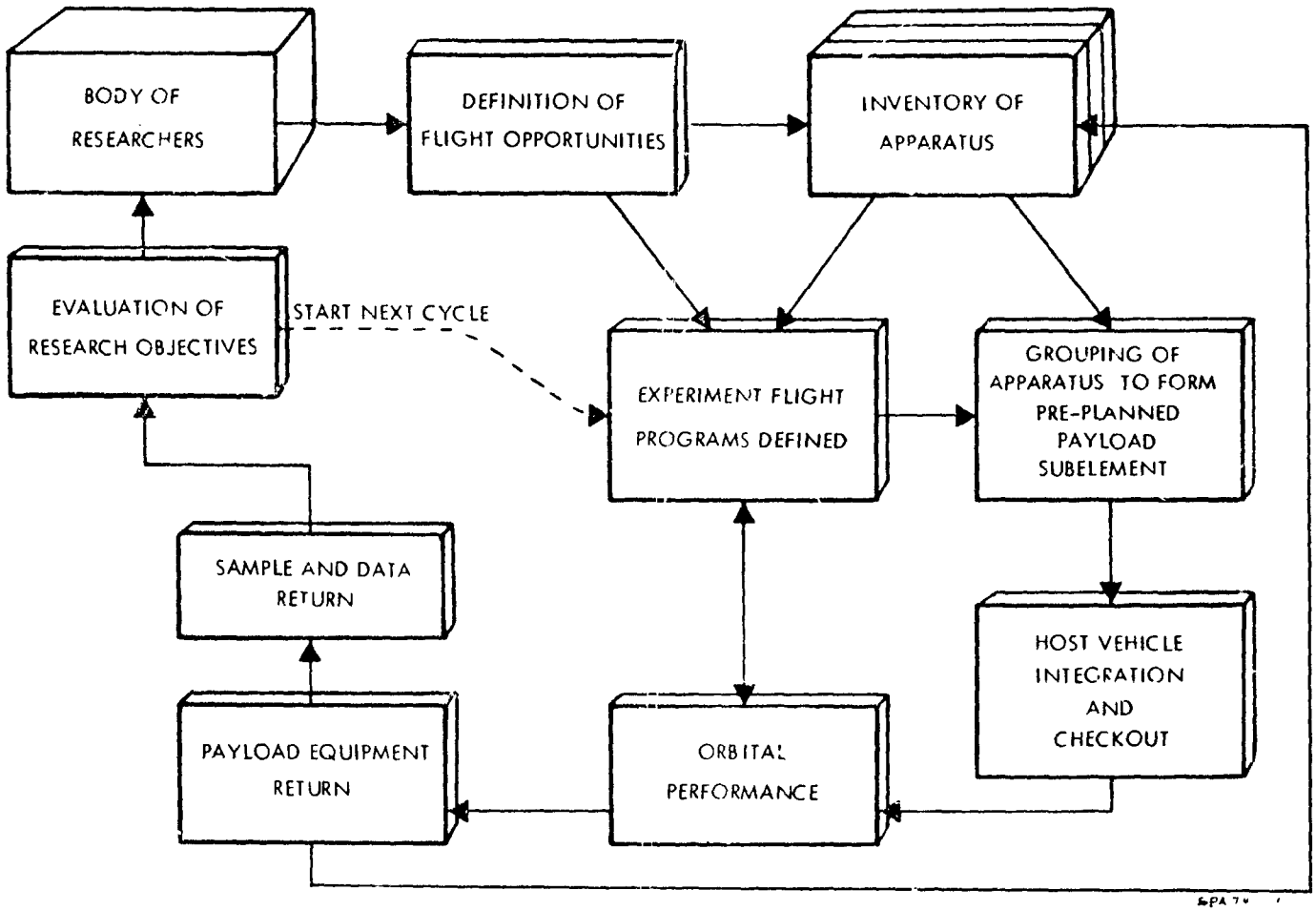

FIGURE 17. ILLUSTRATIVE FLOW OF EVENTS.

Space Processing Experiments on Sounding Rockets

N74 29907

by

Hans F. Wuenscher
Marshall Space Flight Center
Alabama 35812

Space Processing Experiments conducted on board the Command and Service Module during translunar flight and during the Skylab missions have shown a high rate of unexpected results. This indicates that all processing changes during the weightless environment, especially chain reaction type modifications of terrestrial processes, are presently not readily predictable by either the existing theoretical treatment or by terrestrial laboratory testing. In processes involving transitions through liquid and or gaseous phases, "the ever-present gravity plays a decisive but normally hidden role, and drastic lowering or elimination of g might yield unique changes in the achievable product. The unique advantage of orbital processing must be seen in the promotion of molecular forces from their negligible role in terrestrial manufacturing to leading process controlling factors, even in the largest bulk processes." (Ref. 1) The Skylab results show that essential process modifications can be caused by the very small changes in weightlessness. For instance Dr. Walters experiment M560 produced a steady decline in dislocations with the undisturbed progression of the solidification front. The major reason for this improvement seems to be that no container was restraining the expansion of the solidifying metal. Furthermore the absence of hydrostatic pressure (deadweight deflection) allowed the formation of optically flat facets. But one must consider that these effects come to pass only after the more readily visible actions of gravity, like sedimentation and convection are eliminated.

Another quite hidden effect of gravity came to light through Dr. Larsons analysis of the Sphere Melting Experiment M553. The triple point of metals is at such very low pressures, that on earth, the hydrostatic head in liquified metals is exceeding the critical pressure already at a couple of microns depth below the surface. Therefore even at high vacuum environment on earth, metals will only vaporize from the surface. In weightless environment, a drastic increase in vapor formation to the point removing a component completely from the alloy at a hoter area, and deposit it at some other place. This might be a contributing factor in the results of M552, Exothermic Brazing and M556,Vapor Growth.

Even the most sophisticated modifications of processes and equipment in order to compensate for the ever present earth gravitational action does not provide for assurance that true weightless environment has been properly simulated. Therefore, only experiments conducted in real weightless environment can validate scientific and engineering projections and help to justify larger efforts towards payload developments for the space shuttle. There is only one more orbital mission scheduled between now and the early Space Shuttle flights. This is the ASTP mission (Apollo Soyuz Test Project) in 1975. Experiments, suitable for a multipurpose furnace type facility, as it was used during the Skylab missions, and some new experiments in the electrophoretic separation field, have been already selected.

In order to asses the chances for earthbound zero-g testing, we have to consider two things: first, what is weightless environment, and second, for how long must we produce it in order to achieve meaningful results.

First, weightlessness is achieved by the elimination of the gravitational action of the earth. The inherent gravitational action of the masses in the experiment and equipment on each other are not eliminated in weightlessness, but is negligibly small. What gravitation is, whether an electromagnetic radiation type action, which would have a finite velocity of propagation for action at a distance, or whether gravitation acts instantaneous on all masses in the universe, is not known. While the latter assumption of instantaneous action over thousands and more light years in distance cannot be explained by presently accepted theories, all practical gravitational calculations for space flight are carried out on this instantaneous basis by means of Newton's equation. Einstein himself admits, "Newton's law (of gravitation) still remains the basis of all astronomical calculations." (Ref. 2)

Besides all these not well understood situations, for the purpose of eliminating all forces caused by the gravitational action of the earth on a processing experiment, it is sufficient to provide for unrestrained motion, commonly called free fall.

The orbit of a spacecraft or any free coasting space craft is in unrestrained motion and produces weightlessness. From this well established fact, one can accept as well another explanation for gravitation in that sense, that it is nothing else but motion which is basically connected with the existence of atomic matter. Atoms appear to exert forces of attraction simply because they are moving inward in space simultaneously, each atom moving towards all others. There is no propagation of force, no action at a distance, no medium, no curved space, no way the effect could be screened off or modified by anything between the masses. Gravitation is a result of basic macroscopic motion. Atoms and Photons are results of basic microscopic motion. The idea of a universe of motion should not surprise anyone who is familiar with the history of science. Past investigators did not succeed in developing a useable theory, because they could not free themselves from the assumption that independent definitions of space and time, as are needed

in a universe of matter, are also a prerequisite for a universe of motion. D. B. Larson reached first the crucial conclusion that motion being nothing but the relation between space and time, also defines space and time. Motion produces space and time, and motion produces matter as a composite of space and time units. (Ref. 3) As strange as this all may sound at first, the "motion" concept can explain not only what gravity is but also what it does beyond the range covered by Newton's law. There is a "gravitational limit" which determines the distance of stars, the sizes of galaxies, and beyond this limit the recession of masses from each other. On the basis of pure theoretical deduction from just that one postulation of "Unit Motion" Larson published in 1955 that Quasars and Pulsars must exist. He also deducted from the same premises a workable liquid state theory, which was very useful in bringing a recent research project about solute diffusion to a clear conclusion. (Ref. 4) I am sorry that I was not able to give a shorter and better founded answer to the question about the nature of weightlessness.

To the second question asking for how long the weightless environment must be avilable in order to achieve useful results, let me start with the assessment of Drop Towers.

The MSFC Drop Tower provides for about 100 m free fall. It did not appear very promising that much could be learned in Space Processing during the 3.8 seconds of weightlessness available. Now we know better. Unique experiment results were achieved and even unexpected results surprised the experimentors, redirecting the conclusions drawn from theoretical and laboratory work.

For instance -

- o Slower cooling rates caused finer instead of coarser dispersion in immiscible or multiphase materials.
- o Liquid metal drop tests already showed vapor phase reactions, as later discovered on Skylab Experiment M553.
- o Liquid deployment concepts showed adverse effects, and also a electromagnetic positioning system which checked out in two dimensions in the laboratory, did not in three dimensions.

Nevertheless, many processing areas for which early verification of feasibility would be of great importance require longer weightlessness time in order to get through a meaningful increment of the critical processing phases.

The flexibility and repeatable low cost operation makes a drop tower an ideal research tool.

During the free fall in a drop tower, the experiment is in or orbit, which would cycle through the center of the earth - out to the other side of the globe and come back. All we would need is a tunnel all the way through. That tunnel is not there, therefore the experiment will impact the earth. After 33 seconds of free fall for instance the impact-velocity reaches already speed of sound.

Furthermore the air-resistance during the fall has to be over-come by pushing down requiring something like the jet engines of a fighter plane for just maintaining the required free fall velocity in air after 30 seconds.

We see drop towers are limited, the practical maximum seems to be at 300 m or 1000 ft drop, yielding close to 8 seconds of experiment time.

Drop facility for longer free fall duration should maintain vacuum in the upper half, in order to avoid the air resistance and contain air in the lower half for gentle deceleration and catching of the experiments. It is not possible to build such a facility, but this environment exists naturally on large scale only, by doing the free fall above the earth atmosphere, while during re-entry in the atmosphere, gentle deceleration occurs followed by parachute recovery. Nothing but the rocket fits this environment and can give us more zero-g.

Sounding rockets are already existing, which can provide with only minor adjustments an ideal cost effective zero-g-test bed.

The first two pictures show the launch of an Aerobee Sounding Rocket and the recovery of the experiment payload. Figure 3 shows the flight trajectory. Burnout of the propulsion stages occurs below 200 ft altitude at about 50 seconds into the flight. The booster burns already out after the first three seconds of flight and drops off. The booster thrust delivers the peak acceleration of about 18 g, while the sustainer engine continues to push only with about one g. At burnout the rocket has reached a velocity of about 4000 miles per hr. or 5 times the velocity of sound and continues to coast upward in nearly vertical direction. At 300,000 ft. altitude, the air density has dropped off to nearly one millions of the density on the gound. A very small air resistance is the only remaining outside force acting on the rocket and causes a deceleration in the order of 10^{-5}g which diminishes to the order of 10^{-10}g at peak altitude. This practically unrestrained motion cycle above 300K ft altitude lasts for 300 to 420 seconds for a range of experiment payload weight from 100 lb. to 250 lb. There is another Sounding Rocket available, the Black Brant, which has about 20% higher payload capacity for the same zero-g time range of 5 to 7 minutes.

Let me mention some more characteristics of Sounding Rockets. The simplicyt and cost effectiveness is achieved through spin-stabilization as shown in picture 5. The fins are aerodynamically set in order to spin up the rocket to about 200 rev. per minute. After burnout a "yo-yo" despin device is deployed consisting of weights on wire cables, causing a drop of the spin rate to below 10 %. For our purpose this residual rotation produces an intolerable inertia force level. Therefore the experiments must be

isolated from the rocket rotation by a "Non Spin Platform."

Picture 5 shows a typical "Baseline Configuration." The red portion consisting of the Non Spin Platform, carrying the experiments and their support systems, is separated rotationwise by ball bearings from the blue colored rocket systems. That way the experiments never spin and they are free from whatever the rocket spin up and despin operations are during the whole flight. The ball bearing friction is compensated by a rotation - sensor-motor servo system. Such non spin devices are commonly used in spin stabilized rocket and satellite systems.

Figure 6 shows the g-level range achievable with the above "single axis rate control system," which a non spin platform represents. By adding up all the residual forces acting on the payload during the "free fall coast"; these are aerodynamic and internal body forces from flight dynamics caused motions like coning, gravity gradient, mechanical tolerances between inertia axis and platform axis and control loop tolerances; we see that a g-level environment in the order of 10^{-3}g to 10^{-4}g if available. (Ref. 5) For higher requirements a three-axis rate control system, employing cold gas jets, can be provided.

This answers the question of what Sounding Rockets can offer.

We have investigated over the past year also the requirements and effectiveness of limited zero-g time experimenting. It was found in one extensive study that "for 17 of the 18 evaluated space processes, a valid representation of the complete process cycle can be achieved at low-g periods ranging 40 to 390 seconds" and that "specific process parameters can be verified in 3 to 8 seconds." (Ref. 6) Another investigation involving a large number of experimentors and the members of the University Space Research Association (USRA) is summarized in figure 7.

A typical processing cycle is shown in figure 8. The art of experimenting lies in arranging only the g-sensitive phase of the processes into this so very hard to accomplish "cycle of weightlessness." Here we see that within a total experiment time of one hour only 130 seconds low-g processing takes place. Pictures 11, gives an impression how a typical payload looks like. Here the processing facilities were mounted on a rocket fixed platform. Therefore only one experiment capsule located along the centerline in each facility, separately shown on picture 9 and 10, could be processed in order to minimize the effects of the spinrate during coast flight. In future flights the full payload volume can be utilized because of the use of single or multiaxis rate control systems. The diameter inside the payload rocket structure is 14 or 16 inches and the total length ranges from 60 to 100 inches, depending on the type of rocket, Aerobee or Black Brant.

Figure 12 depicts the presently considered management concept for the program. The action starts at the outer left block with the release of an AFO (Announcement of Flight Opportunity) by NASA Headquarters, Office of Application. Experiment proposals will hopefully be submitted by researchers in industry, institutions and universities. Another input will come from the investigators presently involved in Space Processing Research and Development activities, and I see many colleguea in the audience today just waiting for that since some time. The AFO will be open for continuous submissions.

The Experiment Selection takes place also in a continuous evaluation process, resulting in contract release and flight scheduling for each experiment. In cases where the investigator delivers the complete experiment including special processing facility, the apparatus goes for integration into the Payload Module to MSFC. There the interface connections with the power supply and telemetry unit is made as required and the complete Payload Module is shipped to the launch site. Here GSFC takes over, assembles the Payload Module by connecting simple field splices with the other rocket modules, also providing the 3-axis rate control system if required. After launch and recovery the Payload Module goes back to MSFC for distribution of the experiments to the investigators, and for refurbishment of the standard payload systems for reuse. A g-level measurement readout is furnished to the experimentor, and also the telemetered experiment measurements.

Many experiments will have sufficient commonality in their processing requirements so that multipurpose facilities can be used. In this case only the experiment materials in minimum enclosures are delivered and MSFC provides integration into the available facility and the processing of ground samples. The best possible combinations will be worked out to keep the operation flexible and cost effective.

The last graph, figure 13 shows the presently anticipated schedule. The AFO release is planned for late this month, May 1974. The operational flight should start in March 1975 and built up to 6 launches, may be even 12 launches per year, depending how effective this program will support the development of Space Shuttle Payloads.

We have seen during this symposium that only an aggressive experimental program can point this Space Processing Applications Program into the right direction. Verification of theoretical and laboratory result by experiments in real weightless environment is necessary for assurance of larger commitments. Furthermore, many effects of gravity and even the nature of gravitation is presently not yet well understood, maybe because the earth gravitational action was not even recognized as a dominating environmental factor, until recently the space age enable man to really see our planet earth hanging free in space. The awareness that all other natural terrestrial environments are finally controlled by the dominating terrestrial gravitation is growing. Besides verification, a lot of explorator. experimenting must be done in order to find out which of many thinkable and mathematically logical concepts nature is using and which not. Hopefully the

the projected program will provide enough flexibility and enough chances for repeated testing, so that we can learn by correcting our failures and use it as a true research tool.

References

1. H. F. Wuenscher, Low and Zero "G" Manufacturing in Orbit, p. 5 & 6, AIAA Paper No. 67-842, Oct. 67 (First Paper published about Space Processing).

2. Einstein and Infeld, The Evolution of Physics, Simon and Schuster, New York, 1938, page 249.

3. D. B. Larson, The Structure of the Physical Universe, Beyong Newton, Quasars and Pulsars, North Pacific Publishers, Portland 13, Oregon.

4. B. N. Bhat, Solute Diffusion in Liquid Metals, p. 3 NASA TR-417, Oct. 73.

5. H. F. Wuenscher, The Non-Spin Platform, MSFC-S&E-PE-IN-73-5.

6. W. H. Steurer, S. Kaye and D. J. Gorham, General Dynamics, Space Processes for Extended Low-g Testing, NAS8-28615, June 73.

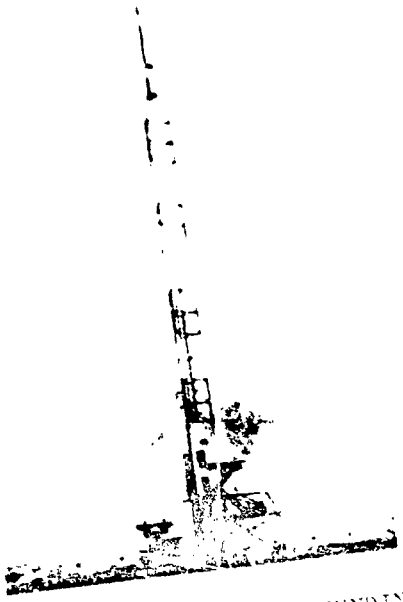

FIGURE 1 LAUNCH OF AN AEROBEE SOUNDING ROCKET

FIGURE 2 RECOVERY OF AN A

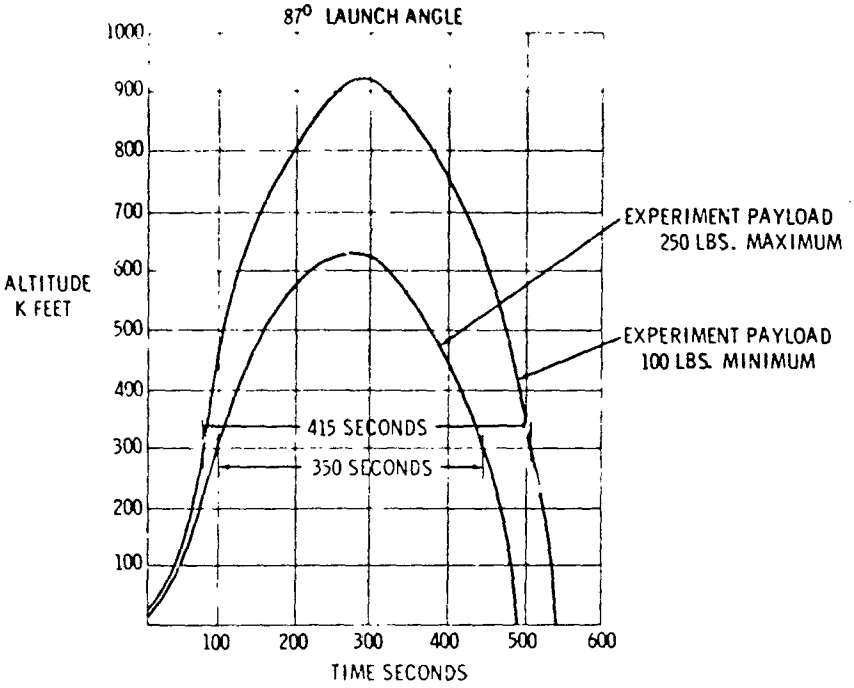

FIGURE 3 AEROBEE 200 ALTITUDE VS. TIME

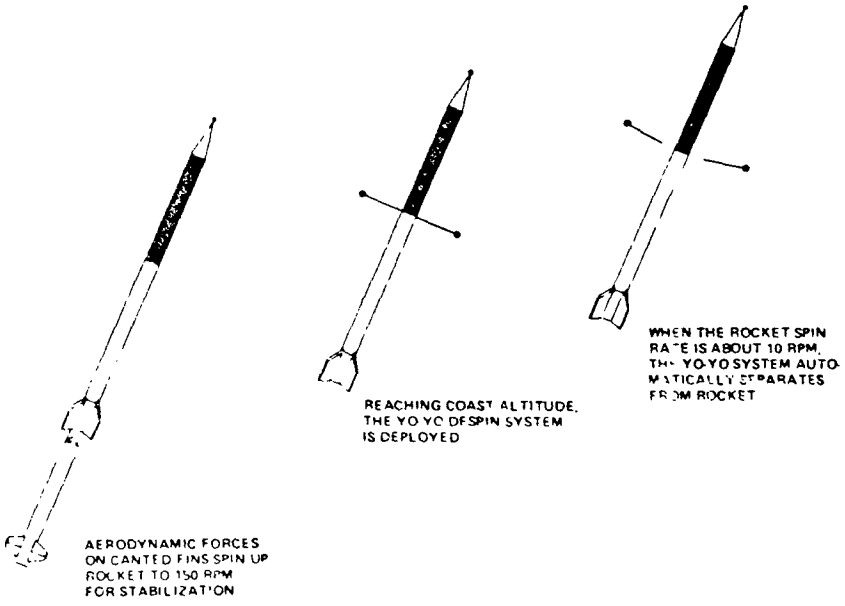

FIGURE 4 TECHNICAL ANALYSIS - ROCKET ROTATION

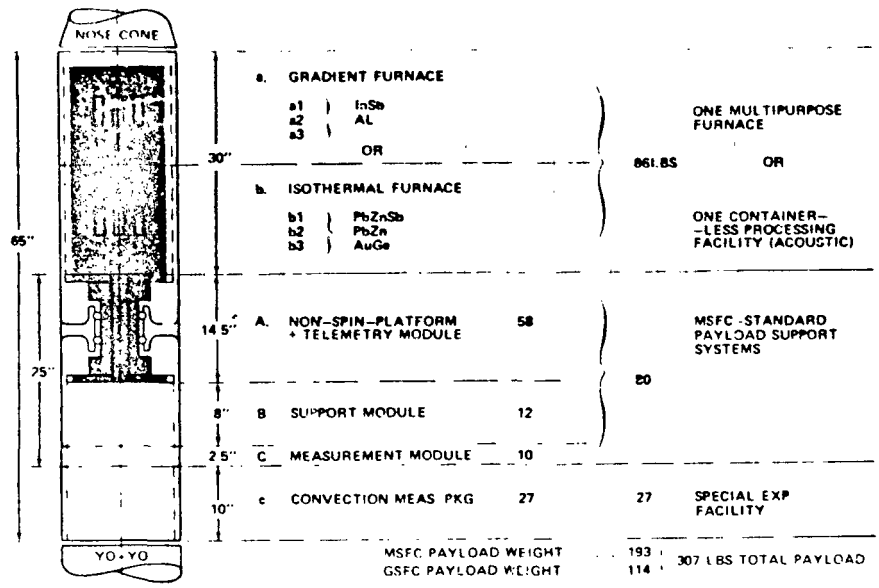

FIGURE 5 AEROBEE 200 - PAYLOAD BASELINE CONFIGURATION

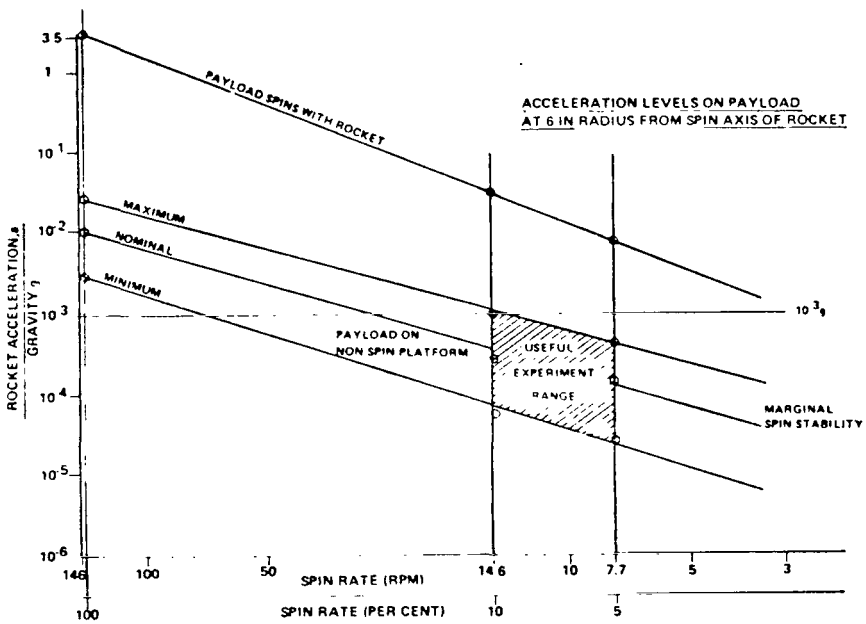

FIGURE 6 G-LEVEL RANGE ACHIEVABLE WITH A SINGLE AXIS RATE CONTROL SYSTEM

	GRAVITY LEVELS		PROCESSING TIME	
	MINIMUM REQUIREMENT	ESTIMATED AVAILABLE	MINIMUM REQUIREMENT	MAXIMUM AVAILABLE
CRYSTAL GROWTH FROM MELT	10^{-3}	10^{-3} to 10^{-4}	150 sec	415 sec
SOLIDIFICATION OF COMPOSITES	10^{-3}	10^{-3} to 10^{-4}	200 sec	415 sec
SOLIDIFICATION OF GLASS	10^{-3}	10^{-3} to 10^{-4}	300 sec	415 sec
BIOLOGICAL SEPARATION	10^{-3}	10^{-3} to 10^{-4}	400 sec	415 sec
SOLIDIFICATION OF METASTABLE ALLOYS	10^{-3}	10^{-3} to 10^{-4}	60 sec	415 sec

FIGURE 7 COMPARISON OF REQUIREMENTS AND CAPABILITIES DURING ROCKET COAST ABOUT 300K FT.

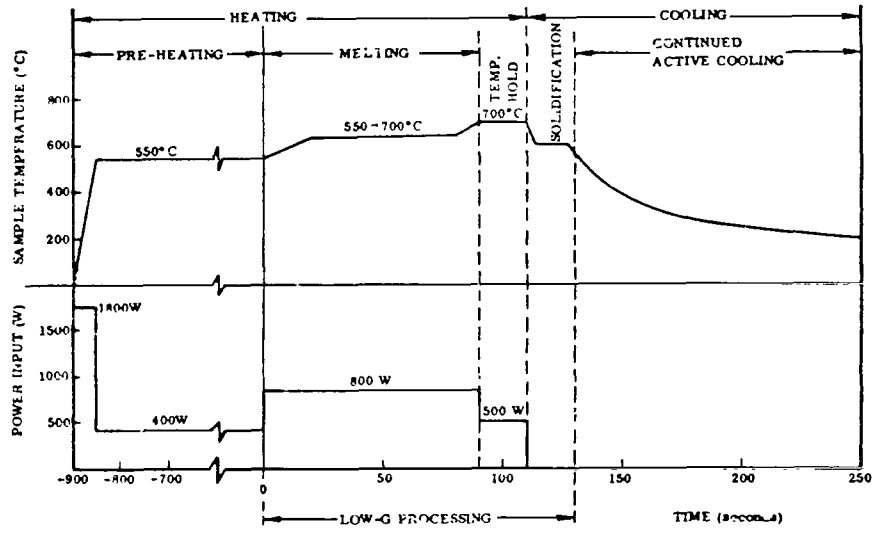

FIGURE 8 SAMPLE TEMPERATURE AND POWER PROFILES - PROCESSING OF COMPOSITES IN ELECTRICAL FURNACES

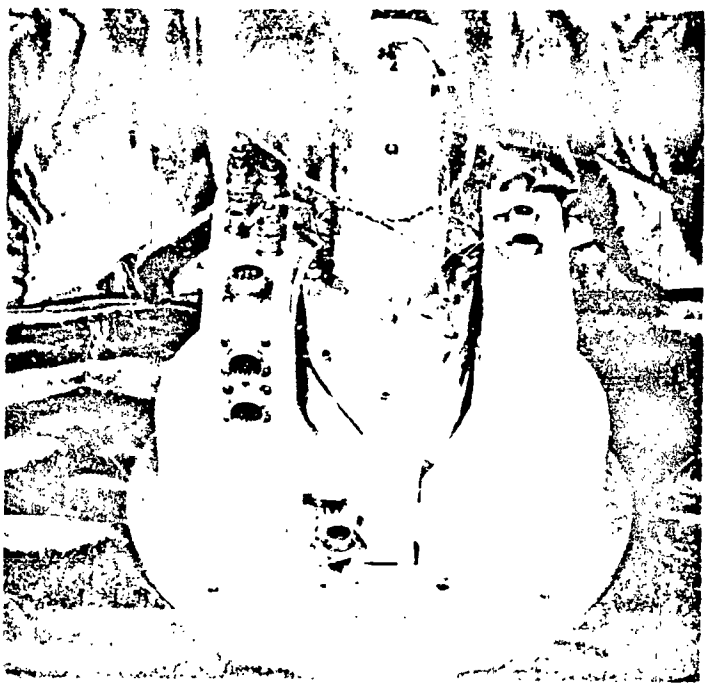

FIGURE 9 TIN CRYSTAL GROWING TEST - AEROBEE 200
NASA 26.013 RE-FLY

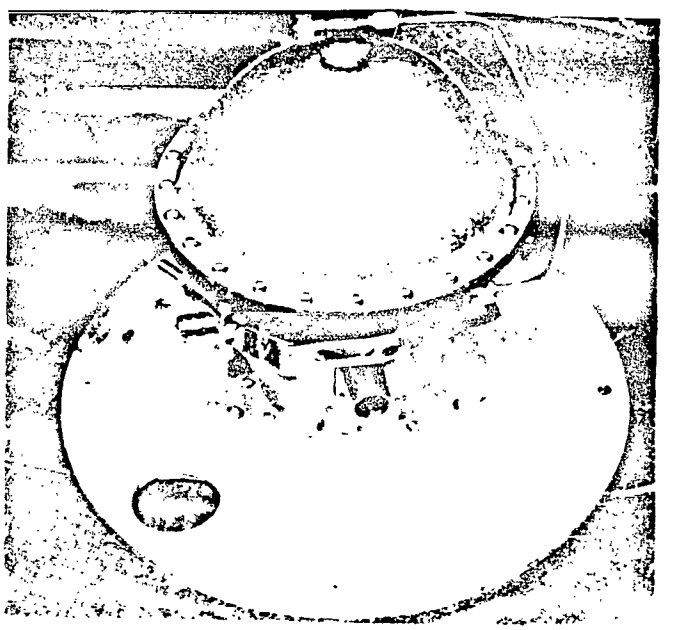

FIGURE 10 METAL MELTING TEST - AEROBEE
NASA 26.013 RE-FLY

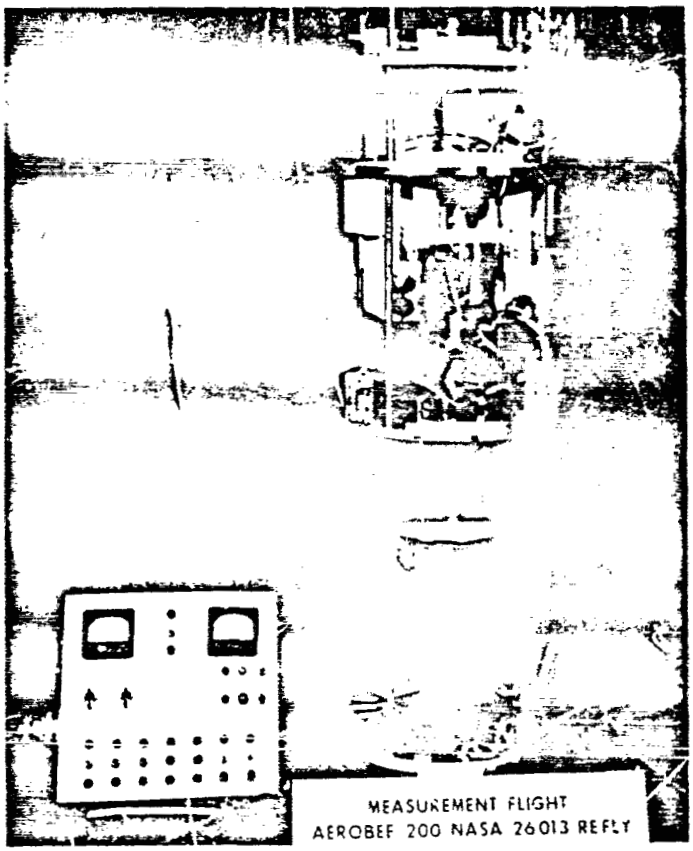

FIGURE 11 TYPICAL PROCESSING FACILITIES FOR AN AEROBEE 200 PAYLOAD

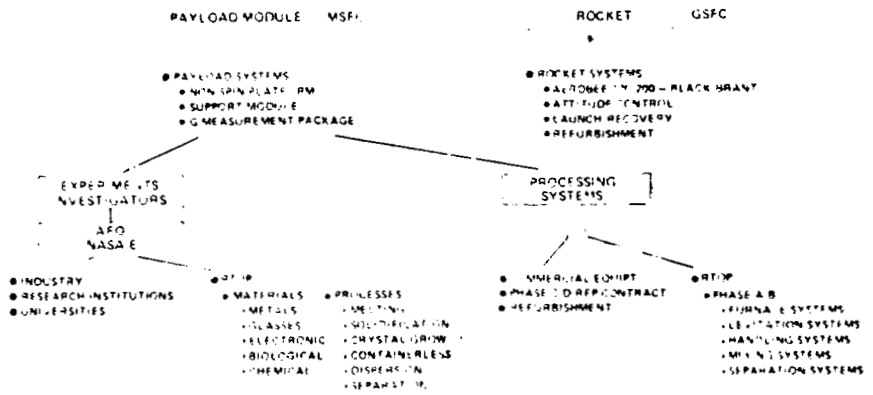

FIGURE 12 SPACE PROCESSING EXPERIMENT DEVELOPMENT AND INTEGRATION

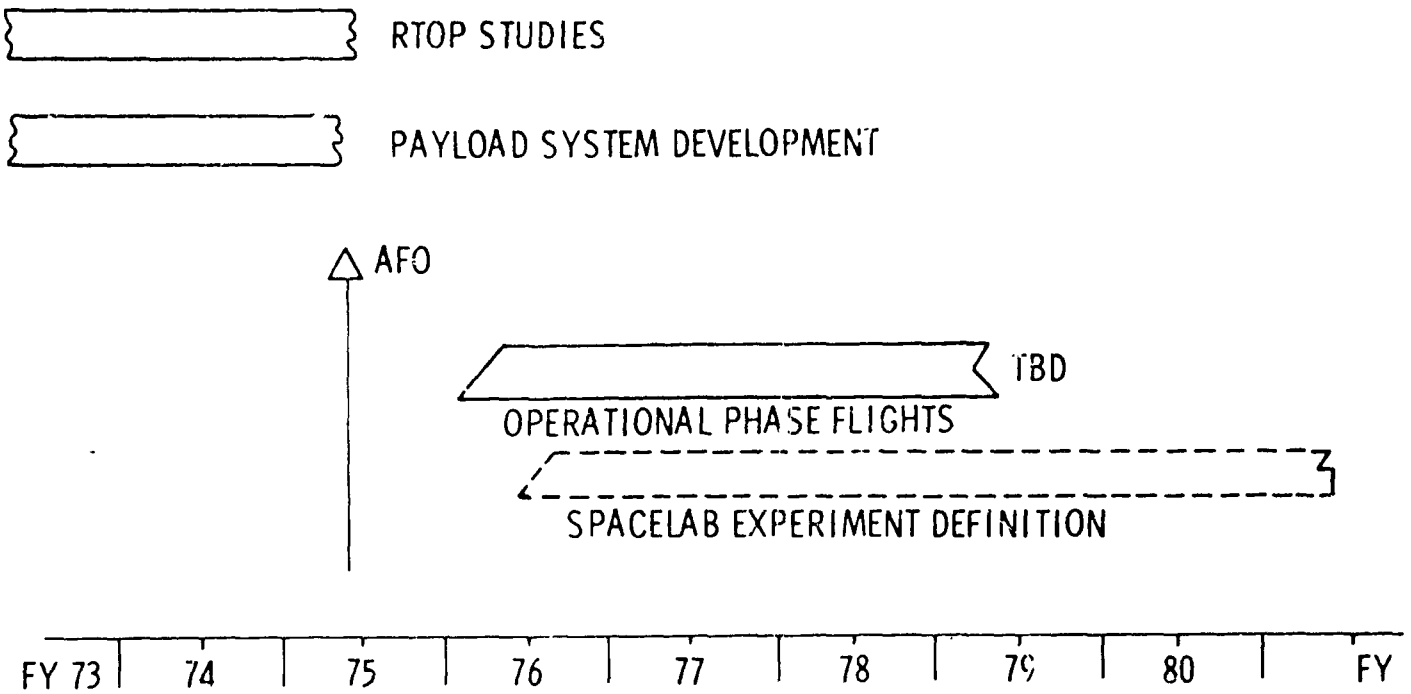

FIGURE 13 SUMMARY PLANNING SCHEDULE FOR SPACE PROCESSING EXPERIMENTS ON SOUNDING ROCKETS

FURNACE SYSTEMS DEVELOPMENT

By

B. R. Aldrich
Marshall Space Flight Center
Huntsville, Alabama 35812

SUMMARY

The advent of the space flight era has provided many new and challenging opportunities. Perhaps the most promising of these is the opportunity to utilize the low gravity of space in the production of new materials for use on earth. The first studies in this field were conducted on Apollo flights during the translunar and transearth coast periods. These were followed by more sophisticated experiments on Skylab. The encouraging results achieved from these studies has led to the planned expansion of activities in the field; with experiments now under development for flight on sounding rockets, the Apollo/Soyuz mission and Shuttle/Spacelab. This effort will provide a sound background for the eventual development of industrial space processing facilities. The reusable characteristics and the low payload cost per pound of the Space Shuttle will make materials processing in space economically feasible.

Space processing facilities, including furnace systems, will only vagely resemble their laboratory and industry counterparts. Within the constraints imposed by the host vehicle, flight furnaces will be more versatile. They will provide a wider range of controlled heating, cooling and sample positioning to accommodate the requirements of experiment scientists, and will be more efficiently packaged. The development of these advanced furnace systems will be an essential element in the orderly evolution of space processing technology.

INTRODUCTION

Successful scientific experiments in the field of materials processing have been conducted aboard the Apollo moon flights and the Skylab missions with more advanced studies planned for sounding rockets, the Apollo/Soyuz mission and the Shuttle/Spacelab era. All of these studies utilize the extended low acceleration environment available only in space to achieve processing conditions that are impossible to maintain on earth.

Furnace systems were and are a major element in all materials processing facilities. Experience gained in the development of these facilities have shown that laboratory or industrial type furnace systems designed for use on the ground cannot simply be modified or adapted for use in space. Space processing facilities must meet the stringent requirements of low power consumption, low weight, small size, mechanical loading, and most important, complete safety, when operating on board manned space vehicles.

Furnace systems are also required to provide flexibility, in controlled heating and cooling in order to accommodate a wide range of experiments in the general fields of crystal growth and materials melting and solidification.

As the era of manufacturing in space progresses, the needs of participating scientists will increase, posing an even greater challenge to the developers of furnace systems to keep pace.

HEAT SOURCES

In the initial phases of space processing furnace development, a study was made of the many different heat sources and classes of equipment commercially available. These studies formed the basis for design and construction of the initial flight systems. Some of the energy sources investigated were: Induction Heating, Electron Beam Gun, Electron Beam Plasma Gun, Laser, Electric Arc, Hot Gas, Electrical Resistance, Solar Radiation, Chemical, Ultrasonics, Infra-Red Radiation and Microwave Radiation.[5] Each heating source had its particular advantages and limitations and possible application in space-oriented furnaces. From these, the electrical resistance heating element proved to be the most practical heat source for a melting and controlled solidification type furnace. This was determined because of the relatively high efficiency of heating as well as small size, good temperature distribution control, and freedom from sample contamination. The electron beam gun and chemical energy sources respectively were selected for welding and brazing experiments. The most efficient insulation and thermal design had to be utilized in developing the melting and controlled solidification type furnace in order to reduce intrinsic heat losses and conserve energy. The insulation found most effective in furnaces operating in a vacuum was multifoil insulation made up of very thin, highly reflective, high temperature, shields separated by thin layers of silica fabric. This was determined by an evaluation of different material systems over a wide range of transient and steady state temperature and vacuum conditions.

APOLLO 14

The first opportunity to fly a materials processing furnace was on the Apollo 14 mission during the translunar and transearth coast periods. The apparatus developed by MSFC for this flight is shown in Figure 1 and consisted of an electrical heater, a heat sink device for cooling, and sealed metal capsules containing the sample material. This experiment met all the manned space flight requirements, such as light weight, low power consumption, maximum touch temperature and approved materials, and was capable of processing eighteen different experiment cartridges. These cartridges consisted of a variety of immiscible materials, particle and whisker composites, powder compacts, metal foam, crystal growth, and eutectic solidification experiments. The temperature limitation of this first generation furnace was 130°C. The furnace parameters were obtained by heating the charge to the desired temperature and then cooling it passively by conduction into a heat sink.

Generally speaking, the [illegible] first low-G experiments served their purpose, in that [illegible] were produced that cannot be duplicated on earth. Enhanced dispersion and distribution of fibers, particles and gases were found in the space processed samples.[2]

These initial demonstrations in space led the way to the development of materials processing systems available today. Continued advancement of these systems will lead to future processing facilities on an industrial level.

GALLIUM-ARSENIDE SOLUTION GROWTH EXPERIMENT (M555)

Experiment M555 (Figure 2) was developed for flight on Skylab as one of the M512 Manufacturing in Space experiments. This experiment involved growing single crystal gallium-arsenide from solution. It was designed to operate at 720°C for 115 hours. The experiment package consisted of three sealed quartz ampoules, each containing high purity, polycrystalline gallium arsenide source material, single crystal gallium arsenide seed material and liquid gallium solvent. Each ampoule was individually heated with a resistance heating coil. During this experiment, gallium-arsenide goes into solution at the hot end of the ampoule, is transported across a steady state thermal gradient to the cold end by diffusion, and precipitated out on the seed crystal. This experiment was not processed during the Skylab mission because of the impact created by loss of the solar wing.

COPPER-ALUMINUM EUTECTIC EXPERIMENT (M554)

The M554 Experiment furnace (Figure 3) was also developed for use in the M512 Manufacturing in Space facility. This experiment furnace had a maximum temperature capability of 900°C, and was designed to unidirectionally solidify three copper-aluminum eutectic samples. The furnace consisted of three graphite crucibles, each individually heated. To reduce the sample return weight and make the furnace reusable, the experiment package was designed so that the astronaut could open the furnace and remove the processed samples. New samples could then be installed for another test. A thermal gradient was established across the crucible by actively controlling the energy input to the hot end and passively cooling the cold end. Once the desired maximum temperature conditions were obtained, the control system was switched to the furnace cool mode. The temperature of the charge was then reduced at the desired solidification rate, maintaining a reasonably constant thermal gradient, as the sample froze.

The M554 Experiment furnace was replaced with the more versatile M518 multipurpose furnace system. The M554 Experiment itself was re-configured to mate with the M518 hardware and was processed on Skylab 3 and 4.

MULTIPURPOSE ELECTRIC FURNACE (M518)

Development of the M518 furnace increased both the temperature and control capabilities over previous furnace systems. It also provided a reusable materials processing facility capable of supporting a wide range of experiments. As shown in Figure 4, this system was designed to operate at 1000°C and provide active control at the hot end of the furnace to accommodate a range of soak temperatures, solidification rates, and thermal gradients. Eleven different experiments were processed during the Skylab 3 mission, and six of the eleven experiments were repeated utilizing the same furnace during the Skylab 4 mission. Each experiment consisted of three samples processed simultaneously in sealed stainless steel cartridges. The cartridges were installed in the furnace for processing by removing the plugs in the cold end of the furnace housing, attaching the cartridge, and inserting them into the three heating cavities. The proper processing conditions were then set on the control box and the experiment initiated.

APOLLO-SOYUZ

The joint endeavor to link up Soviet and American space ships in near earth orbit has provided another opportunity to perform a series of low-G materials processing experiments. The M518 Multipurpose Furnace is being modified for this purpose. During the Apollo-Soyuz mission, seven different experiments will be conducted. Six of these experiments will be developed by Principal Investigators within the United States and one from the Union of Soviet Russia. Experiments will be performed to investigate convection in the liquid melt, crystal growth by both directional solidification and vapor transport, composites, solidification of material with widely different specific gravities, directional solidification of eutectics, and the production of high coercive strength magnets.

Several modifications are necessary to adapt the M518 furnace system to the Apollo-Soyuz docking module. The furnace housing, control package, and electrical cables will be hard mounted to the wall of the docking module. A thermal protection shield will be placed around the furnace housing to protect the astronaut from hot portions of the furnace. The 5/8-inch thick aluminum wall of the docking module will provide an excellent heat sink to absorb and distribute the thermal energy generated by operating the furnace. A helium purge system will be added to provide a rapid furnace cooldown. This faster cooldown will decrease the experiment turn around time and allow more experiments to be performed in the same time period. The thermal efficiency of the furnace has been increased by reducing furnace heat losses, thus raising the maximum operating temperature from 1000°C to 1150°C without increasing the power required. A vacuum line was also needed to vent the furnace housing to outer space. Additional circuitry, to provide a linear solidification velocity feature, and protection against a shorted control thermocouple was added to the control package. The Apollo-Soyuz mission is scheduled for the summer of 1975.

SOUNDING ROCKETS

The ultimate potential of developing commercial products or processes in space will only be realized on long duration missions of the type proposed for Spacelab; however, many basic studies can be performed in the interim, at relatively low cost, through use of low-G simulation devices. Research and development in materials processing systems and materials science will continue between long duration flight opportunities through the use of short duration flights available with sounding rockets and the free-fall time offered by the drop tower.

A multipurpose, materials processing facility, Figure 5, is being developed for use on NASA's first dedicated sounding rocket scheduled for flight in December 1974.[4] Experiment data will be obtained and telemetered to ground by a measurement module designed to sense all aspects of the vehicle payload environment such as high and low acceleration, temperature, pressure and the acoustic conditions. A metallurgical evaluation of the flight samples, in conjection with the instrumentation data, will provide Principal Investigators with a good understanding of the materials processing conditions made available by the sounding rocket.

This multipurpose rocket furnace system will basically consist of the following: (1) a three cavity furnace, designed to process samples of the widest possible range of materials and thermal requirements. (2) an automatic control system capable of independent control of the three heating modules, each containing three heating elements. (3) a heat removal mechanism to extract the excess heat buildup in each heating module. This will provide the capability, in conjunction with the programmable control system of establishing an isothermally heated cavity or a wide range of thermal gradients and cooldown rates. (4) a thermal monitoring system compatible with the research rocket telemetry, to provide furnace performance and sample growth rate data throughout the processing cycle. The processing facility will be mechanically and thermally designed to withstand rocket vibration and shock loads encountered during launch and recovery and will be capable of withstanding these loads at operating temperatures repeatedly without significant damage.

In addition to the multipurpose furnace, two special purpose furnace systems, Figures No. 6 and 7, are being developed for later Sounding Rocket flights. These processing systems are being designed to accomplish specific objectives with limited variation in processing conditions. These systems

include a Float Zone Stability experiment, Figure 6, and a glass processing furnace, Figure 7. The Float Zone Stability experiment will determine the zone shape of molten materials, at various rotation rates and obtain the mode of instability and corresponding maximum zone dimensions. The Glass Processing Furnace will be utilized basically to process two types of glass systems. First, pure oxide or mixtures of several pure oxide compositions will be melted and cooled in a low-G environment. Secondly, glass materials will be heated and allowed to form nuclei in low-G resulting in glass-ceramics.

ELECTRICALLY CONDUCTING CERAMIC HEATING

The use of electrically conducting ceramics, as heating elements, has significantly raised the processing temperatures available for space flight furnace systems. Zirconia and thoria-based ceramic oxides, which are used as heating elements are electrical insulators at room temperature, but become excellent high temperature ohmic heaters above some transition temperature.[1] Heating elements now under development can operate at 2200°C in oxidizing inert or vacuum atmospheres for extended periods of time. The first ceramically heated furnace system (Figure 8) is being developed for use on the Marshall Space Flight Center drop tower. This furnace system will provide an isothermal processing cavity, 2.5 cm dia. X 10 cm long, with the capability of operating from room temperature to 2200°C max. The axial temperature variation throughout the isothermal cavity will be less than 10°C. By replacing the isothermal heating element with an axial gradient element, temperature gradients of up to 200°C/cm for distances of approximately 5 cm can be obtained. The operating temperature of this furnace system is controlled via a resistance signal from the ceramic heating element and is maintained within 1/2% accuracy or 11°C at the maximum operating temperature.

Additional furnace systems utilizing the ceramic heating concept will be developed in the near future for use on sounding rockets.

FUTURE PLANS

Future plans in the area of manufacturing in space include the development of advanced materials processing systems with special features such as containerless melting, sample positioning, materials mixing devices, high temperature processing systems, and automated processing systems.

Several methods of levitation and sample positioning are being studied for use in conjunction with furnace systems, for the purpose of eliminating contact between the sample melt and crucible. Levitation systems now under investigation or proposed for further study include electromagnetic, acoustic, electrostatic forces, gas jets, electrohydrodynamics, and microwaves. These terrestrial levitation experiments will be studied and or developed and scaled up for testing in the low gravitational environment of space. Possible applications are the preparation of ultrapure materials and solidification under conditions of extreme subcooling. Ultrapure refractory materials which are easily contaminated by molds are logical candidates.[3]

Both acoustic and electromagnetic mixers are being developed for use in space. These systems will be used in conjunction with furnace systems to process materials in space that require mixing such as immiscibles and the dispersion of fibers or particles in a liquid metal matrix.

Research and development of space processing facilities and the technology development associated with low-G experiments will continue through the ASTP mission, Advanced Sounding Rocket flights and the initial Spacelab missions, with an end item goal of providing the basis for commercial manufacturing operations in near earth orbit. The availability of Spacelab as a test bed for commercial low gravity manufacturing operations will add the vast volume of near earth space to the habitable regions of earth already used by mankind.

REFERENCES

1. Halbach, C. R. and Page, R. J., 2200°C Oxidizing Atmosphere Furnace for Space Manufacturing, ARTCOR, Irvine, California, January 1974

2. Yates, Jr., I. C., Apollo 14 Composite Casting Demonstration, Final Report, S&E-PE-A, Marshall Space Flight Center, Alabama, October 1971

3. Frost, R. T., Weightless, Containerless Melting and Solidification of Potential New Metal and Ceramic Products. General Electric Company, Philadelphia, Pennsylvania

4. Aldrich, B. R., Multipurpose Furnace for Research Rockets, S&E-PE-MXX. Marshall Space Flight Center, Alabama, January 1974.

5. Aldrich, B. R., Spaceflight Furnace Development, S&E-PE-MXX, Marshall Space Flight Center, Alabama, February 1973

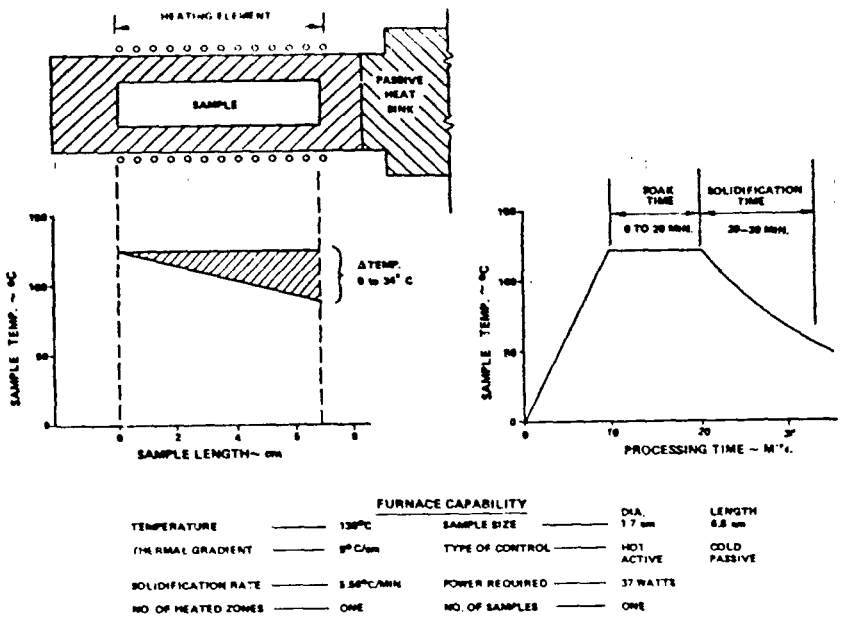

FIGURE 1. APOLLO 14 MATERIALS PROCESSING FURNACE.

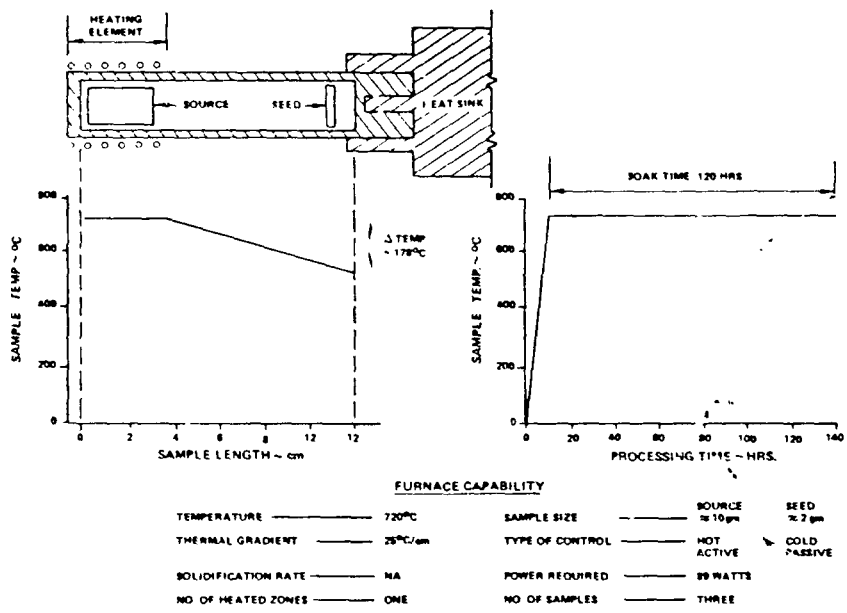

FIGURE 2. GALLIUM-ARSENIDE SOLUTION GROWTH EXPERIMENT M-555.

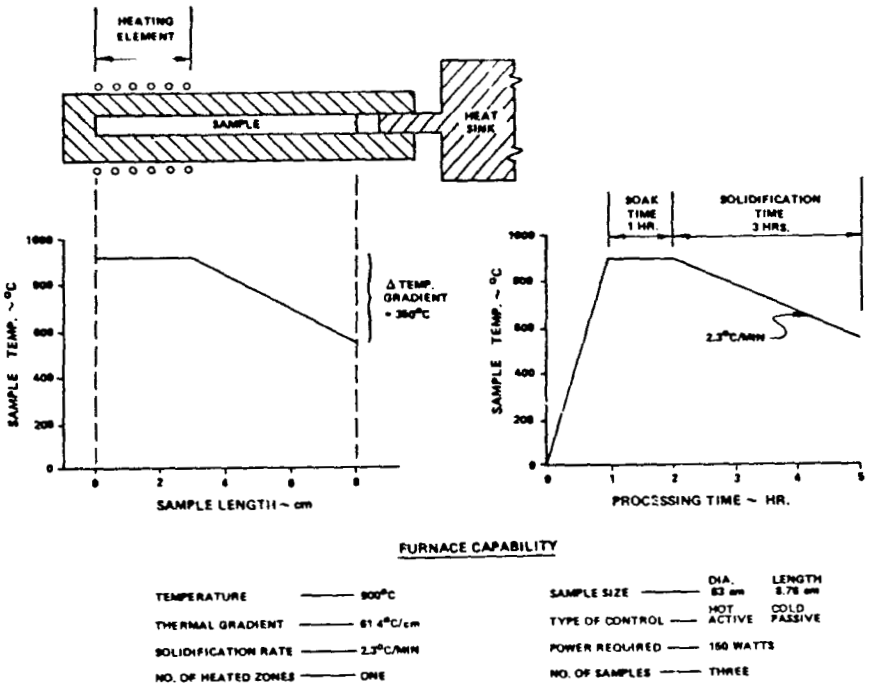

FIGURE 3. M554 COPPER-ALUMINUM EUTECTIC EXPERIMENT.

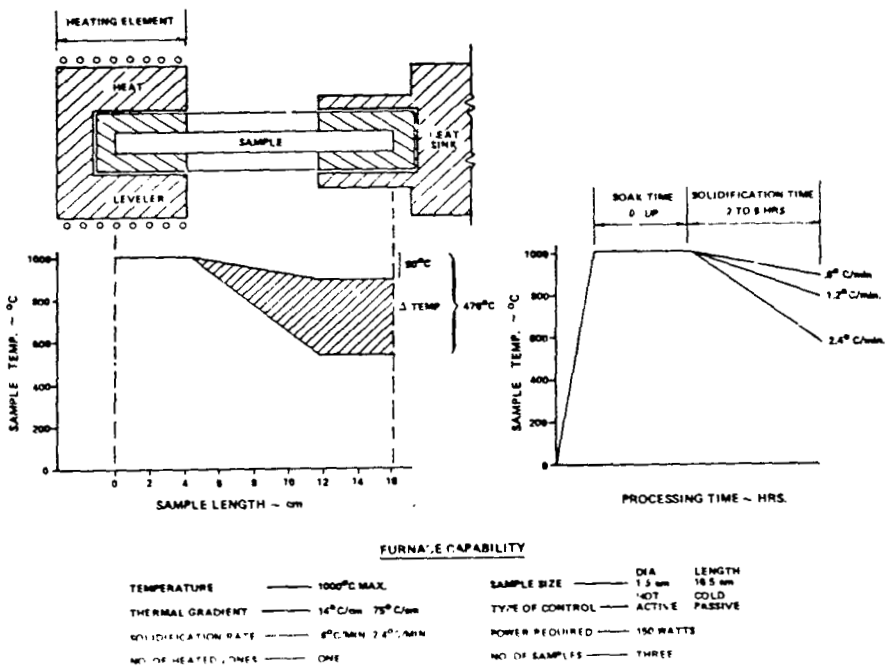

FIGURE 4. MULTIPURPOSE ELECTRIC FURNACE M518.

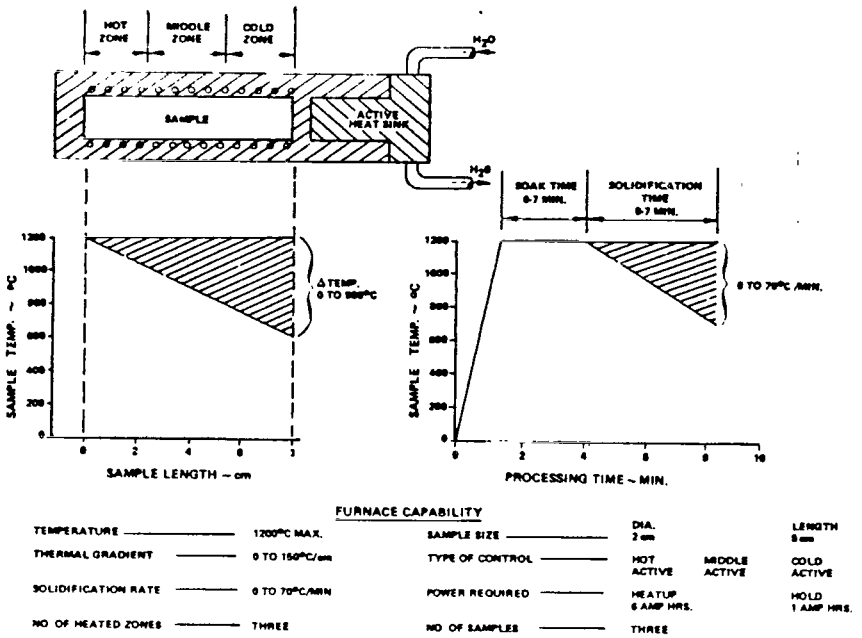

FIGURE 5. SOUNDING ROCKET MULTIPURPOSE FURNACE.

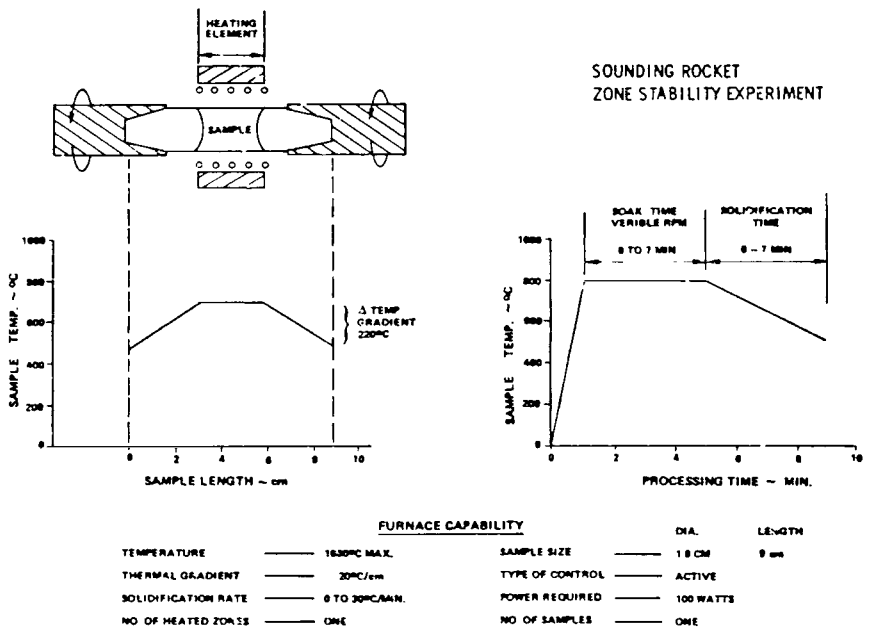

FIGURE 6. SOUNDING ROCKET ZONE STABILITY EXPERIMENT.

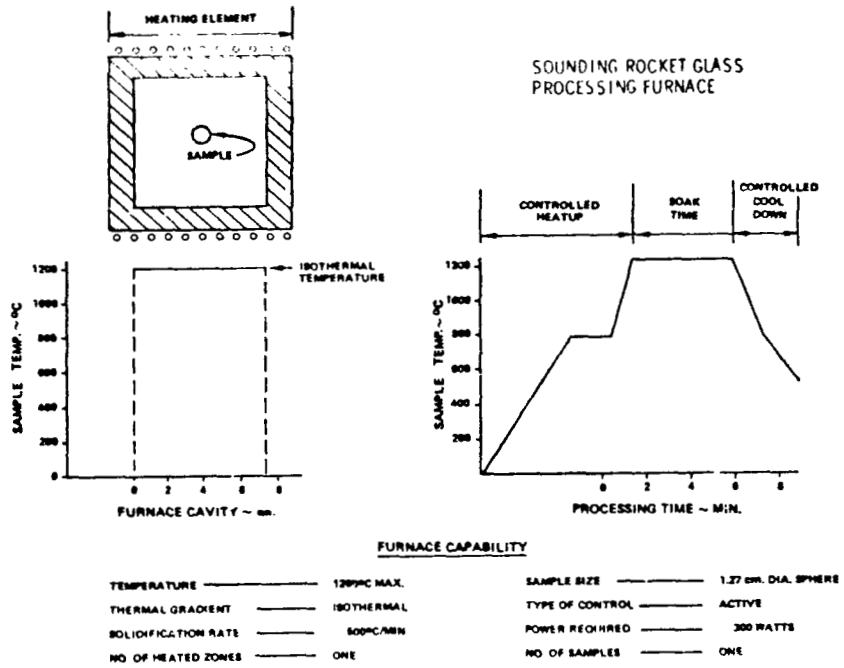

FIGURE 7. SOUNDING ROCKET GLASS PROCESSING FURNACE.

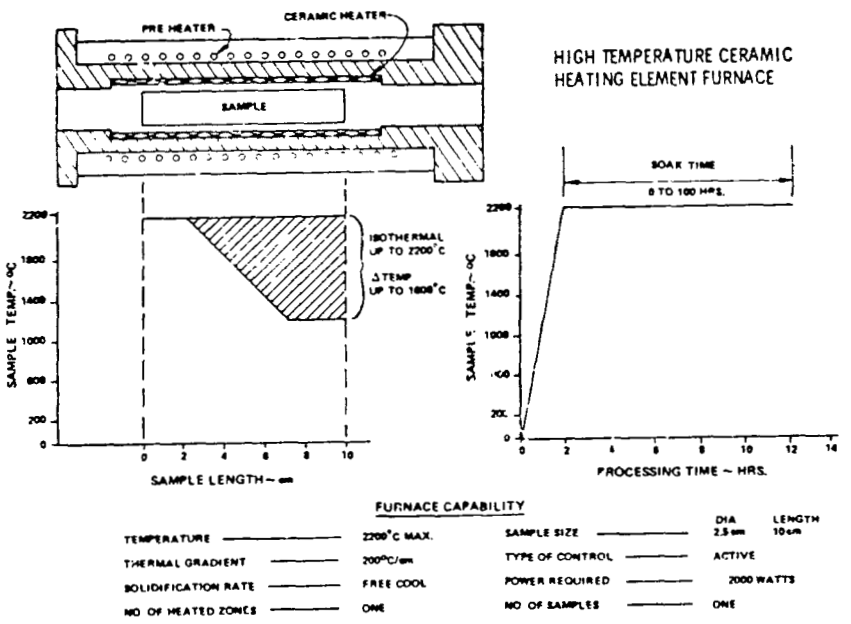

FIGURE 8. HIGH TEMPERATURE CERAMIC HEATING ELEMENT FURNACE.

SYSTEM DESIGN CONSIDERATIONS FOR FREE-FALL MATERIALS PROCESSING

By

R. G. Seidensticker
Westinghouse Research Laboratories
Pittsburgh, Pennsylvania 15235

SUMMARY

The design constraints for orbiting materials processing systems are dominated by the limitations of the flight vehicle/crew and not by the processes themselves. Although weight, size and power consumption are all factors in the design of normal laboratory equipment, their importance is increased orders of magnitude when the equipment must be used in an orbital facility. As a result, equipment intended for space flight may have little resemblance to normal laboratory apparatus although the function to be performed may be identical.

The same considerations influence the design of the experiment itself. The processing requirements must be carefully understood in terms of basic physical parameters rather than defined in terms of equipment operation. Preliminary experiments and analysis are much more vital to the design of a space experiment than they are on earth where iterative development is relatively easy.

Examples of these various considerations are illustrated with examples from the M518 and MA-010 systems. While these are specific systems, the conclusions apply to the design of flight materials processing systems both present and future.

INTRODUCTION

When reduced to basic principles, the requirements for materials processing in free-fall conditions are no different from the requirements on earth. So far as I know, there are no proposed materials processing techniques which differ in principle from those currently used in earth bound laboratories. Materials must still be heated, cooled, compressed, etc., in order to achieve some goal. The only novel considerations arise from either new handling techniques such as containerless melting or the absence of gravity driven phenomena such as density driven convection or phase separation.

The most important design constraints for materials processing systems arise from limitations imposed by the flight vehicle capabilities and crew availability. These considerations are far from minimal and influence not only the design of equipment but should be considered in the design and development of the experiment itself.

The balance of this paper will be devoted to examining these constraints both generally and in the context of the M518 and MA-010 MEF systems.

VEHICLE/CREW LIMITATIONS

The general design limitations imposed by the flight vehicle and crew are summarized briefly in Table I.

Table I.

Parameter	Earth Laboratory	Space Laboratory
Weight Volume Power Input Heat Dissipation Human Interaction Time	Negligible Consideration	Constrained

Under normal laboratory conditions, the basic requirement of a furnace system is that it can perform the necessary function; weight and size are secondary considerations. Similarly, within rather wide limits, the power consumption and efficiency of apparatus is relatively unimportant. Finally, manpower considerations, while present in any operation, are generally not a key factor in the selection of equipment on a laboratory scale. When a materials process moves from laboratory to manufacturing, then considerations of space, power and manpower increase in importance but still cannot be compared with the situation encountered in an orbiting facility.

Space flight conditions change the priorities drastically. The inherent capabilities of any flight vehicle are limited whether it is an Apollo command module or a Space Shuttle. Every kilogram placed in orbit must be accounted for and every cubic decimeter carefully planned; the vehicle type only changes the scale of the planning. Similarly, every watt that is consumed must be utilized in as efficient a manner as possible and every joule must be accounted for. Again, the manpower available for interaction with the equipment is limited and equipment therefore must be capable of performing the required task with a minimum of human interaction. There are obvious tradeoffs possible between manual operation and equipment complexity and the problem can be summed up by saying that the integrated weight, power and manpower should be minimized.

All these considerations are in addition to the primary requirement that the job itself be done. The integrated effect is that the manner of doing the job may differ substantially from the way it might be done in normal laboratory practice.

EXPERIMENT DESIGN

When the system limitations imposed by space flight are factored into the overall economics of an experiment, the ordering of priorities in the experiment design process changes. In normal laboratory practice,

empiricism usually dominates analysis in the development of an experiment. It is usually more economical to add a few thermocouples to a system than to develop and evaluate a complicated thermal model. In the case of flight experiments, however, the reverse may well be true. Fortunately, for free fall conditions, the task is frequently simplified since heat transfer which is frequently dominated by convection on earth is more likely to be controlled by thermal diffusion. This simplifies the necessary calculations and the results can be viewed with greater confidence.

This approach does demand that the experiment be well defined in terms of the experiment conditions rather than the experimental conditions before it is actually run. That is to say that the thermal conditions in the sample must be specified rather than the thermal conditions of the furnace since various processes of heat transfer and dissipation may make the two quantities quite different. Although analysis is essential in the design and evaluation of an experiment, the general availability of the requisite thermal parameters makes experimental verification of any model an absolute necessity. Preliminary ground based testing must be done to provide the missing thermal data. Also because of intrinsic cost of space processing, the economics dictate that maximum information possible be derived in GB tests.

The element which distinguishes this approach from usual investigations is that the goal of laboratory studies is as much to verify the model of the experiment configuration as to generate material samples for evaluation. Even with future space processing systems, it will probably be cheaper to do extensive ground evaluation than to use an iterative process based on the results of flight experiments.

EXAMPLES FROM CURRENT SYSTEMS

The M518 Multipurpose Electric Furnace System from the Skylab mission or its modified version, the MA-010 System for the ASTP Mission, may be used as examples of the various design considerations discussed in the previous sections. The components of these systems are shown in Fig. 1, and their functions are listed in Table II. A brief description of these components and some of the design considerations are as follows.

Table II

Component	
Control Package	• Temperature Control • Time/Temperature Programming • Measurement Signal Conditioning
Multipurpose Electric Furnace	• Heat Experiment Cartridges
Experiment Cartridges	• Confine Samples • Generate desired temperature distribution in sample
Helium Package (MA-010 only)	• Rapid Furnace Cool

Control Package (CP)

The Control Package serves as the "brain" of the processing system. In order to accommodate the limited astronaut time available for the experiments, the Control Package not only provided temperature control during the soak and cool-down periods, but also automatically sequenced the entire experiment program from the beginning of heat-up to the end of the final passive cool-down. The only astronaut participation required was to load the experiment cartridges, set the proper operation parameters and press the "start" switch. As a convenience, the Control Package also provided a digital display of the furnace temperatures and the status of the system.

Multipurpose Electric Furnace (MEF)

The Multipurpose Electric Furnace was the processing unit of the system providing a temperature controlled hot zone for heating the experiment cartridges. The essential design constraints for this unit were of size and power since the unit had to interface with the heat sink in M512 Materials Processing Facility and present an acceptable load to both the spacecraft power system and heat dissipation capability. Also, to be consistent with constraints on space and weight, only the single heated zone was available; the required temperature distribution in the experiment samples was provided by the experiment cartridges. Further, manual loading of the experiment cartridges was more efficient than an automated system for the conditions of the Skylab and ASTP missions.

Helium Package (HP)

In the MA-010 System, the heat losses from the furnace were reduced to a level where the cooldown time of the samples would take a disproportionately large fraction of the experiment time line. With only a relatively limited flight time available, a means was needed to increase the cooling rate of the furnace once the critical phases of an experiment were completed. Since the furnace insulation is primarily radiation shielding, the introduction of helium increases the losses ten-fold and reduces the experiment cycle to an acceptable length.

Experiment Cartridges

In the M518/MA-010 systems, the experiment cartridges serve as more than convenient containers for the sample ampoules. By controlling the heat fluxes through the cartridges, a much wider range of temperature distributions can be achieved in the samples than could be generated by the furnaces alone with their single variable temperature zone. An example of one mode of control is shown in Fig. 2, where the emissivity of the cold end of the cartridge is used as the variable. The temperature

of the hot end of the cartridge remains relatively constant, while the temperature of the colder end varies by several hundred degrees. Another mode of control is the use of different thermal conductances along the axis of the cartridge. Each cartridge was designed to provide the appropriate temperature distribution for the experiment.

Experiment Design

Limitations on instrumentation dictated that only the furnace temperatures (hot and cold end) could be measured in flight. Therefore, in order to determine the temperatures of interest in the samples themselves, it was necessary to develop analytical models for the temperatures in the experiment cartridges. These analytical models were refined during an extensive development test program so that during the final flight, the sample temperatures could be predicted accurately for any set of actual furnace conditions.

CONCLUSIONS AND RECOMMENDATIONS

The challenge in designing materials processing systems for space flight lies in accommodating the requirements of the particular experiments to the constraints imposed by the flight vehicle. Success in achieving a good design depends on having an adequate definition of both the requirements and limitations in terms of basic parameters. Further, careful ground based testing and analysis is essential for the efficient utilization of flight facilities.

Although the previous discussion has emphasized various design constraints with reference to a furnace system, weight, volume and power are constraints on any system. Human interaction was not stressed in the discussion; any temperature-time programs were automated in previous systems. Future programs may require automation of material handling and more sophisticated control programming. In all cases, however, the guiding consideration for the design of materials processing system will be the optimum allocation of available resources including time, human availability, launch fuel and spacecraft power.

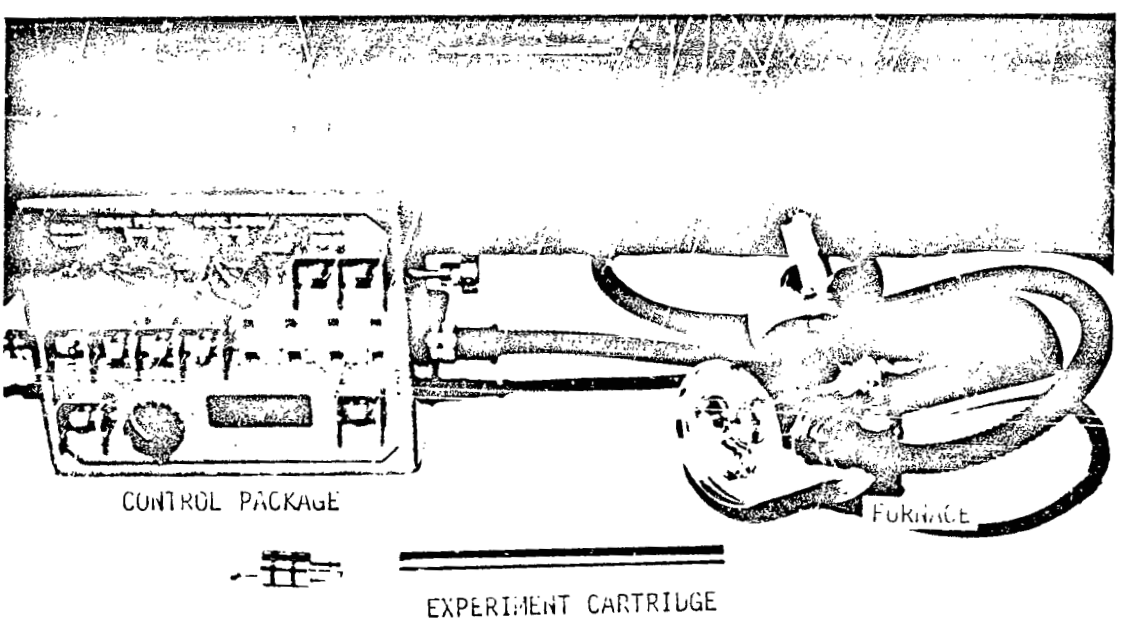

FIGURE 1. SKYLAB M518 MEF SYSTEM.

Curve 642222-A

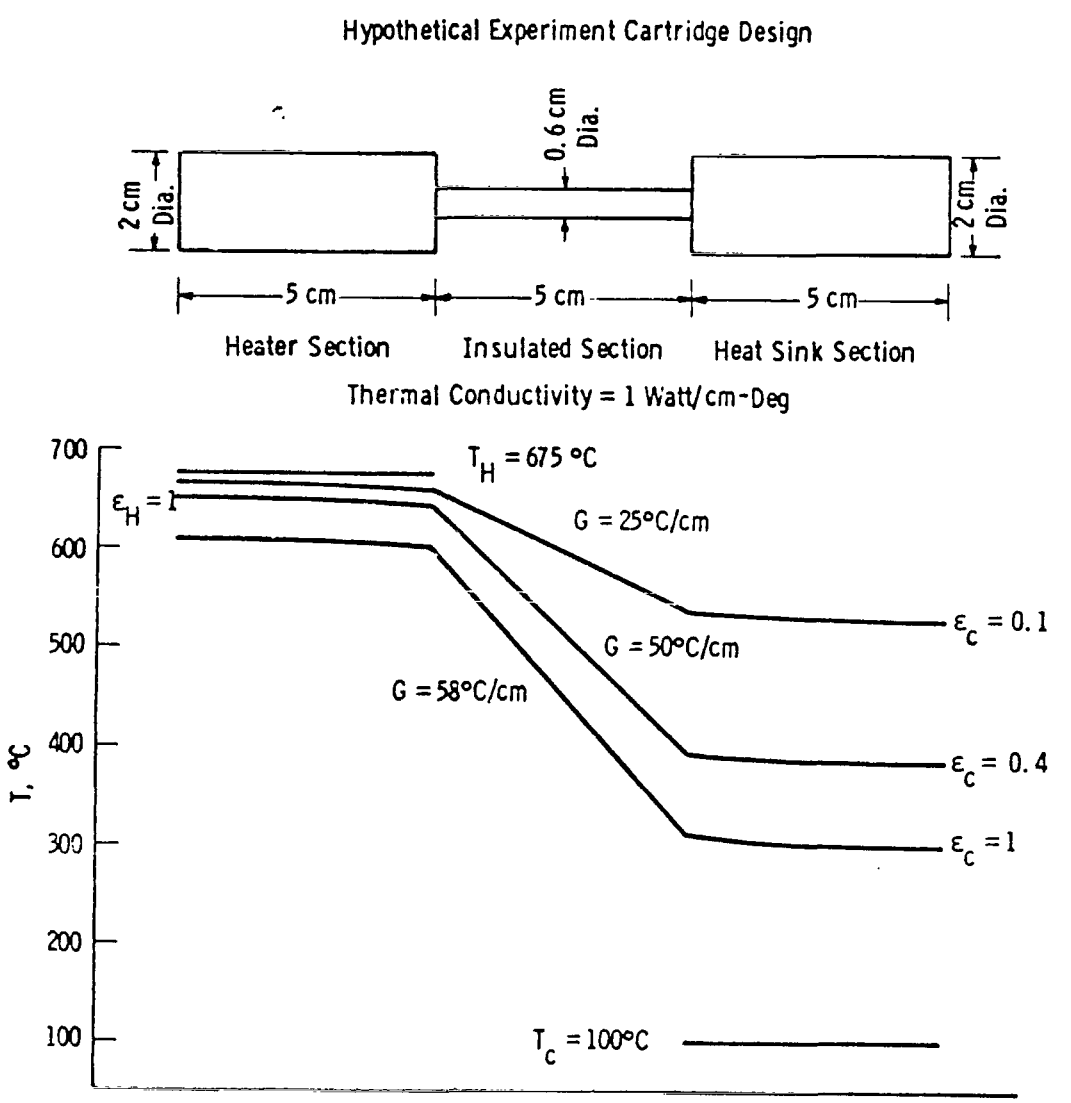

FIGURE 2. TEMPERATURE DISTRIBUTIONS FOR A HYPOTHETICAL EXPERIMENT CARTRIDGE.

ELECTROMAGNETIC CONTAINERLESS MELTING AND SOLIDIFICATION IN THE WEIGHTLESS ENVIRONMENT

By

R. T. Frost,* E. H. Stockhoff, G. Wouch
General Electric Company
Philadelphia, Pennsylvania 19101

SUMMARY

A wide range of important materials science experiments and materials processes which depend upon melting, reaction or resolidification in the freely levitated state has been identified. These materials range from alloy systems of relatively good electrical conductivity to glasses of electrical resistivities when preheated on the order of one ohm-centimeter. For these materials, application of positioning forces by means of electromagnetic fields in a Containerless Processing Facility is practical with present day technology. Ground based studies and theory indicate many possibilities for formation of new phases and crystal structures through elimination of gravity and the influence of crucible walls. Within the resistivity range considered are included many interesting possibilities for new types of containerless melting and solidification experiments. These include possibilities for formation of amorphous metals and semiconductors through the exploitation of the undercooling made possible by containerless solidification, refractory metals and oxides formed or purified free of the influence of crucible contamination, immiscible alloys and cermets, and transition metal carbides and nitrides of high purity which are difficult to prepare by powder metallurgy.

Because the range of physical parameters of the materials which can be processed free of the influence of containers is extremely large compared to the experience in terrestrial levitation experiments, it is inappropriate to utilize without major change the electromagnetic levitation techniques which have been developed over the past decades in terrestrial laboratories. The material property to which the containerless facility physical specifications are most sensitive is the specimen electrical resistivity in and at temperatures just below the molten state. This parameter has a major effect upon the specification of an optimum frequency for the electromagnetic fields used for specimen position control and eddy current heating. The efficiency for achieving required positioning forces and for induction heating of the specimen depends sensitively upon specimen resistivity and size, both of which can be considered to vary over a much greater range than can be

*Paper presented by - R. T. Frost

tolerated in terrestrial levitation experiments. Since available electrical power in the Space Laboratory will be limited, much attention is given in the present study to optimization of facility power efficiency. It is considered inappropriate to carry out Space Laboratory experiments at high power with the very poor efficiencies which are normally tolerated in terrestrial levitation experiments with small samples.

In a recent NASA study [1] a comparison has been made amongst what are believed to be all reasonable candidate coil configurations for a Containerless Processing Facility. After optimizing each specific coil type with respect to efficacy for electromagnetic position control and eddy current heating for spherical conducting specimens, a comparison was made amongst the optima so found within each coil "family." This intercomparison was made on the basis of a number of engineering criteria in addition to the achievement of high force and heating per unit power. A brief summary of this work is given here which indicates that a baseball or "cusp" coil are especially suitable for an early Space Laboratory Facility. An orthogonally wound circular coil can be added to either to provide for specimen rotation control.

The cusp coil is preferred for use with electron beam heating because of its greater "stiffness" for specimen displacements. Measurements have been made to compare eddy current heating efficiencies for both types of coils. The induction heating efficiency is greater for the baseball when the ratio of specimen diameter to coil diameter becomes small. Since a versatile Space Laboratory facility will require both types of heating in order to be compatible with the widest possible range of materials and since both coils are compatible with the same type of RF power amplifier and servo equipment, it is recommended that the coils be modularly replaceable elements in the facility. The requirement for easily exchangeable modular coils is indicated, in any event, by the requirement for changing coil size when significant changes in specimen size are made so as to maintain reasonable power efficiencies within the facility.

Because most of the materials process examples which have been identified are included within a range extending six decades in resistivity above the good conductors, coil power frequencies ranging over about three decades, from 0.01 to 10 or 15 mHz will be required. Continuous frequency variation over this range is not required. Rather, one octave steps will be sufficient, leading to power amplifier requirements similar to the band switching techniques used in commercial radio transmitter gear which can, in a single unit, typically cover five or six octaves of frequency at power levels of 1 kw and above. Tuning within such bands is not required in an electromagnetic Containerless Processing Facility.

For early Space Lab applications, available power will be the principal limitation to the variety of materials which can be processed in quantities larger than experimental amounts. The maximum sample diameters for reasonable assumed Space Laboratory facility power range from 16 cm for the lower melting materials such as glasses and many alloy systems to about 2 cm for the highest

melting materials such as tungsten. For later manufacturing facilities, however, the system can be scaled up to commercial quantities if adapted to the use of solar heating at the focus of a large reflector.

INTRODUCTION

During the late 1960's a number of conversations were held between representatives of industry and NASA officials regarding the possibilities for exploiting the weightless environment of space to carry out new types of materials processing experiments which could lead to new materials and products. Perhaps the most obvious of the suggestions was to utilize the natural tendency of all objects to float freely in a "levitated" state in a freely orbiting space vehicle. This would allow consideration of melting and solidification experiments free from the influence of crucibles and molds since the specimen integrity could be maintained by surface tension forces alone. It was apparent that many of the restrictions of terrestrial levitation techniques utilizing electromagnetic fields would be removed. In the weightless environment, electromagnetic fields could be used to remove kinetic energy from the specimen relative to the laboratory and to prevent the melt from touching nearby equipment. Since the required forces would be relatively small, containerless melting and solidification can be carried out for materials having resistivities orders of magnitude above those which can be considered in terrestrial experiments. The mass of the melt processed would be limited only by the onset of hydrodynamic instabilities and heat transfer considerations, and calculations show that masses of many kilograms can be considered. These early ideas have been developed in some detail through NASA contract studies over the past several years. The purpose of the present report is to indicate general facility concepts capable of processing the widest range of possible important containerless processing experiments within reasonable technology constraints. An important part of the work has been to make an up-to-date summary of these experiment possibilities. An attempt has been made to consider materials based on importance in terms of new scientific data or possible future commercial applications.

CANDIDATE CONTAINERLESS MATERIALS PROCESS EXPERIMENTS

The motivation for earth based electromagnetic levitation experiments has generally been the achievement of one or more of the following objectives.

1. Purification and outgassing of specimens free from crucible contamination

2. Observation of extreme degrees of supercooling

3. Production of well homogenized alloys.

Although terrestrial work in this area has been mainly with metals and their alloys, some investigators have recently extended these techniques to the study of high temperature inorganic synthesis [2, 3]. The present paper indicates that, in the weightless space environment, containerless levitation with electromagnetic position control is applicable to materials whose resistivities just below their melting point may be six decades higher than the resistivity of the best conductors and may be processed in masses of many kilograms, provided that sufficient power is available.

In a recent contract carried out for the Marshall Space Flight Center Process Engineering Laboratory, a review was made of the very wide range of suggestions which have been made for exploiting such containerless processing to carry out basic materials experiments in space leading to new knowledge and in many cases to the probable preparation of new and unique materials [1, 4, 5, 6, 7, 8, 9, 10, 11, 12]. A review of this work will be given in another paper [13]. We shall here only briefly summarize those classes of materials which would most benefit from the new possibilities of containerless processing in space. We shall emphasize primarily the range of electrical resistivities covered by the most interesting candidate materials since this parameter has the greatest effect upon specification of optimum electromagnetic field frequencies required for position control and heating of the melt. Also considered is the range of melting temperatures which, together with the size of the specimen, is most important in determining power required for melting of a free levitated mass.

The materials of greatest interest can be grouped as follows.

1. Alloys, intermetallic compounds and cermets
2. Transition metal carbides and nitrides
3. Glasses.

These are discussed briefly following.

Alloys, Intermetallic Compounds and Cermets

Carbides, Nitrides, Silicides, Borides, Beryllides and Sulfides

These materials are beginning to be used widely in various fields of modern technology because of their high melting points, hardness, chemical stability, high temperatures of transition into the superconducting state, metallic conductivity or semiconductivity or strength at high temperatures [2, 3, 14, 15, 16]. The preparation of high purity polycrystalline solids of these materials with adequate homogeneity and grain size as well as the preparation of high purity single crystals of low defect density has been a problem. Also, it is desirable to produce these materials with better characterization of bulk samples to assist in understanding how deviations from stoichiometry, crystal structure, lattice parameters and

impurity levels should be specified. The following examples are discussed in Reference [1].

1. TaN and NbN based alloys

2. Hexaborides such as lanthanum boride (LaB_6)

3. Carbides such as TiC, ZrC, TaC

4. Amorphous metallic conducting glasses such as palladium silicon.

Amorphous Semiconductors and Semiconducting Glasses

These materials should find wide applications in electronics in future years. Due to their amorphous nature, these materials show homogeneous and isotropic electronic and optical properties. They are not as much affected by impurities as are the crystalline semiconductors. Many of these glasses exhibit the property of "switching" their conductivities from low to high and should be useful in electronic switching and computer applications. The semiconducting glasses and amorphous semiconductors fall into three main categories. These are

1. The chalcogenide glasses, in which one or more of the elements, S, Se, or Te is combined with one or more of the elements such as metals Si, Ge, P, As, Sb, Bi, Tl and Pb,

2. The Transition-metal oxide glasses, which are glasses in which the major constituent is a transition metal oxide such as V_2O_5 (vanadium pentoxide),

3. Amorphous germanium and silicon,

4. Recently, "diamond lattice type" glassy semiconductors such as Cd-Ge-As have been reported and may form a fourth category.

All of these glasses may be prepared by supercooling from the melt, bypassing crystallization. Thus they are ideal candidates for containerless processing experiments. At room temperature many of these semiconducting glasses have resistivities above 10^5 ohm-meters, but at elevated temperatures and when molten, resistivities which fall below 10^{-2} ohm-meters.

Alloy Melts having a liquid miscibility gap

These are the monotectics and exhibit the phenomenon of segregation of the two liquids, on earth, by virtue of density differences [5]. In the weightless environment this separation should not occur and a matrix of one phase with dispersion of the other phase throughout should be obtained. Unique new alloys and

intermetallic compounds with unique electronic properties may be prepared from melts of monotectic composition and hypermonotectic composition. Tungsten-copper is an alloy which is totally immiscible in the liquid and solid states [5]. Tungsten-copper is produced commercially at the present time by liquid copper infiltration of a Tungsten skeleton. By solidifying a tungsten power dispersion in a copper melt using containerless processing, new materials could be prepared with possible unique applications to wear resistant, high temperature circuit breakers, relays and electric switches.

If thermal gradients can be adjusted across a freely floating melt, then directionally solidified composites could be produced. An example is Fe-Pb which would have unique magnetic properties. Another example is Hg-Te which forms the semiconducting intermetallic compound HgTe. Through supercooling melts of monotectic or hypermonotectic compositions, new intermetallic compounds, new alloy compositions, or amorphous materials may be formed. The chalcogenic glasses SeSb and SeTl are other examples.

Eutectics

By adjusting the thermal gradients across a freely floating melt, directionally solidified composites may be prepared with unique electronic and optical properties [6]. Some examples are InSb-Sb for the thermoelectric applications, FeSb-InSb for magnetoresistive and infrared polarizing applications, NaF-LiF for optical properties and Fe-FeS for ferromagnetic applications.

New alloys and compounds, prepared by supercooling melts

If a high degree of supercooling can be attained through containerless processing then many new materials may be prepared with unique features through solution broadening or bypassing crystallization [8]. One example is Ni-Ge which has been studied through SPLAT cooling.

Transition Metal Carbides and Nitrides

Transition metal carbides and nitrides are of extreme interest and importance in modern technology [14, 15, 17]. At the present time their main commercial interest is due to their hardness. The carbides in this group form the basis for "cemented carbide" cutting tools and wear-resistant parts. Due to their excellent high-temperature strength and good corrosion resistance they are also used as high temperature structural materials.

There are other, more exciting, properties possessed by these materials which hold great promise for future technological applications. The transition metal nitrides are being used increasingly not only for their electrical properties

in integrated circuitry but are also being studied for their superconducting properties. Niobium nitride based alloys have some of the highest superconducting critical temperatures. Containerless processing in space would open up possibilities for purification, melting, and supercooling melts of nitrides and carbides in attempts to produce new superconducting materials. Many of the superconductors with high critical temperatures, critical magnetic fields, and critical current densities are transition metal carbides and nitrides.

Thin-film nitrides seem to have the most potential for application in such devices as Josephson junctions. Their refractory nature and corrosion resistance results in little chemical diffusion and hence decay of the junction with time. Junctions in use today are not chemically stable after cycling a few times between room and liquid helium temperatures.

Preparing melts of carbides and nitrides poses many problems [14]. Many of them have very high melting points. Tantalum Carbide has the highest melting point known for any material (about 3983°C). The melting points of the carbides are generally higher than those of the parent transition metal element while those of the nitrides are comparable. There are no crucible materials to contain these very high temperature melts.

Contamination by impurities such as oxygen has a significant effect on the properties of carbides and nitrides and, since it forms a solid solution with both carbides and nitrides, oxygen is extremely difficult to eliminate [14, 17]. Carbon deoxidation is possible by heating under vacuum conditions at elevated temperatures and with excess carbon. It appears likely that vacuum purification and melting of these very high temperature materials without a crucible such as in containerless melting in the weightless environment may enable very high purity polycrystalline or single crystal transition metal-carbides and nitrides to be produced for electrical and superconducting applications.

Glasses

Of the glasses, electromagnetic position control can be used for those whose resistivity falls below 10^{-2} ohm-meters at elevated temperatures such as many of the oxides and those with sufficient metallic or semiconductor particles dispersed within them. Most of these materials will require preheating before release. They may also be prime candidates for electron beam heating and melting.

High index glasses for new optical systems [9, 10] may be prepared from melts of oxides such as CeO_2, ZrO_2, Nb_2O_5, TiO_2, etc. These glasses would be prepared by heating, melting and, possibly, superheating the crystalline oxides, and then supercooling the melt in the absence of a crucible.

New single crystal materials may be produced from oxides of very high melting point such as ZrO_2. One process contemplated is the production of the

oxide glass and then conversion of the glass to a crystalline form. This would avoid polymorphic transitions which occur in ZrO_2 and BeO as they are cooled. Other materials such as $2BeO:SiO_2$ (phenacite) [10] and ZrO_2: SiO_2 (zircon in which the composition melts incongruently should also be considered for production of single crystals by conversion from the glass. They have not been produced in usable form by conventional crystal growing techniques.

Review of User Interests and Requirements

In an effort to initiate the establishment of a uniform set of processing requirements for materials of interest to the potential user community, a user survey was carried out as part of this contract. Extensive discussions were held with key individuals from various industrial laboratories. Data was extracted from publications and reports documenting space processing concepts, experiments and tests recommended by various individuals and groups involved in materials research.

As a result of these dialogs and literature reviews, a tabulation was compiled of some 18 areas of user interest, from such specific commercial applications as tungsten with improved grain structure for x-ray targets to such potential applications and research areas as more uniform dispersions of eutectic and monotectic alloys. In all, the tabulated user areas of interest are representative of approximately 400 different materials and material combinations. This work is the subject of another paper [13]. The most important output of these studies is the establishment of the ranges of electrical resistivity of the various candidate materials and processes. These results will be discussed below.

RANGE OF MATERIALS PARAMETERS AND SOME PROCESS REQUIREMENTS

Key Material Properties

The important material parameters for the specific examples of each area of interest were compiled. Subsequently, a representation of the number of examples versus resistivity (in the range of 10^{-8} to 10^{-2} ohm meters) was prepared. Figure 1 is a histogram showing the numbers of candidate cases falling within a number of ranges of electrical resistivity. Also identified in this histogram are the general ranges which include examples already discussed of carbides, borides, nitrides, silicides, beryllides, sulfides, and oxides of metals (when heated), chalcogenic glasses (when heated), pure metals, alloys of metals, and semiconductors (some require heating). The overwhelming number of cases of these materials considered fell within the range of resistivity illustrated and are thus suitable for processing in an electromagnetic containerless system.

Also considered was the number of examples for which the "second crossover point" in secondary electron coefficient versus energy lie in various ranges from 0.5 kev to 20 kev. The "second crossover point" is defined as that electron

energy at which the total secondary electron emission falls below unity, precluding electron beam melting of free specimens with electrons of greater energy. Electron beam heating can be considered for materials for which the "second crossover point" is no less than two or three kilovolts.

The density to surface tension ratio determines the maximum specimen rotation speeds which can be considered for gas bubble removal without causing excessive deformation of a molten specimen. These matters are discussed in Reference [1]. Density is also important in determining the relative accelerations that will be caused by application of positioning forces.

Cooling to Solidification Temperature and Time Required for Solidification

These questions have been discussed numerically in Reference [18] including the effects on onset of solidification at temperatures well below the normal solidification point. Because of the absence of crucible walls to furnish sites for heterogeneous nucleation in the melt, the subcooling phenomenon is expected to be encountered relatively frequently. Extreme subcoolings may be observed in many cases of interest (and in fact provides one of the principal motivations for the containerless experiments). Procedures for computing upper and lower bounds on time to solidification are given in Reference [4].

RF Induction Heating

This subject has been adequately treated in the literature [18,19]. In a recent report [1] computations of efficiency for heating are given and compared with experiment. The efficiency for RF heating and for applying position control forces is a function of a parameter x which is the ratio of the radius of the material specimen considered to the electromagnetic skin depth in the specimen. In practice, reasonable efficiencies are achieved only at frequencies high enough that the skin depth becomes of the order of the specimen radius or less. Because of the importance of the skin depth parameter, we show in Figure 2 the variation of skin depth as a function of frequency for various resistivities.

Because of the wide range considered, the straight lines have been chosen to correspond to constant resistivities, each differing from the other by two orders of magnitude (factors 10^2). Also indicated by the arrows and labels are the ranges of specimen resistivities discussed previously. It can be seen that electromagnetic skin depths of one centimeter or less (x values of unity or greater for reasonable size specimens) can be achieved for frequencies no higher than 20 MHz. Employment of microwave equipment does not appear to be necessary for the range of materials and processes which are considered here.

For very high resistivity specimens such as cold glass, alternate position control techniques, such as standing sound waves in gas filled cavities, can be

considered. Here it is anticipated that alternate methods of heating other than the HF or electron beam techniques considered in this report must be employed. The work coils required for the former would likely interfere with the standing sound wave pattern. Electron beam melting, at the required electron energies, would not be applicable due to electron scattering from the working gas in the sonic system and radiant or microwave heating may be required. It should also be noted that many containerless experiments and processes call for controlled gas environments at pressures too low to be practicable for the sonic positioning technique. Other experiments and processes adaptable to sonic position control are being studied in other laboratories [20,21].

The above considerations indicate that eddy current induction heating of both good and relatively poor conductors is feasible provided magnetic fields of adequate intensity can be provided over a frequency range up to 10 or 20 MHz, the higher frequencies being employed for the poorer conductors in order to achieve adequate x values.

Electron Beam Heating and Melting

There is a large class of material examples which can be electron beam heated and melted in the levitated condition, without the need for grounding of the material. This possibility arises from the circumstance that the total secondary electron emission coefficient can exceed unity for these materials if proper selection is made of electron beam energy. The electrostatic potential of the levitated material will automatically adjust itself to that value, in the range of a few tens of volts positive, which causes an adjustment of the net number of low energy secondaries emitted such that the total electron flux leaving the specimen equals the total flux of electrons in the impinging beam.

Reference [1] lists a large number of material candidates for containerless processing for which the secondary electron emission coefficient rises above unity for electron energies suitable for use with electron beam heaters. In Figure 3 we show a gross representation of the numbers of candidate materials considered for which this possibility for electron beam heating exists. Specifically, EB heating can be considered when the second crossover point exceeds 2 to 3 kilovolts.

Other Process Requirements

The physics and engineering analysis of providing controlled rotations to levitated specimens by providing rotating magnetic fields is discussed in Reference [1] and will not be given here. The synchronous motor principle can be easily applied by providing another magnetic field coil which produces a field orthogonal to that of the main magnetic field used for positioning and heating. Relatively modest rotating fields to impart spin to the levitated specimen can be provided by introducing separate excitation to the coils which are phased in quadrature. Because of the relatively low spin rates required to produce reasonable centrifugal

fields for gas bubble removal, field frequencies in the range below 100 Hz will normally be sufficient. The specimen rotation frequency is limited, in any event, by hydrodynamic instabilities which would set in for excessive oblate deformation.

Position Force Requirements

Translational forces must be applied to the specimens in the Containerless Processing Facility in order to prevent contact of the melt with surrounding equipment. In addition it is necessary that specimen position oscillations within the potential well provided by the magnetic field configuration be damped to a high degree within reasonably short times so that the forces provided by the field may, for some processes, be reduced to very low quiescent levels. A simple analysis given in Reference [1] indicates that an acceleration capability on the order of 10^{-3} gravities will be adequate to rapidly control the position of the specimen relative to the center of mass of the total Space Laboratory. Accelerations of the laboratory as high as 10^{-3}g would be expected only from relatively violent astronaut body motions. In Reference [1] it is argued that these body motions will lead to displacements of the laboratory center of mass relative to a free specimen within the facility small enough that rigid position control is not required and that an acceleration capability for the Containerless Processing Facility of 10^{-4}g will probably be adequate.

Forces on the levitated specimens may arise from electrostatic charges, differential outgassing or vaporization and forces due to impingement of an electron beam if this heating method is employed. As discussed in Reference [1], these various forces are expected to be of a magnitude which would impart accelerations to the specimen on the order of 10^{-3}g or less. For this reason 10^{-3}g is chosen in the facility capability studies given at the end of this paper. It will be noted that for most materials and processes, the power required to provide positioning forces is relatively small as compared to the power required for heating and melting so that higher acceleration capability could easily be provided if early space experiment experience indicates spurious forces higher than anticipated.

Environmental Gas Requirements

Degassing of metals in the solid state and the liquid state is employed to significantly reduce the interstitial impurities which cause embrittlement, high ductile-to-brittle transition temperatures, and other effects detrimental to the service properties of the metal [22,23]. The residual gases present in vacuum systems are, generally, H_2O, O_2, N_2, CO, CO_2, H_2, and CH_4. These gases originate from system leaks, outgassing of the hot furnace surfaces, the pumping system, and the metal being heated. The pressure of each of these gases is dependent upon the furnace history and the test conditions. During the heating-outgassing cycle, the total pressure of these gases will increase to a maximum value and then decrease to a value characteristic of the pumping system. In order

to perform certain processes, then, such as decarburization, the partial pressures of residual gases, such as O_2 in this case, must be adjusted to favor the degassing reactions.

Careful consideration must be given to the use of an inert gas during degassing. A major disadvantage of the use of an inert gas is the great difficulty of measuring precisely the concentrations of the active impurity gases [22, 23]. With permissible partial pressures for degassing reactions at the level of 10^{-4} torr or less, the allowable concentrations of impurity gases in an inert gas at one atmosphere pressure will range from fractional parts per million to 10^{-5} parts per million or less. Thus the allowable impurity concentrations in the inert gas may be so low as to prevent precise measurement and to impose purity restrictions on the inert gas which are not attainable by present technology. Another disadvantage is that the presence of the inert gas will lower the reaction rate between the metal and the active gas. Active gas must collide with and must diffuse through the inert gases to reach the metal surface. Thus the surface collision rate at a given pressure of an active gas at the metal surface is lower in an inert gas than in a vacuum. When active gases are used, as for example in decarburization, this may prolong the degassing dwell. For these reasons degassing is usually performed in a vacuum of the required partial pressures of active residual gases.

With higher temperatures achievable in the solid state due to the lack of the necessity for supporting the solid in the weightless state, the prolonged dwell times employed in solid state degassing on the earth may be significantly reduced in the weightless environment. A short dwell time after melting, with some superheating, may result in evaporation of such minor constituents as phosphorous and potassium. This will depend upon the vapor pressure of the metal versus the vapor pressure of the minor constituent at this temperature. It is clear, then, that the advent of processing in the weightless environment will require modification of degassing processes normally performed on the earth to take advantage of the lack of necessity for support or containment of the metal.

It is most likely that the production of many glasses such as zirconia, alumina, silica, etc., will require an ambient pressure ranging from a low vacuum (about 10^{-3} torr) to one atmosphere pressure. However, the atmospheres considered should be those designed to prevent degassing and volatilization of oxides. An oxygen atmosphere might be used to prepare many glasses [10]. Adjustments of the partial pressures of active gases to the point at which degassing and volatilization cease will be a prime requirement. As an example, BeO tends to form polymeric vapor species as $(BeO)_n$, where n = 2, 3, 4, 5, 6. Even a small partial pressure of O_2 will suppress this incongruent vaporization.

Position Control Forces - Computation Methods

The basic mechanism for the provision of a translational force upon an electrically isolated conducting object by means of an applied alternating electromagnetic field is the following. The alternating applied magnetic field induces

circulating eddy currents in the specimen. Between these induced currents and the applied magnetic field there are Lorentz magnetic forces. In the case of a uniform applied field these forces will balance out to zero by symmetry. However, if the applied field is nonuniform, there will be a net translational force on the specimen. The most accurate way to solve the problem is to calculate the eddy current distribution within the specimen which satisfies the appropriate boundary conditions, to compute the distributed electromagnetic forces $\mathbf{j} \times \mathbf{B}$ and then integrate over the specimen volume. This problem is tractable for certain simple geometries such as a spherical specimen and an applied field having axial symmetry. Some such calculations are reported in the following sections. For a general conceptual facility study as reported here, however, it is more appropriate to utilize a simpler theoretical approach which allows a rapid comparison amongst various coil and field configurations for screening purposes. Such an approach is allowable as long as the differences among the various configurations considered are greater than the errors incurred in use of the approximation. Thus in the sections which follow, the simple formulae derived by Smythe [18] and Okress [19] are utilized for the initial screening and elimination of many non-optimum coil types. Subsequent computations to evaluate the forces more accurately are used when studies or comparisons are made amongst the final candidate systems.

Approximate Formula for Translational Force on Specimen

The problem of a spherical conductor immersed in an alternating uniform magnetic field was solved by Smythe [18]. Okress [19] applied these formulae to the calculation of the net forces exerted upon the induced current system for problems of interest in terrestrial levitation experiments. This work used the approximation that the applied field is sufficiently uniform that, before introduction of the spherical specimen, the variation in applied field over the volume to be occupied by the specimen is small compared to its average value within the specimen. The resulting formula for the force acting on the specimen is $F = -(a^3/4)\,G(x)\,\text{grad}\,B^2$. Here a is measured in centimeters, B in gauss (10^4 gauss = 1 weber m^{-2}) and the force in dynes. A plot of the function G(x) is shown as Figure 4. For large x (skin depth short as compared to specimen radius) the function G(x) approaches unity. This is the normal mode of operation for the facility discussed at the end of this report. For decreasing x the forces achievable with reasonable power levels drop precipitiously when $x < 1$.

The equation involves an inconsistency in that the dipole moment is calculated on the basis of a uniform applied field which later is assumed to have a gradient in order that it be able to exert a force on the specimen. The error involved in this approximation is small provided the specimen does not approach too closely to the field producing windings or if magnetic fields having a cusp-like [illegible] specimen volume are [illegible]. The [illegible] was [illegible] of the simple formula. Two types of more exact computations were utilized.

The first involved a computation of the actual Lorentz forces acting on each of 20 discs into which the spherical specimen was divided. The large x (small skin depth) regime was considered and the 20 self-consistent loop currents in each disc were calculated which satisfied the boundary condition that the magnetic field just exterior to the spherical surface would be parallel to that surface. Individual forces on each eddy current loop were then calculated and summed. Results of these calculations are given in following sections where appropriate. A second method was to use the simple formula but to compute grad B^2 on the basis of the applied field B^2 averaged over the specimen volume. This approximation, for the circular coil, yielded forces which agreed better with the more exact 20 segment calculations and with experiment than those computed from the simple formula with B evaluated at the specimen center.

Selection of Magnetic Field Configuration

With each coil type, studies were done where appropriate to find that set of coil parameters representing an optimum. Comparisons were then made among these optima for various coil types based on several criteria applying to the achievable translational forces for a given expenditure of electrical power. The coil types were also compared on the basis of efficiency for electromagnetic induction heating since, as discussed above, this represents probably the most efficient heating method to be considered in those cases where electron beam heating is inappropriate. Induction heating will represent, for initial Space Lab experiments, a heating method easier to implement than radiant heating or solar heating through the use of large sun-oriented flux-collecting mirrors. The latter approach will almost certainly be considered for large manufacturing facilities but will require constraints to be placed upon the orientation and possibly orbit parameters of the space facility.

As the study proceeded, it became clear that some of the coil configurations thought to be distinct candidates could alternately be considered as variants upon the same basic topological configuration. For example, the Alice coil can be considered as the simplest Joffe bar configuration in which account is taken of two single end loops serving as mirrors for the quadruple bars (see Figure 5). In fact this realization historically led to the evolution of the Alice system from the original Joffe configuration. Likewise, the member of the baseball family in which the coil loops lie in orthogonal planes closely resembles the Alice configuration and its properties are not greatly changed by the rounding of the corners of the Alice cube. Detailed studies carried out on optimizing coil plane angles in the baseball family thus represent what can be considered the final evolutionary stage in a whole series which included several other coil types.

Similar detailed studies of the opposing hemisphere coil configuration showed an optimum consisting of three contiguous turns near the equator of each hemisphere with the remaining turns greatly reduced in influence. It was later found that operating the coil pair in phase opposition (the so-called cusp

configuration) gave, when optimized, symmetrical force fields, reasonable RF heating efficiency and permitted elimination of the coil turns of smaller diameter on the hemispherical surface. This simplification of coil geometry provides the great advantage of greater accessibility to the specimen position for injection or ejection into, or out of, the coil.

A third example of the "dequantization" of formerly discrete, qualitatively different systems through discovery of intermediate cases resembling a continuum is related to the cusp and 6-coil configurations. The cusp, when it is considered in a system which can provide rotation control, must be used in conjunction with a second orthogonal system. If this second coil system is chosen to be a second pair of opposing coils, the resulting configuration resembles very closely the original 4-coil mock-up of the 6-coil system which was used in this laboratory to demonstrate position control and damping in a horizontal plane for a specimen suspended on a long pendulum. In a sense, it may be said that it has been learned how to achieve both three axis position and rotation control about a single axis with only four coils of the 6-coil system.

Although there are probably other equally valid alternate ways to consider the comparisons among coil types, in the present study the sense of an evolutionary development proceeding on detailed numerical studies of each coil type has been very strong.

Magnetic Flux Density for Circular Coil

Because of its importance as an element in several coil configurations, special attention is first given to the simple circular coil. In arrangements in which several separate circular windings (e.g., cube, tetrahedron, opposing hemispheres) are operated at discrete frequencies, it may be shown that the time averages of the squared field intensity, $\overline{B^2}$, add linearly for the combination of the separate coils. This is also true for grad B^2. Thus the calculation for single circular turns were used later to construct force fields for some of these other more complicated coil configurations which are composed of circular coils.

Smythe [18, p. 270] gives the flux density anywhere for a circular coil in terms of an axial component, B_z, and a radial component, B_r, expressed as functions of complete elliptic integrals. These analytic expressions were used to derive maps of B^2 and grad B^2 which were used first to make detailed comparisons between calculated and measured forces for circular turns and secondly to construct force fields for arrays consisting of a number of circular turns, e.g. cube and tetrahedral geometries.

Force Measurements and Calculations for a 3-turn Circular Coil

In order to test the validity of the several computational procedures for total body force, these were applied to circular geometry force measurement:

carried out in the laboratory. The coil consisted of three turns of one-quarter inch diameter copper tubing 5.5 cm in diameter. A solid aluminum sphere 2.54 cm diameter was used as a test body. The coil was mounted with its axis of symmetry in the vertical direction and mounted upon a positioning device which permitted the coil to be raised or lowered. The solid aluminum sphere, mounted upon a non-conducting, counterbalanced arm which hung from a balance, was positioned on the axis of the three turn coil. The distance between the coil and sphere was measured with the aid of a telescope 170 cm from the sphere. An alternating current (frequency ≈ 100 KHz) of 50.5 amp rms was introduced into the coil and the balance was used to measure the force exerted upon the sphere. The accuracy of each individual force measurement for this experiment is estimated to be ± 0.001 gram or ± 1 dyne. The forces measured, plotted in Figure 6, ranged from 13 to 239 dynes.

The computer program which sums the individual forces on each of 20 planar discs into which the sphere was conceptually divided yielded results which are plotted in Figure 6. We note that there is excellent agreement between the measured forces and those calculated on the basis of the 20 disc eddy current ring model over most of the range but that there is a noticeable discrepancy as the sphere approaches close to the coil plane. These differences are attributed to dimensional uncertainties arising from the representation of the current flowing in the three windings of the coil by a single filamentary winding in the computational model. It should be noted, however, that the region of good agreement between the theory and measurements is just that region which will be considered as the confinement region for specimens in practical coil systems. Other computations discussed below take explicit account of individual turns in multiple turn windings.

Since it is expected from the simple force model that the force will be proportional to $a^3 G(x) \text{grad } B^2$, it is of interest to compute the ratio $F/a^3 G(x) \text{grad } B^2$ from the measured values of F and to compare to the ratio 0.25 predicted by the simple force model. The values of this ratio using the measured force values given in Figure 6 and the conveniently available calculated values of B^2 are shown as the hexagonal points in Figure 7. Here the values of B^2 are taken corresponding to the central position of the spherical specimen volume. The ratio approaches a constant of about 0.28 using this procedure.

The procedure used for most of the coil comparisons carried out during the study was next tested. This consists of averaging the values B^2 over the spherical specimen volume before calculating $\text{grad } B^2$. This procedure yields the points shown as triangles in Figure 7. We see that the ratio is quite accurately 0.25 if we avoid positions too close to the coil winding. It may be concluded that the use of the simple formula $F = 0.25\, a^3 G(x) \text{grad} B^2$, where B^2 is evaluated as an average over specimen volume, is to be preferred over the use of the simple formula without averaging. In fact, for this particular case, the averaging procedure yields results equally as good as the 20 disc model.

Force Calculations for Cube and Tetrahedron Arrangements of Circular Coils

If it is assumed that there are no large effects due to mutual inductances among the several coils in an array of circular coils, the single coil data can be used to calculate the grad$(B/NI)^2$ at any location within such an array. This has been done for certain directions for four such systems; two are the cube and tetrahedron systems studied previously in this laboratory in which the radius of the spherical volume enclosed by the coils is equal to twice the radius of each coil; the other two are the cube and tetrahedron systems in which the radius of the spherical volume enclosed by the coils is equal to one-half the radius of each coil. The latter arrangement will be referred to as an "overlap" configuration due to the fact that windings of the coils must cross windings of other coils in the configuration.

The reason for the sharp division in values of the parameter which is the ratio,

$$\frac{\text{spherical volume radius}}{\text{coil radius}}$$

into ranges near two or one-half is the desire to avoid values of this parameter near unity. A coil radius nearly equal to the radius of the sphere on which the coils are circumscribed would lead to very large mutual inductances between coil pairs. Laboratory studies had previously indicated engineering complications in operation of such a highly inductively coupled system. Experiments had indicated that the mutual inductance effects were tractable when the coil radius did not greatly exceed 1/2 the radius of the sphere to which the coil planes are tangent. Since it is known that these mutual inductances would also be small if the coils are large enough so as to cross nearly at right angles, this latter configuration, known as the "overlap" configuration was also studied. As reported in detail in ref.(1), however, the overlap configurations must be rejected on the grounds of unsuitability of the force fields which they produce.

The component of the total force directed inward along three axes of symmetry was calculated for each of these systems by computing grad B^2 and its direction by superposing results from the several single coils along appropriate axes.
These three axes are listed below.

1. Axis of a single circular coil
2. Axis of symmetry between two adjacent coils (angle for cube is 45°; for tetrahedron 54.8°)
3. Axis of symmetry among three adjacent coils (angle for cube is 54.7°; for tetrahedron 70.8°).

These data are plotted for an enclosed spherical volume of diameter 5.0 cm in Figure 8 for the cubical coil arrangement with coil radius equal to one-half of the enclosed sphere radius. Because of the existence of gradients within the

specimen volume, these calculated values of force for a conducting sphere of any appreciable size (such as a 1 cm diameter sphere in a 5 cm diameter volume) are expected to be somewhat smaller than the actual forces.

Other calculations were done for circular coils in a tetrahedral arrangement and for a cubical arrangement of the overlap variety. The resulting values of grad B^2 were less favorable for these other arrangements and so are not shown here.

Field and Force Computations for Opposing Hemispherical Coils

The earliest work to develop simplified position control servo damping for specimen oscillations by means of electromagnetic position sensing was carried out in this laboratory in late 1972 utilizing a single hemispherical coil with vertical axis. This type of coil, or variations thereof, had previously been studied for terrestrial levitation work in which the axial field gradient is made large compared to the radial gradient in order to maximize levitation forces. This type of coil is known to have relatively high efficiency for RF induction heating which can be increased when utilized with the position stabilizing servo which allows much tighter coupling to the specimen through minimization of coil size.

We give here a summary of results of computations carried out to adapt an opposing pair of such coils to the zero gravity environment. The second opposing coil substitutes for the role of gravity in the simplest terrestrial arrangement in that it returns a specimen to the first coil as the specimen drifts away from the first coil and vice versa. A number of variations of coil spacings and windings were analyzed to find that configuration giving nearly equal square field gradients (grad B^2) in the three orthogonal directions. In Figure 9 the results of calculation of $(H/I)^2$ ($=(B/I)^2$ in gauss units) vs. distance from the center of such a pair of coils is shown. It was assumed in this calculation that each coil of each pair is as described in the sketch of a single coil above the graph and that each coil of each pair has the same amount of current flowing through it but at different frequencies so the force fields due to the two coils in each pair may be considered to be independent of one another. This situation is one which would be found in a cup coil pair when the pair is inductively heating a specimen, while also containing the specimen assuming no benefit of any position sensing system and control loop. The force at a point may be obtained by taking the slope of the plotted curves. The cup coil pair labelled "D" was the system chosen for use in the preliminary coil comparison based upon point values of H.

Magnetic Flux Density Calculation for Several Baseball Coils

The term "baseball coil" in this report is used to describe a coil wound on the surface of a sphere, much like the seam of a baseball, in such a manner that the coil results in four arcs or segments of a plane circle, each arc joined to two others at its ends. A sketch of such a coil is given in Figure 10. Other

configurations are possible where the winding does not consist of such planar segments. However, it is found that by considering the coil family consisting of four such contiguous planar sections where only the angles of the planes with respect to one another are varied over a large range, configurations can be found which give nearly symmetrical field gradients in the central region.

In Figure 11, the several baseball coils are identified by the parameter "s" which is the closest spacing between two portions of the coil in the x-y or x-z planes, defined in that figure. The parameter s is given in increments of 0.50 cm except in two cases. Instead of 3.50, a value of 3.54 was selected to give a coil in which the plane arcs on opposite sides of the x-axis are parallel to one another, i.e. the coil is then somewhat like an "Alice" coil, and a value of 2.15 cm is given because this is the value of s for the coil used in force measurements in the laboratory.

We note that s = 2.5 represents an optimum with respect to yielding approximate symmetry to the height of the "potential barrier" B^2 in orthogonal directions.

Optimization of Cusp Coil

A number of computations were carried out for flux densities and gradients of B^2 (or equivalently H^2) for cusp coils over a range of ratios of coil diameter to coil plane separation. The sketch shows the coil configuration and nomenclature for the separation s of the two coil planes. Figure 12 shows the values of grad B^2 when the squared field is averaged over the specimen volume to compute grad B^2. It is seen that a coil separation of 2.6 cm gives approximate symmetry in the radial and axial forces for small specimens for displacements as great as 0.75 cm. from the center.

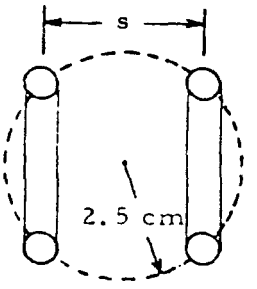

Forces From Cusp Coil

Some forces were measured in the laboratory in order to confirm the magnitude of the computed forces, since in the case of cusp coil near the central position where the field vanishes, the difference obtained in computations with or without field averaging over specimen volume should be especially important. The coil configuration for the laboratory test set-up is shown in the sketch on Figure 13. The two turn cusp coil had a 2.0 cm mean radius with a 2.7 cm spacing between coils. The calculations took actual account of the two separate but closely spaced windings on each coil and also computed grad B^2 averaged

over the spherical specimen volume at each point. Since a computer program was available which averaged B^2 values over a 2.0 cm diameter sphere whereas the experiment utilized a 2.5 cm diameter aluminum sphere, scaling of the theoretical computation were made before plotting as the solid curves in Figure 13. Scaling will be discussed below. Also shown as the dashed line are the axial forces measured with the balance arrangement described previously.

Comparison of Several Coil Types When Used With Small Specimens

Coil Types and Assumptions

The coil comparisons of Reference [1] are all made corresponding to a configuration for which the coils are wound upon a 5 cm diameter volume within which the specimen is free to move. The scaling laws for B^2 and grad B^2 which show that the comparisons given below will be valid when comparing any two systems of the same dimensions will be discussed later.

The types of coils considered in detail were 6-coil cube, baseball, cup coil pair, and cusp coil. The same relatively small spherical specimen is assumed to be present in each coil. The assumptions in the comparisons are listed below.

A simple sketch of each type of coil, of the dimensions assumed in this comparison, is given in Figures 14 through 17. The configurations given here have been optimized based upon computations described previously.

Numbers illustrating the relative resistance of each coil type are developed in Table 1 in which it is assumed that the skin depth in the copper tubing of which the coils are made is considerably smaller than the radius of the tubing. Hence the relative power dissipation P is proportional to the total length of tubing through which current passes and inversely proportional to the diameter of the tubing. In magnetic field and winding length calculations the current is assumed to lie on a filament on the tubing's axis. Computations given later take account of skin depth and proximity effect for the multiple turn coils finally selected.

Table 1. Relative Resistances of Coils

Coil Type	No. of Coils Excited, n	Length of Coil, ℓ	Dia. of Tubing*, d	Relative Power, P**
Cube	1	7.9 cm	1.1 cm	7.2
	3	23.7		21.6
	6	47.4		42.2
Baseball		24.9	0.9	27.7
Cup Coil Pair	1	92	0.6	153
	2	184		306
Cusp Coil		26.4	1.1	24.0

*Maximum size consistent with the volume which is available
**Per unit current

Containment Ability per Unit Power

The value of H^2/I^2 at the center of each coil and the maximum value of H^2/I^2 on the surface at which the force exerted upon the spherical specimen is zero are given in Table 2 as well as the difference $\Delta(H/I)^2$ between these two values. This difference is proportional to the depth of the potential well (from the fact that force is proportional to grad H^2) which contains the specimen, and in the case of coil types containing more than 1 single-frequency coil, e.g. cube and cup coil pair, this assumes suitable position sensing and switching of power to the proper coil(s). The last column in Table 2 gives the ratio of the differences to the corresponding figures from Table 1 to yield numbers proportional to the depth of the potential well per unit power dissipated in the coil. Note that no dimensions are given here since the absolute resistivity of the coil has been omitted for simplicity.

Table 2. Ability to Contain a Specimen

Coil Type	No. of Coils Excited, n	H^2/I^2 at Center	(H^2/I^2)min on F=0 Surface	$\Delta\left(\frac{H}{I}\right)^2$	$\Delta\left(\frac{H}{I}\right)^2/\frac{P}{I^2}$
Cube	3	0.006	0.018	0.012	5×10^{-4}
Baseball		0.008	0.051	0.043	16×10^{-4}
Cup Coil Pair	2	1.3	1.9	0.6	20×10^{-4}
Cusp Coil		0.0	0.050	0.05	21×10^{-4}

Positioning Ability per Unit Power

The maximum force per unit power dissipated in the coil is evaluated in Table 3 by starting with the maximum average gradient in H^2/I^2 between the center of the coil and a distance 0.5 cm from the center and then again dividing by the corresponding relative resistance.

Table 3. Ability to Resist an External Force Along Strongest Axis

Coil Type	No. of Coils Excited, n	Maximum Gradient Near Center	Max. Grad/ $\frac{P}{I^2}$
Cube	1	0.012	17×10^{-4}
Baseball		0.03	11×10^{-4}
Cup Coil Pair	1	0.59	38×10^{-4}
Cusp Coil		0.04	17×10^{-4}

If the Table 2 value for the heating efficiency of the cusp coil be expected as an anomaly to be treated later, all of the systems considered receive appreciable scores in all areas. The cup coil pair receives the highest score when all

columns are considered. When account is taken of the anomalous situation of the cusp coil as regards this simple comparison it appears that all of the above four systems are capable of adequate performance.

In conclusion it may be said that the studies of magnetic field configurations summarized here have served to optimize each coil configuration type but do not serve to make the final recommended choice, other than the rejection of a few coil types. The final choice rests upon overall engineering considerations, including accessibility, efficiency for RF heating, suitability for use with simple electromagnetic position sensing(which is closely related to induction heating efficiency) and suitability for use in conjunction with electron beam heating.These require more detailed considerations.

In the facility capability studies given later it is seen that the primary limit to the capabilities of the Containerless Processing Facility will be the total power availability. The main power requirement is for furnishing surface radiation loss for the highest melting specimens such as tungsten. Since electron beam heating should be considered for many specimens for which it can yield a higher efficiency than RF heating. The ability of the facility to maintain the specimen accurately in the focus of an electron beam when subject to forces due to electron or ion bombardment and differential outgassing is important. For RF heating efficiency, it is necessary to consider specimen volume field averaging and to place great reliance on laboratory measurements because of the importance of this parameter.

Overall Facility Engineering Considerations

The optimization of the various coil and field configurations with each coil type and the elimination of a few of the candidate types was made possible by the field and field gradient considerations given previously. Amongst the remaining candidates, namely the b-coil, baseball, opposing hemisphere (or cup pair) and cusp configurations, some overall considerations of facility engineering and complexity may be applied. We may consider the finalists in more detail with regard to the following engineering criteria.

1. Mechanical accessibility for specimen introduction and removal including accessibility for observation of the process.

2. Compatibility with the simplest electromagnetic position sensing for damping of position oscillations.

3. "Stiffness" of control near the central position or the ability to maintain the specimen in the focus of an electron beam when subject to the attendant thrusts.

4. Engineering complexity due to cross coupling of multi-coil systems. Especially important because of the requirement (to be shown later) for operation over a wide frequency range.

Specimen Accessibility within Coil Configuration

Figure 17 shows that the cup coil pair receives a low score in this area unless the opposing coils would be made mechanically movable with respect to one another. The cubic arrangement also gives relatively poor accessibility for specimen introduction or ejection when large specimens are considered. Scaling up the size of the coil for a given specimen size would increase accessibility but would also cause a large decrease in RF heating efficiency and achievable force per unit power so that it is necessary to consider the comparison between coils on the basis of equal relative scaling of specimen and coil dimensions.

Compatibility with Electromagnetic Position Sensing

Detailed analysis has shown that the 6-coil system is not adaptable to electromagnetic position sensing unless considerable electronic development were to be carried out. This is due to the large number of mutual inductances amongst coils. Detailed measurements also showed that the signal sensitivity for electromagnetic position sensing with opposing hemispherical coils is quite low.

Although work has been done to develop an electro-optical position sensing system for use with the 6-coil arrangement, this system is much more complex than the corresponding electromagnetic position sensing scheme later developed in this laboratory. The latter is expected to be much less subject to influence of metallic vapor deposits, etc. than would electro-optical sensors even when such sensors are protected by mirror optics and baffles. The recent development of this servo control system which can damp specimen oscillations by detection of changes in RF loading upon the coil system can be regarded as a development which has superseded the earliest development of three dimensional position control and damping. This servo system is adaptable to the other final system candidates, e.g. baseball and cusp.

"Stiffness" of Control Near Central Position

Since, for some low resistivity specimens, electron beam heating and melting may be more efficient as regards total required power, than eddy current heating, the suitability of the position control system to maintain the specimen accurately at the focal point of an electron beam will be important. For this reason the following computations were made of the distance through which a 2.0 cm diameter sphere with large x-parameter (ratio of radius to skin depth) will be pushed by a constant external force, such as might be caused by an electron beam, while suspended in a coil system in a weightless environment. Three different coil systems were assumed, all circumscribed on a 5 cm diameter sphere. Because of the low sensitivity of electromagnetic position sensing mentioned for the opposing hemispherical coils it was known that the "stiffness" of this system would be low and hence was not evaluated.

By assuming several amounts of power absorbed by a facility containing such coils, as listed in Table 4, a displacement from the center of the coil may be found at which the force generated is equal and opposite to the external forces given.

Table 4. Coil Stiffness

	Total Power to Facility	Displacement from Center for F = 5 dynes	10 dynes	50 dynes
Baseball Coil	1000 watts	0.1 cm	0.2 cm	0.4 cm
	500	0.2	0.3	0.5
	250	0.3	0.4	0.8
	100	0.4	0.5	1.1
	50	0.5	0.8	*
Cusp Coil	1000	0.0005	0.001	0.005
	500	0.0009	0.002	0.009
	250	0.002	0.003	0.02
	100	0.005	0.01	0.05
	50	0.009	0.02	0.09
Six-Coil Cube	1000	0.01	0.02	0.08
	500	0.02	0.04	0.12
	250	0.04	0.07	0.23
	100	0.09	0.15	0.42
	50	0.15	0.24	0.58

*Coil unable to contain sphere.

Comparison of the data of Table 4 shows that the "stiffness" of the particular cusp coil studied exceeds by about an order of magnitude the stiffness of even the 6-coil cube system in which unequal excitation of opposing coils is employed. The particular cusp coil selected for study here is one which has somewhat more axial stiffness than the configuration giving equal axial and radial gradients referred to previously. It is believed that such a choice would be appropriate when high powered electron beams are employed in order to minimize displacement of the specimen being heated. Thus the cusp appears to be a logical choice to be made for those situations in which electron beam heating is employed at high powers and rather rigid control of specimen position is required.

Computations of Induction Heating Efficiency

From the detailed results which are available for magnetic field distributions and coil losses including proximity effect, it is possible to compute the fraction of total coil power which is transferred to the specimen. These evaluations are important not only to estimate total power requirements for heating

and melting various specimens but also are important in determining feasibility for electromagnetic position sensing which depends upon appreciable changes in specimen power absorption as the specimen position changes. Figure 18 shows results of computations for a specific baseball winding at several frequencies as a function of specimen resistivity. It is seen that the heating efficiency increases with specimen resistivity up to a maximum value which depends upon the operating frequency. In the limit of very high facility frequencies the heating efficiency increases continuously with specimen resistivity until an asymptote is reached.

Computations and measurements were made for heating efficiency of a 5.0 cm diameter baseball winding, versus frequency, with 2.50 cm diameter specimens of resistivities corresponding to those of aluminum and steel. These results are shown in Figure 19 as the solid curves. Figure 20 gives corresponding calculational data for a cusp coil of dimensions as illustrated in that figure. The equation $P = 3\pi F(x)a\rho H^2$ (MKS) was used for values of frequency ranging from 1 KHz to 300 KHz and resistivity values of 4×10^{-6} ohm/cm and 74×10^{-6} ohm/cm. The latter were chosen to represent the electrical resistivity of the aluminum and steel spheres used in experimental measurements about to be described. The heating efficiencies were obtained by dividing the computed power dissipated in the specimen by the sum of that power and the power dissipated in the coil. An average value of H^2 over the regions concerned was estimated from computer calculations of H^2 for several points in, or near, those regions.

Recommended Coil Configurations for Early Space Laboratory Electromagnetic Containerless Processing Facility

The two systems which appear from an overall engineering point of view the best based on all of the above considerations appear to be the baseball and cusp arrangements. RF heating efficiency measurements for relatively large specimens do not serve to markedly distinguish between these two types of coil. For specimens whose size is small compared to the coil dimensions, however, the baseball heating efficiency will obviously be greater than that for the cusp coil because of the field null at the center of the latter. However, the cusp coil shows a much greater "stiffness" to maintain the specimen accurately at an electron beam focus than the baseball. Since, as will appear in the sequel below, both types of specimen heating and melting should be considered in a facility having the widest capability for processing materials of various melting temperatures, it is recommended that the facility for Space Lab be designed to accommodate either type of coil interchangeably. For maximum power efficiency for both positioning or for induction heating, when the latter is used, exchangeable modular coils of sizes commensurate with the specimen size being processed should be considered, just as in the case of terrestrial levitation work. For the higher melting temperature specimens, conservation of total facility power will not allow the low efficiencies customary in terrestrial work when a coil size far from optimum is employed. The consideration of two types of coil configuration

is compatible with the consideration of an interchangeable set of coils of various sizes. In the following, facility capabilities for handling the various materials and processes considered above are delineated. Both electron beam heating and induction heating are considered.

SPACE LABORATORY FACILITY CAPABILITIES AS FUNCTION OF AVAILABLE POWER

This section summarizes the results of calculations performed to indicate the largest sizes of specimens, for fixed total power, which may be suspended in a cusp coil facility and melted either by electromagnetic induction or by some other source of heat, such as an electron beam. Because of the similarity of efficiency of the baseball for RF heating for larger specimens, which represents the main factor determining required facility power, these capability estimates can also be taken as typical of a baseball facility. These calculations have been performed from the consideration of power dissipated at or near the specimen's melting point, do not account for limitations in the dissipation and removal of large amounts of heat in very small coils and have been based upon laboratory data for which forces acting upon and power dissipated in actual specimens were measured. These laboratory data permit calculation of constants relating magnetic field strength and gradient averages to coil current, actually geometrical relationships, which were then used to calculate the behavior of the coil-specimen system for a range of specimen resistivities, sizes, and optimum frequencies.

The force measuring apparatus described previously and lab measurements of heating efficiency were used to obtain data for this section. The characteristics of the aluminum sphere and of the copper cusp coil were as follows

aluminum sphere		copper cusp coil	
diameter	= 2.54 cm	diameter (spherical)	= 5.0 cm
resistivity	= 4×10^{-6} cm	spacing between loops	= 2.7 cm
		number of turns	= 2
		diameter of conductor, d	= 0.64 cm
		length of conductor, ℓ	= 53 cm
		coil proximity factor	= 1.2

With a frequency of approximately 100 KHz for both force and heating efficiency measurements and a current of 67 amperes rms for the force measurements, the following were measured: Force: 100 dynes, 0.5 cm from center of coil, both on axis and on central plane. Heating efficiency: 10%, at center of coil.

Using the equations

$$F = \frac{1}{4} a^3 G(x) \operatorname{grad}\left(\frac{H}{I}\right)^2 I^2 \quad \text{CGS} \tag{1}$$

$$P_{specimen} = 3\pi F(x)\, a\rho \left(\frac{H}{I}\right)^2 I^2 \quad \text{MKS} \qquad (2)$$

values of the desired constants were obtained, viz.

$$\text{grad}\left(\frac{H}{I}\right)^2, \text{ (0.5 cm from coil center)} = 0.49 \text{ oersteds}^2/\text{amp}^2\text{cm}$$

$$\left(\frac{H}{I}\right)^2, \text{ (at coil center)} = 0.28 \text{ oersteds}^2/\text{amp}^2$$

Selection of Optimum Frequencies

The efficiency of heating an electrically conducting sphere rises continuously with increasing frequency but the rate of increase is relatively slow for values of x greater than 3 and has virtually attained its asymptotic value for values of x greater than 20. The force exerted upon such a sphere per unit power is at a maximum at a value of x of about 3. It decreases rapidly for values less than 3 and less rapidly for values greater than 3. Thus, in general, it is desirable to operate a free suspension system with values of x greater than 3, and no great disadvantage is incurred when operating at values of x not greatly in excess of 20.

Because the cusp coil used in the laboratory was operated with no difficulty at 400 KHz, because a value of x of 3 or greater is attained with 400 KHz for resistivities less than 3×10^{-3} ohm-cm and because the force per unit power changes little with resistivities less than 3×10^{-3} ohm-cm at 400 KHz, 400 KHz was chosen to be the nominal operating frequency corresponding to the laboratory size coil in the calculations for 10^{-5} and 10^{-3} ohm-cm. For calculations at 10^{-1} ohm-cm a frequency of 15 MHz was selected because x = 3 with this combination. For 1 ohm-cm, the same frequency, 15 MHz, was used despite a resulting value of x of 1, because it is at frequencies greater than 15 MHz that losses in the auxiliary circuits are expected to become noticeable by decreasing the efficiency of conveying power into the coil.

Extension to Coils of Different Sizes

In the following, the power required by a cusp coil to position and to melt specimens of varying properties is calculated for the 5.0 cm dia. coil described above and for a 2.5 cm dia. specimen. Then, to determine the maximum size the specimens may have, for a particular limiting value of available power, it is necessary to examine how the power absorbed by the coil and the power absorbed by the specimen vary with the size of the specimen and coil. This section establishes the basis for the "scaling" of the power as the physical dimensions of the system are "scaled."

Let a scale factor K be defined by $K \equiv a/1.25$ cm where a is the specimen radius so that any specimen of radius a is K times greater than the sphere used

in the laboratory. Also, let all physical dimensions of the coil have the same scale factor relationship with the corresponding dimension used in the laboratory. Because the magnetic field intensity in the central region created by current flowing in a coil is inversely proportional to the size of the coil, for constant current, it may be seen that $(H/I)^2$ is proportional to K^{-2} and grad $(H/I)^2$ is proportional to K^{-3}.

Once the operating frequency has been selected for the 5.0 cm dia. coil the resulting value of x must be maintained near optimum with scaling of the coil. This means that the frequency is a function of K. The ratio of sphere radius to skin depth is x, the sphere radius is proportional to K and the skin depth is proportional to the reciprocal of the square root of frequency. Thus if x is to be kept constant, the frequency must be proportional to K^{-2}.

The resistance of the coil is

$$R_{coil} = \frac{\rho_{coil}\, \ell_{coil}}{\pi \delta_{coil}(d-\delta_{coil})} \tag{3}$$

If $d \gg \delta_{coil}$, as is true in all of the calculations in this section, the resistance is proportional to $\ell/\delta d$ which is proportional to $K\sqrt{f}/K = \sqrt{f}$ which is proportional to K^{-1}. Thus R_{coil} is proportional to K^{-1}, when x is kept constant.

In summary, $(H/I)^2$ is proportional to K^{-2}, grad$(H/I)^2$ is proportional to K^{-3}, f is proportional to K^{-2}, R_{coil} is proportional to K^{-1}. The application of these relationships is in the scaling of several equations used in the following.

Induction Heating

The power, P_{spec}, required to melt and superheat specimens with melting points of 1000, 2000 and 3000°C was assumed to be 1.2 times the power required to maintain the specimen (with emissivity of 0.8) at 1000, 2000 and 3000°C. From the equation and $P_{coil} = I^2 R_{coil}$, the power dissipated in the coil was calculated for several values of resistivity, ρ, using

$$P_{coil} = \frac{P_{spec}\, R_{coil}}{3\pi F(x)\, a\, \rho \left(\frac{H}{I}\right)^2 (0.63)} \tag{4}$$

(the factor 0.63 being required to use the equation for P_{spec} with cgs units except for P measured in watts). The sum of the total power consumed by the coil and specimen, $P_{coil} + P_{spec}$, was then calculated and, assuming efficiencies of power conversion as described previously, this sum was multiplied by 2 to obtain the total maximum power required of such a free suspension system. The factor 2 assumes 50 percent for the combined efficiency of power amplifier and power conditioning equipment. The 10 percent heating efficiency already discussed as the base measurement which was scaled for frequency and resistivity

already included the transformer, tank circuit and transmission line losses. A product of RF generator and power conditioning efficiency of 50 percent will be conservative for low and intermediate frequencies where solid state devices can be used and operated directly from batteries. For the case of the smallest, highest resistivity specimens, which require the highest frequencies, vacuum tube amplifiers must be used so that 50 percent would not be conservative for the overall power amp/power conditioner.

In order to account for the need for the coil to supply a restraining force to the specimen it was assumed that a force of the form $F = ka^3$ is required which means $k = 4/3\ \pi\sigma\alpha$, where σ is the density of the specimen and α is the acceleration of the specimen resulting from the application of the force. Assuming an acceleration of 1 cm $sec^{-2}(10^{-3}g)$ and a density of 10 gm/cm^3, a value of 40 was selected for k. Thus $F = 40\ a^3$ in which F is in dynes if a is in cm. This yields a force of 40 dynes for a specimen radius of 1 cm, which is considered adequate as discussed in reference 1. We shall henceforth drop the density variable in order to facilitate an overview of facility capabilities. Acceleration minimums will thus be higher than $10^{-3}g$ for materials whose density is less than 10 gm cm^3. Provision of accelerations considerably above $10^{-3}g$ even for density 10 requires little additional power for most cases considered here. By combining equations (1) and (3), a value of minimum allowed P_{coil} required for positioning alone may be calculated.

$$P_{coil}(\min) = \frac{160\ R_{coil}}{G(x)\,\mathrm{grad}\left(\frac{H}{I}\right)^2}$$

Whenever the value of P_{coil} calculated by equation (4) fell below $P_{coil}(\min)$, the value used in obtaining the total power required by the system was $P_{coil}(\min)$ in place of P_{coil} and with P_{spec} increased a proportionate amount. (They are proportional, one to the other, by equation (4).

Calculation of Maximum Radii

The power radiated by a spherical surface is proportional to the square of its radius, hence P_{spec} is proportional to K^2. By application of the scaling relationships discussed above, P_{coil} is proportional to $\frac{P_{spec} R_{coil}}{a\left(\frac{H}{I}\right)^2}$ which is proportional to $\frac{K^2 K^{-1}}{K K^{-2}} = K^2$. Thus $(P_{coil} + P_{spec})$ and the total power required by the facility is proportional to K^2.

To calculate the radius of the largest meltable specimen at 5000 watts available peak power, the ratio of 5000 watts to the power required for a 2.5

cm dia. specimen was set equal to K^2 and a(max) calculated from 1.25 K cm. Higher peak powers of 10 and 20 kW were also assumed. Reference 1 indicates that peak powers are normally required for times not exceeding a few minutes, which makes consideration of battery furnished peak powers practical. Thus the data for Figure 21 were obtained.

Electron Beam Heating

The power radiated by a spherical surface is proportional to the square of its radius, hence $P_{spec} + P_{eb}$ is proportional to K^2. From equation (1)

P_{spec} is proportional to $\frac{a(H/I)^2 P_{coil}(min)}{R_{coil}}$ which is proportional to $\frac{a(H/I)^2}{grad(H/I)^2}$ which is $K\,K^{-2}/K^{-3} = K^2$. Thus, again the total power required of the system is proportional to K^2 and the maximum specimen radii were calculated as indicated above, for induction heating. The results of these calculations are given in Figure 22.

Discussion of Results

Figures 22 and 23 should not be mistaken for a description of a continuum of possible specimen sizes all obtainable with a single coil. It must be remembered that these figures were drawn for a specific, optimized ratio of specimen to coil size for specific optimized frequencies, for a specific force for each size specimen and for a series of several different coil sizes as identified on the ordinate as a series of specimen sizes. One way Figures 22 and 23 are readily used is by selecting the size of specimen to be processed and then reading to the right to determine the maximum melting temperature that can be attained for the amount of power which is available.

In Figure 22, on the graphs for 10^{-1} and 1 ohm-cm, it may be seen that each of the curves becomes horizontal at its left end. This indicates a region on the graph for which the available power results in insufficient force to meet the minimum force requirement for specimen sizes greater than those indicated by the horizontal line. For systems operating on such a horizontal line, the power dissipated in the specimen, as a result of meeting the minimum force requirement, is in excess of the quantity deemed necessary to heat and melt specimens. If operation on a horizontal line is considered, it will necessitate operating the Containerless Processing Facility at full power only a fraction of time such that the desired temperature is attained without severe superheating. In view of the considerations of accelerations to be encountered in a Space Laboratory, the minimum acceleration requirements of 1 cm/sec^2 may be conservative with 0.1 cm/sec^2 perhaps more likely. If the required minimum acceleration were reduced, the horizontal lines in Figure 22 would rise to higher values of specimen radius.

In Figure 22, the regions described immediately above are left blank because the excess induction heating due to the minimum force requirement renders the electron beam unnecessary. The points, in Figure 23, at which the induction heating just equals the power radiated are marked by large dots inside the data points.

It should be noted that additional consideration must be given to the feasibility for processing the largest size specimens indicated in Figure 22. For specimen radii exceeding several centimeters, hydrodynamic stability of the molten mass whose integrity is maintained solely by surface tension forces must be considered. Elementary estimates indicate that positioning forces will lead to only moderate shape distortions for the largest sizes indicated in Figure 22. Another important physical consideration for these larger size specimens is heat transfer mechanisms within the specimen which will have a major effect upon the time required for melting and may indicate heating power margins other than the 20 percent assumed here to optimize the trade-off between facility peak power and duration of demand for peak power. It is expected that the distribution in depth of joule heating obtained with the higher resistivity specimens and stirring due to electromagnetic Lorentz forces will be important factors to be exploited.

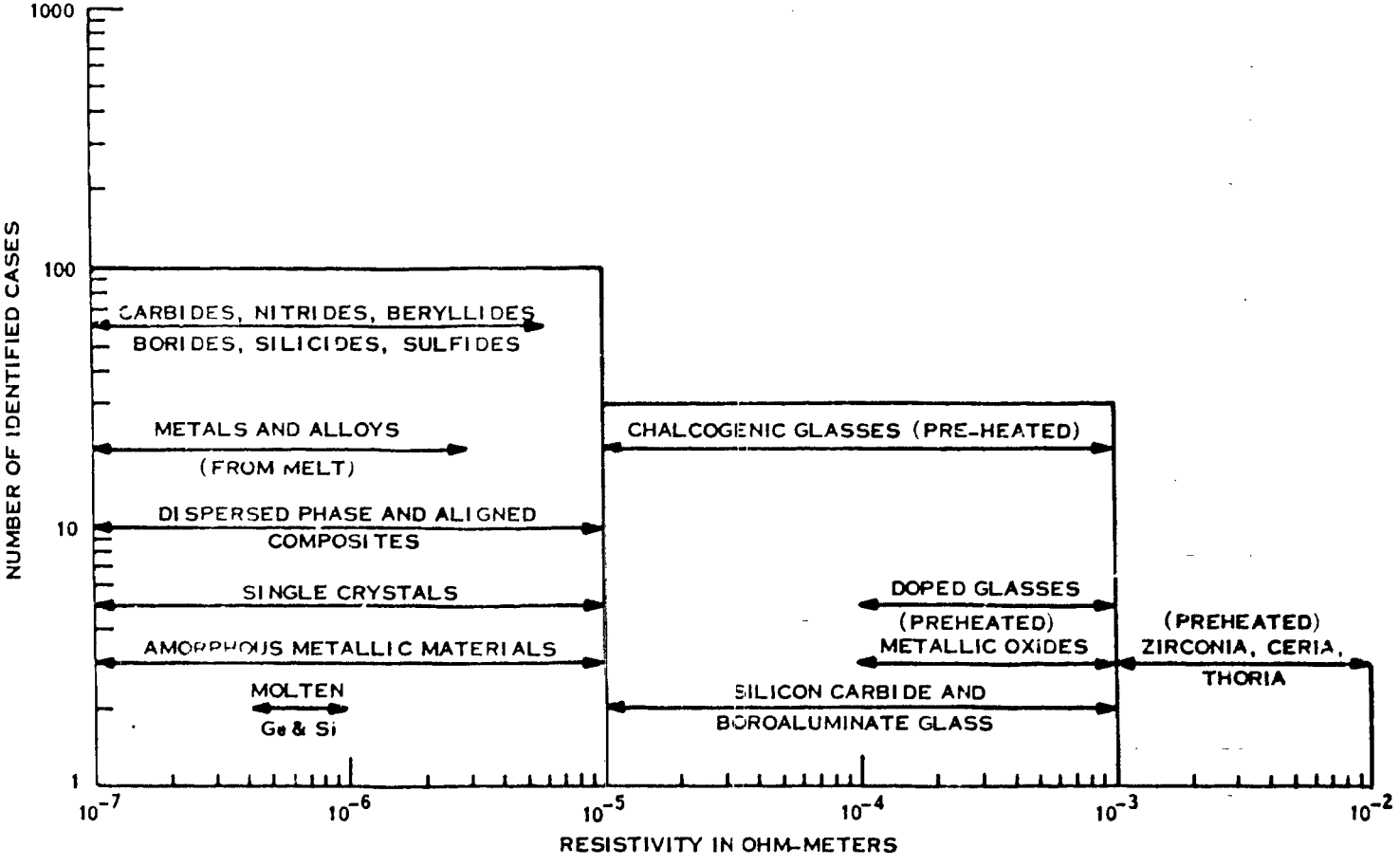

Figure 1. Numbers of Identified Candidate Materials with Various Ranges of Electrical Resistivity

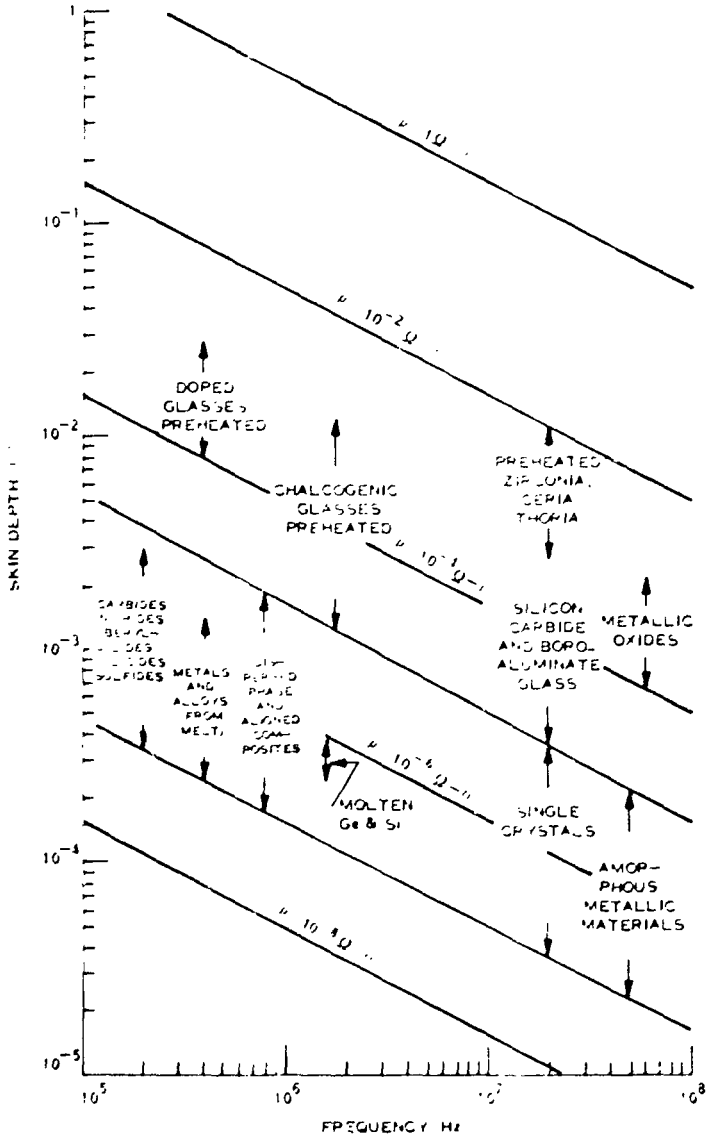

Figure 2. Electromagnetic Skin Depth Versus Frequency and Resistivity

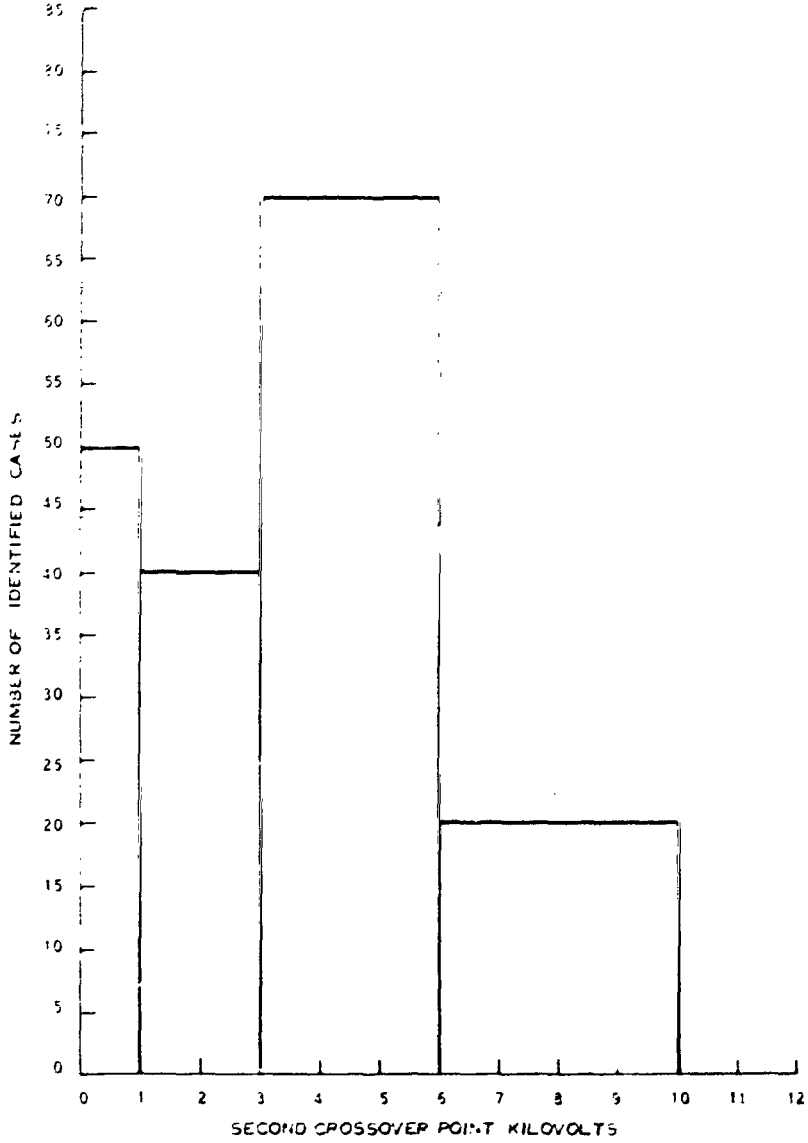

Figure 3. Numbers of Candidate Materials Arranged According to Second Crossover Point in Electron Emission

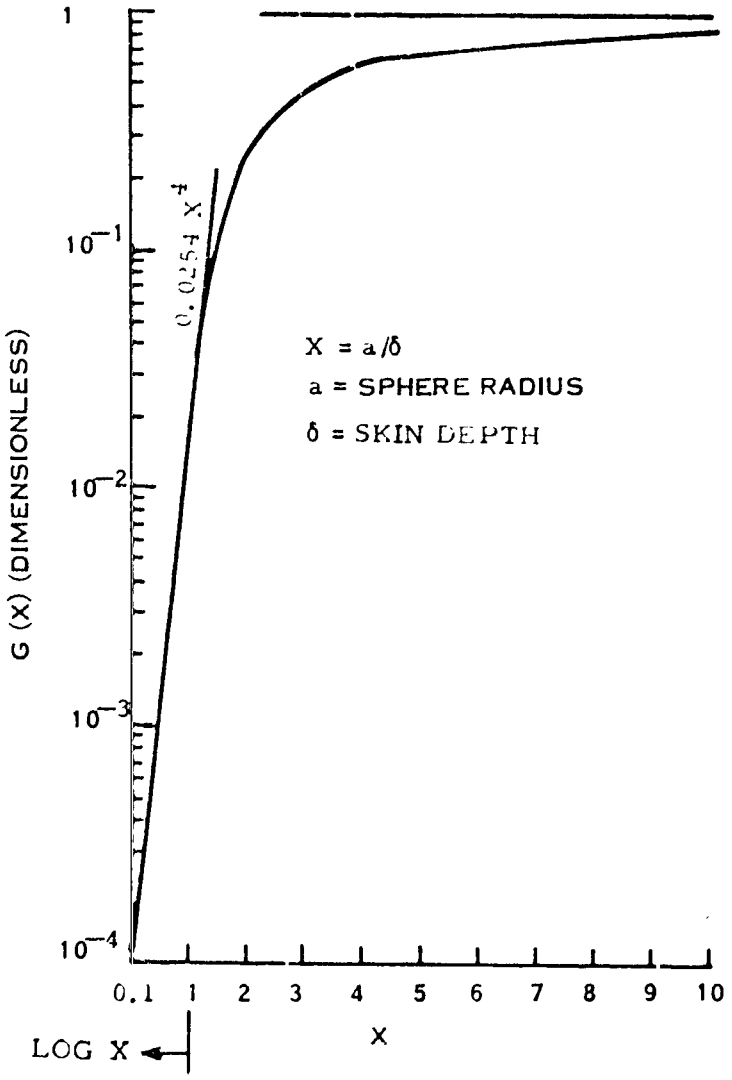

Figure 4. Body Force Function

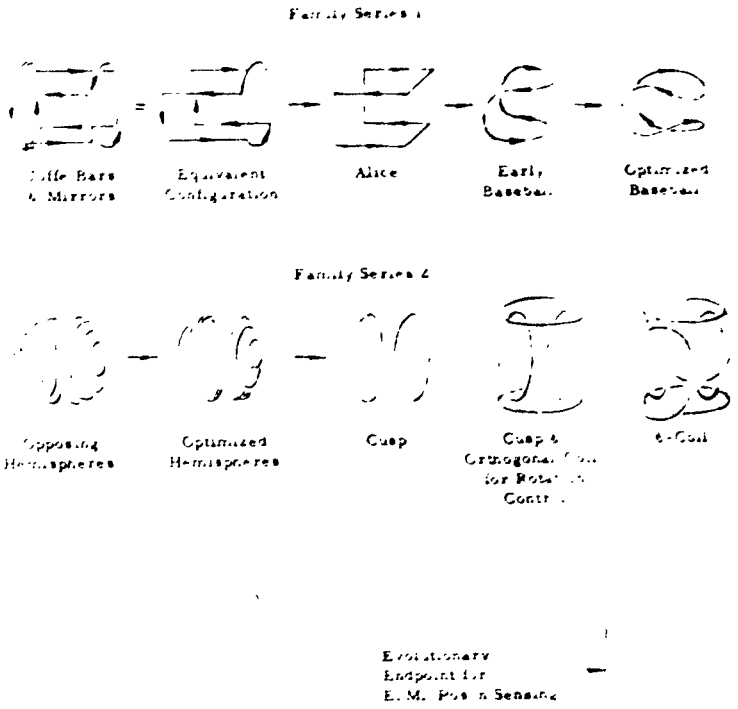

Figure 5. Family Relationships Amongst Various Coil Types

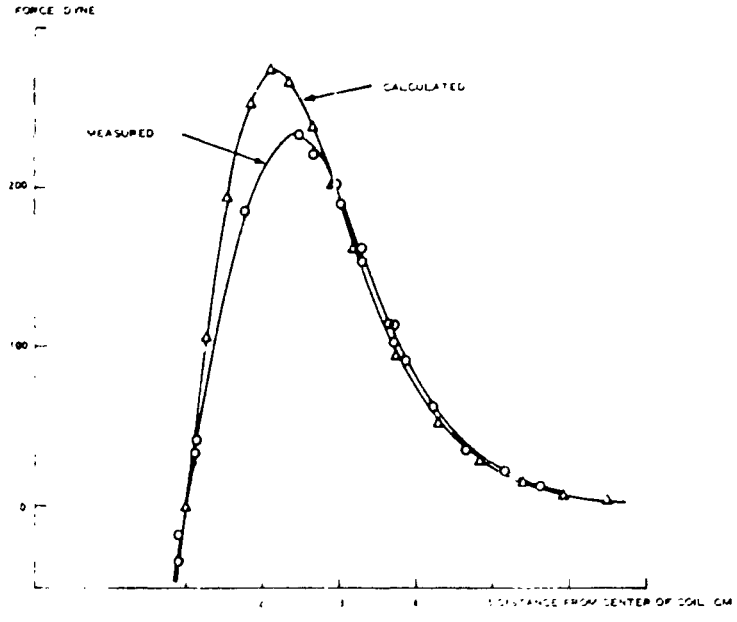

Figure 6. Force Exerted Upon a 2.54 cm Diameter Solid Aluminum Sphere By a 5.5 cm Diameter 3-Turn Circular Coil Carry 50.5 amp (rms), f=100 KHz

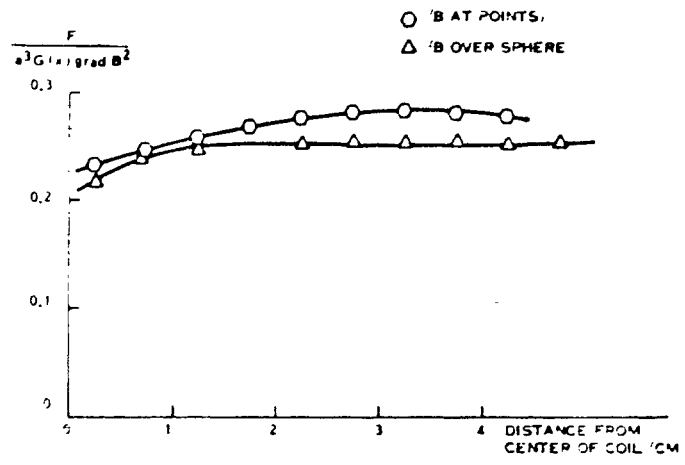

Figure 7. $F/a^3G(x)$ grad B^2 (dimensionless) vs. Distance

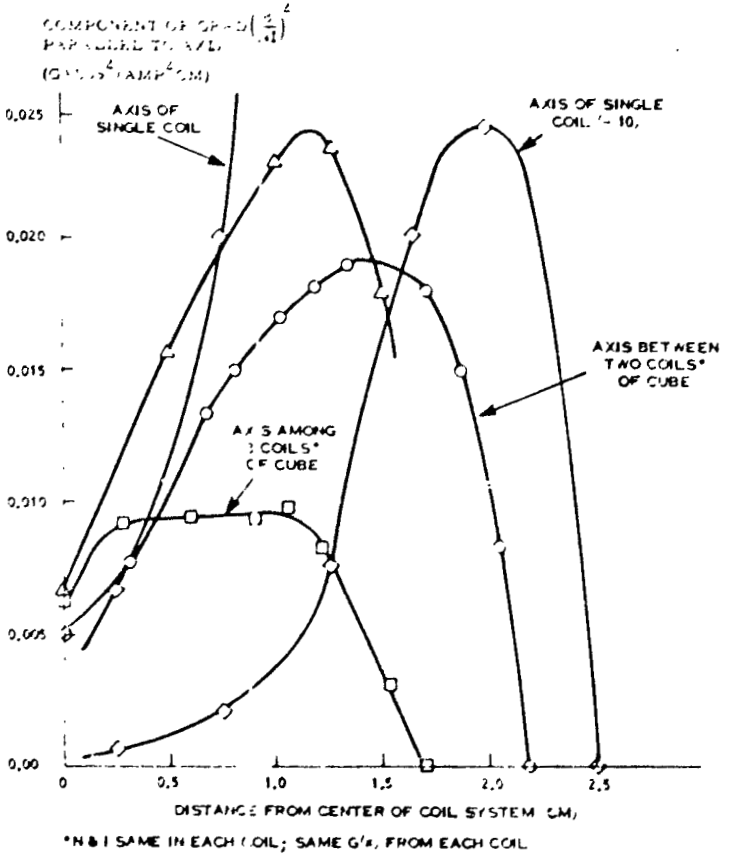

Figure 8. Calculated Force Along Axes of Symmetry for Cube with Coils of Radius 1.25 cm, a Distance 2.5 cm from the Center of the Coil System

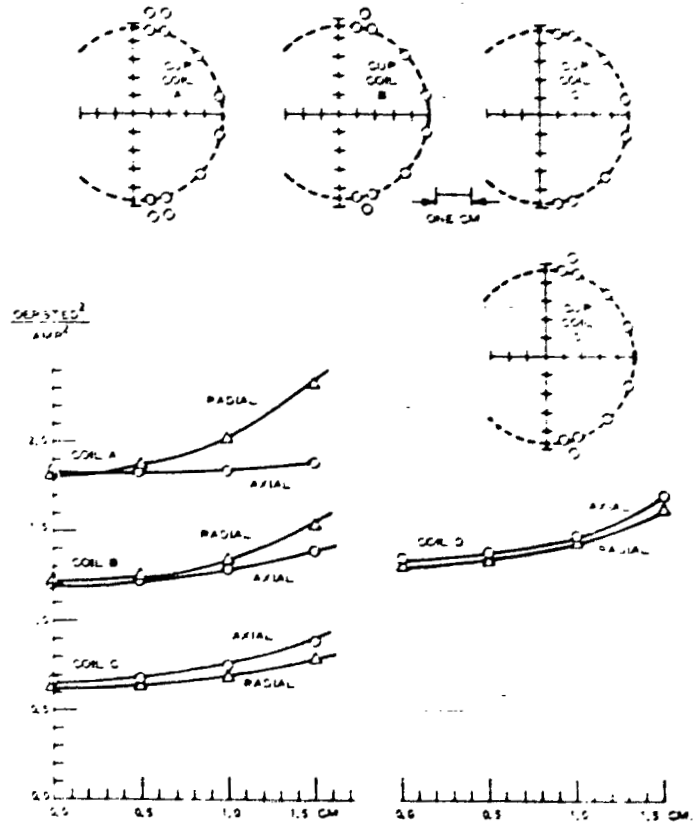

Figure 9. $\left(\frac{B}{I}\right)^2 = \frac{H^2}{I^2}$ vs. Distance From Center of Cup Coil Pair For Several Different Cup Coils

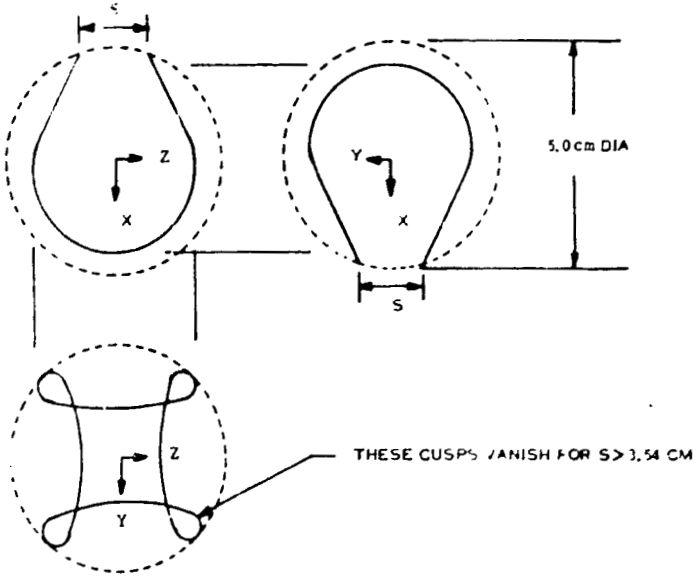

Figure 10. Baseball Coil Geometry

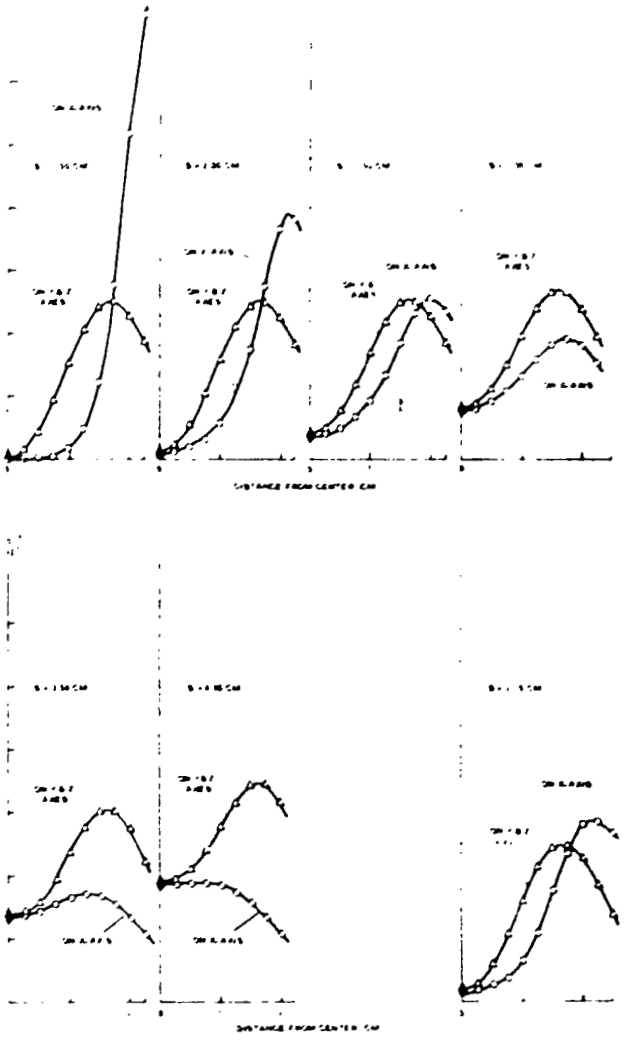

Figure 11. Total Flux Density Squared on Each Axis for Baseball Coil of 5.0 cm Diameter

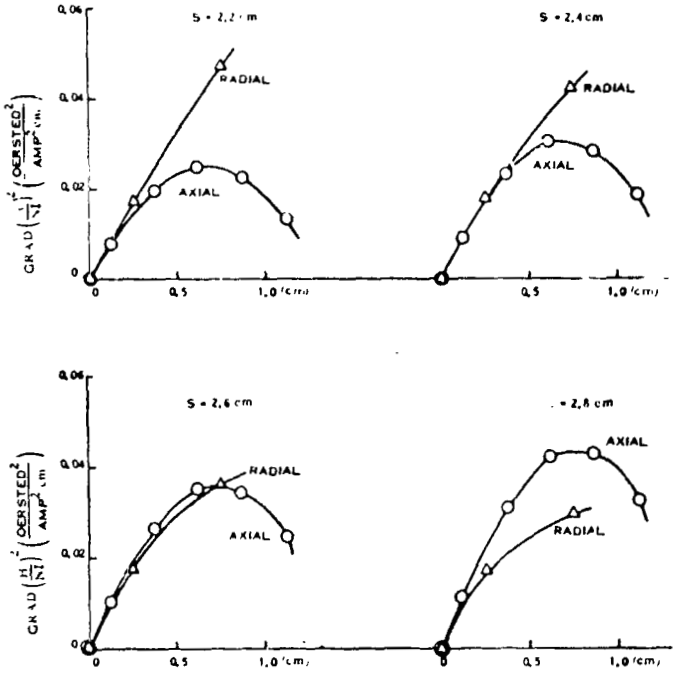

Figure 12. Radial and Axial grad $(H/I)^2$ (Vol. Aver.) for Cusp Coil vs. Distance From Center of Coil for Several Different Coil Spacings (Coils wound on 5 cm dia. sphere)

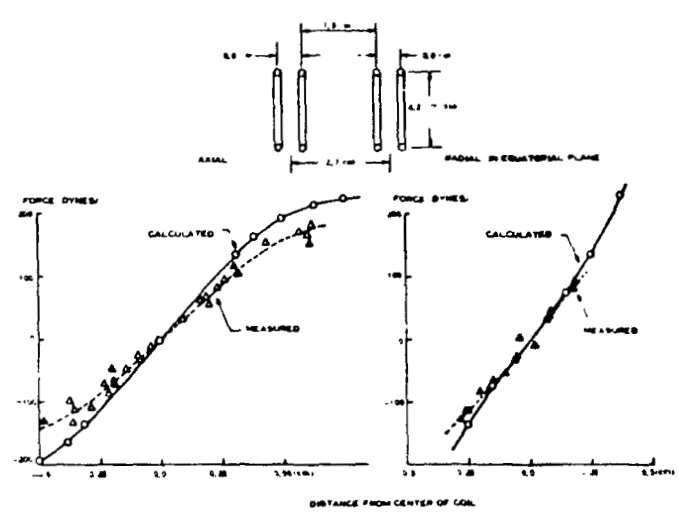

Figure 13. Measured & Calculated Forces In a Two Turn Cusp Coil, 2.1 cm Radius, 2.7 cm "Spacing" with a 2.5 cm dia. Aluminum Sphere. (I = 67 amp, rms)

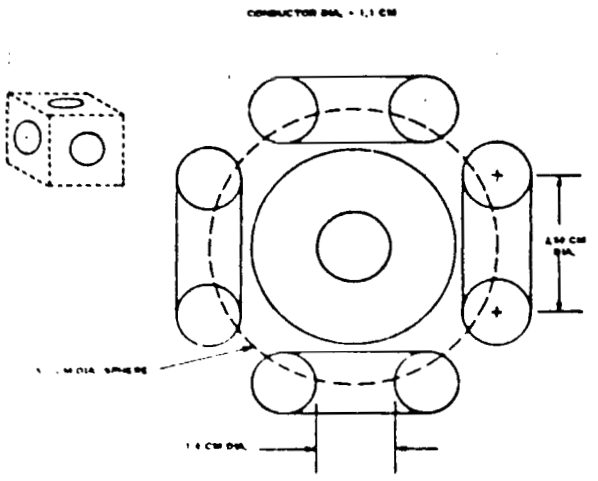

Figure 14. Cube

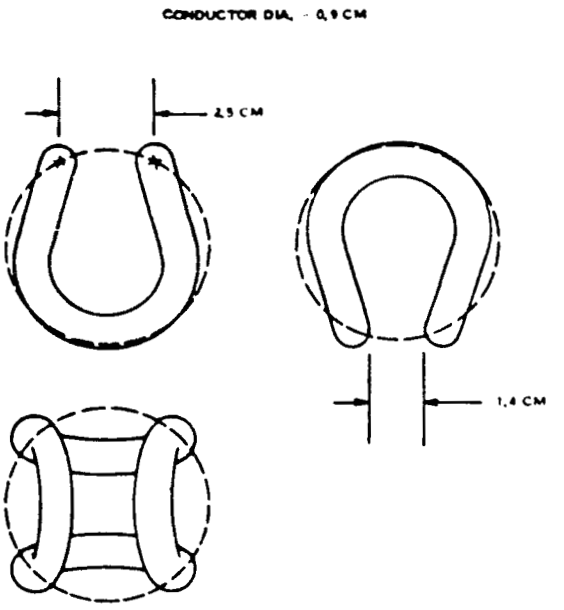

Figure 15. Baseball

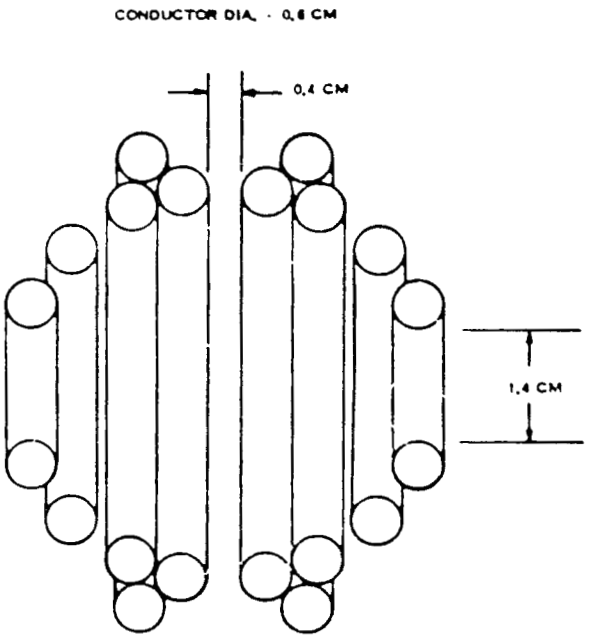

Figure 16. Cup Coil Pair

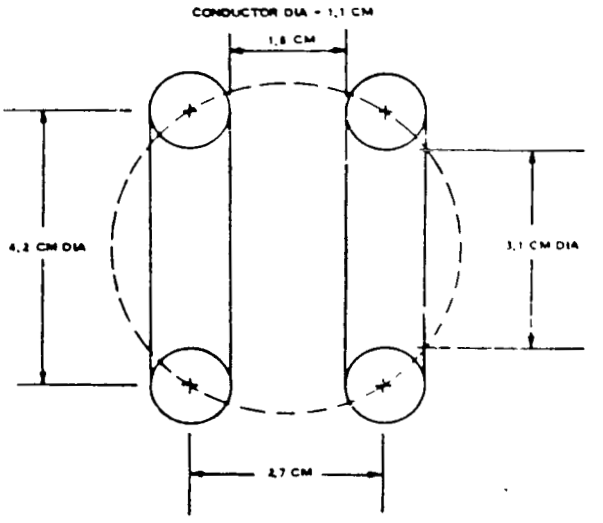

Figure 17. Cusp Coil

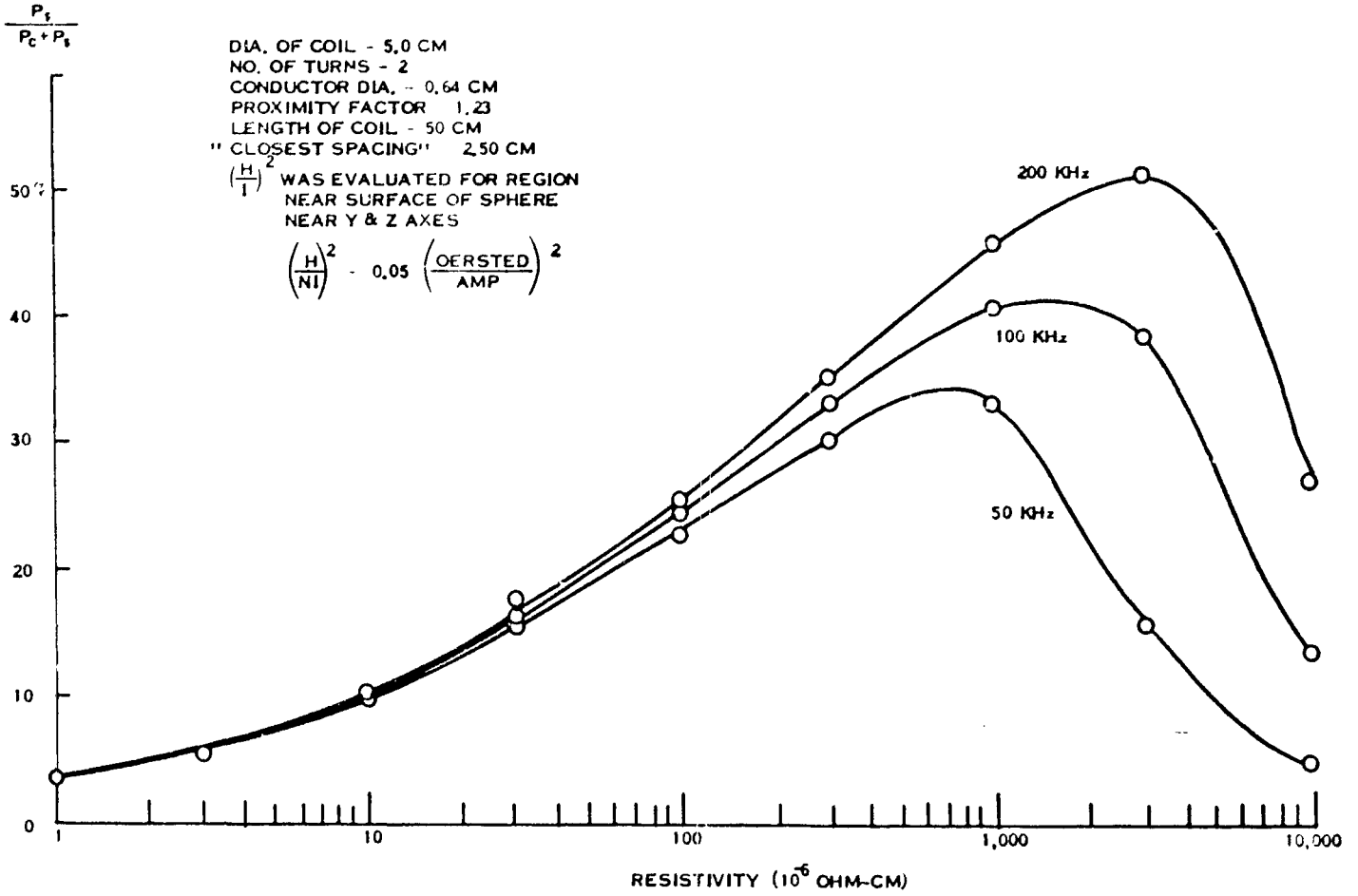

Figure 18. Efficiency of Heating a Specimen vs. Resistivity for a Baseball Coil

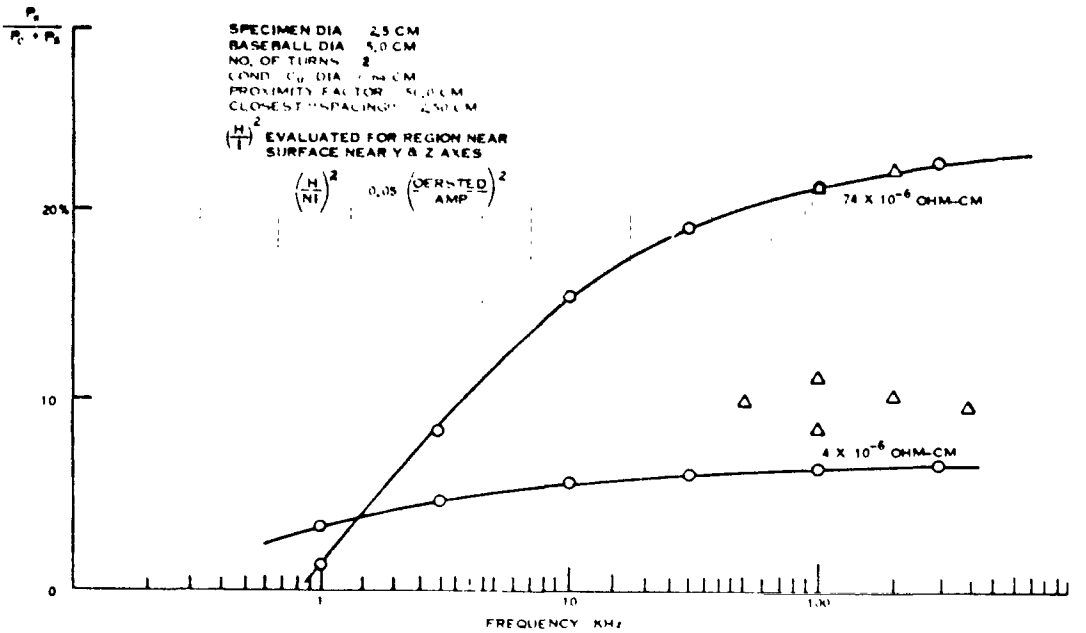

Figure 19. Efficiency of Heating A Specimen In A Baseball Coil

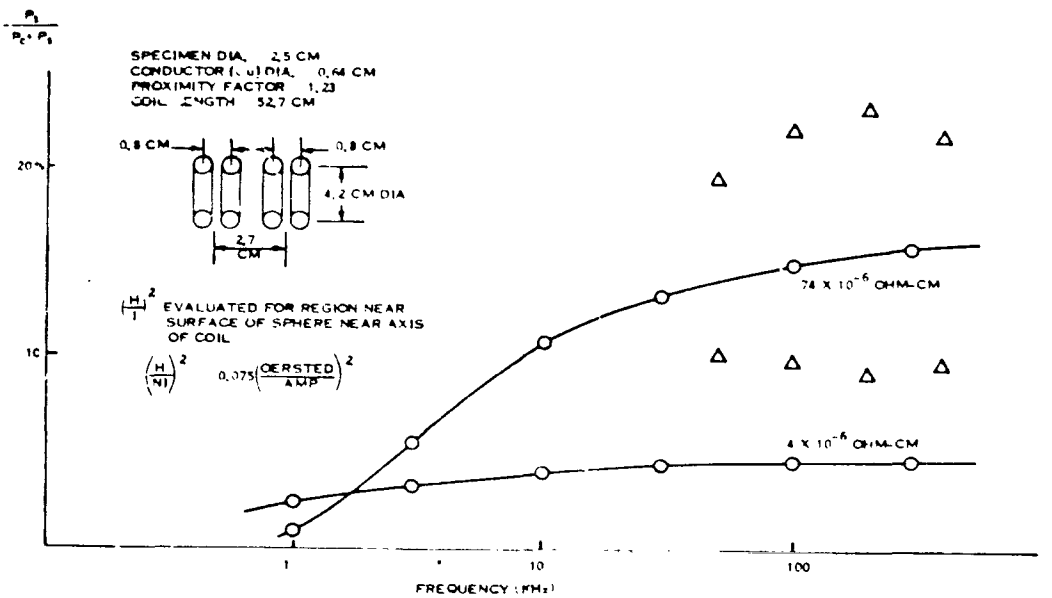

Figure 20. Efficiency of Heating A Specimen In A Cusp Coil

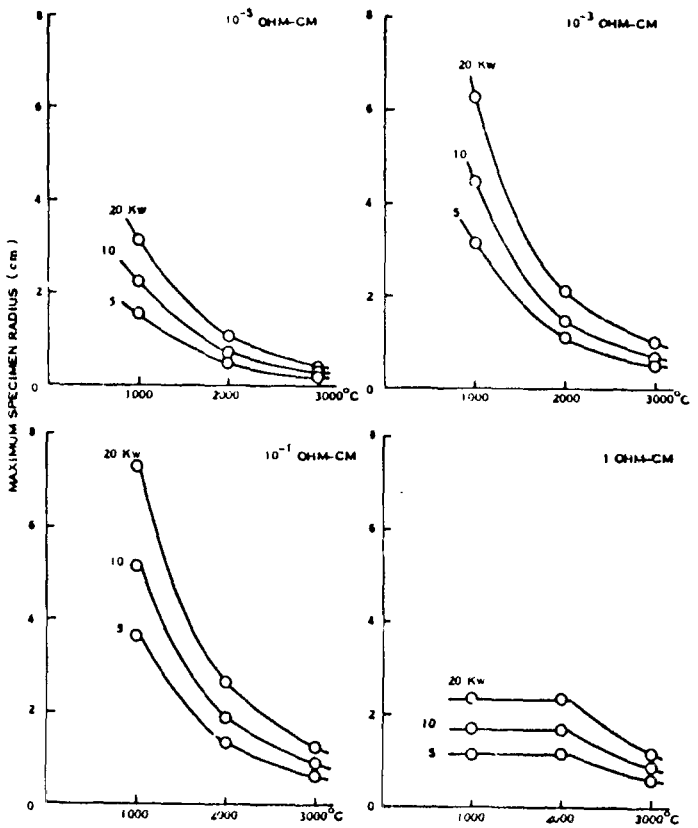

Figure 21. Maximum Radii of Specimens For Various Melting Temperatures and Assumed Total Facility Powers, RF Induction Heating

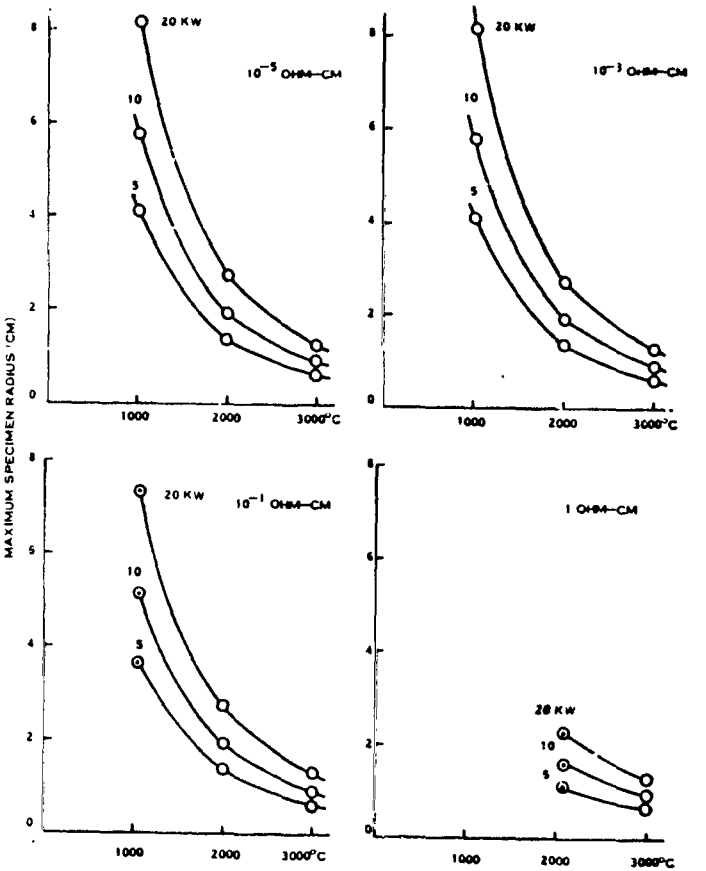

Figure 22. Maximum Radii of Specimens For Various Melting Temperatures and Assumed Total Facility Powers, Electron Beam Heating

REFERENCES

1. Electromagnetic Containerless Processing Requirements and Recommended Facility Concept and Capabilities for Space Lab, General Electric Company, Final Report (Preliminary), Contract NAS8-29680, March 20, 1974.

2. Roberts, O. C., Robertson, D. G. C. and Jenkins, A. E., "The Electromagnetic Levitation of Liquid Metal Sulfides and Their Reaction in Oxygen," Trans. AIME, 245, pp 2413-2420, Nov., 1969.

3. Nelson, L. S., "Techniques for Studying Liquids and Solids at Extreme Temperatures," Advances in High Temperature Chemistry, 4, ed. by Leroy Eyring, Academic Press, N.Y. & London, 1971.

4. Free Suspension Processing Systems for Space Manufacturing, General Electric Company, Final Report Contract NAS8-26157, June 15, 1971.

5. Wuenscher, H. F., "Manufacturing in Space," Astronautics and Aeronautics, 10, p. 42, Sept. 1972.

6. Wechsler, A. E., "Spherical Forming and Composite Casting in Zero-G," Space Processing and Manufacturing, NASA Pub. ME-69-1, 1969.

7. Reger, J. L., "Reduced Gravity Processing of Homogenized Immiscible Metal Alloys," Space Processing and Manufacturing, NASA Pub. ME-69-1, 1969.

8. Frost, R. T., "Techniques and Examples of Zero-g Melting and Solidification Processes," Unique Manufacturing Processes in Space Environment, NASA Pub. ME-70-1, April, 1970.

9. Deeg, E. W., "Glass Preparation in Space," Space Processing and Manufacturing, NASA Pub. ME-69-1, 1969.

10. Happe, R. A., "Possibilities for Producing New Glasses in Space," Space Processing and Manufacturing, NASA Pub. ME-69-1, 1969.

11. Space Processing and Manufacturing, George C. Marshall Space Flight Center, NASA Pub. ME-69-1, October 21, 1969.

12. Study for Identification of Beneficial Uses of Space, Final Report, NAS8-28179, General Electric Company, April 23, 1973.

13. Wouch, G. and Bloom, H. L., "Free Suspension Processing - A Review of Selected User Interests and Requirements," paper to be presented at AIAA/ASME Thermophysics and Heat Transfer Conference, Boston, Mass. July 15-17, 1974.

14. Toth, Louis E., Transition Metal Carbides and Nitrides, Academic Press, N. Y. & London, 1971.

15. Samsonov, G. V., Refractory Transition Metal Compounds, High Temperature Cermets, Academic Press, N. Y. & London, 1971.

16. Margrave, J. L., Treverton, J. A. and Wilson, P. W., "The Use of Levitation in Inorganic Synthesis," High Temperature Science, 3, pp 163-167, March, 1971.

17. Machlin, I., Begley, R. J. and Weisest, E. D., Refractory Metal Alloys, Metallurgy and Technology, Plenum Press, N. Y., 1968.

18. Smythe, W. R., Static and Dynamic Electricity, McGraw-Hill, New York, 1950.

19. Fromm, E. and Jehn, H., "Electromagnetic Forces and Power Absorption in Levitation Melting," Brit. J. Appl. Phys., 16, 653, 1965.

20. Wang, T. G., "Acoustic Positioning Chamber," to be presented at the Third Space Processing Symposium at the George C. Marshall Space Flight Center, 1974.

21. Whymark, R. R., "Acoustic Field Positioning for Containerless Processing," to be presented at the Third Space Processing Symposium at the George C. Marshall Space Flight Center, 1974.

22. Bunshah, R. F., Vacuum Metallurgy, Reinhold Pub. Corp., N. Y., 1958.

23. Okress, E. C., Wroughton, D. C. Comenetz, G., Brace, P. H. and Kelly, J. C. R., "Electromagnetic Levitation of Solid and Molten Metals," Jrnl of App. Phy., 23, No. 5, p. 545, May, 1952.

N74 29911

ACOUSTIC FIELD POSITIONING FOR CONTAINERLESS PROCESSING

By

R. R. Whymark
Intersonics Incorporated
Chicago, Illinois 60611

SUMMARY

The non-contact positioning of materials in a space processing chamber is accomplished using a new type of acoustic levitator. Liquid and solid materials are positioned using a single source of sound. Fine control of position may be obtained by motion of an acoustical reflector. Electrical power required is usually less than 100 watts. The system operates satisfactorily at high and low temperatures and is adaptable as an "add-on" feature to existing space experiments. Containerless melting and solidification can be performed and a freely suspended liquid can be shaped to the contour of the sound field. Experiments are described in which aluminum, glass and plastic materials are melted and solidified in the containerless state. The system has applications to containerless crystal growth, melting and related processes.

INTRODUCTION

Manufacturing processes undertaken in an orbital space station may be seriously effected by drift of the material being processed. Control of the position of the material is generally desirable. The objective of this paper is to describe a new type of acoustic position control system that can be adapted to existing space processing chambers with minimum modifications to the chambers. The acoustic system to be described departs from existing systems in that only one sound source is used. The single sound source is used to excite the chamber volume into normal modes of vibration. Whenever there is a region in the experiment chamber at which the acoustic potential energy is a minimum, the specimen will be urged towards this region and remain freely suspended, if the acoustic forces are strong enough. Liquid and solid materials can be freely suspended by this method, up to several ounces in weight under 1-g. The shapes of the levitated materials can be spherical or disc-shaped. The spherical bodies are limited in size to about one half wavelength of sound (1.7 cm diameter for a 10kHz levitator). Flat blanks of material can be considerably larger than the half wavelength criterion and still remain stably levitated. Specimens can, under certain conditions, be spun on an axis for degassing purposes, without touching the specimen. The shape of a liquid specimen can also be made to conform to the shape of the localized acoustic field. The system

has been operated in a range of configurations of experiment chambers including rectangular and cylindrical experiments units.

Experiments have been conducted, and will be described later, in which the effect of the levitator sound field on a supercooled liquid has been determined. The indications are that the sound energy coupled into the specimen must exceed the cavitation threshold in the liquid. The cavitation threshold is several orders of magnitude larger than the sound levels that can reasonably be expected to be coupled into the specimens. The indications are that the levitator sound field will not disturb the material processes. This point is given greater credence when the levitator is operated under the low-g conditions pertinent to space processing. The acoustic field strengths can be reduced greatly and thereby further reduce the effects of these fields upon the material being processed.

Several position control systems for space manufacturing have already received study and development by other investigators. The triaxial system developed at the Jet Propulsion Laboratory utilizes three low frequency sound sources and relies upon the opposing action of the acoustic radiation pressure in three crossed sound beams for positioning the object. The electromagnetic position control system, a version of which has been developed at the General Electric Laboratories, utilizes three field coils. The electromagnetic system has the unique advantage of operating in a vacuum but is limited in use to electrically conducting materials.

PRINCIPLE OF OPERATION

A simplified version of the levitator is shown in Figure 1. The sound source consists of a plane circular piston that radiates a beam of sound toward a parallel reflecting surface placed a distance $n\lambda/4$ away, where λ is the sound wavelength in the levitator atmosphere and n is any integer. A standing wave is established between the sound source and reflector as shown by the pressure profile in Figure 2. A body introduced into the sound field will move towards planes of minimum potential energy, corresponding to the planes of minimum sound pressure drawn in Figure 2.

The levitated material is constrained in the sideways direction by the near field pressure of the sound source. Three typical near field pressure profiles are drawn in Figure 2 for successive planes normal to the axis of the levitator. These pressure profiles are obtained by the methods described in Reference 1 and are for a piston radiator 4 sound wavelengths in diameter corresponding to a sound source 7.5 cm diameter resonated in air at 20kHz. The positions of stable levitation correspond to the regions where the pressure is minimized in the combined standing wave field and the near field. These regions are indicated by the small circles in Figure 2. The near field pressure distribution

is circularly symmetric about the levitator axis so that stable levitation is obtained anywhere in a series of successive circular zones spreading outward from the levitator axis, each levitation zone being parallel, and closely neighboring the minimum pressure planes.

For the levitator to operate satisfactorily, the material being levitated should not be so large as to overlap successive pressure minima. The diameter of a sphere, for example, should not exceed one half of a sound wavelength in the gas atmosphere, otherwise pressures will tend to cancel. The limiting sphere size for stable levitation in a 10kHz air-filled levitator at room temperature is 1.7 cm diameter. Flat blanks of material can be levitated larger than the sphere. A specimen blank will come to equilibrium with the plane of the blank parallel to, but displaced a small distance from a minimum pressure plane. The blank thickness (measured in a direction normal to the planes of minimum pressure) should not exceed the half wavelength limit alluded to earlier. However, the lateral dimensions may exceed a half wavelength and are limited by the radial distances between the pressure troughs in the near field. For example, a disc approximately 5.5 cm diameter could be levitated at the minimum pressure plane cc', Figure 2. This distance of 5.5 cm corresponds to the distance between the outer pressure troughs in the near field, at this plane. The estimates of maximum blank diameter are modified by the reflection of sound from the blank itself. The sound reflection from the blank will enhance the standing wave between the blank and the sound source but tend to smear the near field. The sideways restoring forces are reduced so that levitation of the blank may be less stable.

An acoustic standing wave is shown in Figure 3, measured along the axis of an experimental nucleation tube. The nucleation tube was 7.5 cm in diameter and 30 cm in length, driven at one end by a 7.4 cm diameter piston radiator oscillating at 20kHz.

The far end of the metal tube was closed by a close fitting circular reflector that could be moved precisely along the tube axis. The upper curve of Figure 3 shows the increase in sound pressure and the corresponding increase in the gradient of the sound pressure as the gas column is tuned by adjusting the position of the reflector. Maximum sound pressure amplitude is obtained when the separation distance between the source and the reflector is $n \lambda /4$. The completely untuned condition, separation equal to $n \lambda/2$, (the lower curve of Figure 3), results in a reduction in the sound pressure and hence in the levitation force. The reduced gradients of sound pressure in the untuned condition would result in a longer time to restore the levitated body. Plastic spheres inserted into the tuned and excited tube reached their equilibrium positions close to the planes of minimum pressure. The small open circles in the upper curve of Figure 3 show the observed levitation points.

The magnitude of the sound radiation force on a small sphere in a plane standing wave is given in Reference 2 by the equation:

$$F = \pi R^2 \ (kR) \ \rho \ v_o^2 \ .f\left(\frac{\rho_b}{\rho} \ , \ \frac{C_b}{C}\right) \qquad 1.$$

where

R = radius of sphere
k = $2\pi / \lambda$ for the gas atmosphere
ρ = density of the gas
v_o = acoustic particle velocity

$f\left[\frac{\rho_b}{\rho} \ , \ \frac{C_b}{C}\right]$ = 5/6 for solid or liquid bodies suspended in a gas.

The minimum potential energy exists at the velocity antinodal planes as described in Reference 2 at which planes the sound pressure is a minimum.

A solid sphere 0.4 cm radius would experience a radiation force of approximately 1800 dynes which when placed at a velocity antinode in a 20kHz plane standing wave, in which the radiated sound intensity of the source was $1 w/cm^2$ (160 db sound pressure level) and the standing wave gain was threefold. At this acoustic field strength, the 0.4 cm radius sphere could weigh approximately 1.8 grams and remain levitated on earth. This corresponds to a density of about 7 for the sphere. Since higher sound intensities are available, the dense elements evidently can be levitated terrestially, if desired.

Sound adsorption in the levitator gas reduces the distance at which a body can be levitated. For example, the pressure troughs in the standint wave shown in Figure 3 are considerably less pronounced as one moves away from the sound source.

The adsorption of a low intensity plane harmonic sound wave is given in Reference 2 and 3 by the equation:

$$I = I_o \ \varepsilon^{-\alpha\chi} \qquad 2.$$

where

I is the sound intensity
χ is the distance measured in a direction normal to the wavefront
α is the attenuation constant

The attenuation constant is given by the equation:

$$\alpha = \frac{\omega^3}{2\rho C^3}\left[\frac{4}{3}\eta + \eta' + \chi\left(\frac{1}{c_v} - \frac{1}{c_\rho}\right)\right] \qquad 3.$$

where

ω is the regular frequency
η is the shear viscosity coefficient of the gas
η' is the compressional viscosity coefficient
ρ is the density of the medium
c is the velocity of sound
c_v, c_p } specific heats

It is seen that the attenuation coefficient varies as the square of the wave frequency. Thus, operation of the levitator at the lower ultrasonic frequencies results in a greater distance at which the object can be levitated. Also, the absorption given by equation 2 holds only for distances close to the source as mentioned in Reference 2, p 30. At greater distances than one wavelength from the source the absorption is considerably greater than that given by equation 2. The increase in absorption at the fundamental frequency depends upon the wave amplitude and may be an order of magnitude larger than that predicted by equation 2. The curves shown in Figure 3 can be used as a guide to indicate the absorption losses in a 20kHz levitator and the absorption in lower frequency systems can be scaled from these curves.

ACOUSTIC CAVITY ENERGY WELL LEVITATOR

The levitator described in the preceding section represents a limited version of the more general energy well levitator in which resonances are developed throughout the entire three dimensions of the experiment chamber. In this sense, the experiment chamber is viewed as an acoustic cavity that can be excited in a range of high and low order modes - the normal modes of vibration. Typical acoustic cavities are represented by experimental furnace tubes or the interior volume of a muffle furnace, all of which volumes are adaptable directly to energy well levitation through normal mode excitation.

The normal modes of vibration of a rectangular enclosure are given by the following equations obtained from References 4 and 5:

$$\rho_{n_x\, n_y\, n_z} = \begin{matrix}\cos \\ \sin\end{matrix}\left(2\pi\frac{x}{\lambda}\right) \begin{matrix}\cos \\ \sin\end{matrix}\left(2\pi\frac{y}{\lambda_y}\right) \begin{matrix}\cos \\ \sin\end{matrix}\left(2\pi\frac{z}{\lambda_z}\right) \qquad 4.$$

$$f = \frac{c}{2}\left[\left(\frac{n_x}{\ell_x}\right)^2 + \left(\frac{n_y}{\ell_y}\right)^2 + \left(\frac{n_z}{\ell_z}\right)^2\right]^{\frac{1}{2}} \qquad 5.$$

$n_x, n_y, n_z, = 0, 1, 2, 3 - - -$

where

p = sound pressure
c = sound velocity in the gas
λ = sound wavelength

A rectangular cavity is shown in Figure 4 excited in normal mode M_{228}. The dimensions of the cavity are $\ell_x = 8$ cms, $\ell_y = 8$ cms with $n_x = 2$, $n_y = 2$ and $n_z = 8$. For an acoustical signal of frequency 20kHz, injected into the chamber, the distance ℓ_z is calculated to be 7 cms, obtained from equation 5. These dimensions may be typical of a small space processing chamber.

The normal mode corresponding to any particular set of values of n_x, n_y and n_z can be produced by starting a plane sound wave in the direction given by the direction cosines ω_x/ω, ω_y/ω, ω_z/ω where $\omega_x = C\pi n_x/\ell_x$ --- and letting the wave reflect until it becomes a standing wave. Thus, the sound generator used to produce levitation in a cavity experiment chamber should be inserted at an angle given by the direction cosines. If this is not effected, the resultant wave in the experiment chanber will not be periodic and will not correspond to a normal mode (See Reference 4, p. 390).

The sound pressure isobars for the cavity shown in Figure 4, are plotted in Figure 5 for the X-Y plane at Z = 0. Note that there are four pressure minima and consequently four levitation points in the X-Y plane at Z = 0.

The isobars shown in Figure 5 are repeated periodically as one moves along the Z axis. Since there are 8 half wavelengths in the Z direction ($n_z = 8$), there are consequently 32 distinct levitation regions in the cavity. However, the depth of each energy trough will be governed by the absorption of sound. The energy troughs near to the sound source will be stronger than those a distance away.

Various examples of acoustic cavity levitators are given in the next section.

APPARATUS

The sound source used throughout the investigations is shown in the photograph Figure 6. The source consists of a cylinder of magnesium-aluminum alloy about 7.5 cm in diameter and of length equal to a one half sound wavelength in the alloy. The vibrator is supported by a flange at the midsection - a displacement node - and excitation of the vibrator is provided by inducing eddy currents in a metal tube turned integrally with the base of the vibrator. A full description of an early version of this vibrator is given in Reference 1.

A muffle furnace shown in Figure 7 is adapted for use with the sound source. This is accomplished by removing a firebrick from the underside of the furnace and placing the front end of the sound source so that it is centered in the firebrick hole, pointing vertically upwards. A fixed reflector, consisting of a flat slab of stainless steel is supported within the furnace at a distance equal to 4 half wavelengths of sound from the vibrator surface and parallel to it. To reduce heating of the vibrator by the furnace heat, a series of parallel 200 mesh, stainless steel wire mesh screens are placed immediately above the vibrator in a plane parallel to the vibrator surface. The wire mesh screens introduce very small absorption of the sound wave, but effectively conduct away the heat that otherwise might impair the performance of the vibrator. A detailed description of acoustical transmission through wire mesh screens is given in Reference 6.

An experimental furnace module, suitable for drop tower and rocket experiments, is shown in Figure 8, equipped with the acoustic levitator, for levitating specimens of chalcogenide glass. The furnace operates at 800°C, at which temperature solid specimens can be levitated and melted. The furnace module consists of a fused quartz tube measuring 7.5 cm diameter by 15 cms in length, outside of which are placed two nickel-chromium heating elements. The top end of the quartz tube is closed by a refractory cap through which an inert gas can be passed by means of an inlet tube. An adjustable metal reflector is provided inside the quartz tube to increase the levitation forces.

PERFORMANCE EVALUATION

The stability of the acoustic energy well levitation process can be gaged from the three photographs shown in Figure 9. The upper photograph shows the levitator (frequency 20kHz) mounted inside a drop tower cage and pointing vertically upwards. A specimen can be seen levitated approximately halfway between the upper surface of the vibrator and the reflector. The center photograph in Figure 9 shows the specimen remaining levitated when the entire assembly is rotated through 90°. The lower photograph shows the system pointing vertically downwards. The system is stable and independent of the direction of the sound beam. We thus conclude that the energy wells are closed. In the center photographs of Figure 9, the levitated specimen is shown pulled by gravity to a position slightly below the position originally occupied in the upper photograph. The deflection of the specimen provides the means to measure the "sideways" restoring forces in the levitator. In the instance cited, the lateral restoring forces are about 10% of the levitation forces in the direction of the main sound beam.

The photographs shown in Figures 10 and 11 demonstrate levitation of liquid and solid materials. The levitator frequency was 20kHz and the electrical power input into the vibrator was approximately 85 watts throughout. The left photograph in Figure 10 shows a levitated water droplet

measuring approximately 0.4 cm in length. A considerable degree of flattening is observed. The flattening results from the sound radiation force. The droplet shape is governed by the surface tension of the water and the shape and strength of the acoustic energy well in which it resides. By deliberately shaping the energy well, the liquid could, in principle, be formed to a desired shape without contacting surfaces. The right photograph in Figure 10 shows a solid aluminum sphere levitated brass disc measuring about 5 cm diameter by 0.5 cm thick. Levitation of the disc is obtained without a separate reflector since the disc acts as its own reflector. Here, gravity is needed to retain the specimen in position. For space applications, a separate reflector would be required. The upper photograph in Figure 11 shows five spheres simultaneously levitated in the standing wave as indicated in Figure 3.

Position control in the levitator is effected by simply moving either the reflector or the sound generator. The specimen will follow the motion of the surface that is moved.

Acoustic "lift-off" of a specimen from a wire mesh screen is shown in Figure 12. The specimen will lift from the position of the spoon in the lower photograph to the position of the specimen in the upper photo.

APPLICATIONS

Free Suspension Melting

Low temperature containerless melting is demonstrated in the sequence of photographs in Figure 13. A picoelastic material, melting point 80°C, is introduced in the levitator and is shown in the top left-hand photograph. Partial melting of the material, obtained by means of a quartz lamp, is shown in the top right-hand photograph. It is observed that the material has taken an approximately spherical form. As the viscosity of the material reduces with increasing temperature, the sphere flattens (lower left-hand photograph) and finally the material is compressed by the sound vibration forces to a flattened disc-like shape. The spherical form could be retained by reducing the intensity of the sound field. In low gravity, for example, the sound fields could be reduced in proportion to the reduction in the gravity field. Consequently, little distortion of a spherical body should result from the acoustic levitation. A penalty, however is the increasing time to restore the body to equilibrium, when the sound fields are reduced.

High temperature containerless melting of aluminum and glass is shown in Figures 14 and 15, respectively, undertaken in the muffle furnace levitator described in the previous section. The top photograph in Figure 14 shows an irregular, solid, aluminum ball introduced into the furnace. The sound vibrator is directed upwards through the bottom of the furnace as described previously. The flat plate, situated midway between the bottom

and top of the furnace, is the reflector. Furnace temperature, measured at a distance of 7 cms to the rear of the specimen, was 1000°C. After an elapsed time of 40 seconds a photograph was taken, shown at the bottom of Figure 14. At this point, the aluminum had melted and was approximately spherical in form.

Figure 15 shows two photographs of containerless glass melting. Each photograph was taken 30 seconds apart. In the top photograph a glass disc, 1 cm in diameter, was inserted into the furnace and levitated. The disc is situated towards the top right-hand side of the picture. The bottom photograph shows the glass disc melted to form a sphere of molten glass that remained stably levitated. The furnace temperature was 800°C for this sequence of photographs. Electrical power into the levitator was 200 watts. Small random motions of the levitated sphere were observed. Those random motions were mostly caused by drafts entering the open front door of the furnace.

Liquid Injection

Injection of liquids into the levitator may present a problem if the liquid is not injected into an energy well and if too much liquid is inserted at any one time. Improper liquid injection results in break-up of the liquid droplet and consequent fouling of the experiment chamber. A method of liquid injection consists of detaching the droplet from the end of a capillary tube. The weight of the largest drop that can hang from the end of a tube of radius a, is $mg = \lambda\pi a \gamma \cos\alpha$ where γ is the surface tension and α is the angle of contact with the tube. By choosing a tube of diameter calculated from this equation the size of the drop can be obtained, that the levitator will accept without liquid break-up. This is demonstrated by the two photographs shown in Figure 16. The top photograph shows a water droplet growing at the end of a capillary tube that is inserted into the levitator. As the drop grows, it will tend to move in the sound field, but remain attached to the capillary tube. The capillary tube is now moved until an energy well is found where the droplet reaches equilibrium and shows no tendency to translate. After a few seconds the droplet will detach when it reaches critical size and remain levitated. The detached droplet is shown in the bottom photograph in Figure 16. Under low gravity a slight gas overpressure in the capillary tube should suffice to eject the liquid from the capillary tube.

Liquid Shaping

Levitated liquids may be shaped by increasing or decreasing the sound pressure or, alternatively, by shaping the acoustic energy well in which the levitation takes place. A sequence of photographs of a levitated water drop is shown in Figure 17. The photographs were each taken at a different sound pressure level. It can be seen that the drop progressively flattens as the sound pressure is increased.

EFFECT OF THE LEVITATOR SOUND FIELDS ON THE PROCESSING OF MATERIALS

A series of experiments was conducted to indicate the effect, if any, of the levitator sound field on the material being processed. From the viewpoint of classical acoustics, the mismatch in acoustical impedance between the levitator gas in which the sound field propagates and the material levitated, is considerable, and the energy transfer should be extremely small. For example, the acoustical impedance of air is 42 cgs units and that of water 1.5×10^5 cgs units. The impedance mismatch is about 3500 to 1 resulting in an energy transfer ratio equal to the square of this ratio, or about 1.2×10^7 to 1. However, other disturbances could arise in a levitated material such as surface or volume resonances that may increase the energy transfer from the sound field.

To check the sensitivity of a material process to the levitator sound field, the following experiments were conducted. A droplet of benzophenone (M.P. 47°C), measuring 4 mm diameter, was levitated and allowed to supercool in the levitator while freely suspended. It was observed that the droplet supercooled by 16% of the melting point temperature without any indication of crystallization. During the cooling process the drop was viewed continuously under a microscope using a polarized light source to indicate any tendency of the liquid to solidify.

In the second experiment, it was decided to irradiate a supercooled liquid by soupling sound into the liquid by direct immersion of an ultrasonic transducer. The acoustic energy transfer is high, in this condition, such that 50 to 60% of the sound energy generated in the transducer is propagated into the liquid. The experimental apparatus is shown in the top photograph of Figure 18. The metal cylindrical stub of the acoustic transducer can be seen immersed in the liquid (benzophenone) in the foreground of the photograph. At the bottom right side a small acoustic probe can be seen which is used to detect the sound field. This probe is connected to a narrow band electrical filter that can be switched into the circuit and used to suppress the direct acoustic signal received from the transducer. The liquid was supercooled, as shown by the bottom curve of the supercooling curves plotted in Figure 19. At a temperature of 30.8°C the transducer was excited at the increasing voltages labelled on the curve. At a transducer drive voltage of 220 volts, acoustic cavitation was visually observed in the liquid benzophenone, whereupon the liquid crystallized at a high rate, shown by a sharp increase in temperature of the liquid - the lower curve in Figure 19 - and shown by the crystallization evident in the photographs in Figure 18. Just prior to the inception of crystallization, the acoustic probe indicated a noise signature shown by the oscilloscope traces in the photographs. The noise signature was characteristic of sonic cavitation (See References 1, 7 to 11). Prior to the inception of cavitation the acoustic intensity in the liquid was substantial, and from the acoustic probe reading, was calculated to exceed 0.1 watt/cm^2. At the 0.1 watt/m^2 acoustic radiation level, no effect on the crystallization process could be observed as shown in Figure 18.

The evidence appears to indicate that the sound fields must reach the cavitation level for these fields to effect crystallization of the material. An exception would be in a specific instance in which a deliberate attempt was made to couple the gas-born sound energy to the material, for purposes of acoustic mixing of the material, homogenization or other acoustic processing factors. In this event, the sound frequency could be adjusted to resonate the material and increase the energy coupling. These factors considered further in the Appendix.

CONCLUSIONS

The acoustic energy well levitator is capable of levitating and positioning liquids, and solid dense materials of sizes useful in space processing experiments. The method can be scaled to a full scale space manufacturing process. The virtue of simplicity is retained in the levitator, while operating in high temperature environments exceeding 1000°C. A gas atmosphere is necessary to conduct the sound, but the gas pressure can be reduced at the cost of reducing the levitation forces. Containerless shaping of materials can be accomplished, though precise shaping would require careful design of the experiment chamber to form the energy wells to the proper shape. Precise positioning can be obtained by moving a reflecting surface or by moving the sound source. By this means, a specimen can be translated from a hot region to a cold region. The energy well levitator is adaptable to a range of space experiments. Strip materials, flat blanks and discs are particularly easily handled.

ACKNOWLEDGEMENT

The author wishes to acknowledge the work of Mr. B. A. Durley III who contributed much to the investigations described in this paper. Mr. Durley contributed substantially to the experiments and the design of the hardware.

REFERENCES

1. T. Heuter and R. H. Bolt, "Sonics",
   John Wiley and Sons, New York, 1955,
   p. 68 for calculations of near field
   p. 228 for cavitation noise spectra.

2. L. D. Rozenberg, "High Intensity Ultrasonic Fields",
   Translated from the Russian by J. S. Wood,
   Plenum Press, New York, 1971,
   p. 114.

3. A. B. Wood, "A Text Book of Sound",
   Bell and Sons, London, 1953.

4. P. M. Morse, "Vibration and Sound",
   McGraw Hill Book Company, New York, 1948,
   p. 397.

5. E. Mori and K. Itom, "Measurements and Applications of Normal Modes
   of Vibration in a Rectangular Bath",
   Ultrasonics International, Conference Proceedings,
   Published by IPC Science and Technology, London, 1974.

6. W. P. Mason, "Piezoelectric Crystals and Applications to Ultrasonics",
   D. Van Nostrand Co. Inc., New York, 1956.

7. B. E. Moltingk and E. A. Neppiras, "Cavitation Produced by Ultrasonics",
   Proc. Phys. Soc., 63B: 675 (1950), 64B: 1032 (1951).

8. H. G. Flynn, "Physics of Acoustic Cavitation in Liquids",
   Physical Acoustic (W. P. Mason, ed), Vol. 13,
   Academic Press, New York (1964).

9. M. G. Siroryuk, "Energetics and Dynamics of the Cavitation Zone",
   Akust. Zh., 13(2): 265 (1967).

10. L. Bohn, "Sound Spectrum of Vibration Induced Cavitation",
    Akust. Beih. 2:201 (1952).

11. V. A. Akulichev and V. I. Ilichev, "Spectral Indication of the Origin
    of Ultrasonic Cavitation in Water",
    Akust. Zh., 9(2):158 (1963).

APPENDIX

Mechanisms of Acoustic Cavitation and Effect On Crystallization

We have concluded earlier that cavitation levels of sound evidently are necessary to induce nucleation and crystallization of a supercooled liquid. We disgress at this point to evaluate how these cavitation-related effects can occur and what their significance may be.

Cavitation processes start when a bubble or other nucleant enters a sound field. A bubble trapped in a sound field will begin to grow - a process known as rectified diffusion. If the localized sound intensity is low, the bubble will continue to oscillate. The bubble may grow to resonant size or coalesce with other bubbles and become visible to the naked eye. Gaseous cavitation such as this gives rise to a line spectrum of acoustic noise that may be measured with a broad band acoustic probe, as mentioned earlier. Pressure and particle velocities in the gaseous cavitation state do not much exceed those in the incident sound field. As such, gaseous cavitation generally is found to play only a minor role in changing the properties of liquids. This fact is brought out in a multiplicity of references of which References 7 to 11 have been selected. High sound intensities, usually of the order of $0.3W/cm^2$ or greater give rise to vaporous cavitation. Vaporous cavitation arises as follows: Bubbles of a size such that their resonant frequency is higher than the incident sound frequency behave nonlinearly as shown in Reference 7. These bubbles grow at about the rectified diffusion growth rate, but at a critical size, the bubbles collapse with extreme violence generating localized shock waves that further nucleate the liquid that surrounds the original voids. Temperatures in the collapsing void may be extreme, and may exceed 10^4 degrees Kelvin. The acoustic noise shows a continuous spectrum and this spectrum can be used as a "label" for the existence of vaporous cavitation in a liquid. Vaporous cavitation is the principle mechanism whereby sound can induce fundamental changes in a liquid such as, for example, increasing the nucleation rates of a liquid.

The evidence from the photographs in Figure 18, showing the effect of direct sound irradiation of supercooled benzophenone, is reconsidered in the light of these considerations. The top left-hand photograph shows the condition with no sound radiation - the oscilloscope trace shows no vertical deflection indicating that no sound is being received at the acoustic probe.

The bottom left-hand photograph shows a small vertical trace produced by $0.1\ W/cm^2$ sound radiation at 20kHz of the liquid. This trace is found to be a noise signal consisting of a line spectrum and corresponds to the gaseous cavitation, as alluded to earlier. Vaporous cavitation is incepted very suddenly at a slightly higher sound level as seen visually in the top right-hand photograph taken 100 milliseconds later. The vaporous cavitation is identified by the streamers emanating from the bottom

face of the transducer and moving in a curved path to the right of the picture. The oscilloscope trace shows the characteristic jump in the acoustic noise level due to the addition of the continuous noise - further identifying the existence of vaporous cavitation. Almost instantly with the start of vaporous cavitation, we have the start of nucleation and crystallization in the liquid as shown in the bottom right photograph. A few seconds after this picture was taken the whole container of supercooled benzophenone had solidified. Note that the oscilloscope trace has disappeared even though the sound remains on. This is because the crystals of benzophenone absorb the sound and prevent the sound from reaching the acoustic probe.

The evidence from this experiment is that the vaporous cavitation threshold must be exceeded for the sound to cause crystallization and nucleation of the material. As discussed earlier, it is very improbable that these levels of sound energy can be coupled from the levitator to a fully suspended liquid.

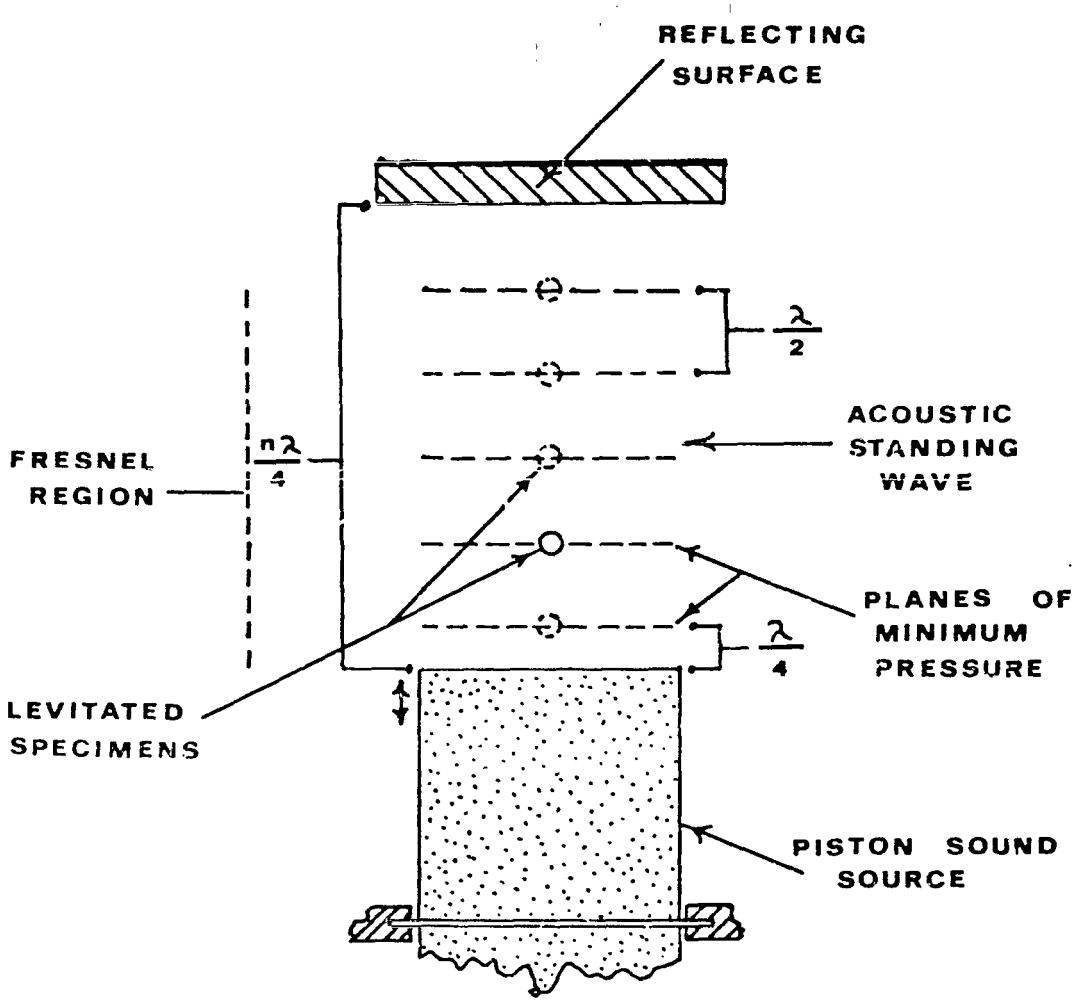

FIGURE 1. THE ENERGY WELL LEVITATOR

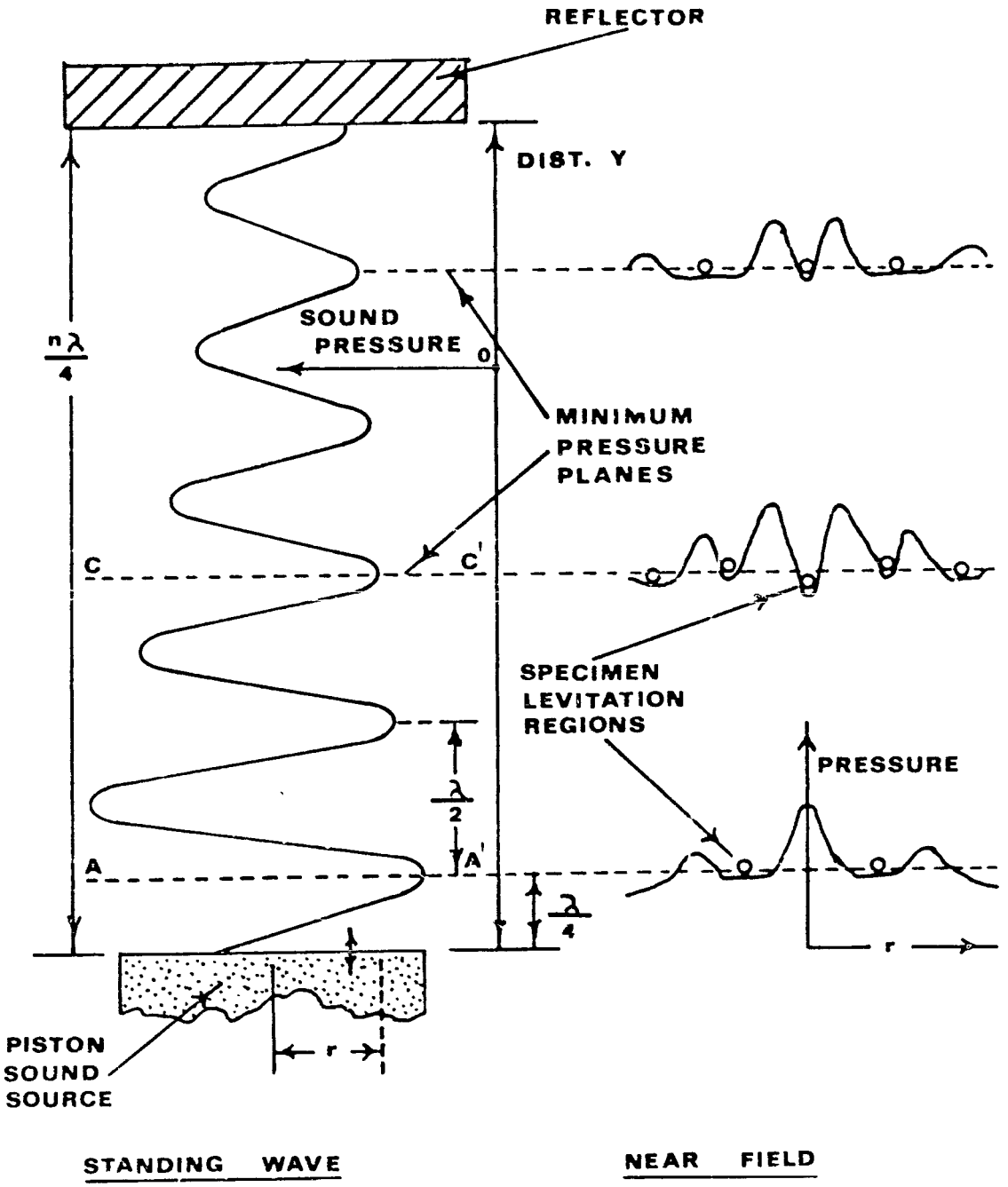

FIGURE 2. DISTRIBUTION OF SOUND PRESSURE

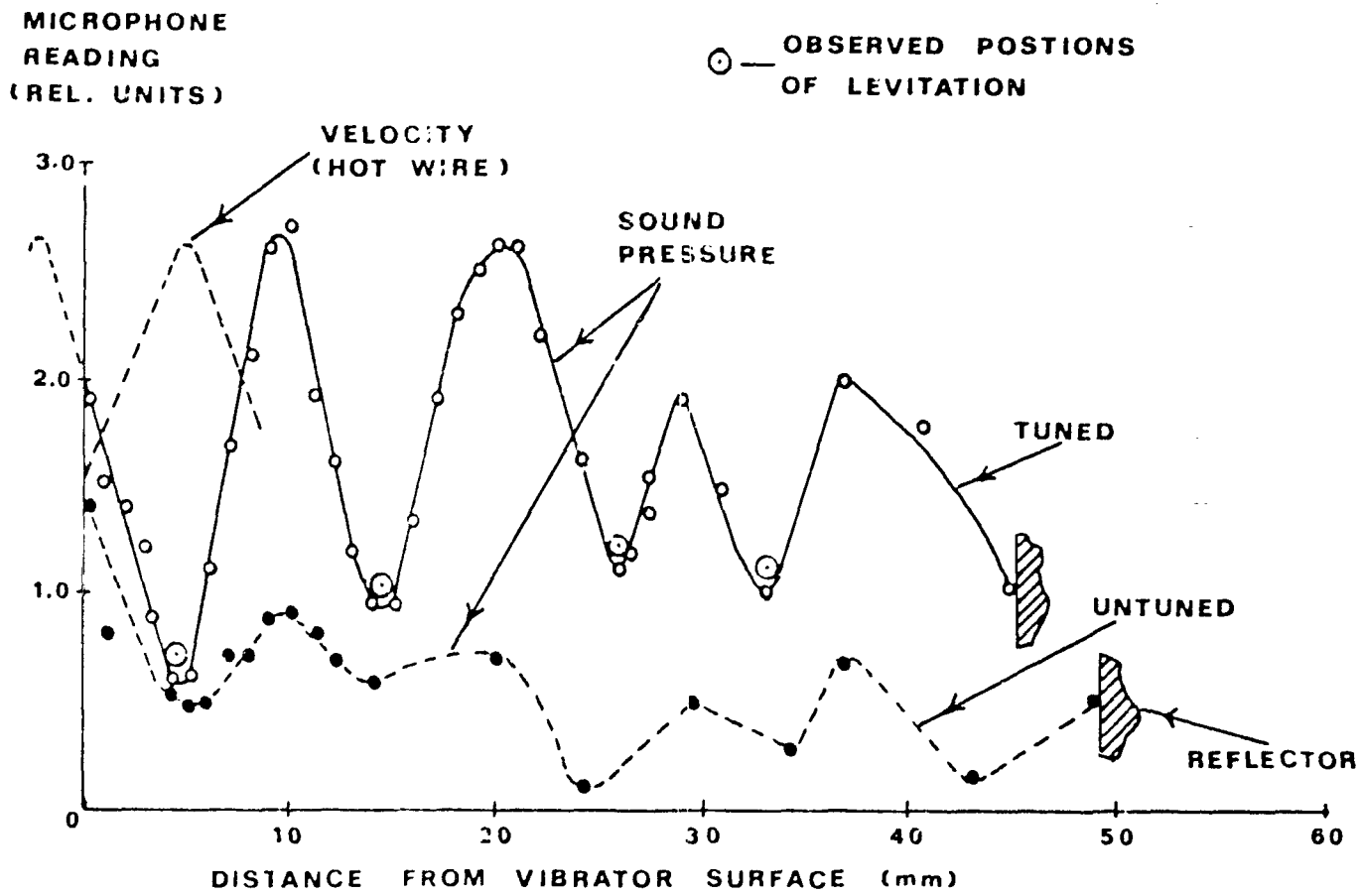

FIGURE 3. LEVITATOR STANDING WAVE

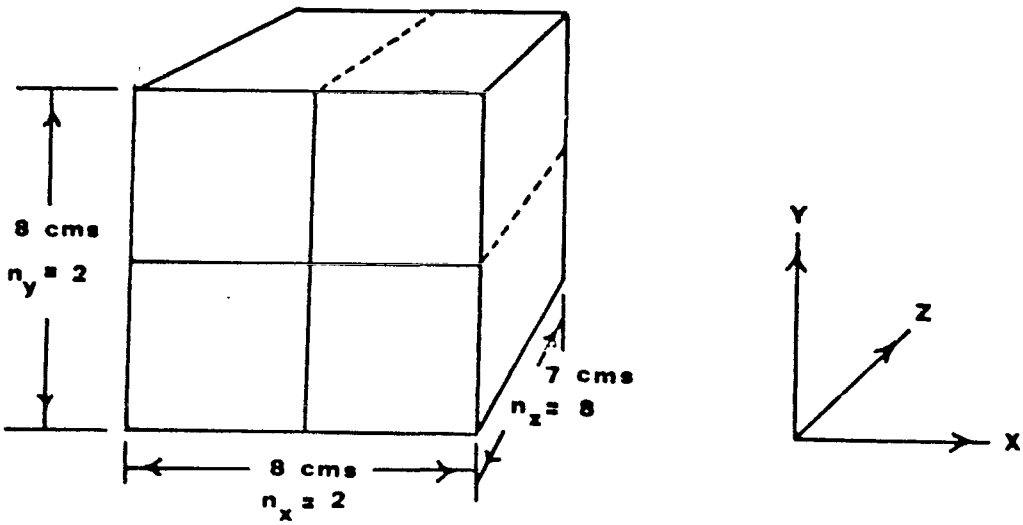

FIGURE 4. ACOUSTIC CAVITY LEVITATOR

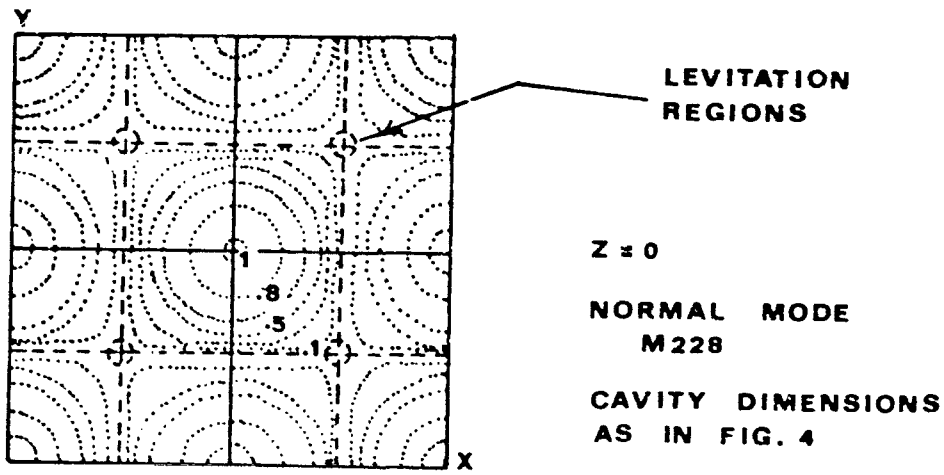

FIGURE 5. ISOBARS FOR A RECTANGULAR CAVITY.

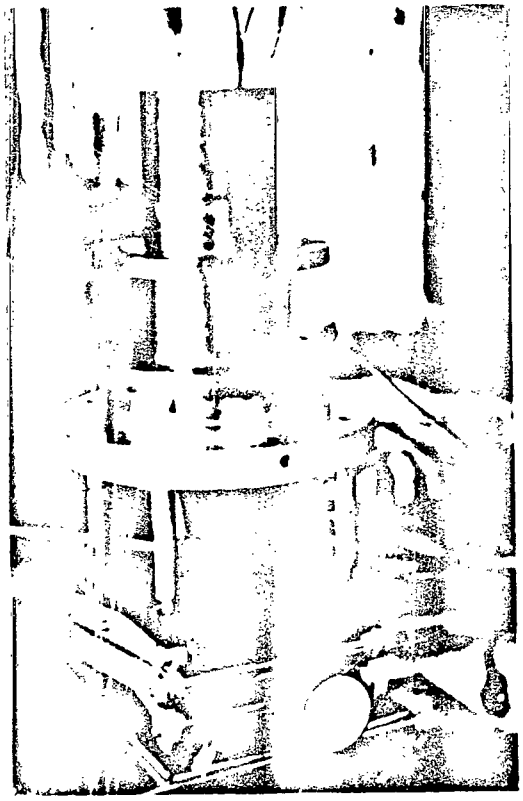

FIGURE 6. ULTRASONIC INTENSE SOUND SOURCE.

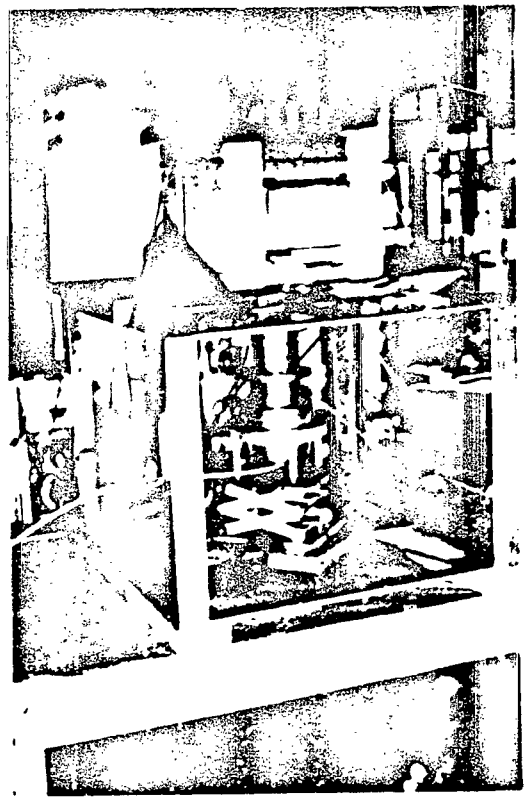

FIGURE 7. SOUND SOURCE COUPLED TO MUFFLE FURNACE .

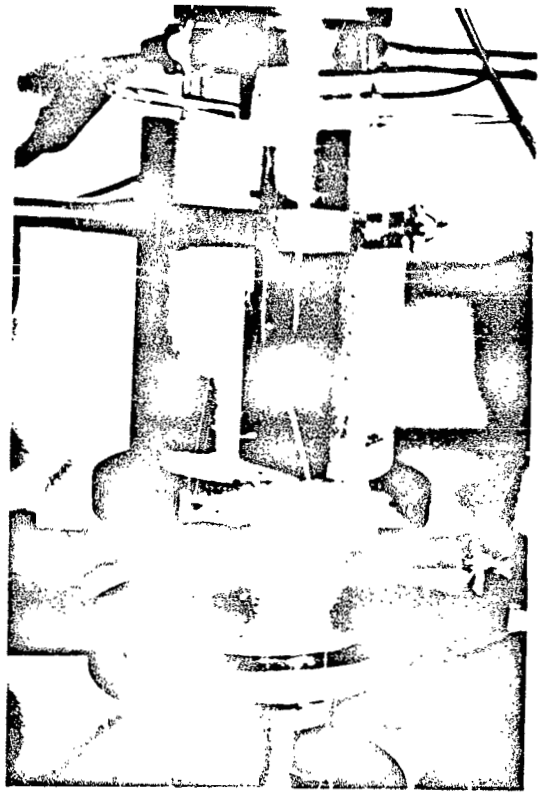

FIGURE 8. FUSED QUARTZ FURNACE FOR CONTAMINATION MELTING.

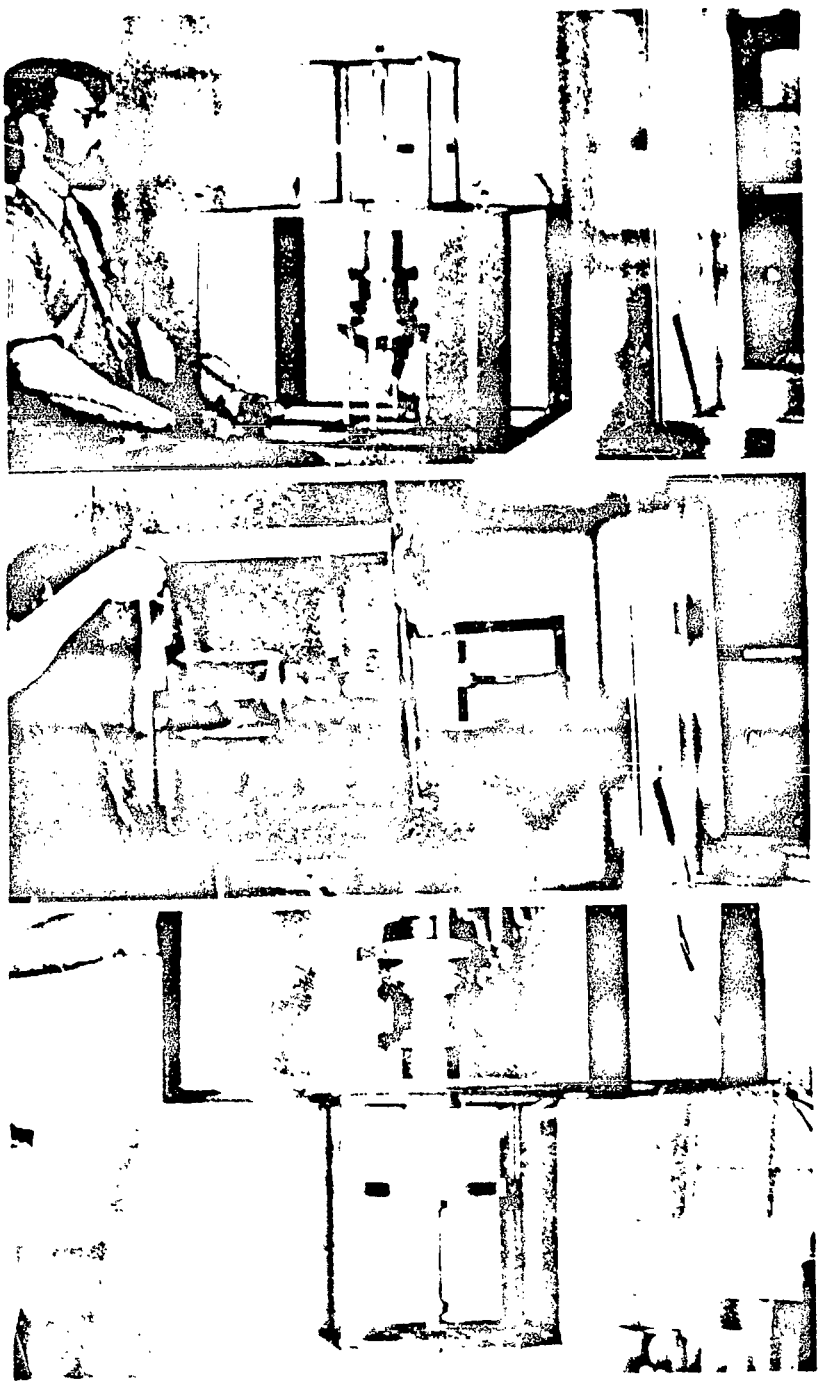

FIGURE 9. LEVITATION IS POSITION-STABLE AND INDEPENDENT OF THE ORIENTATION OF THE SOUND BEAM.

FIGURE 10. LEVITATION OF A 3mm WATER DROP (LEFT-HAND PHOTO). FREE SUSPENSION OF SOLID 0.6 cm DIAMETER ALUMINUM SPHERE (RIGHT-HAND PHOTO).

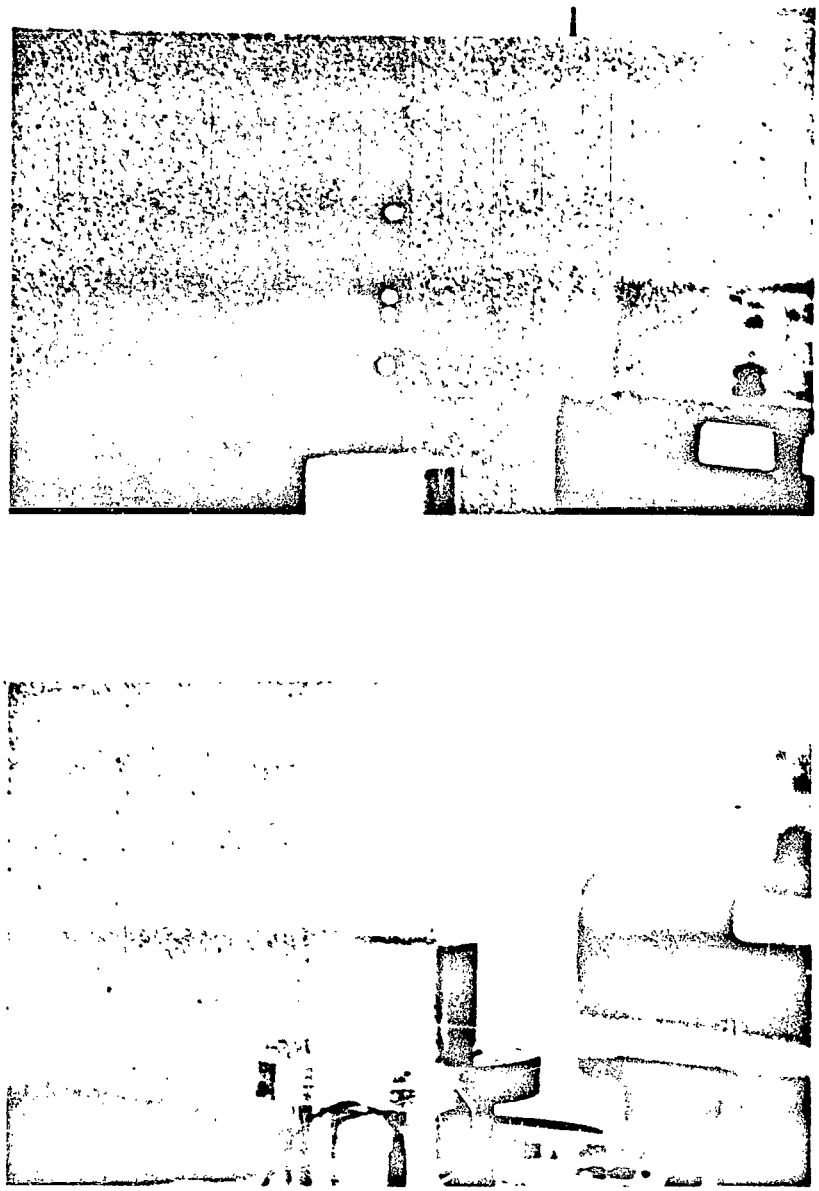

FIGURE 11. FREE SUSPENSION OF A 7.0 cm DIAMETER BRASS DISC (LOWER PHOTO). LEVITATION OF MULTIPLE SPECIMENS IN AN ACOUSTIC STANDING WAVE (UPPER PHOTO).

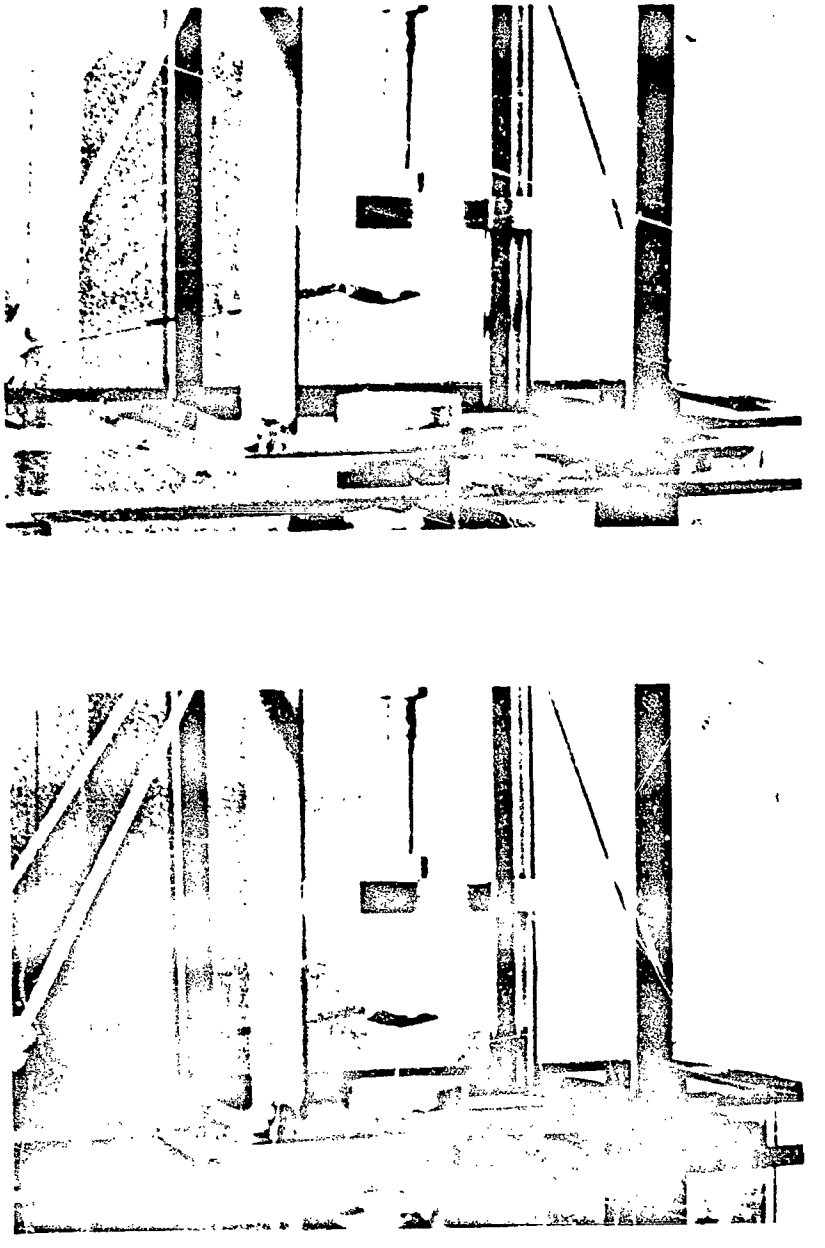

FIGURE 12. ACOUSTIC LIFT-OFF OF A SPECIMEN FROM A WIRE MESH SPECIMEN SUPPORT.

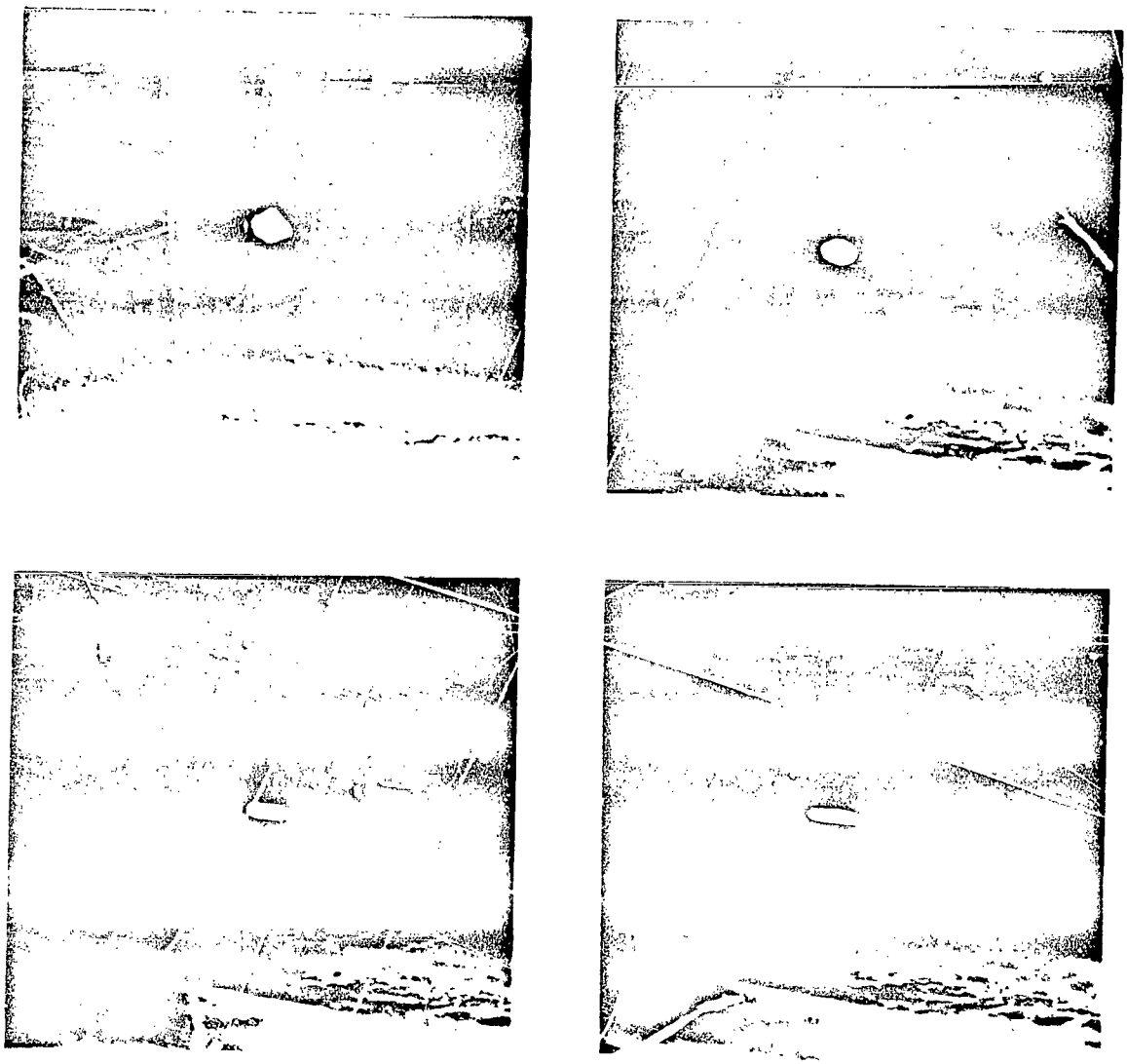

FIGURE 13. CONTAINERLESS MELTING SEQUENCE FOR PICOELASTIC MATERIAL. PHOTOS TAKEN AT 45 SECOND TIME INTERVALS.

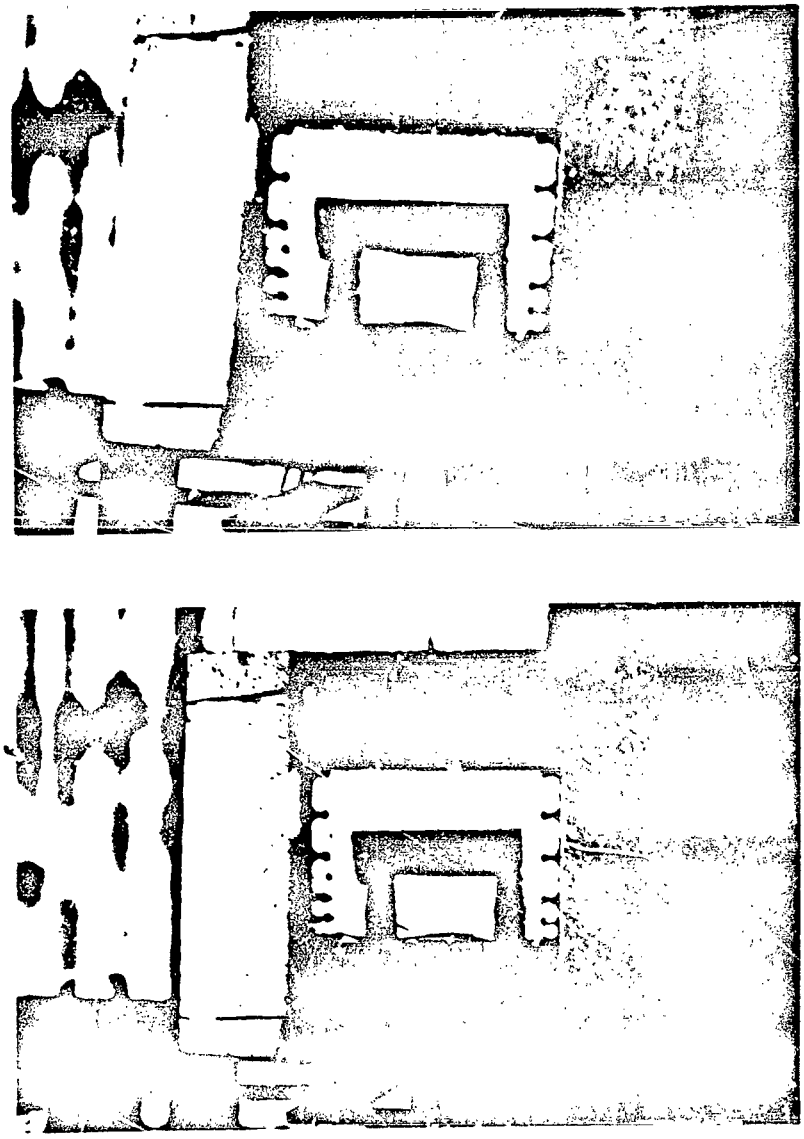

FIGURE 14. CONTAINERLESS MELTING OF ALUMINUM.

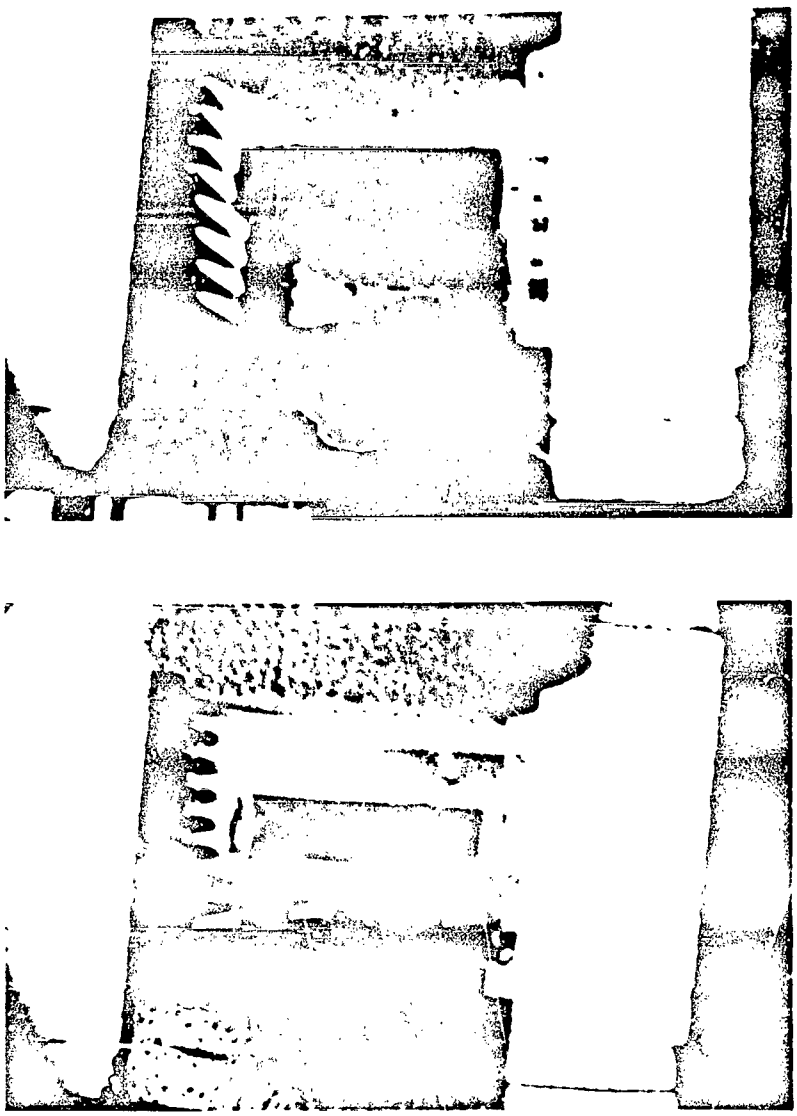

FIGURE 15. CONTAINERLESS MELTING OF GLASS.

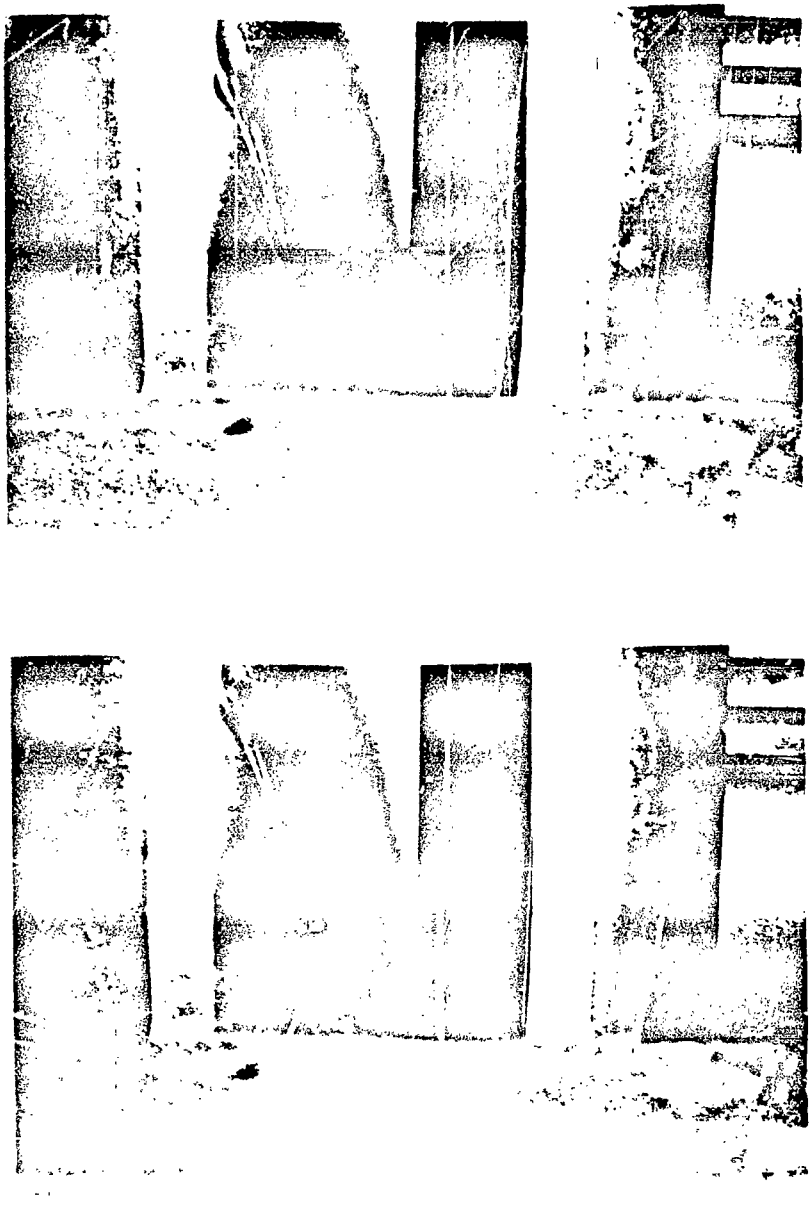

FIGURE 16. INJECTION OF LIQUIDS USING DROPLET DETACHMENT METHOD.

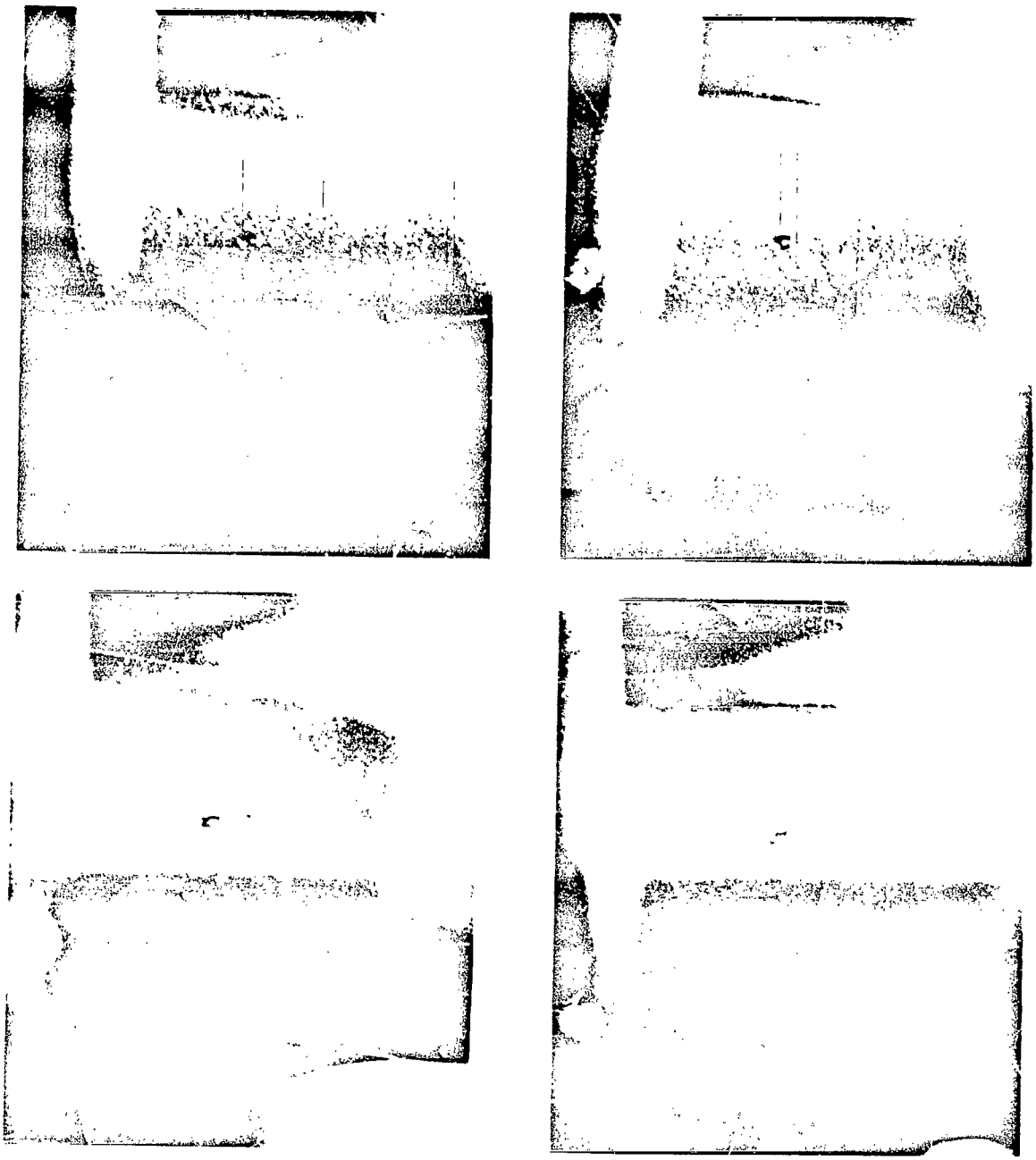

FIGURE 17. SHAPING OF A WATER DROP BY INCREASING THE SOUND INTENSITY. TOP LEFT PHOTO WAS FOR 130db S.P.L. TOTAL. TOTAL INCREASE IN S.P.L. ABOUT 6db.

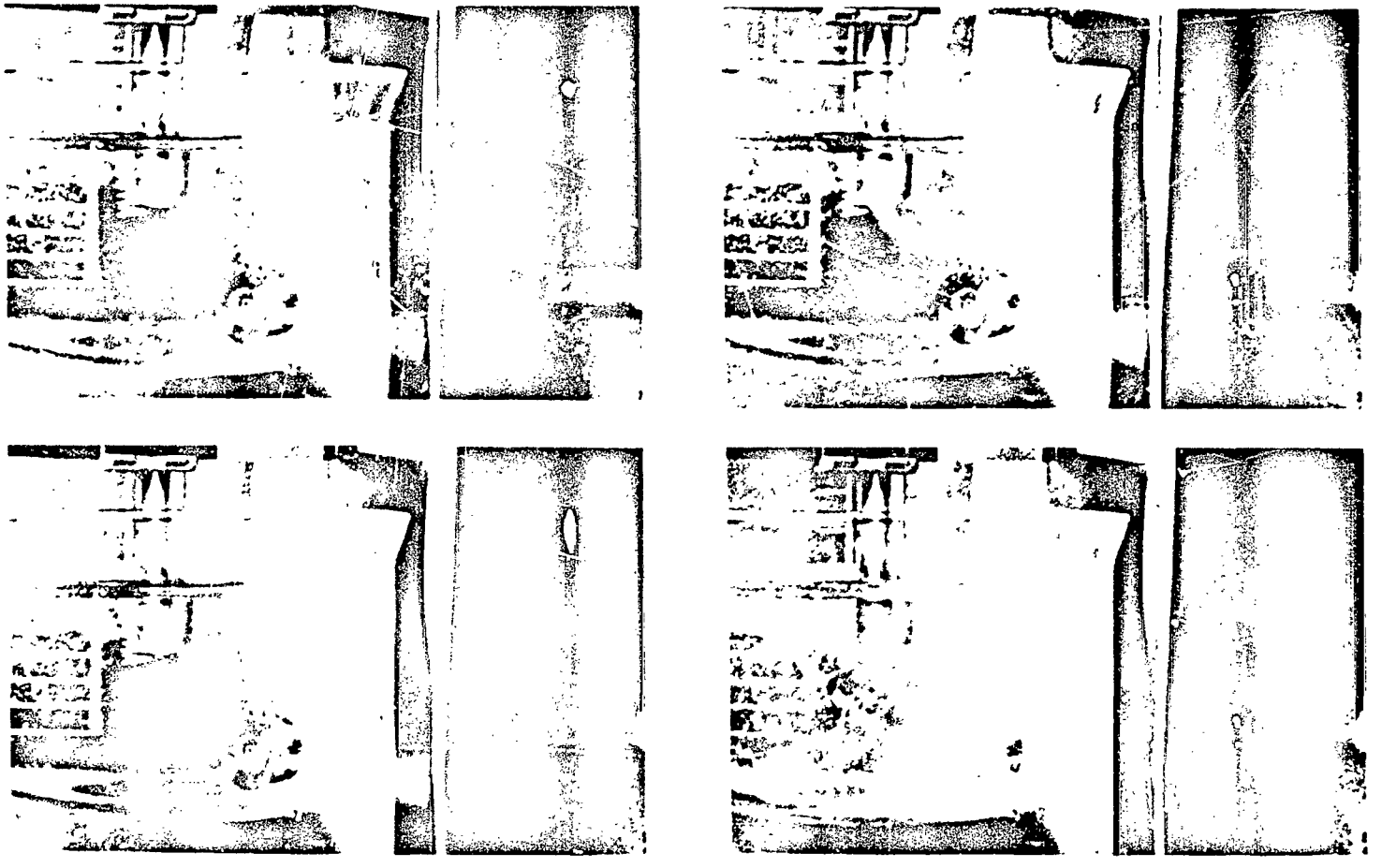

FIGURE 18. DIRECT ACOUSTIC IRRADIATION OF SUPERCOOLED BENZOPHENONE. CRYSTALLIZATION OCCURS AT THE VAPOROUS CAVITATION LEVEL (BOTTOM RIGHT PHOTO)

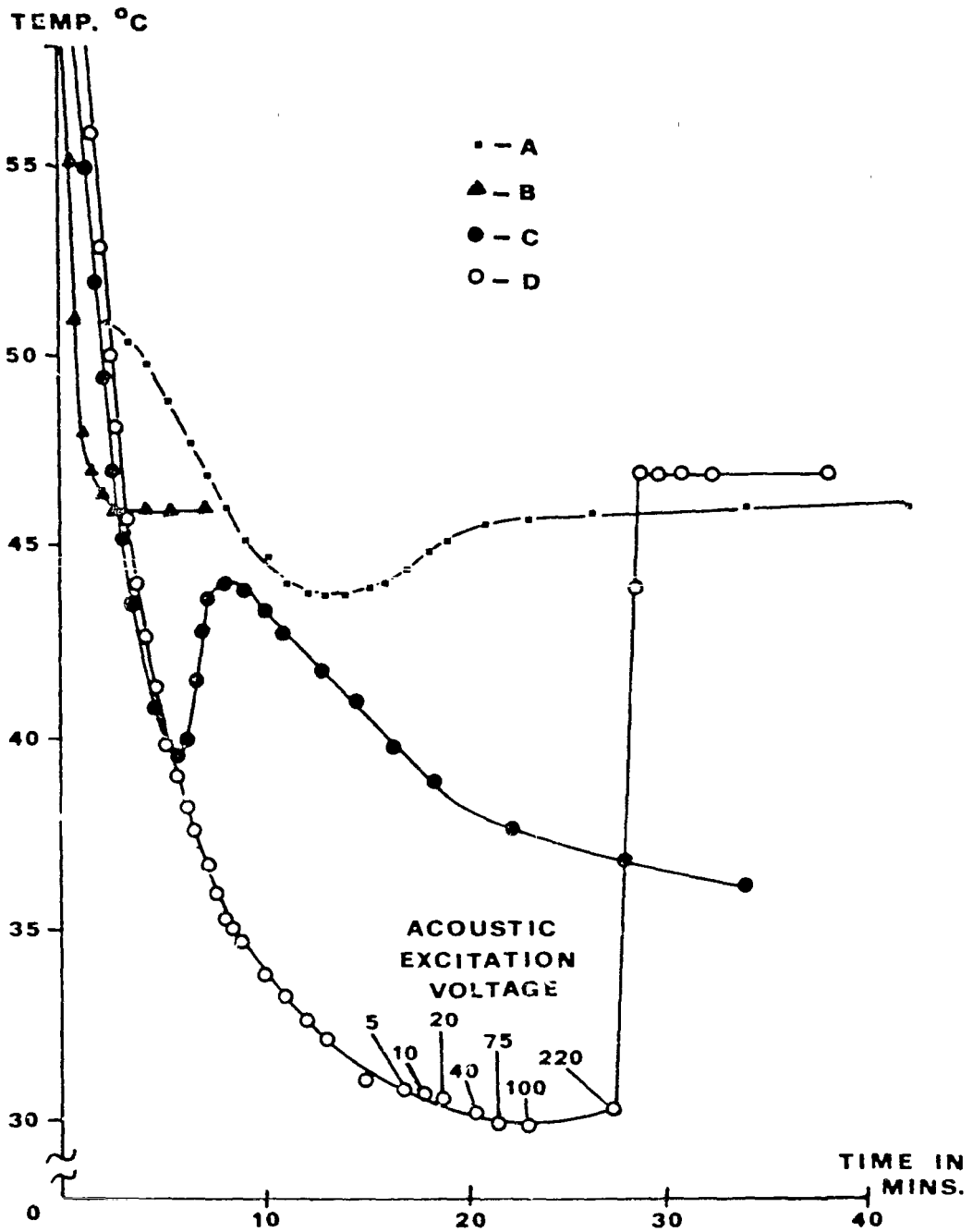

FIGURE 19. SUPERCOOLING OF BENZOPHENONE

ACOUSTICAL POSITIONING CHAMBER FOR SPACE PROCESSING

By

T. G. Wang*, M. M. Saffren, and D. D. Elleman
Jet Propulsion Laboratory
Pasadena, California 91103

SUMMARY

By readily levitating, positioning, and manipulating materials placed in it, the acoustical resonator can serve a variety of space processing operations, such as drawing crystals, degassing, and stirring of melts, and casting.

*Paper presented by T. G. Wang.

Many space manufacturing processes will require manipulating weightless molten material within a container without the material making contact with the walls. Electromagnetic fields can position and shape electrically conducting melts. The acoustical method described here can control any molten material including nonconductors such as glasses.

The method utilizes the fact that when an acoustical standing wave is excited within an enclosure, or resonator, the pressure is greater at the nodes of the wave amplitude than the antinodes (there, practically zero); consequently, liquids and particles introduced into the resonator will be driven away from the nodes at the chamber walls toward the antinodes, where they collect and remain until the excitation ceases. Slightly modifying the acoustic field will rotate the collected material, a technique recently proven in our laboratory by positioning and rotating soap bubbles and styrofoam balls.

The technique has many applications to space processing: zone melting, casting, crystal growing, casting of composites, casting materials with dispersed voids, and chemical synthesis. Altering the shape of the resonator will alter the shape of the antinodal region and cause a melt to assume a particular form -- for instance, that of a cylinder, one particularly suited to zone-refining a melt. Introducing sound waves at frequencies corresponding to resonant modes of the melt will oscillate, and so stir it. A movable wall in the resonator can [illegible] by making the anitnodes move apart. Rotating the melt can degas and control the segregation of substances within it. Laser and ion beams can be used for contactless heating of the melt.

The laboratory model of the rectangular resonant chamber as shown in Figure (1) consisted of a 4" x 4 1/2" x 5" plexiglass rectangular box and three commercially made speaker drivers. Those drivers are mounted at the center of the orthogonal planes of the box. In order to maximize the efficiency of the system, three aluminum spacers were used to make the total distances from the diaphrams of the speakers to the inner walls of the chamber equal to the inner dimensions of the resonant chamber.

The resonant chamber and the speaker driver units are acoustically coupled through the twelve 1/8" holes which are drilled radially symmetrically around the center of three orthogonal planes. This arrangement will pick out the part of the wave front that has same phase angle to enter the resonant box. When the chamber was driven at the one of its resonance nodes by acoustical compressional drivers, the ambient pressure is maximum at the nodes of the wave and is minimum at the anti-nodes. Consequently there is a tendency for liquids and particles introduced into such enclosures to be drive toward the antinodes where the materials collect and remain until excitation ceases.

The average ambient pressure change ΔP in a sound wave is

$$\Delta P = \frac{\overline{P^2}}{2\xi C^2} - \frac{1}{2}\,\xi\,\overline{U^2} \qquad (1)$$

Where P is the excess pressure, U is the particle velocity, and ξ is density of medium.

The pressure profile in our system can be derived as following:

The wave equation ϕ for our rectangular chamber can be expressed as

$$\phi = \phi_x \cos k_x X\, e^{i\omega_x t} + \phi_y \cos k_y Y\, e^{i\omega_y t} + \phi_z \cos k_z Z\, e^{i\omega_z t} \qquad (2)$$

Where $\phi_{x,y,z}$ are the complex velocity potential amplitudes of standing waves of frequency $\omega_{x,y,z}$ and wavelength constant $k_{x,y,z}$ with a velocity C.

the particle velocity U by definition is

$$U = \Delta\phi \tag{3}$$

The momentum conservation condition gives us

$$P = -\zeta\dot{\phi} \tag{4}$$

Thus, ΔP is minimum at center of the chamber as shown in Figure (II), when drivers are operated at lowest resonance modes of the chamber.

For this acoustical-levitation device to position and shape a melt, it must be able to maintain resonance even as the ambient temperature changes from one extreme to another. Temperature extremes will be caused by first melting and then resolidifying the material within the chamber. JPL has developed an automatic frequency control (based on a phase-locked loop) to maintain resonance despite temperature excursions within the chamber.

In a forced oscillation system the complex displacement X is

$$X = \frac{-j\ Fe^{j\omega t}}{w\ [Rm + j\ (wm - s/w)]} \tag{5}$$

where F is the driving force, R is the resistance, M is the mass, and S is the restoring constant. Without solving the real part of this equation, one can easily see that a resonance where $wm = s/w$, the complex displacement X is 90° phase lag with respect to the driving force. This is a well known but rarely mentioned property of acoustical systems. The principle of phase locking is to monitor the driving frequency so that the input signal has 90° phase lead with respect to the acoustical signal inside the chamber at all times.

We tested the controller by simulating a temperature shift with helium-air mixtures--changing the gas in the chamber from 100% air through intermediate mixtures to 100% helium. This variation in gas density and resulting change of velocity of sound simulated a change of temperature from 25° to 2000°C. The fundamental resonance frequency of the chamber varied from 1.5 to 4.2 KHz during the simulated temperature rise. The automatic controller maintained the pressure profile in its original pattern throughout the test. Significantly, a styrofoam sphere levitated at the center of the chamber remained there throughout the test with no measured motion or oscillation; this indicated that no unwanted oscillation was occurring in the servo system.

The acoustical wave pattern does change as a function of boundary conditions at the walls. Would this change make material being processed come in contact with the wall of the chamber, and then the material on the wall distort the wave pattern and produce instabilities, causing catastrophic failure of levitation? The answer is no. We mapped out the acoustical pattern of the chamber with a layer of water in it. As you can see from F-3, the sound intensity maintained its symmetry until the water layer reached a thickness of 3 cm. A thick layer of water on the wall has the same effect as decreasing the chamber dimensions by the water layer's thickness. Repeating the experiment with oil and with alochol gave the same results. So we see no fundamental difficulty in using this device for splat cooling as developed by Bell Telephone Laboratory where by melts are quickly cooled by projecting them onto a wetted surface.

How does a temperature gradient affect the acoustical wave patterns in a space-manufacturing furnace? A zero-g environment eliminates gravitation-induced convection. A molten material positioned in the middle of the chamber can only disperse its heat by radiation. Due to this inefficient heat transfer, the temperature around the molten material will be much higher than at the wall. Will this extreme temperature gradient affect the sound-intensity profile, and what will the acoustic wave do to the temperature gradient? As you will see, not much happens.

We took a glass cylinder 24-in. long and 7-in. in dia. and fitted a disk heater into one end and a speaker driver on the other; we measured the temperature and sound intensity profiles first independently then simultaneoulsy. F-4 and F-5 show the results. The temperature gradient doesn't distort the resonant condition. The acoustical field slightly improves the heat conductivity of gas without much altering of the shape of the profile. That is, neither will the temperature gradient affect the positioning ability of the chamber nor the acoustic field significantly modify melting and solidification processes.

As one anticipated use, an acoustical-levitation "furnace" can serve to grow ultra-pure single crystals with a minimum of defects. Moreover it would be convenient to be able to grow a crystal and then test it in the same chamber to prevent contaminating or flawing it in a transfer from the furnace to a separate test-chamber. Testing in the furnace would also save time. To test the purity of ultrapure metals, for example, a convenient method is to measure its resistivity at very low temperatures. The resistivity measurements could be made by the eddy-currents magnetically induced in a levitated sample eliminating any need to put electrical leads on the sample. Measurements of this type are often conducted at temperatures below 2.0K.

How does such a temperature affect the acoustic levitation chamber? Tests were carried out a 1.8K, and the acoustic pattern showed no dramatic deviation from that at room temperature.

While we can expect significant evolution of this and many other space processing equipment once space processing begins, this evolution can begin now on Earth. In this respect we should mention the apparatus utilizing a high-power acoustic driver shown in F-6. The driver is a high-Q aluminum cylinder with a resonance frequency of approximately 16 KHz. In a 1-g field the apparatus can levitate water droplets, glass spheres, and metal plates as shown in F-7, F-8 and F-9. We plan to use it in the laboratory to study crystal growth of levitated melts.

Acknowledgement

The authors wish to thank Professor I. Rudnick of UCLA for his valuable suggestions, and Mr. E. E. Olli and D. Parry of JPL for their excellent help in conducting the experiment.

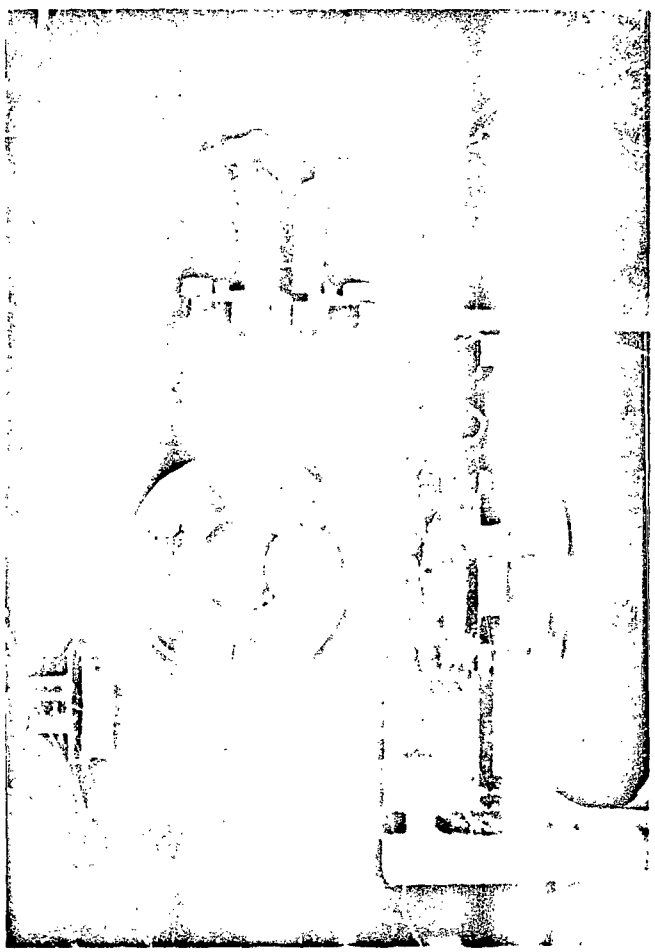

FIGURE 1. TRI-AXIAL ACOUSTIC POSITIONING CHAMBER.

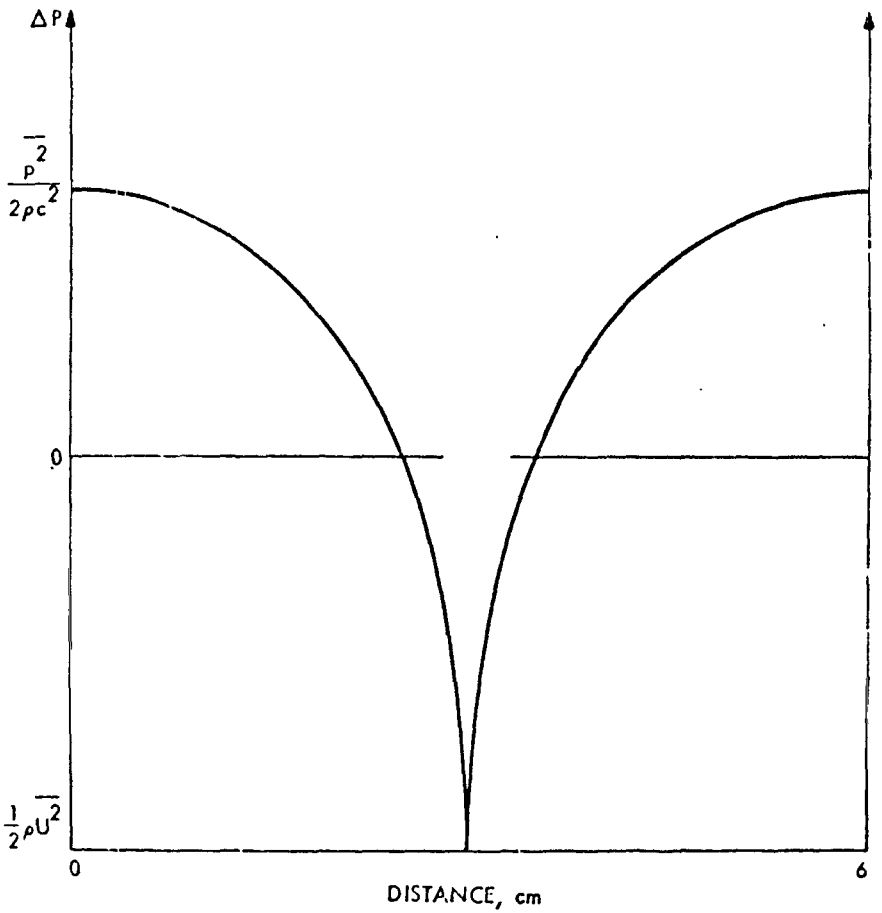

FIGURE 2. THE ONE-DIMENSIONAL PRESSURE PROFILE.

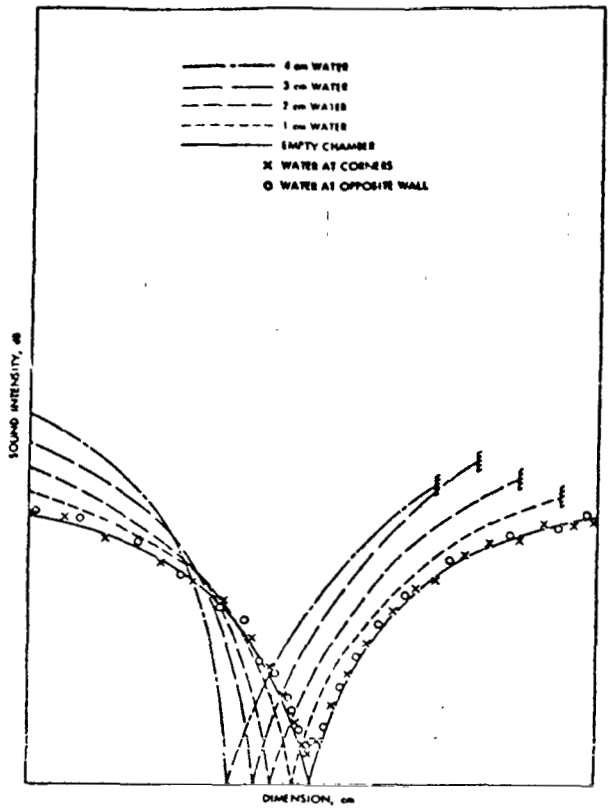

FIGURE 3. THE BOUNDARY EFFECT.

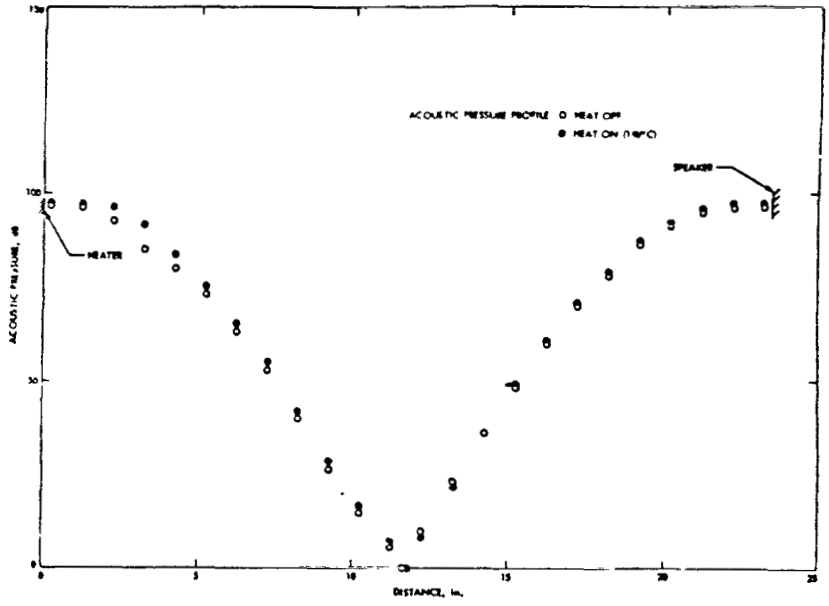

FIGURE 4. THE TEMPERATURE PROFILE.

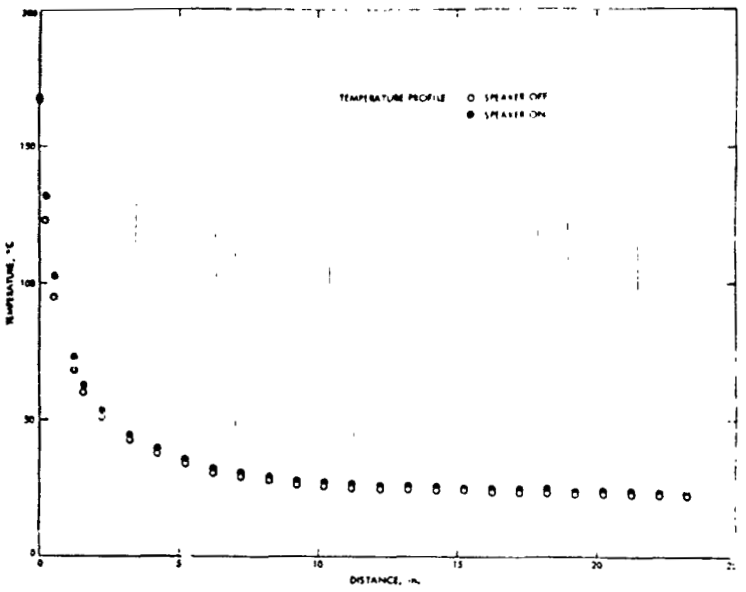

FIGURE 5. THE ACOUSTIC PROFILE.

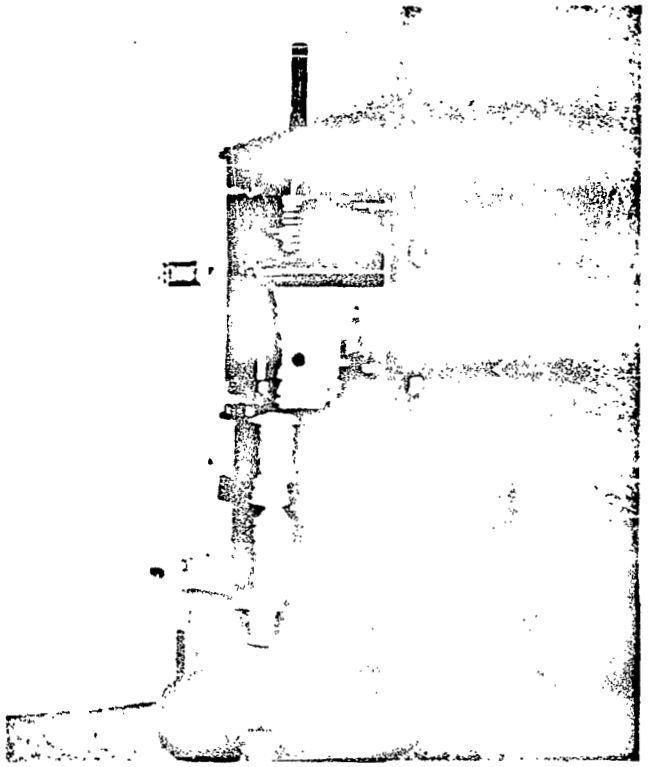

FIGURE 6. THE HIGH POWER ACOUSTIC DRIVER.

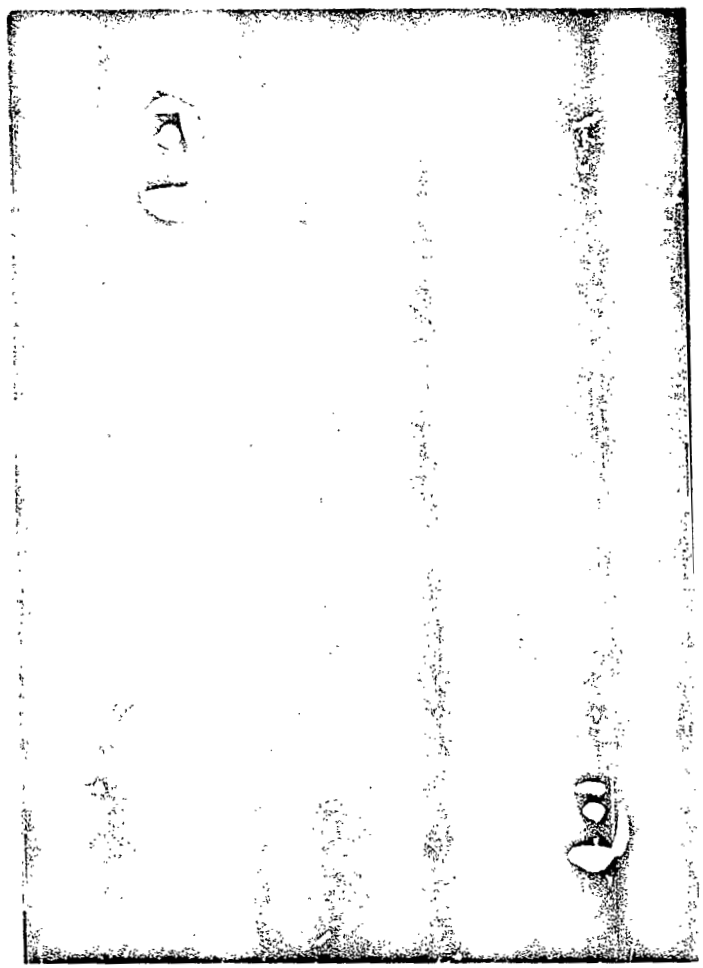

FIGURE 7. ACOUSTICAL LEVITATED WATER DROPLETS.

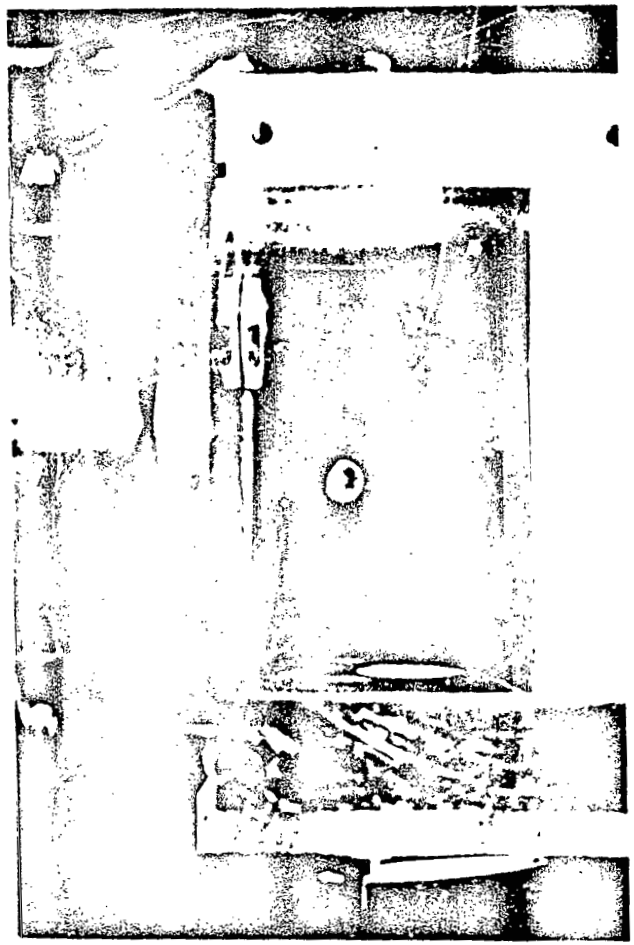

FIGURE 8. ACOUSTICAL LEVITATED GLASS SPHERE.

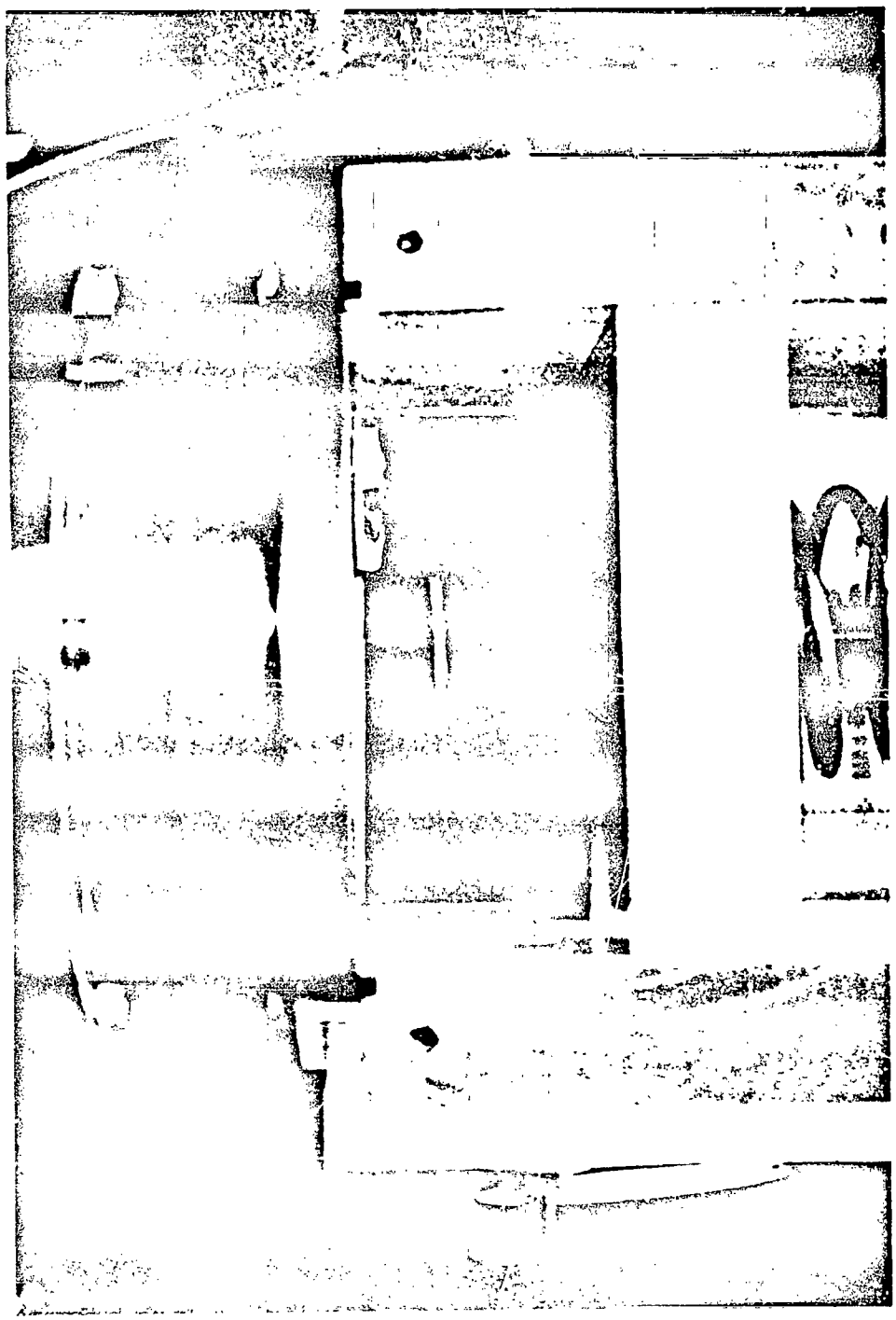

FIGURE 9. ACOUSTICAL LEVITATED METAL PLATE.

FLUID MOTIONS IN A LOW-G ENVIRONMENT

By

P.G. Grodzka*, S.V. Bourgeois, M.R. Brashears,
and L.W. Spradley
Lockheed Missiles & Space Company, Inc.
Huntsville, Alabama 35807

SUMMARY

The importance of natural convection and other fluid motions in low-g space processing is now well recognized. Recent space experiments in the areas of natural convection and material processing, as well as results of theoretical studies, have yielded much needed information on fluid behavior in low-g environments. The state of knowledge of fluid motions in low-g environments is reviewed and the dimensional analysis approach used to assess the relative importances of various driving forces for fluid flow in four of the Skylab material processing experiments outlined. Results of dimensional analyses for the Skylab experiments, subsequently confirmed by actual space data, are presented. Finally, the limits of dimensional analysis in assessment studies are indicated.

INTRODUCTION

Fluid phases are an inherent feature of most projected space manufacturing processes. In these processes products are produced from fluids which are manipulated in a variety of ways. Fluid manipulations in low-g may consist of levitating heated, uncontained fluid masses; heating and cooling contained fluid masses; applying various forces to fluid masses for shaping purposes; and applying various force fields for mixing, separating or positioning purposes. Fluid motions resulting from various manipulations may be generally classified as those arising from direct force application (stirring, pumping, and film forming) and spontaneous fluid motions arising from a variety of indirect causes. Among these latter spontaneous motions are natural convective motions caused by various combinations of thermal or concentration gradients and various force fields. Flows such as spreading of a liquid on a solid or on another liquid which occur in order to decrease system free energy are also examples of the latter category. In low-g environments most of the aforementioned motions, both forced and spontaneous, will differ substantially from motions initiated by similar means in a one-g environment. Fluid motions as a function of gravity level are of concern in low-g space processing applications because fluid motions can affect not only the shapes of fluid masses but also internal profiles of temperature, concentration, and immiscible particle distribution. These possibilities can

*Paper presented by P.G. Grodzka

afford unique opportunities for processing advantages or can be the source of undesirable problems.

Until recently, little information on actual fluid behavior in the low-g environment was available. Experiments and demonstrations performed aboard Apollo 14, 15, 16, 17 and Skylab II, II, and IV as well as results of recent theoretical studies, however, have begun to narrow the knowledge gap in the area. In the remainder of this paper the state of knowledge of fluid motions in low-g environments is reviewed. The review is divided into the following fluid flows and behaviors: natural convection; flows associated with spreading; flows associated with surface deformation; shear induced flows; and trajectories of levitated fluid masses. Following the review of low-g fluid behaviors, a brief outline of the dimensional analysis approach used to assess the relative importance of various driving forces for fluid flow in four of the Skylab material processing experiments is outlined. Results of dimensional analyses for the Skylab experiments subsequently confirmed by actual space data, are presented. Finally, the limits of dimensional analysis in assessment studies are indicated.

REVIEW OF LOW-G FLUID MOTIONS

A. NATURAL CONVECTION

Convective flows are classified as internal or external. Internal flows are those in which the total fluid contained within a cavity or enclosure is affected; the motions of water heated in a kettle, for example. In external flows only a small portion of the total fluid is affected significantly; a plume of warm smoke rising from a cigarette, for example. Both cases are of interest for space manufacturing purposes. Internal convection, however, is of immediate relevancy because of many current space experiment design considerations. External convective flows are more relevant to specific details of a processes mechanism, e.g., convective plumes from a growing dendrite. Theoretical treatments of the two cases are quite dissimilar. Boundary layer solutions, assuming that the fluid outside the boundary layer is unaffected, are usually adequate to describe external problems. More complex solutions are usually required for internal problems. Internal convective flows in low-g environments were reviewed in a recent paper [1]. Highlights of that work along with brief accounts of some developments are presented subsequently. External convection is also reviewed briefly. Before these reviews are considered, however, it may be well to reiterate the caution stated in Reference 1 regarding extrapolating experimental or theoretical results on convection obtained for one set or range of boundary conditions to another set or range of boundary conditions. Such action, if done without careful consideration, can result in serious error.

Internal Convection (Highlights of Reference 1 and Some Recent Developments): In low-g environments convective driving forces other than gravity will be of comparable or predominant importance. Among these possible driving forces are various accelerations (including gravity), surface tension (vapor/liquid interface), interfacial tension (liquid/liquid interface), electric fields, magnetic fields, and internal molecular forces.

On earth a constant gravity acceleration of 980 cm/sec^2 (one-g) is experienced by bodies. In a spacecraft both constant and varying accelerations occur to varying extents depending on the mission phase. Steady g-levels result from spacecraft rotation, gravity gradients, solar wind and solar pressure. Varying g-levels result from engine burns, attitude control maneuvers, and onboard vibrations from machinery or astronaut movement. Varying g-levels have been called g-spikes, disturbance environments, or g-jitter.

Convection caused by constant gravity accelerations can be of significant vigor in certain situations even at the 10^{-8} g-level or lower. The major determining parameters are amount of fluid involved and heating direction with respect to the gravity vector. Data from the Apollo 14 and 17 heat flow and convection experiment [2, 3, 4, 5], as well as temperature and pressure data from the Apollo 15 cryogenic tanks [6, 7] show that g-jitter also can result in convection of significant vigor even in relatively small containers. Furthermore, g-jitter is apt to be more of a problem in low-g environments than in a one-g environment because steady g-accelerations have a damping effect on g-jitter. Computer studies are currently underway to determine frequency, amplitude, and vibration form effects. These studies are utilizing an existing computer solution of the Navier-Stokes equations for natural convection in an enclosure [8]. The solution was modified to include the effects of a time-varying g-level. Two g-jitter profiles have been used as test cases: (1) a sine wave g versus time with a period of 1 second and (2) a saw-tooth profile with a period of 0.5 second. The mean g-level was varied from g = 1.0 to g = 10^{-5}. A matrix of cases was processed with amplitudes ranging from 10^{-2} to 10^{-5} g. Three different configurations have been used to determine the effect of geometry on g-jitter convection. A cylinder of mercury, a rectangular box of water, and a cylinder of helium gas were used as typical configurations.

Analysis of the results of the computer runs is still in progress, but preliminary data does show some interesting trends and effects. These can be summarized as follows: (1) the sine wave g-profile has very little effect on the heat transfer; (2) the saw-tooth g-jitter profile significantly affects the flow patterns and heat transfer for g-levels of 10^{-3} and larger; (3) the liquids show more g-jitter effects than the gas; (4) maximum temperature differences of 10% were observed between the constant g solutions and the g-jitter solutions. (This corresponds to 20°C out of 200°C on the average); (5) g-jitter changed the constant g unicell flow patterns in the cylinder of mercury to a multicell pattern; and (6) g-jitter appears to have more of an effect on "heating from the side" problems than on "heating from below" problems. No quantitative results will be presented at this time pending a more complete analysis of the analytical data.

Closely related to g-jitter convection is thermoacoustic convection. A suddenly heated wall causes adjacent fluid to expand. This sudden expansion sets up acoustic waves which propagate into the fluid. Given a sufficient heat rate, certain container dimensions, and dissipative mechanisms, a thermoacoustic vibration can be sustained as long as the appropriate boundary conditions are maintained. Recent theoretical studies

predict significant low-g thermoacoustic convection in gases given a sufficiently high heating rate [8].

Surface tension-driven cellular convection was demonstrated on both the Apollo 14 and 17 spaceflights [2, 3, 4, 5]. The cellular convection observed in the Apollo 14 flight experiment showed conclusively that cellular convection can be caused by surface tension alone. The Apollo 14 experiment further showed that, as in 1-g, a critical value of the temperature gradient must be exceeded before cellular convection is initiated. Furthermore, a polygonal cellular pattern was seen as the preferred pattern in a thin liquid layer of uniform thickness. Similar flow pattern experiments were conducted aboard Apollo 17. The Apollo 17 data showed that the sizes of the observed surface tension cells compared quite well with the values predicted by Pearson's linear analysis of surface tension-driven cellular convection [9]. The experiments further showed that the surface tension-driven cellular convection occurs at lower temperature gradients in low-g environments than in 1-g environments. The easier convection onset in low-g than in 1-g was surprising because Nield's linear analysis of cellular convection [10] which considers the coupling between surface tension and gravity predicts that surface tension and gravity reinforce each other strongly. Furthermore, Nield's analysis has received experimental verification in one-g [11]. A number of explanations for the surprising Apollo 17 result were considered. It was concluded that the formation of large surface tension-driven cells which tend to be the same size as those caused by gravity is hindered by gravity. Smaller size surface tension-driven cells, however, reinforced gravity-driven cells. The occurrence of a critical condition for convection onset in the Apollo 17 case is the result of the influence of the retaining side walls. Data were also obtained from the Apollo 17 experiments on the flow patterns at the onset of convection in low-g. Both rolls and cells were observed, an observation somewhat at variance with the general belief that rolls are associated with gravity-driven convection and cells with surface tension-driven convection.

Figures 1, 2 and 3 show cellular convection obtained in a ground test, in the Apollo 14 flight test, and in the Apollo 17 flight test. In these pictures a pan of oil containing suspended aluminum flakes to render the flow pattern visible was heated from below.

Non-cellular, surface-tension-driven convection was demonstrated or observed in a number of flight experiments (see Reference 1 for details). Ripples observed on some of the samples crystallized from the melt in the Skylab multi-purpose furnace furthermore bring to mind the surface-tension generated phenomenon of rythymic crystallization. This phenomenon was observed in ground experiments over forty years ago. Thin films of a number of molten substances have been observed to crystallize in a rythymic fashion [12]. One explanation of rythymic crystallization [13] is that the evolution of latent heat, once crystallization begins, renders surrounding melt more mobile and diminishes its surface tension. The mobile melt is therefore drawn toward cooler portions of the melt by the higher surface tension of the cooler melt. A ridge of melt forms which quickly crystallizes, repeating the cycle.

Electrically-driven fluid flows were observed in the Apollo 16 Electrophoresis Demonstration [14]. The Apollo 16 data indicate that the observed flows were probably of the electro-osmotic variety. Recent exploratory work, however, indicates that flows caused by polarization forces in aqueous electrolyte solutions are also possible (see Reference 1 for details).

Finally, some inferred evidence was found for phase change convection in some returned flight samples. When a liquid freezes the solid formed usually has a somewhat higher density than the liquid and hence a smaller volume. This shrinkage on freezing causes a corresponding fluid flow in the liquid; liquid flows toward the solidifying interface. Depending on the speed of crystallization, a number of fluid flow phenomena can occur. At high crystallization speeds (such as occurs when super-cooled metals crystallize), acoustical disturbances, cavitation effects, grain size transition, development of cavitation pits on constrained surfaces, and the presence of pressure pulses can occur. (See Reference 1 for details.)

External Convection: Analytical solutions for steady laminar convection have been obtained for the following cases [15]:

Vertical surface in a thermally unstratified medium

Vertical surface in a stably stratified medium

Vertical surface in a stably stratified medium with viscous dissipation

Vertical surface with a distributed energy source in the fluid

Vertical surface with mass addition

Plumes arising from concentrated energy sources, and

Axisymmetric flows.

The last two cases are of particular interest at the moment because of their relevancy to convection associated with growing dendrite crystals. For example, silver crystals were grown from silver nitrate solution aboard Skylab IV (Skylab IV Science Demonstration TV 106). The growth mechanism involved electrochemical reduction of silver ions by copper metal. During a ground performance of the demonstration convective plumes could be seen with the aid of a schlieren system to be rising from growing silver dendrites and falling from the copper wire. Needless to say the silver crystals returned from the Skylab IV demonstration were different in a number of respects from the ground grown crystals, the differences being the result of different convection vigors and patterns. Analyses of the experimental data are still in progress. A brief report of preliminary results, however, is available [16].

Boundary layer flow associated with a heated vertical wall is a well-known concept in fluid mechanics. A schematic of the streamlines associated with a convective boundary layer is shown in the sketch on the following page:

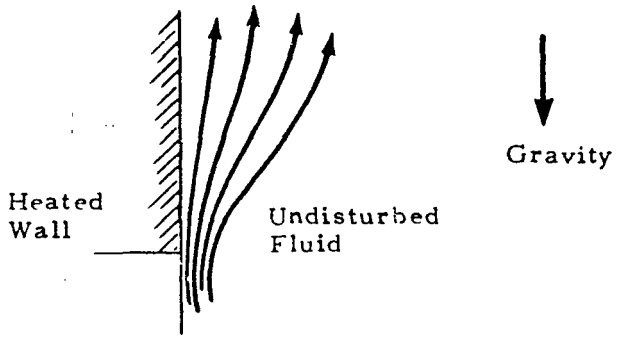

Temperature and velocity profiles associated with a convective boundary layer may be represented as follows [17]:

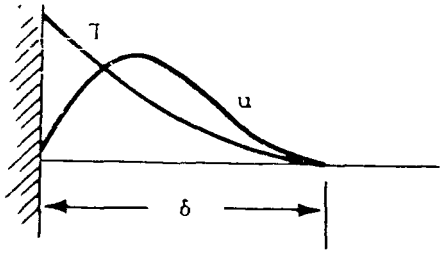

where T is temperature
u is velocity
δ is boundary layer thickness.

It may occur in some cases that velocity and temperature do not fall off to their values in the bulk of the fluid at the same point. In that case we speak of thermal and momentum boundary layers separately. In cases such as solution growth, concentration boundary layers also apply [18]. Obviously if a process is controlled in one-g by mass or heat transport rates, the process will be very much affected by a reduced gravity environment. In the case of dendrite growth we can expect significant gravity effects because dendritic growth is generally agreed to be a mass or heat transport controlled process. The streamlines associated with a dendrite growing from solution in a one-g environment would probably appear somewhat as shown in the sketch on the following page:

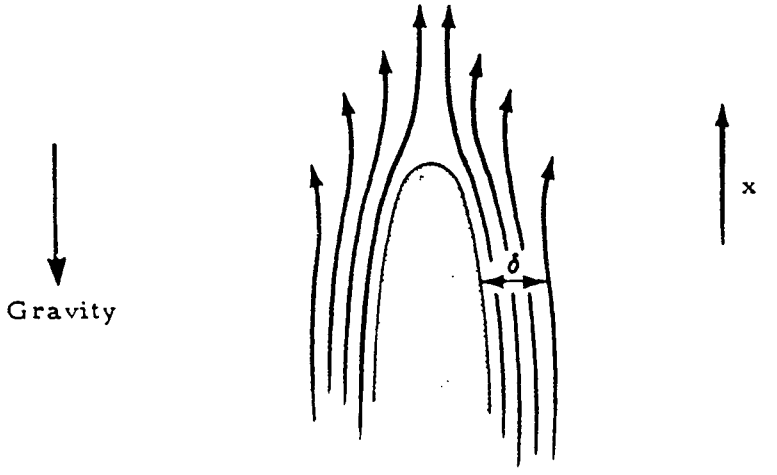

In the classical case of convection from a vertical plate the thickness of the boundary layer is proportional to

$$x\ Gr_x^{-1/4}$$

where Gr is the Grashof number and is given by

$$Gr_x = \frac{g\ \beta\ \Delta T\ x^3}{\nu^2}$$

where

x = vertical distance from bottom of plate

g = gravity acceleration

β = volumetric expansion coefficient

ΔT = the temperature difference at x

ν = kinematic viscosity.

At low-g the Grashof number becomes quite small and the boundary-layer approximation no longer applies [19]. The exact point at which a boundary-layer approximation no longer applies, however, is an individual matter depending on the particular circumstances or boundary conditions of an experiment or process. Also even at very low-g or small Grashof numbers all convection cannot be automatically assumed unimportant. For example, it has been shown that while convection is negligible in comparison with conduction near a heated body, it becomes as important at distances from the body of the order of $(Gr)^{-n}$ where n varies between 1/3 and 1/2 depending on body shape [20].

It is expected that the Skylab IV silver crystal growth demonstration will provide information on how convection affects dendritic growth. The only other known, reported study which has considered this question explicitly is one in which tin crystals were grown in a centrifuge [21]. It was found in that study that the first stages of crystal growth consisted of plate-like dendrites. The crystals exhibited no preference in orientation until approximately 4g - 5g. It is speculated that the observed change in crystal growth direction at 5 g was caused by convective effects.

B. SPREADING FLOWS

Low-G Liquid Configurations and Films: Low-g liquid behavior dependent on one liquid spreading or wetting a solid or another liquid has a number of potential low-g space processing applications: casting, formation of inverse bubbles, coating, encapsulation, and braze joining.

A liquid transferred from one container to another or from one gravity environment to another will exhibit various fluid motions until an equilibrium configuration is attained. Not only is the equilibrium attained as a function of gravity but so also is the attainment rate. The types of equilibrium configurations attainable at zero-g are summarized in Figure 4.

In the Apollo 14 Heat Flow and Convection Demonstration [4, 5] the flow pattern experiment was designed to contain a thin, uncovered layer of oil in a pan whose bottom was to be heated. The pan was designed with a wettable bottom and unwettable sides. It was expected, therefore, that a layer of oil somewhat as shown in the rectangular geometry, 10% full case c, of Figure 4 would be obtained. However, either because of aging or other unknown effects, the sidewalls were wetting when the experiment was performed in low-g so that a configuration somewhat as shown in the rectangular geometry, 10% full case a, of Figure 4. The cell was redesigned with baffles as shown in the following schematic for Apollo 17.

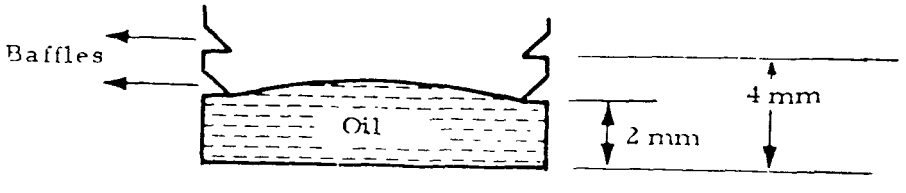

The new arrangement performed well and significant data were obtained [2,3].

During the Skylab IV Science Demonstrations, Astronaut Pogue delightedly reported that he had invented a zero-g drinking cup. His invention consists of the following essentials:

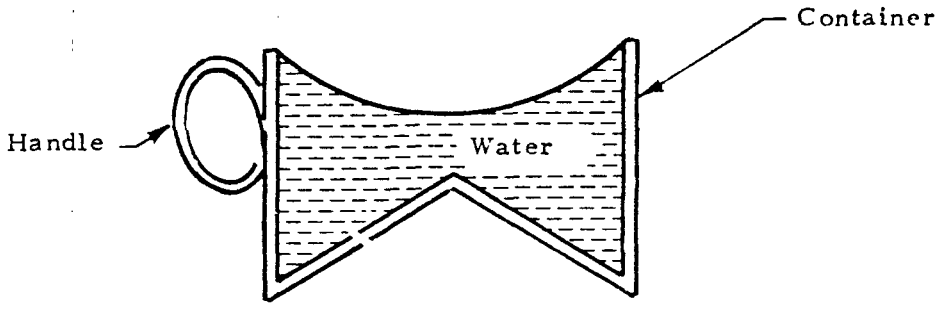

Zero-g Drinking Cup Invented by Astronaut Pogue

Astronaut Pogue demonstrated his invention and even showed a drawing of it on TV tape [23].

The time interval, t, for a liquid to attain a new configuration when its gravity environment is suddenly changed, e.g., drop tower or sounding rocket tests, can be estimated from the following formula [24]

$$t = K D^{3/2} \left(\frac{\rho}{\sigma}\right)^{1/2}$$

where

K = a constant dependent on container geometry and magnitude of gravity change

D = significant container dimension

ρ = liquid density

σ = liquid/vapor surface tension.

The preceding formula resulted from an experimental study. More insight into the roles of contact angle and gravity can be gained by considering the complete momentum conservation equation for liquid flow in capillary tubes [25]. This is given by:

$$\frac{2\sigma \cos\theta}{r} - \rho g h - \frac{8\mu}{r^2} h \frac{dh}{dt} - \rho\left(\frac{dh}{dt}\right)^2 - \rho h \frac{d^2h}{dt^2} = 0$$

where

r = tube radius

θ = contact angle between liquid and tube

h = liquid height in tube

μ = coefficient of viscosity.

This equation does not have a simple solution. However, the equation does tell us that the rate of capillary climb is dependent both on the contact angle and the gravity level.

A preflight analysis of the Skylab M552 Exothermic Brazing Experiment [26] based on considerations such as discussed in the preceding paragraphs predicted an increased rate and uniformity of spreading in low-g and better brazed joints as a result. Another predicted low-g effect was a more symmetrical interface at the free surface of the filler and capillary spreading in a wider gap than possible in a one-g environment. Both predictions were fulfilled in the flight experiment.

Related to rates of spreading or capillary rise are thicknesses of liquid films. Formulas have been derived for determining the liquid film thickness, h_o, on the surface of a solid withdrawn from a liquid at rest [27]. These formulas are as follows:

- For small withdrawal velocities ($u_o \mu << \sigma$)

$$h_o = 0.93 (\mu u_o)^{2/3} \sigma^{-1/6} (\rho g)^{-1/2}$$

- For large withdrawal velocities ($u_o \mu >> \sigma$)

$$h_o = \left(\frac{\mu u_o}{\rho g}\right)^{1/2}$$

Spreading in zero-g on a flat surface will occur if

$$\bar{S} = \sigma_{SV} - \sigma_{SL} - \sigma_{LV} \geq 0$$

where σ represents interfacial tension and the subscripts S, L, and V indicate the solid, liquid and vapor phases, respectively [28, 29]. If $\bar{S}$ is negative, the liquid will again conform to its minimum energy configuration which is a spherical segment with a solid-liquid control area, A, defined by [30]

$$A = \frac{\pi^{1/3} \sin^2\theta \, V^{2/3}}{(1 - \cos\theta)^{4/3} \left(\frac{2 + \cos\theta}{3}\right)^{2/3}}$$

where

θ = contact angle

V = volume of the liquid

For $\bar{S} \geq 0$, the rate of spreading depends on the viscosity and density of the liquid and the surface roughness. Many analyses exist for the rate and manner of spreading and film thickness under the controlling influence of gravity [31, 32], but these relationships cannot be applied to zero-g cases. The preceding discussions of spreading or wetting also have not considered any rate effects connected with the contact between liquid and solid. In reality, however, a number of contact angle non-equilibrium effects have been observed [33].

A surface wetting demonstration was proposed and approved for Skylab IV. The purpose of the wetting demonstration was to investigate the manner in which liquids spread over solids. This is important in the possible space manufacturing of thin film materials, especially in the adhesion casting process. The spreading speed and thickness uniformity will determine the feasibility of this processing technique. Practical applications include semiconductors, unique laminated structural materials, electromagnetic switching devices for computers, electro-optical and magneto-optical materials for laser communications devices. Only materials normally onboard Skylab were required for this demonstration.

The technical objective of this demonstration was to observe the spreading rate and the uniformity of thickness of a wetting liquid as it spreads over a solid substrate. Initially, a thin layer of liquid will immediately spread over the entire surface with a thickness on the order of molecular spacings. The driving force for this spreading is solid-liquid-gas surface energies. Further intrinsic spreading of the remaining liquid occurs by liquid-gas interfacial energy. This latter spreading will be much slower; or may stop completely. No data exist for the prediction of the intrinsic bulk spreading rate, but time to approach uniform thickness may exceed reasonable process times by orders of magnitude [28,31].

The Skylab IV astronauts were unable to conduct the surface wetting portion of Science Demonstration TV-107, Fluid Mechanics Series [23]. The TV-107 series consisted of:

A. Oscillation Damping Time
B. Surface Wetting
C. Droplet Impacts and Coalescence
D. Vortex Formation and Damping.

The A, C and D portions were completed, however, during the Skylab IV mission.

Preliminary review of the available TV films indicates that contact angles of grape-colored water on glass were approximately 90 degrees for a 1.5-inch diameter droplet which was filmed during TV 107-A. Wetting of Krytox oils on solid substrates may have been filmed during the floating zone demonstration, TV-101.

Drops and Inverse Drops: Producing unique composites by dispersing one immiscible material within another is a current space processing concept [34]. In the Apollo 14 Composite Casting Demonstration Experiment [35] greater degrees of dispersion of two immiscible materials (paraffin and sodium acetate trihydrate) within each other were obtained in samples processed during flight than in samples similarly processed on the ground. Another notable feature of the space processed samples was the formation of duplex dispersions or closed shells of one fluid surrounding and surrounded by another fluid. A number of various samples were also processed in the low-g environments of a drop tower, an aircraft during a climb-dive maneuver, and aboard Skylab [36, 37]. These also showed greater degrees of dispersion than samples processed on earth.

Drop formation is governed by the sum of a number of forces, as given by the following relationship [38].

$$F = F_g + F_k - F_\sigma - F_d$$

where F_g is a gravity force, F_k a kinetic force, F_σ an interfacial tension force, and F_d a drag force. The drop volume at the moment of drop formation, V_{dr}, can be thought of as composed of two parts [38]: an equilibrium volume, V_{eq}, and a dynamic volume, V_d or

$$V_{dr} = V_{eq} + V_d$$

and

$$V_{dr} = V_{eq} + q\, t_{rl}$$

where q is the flow rate of liquid into the drop, cm^3/sec, and t_{rl} is the time period during which the drop is released. The work from which the preceding relationships were obtained [38] presents further mathematical development of relationships predicting drop volumes for drops formed at non-wetted capillaries in liquid-liquid systems. The cited work, however, does not take into account the role of interfacial tension-driven convection in determining V_d.

To the authors' knowledge a full mathematical treatment including interfacial tension convection has as yet not been published. The work of J. T. Davies and others [39], however, indicates that interfacial tension convection does play a very important role in drop or emulsion formation. For example, the spontaneous emulsification of benzene, toluene, or xylene and strong solutions of dodecylamine hydrochloride is attributed to interfacial turbulence generated by interfacial tension gradients. The turbulence has the effect of tearing away drops.

Very little is known about the formation of duplex dispersions or closed shells of one fluid surrounding and surrounded by another fluid. Such closed fluid shells have been found in a number of liquid-liquid systems [40]: oil in water and water in oil. Closed shells of gas within a liquid (inverse bubbles)

have also been reported. The possibility of producing duplex dispersions (sometimes called inverse bubbles) in zero-g was discussed in an earlier report [41]. The mechanism by which inverse bubbles are formed is shown in the following sketch taken from Reference 42.

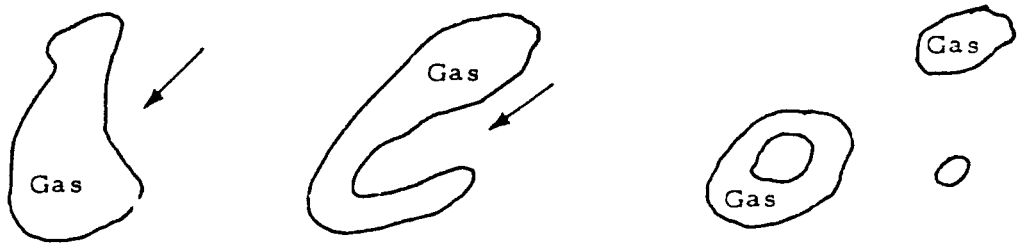

If two immisible liquids are present in a third liquid, a possibility of still another type of inverse bubble exists. Suppose one liquid preferentially "wets" another. Bubble (droplet) coalescence may then occur as illustrated in the following sketch,

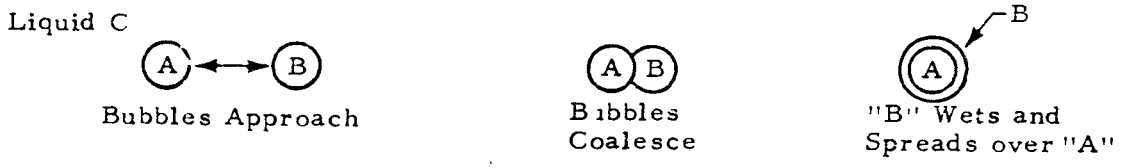

Recent experiments with pure water and with water containing surface active agent [43] have shown that inverse bubbles (thin, spherical films of air enclosed by liquid) are sensitive to electric fields. Application of an electric field destroys the bubbles, suggesting that self-generated electric fields may be responsible for inverse bubble stability. Another study [44], however, indicates that fluid flow may also play a role. Drops of water were floated on a water surface. It was demonstrated that a concave film of vapor flowing radially supports the floating drops. The radial flow also causes internal motions in the floating drops. Still other investigators [43], interestingly enough, determined that an inverse bubble is more stable if the effect of gravity can be overcome, so that the bubble would not rise or sink. They devised an experiment in which the inverse bubble is held in the center of a rotating liquid mass and found that as expected the inverse bubbles

lasted as long as the rotation continued. The area of interfacial forces and dynamics is clearly one which should receive more development.

C. SURFACE DEFORMATION-INDUCED FLOWS

Flows in this section are addressed to motion induced by normal (perpendicular) stresses at a liquid-vapor interface. These normal stresses are typified by the mechanical (jetting) force of the electron beam in the Skylab M551 (Electron Beam Welding) and M553 (Sphere Forming) experiments [26]. Such stresses result in surface deformations; and, in combination with surface tension and inertia forces, can lead to sloshing actions and even splattering (unstable sloshing). These motions are accentuated in low gravity. The following discussion illustrates surface deformation-induced flow in space processing applications.

Sloshing: During electron beam welding, sloshing of the molten metal leads to the phenomenon known as spiking which occurs in the partial penetration welds of the stainless steel samples in the M551 experiment. This phenomenon is illustrated in Figure 5. The following mechanism was proposed for spiking [45, 46]. Each time the electron beam penetrates to the base of the weld (no melt barrier remains), a spike is formed. The severity of the spiking depends on the frequency of the oscillation and the welding speed as well as the material properties. The sloshing of the melt can give rise to increased porosity in the fusion zone if contaminant gas bubbles are trapped at the weld base when the molten metal flows back into the cavity. These bubbles are then frozen if the cooling rate is sufficiently rapid. Sloshing may also induce cold shuts and cracks as the melt falling back into the cavity might not bond to the already frozen spike walls. It also leads to very efficient mixing in the melt and should produce a very homogeneous fusion zone.

A theoretical analysis of the melt-beam dynamics described above and in Figure 5 show that spiking frequency is predicted by [26, 46]

$$\omega = \frac{\frac{1}{4}\sqrt{\frac{g}{h}}}{\sqrt{\frac{P_V - \frac{2\sigma}{a}}{\rho g h}} - \sqrt{\frac{P_V - \frac{2\sigma}{a} - gh_1}{\rho g h}}} \qquad (1)$$

The preceding analysis considered welding a horizontal plate from above. Equation (1) should not be expected to generate exact, rigorous results to match actual M551 experimental data. It can, however, be utilized to predict a low gravity variation in the stainless steel electron beam welds. As predicted in Equation (1), spiking frequency varies inversely with gravity level. Using the experimental conditions, physical properties and beam parameters for the M551 stainless steel experiment and assuming levels of superheat in the melt, Equation (1) predicts oscillation frequencies shown in Figure 6.

In the limit as $g \rightarrow 0$, Equation (1) yields,

$$\omega = \sqrt{\frac{P_V - 2\sigma/a}{4\rho h^2}} \qquad (2)$$

which means that spiking cannot occur below 2027°C for stainless steel. The surface tension force overcomes any jetting due to vaporization at lower surface temperatures. This is indicated by imaginary numbers in Equation (2).

Splattering: In the M551 experiment a question arises as to the stability of the molten dwell pool in low gravity. An instability might develop in the molten puddle formed during the dwell mode of the M551 experiment, wherein the liquid might not adhere and separate from the solid disk or violent splattering may occur due to unstable oscillation of the melt/vapor interface. This splattering could be caused by the momentum force associated with the impinging electron beam.

The latter instability mechanism has been treated recently by Berghmans [47]. He performed a theoretical study of fluid interface stability with special attention being given to the role of surface tension. It was motivated by its possible application to the splattering of molten metal as observed during electric arc welding.

Berghmans' study concluded that the weld pool interface would be stable if the following condition was met,

$$We^2 \leq 1.04 + 3.3\ Bo^2 \qquad (3)$$

where $We = 2\ P_m\ R/\sigma$ is a modified Weber number, $Bo = (\rho_L - \rho_V)\ g\ R^2/\sigma$ is a Bond number, P_m is the average beam mechanical pressure exerted over the dwell puddle and R is the beam radius. The analysis is exact if viscous and inertia effects are unimportant as far as stability is concerned. Other assumptions are the radial pressure distribution in the beam impingement area is exponential and the beam radius is negligible in comparison to the dwell pool radius.

The criterion expressed by Equation (3) was applied to each of the M551 materials and for gravity levels between ground tests (g_E = 980 cm/sec^2) and those of Skylab ($g = 10^{-5}\ g_E$). Beam diameter was also varied between 0.635 and 0.07 cm with corresponding average beam pressures of 15.3 and 1060 dynes/cm^2, respectively. For each of the preceding cases,

$$We^2 < 10^{-2}$$

therefore, the momentum force of the electron beam will not be a cause of weld pool splattering in the M551 experiment.

D. SHEAR-INDUCED FLOWS

When liquid containers rotate or vibrate, the walls induce tangential stresses on the liquid which induce nonuniform flow within the liquid. Excellent treatises on this type of flow in low-g are given by Habip [48], Abramson [49, 50], and Moiseyev [51] for vibrating containers; whereas Greenspan [52] and Benton [53] give analyses for rotating containers.

Transient rotation and vibration of containers may be significant in certain space processing applications, such as during sounding rocket flights. Just before the low-g portion of these flights, the rockets are despun from 150 down to 15 rpm. Even with despin platforms, despin will lead to spindown ratios of 5 rpm down to 1 rpm.

The time to reach a new steady-state flow profile when container rotation is suddenly increased from a constant angular velocity to another is termed spinup, while the converse situation is referred to as spindown time. For a finite cylindrical container completely filled with liquid, spinup and spindown times are shown in Figure 7 for various Rossby numbers. The Rossby number, ϵ, is given by $\epsilon = 1 - \Lambda_o/\Lambda_1$ for spinup and by $\epsilon = (\Lambda_1/\Lambda_o) - 1$ for spindown where Λ_o = initial container angular velocity and Λ_1 = final angular velocity.

In a sounding rocket with a despin platform, ϵ is approximately -0.8. Utilizing typical space processing container dimensions ((cylinder 8 inches long by 0.75 inch diameter), the spindown times (to reach 1% of final state) for various fluids are shown below:

Fluid*	Spindown (Seconds)
Mercury	120
Water	50
Krytox oil (AZ)	28
Carbon dioxide	13
Helium	4

Thus it can be seen that these shear induced flows can be important when three-minute low-g sounding rocket flights are contemplated. For other space processing environments such as Skylab or ASTP, vibration rather than rotating shear flows are more important [2].

E. TRAJECTORIES OF LEVITATED FLUID MASSES

A practical consideration in a number of low-g space processing concepts is how to manipulate matter so that a liquid mass can be freely levitated and then heated, cooled, or stirred. The first consideration in achieving this objective is how to position the liquid or solid mass in a freely levitated

*At 1 atm and room temperature.

condition. The second consideration is how to keep the liquid positioned during processing.

In low-g a fluid mass may be set into relative motion (internal or convective motions are here excluded) by a number of forces. Among these may be

- Reaction forces due to vaporization or degassing
- Various action forces such as the impingement of an electron beam or jet of gas, and
- Attractive and repulsive forces generated by gravity and electric or magnetic fields.

Relative motion is opposed by cohesive and adhesive forces.

These concepts were applied to the M553 experiment flown aboard the Skylab [30]. The objective of the experiment was to deploy liquid spheres (obtained from electron beam melting) in a vacuum chamber and achieve containerless low gravity solidification. In order to predict the motion of the molten sphere, a trajectory program was developed that included allowances for the electron beam force, deployment velocity considerations (surface tension effects), vaporization force based on three-dimensional temperature history, Skylab orbit considerations, and additional general force routine. The general force routine was included specifically to allow analysis of experiments conducted in KC-135 aircraft flying ballistics trajectories to achieve low-g environments. Accelerometer data recorded during the flights served as input to the routine.

A typical sequence of events consisted of initiation of the electron beam with impingement on a solid metal cylinder. Formation times for spherical portions occurs very rapidly after melting as shown by the calculation in Table I. Fully molten spheres were usually obtained in 3 to 6 seconds. Oscillations (30 to 40 Hz) occur due to perturbations and to "overshoot" as a result of surface tension surface area minimization.

Table I - Formation Times for M553 Materials

M553 Materials	ρ	σ	R	T
	(g/cm^3)	(dyne/cm)	(cm)	(sec)
Ni	7.85	2050	.3175	.011
Ni-12% Sn	7.80	1500	.3175	.013

Viscous effects will damp out the oscillation in time; however due to the relatively low viscosity of liquid metals, the time is on the order of tens of seconds for spheres of a fraction of a centimeter in diameter. In fact for a 0.6 cm nickel sphere, a 3 second decay time constant results requiring 15 seconds for 99% decay and 30 seconds for 99.99%.

After complete melting, the experiment was designed to deploy the molten sphere. It was found that the vaporization force controlled the trajectory if deployment occurred rapidly after electron beam cutoff. A schematic of this situation is shown in Figure 8 corresponding to a particular run in a March 1972 KC-135 experiment.

A photographic sequence from the same flight is shown in Figure 9. Here the specimen adhered to the pedestal for 0.3 second after completely melting (t = 0 corresponds to a completely molten sphere). This time allowed isothermal correlations to result before deployment thus producing a gravity controlled motion (the gravity component in the film was directed to the lower left). The oscillations about the spherical shape are also evident in the photographs. For a detailed discussion the reader is referred to References 30 and 54.

PREDICTING LOW-G FLUID MOTION VIA DIMENSIONAL ANALYSIS

Dimensionless parameters, such as the Rayleigh and Marangoni numbers, may be thought of as ratios of physical forces. Thus when a particular ratio is >> 1, the force associated with the numerator dominates that of the denominator, and vice versa when the ratio is << 1. In certain well studied problems, critical values exist for these dimensionless parameters (ratios) such that a change of state occurs as the critical value is exceeded and one force overcomes the other.

The likelihood of natural convection arising in a fluid and its order of magnitude if it does occur can be estimated for buoyancy (gravity) induced conditions by examining a dimensionless parameter called the Rayleigh number (Ra). A similar analysis can be applied for surface tension-induced motion in fluids with free surfaces by examining a dimensionless parameter termed the Marangoni number (Ma). These numbers are defined by

$$Ra = \frac{g\beta \Delta T L^3}{\nu \alpha}$$

$$Ma = \frac{\left(\frac{d\sigma}{dT}\right) \Delta T L}{\mu \alpha}$$

where

g = gravity
β = thermal expansion coefficient
ΔT = temperature difference across the fluid
L = depth or width of the fluid
σ = surface tension
μ = absolute viscosity
ν = kinematic viscosity
α = thermal diffusivity.

The Rayleigh number is, therefore, the weighted ratio of the buoyancy force to the viscous force, whereas the Marangoni number is the corresponding ratio of surface tension to viscous force. In each number, the numerator contains the driving force with the denominator representing the restraining

force. Thus the tendency for achieving sustained convective motion is greater as the numbers increase. As they surpass their critical values, the driving forces overcome viscous restraining forces and a change in flow occurs; i.e., a transition from no-flow to laminar convection or from laminar to turbulent convection occurs.

The ratio of Ra and Ma to their respective critical values (Ra_c and Ma_c), which are determined by geometry, type of containment and direction of heating, determines the onset and magnitude of fluid flow. If either Ra/Ra_c or Ma/Ma_c exceed unity, flow will occur and heat transfer through the fluid increases because the convective heating is superposed to the conductive and radiative modes existing before flow initiates. As these ratios increase, the magnitude (velocity) of flow increases until turbulence finally occurs and the amount of convective heat transfer also increases. Normally this relation is linear on a log-log plot in a given regime. When heating from the side in a gravity field, for example, the critical Rayleigh number is shown to be zero from theoretical considerations [55]. Experimental results have shown, however, that a certain finite critical condition must be exceeded before heat transfer is increased over that of conduction and radiation [56]. Upon heating from below, the liquid layer remains stable to fluid flow as well as convective heat transfer until a relatively large critical condition is exceeded. For a liquid layer bounded on bottom with a solid wall (heating element) and on top with a free surface, Ra_c is approximately 1100 [57].

The preceding quantities, Ma_c and Ra_c, are dependent on such properties of the fluid and container as the Prandtl number, Biot number, aspect ratio, heater versus fluid thermal conductivity, sidewall thermal conditions, and surface deformability (crispation and Bond numbers). The Prandtl, Biot, and Bond numbers are dimensionless ratios which often appear in many other engineering problems. The aspect ratio is a measure of the geometrical symmetry of the fluid container, and as such it also appears frequently in many engineering problems. The crispation group appears less frequently and is utilized in the study of capillary waves. The definition and utility of each of these dimensionless numbers are discussed in Reference 2.

The preceding discussion has demonstrated the utility of dimensionless numbers for describing certain fluid flow phenomena. It was noted that these numbers are extremely useful in well studied problems where ranges in their values have been identified with flow regimes. In other less studied problems, the state of the art of nondimensional numbers is at a very primitive stage and they must be used discretely. An example of their use in a complex situation follows.

One of the Skylab M512 experiments, M553 Sphere Forming, involved melting nickel specimens in a vacuum chamber and allowing the molten sphere to deploy [54]. The ensuing free-float time would then give rise to containerless freezing. The nickel was melted by an electron beam (eb).

Application of dimensional analysis [58, 59] to the governing equations for eb melting, coupled with ground-based and low-gravity experiments, enabled prediction of the extent of reduction or increase of motion in the molten metal and/or the change in flow pattern in eb melting in space. Possible

physical forces which could induce fluid flow in the M553 experiment and their causes include [54]: gravity, Lorentz forces, electrostriction, magnetostriction, electrostatic forces, surface tension, solidification shrinkage, electron beam mechanical, thermal expansion, vibration, centrifugal and coriolis, vapor pressure, inertia forces and viscous forces.

The preceding forces, which could influence fluid flow and solidification, appear explicitly in the conservation equations which apply to formation of a molten pool by electron beam heating [54]. From the many possible forces, the controlling physical forces can be determined by non-dimensioning each of the preceding equations and performing an order-of-magnitude comparison on the various dimensionless groups which result [58, 59]. The key to successful analysis is in choosing the proper reference values; i.e., since no freestream velocity exists, which forces do we equate to estimate a "characteristic" or "typical" velocity. Choosing the proper characteristic velocity is very important, since the reference time, temperature, etc., usually depend on this velocity.

Examination of film taken during both KC-135 low gravity flight experiments and ground tests indicated that surface flow velocities for nickel specimens were approximately 20 cm/sec. Of the possible forces affecting electron beam melting only those shown in Table II yield characteristic velocities of this order of magnitude. These driving forces consist of couplings involving surface tension, gravity or Lorentz (electromagnetic) forces with inertia forces.

Table II - Probable Characteristic Velocities in Electron Beam Melting [54]

Controlling Forces	Velocity	
	Functional Form	Value (cm/sec) for Nickel in M553
Inertia = Surface Tension	$(ST/\rho L)^{1/2}$	20
Inertia = Lorentz	$(\sigma' E^2 L/\rho)^{1/3}$	1
Inertia = Gravity	$(gL)^{1/2}$	18 at 1 g_E 6 at 10^{-4} g_E
Viscous = Lorentz	$(\sigma' E^2 L^2/\mu)^{1/2}$	7

The dimensionless momentum equation which determines fluid flow in electron beam melting becomes (upon choosing the surface tension-inertia characteristic velocity),

$$\frac{1}{N_{St}} \rho \frac{\partial \vec{V}}{\partial t} + \frac{1}{N_{Oh}} \rho(\vec{V} \cdot \nabla) \vec{V} = - \frac{1}{2N_{Oh}} \nabla P + \nabla^2 \vec{V} + \frac{N_{Bo}}{N_{Oh}} (\rho \vec{g}) + \frac{2N_{MI}}{N_{Oh}} (\vec{V} \times \vec{B}) \times \vec{B} \quad (4)$$

where

N_{St} = Stokes number = $\mu t/\rho L$

= duration of process/residence time

N_{Oh} = Ohnesorge number = $\mu/\sqrt{\rho L S T}$

= viscous force/surface tension force

N_{Bo} = Bond number = $\rho g L^2/ST$

= gravity force/surface tension

N_{MI} = magnetic interaction number

= $B^2 L/2\mu 'ST$

= magnetic force/surface tension

Using physical property data for nickel and the beam parameters for the M553 experiment, the equation reduces to

$$10^3 \rho \frac{\partial \vec{V}}{\partial t} + 10^3 \rho(\vec{V} \cdot \nabla)\vec{V} = -10^3 \nabla P + \nabla^2 \vec{V} + G(\rho \vec{g}) + 10^{-1} (\nabla \times \vec{B}) \times \vec{B} \qquad (5)$$

where

$G = 10^3$ for earth gravity

$G = 10^{-1}$ for expected Skylab gravity.

This order-of-magnitude analysis indicates that surface tension driven convection will occur both in ground tests and for Skylab conditions because $N_{Oh} << 1$. This is confirmed by KC-135 M553 tests. Furthermore, a comparable degree of gravity driven convection will exist on ground tests, but will be negligible in the reduced gravity of Skylab. Thus different forces will control convection on earth versus Skylab. The preceding analysis also indicates that electromagnetic or Lorentz forces will be negligible with regard to causing fluid motion.

The surface tension driving force considered above is actually a surface tension gradient caused by radial and lateral temperature gradients. Ignoring convection, gradients of at least several hundred degrees Celsius per centimeter have been predicted during melting. It can be shown by dimensional analysis (equate inertial and viscous terms) that the motion caused by the initial temperature gradients will occur in less than 0.1 second and can persist for 60 seconds after removing the driving force. This means that there will be some fluid motion during solidification if the M553 specimens freeze after 32 to 48 seconds as predicted Melting time for these specimens is approximately 3 seconds.

Values of the pertinent dimensionless groups for the remaining M553 materials are given in Table III. As can be seen, no significant changes are evident from the preceding conclusions for pure nickel.

Table III - M553 Dimensional Analysis

Material	N_{Oh}	N_{Bo}	$\frac{1}{N_{Oh}}$	$\frac{N^{*}_{Bo}}{N_{Oh}}$	$\frac{N^{+}_{Bo}}{N_{Oh}}$
Ni-Sn	4.4×10^{-4}	1.50	2292	3437	.34
Ni-Ag	5.0×10^{-4}	1.53	1991	3043	.30
Ni-Cu	4.45×10^{-4}	1.54	2107	3241	.32

*With earth gravity (9.8 m/sec^2).
+With 10^{-4} earth gravity.

Early examinations of KC-135 and ground film indicated fluid velocities of 300 cm/sec. Dimensional analysis based on a characteristic velocity of 300 cm/sec would have yielded the following controlling forces rather than those shown in Table 2: coupling involving surface tension, gravity or Lorentz forces with viscous forces. This would have led to erroneous coefficients appearing in Equation 2 and entirely different conclusions as to decay times and controlling forces on earth versus Skylab processing. This indicates the importance of choosing the proper characteristic velocity and the importance of discrete application of dimensional analysis to complex problems.

A compilation of fluid velocities (on the molten sphere surfaces) measured from movies taken during Skylab, KC-135 aircraft and terrestrial processing is shown in Table IV [54]. The variations in results are probably due to differences in material compositions and beam settings (i.e., focus, impact point, voltage and amperage) rather than gravity effects. As discussed earlier only surface tension and gravity forces are predicted to produce these velocities. The one velocity measurement obtainable from the Skylab movie was an order of magnitude lower than that obtained from some low gravity KC-135 aircraft and ground-based movies, but was similar to ground and KC-135 measurements also obtained long after complete melting. It can be concluded that no significant difference in magnitude of convection occurred between Skylab, KC-135 and ground processing, which reinforces the theory of surface tension as the dominating force for fluid motion. This demonstrates the utility of dimensional analysis in the evaluation of complex physical problems:

- Prediction of vigorous convection on Skylab
- Selection of controlling driving forces and characteristic times and velocities for fluid motion.

Table IV - M553 Surface Velocity Measurements

Processing Environment	Gravity Level* (g)	Sphere Material	Fluid Velocity (m/sec)	Time of Measurement
Skylab	10^{-4}	Ni-Ag	0.02	Very long after melted
Ground	1	Ni-Ag	0.35 to 0.40	From early to complete melt
KC-135	$6 \cdot 10^{3}$	Ni-Ag	0.20 0.10	Before full melt Right after full melt
Ground	1	Ni	0.15 0.20 0.33	Before complete melt
Ground	1	Ni	0.12	Half melted

*Normalized by Earth gravity.

Limits of Dimensional Analysis: In conclusion, the preceding discussions have demonstrated the utility of dimensionless numbers for describing certain fluid flow phenomena. It was noted that order-of-magnitude, dimensional analysis is extremely useful in well studied problems where ranges in their values have been identified with flow regimes. In other less studied problems, the status of nondimensional numbers is at a very primitive stage and careful, discrete use must be made of them.

At a minimum, the following information must be known before realistic results can be obtained:

- All the possibly important physical forces and energy transfer mechanisms,
- Confident estimates of important characteristic or reference quantities such as velocity, temperature, length, etc., and
- The algebraic manipulations [58, 59] required to evaluate order-of-magnitude and dimensional analyses.

Meaningful dimensional analysis, however, requires both physical insight and comprehension and is not merely an exercise in algebra. A great deal of information can thus be obtained if dimensional analysis is coupled with the general equations and boundary conditions that describe the problem. Furthermore, its success depends on the validity and existence of these basic general equations that describe the related physical phenomena.

REFERENCES

1. Grodzka, P. G., and T. C. Bannister, "Natural Convection in Low-g Environments," Paper No. 74-156, AIAA 12th Aerospace Sciences Meeting, 30 January - 1 February 1974, Washington, D. C.

2. Bannister, T. C., P. G. Grodzka, L. W. Spradley, S. V. Bourgeois, R. O. Hedden and B. R. Facemire, "Apollo 17 Heat Flow and Convection Experiments, Final Data Analyses Results," NASA TM X-64772, 16 July 1973.

3. Grodzka, P. G., and T. C. Bannister, "Heat Flow and Convection Experiments Aboard Apollo 17," submitted for publication.

4. Grodzka, P. G., C. Fan and R. O. Hedden, "The Apollo 14 Heat Flow and Convection Demonstration Experiments; Final Results of Data Analysis," LMSC-HREC D22533, Lockheed Missiles & Space Company, Huntsville, Ala., September 1971.

5. Grodzka, P. G., and T. C. Bannister, "Heat Flow and Convection Demonstration Experiments Aboard Apollo 14," Science, Vol. 176, 5 May 1972, pp. 506-508.

6. Barton, J. E., and H. W. Patterson, "Post-Flight Analysis of the Apollo 15 Cryogenic Oxygen System," Boeing Company Report D2-1189422-1, 15 December 1971.

7. Barton, J. E., and H. W. Patterson, "Apollo Oxygen Tank Stratification Analysis — Final Report," Report D2118406-2, Vol. 2, Boeing Company, Huntsville, Ala., 31 January 1972.

8. Spradley, L. W., "Thermoacoustic Convection of Fluids in Low Gravity," Paper 74-76 presented at the 12th AIAA Aerospace Sciences Meeting, 30 January - 1 February, Washington, D. C., 1974.

9. Pearson, J. R. A., "On Convection Cells Induced by Surface Tension," J. Fluid Mech., Vol. 4, 1958, pp. 489-500.

10. Nield, D. A., "Surface Tension and Buoyancy Effects in Cellular Convection," J. Fluid Mech., Vol. 19, 1964, pp. 341-352.

11. Palmer, H. J., and J. C. Berg, "Convective Instalability in Liquid Pools Heated from Below," J. Fluid Mech., Vol. 47, 1971, pp 779-787.

12. Dippy, J. F. J., "The Rhythmic Crystallization of Melts," J. Phys. Chem., Vol. 36, 1932, pp. 2354-2361.

13. Hughes, W., "Spiral Markings on Carborundum Crystals," Nature, Vol. 1 123, 20 April 1929, pp. 603-604.

14. Snyder, R. S., "Electrophoresis Demonstration on Apollo 16," NASA TM X-64724, November 1972.

15. Gebbart, B., "External Natural Convection Flows," Appl. Mech. Rev., 1969.

16. Grodzka, P. G., and B. Facemire, "Growth of Silver Crystals Aboard Skylab IV; Quick-Look Report," available from B. Facemire, Space Sciences Laboratory, NASA-Marshall Space Flight Center, Ala.

17. Eckert, E. R. G., and R. M. Drake, Jr., Heat and Mass Transfer, McGraw-Hill, New York, 1959, p. 312.

18. Brice, J. C., The Growth of Crystals from Liquids, American Elsevier Publishing Co., Inc., New York, 1973, p. 129.

19. Ede, A. J., "Advances in Free Convection," in Advances in Heat Transfer, Vol. 4, 1967, p. 44.

20. Mahony, J. J., Proc. Roy. Soc. (London), Vol. A238, 1957, pp. 412-423.

21. Johnston, M. H., "Influence of Gravity on Growth Orientations of Tin Single Crystals," J. Crystal Growth, Vol. 19, 1973, pp. 79-80.

22. Otto, E. W., "Static and Dynamic Behavior of the Liquid-Vapor Interface During Weightlessness," AIChE Chem. Engr. Progr. Sympos., Vol. 62, No. 61, 1966.

23. Bannister, T. C., Space Sciences Laboratory, NASA-Marshall Space Flight Center, Ala., is the person to contact for further details.

24. Reynolds, W. C., and H. M. Satterlee, "Liquid Propellant Behavior in Low and Zero g," in The Dynamic Behavior of Liquids in Moving Containers, Editor: H. Norman Abramson, NASA SP-106, 1966.

25. Pickett, G., "Rate of Rise of Water in Capillary Tubes," J. Appl. Phys., Vol. 15, 1944, p. 623.

26. Bourgeois, S. V., "Convection Effects on Skylab Experiments M551, M552 and M553 — Phase C Report," LMSC-HREC TR D306955, Lockheed Missiles & Space Company, Huntsville, Ala., 1 December 1973.

27. Levich, V. G., and U. S. Krylov, "Surface-Tension-Driven Phenomena," in Ann. Rev. Fluid Mech., Vol. 1, 1969, p. 308.

28. Steurer, W. H. et al., "Processes for Space Manufacturing Definition of Criteria for Process Feasibility and Effectiveness," NASA CR-61334, June 1970.

29. Zisman, W. A., "Relation of Equilibrium Contact Angle to Liquid and Solid Constitution," in Contact Angle, Wettability and Adhesion, Adv. Chem. Ser., No. 43, American Chemical Society, Washington, D. C., 1964, pp. 1-51.

30. Brashears, M. R., and S. J. Robertson, "Research Study on Materials Processing in Space Experiment M512," Final Report, LMSC-HREC TR D306954, Lockheed Missiles & Space Company, Huntsville, Ala., 1 December 1973.

31. Ludvikson, V., and E. N. Lightfoot, "The Dynamics of Thin Liquid Films in the Presence of Surface-Tension Gradients," AIChE Journal, Vol. 17, 1971, pp. 1166-1173.

32. Padday, J. R., "Cohesive Properties of Thin Films of Liquids Adhering to a Solid Surface," in Thin Liquid Films and Boundary Layers, 1970, p. 64.

33. Lightfoot, E. N., and V. Ludviksson, "Deformation of Advancing Menisci," AIChE J., Vol. 14, 1968, pp. 674-677.

34. Lacy, L. L., and G. H. Otto, "The Electrical Properties of Zero-Gravity Processed Immiscibles," AIAA Paper 74-208, AIAA 12th Aerospace Sciences Meeting, Washington, D. C., 30 January - 1 February 1974.

35. Yates, I. C., Jr., "Apollo 14 Composite Casting Demonstration — Final Report," TM X-64641, NASA-George C. Marshall Space Flight Center, Ala., October 1971.

36. Reger, J. L., and I. C. Yates, Jr., "Preparation and Metallurgical Properties of Low Gravity Processed Immiscible Materials," Paper given at the AIAA 12th Aerospace Sciences Meeting, 30 January - 1 February, 1974, Washington, D. C.

37. Skylab Science IV Demonstration TV 102, L. L. Lacy, NASA-Marshall Space Flight Center, Space Sciences Laboratory is the person to contact for further details.

38. Heertjes, P. M., L. H. de Nie, and H. J de Vries, "Drop Formation in Liquid-Liquid Systems — I Prediction of Drop Volumes at Moderate Speed of Formation," Chem. Engr. Sci., Vol. 26, 1971, pp. 441-449.

39. Davies, J. T., and D. A. Haydon, "Spontaneous Emulsification," Proceed. 2nd Internat. Congr. of Surface Activity, Vol. I, Butterworths Scientific Publications, London, 1957, pp. 417-425.

40. Davies, J. R., and E. K. Rideal, Interfacial Phenomena, Academic Press, Reading, Mass., 1963.

41. Grodzka, P. G., "Zero-Gravity Solidification," LMSC-HREC D148619, Lockheed Missiles & Space Company, Huntsville, Ala., March 1970, p. 27.

42. Baird, M. H. I., "The Stability of Inverse Bubbles," Trans. Faraday Soc., Vol. 56, 1960, p. 214.

43. The Amateur Scientist, Scientific American, August 1973, pp. 104-109.

44. The Amateur Scientist, Scientific American, April 1974, pp. 116-121.

45. Weber, C. M., E. R. Funk and R. C. McMaster, "Penetration Mechanism of Partial Penetration Electron Beam Welding," Welding J., February 1972, pp. 90s - 94s.

46. Tong, H., and W. H. Geidt, "A Dynamic Interpretation of Electron Beam Welding J., June 1970, pp. 269s - 266s.

47. Berghmans, J., "Stability of a Gas-Liquid Interface and Its Relation to Weld Pool Stability," J. Phys. D: Appl. Phys., Vol. 5, 1972, pp. 1096-1105; and "Theoretical Investigation of the Interfacial Stability of Inviscid Fluids in Motion, Considering Surface Tension," J. Fluid Mech., Vol. 54, 1972, pp. 129-141.

48. Habip, L. M., "On the Mechanics of Liquids in Subgravity," Astr. Acta, Vol. 11, No. 6, 1965, pp. 401-409.

49. Abramson, H. N., "Dynamic Behavior of Liquid in Moving Container," Appl. Mech. Rev., Vol. 16, No. 7, 1973, pp. 501-506.

50. Abramson, H. N., "The Dynamic Behavior of Liquids in Moving Containers," NASA SP-106, 1966.

51. Moiseyev, N. N., and V. V. Rumyantsev, Dynamic Stability of Bodies Containing Fluid, Springer-Verlag, New York, 1968, pp. 42 and 207.

52. Greenspan, H. P., The Theory of Rotating Fluids, Cambridge Press, Cambridge, Mass., 1968, pp. 34, 35, 36, 161, 175, 272, 274 and 290.

53. Benton, E. R., "Nonlinear Hydrodynamic and Hydromagnetic Spin-Up Driven by Elemann-Hartmann Boundary Layers," J. Fluid Mech., Vol. 57, Part 2, 1973, pp. 337-360.

54. Bourgeois, S. V., and M. R. Brashears, "Fluid Dynamics and Kinematics of Molten Metals in the Low-Gravity Environment of Skylab," AIAA Paper 74-205, AIAA 12th Aerospace Sciences Meeting, January 1974.

55. Batchelor, G. K., "Heat Transfer by Free Convection Across a Closed Cavity Between Vertical Boundaries at Different Temperatures," Quart. Appl. Math, Vol. 12, October 1954, p. 214.

56. Eckert, E. R. G. and W. D. Carlson, "Natural Convection in an Air Layer Enclosed Between Two Vertical Plates with Different Temperatures," Int. J. Heat Mass Trans., Vol. 2, 1961, pp. 106-120.

57. Sparrow, E. M., R. J. Goldstein, and V. K. Jonsson, "Thermal Instalibility in a Horizontal Fluid Layer: Effect of Boundary Conditions and Non-Linear Temperature Profile," J. Fluid Mech., Vol. 18, 1963, p. 513.

58. Ostrach, S., "Role of Analysis in the Solution of Complex Physical Problems," Third Intl. Heat Trans. Conf., Chicago, August 1966.

59. Churchill, S., and J. D. Hellums, "Dimensional Analysis of Natural Convection," Chem. Engr. Prog. Symp. Ser., Vol. 57, 1964, p. 75.

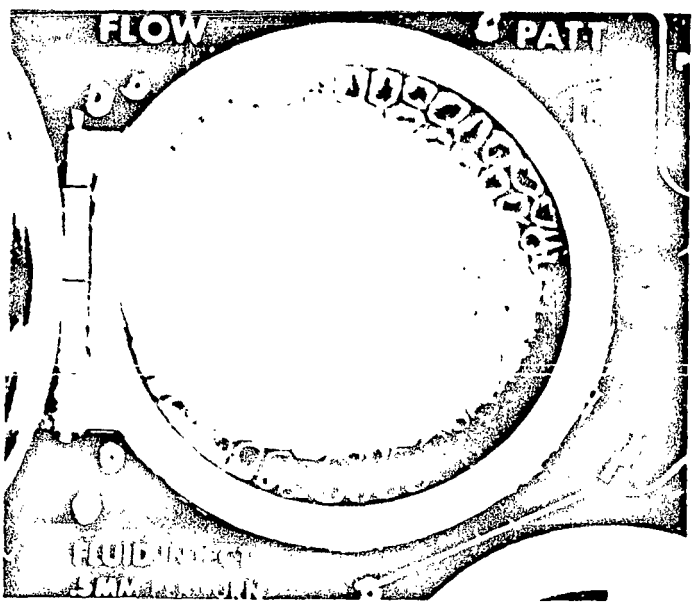

FIG. 1 - BENARD CELLS GENERATED IN GROUND TEST

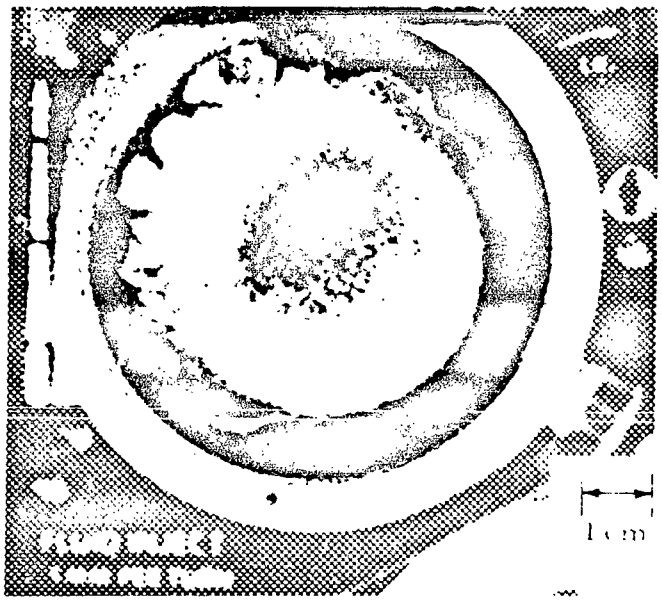

FIG. 2 - CELLULAR CONVECTION OBSERVED IN APOLLO 14 TEST. NOTE THE CONCENTRATION OF LIQUID IN THE CREVICE AT THE EDGE OF THE PAN.

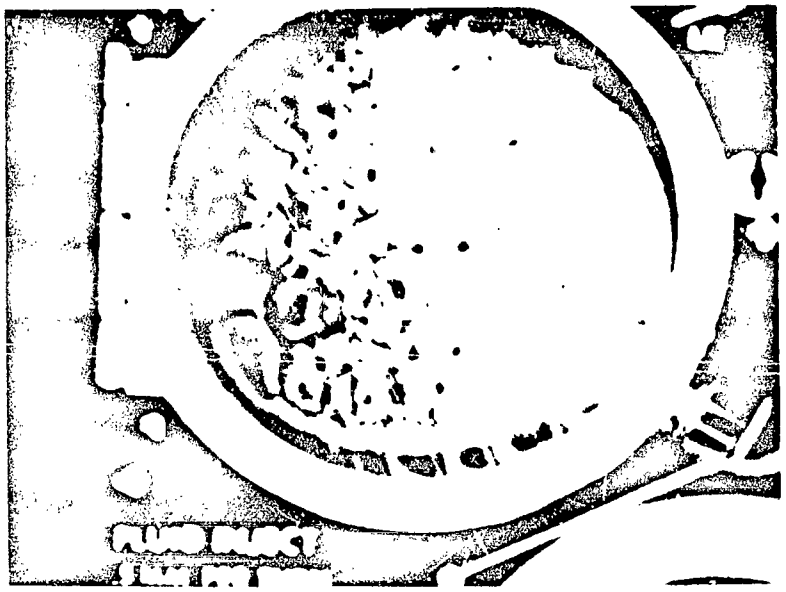

FIG. 3 - CELLULAR CONVECTION OBSERVED IN APOLLO 17 TEST

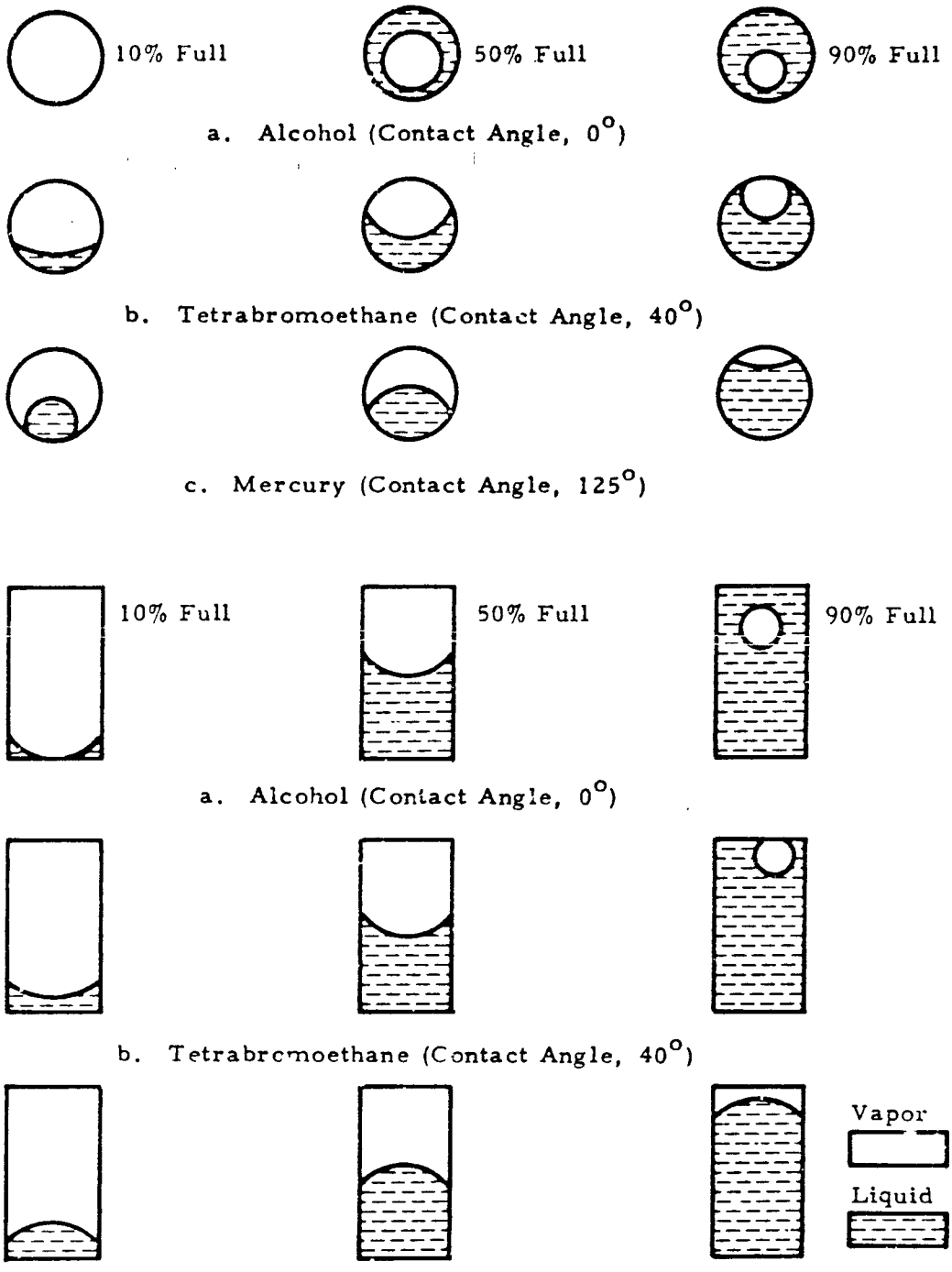

FIG. 4 - EQUILIBRIUM CONFIGURATIONS OF LIQUIDS IN ZERO-g [22]

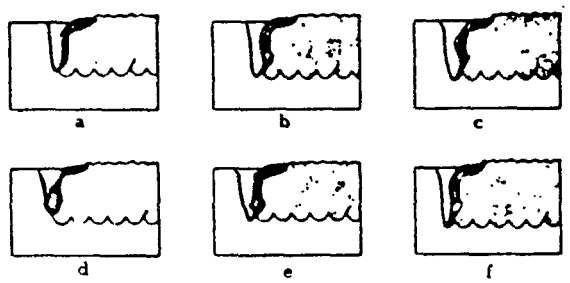

FIG. 5 - SPIKING MECHANISM IN ELECTRON BEAM WELDING [46]

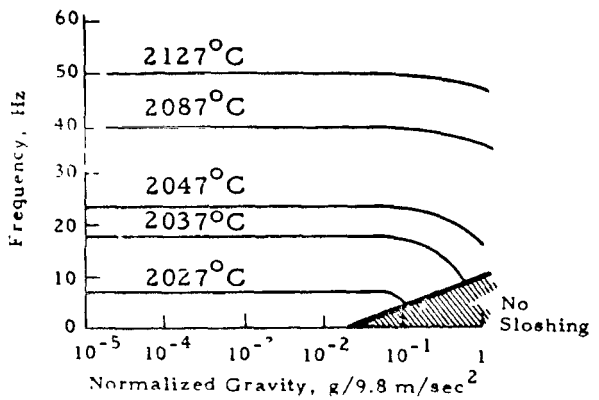

FIG. 6 - MELT SLOSHING IN M551 ELECTRON BEAM MELTING OF STAINLESS STEEL

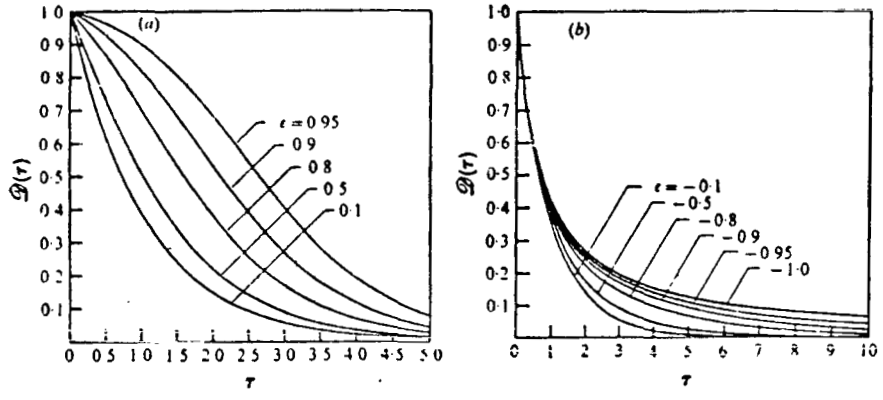

FIG. 7 - NORMALIZED INSTANTANEOUS DEVIATION $\mathscr{D}$ OF ANGULAR VELOCITY FROM THE FINAL VALUE VERSUS DIMENSIONLESS TIME τ IN (A) HYDRODYNAMIC SPIN-UP AND (B) HYDRODYNAMIC SPIN-DOWN, FOR VARIOUS ROSSBY NUMBERS ϵ 53

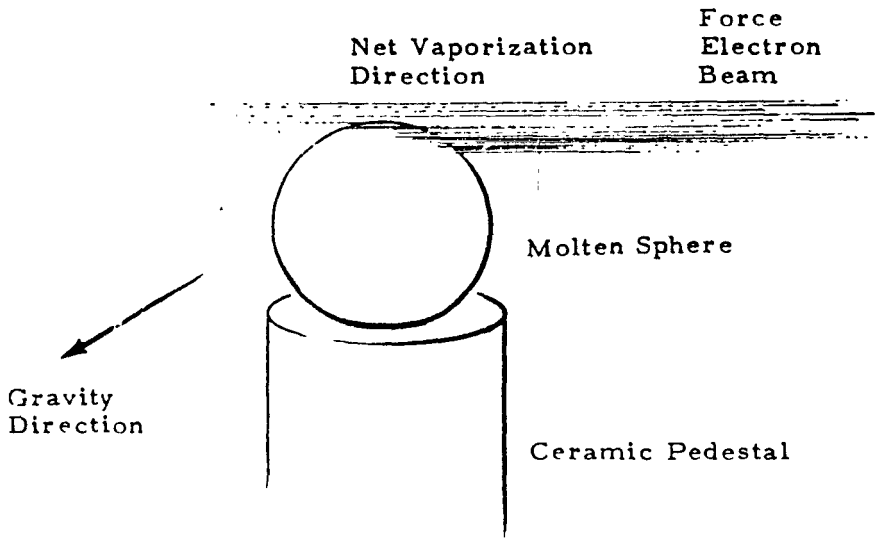

a. Just Before eb Cutoff Isothermal Conditions Reached

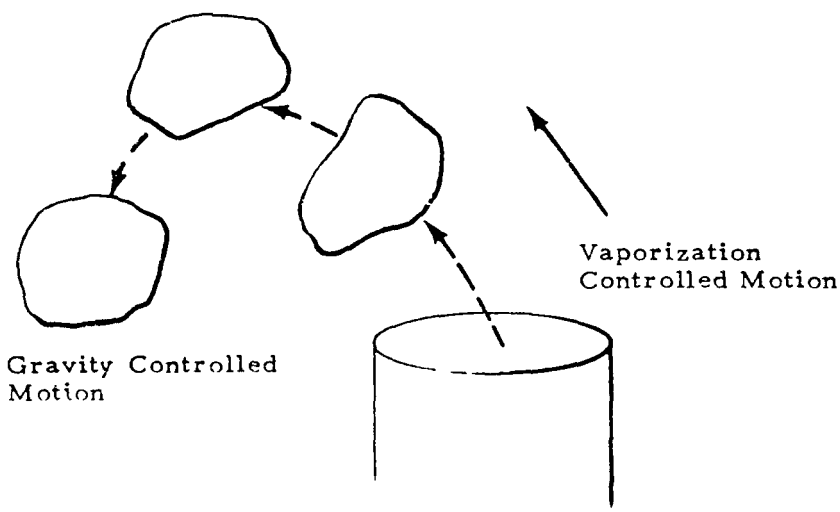

b. Trajectory After Deployment

FIG. 8 - SCHEMATIC OF TRAJECTORY SEQUENCE

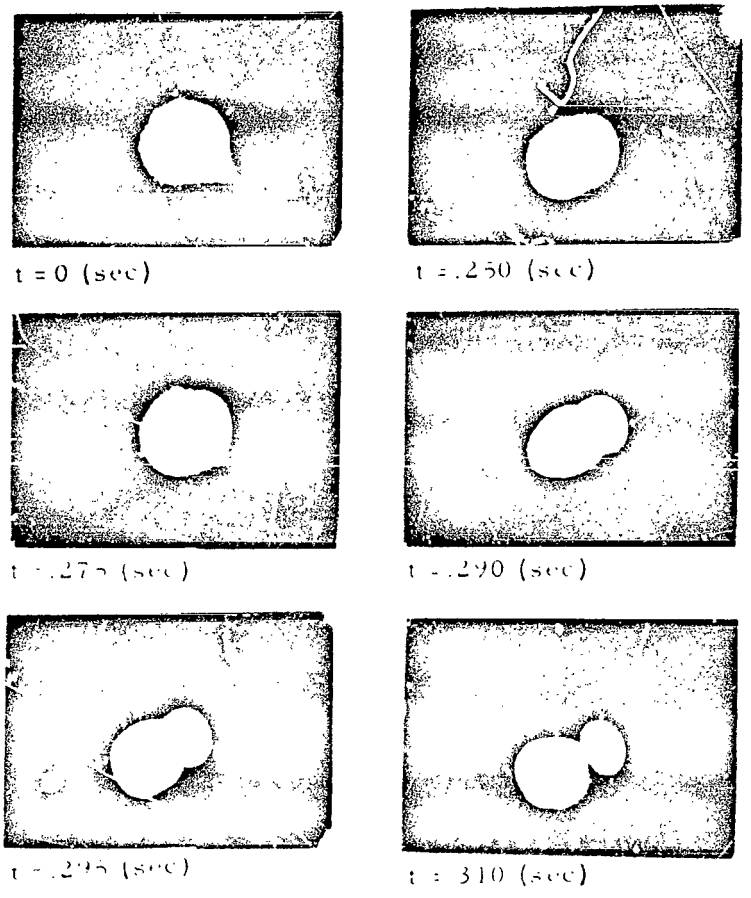

FIG. 9 - TRAJECTORY SEQUENCE - MARCH 1972 KC-135 FLIGHT (NICKEL)

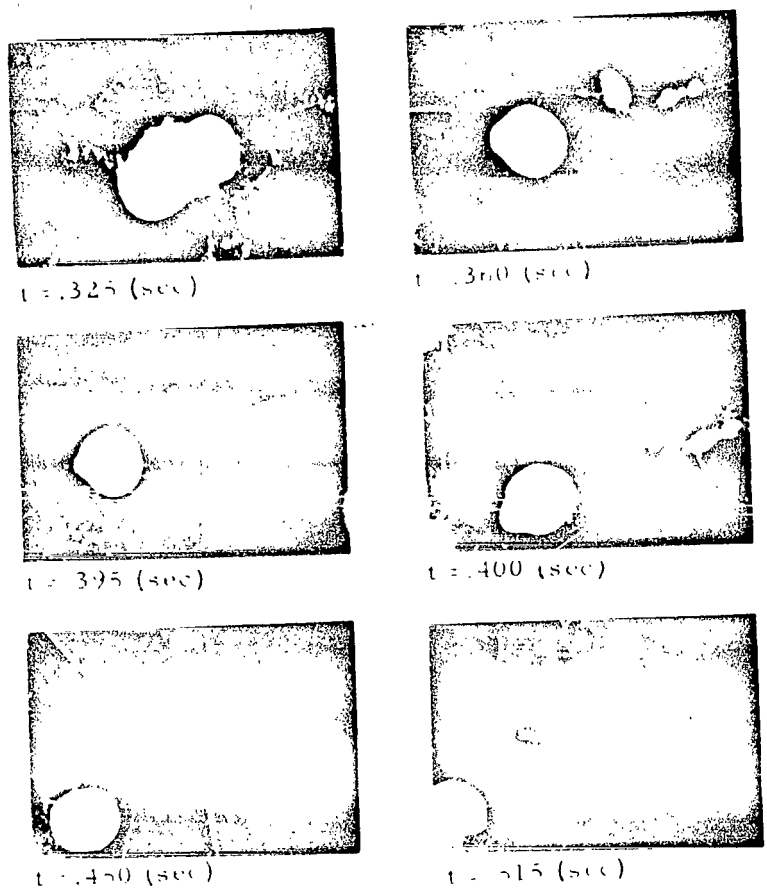

FIG. 9 - (CONCLUDED)

ROLE OF GRAVITY IN PREPARATIVE ELECTROPHORESIS

N74 29914

By

M. Bier, J. O. N. Hinckley and A. J. K. Smolka
Veterans Administration Hospital and
University of Arizona, Tucson, Arizona 85713

M. J. Binder, M. Coxon, T. W. Nee, M. O. Scully and H. S. T. Shih
University of Arizona, Tucson, Arizona 85721

and

R. S. Snyder *
Astronautics Laboratory
Marshall Space Flight Center, Alabama 35812

SUMMARY

Electrophoresis has contributed significantly to the methodology of biological sciences, and shows the potential for large scale fractionation of a wide range of medically important substances, including living cells. Gravity plays an important role in the electrophoretic process, and hence the importance of the Nasa effort to develop a zero-gravity separation facility as part of its shuttle program. The present paper reviews the current state of art in electrophoresis, with particular emphasis on the role of gravity and the possible use of istachophoresis. This technique utilizes a discontinuous buffer system, and appears to be the only high resolution electrophoretic technique currently available for separation of living cells.

INTRODUCTION

Electrophoresis is defined as the transport of electrically charged ions or particles in a direct current electric field. It is the most elegant and useful technique for separation of complex biological mixtures of proteins. As a result, there has been a great proliferation of electrophoretic techniques which have been applied to a wide array of other substances as well (1-3).

Most of the applications of electrophoresis are on an analytical or micropreparative scale. It has not yet been possible to scale up electrophoresis to provide commercially significant quantities of materials with the resolution obtainable on a small scale. Another area in which electrophoresis has yet to reach its full potential is in separations of living cells. At least in part, both of these shortcomings are attributable to gravity. This is why Nasa's concept of a zero gravity electrophoresis facility has stimulated the imagination of so many scientists. The development of such a facility may constitute a major breakthrough in this field and bring about the realization of the full potential of the separating capabilities of electrophoresis.

* Paper presented by R. S. Snyder

The scientific, biomedical and even economic implications of such a development could be of major significance. Large quantities of human blood proteins are daily fractionated by rather archaic methods involving alcohol and salt fractionation, resulting in low purity and poor yields, some of the fractions being completely unavailable on a commercial scale (4). The same situation prevails with enzyme and protein-hormones. All of these products have widespread clinical and research applications.

Even more promising is the possibility of applying electrophoresis to cell separation. While it is well established, on an analytical scale, that different cells have characteristic electrophoretic mobilities, their electrophoretic separation is as yet very difficult and none of the techniques has yet shown the high resolution obtainable with proteins (5-7). Pure cell populations have widespread potential uses in a variety of applications ranging from their direct transplantation to tissue culture, preparation of specific antisera, vaccines, etc.

ROLE OF GRAVITY IN ELECTROPHORESIS

At first, electrophoresis was carried out in free solutions, but it was soon realized that problems arise due to convective disturbances in the bulk of the liquid. We can outline several major causes of these disturbances:

(a) the sample to be separated, be it proteins or cells, contribute to the density of the solution or suspension, causing it to be higher than that of the pure solvent, which is usually an appropriate buffer. The difference in density between solution and pure solvent is in itself sufficient to cause convective disturbances if the solute is present in significant concentration. The problem is compounded during the separation process, as the original sample separates into different compartments or zones, according to the characteristic mobility of each component of the mixture. Each such zone is accompanied by its own individual density gradients.

(b) In some instances the particles may be sufficiently large to sediment noticeably, which, of course, is the case with living cells. While there are a number of techniques which utilize differential sedimentation for meaningful separations (8), in the context of electrophoresis, this is usually undesirable, especially as it is superimposed upon the convective flow of the suspension as a whole, described above.

(c) The passage of electrical current causes heating of the solution. As the vessels are externally cooled, radial temperature gradients arise, again causing gravity-conditioned convection. Even in absence of convective disturbances, unequal temperature results in unequal transport rates, causing bowing of zones.

(d) Characteristic electrical charge is exhibited by most interfaces, including the walls of the vessels within which electrophoresis is carried out. These charges are neutralized by local accumulation of opposite charge within the fluid, in the immediate neighborhood of the interface. When an electric field is applied, it

causes a flow of the charged fluid along these interfaces, referred to as electro-osmosis. Often, this again causes a typical parabolic bowing of the boundaries of migrating solutes.

Gravity is the obvious causative agent in the first three of above disturbances, it being, however, without effect on electroosmosis. Thus, by the simple stratagem of going into zero gravity, some of the major disturbances in electrophoresis are eliminated.

Other approaches to the control of these phenomena are possible. Complete avoidance of all gravity effects is obtainable by working in gels or other solid supporting media of fine enough porosity to effectively hinder bulk flow, but not fine enough to prevent molecular transport phenomena. A complex electrophoretic methodology has evolved around the use of such solid supporting media which we need not review here, since they do not enter into consideration for space processing. It is those techniques which have given us the best methods for analysis and micropreparative separation of proteins. Unfortunately, these are mostly inapplicable to living cells, because of their large size. Our next speaker, Dr. Van Oss, will surely have more pertinent comments on this subject. Surprisingly enough, the use of these anti-convective supporting media has not solved the problem of large scale protein separation, for a variety of reasons too complex to discuss at the present time.

Another anticonvective measure is to use a stabilizing density gradient. In the Tiselius method, the proteins themselves fulfill this role, but as a result their complete separation is not possible, and only frontal analysis is used. More versatile is the use of sucrose (or other similar solutes) gradients, steeper than any density gradient engendered by the electrophoretic process. Sucrose of different concentrations is layered in a vertical column, and remains essentially undisturbed by the electrophoretic process, as the sucrose is not electrically charged. This approach not only overcomes density-caused convective flows, but also completely suppresses electroosmosis. It is not quite clear, at present, why this is so. Sucrose itself, could have a dampening effect on the electrical potential of the wall vessels, similarly to the well known effect of more complex polysaccharides, such as agarose. On the other hand, it is also possible that the sucrose density gradient is sufficient to prevent the flow of the fluid in the vertical direction, along the vertical walls of the column, simply causing microcirculation of the fluid at each level of the concentration gradient.

Another method of stabilizing fluids against gravity effects has been pioneered by Hannig (6). A thin film of fluid (0.1-0.2 cm) is contained between two parallel plates of glass, and the viscosity of this film is sufficient to minimize convective flows. This system is used in so-called continuous curtain electrophoresis type of apparatus, where the whole film of fluid is continuously flowing downwards between the cooled plates, while the electrophoretic transport is carried out in a direction perpendicular to the flow of liquid. While the viscosity of the film is sufficient to minimize the convective effects, it causes parabolic zone profiles due to the downward flow of the whole liquid, as discussed by Strickler and Sacks (9). These shortcomings notwithstanding, this technique has given so far the best published data on separations of living cells. An ingenious apparatus based on this principle has been proposed for space testing, and is scheduled to be tested in the forthcoming Apollo-Soyuz flight. Space does not permit us

to describe the apparatus in detail, and it is to be regretted, for the completeness of the present symposium, that a separate paper on this subject was not included.

Numerous other methods have been suggested for overcoming the gravity effects, such as the rotating horizontal tubes explored by Hjerten (10), but have not gained generalized acceptance.

It is thus obvious that consciously or not, the whole methodology of electrophoresis has evolved around the need to circumvent the effect of gravity; this has given rise to the multiple methods involving anticonvective support media, and the various other approaches just outlined.

Basically, two alternatives are available in free solutions: various static column techniques or the flowing techniques. In either case, if we deal with a background of homogeneous electrolyte distribution, we have Tiselius electrophoresis (frontal analysis), various zone electrophoresis methods (differing from the Tiselius technique in giving complete separation of components into separate zones), or the microscope electrophoresis (no separation at all - just microscopic examination). On the other hand, it is possible to superimpose discontinuities onto the electrolytic system. In many ways these techniques are far more interesting, the discontinuities adding new discrimination parameters onto the electrophoretic process:

(a) If membranes and/or filters are inserted into the migration pathway, we have a family of allied techniques known as forced-flow electrophoresis, electrophoresis-convection, or electrodecantation (11-12). All are high throughput methods, capable of large-scale industrial application, but have only limited resolution, and are therefore outside the scope of the present inquiry.

(b) If gel density is made sufficiently high, an element of molecular sieving is superimposed upon the electrophoretic separation (13). This results in far better resolution than zone electrophoresis, but the method has low throughput. Unfortunately, it has not been possible to devise sufficiently porous gels to permit the application of this principle to cells.

(c) Equally high resolution is obtained in isoelectric focusing, (14), where a continuous pH gradient is created in the pathway of migrating particles. The technique is applicable either in free solution or in gels, but is unfortunately not usable with cells, their isoelectric point being incompatible with their survival.

(d) One can also introduce the sample to be separated in the interface between two homogenous buffers, meeting some special requirements. This technique is referred to as isotachophoresis, and has characteristics quite different from the above methods. We set upon examining this in detail for possible use in the space facility, as it seemed to offer some unique advantages for both high resolution cell separation, and large scale protein fractionation.

PRINCIPLE OF ISOTACHOPHORESIS

The fundamental theoretical basis of this technique was provided by Kohlrausch in 1897 (15), and his principles were first applied to electrophoresis by Kendall (16). The method was revived largely by Martin and Everaerts (17), but only in recent years have various researchers realized the potential usefulness of the principles involved (18-21).

These can be illustrated with the aid of the simple diagram presented in Fig. 1. The sample anions S^- to be fractionated are inserted between two homogeneous buffer zones formed by the leading anions L^-, and the terminating anions T^-, the unique requirement for the leading and terminating anions being that they bracket the electrophoretic mobilities (m) of all the sample anions, with the leading ion mobility being higher, and the terminating ion mobility lower than those of the sample ions: ($m_L > m_S > m_T$). Electric neutrality is preserved by having in all compartments the same counterion C^+. When an electric field is applied, the leading ions will migrate towards the anode at their characteristic velocity in the given field. The sample ions and the terminating ions will have to migrate at the same velocity or the leader ions (isotachophoresis = equal rate transport), as otherwise an ion-free gap would separate the migrating ionic compartments. As the mobility of sample and terminator ions is lower, the field (volts/cm) in each compartment automatically adjusts itself to assure equal velocity. In the course of the fractionation, the sample ions separate into their constituent components, arranged in order of decreasing mobilities. This field change in each compartment is illustrated in Fig. 2, together with the mobility profile.

Several important consequences ensue:

(a) There is a relatively simple relation between concentration of leading C_L and terminating ions C_T, given by the Kohlrausch regulating function, where the indexes 1 and 3 refer to the respective zones according to diagram in Fig. 1. In its simplest form,

$$\frac{C_L}{C_T} = \frac{m_L\,(m_T + m_{C_3})}{m_T\,(m_L + m_{C_1})}$$

The same relationship prevails for each species of the sample ions of intermediate mobilities. Thus, the concentration of sample ions after equilibrium is reached is independent of the concentration at which they were applied. Instead, the concentration is exclusively dependent on the leader ion concentration, and the sample compartment expands or contracts to fill its Kohlrausch regulated volume. As an indication of the order of magnitude, for a 20mM chloride leader concentration, the corresponding protein concentration may be of the order of 10%. This is the basis of the "stacking gel" principle in discontinuous or disc electrophoresis according to Ornstein (22) and Davis (23), where isotachophoresis is employed to sharpen the initial boundaries.

(b) The concentration of each ion within the Kohlrausch regulated compartments is constant, rather than presenting the usual Gaussian distribution curve, characteristic of other forms of electrophoresis.

(c) The boundaries separating the various ionic compartments are extremely sharp, there being a minimum of overlap between ionic species. This will be discussed at greater length in the following section.

(d) Once equilibrium is established, the separated compartments will migrate without further change for as long as space is available. Thus, unlike in zone electrophoresis, there is no progressive spreading or deterioration of zones, due to diffusion.

(e) The boundaries separating ionic compartments are self-restoring, and the sharp boundaries will reform if disturbed due to a random movement of the fluid. Both convection and diffusion are thus counteracted by the sharp potential drop existing between the subsequent compartments.

(f) Sample compartments are contiguous to each other and never separate from each other to form an intermediate buffer zone characteristic of other forms of electrophoresis. If separation is desired, a so-called spacer ion of suitable mobility has to be added. For this purpose the commercial product Ampholine is frequently used (LKB Producter - Stockholm), which is a mixture of near infinite distribution of similar condensation products of polyamino-polycarboxylic acids (24), providing a continuous mobility and pH spectrum.

(g) The heating in the column is not uniform, as different ionic compartments have different applied fields. The temperature rise is thus a complicated function of both radial cooling and frontal migration of each ionic compartment. This point is also discussed in one of the following sections.

We have not found a single literature reference indicating that isotachophoresis might be applicable for cell separations, but there appeared to be no theoretical reasons why this could not be done. It was felt, therefore, that several of above factors make isotachophoresis a particularly attractive technique for the space facility. Our research effort has been directed largely towards this goal, and comprised theoretical, engineering and experimental evaluation of the problem.

STRUCTURE OF THE IONIC SPECIES INTERFACE IN ISOTACHOPHORESIS

While it is well known that the interface between contiguous ion compartments in isotachophoresis is very sharp (17-21), its exact structure has never been calculated. We have therefore proceeded with a theoretical evaluation of this interface. A preliminary paper treating this subject, but neglecting the effect of diffusion, is presently in press (25, cf also 26).

At present we wish to give a resume of the extension of this work including the effects of diffusion (27), which causes a broadening of the interfaces, and a continuous distribution of all ions throughout the entire electrophoretic column. However, in discrete sample (as opposed to continuous frontal) separations, the bulk of the concentration change of the individual ion species occurs in a very short length of the column. We refer to the distance over which the concentration changes from 99% to 1% of its initial value (as determined by the Kohlrausch regulating function) as the interface thickness, Δ . A theoretical prediction of the thickness of isotachophoretic interfaces is of importance in evaluating the maximum resolution of the method for preparative applications, and in determining in what ways experimental parameters may be varied to achieve optimal performance.

We consider a steady state, isothermal, one-dimensional analysis of the interface which would exist between leader and terminator in a sample-free model. The leader and terminator are taken to be cations having a common counterion (anion). The governing equations for the one-dimensional interface in isotachophoresis are the species continuity equations for the leader, terminator, and common counter-ion, and Gauss's law. These equations may be put in dimensionless form and manipulated to yield the following third-order differential equation:

$$2n_1^2(1 + e^{\alpha x}) + n_1\alpha e^{\alpha x} - \varepsilon\frac{n_1^{2}\,''}{n_1} + \varepsilon\frac{n_1^{2}\,'}{n_1}(3 - \beta)$$

$$- \varepsilon\left(\frac{n_1^2}{n_1}\right)^3 - \varepsilon\frac{n_1^2 n_1^{2}\,'}{n_1^{2}} + \beta\varepsilon\left(\frac{n_1^2}{n_1}\right)^2 + \beta n_1(1 + e^{\alpha x}) = \frac{\alpha\vartheta_2}{1-\theta_2} \quad . \qquad (1)$$

The boundary conditions are determined from the Kohlrausch regulating function and electroneutrality considerations for regions removed from the interface.

A solution to equation (1) is assumed of the form

$$n_1 = \frac{\theta_2}{(1 + Ke^{\alpha x/N_1})N_1}$$

where $K = \theta_2^{1/N_1}$.

Substitution of the assumed solution in equation (1) yields an equation of the form

$$f(x) = \beta\theta_2 .$$

As an indication of how well our assumed solution satisfies equation (1) we define the error in the system to be

$$\text{Error } (\%) = \left| \frac{100[f(x) - \beta\theta_2]}{\beta\theta_2} \right| .$$

In general, the error will be a function of x, and the exponent N_1 must be chosen in such a way as to minimize the maximum error for each set of experimental conditions considered

The results of the numerical calculations indicate that the assumed solution satisfies equation (1) with a maximum error of about 7 1/2% for values of θ_2 greater than 0.5 Leader and terminator interface thicknesses were found to be equal and their variation with α is shown in Fig 3 for various values of the parameter β_2 Typical concentration and electric field profiles are shown in Fig. 4. Further details of this analysis may be found in reference 27

As a numerical example, for the separation of Sodium and Potassium ions with chloride as the counterion, at a temperature of 10°C and a terminator voltage gradient of 20 volts/cm, the interface thickness is of the order of 0.15 mm For a terminator voltage gradient of 200 volts/cm the interface thickness is of the order of 0.04 mm It should be reemphasized that this interface thickness is independent of the length of each ionic compartment - throughout each of which, no matter how long, uniform concentration prevails

DETERMINATION OF TRANSVERSE TEMPERATURE DISTRIBUTIONS IN ISOTACHOPHORESIS COLUMNS

We have also given special consideration to the problem of temperature gradients in isotachophoresis. The temperature gradients are, of course, of basic importance for all electrophoretic processes, but more so for isotachophoresis, where we need to consider not only radial but also longitudinal gradients (28). Longitudinal gradients arise because of the advancing sample and terminator fronts, each of which compartments has a higher electrical field. We must also be concerned with non-equilibrium conditions, because of the speed at which meaningful separations may be obtained, often before the temperature equilibrium has been reached. The problems of radial temperature distribution in a column of circular cross-section and of transverse temperature distribution in a column with rectangular cross-section have been solved for both steady state and transient conditions. The solutions obtained are valid away from the vicinity of any separation fronts subject to the following assumptions:

(1) Operation occurs in a gravity free environment;
(2) Convection may be neglected;

(3) Temperature dependence of thermal properties (density, specific heat, and thermal conductivity) may be neglected;
(4) Electrical conductivity of the supporting medium is linearly dependent on temperature in the range of temperature of interest;
(5) The supporting medium is essentially at rest with the ionic species drifting through it in the axial direction.

Assumption (2) is reasonable, in view of (1), provided that electroconvective effects may be ignored; this point remains to be investigated. Assumption (3) has been checked against a perturbation solution which permits variable properties to be accounted for (in the steady state) and it appears that the assumption is justified and further leads to conservative estimates from a design standpoint. Assumption (5) will need to be relaxed for a system which employs counterflow of the supporting medium (e.g. in free fluids).

Numerical calculations have been performed for the case of an isotachophoretic column of circular cross-section. Fig. 5 shows the variation of temperature θ with time t for a range of heating rates S, for one value of wall thickness ξ_1. Assuming a cooling bath temperature of 0° C and allowing a maximum temperature in the tube of 37° C (to avoid "cooking" living cells), the maximum allowable value of θ is accordingly 0.1355 (denoted θ_c).

An inspection of Fig. 6 shows that for a given value of ξ_1, there will be some value of S above which θ_c will always be exceeded in some finite amount of time. We term this value of S for which θ_c is approached asymptotically S_{max}.

Since the electric field decreases in going from terminator to leader electrolyte zones, S will also decrease from terminator to leader. Fig. 6 depicts the steady state temperature profile for various values of S. Since ionic mobility is proportional to temperature, this leads to velocity profiles which become progressively less "bowed" from terminator to leader zones.

Since the sharpness of the ionic interfaces increases with increasing electric field strength, it may be desirable to operate at values of S greater than S_{max}. This requires that E^* and R_1 be chosen in such a way that the time required for separation is less than the time at which θ_c is exceeded. An analysis of the limitations imposed by this requirement is in the process of being completed at this time.

Numerical calculations for the case of a rectangular cross-section are presently under way, and it is hoped that the results of the analyses described here will be published in the near future.

STUDIES ON POSSIBLE INSTABILITIES IN ELECTROPHORESIS

As part of our theoretical studies, we have undertaken an analysis of fluid behavior in electrophoresis. A detailed manuscript is now in preparation (29), and we wish to report here only the approach taken. In the study of electrophoretic phenomena, laminar flows are usually assumed, but instabilities could occur. One example is due to the combined effects

of large electric fields and temperature variations in the charged fluids It is analogous to the Benard instability (for a layer of fluid heated from below) in hydrodynamics (30), with the electric field E playing now the role of gravity .

As a preliminary step we study the "Benard instability" in very much the same spirit as in the Lamb's semi-classical theory of "laser instability" (31) Corresponding to Maxwell equations, hydrodynamic equations are employed By restricting our attention to the threshold region, the normal-mode method is used and an equation of the form

$$(R - R_c)\, V - \xi V^3 = 0$$

is obtained at steady state. R is the Rayleigh number and the mode amplitude V is the "order parameter". The saturation term ξV^3 is due, in our theory, not to the nonlinear constituent relations like in the laser case, but to the non-linearities inherent in the hydrodynamic equations themselves. In other words, the convective processes are responsible A simple application of the result is given to explain the experimentally observed dependence of the Nusselt number on the Rayleigh number.

EXPERIMENTAL ISOTACHOPHORESIS

Isotachophoresis has received mainly two applications: (a) as an analytical technique for rapid separation of small molecular weight ions, such as acetate, bicarbonate, etc. These separations are usually carried out in free solution, using capillaries. (b) Isotachophoresis shows considerable promise for preparative protein separations, because of the high concentration of proteins in the separated compartments, and the sharp intercompartmental boundaries. Though some protein work has been carried out in free solutions in capillaries, (21, 32) most work is carried out in gels.

Our initial efforts were centered on obtaining protein separation in capillaries, where viscous effects tend to minimize convective disturbances. Three additional modes of anti-circumventing gravity effects were employed. These were rotation of capillaries around their horizontal axis, the inclusion of high viscosity soluble polysaccharides into the electrolyte system, and rapid migration at high potential gradients. With these systems, one can easily demonstrate the unusual properties of isotachophoresis: the extremely sharp boundaries between sample and buffer, the self stabilizing properties of the boundaries, etc. Unfortunately, a major problem of protein isotachophoresis also became painfully obvious: this is the very large density gradient between concentrated protein compartments and the leading and terminating buffers. As a result, the boundaries could not be stabilized by any of the palliative methods employed, and a complex series of phenomena were observed, such as boundary slumping, bowing, etc. In Fig. 7 we show a typical photograph of separation of red cells from stained albumin in a capillary tube.

We had to turn to gels, therefore, for optimal protein separation. Two gels were employed, agarose and polyacrylamide. In such gels protein separation is readily obtainable. The length of protein compartments is proportional to the protein quantity applied

as is apparent from Fig. 8, showing increasing length of the ferritin bands, approximately proportional to the volume of the 10% protein applied (cf 21, 32). Unfortunately, the rear boundaries in proteins are not always flat, but at times show an upward curvature, which we call doming. Considerable efforts have gone into understanding of the doming effect, which at present still remains ill understood. There are obviously some strong radial fields in isotachophoresis, which have been previously not described in the literature.

Best example of this radial field effect is obtainable with dyes. In the sequence of photographs presented in Fig. 9, we show a sample of Ponceau S, which was applied in a stab-application into polyacrylamide gel, just below the leader-terminator interface. In the sequence of photographs presented, one can readily see the near instantaneous spreading of the dye across the whole cross-section of the tube, as the terminator front is sweeping across the sample area. This spreading is far more rapid than accountable for on the basis of diffusion alone, and clearly demonstrates the unusual properties of isotachophoretic interfaces. It is also significant that the front boundaries of both dyes and proteins are always flat, showing no trace of the bowing that one could expect on basis of radial temperature gradients. This absence of bowing, and rapid spreading of boundaries across the aviable interface are indications of radial electric fields, presently under both theoretical and experimental investigation.

In Fig. 10 we are presenting another series of photographs, illustrating the unusual behavior of isotachophoretic systems. In the Polyacrylamide gel, first a regular isotachophoretic run of the Ponceau S dye was carried out, allowing the migration of the dye to proceed till about half the length of the gel column. Then a second sample of the dye was applied to the top of the gel, but this second sample was now located in the terminator compartment, and not the leader-terminator interface. The migration of this second dye sample proceeds by regular zone electrophoresis, and the dye migrates much more rapidly than at the interface, the electric field being higher in the terminator than in the sample. The difference between the sharpness of the isotachophoretic bands, and the diffuse zone bands is obvious and can also be shown in free solution. Within minutes, the second dye sample catches up with the first sample, and forms a single isotachophoretic boundary of greater length, with the usual sharp boundaries. These few illustrations are presented only to illustrate the restorative properties of isotachophoretic boundaries.

Other work has been carried out in sucrose density gradients, borrowing the technique and instrumentation of isoelectric focusing. This has shown excellent resolution of dyes, where concentration gradients due to sample are smaller than with proteins. With proteins, only transitory sharpening of boundaries was observed, these soon degenerating and convecting as a result of the sharp density gradients. Similar is the behavior of cell suspensions, and in Fig. 11 we show the transitory separation in ficoll gradients of human and sheep red blood cells. With further boundary sharpening, convection unfortunately sets in. We are at present studying much steeper density gradients as possible means of boundary stabilization.

SKYLAB EXPERIMENTS

An opportunity presented itself to include a simple electrophoresis experiment into

the last Skylab mission, as part of the demonstration experiments. The main limitations imposed were the short lead time in which the experiment had to be prepared, the limited power available (only 28 volts), and the requirement for the whole package to fit a volume defined by a cylinder of 3.5" diameter, 3.5" long. Within these narrow confines it appeared possible to design an apparatus which would give the answers to two important questions:

(a) will proteins, at zero gravity, give comparable patterns to those presently obtainable in gels only, or will other factors, notably electroosmosis, cause distortion of the patterns?

(b) will cells at zero gravity provide sharp boundaries comparable to those of proteins?

Both of these questions appeared of significance for the future direction of the isotachophoresis work.

To this end, a simple electrophoretic assembly was constructed, consisting of two plexiglas modules. The observation channel was 3/16" in diameter, 1" long, and two electrode vessels were commensurate. Non-gassing electrodes were used, a silver anode and a palladium cathode. The modules were made in Tucson, (thanks are due to Mr. Anthony Clarkson for the construction) and the assembly completed in Huntsville. Fig. 12 shows the completed apparatus. The two modules were completely filled with degassed fluids in the high altitude chamber, also in Huntsville, largely through the efforts of Mr. Hall of MSFC and Mr. Smolka.

One of the two modules contained a mixture of two colored proteins, ferritin and hemoglobin contained within the movable slide, which was used as the sample injector. Laboratory experiments in gels have clearly shown that under the conditions of the flight experiments, it is easy to obtain the separation of the two proteins, provided a colorless spacer, Apmpholine, is added. The leader buffer was 20 mM chloride-tris buffer, pH 7.2, and the terminator was 380 mM tris-glycine, pH 8.3.

The second module contained a suspension of human red blood cells. The most immediate problem was the preservation of the RBC over the several weeks between launch-time and execution of the experiment. Laboratory experiments had indicated that the best preserving medium was defibrinated whole plasma. This sample was thus prepared by defibrinating whole blood, (human) by shaking it with glass beads. Gentamycin was added as preservative. The leading buffer was the same as above, with 5% dextrose added for isotonicity. Because of the probability of cell sedimentation during the centrifugal effect of lift-off, the whole cathode compartment was filled with the cell suspension, and a small stirrer was incorporated into it, to permit the astronauts a resuspension of the cells.

This permitted only a frontal analysis of the cell migration. Numerous laboratory experiments had been conducted to prove beforehand that cells do migrate isotachophoretically from such a plasma suspension. This was possible to accomplish also by frontal analysis, in a vertical upward migrating mode, the cell suspension being self-stabilized against convection by the autogenic density gradient. It showed that in such a system, the Kohlrausch

regulated cell concentration is considerably less than that of the whole blood. A range of concentrations of cells is obtained, as the plasma proteins contribute to forming a series of mixed isotachophoretic steps, with the plasma proteins and other plasma ions.

The results of the two experiments were unfortunately quite disappointing. The main reason for this appeared to be significant leakage of the fluids from both modules, resulting in many air bubbles in the chambers, though all fluids were carefully degassed prior to cell loading. It is most likely that the leakage occurred during the lift-off phase, as a result of the increased acceleration, the testing of the seals not having been carried out under these conditions. The protein experiment was a complete failure, as there was no observable migration of any colored proteins when the astronauts pushed in the sliding gate with the sample. Spectrophotometric examination of the modules' contents, upon return from the Skylab, showed a uniform distribution of the sample in all fluids. An examination of the silver anode showed that at no time was there any current through the cell, though there was electrical continuity of all connections. The most likely explanation is that an air bubble completely prevented passage of the electrical current.

The results with the cell suspension were better, though it was also marred by presence of air bubbles. Nevertheless, the advancing front showed little bowing, the view being partially obstructed by air bubbles. A typical photograph is shown in Fig. 13. Upon completion of forward migration, the current polarity was reversed, and the astronauts cleared the air bubbles from the observation channel by mechanical agitation. They then repeated the frontal migration a second time. The photograph reproduced in Fig. 14 shows an extremely sharp boundary, with a blunt parabolic profile. It is unfortunately not possible to state clearly if this is due to electroosmosis only, or to contribution of other events which occurred, including the reversed polarity migration step. Nor was this second migration passage necessarily a purely isotachophoretic run, as there may have been considerable mixing of buffers in the preceeding operations. Reversal of polarity rendered the boundary strikingly more diffuse, this reverse migration being in a zone mode, as shown in Fig. 15.

CONCLUSIONS

The sharpness and self-restoring properties of boundaries in isotachophoresis make it an attractive candidate for space applications. This is most obvious from the comparison of the sharp boundaries obtained in the Skylab experiment, as compared to the diffuse boundaries obtained in prior Apollo experiments (33, 34). It is most unfortunate, nevertheless, that the Skylab experiment did not provide more definitive answers as to boundary shapes in zero-gravity isotachophoresis. It is hoped for that these questions will be answered by the planned experiments for the forthcoming Apollo-Soyuz test program, where two modified isotachophoresis modules will be flown, together with several zone electrophoresis modules.

Nevertheless, earth-bound laboratory experiments and the Skylab demonstration have shown that isotachophoresis is applicable to separation of living cells. This may eventually permit the development of techniques of cell separation with sharper resolution than possible by zone electrophoretic methods.

The results so far obtained from the Apollo missions, and the Skylab demonstration, have clearly indicated the advantages of a zero gravity electrophoresis facility. Numerous problems remain, such as the development of optimal buffers systems compatible with cell survival, etc.

Nor are all problems confined to isotachophoresis. For the development of the space facility numerous technical details remain to be solved. These include some hardware problems, which appear to be rather trivial at first glance, but which present serious engineering problems, when coupled with fluid behavior at zero gravity. The most obvious of these is the collection of the separated fractions. The Hannig approach of continued collection of fraction is one possible solution. Another approach has been developed at Huntsville by Dr. Snyder and his collaborators. This is the radial freezing of the whole electrophoretic column, which is then sectioned while still frozen. This is the approach which will be taken in the forthcoming Apollo-Soyuz mission. It has the notable advantage that a number of different samples can be run with the same basic electrophoretic apparatus, each sample being confined to a different tube. A third approach has been proposed by John G. Watt of the Protein Fractionation Center in Edinburgh. It comprises the isoelectric focusing of proteins in a square column, and the lateral expulsion of the fluid content into a series of collecting tubes, arranged along the whole length of the electrophoretic column. Several other possibilities are still on the drawing boards.

In conclusion, one may only say that the recent Apollo and Skylab experiments have clearly demonstrated the promise of Nasa's electrophoresis program, and the possible advantages of electrophoresis at zero gravity. The potential benefits of the development of a zero gravity electrophoretic facility may fully warrant the considerable energies expended in this direction.

LIST OF SYMBOLS

SYMBOL	MEANING
E	Dimensionless electric field
E^*	Electric field (volts/cm)
n_1	Dimensionless terminator ionic number density
S	Dimensionless heating rate
x	Dimensionless distance along axis of tube referred to moving coordinate system
α	Dimensionless leader mobility parameter
β	Dimensionless counterion mobility parameter
γ	Dimensionless heat transfer coefficient
δ_1	Dimensionless terminator interface thickness
δ_2	Dimensionless leader interface thickness
Δ	Leader or terminator interface thickness (mm)
ϵ	Dimensionless dielectric constant
θ	Dimensionless temperature
θ^s	Dimensionless steady state temperature
θ_2	Dimensionless number density in terminator zone
ξ	Dimensionless radial distance
ξ_1	Dimensionless wall thickness
τ	Dimensionless time

REFERENCES

1. H. A. Abramson, "Electrophoresis of Proteins" Hafner Publishing Company, Inc. New York,1964.

2. M. Bier, ed., "Electrophoresis", Vol. I and II, Academic Press, New York, 1959 and 1967.

3. D. J. Shaw, "Electrophoresis", Academic Press, New York, 1969.

4. G. A. Jamieson, ed., "The Development of Plasma Derivatives for Clinical Use", S. Karger, New York, 1972.

5. C. C. Brinton, and M. A. Lauffer, in "Electrophoresis", Vol. I, p. 427, M. Bier, ed., Academic Press, New York, 1959.

6. K. Hannig, in "Methods in Microbiology", J. R. Norris and D. W. Ribbons, eds., Academic Press, London, 1971.

7. E. J. Ambrose, ed., "Cell Electrophoresis", Little, Brown and Company, Boston, 1965.

8. J. Harry Cutts, " Cell Separation", Academic Press, New York, 1970.

9. A. Strickler, and T. Sacks, Annals of the New York Academy of Sciences, 209, 497,1973.

10. S. Hjerten, Chromatog. Rev. 9, 122, 1967.

11. M. Bier, in "Electrophoresis", Vol. I, p. 263, M. Bier, ed., Academic Press, New York, 1959.

12. M. Bier, in "Membrane Processes in Industry and Biomedicine", M. Bier, ed., p. 233, Plenum Press, New York, 1971.

13. H. Bloemendal in "Electrophoresis", Vol.II, p. 379, M. Bier, ed., Academic Press, New York, 1967.

14. H. Haglund, Science Tools, 17, 1, 1970.

15. F. Kohlrausch, Ann. Phys. (Leipzig) 62, 209, 1897.

16. J. Kendall, Science, 67, 163, 1928.

17. A.J.P. Martin, and F. M. Everaerts, Anal. Chim. Acta, 38, 233, 1967.

18. A. Chrambach, G. Kapadia, and M. Cantz, Separation Sci. 7 (6), 785, 1972.

19. N. Catsimpoolas, N. & J. Kenney, Biochim. Biophys. Acta, 285, 287,1972.

20. F. M. Everaerts, J. L. Beckers, and Th. P.E.M. Verheggen, Annals of the New York Academy of Sciences, 209, 419, 1973.

21. D. Peel, J.O.N. Hinckley, and A.J.P. Martin, Biochem. J. 117, 69P, 1970.

22. L. Ornstein, Annals of the New York Academy of Sciences, 121, 321, 1964.

23. B. J. Davis, Annals of the New York Academy of Sciences, 121, 404, 1964.

24. O. Vesterberg, Annals of the New York Academy of Sciences, 209, 23, 1973.

25. T. W. Nee, and G. T. Moore, J. Chromatog. In Press.

26. J.O.N. Hinckley and R. Hall, written communications, 1971.

27. M. Coxon, and M. J. Binder, submitted to J. Chromatog.

28. J.O.N. Hinckley, in "Methodological Developments in Biochemistry", Vol. II, p. 201, E. Reid , ed., Longman, London, 1973.
and
J.O.N. Hinckley, Biochem. Soc. Trans., 1, 574, 1973.

29. H.S.T. Shih, M.O. Scully, and T. W. Nee, in preparation.

30. S. Chandrasekhar, "Hydrodynamic and Hydromagnetic Stability", Oxford University Press 1961.

31. W. E. Lamb, Jr., Phys. Rev. 134, A1429 1964.

32. J.O.N. Hinckley, Abstract, 6th Annual Symposium on Advanced Analytical Concepts for the Clinical Laboratory, Oak Ridge National Laboratory, 1974.

33. R. S. Snyder et al., Separation and Purification Methods, 2 (2) 259, 1973.

34. M. Bier and R. S. Snyder, AIAA Paper No. 74-210, AIAA 12th Aerospace Sciences Meeting. Washington, 1974.

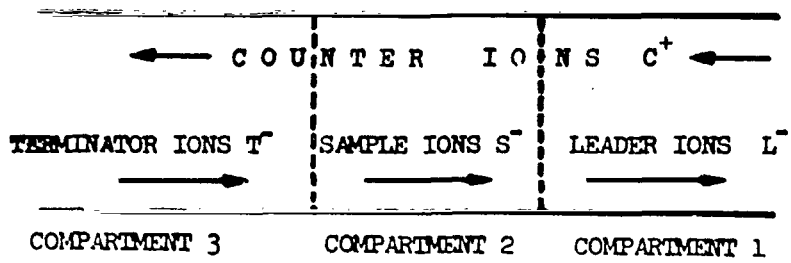

FIG. 1 SCHEMATIC PRESENTATION OF ION DISTRIBUTION IN ISOTACHOPHORESIS. LEADER IONS HAVE THE HIGHEST MOBILITY, TERMINATOR IONS LOWEST. COUNTERIONS MAY HAVE BUFFERING ACTION.

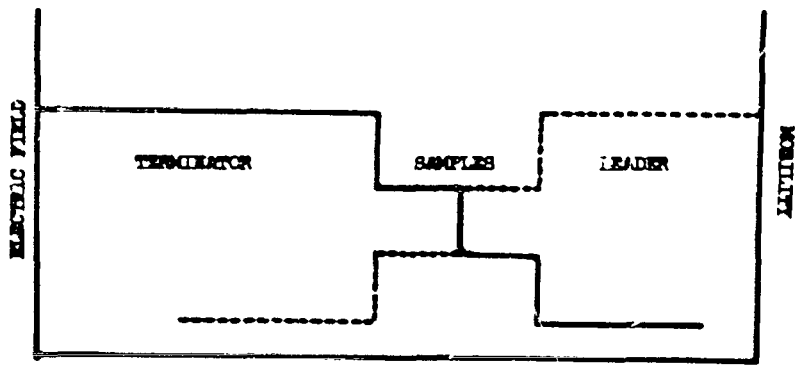

FIG. 2 SCHEMATIC FIELD AND MOBILITY PROFILES AFTER KOHLRAUSCH EQUILIBRIUM HAS BEEN ESTABLISHED. L^-, LEADER IONS, T^-, TERMINATOR IONS, S^-_1 AND S^-_2, RESOLVED SAMPLE IONS. FIELD STRENGTH IS INVERSE FUNCTION OF MOBILITIES.

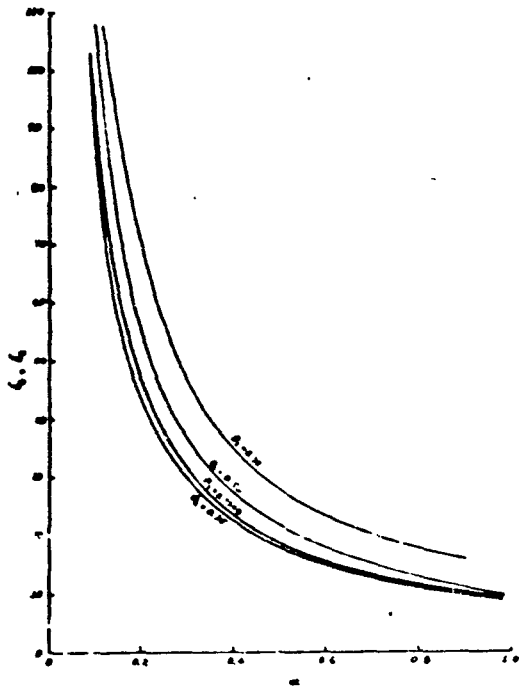

FIG. 3 LEADER AND TERMINATOR INTERFACE THICKNESS.

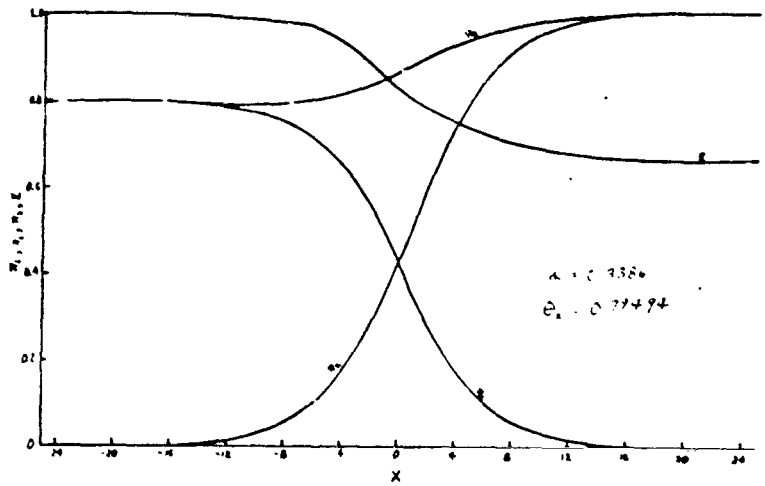

FIG. 4 CONCENTRATION AND ELECTRIC FIELD PROFILES.

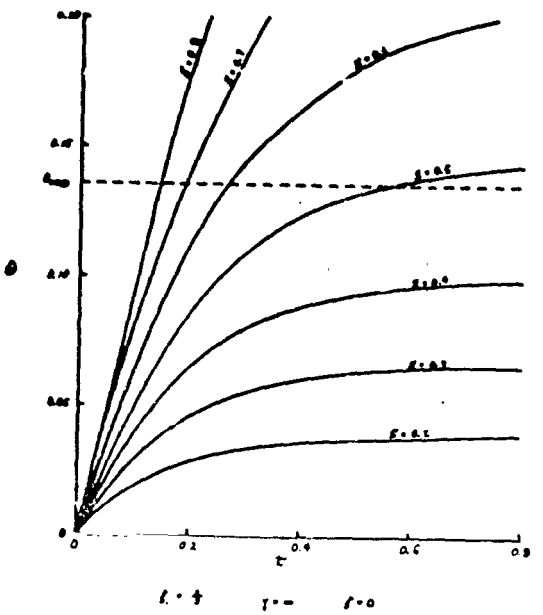

FIG. 5 TEMPERATURE AS A FUNCTION OF TIME FOR $\xi_1 = 2/3$.

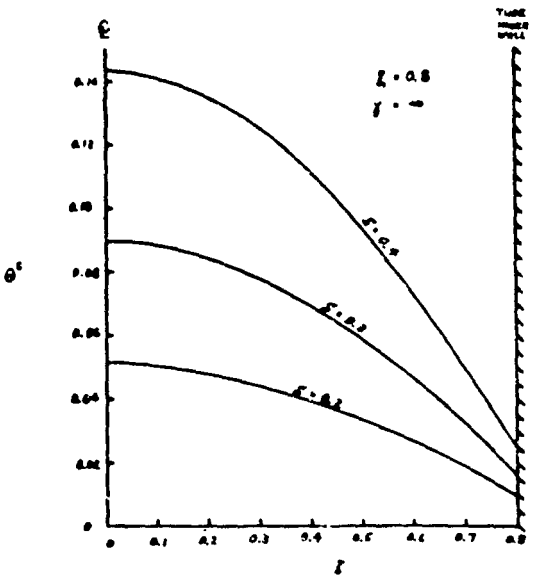

FIG. 6 STEADY STATE TEMPERATURE PROFILES FOR VARIOUS HEATING RATES AT $\xi_1 = 0.8$.

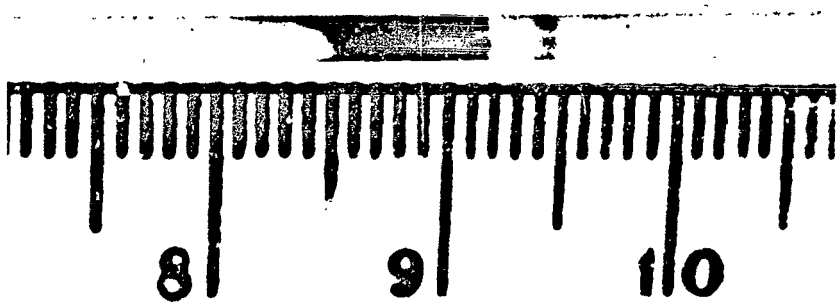

FIG. 7 ISOTACHOPHORETIC SEPARATION OF ERYTHROCYTES (LONG ZONE) FROM STAINED ALBUMIN IN A CAPILLARY.

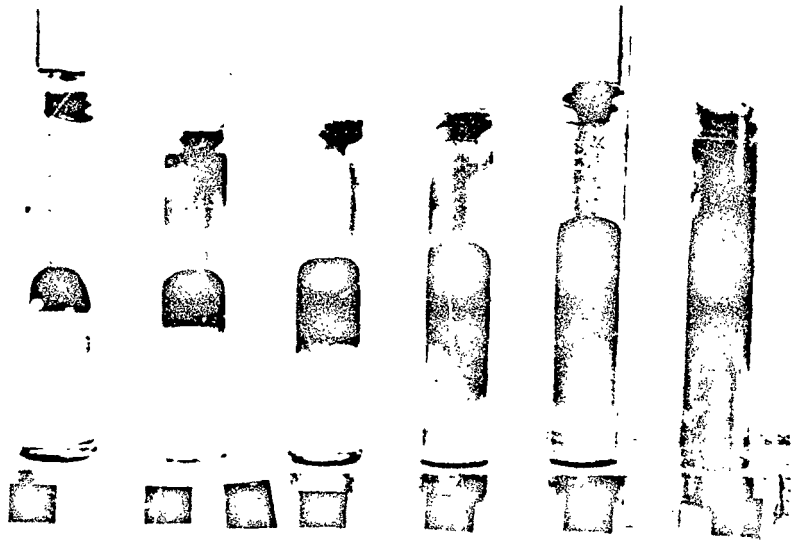

FIG. 8 PROPORTIONALITY OF ISOTACHOPHORETIC COMPARTMENT LENGTH TO QUANTITY OF PROTEIN ADDED. FERRITIN WAS USED, AND ITS SELF-REGULATED CONCENTRATION IS ABOUT 10% WITH 20 mM LEADER CONCENTRATION.

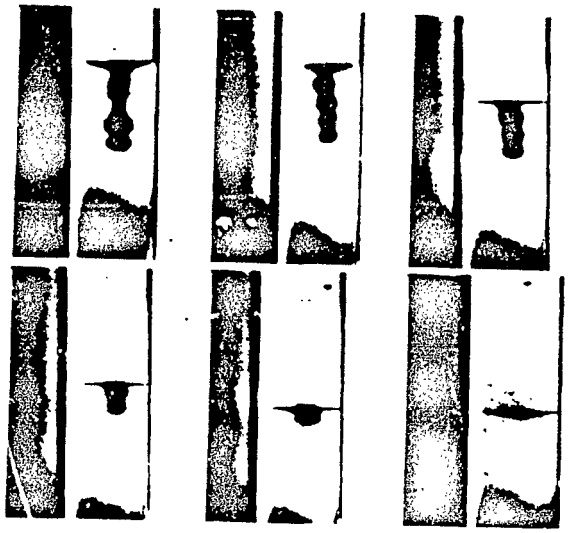

FIG. 9 SPREADING OF DYE SAMPLE AT LEADER-TERMINATOR INTERFACE. THE PONCEAU S DYE WAS CENTRALLY INJECTED INTO THE LEADERGEL, AND SPREADS SHARPLY ACROSS THE ENTIRE TUBE WITH THE ADVANCING INTERFACE.

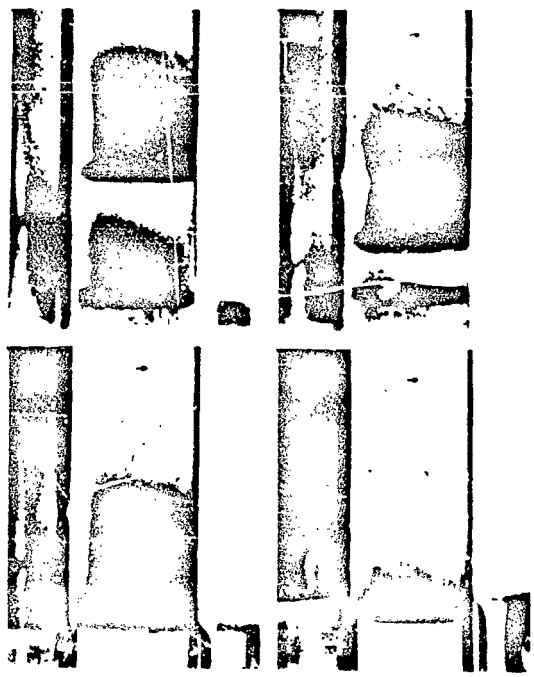

FIG. 10 RESTORATION OF ISOTACHOPHORETIC BOUNDARIES. A SECOND SAMPLE WAS APPLIED ON TOP OF A PREVIOUSLY FORMED ISOTACHOPHORETIC DYE COMPARTMENT. THIS SECOND SAMPLE, APPLIED IN THE TERMINATOR, MIGRATES FASTER, AND CATCHES UP WITH THE FIRST SAMPLE, FORMING AT THE END A SINGLE BOUNDARY. THE DIFFERENCE BETWEEN THE SHARPNESS OF ISOTACHOPHORETIC BOUNDARIES AND THE DIFFUSE NATURE OF ZONE BOUNDARIES OF THE DYE IN THE TERMINATOR IS OBVIOUS.

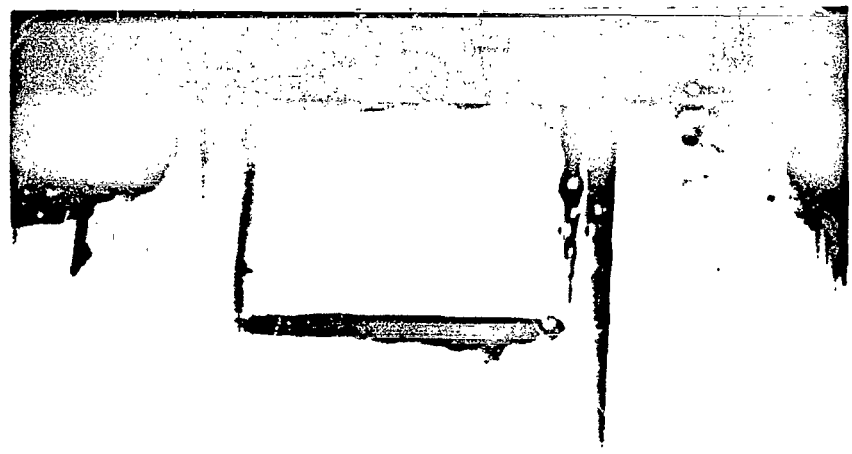

FIG. 11 SEPARATION OF HUMAN AND SHEEP RED CELLS IN A FICOLL GRADIENT. SEPARATION WAS ONLY TRANSITORY DUE TO CONVECTIVE DISTURBANCES.

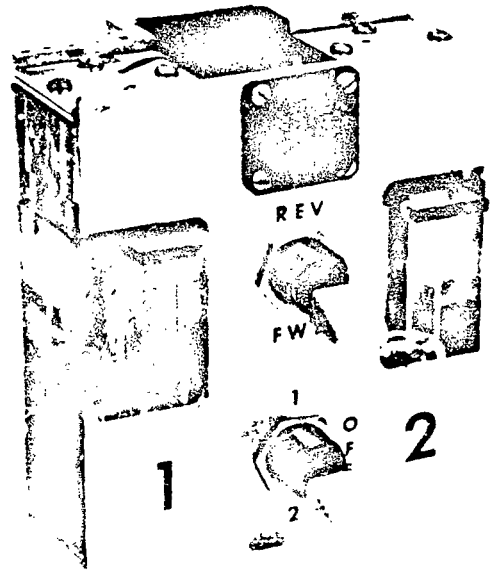

FIG. 12 SKYLAB APPARATUS SHOWING THE MOUNTING OF THE TWO SAMPLE - CONTAINING MODULES.

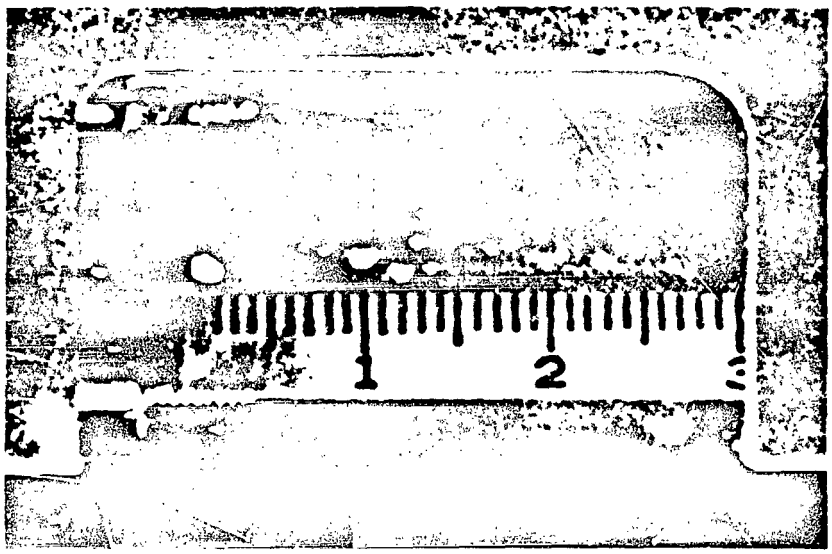

FIG. 13 SKYLAB PHOTOGRAPH OF ADVANCING ISOTACHOPHORETIC FRONT OF THE RED BLOOD CELL SUSPENSION. THE EXACT SHAPE OF THE BOUNDARY IS BLURRED BY AIR BUBBLES.

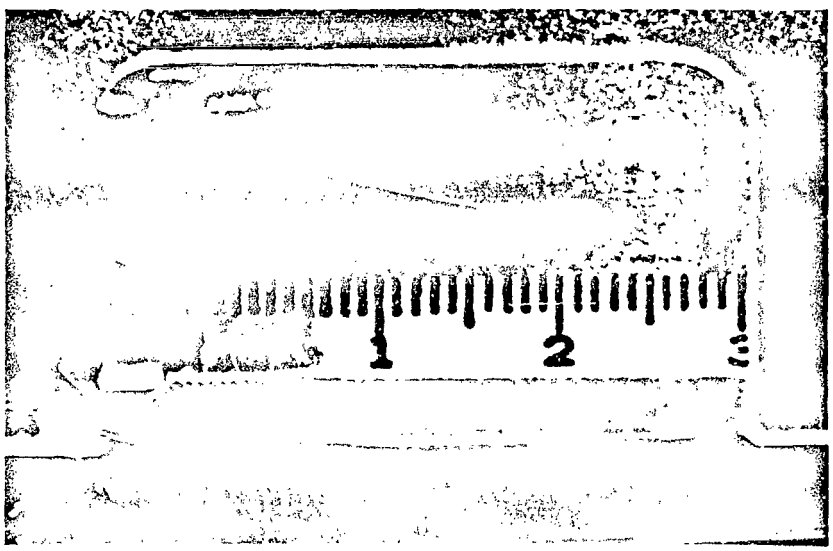

FIG. 14 SKYLAB PHOTOGRAPH DURING SECOND RUN OF THE BLOOD MODULE. THE SHARP BOUNDARY HAS THE PROFILE OF A BLUNTED PARABOLA.

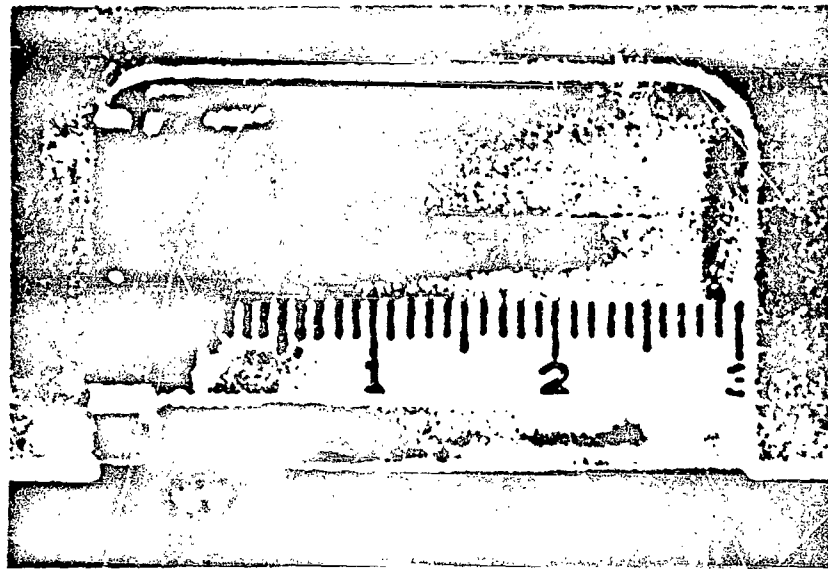

FIG. 15 REVERSAL OF CURRENT IN SKYLAB EXPERIMENT SHOWS THE DIFFUSE BOUNDARY TYPICAL OF ZONE ELECTROPHORESIS.

N74 29915

PREPARATIVE ELECTROPHORESIS OF LIVING LYMPHOCYTES

By

C. J. van Oss*, P. E. Bigazzi, C. F. Gillman
Department of Mocrobiology and The Center for Immunology
School of Medicine, State University of New York at Buffalo
Buffalo, New York 14214

and

R. E. Allen
Astronautics Laboratory
George C. Marshall Space Flight Center
Huntsville, Alabama 35812

SUMMARY

Vertical liquid columns containing low molecular weight dextran density gradients can be used for preparative lymphocyte electrophoresis on earth, in simulation of 0 gravity conditions. Another method that has been tested at 1 G, is the electrophoresis of lymphocytes in an upward direction in vertical columns. By both methods up to 10^7 lymphocytes can be separated at one time in a 30 cm glass column of 8 mm inside diameter, at 12 v/cm, in 2 hours. Due to convection and sedimentation problems, the separation at 1 G is less than ideal, but it is expected that at 0 gravity electrophoresis will prove to be a uniquely powerful cell separation tool. The technical feasibility of electrophoresing inert particles at 0 G has been proven earlier, during the flight of Apollo 16 [1].

INTRODUCTION

Certain cells with quite different biological properties (notably T and B lymphocytes) differ physio-chemically only in their surface potential [2]. Thus the only physical methods for separating such cells into groups of cells with different surface potentials are electrophoretic ones. Normally, however, cells sediment to the bottom of the experimental vessels in the time required for electrophoretic separation. Increasing the medium's density by adding solutes creates osmotic and other problems. Thus the ideal condition for the electrophoretic separation of cells must be sought at 0 gravity, in space. Nevertheless, the methodology for electrophoretic cell separation in space first has to be worked out on earth, at gravity = 1.

To that effect two approaches can be used: 1) Descending electrophoresis in a vertical column, stabilized by a density gradient, and 2) Ascending electrophoresis in a non-stabilized vertical column. Both approaches are studied here and both yield valuable information, indispensable for the

*Paper presented by C. J. van Oss.

elaboration of O G electrophoresis methodology.

T and B lymphocytes, once separated, will not only serve in further in vitro research, but also in the treatment of a variety of immunological diseases (agammaglobulins, DiGeorge's syndrome), various malignancies such as Hodgkins disease and chronic lymphatic leukemia, and other types of cancer and chronic infections.

DESCENDING ELECTROPHORESIS IN A DENSITY GRADIENT

Electrophoresis Buffer

A phosphate buffer, of pH 7.7, $\Gamma/2 = 0.022$, with a conductivity of 0.26 mho cm and an osmolality of 265 m.Osm/L. (When, for practical reasons, the cells must be electrophoresed in a medium that is sufficiently cryoprotectant to allow them to be frozen, 4% glycerol is added to this buffer, which then raises the osmolality to 780 m.Osm/L). The buffer consists of 12 parts of:

A
- 0.18% Na_2HPO_4
- 0.02% KH_2PO_4
- 4.32% glucose

plus one part of:

B
- 0.18% Na_2HPO_4
- 0.02% KH_2PO_4
- 0.80% NaCl.

The density gradient was prepared by overlaying a 5% Dextran T 10 (Pharmacia, Piscataway, N.J.) (average molecular weight = 10,000) solution in the above buffer, on top of an 11% solution of the same material. Other cells have been successfully electrophoresed in density gradients of much higher molecular weight dextrans [3], but in our experience signigicant lymphocyte agglomeration occurred in dextran solutions of practically all molecular weights above 10,000, so that the T 10 dextran variety proved the only one that could be used with this type of cell.

The gradient was established by careful hand mixing. It could also be obtained with a two-vessel stirred gradient maker. The results proved to be the same, as checked by measuring the refractive index at various intervals, with a refractometer.

Electric Field

The lymphocytes were electrophoresed under an electric field of ≈ 10 mA, yielding, at a total potential difference across the tube of 360 V, 3.6 W.

Cooling

Cooling of the cylindrical columns was accomplished by means of a water jacket connected to a Lo-Temprol refrigerated water bath. Continuous circulation of cold water maintained a temperature of +4°C. For the complete apparatus, see Figures 1 and 2.

Cells

Some experiments were done with cultured human lymphoid cells (RPMI

6410), which were grown and maintained in Eagle's Essential Medium with 10% fetal calf serum. The cultured cells were washed twice in phosphate buffered saline (PBS) before being applied to the column. 4×10^6 cells were suspended on top of the gradient.

For fresh human lymphocytes, human buffy coat preparations (courtesy of the Buffalo Regional Red Cross Blood Center) were subjected to Ficoll-Hypaque [4] density gradient centrifugation and the lymphocytes were collected and washed in PBS. 3×10^6 cells were generally used per electrophoresis experiment.

Electrophoresis Tube

A 30 cm long, 8 mm inside diameter glass tube was used, coated on the inside with a 1.5% agarose gel (made in the electrophoresis buffer), and plugged at the bottom with a 2 cm deep 1.5% agarose plug. The bottom stood in the lower electrode vessel, while the top of the tube was connected to the upper electrode vessel by means of an agarose wick encased in a glass U-tube (inverted).

Fraction Collecting

After electrophoresis the cells were collected by piercing the agarose plug with a 21-gauge needle and collecting 5 drops per test tube.

ASCENDING ELECTROPHORESIS

Electrophoresis Buffer

The cells were separated by electrophoresis in an upward direction, using a phosphate buffer, of pH 7.7, $\Gamma/2 = 0.01$ (buffer A), with a conductivity of 0.12 mho cm and an osmolality of approximately 265 m.Osm/L.

Electric Field

With this buffer an electric field of 10 V/cm was obtained, with a current of 5 mA. The cells were electrophoresed for 2.5 hours under these circumstances.

Cooling

The cooling arrangement was the same as described above.

Cells

The cells used were the same as those described above.

Electrophoresis Tube

Either the same tubes (agarose-coated) as described above were used, or in their stead, uncoated lucite tubes of comparable size.

Fraction Collecting

When a plastic tube was used, it was also fitted at the bottom with an agarose plug (see above). After electrophoresis, 3 or 4 1 ml fractions were collected from the top of the electrophoresis tube, by aspiration with a 5 ml syringe, through a 30 cm needle.

METHOD OF ANALYSIS

After the fractions were collected and counted, with a Spencer Improved Neubauer Counting Chamber, they were analysed for surface immunoglobulins by immunofluorescence. An equal volume of 1/16 dilution of fluoresceinated rabbit anti-human IgG was added to the cells. After 30 minutes at 4°C the cells were centrifuged at 2,000 RPM and the excess conjugate decanted. After 2x washing in cold PBS, the percentage of positive fluorescent cells (B cells) was determined by microscopy (Reichert Zetopan fluorescence microscope).

RESULTS OF DESCENDING ELECTROPHORESIS

In Figure 3 the results of a typical density gradient experiment are shown. The two fast batches contained more T than B cells and the fastest of these had 82% T cells (only 18% B cells left), which represents an enrichment factor of 3.3. The yield was close to 90%. Among the fractions only those are shown on which B/T cell ratio analysis by immunofluorescence was done, which, on account of time limitations, was only feasible with one fraction out of three.

Thus, descending density gradient electrophoresis gave fairly good results with cultured human lymphocytes. With fresh peripheral human lymphocytes, this method, possibly due to a somewhat greater overlap of electrophoretic mobilities, proved less satisfactory. The ascending electrophoresis approach, discussed below, appears more promising for that type of cell.

RESULTS OF ASCENDING ELECTROPHORESIS

Ascending electrophoresis gives good results with fresh human peripheral lymphocytes. In an exceptionally successful experiment, shown in Figure 4, the fraction that was enriched from the original 72% T cells to 96% T cells in the first run, was electrophoresed a second time, yielding a fast fraction with 2×10^6 100% T cells, representing 20% of the cells that were made to electrophorese the second time. In Figure 5 two fractions, well separated from one another, are visible inside the electrophoresis tube. In Figure 6 the results are shown that pertain more often than the exceptionally favorable ones given in Figure 4: at the second electrophoresis the proportion of T cells could only be improved from 92% to 95%, at the expense of a 40% loss of cells.

Recovery of B cells from the slow fraction, after two electrophoreses, seldom results in more than 90% pure B cells, due, e.g., to clumping of B cells and trapping of T cells in the clumps. At 0 gravity clumping may be equally difficult to avoid but the sedimentation of the clumps and their contamination of the slowest fractions will not occur.

CONCLUSION

The results of both the descending and ascending electrophoretic lymphocyte separation at gravity = 1 show the possibilities as well as the probable limits to lymphocyte electrophoresis on earth. At the same time the methodology developed will permit, by fairly simple extrapolation to elaborate the methodology to be used at 0 G.

REFERENCES

1. R.S. Snyder, M. Bier, R.N. Griffin, A.J. Johnson, H. Leidheiser, F.J. Micale, J.W. Vanderhoff, S. Ross and C.J. van Oss, in SEPARATION AND PURIFICATION METHODS, Vol. 2, E.S. Perry, C.J. van Oss and E. Grushka, eds., Dekker, New York, 1974, p. 259.

2. P.E. Bigazzi, C.J. van Oss and S. Cohen, in PRINCIPLES OF IMMUNOLOGY, N.R. Rose, F. Milgrom and C.J. van Oss, eds., Macmillan, New York, 1973, p. 205.

3. R.C. Boltz, P. Todd, M.J. Streibel and M.K. Louie, Prep. Biochem. 3, 383 (1973).

4. A. Boyum, Scand. J. Clin. Lab. Invest. 21, Suppl. 97, 51 (1968).

ACKNOWLEDGEMENTS

This work has been supported in part by NASA Contract NAS8-29745. An earlier version of this paper was communicated at the 12th AIAA Aerospace Science Meeting, in Washington, D.C., on February 1, 1974. We are much indebted to Drs. R. M. Lambert and K. Zelenski, of the Buffalo Regional Red Cross Blood Center, for their help in procuring fresh human lymphocytes.

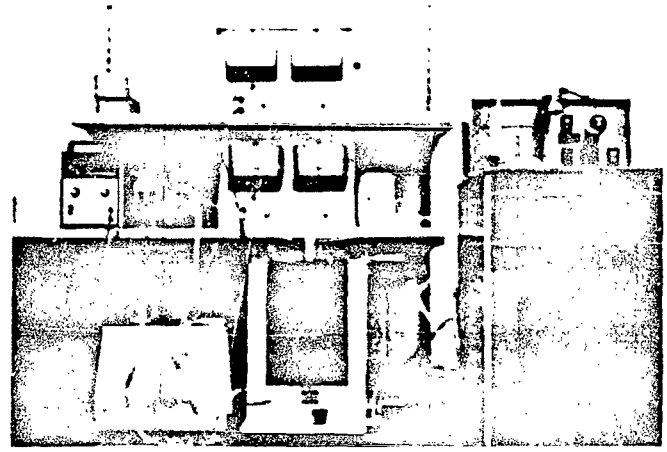

FIG. 1 PHOTOGRAPH OF THE ELECTROPHORESIS TUBES (ONE AT LEFT AND ONE IN THE MIDDLE, BENEATH THE BOTTOM SHELF), THE COOLED WATER CIRCULATOR (RIGHT) AND THE POWER SUPPLIES (IN THE MIDDLE ON THE TOP AND BOTTOM SHELVES).

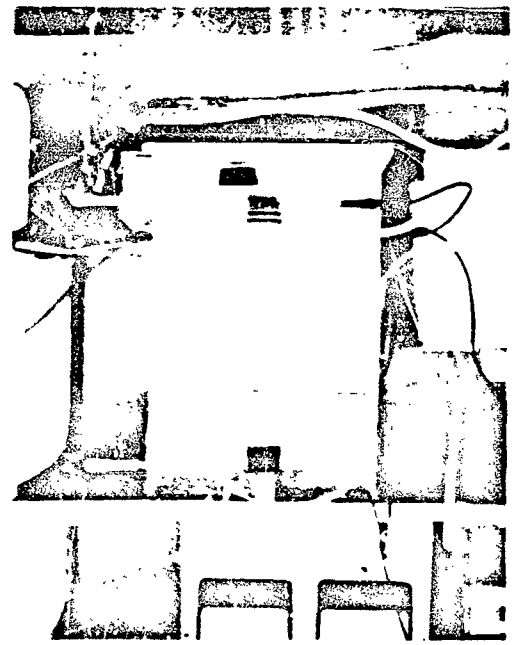

FIG. 2 PHOTOGRAPH OF A JACKETED ELECTROPHORESIS TUBE, WITH ITS POWER SUPPLY STILL PARTLY VISIBLE ABOVE IT, ON THE SHELF.

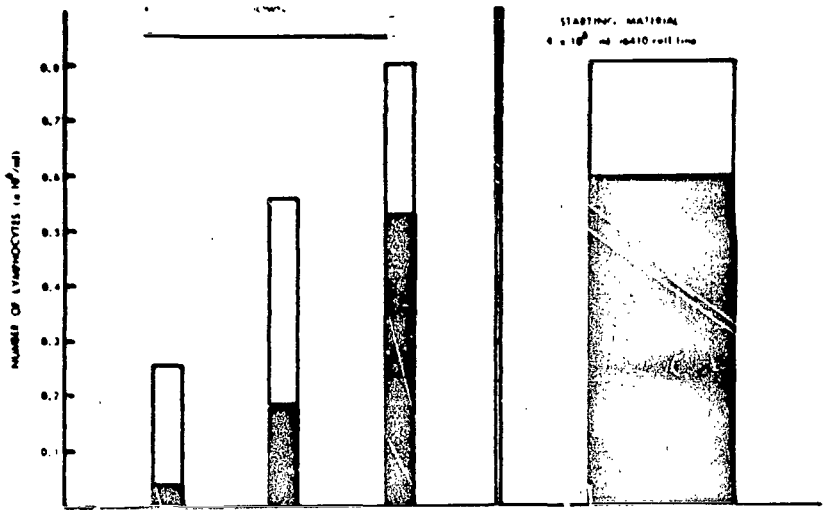

FIG. 3 GRAPH OF THE RESULTS OBTAINED IN A DESCENDING ELECTROPHORESIS OF HUMAN LYMPHOCYTES (RPMI 6410).

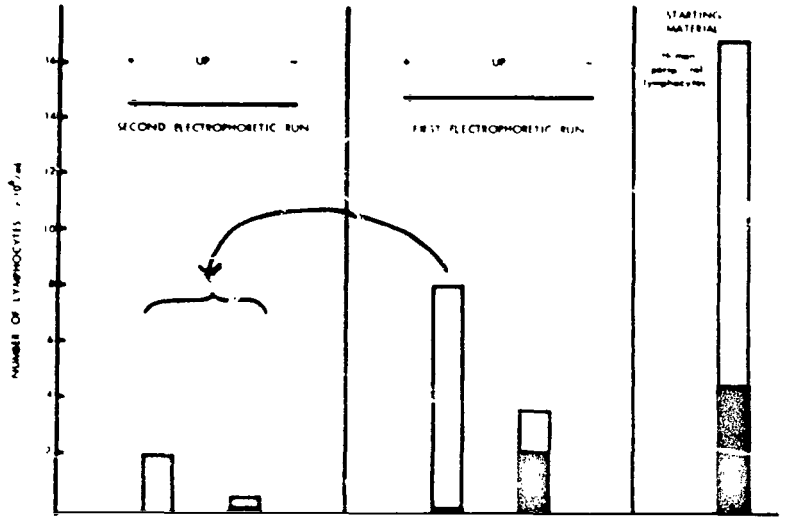

FIG. 4 GRAPH OF THE RESULTS OBTAINED IN A DOUBLE ASCENDING ELECTROPHORESIS OF FRESH HUMAN PERIPHERAL LYMPHOCYTES. THIS WAS AN EXCEPTIONALLY SUCCESSFUL SEPARATION.

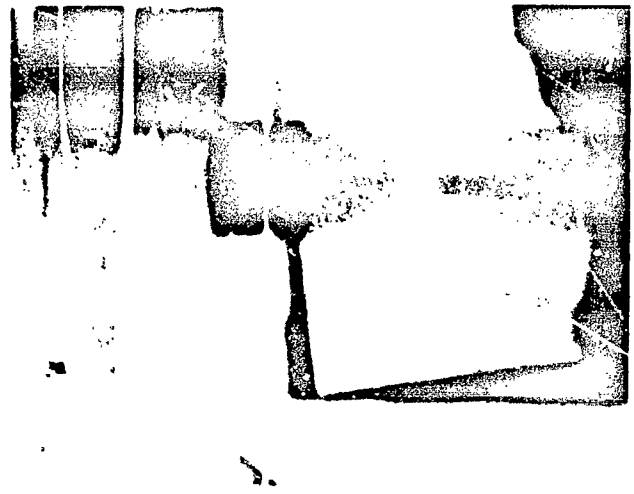

FIG. 5 PHOTOGRAPH OF THE SEPARATED BANDS OF LYMPHOCYTES VISIBLE IN A TYPICAL ASCENDING ELECTROPHORESIS EXPERIMENT WITH FRESH HUMAN PERIPHERAL LYMPHOCYTES.

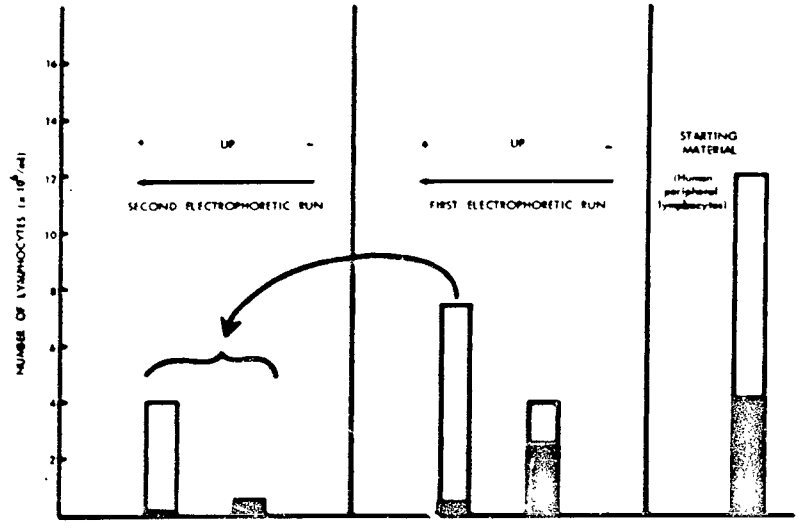

FIG. 6 GRAPH OF THE RESULTS OBTAINED IN A DOUBLE ASCENDING ELECTROPHORESIS OF FRESH HUMAN PERIPHERAL LYMPHOCYTES. THIS IS THE TYPE OF SEPARATION USUALLY OBTAINED.

MATERIALS SCIENCE AND MANUFACTURING IN SPACE: THE NBS PROGRAM OF GROUND BASED RESEARCH

By

E. Passaglia and R. L. Parker*
National Bureau of Standards
Washington, D. C. 20234

INTRODUCTION

NBS work for NASA in support of NASA's Space Processing Program is described. The objectives of the NBS program are to perform ground-based studies of those aspects of space that could possibly provide a unique environment for making materials more perfect or more pure. The approach taken deals primarily with experimental and theoretical studies of the possible effects of the absence of gravitational forces on those materials preparation processes where the presence of gravity may be important in reducing perfection or purity. The materials preparation processes studied comprise 6 tasks in the areas of crystal growth, purification and chemical processing, and the preparation of composites. They are:

(1) Crystal Perfection in Czochralski Growth

(2) Evaporative Preparation of Ultrahigh Purity Materials

(3) Vacuum Effects in the Preparation of Composite Materials

(4) Melt Shape in Weightless Crystal Growth

(5) Vapor Transport Synthesis and Crystal Growth of Oxides

(6) Surface Traction and Other Surface Phenomena

*Paper presented by R. L. Parker.

SUMMARY

This report describes NBS work for NASA in support of NASA's Space Processing program. The objectives of the NBS program are to perform ground-based studies of those aspects of space that could possibly provide a unique environment for making materials more perfect or more pure. The approach taken deals primarily with experimental and theoretical studies of the possible effects of the absence of gravitational forces on those materials preparation processes where the presence of gravity may be important in reducing perfection or purity. The materials preparation processes studied comprise 6 tasks in the areas of crystal growth, purification and chemical processing, and the preparation of composites.

The results obtained for each task are given in detail in the body of the report. Briefly, in Task 1 - Crystal Perfection in Czochralski Growth - an intensive study has been performed, and optimum solidification parameters determined for the production of highly perfect copper crystals by the Czochralski growth process, using x-ray topographs and rocking curve measurements of crystal perfection. In Task 2 - Evaporative Preparation of Ultrahigh Purity Materials - a calculational procedure involving the use of complex chemical equilibria was developed and showed that extensive purification can be obtained in evaporative purification. In Task 3 - Vacuum Effects in the Preparation of Composite Materials - the scanning electron microscope was used to study the effects of strain, surface coatings and specimen tilt in electron channelling patterns. In Task 4 - Melt Shape in Weightless Crystal Growth - the differential equation for the shape of the liquid-vapor interface in the presence of a gravitational field has been extended to the case of very small gravitational fields, and measurements of contact angles in liquids on their own solids have begun. In Task 5 - Vapor Transport Synthesis and Crystal Growth of Oxides - the ZrO_2-Ta_2O_5 system was investigated in chemical vapor transport reactions and met with severe problems in the quartz reaction tubes and resulted in very small crystal sizes; additional experiments in pure vapor phase growth of $HgCl_2$ appear promising. In Task 6 - Surface Traction and Other Surface Phenomena - the pattern of thermocapillary convection cells in a liquid drop with an axially symmetric temperature field on the surface was deduced.

While it would be premature to draw, at this stage, extensive conclusions from these studies on space processing, it is clear that the role of gravity in materials processing can have significant, and possibly limiting, effects on purity and perfection of materials, and that extensive experimental and theoretical investigations, in ground-based environments, are important base-line information needed for the efficient use of the space environment in materials processing.

Table of Contents

Task 1 (Acct. No. 179-11-11-03)

CRYSTAL PERFECTION IN CZOCHRALSKI GROWTH

By

M. Kuriyama, J. G. Early, W. J. Boettinger and H. E. Burdette
Institute for Materials Research,
National Bureau of Standards

SUMMARY

In the absence of gravity, thermal convection, i.e., convection induced by gravity acting on density differences in the melt, would be expected to be negligible. Fluid flow in the melt, including thermal convection, probably affects crystals grown from the melt. At present, the relationship between crystal growth conditions, in particular fluid flow conditions, and the degree of crystal perfection has not been well established for metals. An intensive study has been performed and reported here on optimum solidification parameters for the production of highly perfect copper crystals by Czochralski growth. In this research, the crystal perfection has been assessed by non-destructive methods of x-ray diffraction, such as Borrmann anomalous transmission and rocking curve measurements by double crystal diffractometry. The copper single crystals have been grown under various growth conditions where the rotation of the seed and of the melt and the diameter of the bottle-neck are chosen as variables. X-ray topographs have been analysed along with the data obtained from rocking curve measurements. Tables of growth conditions and quantitative data of rocking curve widths are presented in this report with the x-ray topographs. Optimum growth parameters resulting in highly perfect crystals have been determined. Possible mechanisms for obtaining highly perfect crystals have been discussed.

INTRODUCTION

Although for many years certain semiconducting materials, such as Si and Ge have been grown from the melt phase, free of dislocations, it has not generally been possible to grow sizable metal crystals free of dislocations. The reasons for this are still not entirely clear. The difficulty in growing highly perfect metal crystals may be attributed to their low dislocation energy and high dislocation mobility, compared with those factors for semiconducting crystals. Imperfections can be produced by impurity particles present in the melt which may originate in the container used to hold the melt.

In addition to these defect sources, one certainly cannot neglect sources related to thermal conditions. Among them, the presence of thermal convection and other fluid flow phenomena in the melt may affect solidification processes resulting in the build-up of inhomogeneous strain fields sufficiently large to cause dislocations to multiply. Since thermal convection

is induced predominantly by gravity acting on density differences in the melt, it is usually impossible to control completely fluid flow, especially convection, during crystal growth on the earth's surface.

At the present time, the relationship between the crystal growth conditions and the degree of crystal perfection has not been well established for metals. As a continuation and an expansion of our previous work, an intensive study has been performed and reported here on optimum solidification parameters for the production of large, highly perfect metal crystals by Czochralski growth. In this research as well as in the previous study, a non-destructive assessment of the crystal perfection of the grown crystals is indispensable. Further development has, therefore, been continued on high resolution X-ray diffraction methods for the characterization of such crystals. Hereafter, our previous work will be refered to as Report I*.

In the present report, emphasis will be placed on studying the resultant crystal perfection from the following aspects:

a. reproducibility of crystal perfection for given growth conditions,

b. "bottle-necking" effects in the processes of crystal growth,

c. annealing effects after sample crystals are prepared in a disc form.

In studying crystal perfection as a functional of fluid flow, it is necessary first to establish the fact that there is, indeed, a relation between the crystal perfection and the fluid flow conditions. In Report I, we have discussed such a relation, based on our preliminary experiments. However, it was not conclusive whether or not the variations of crystal perfection are caused by fluid flow conditions, per se, or by other factors, such as the perfection of seed crystals, and the procedures of handling grown crystals. In view of this, it is important to check whether one can reproduce the same degree of crystal perfection for a given fluid flow condition. This check cannot be done without including aspects b and c, although analysing the results in aspect a alone seems sufficient enough to define the optimum fluid flow conditions in the melt for the present purpose.

EXPERIMENTAL PROCEDURES

The details of the experimental procedures and the principles of x-ray diffraction mechanisms which are required to perform the present work have been described in Report I. In the present report, only changes and improvements will be discussed, along with a brief description of the techniques we use.

---

* Government Order H-84832A, National Aeronautics and Space Administration; NBS Report 10873.

The schematic diagram of the Czochralski pulling apparatus is shown in Fig. 1, where the principle variables defining growth conditions are denoted by x (pulling speed), y (seed rotation) and z (crucible rotation). The pulling speed is generally between 0.013 cm/min. and 0.1 cm/min. The speed does not cause as significant a change in diameter, except for crystals having a small bottle-neck diameter (~0.05 cm), as does the temperature in the melt. When the crystal initially grows with a very small bottle-neck diameter, the pulling speed affects the diameter of the growing part significantly until the bottle-neck region completely clears the top of the furnace.

Crystal boules were grown by narrowing the diameter at one region of the boule and increasing the diameter for the rest of the boule till the desired crystal diameter (1.5 cm - 3.0 cm) is reached. Narrowing the crystal diameter (the bottle-neck) can be produced by increasing the temperature of the melt. Two examples of crystal boules are shown in Fig. 2. Because of extremely narrow bottle-necks, the removal of crystal boules from the puller required the following procedures to be adopted to prevent any flexing of the crystal in the neck region which would induce strains and dislocations. When the boule has cooled to room temperature, a mold is placed around the boule, but not touching it. The mold is then filled with molten paraffin (at approximately 40°C). When the wax has cooled, the crystal is released from the puller. The wax supports the neck while the crystal is mounted on an acid saw.

At least three slices of sample crystals were cut from different regions of each boule. One of the slices was annealed at 1000°C for three days in a hydrogen (dew point = -90°F) flow furnace. The thicknesses of the slices were determined by use of the Borrmann (anomalous transmission) effect of x-ray diffraction. Fig. 3 illustrates schematically the experimental arrangement and the derivation of the thickness equation

$$D = (L_0 - L_S)/\tan\theta.$$

In the present work, the slit placed in the x-ray beam before the crystal is 0.01 cm wide. A photograph of a nuclear plate used for the determination of thickness is shown in Fig. 4, where the (111) Bragg diffraction was used with Cu $K\alpha_1$ radiation.

For the characterization of the perfection of sample crystals, we have used two different x-ray optical alignments, namely an asymmetrical topographic camera and a high resolution double crystal spectrometer. The former, which will be called ATC hereafter, was designed in order to enable us to survey a large number of sample crystals effectively in a shorter time period than that required for ordinary topography. Although this was accomplished at the expense of high resolution, the quality of topographs from the ATC remained just as good as in ordinary x-ray topography. (It was one of the requirements for this design to maintain such high quality in the topographs.)

In the ATC, the first crystal is a silicon crystal whose surface makes an angle of 13.5° with the (111) diffracting plane. The incident x-ray beam falls on the crystal surface almost parallel to it, and the (111) diffracted beam appears with a size of 1.7 cm x 2.5 cm, being sufficiently large enough to cover the entire area of sample crystals. Care must be taken with the first crystal so that it would not superimpose its own surface structure on topographs of the structure of the sample crystal. This requirement often induces an unavoidable lack of ideal high resolution in the ATC. The schematic diagram of the ATC is shown in Fig. 5. Topographs are taken from the sample crystal (Cu) both in transmission geometry, where the (111) diffraction of copper is used, and in reflection geometry, where the (220) diffraction is used.

To obtain diffraction rocking curves and high resolution topographs at various locations on the sample crystals, the high resolution double crystal spectrometer (hereafter called the spectrometer) has been used with a scanning stage mounted on it. The schematic diagram of the spectrometer is shown in Fig. 6, where the first crystal is only shown in reflection geometry. A photograph of the spectrometer in operation is shown in Fig. 7. A silicon crystal of disc shape whose surface is a (110) crystallographic plane has been chosen as the first crystal to obtain a well collimated monochromatic beam from the (220) Bragg diffraction both in reflection and transmission geometry. Between the x-ray source of a point focus x-ray tube and the first crystal, a horizontal slit of 6 mm and a vertical slit of 0.3 mm have been inserted. When the first crystal is in reflection geometry, two vertical slits of 0.15 mm and 0.10 mm, respectively, are placed a distance of 3 cm apart from each other before the second crystal. When the first crystal is in transmission geometry, no slits are inserted.

The quality of the beam was checked by measuring the rocking curves of a dislocation free germanium crystal which was placed at the second crystal position. The full width at half maximum (FWHM) of the rocking curve from the (220) germanium diffraction was determined to be 12.8 seconds of arc in the Si (220) surface/Ge (220) surface mode and 15.5 seconds of arc in the Si (220) transmission/Ge (220) surface mode, where Cu Kα radiation is used throughout.

EXPERIMENTAL RESULTS

1. Fluid Flow Conditions

The fluid flow conditions in the melt during crystal growth are classified into groups by different sets of values of the principle variables, angular velocity of crucible and seed rotation, as listed in Table I. By interchanging the values of y and z, we obtain Δ with opposite signs. Based on the results in Report I and the results in the present work, there appears to be no significant difference in the resultant crystal perfection due to the difference in the sign of Δ. Therefore, we do not discriminate fluid flow conditions from each other when the sign of Δ is changed by exchanging the values of y and z.

In addition, we have introduced another parameter indicating the diameter of the bottle-necks grown during the crystal growth process. There are always at least two different bottle-neck diameters chosen in each group; one is very narrow, usually less than 1 mm and the other between 2 mm and 4 mm.

2. Spectroscopic Data

In Table II, we list the values of rocking curve widths (FWHM) observed in both transmission and surface reflection geometry for all the growth conditions, including annealing. The crystal is considered to be more perfect, the smaller the observed width. The crystals are ranked, as shown in the eighth and ninth columns, in increasing order of their widths. The annealed crystals are ranked separately with the letter A accompanied by their rank. The ranks based on the transmission data should be judged along with the values of μL, because, even with the same degree of perfection, thicker crystals show narrower widths.

In most crystals, the perfection is not uniform throughout the crystal. Rocking curves taken at different locations from the same crystal are shown in Fig. 8, where the (220) diffraction is set in reflection geometry. Other examples of local rocking curves are shown in Fig. 9, where the (111) diffraction is set in transmission geometry (μL ~ 25). In this figure, the horizontal axis represents a decreasing glancing angle to the right. The little humps on the right side of the individual profiles correspond to the Bragg diffraction due to Cu $K\alpha_2$ radiation. The separation of the α_1 and α_2 peaks in the Si (220)/Cu (111) non-parallel ($1\bar{1}$) setting is -20.8 second of arc, which is given by the difference between the separation of α_1 and α_2 due to Si (220) and that due to the Cu (111) diffraction.

Typical rocking curve profiles are shown in Fig. 10 and 11 for various crystals. In Fig. 10, the curves were obtained in both transmission and surface reflection geometry of the copper crystal with the first crystal, Si (220), in transmission geometry. The horizontal axis represents an increasing glancing angle to the right. The smaller peaks correspond to the α_2 diffraction: the separation in the reflection geometry is calculated to be +163.0 seconds of arc. Fig. 11 shows the rocking curve profiles from a crystal of good quality (#037303) and a typical rocking curve from a crystal of poor perfection (#035302). The latter crystal did not produce observable anomalous transmission.

3. X-Ray Topographs of the Grown Crystals

As mentioned previously, diffraction topographs were taken by two different x-ray alignments, the ATC and the scanning spectrometer. The topographs taken by the ATC usually gave the entire view of the sample crystals, unless the crystal size was larger than the size of the x-ray beam. Examples of the topographs* are shown in Figs. 12a, b and 13a, b in both the reflection and the transmission geometry from as grown crystals.

* Many of the enlargements of the topographs are formed as composite photographs as a result of limitations of the microscope used in the enlargement technique.

Since for lack of space we cannot show all the topographs here, we shall describe the qualities of the crystals as-grown in various growth conditions, based on their topographs.

The crystals grown in Growth Condition I with a narrow neck generally produced surface topographs (obtained by a surface Bragg diffraction) almost as good as those shown in Figs. 12a and 13a, but with a continuous distribution of darkness (excess intensity) areas which we call "strain contours". The transmission topographs (taken in transmission geometry) indicated, however, much poorer quality in those crystals, showing the anomalous transmission only in about 50% of the total area.

In contrast, the crystals grown in Growth Condition I with a wider neck showed much poorer quality in their surface topographs, in which not only the strain contours, but many lines of imperfections appeared. These crystals usually did not produce good transmission topographs.

The crystals grown in Growth Condition II were of a quality similar to those grown in Growth Condition I with larger necks. The surface topographs showed many strain contours and often the topograph images did not cover the entire exposed area of the crystals. The transmission topographs were broken up into many areas, indicating that the perfect crystal areas were very much limited within small local regions. These results were consistent in this growth condition, regardless of their bottle-neck diameters.

The crystals grown in Growth Condition III with a narrow neck generally displayed the best quality of perfection. Fig. 12a, b and Fig. 13a, b are examples of the topographs from the crystals grown in this condition. The surface topographs showed much fewer crater-type images than those taken from the crystals grown under other growth conditions. The number of visible dislocations in the surface topographs are found to range between 11 and 100 dislocations per cm^2 for the crystals as-grown in this condition. The transmission topographs, however, reveal more imperfections in the interior of the crystals, as shown in Fig. 12b and 13b. One of the common features in the transmission topographs from these crystals is shown in Fig. 13b, although this crystal happened to show this feature in a somewhat exaggerated fashion. In this topograph, many lines runs normal to the <111> direction. The Bragg diffraction in this case is $(\bar{1}11)$. Also, additional lines, though less visible, run normal to the $<\bar{1}\bar{1}\bar{1}>$ direction. In addition, there appear black and white bands parallel to the <110> direction. Those lines are caused by extended dislocations associated with a stacking fault, running almost parallel to the $<10\bar{1}>$ direction. The lines probably represent Lomer-Cottrell locking of the interacting dislocations.

The crystals grown in this condition but with a large neck diameter generally produced topographs of almost the same quality of perfection as the crystals grown in Growth Condition I with a large bottle-neck. The transmission topographs consisted of several regions, indicating that there were few highly perfect regions throughout the crystals.

The crystals grown in Group Condition IV could not be investigated by x-ray topography, as they were not single crystals.

Under Growth Condition V, regardless of the bottle-neck diameter, the crystals displayed typical mosaic structures, as shown in Fig. 14a. No transmission topographs were produced.

Now we turn to the annealing effects. As indicated in Table II, at least one crystal from the boules in each growth condition was annealed. As shown in Fig. 14b, the surface topograph from an annealed crystal of Growth Condition V is just as bad as Fig. 14a, indicating that the mosaic structure was not at all affected by annealing. The annealed crystals of Growth Condition II showed polygonization, which usually resulted in the formation of several subgrains.

All the topographs taken from the annealed crystals in Growth Conditions I and III showed an equally high degree of perfection in both surface and transmission geometry. The resultant degree of perfection was almost independent of the bottle-neck diameters. Examples of the surface and transmission topographs are shown in Fig. 15a, b and Fig. 16a, b, respectively of Growth Condition I and Growth Condition III. As seen in the transmission topographs, the Lomer-Cottrell locks of dislocations disappeared and dislocation networks appeared rather randomly.

The number of dislocations counted on the surface topographs for these annealed crystals was less than 23 dislocations per cm^2, the smallest number observed was 7 disl./cm^2. The dislocation densities can be obtained from the transmission topographs which show all the dislocations in the interior of the crystals. In this case, the dislocation density is equal to the number of dislocations multiplied by the length of each dislocation divided by the volume where the dislocations are counted. The average number of dislocations thus obtained was 15 dislocations per cm^2. The smallest number was 12.8 dislocations per cm^2. In these annealed crystals, there were always subgrain boundaries observed, which were, of course, considered to be piled-up dislocations, but were not included in the count of individual dislocations. These subgrain boundaries would have eventually been driven out of the crystals, if we had annealed the crystals for a longer period of time.

In Fig. 17a and b, we show the composite topographs taken from the same crystal as in Fig. 15a and b by the scanning spectrometer. The resolution is much higher in Fig. 17 than Fig. 15. The striation-like background which is seen in Fig. 15 is not present in Fig. 17. This background was caused by the image structure due to the asymmetrical silicon crystal. In the transmission topograph of the scanning spectrometer, the details of the dislocation networks are clearly visible. A few examples of enlarged topographs taken by the spectrometer are shown in Fig. 18a, b and c, representing a highly perfect region, an intermediate region and a highly dislocated region, respectively.

CONCLUSION AND DISCUSSION

We would like to emphasize one of our principles followed in conducting the present work. At present, many people believe that growing perfect crystals is still an art where personal skills play significant roles. Although we do not object to this view, and often agree with this view based on our experience, we have attempted to eliminate such an art from the present work. This attitude probably resulted in producing crystals less perfect than they could be. However, we see significance in establishing reproducibility of the resultant crystal perfection as a functional of growth conditions, rather than a functional of the "art" part of crystal growth technology. In the present work, we grew crystals as routinely as possible, with the least effort of human control. Once the variables were set, we did not attempt to modify these variables in response to local perturbations which occurred from time to time during growth. During the growth process, we were tempted more often than not to correct the diameter by changing temperatures or to increase the pulling or rotation speed when the melt surface started vibrating occasionally. However, we made none of these possible corrections.

In the present work, the spectroscopic data indicated that Growth Condition III generally produced crystals of higher perfection, along with crystals produced under Growth Condition I with narrow necks. These results are in good agreement with the observations of the x-ray topographs. The topographs obtained by the scanning spectrometer further helped to distinguish the subtle differences in the resultant qualities from conditions I and III. Those topographs indicated that Growth Condition III with narrow bottle-necks usually produced crystals of better quality than Condition I. The other growth conditions are clearly inferior to Conditions I and III. It is, therefore, concluded that Growth Condition III is most optimum for growing a single crystal of high perfection, when the bottle-neck is made less than one millimeter in diameter.

If one anneals as-grown crystals afterward, Growth Conditions I and III with narrow bottle-necks result in almost the same degree of crystal perfection. However, crystals grown in the other conditions did not show much improvement in quality as a result of annealing. It is, therefore, further concluded that annealing becomes most effective only when the grown crystals are already highly perfect.

In the optimum growth condition, the density of dislocations can be as low as 11 dislocations per cm^2 for "as-grown" crystals, and as low as 7 dislocations per cm^2 for annealed crystals. The lowest dislocation density measured from the transmission topographs was 12.8 dislocations/cm^2 which is in good agreement with the dislocation densities determined from surface topographs.

Apart from the growth conditions that we studied from the viewpoint of fluid flow, it may be worthwhile to mention that gravity can be considered as a driving force to produce slip in the crystals during their growth process, as indicated in the previous section. The weight of the crystal may

cause slip when the crystal is being pulled. However, these dislocations interact with each other, forming Lomer-Cottrell locks and becoming immobile. Then the resultant crystal becomes highly perfect. This presumably takes place in Growth Conditions I and III. If wide-spread slip occurs or if many dislocations form randomly, as in the case of the other growth conditions, then the locking would not take place and the dislocations would still be mobile and affect the subsequently grown part of the crystal, resulting in a less perfect crystal. The lack of gravity in space may favor the growing of perfect crystals from this point of view, which may be entirely independent of fluid flow conditions.

Because of the lack of time, we could not investigate crystal perfection in Growth Conditions III in more detail by the use of high resolution scanning spectrometry. It is highly desirable to pursue the study of this growth condition combined with "art" part of crystal growth techniques and establish the correlation between the crystal perfection and the fluid flow motion.

Table 1

Group Number	Crucible Rotation (Y)	Seed Rotation (Z)	Difference (Δ = Y - Z)	Crystal boules*
I	-5.4 rpm	-6.0 rpm	+0.6 rpm	21,22,23,24,25, 29,35,36
II	+6.0 rpm	+10.0 rpm	-4.0 rpm	10,13,16,26,27, 38,39
III	-20.6 rpm	-20.0 rpm	-0.6 rpm	20,28,30,37
IV	+30.0 rpm	+20.0 rpm	+10.0 rpm	31,32,33
V	-6.6 rpm	+6.0 rpm	-12.6 rpm	14,15,34

* Boule number 21, for example, stands for the first three digits 021 of the number of sample crystals.

Table II

Growth Condition	Neck Diameter mm	Crystal Slice Number	Post Growth Treatment	Thickness mm	(220) Surface Reflection FWHM Seconds of Arc	(111) Transmission FWHM Seconds of Arc	Perfection Ranking		μL
							Surface	Transmission	
I	1.4	023302	As Grown	0.40	70	α_1 α_2 not resolved	7	--	22.05
I	1.4	023303	Annealed	0.40	70	α_1 α_2 not resolved	7A	--	22.05
I	<1	024301	As Grown	0.6580	35	18	2	3	36.27
I	2	025303	As Grown	0.5883	35	14	2	1	32.43
I	2	025302	Annealed	0.3488	29	14	1A	4A	19.23
I	1.2	035302	As Grown	0.50	47	Not Observed	5	7	27.56
I	1.2	035301	Annealed	0.7549	36	11	5A	2A	41.60
I	.1	036301	As Grown	0.2463	35	20	2	4	13.58
I	.1	036303	Annealed	0.3838	32	12	3A	3A	21.15
II	1	026301	As Grown	0.5502	46	17	4	2	30.33
II	1	026302	Annealed	0.5629	33	11	4A	2A	31.03
II	4	027303	As Grown	0.2550	50	Multiple Peaks	6	5	14.06
II	4	027301	Annealed	0.1791	40	15	6A	5A	9.87
III	<1	028303	As Grown	0.8934	32	14	1	1	49.24
III	<1	028301	Annealed	0.7989	37	10	2A	1A	44.03
III	>2	030302	As Grown	0.40	43	Multiple Peaks	3	5	22.05
III	>2	030303	Annealed	0.4638	31	12	2A	3A	25.56
III	.1	037303	As Grown	0.1439	35	17	2	2	7.93
III	.1	037302	Annealed	0.7101	31	11	2A	2A	39.14
IV	Polycrystalline Boule								
V	3	034303	As Grown	0.25	Multiple Grains				
V	3	034301	Annealed	0.20	Multiple Grains				

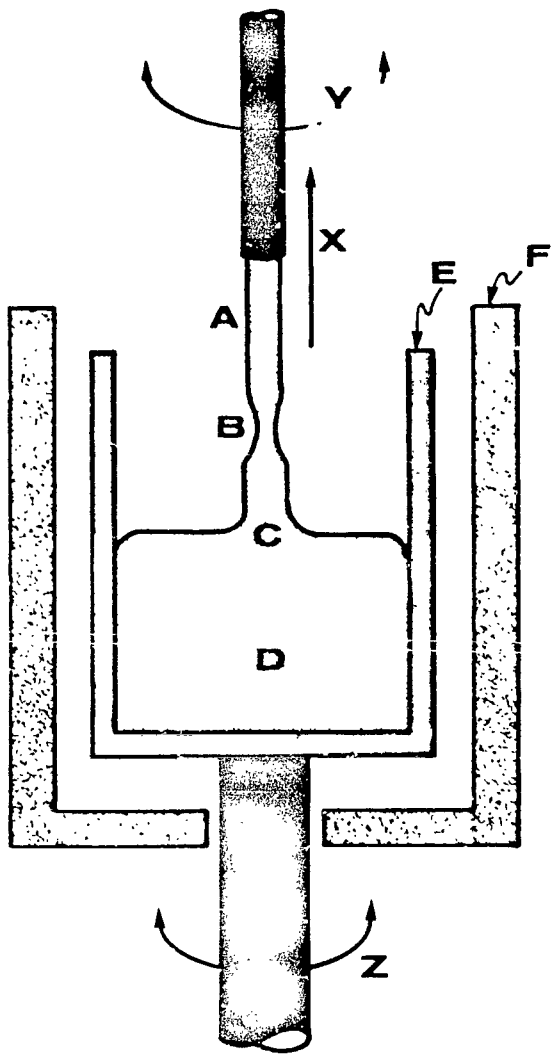

FIGURE 1. SCHEMATIC DIAGRAM OF CZOCHRALSKI CRYSTAL GROWING APPARATUS

A - SEED CRYSTAL
B - BOTTLE-NECK REGION
C - SOLID/LIQUID INTERFACE REGION
D - MELT
E - CRUCIBLE
F - RESISTANCE HEATER
X - PULLING SPEED AND DIRECTION
Y - SEED ROTATION SPEED AND DIRECTION
Z - CRUCIBLE ROTATION SPEED AND DIRECTION

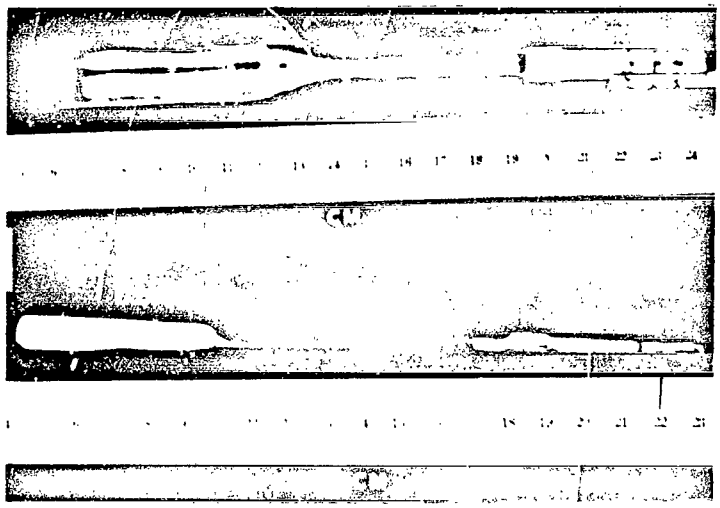

FIGURE 2 PHOTOGRAPH OF CRYSTAL BOULES GROWN WITH DIFFERENT BOTTLE-NECK DIAMETERS.

a. BOTTLE-NECK DIAMETER = 4.7 mm CRYSTAL #020000

b. BOTTLE-NECK DIAMETER - 0.675 mm CRYSTAL #024000

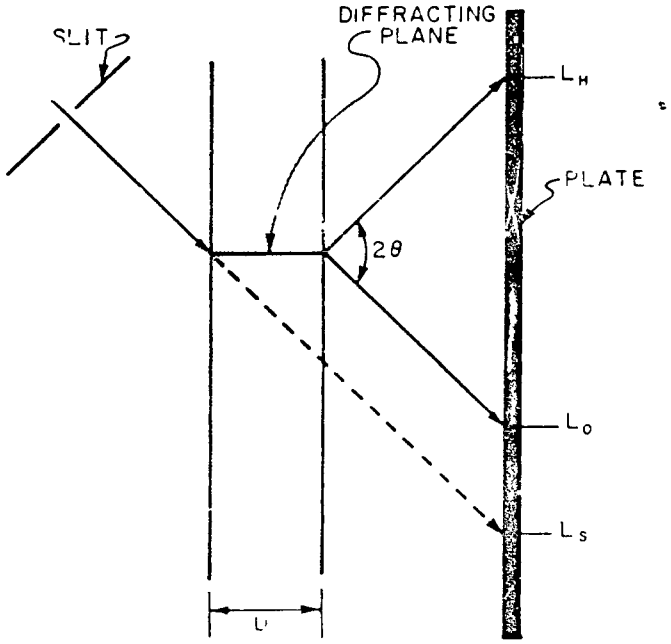

FIGURE 3 SCHEMATIC OF EXPERIMENTAL PROCEDURE USED IN THE DETERMINATION OF THE CRYSTAL THICKNESS

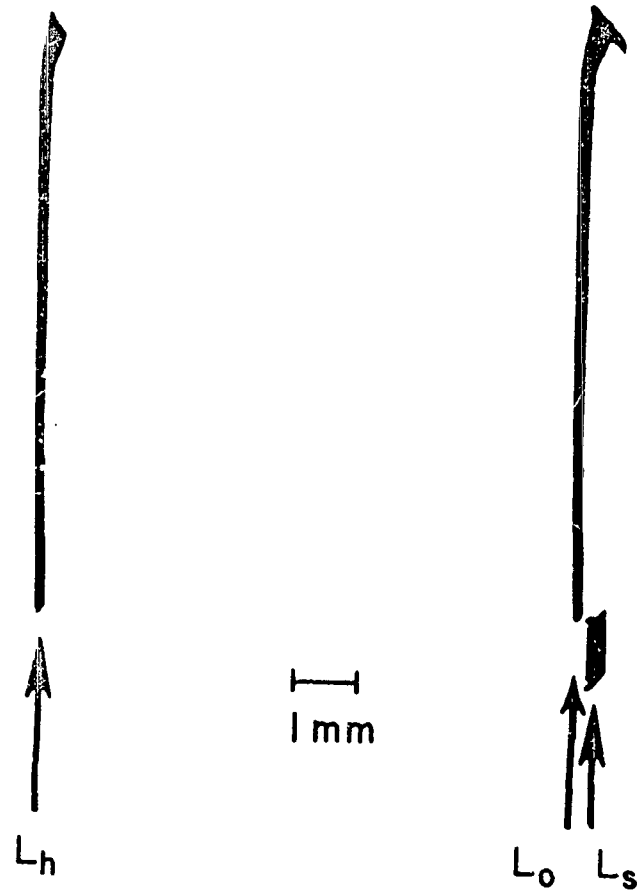

FIGURE 4 PHOTOGRAPH OF NUCLEAR PLATE USED TO DETERMINE THE THICKNESS OF COPPER CRYSTAL #028301

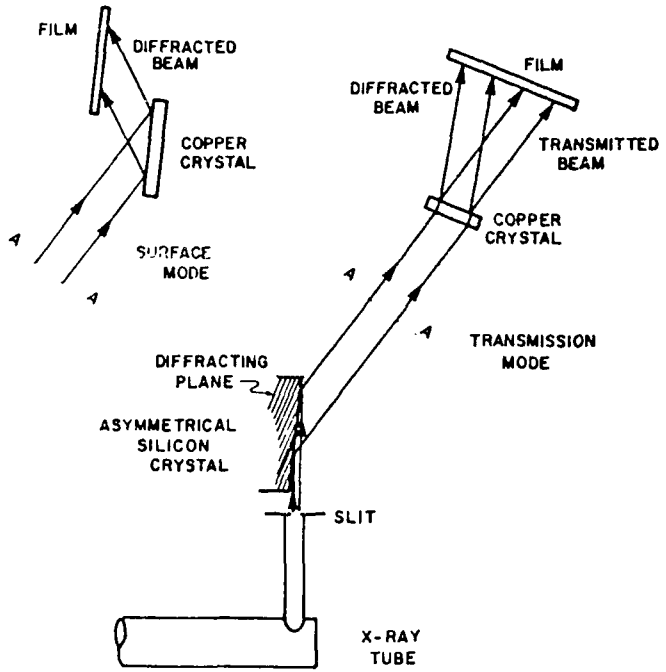

FIGURE 5 SCHEMATIC DIAGRAM OF THE ASYMMETRICAL TOPOGRAPHIC CAMERA ILLUSTRATING BOTH THE SURFACE REFLECTION AND TRANSMISSION MODE

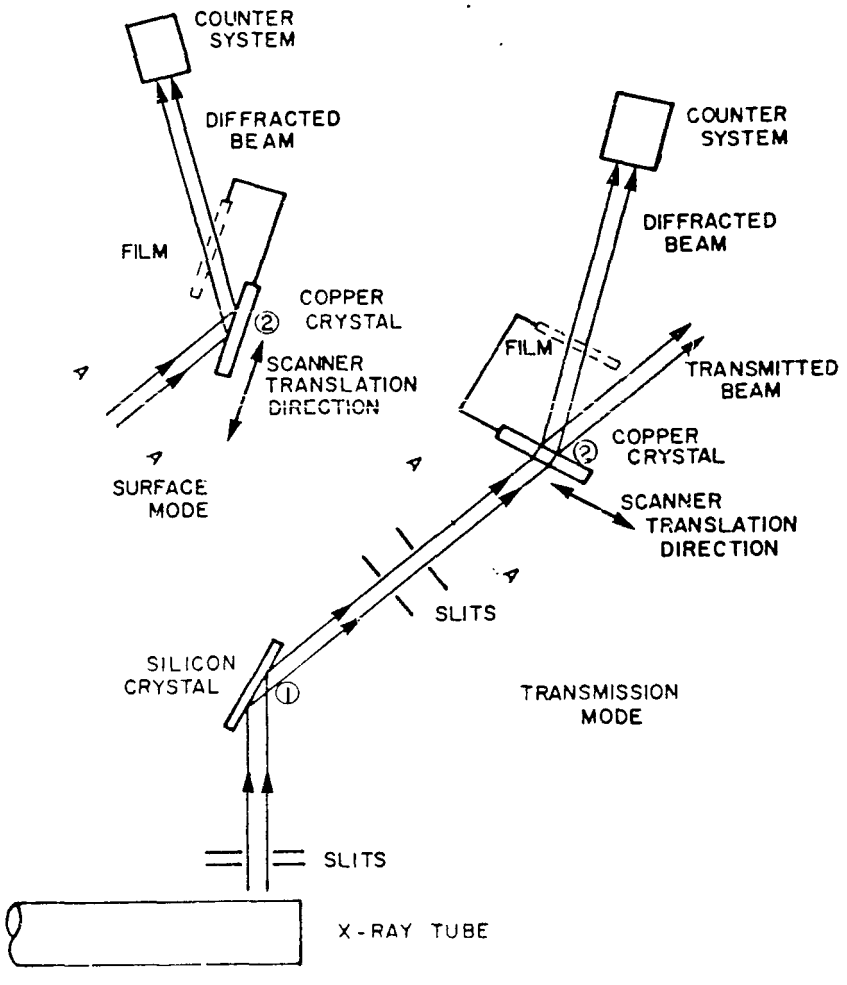

FIGURE 6 SCHEMATIC DIAGRAM OF THE HIGH RESOLUTION DOUBLE CRYSTAL SPECTROMETER WITH SCANNING CAPABILITY ILLUSTRATING BOTH THE SURFACE REFLECTION AND TRANSMISSION MODE.

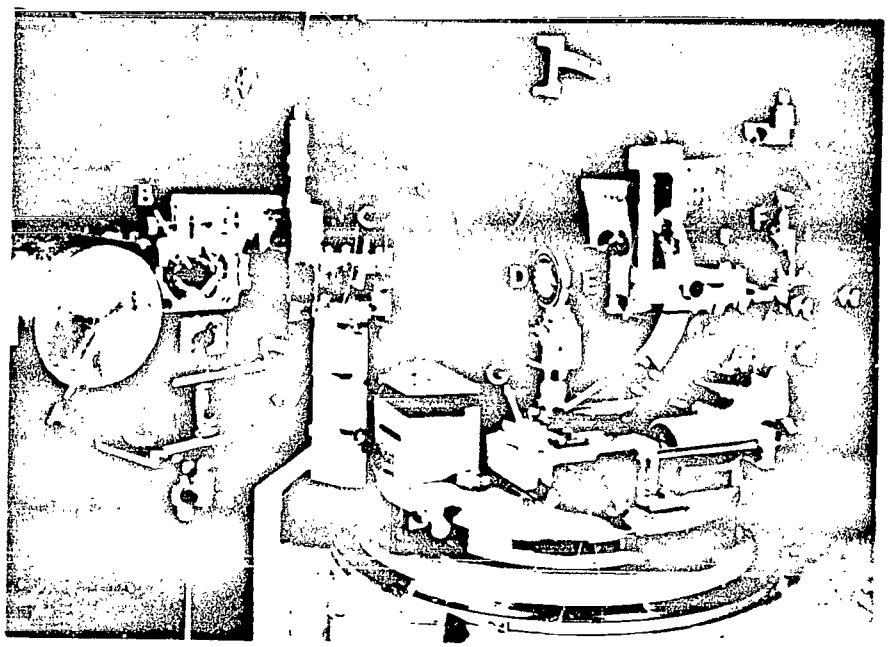

FIGURE 7 PHOTOGRAPH OF HIGH RESOLUTION DOUBLE CRYSTAL SPECTROMETER WITH SCANNING STAGE

A - X-RAY TUBE
B - 1ST CRYSTAL, SILICON, SHOWN IN REFLECTION GEOMETRY
C - SLIT SYSTEM
D - 2ND CRYSTAL, COPPER SAMPLE CRYSTAL SHOWN IN TRANSMISSION GEOMETRY
E - NUCLEAR PLATE
F - COUNTER SYSTEM
G - SCANNER STAGE

NOT SHOWN FOR CLARITY IS ADJUSTABLE SLIT SYSTEM BETWEEN D AND E WHICH STOPS DIRECT AND TRANSMITTED X-RAY BEAMS FROM REACHING FILM.

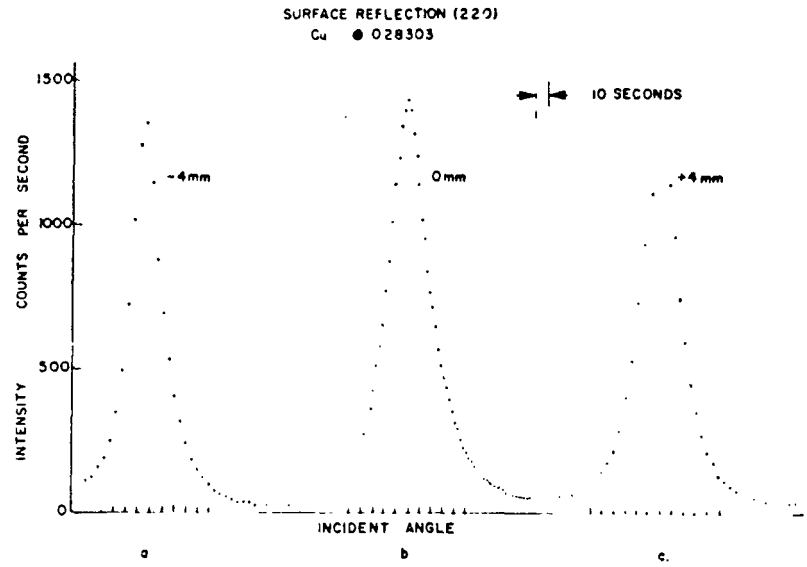

FIGURE 8 DIFFRACTION ROCKING CURVES TAKEN IN THE SURFACE REFLECTION GEOMETRY FOR COPPER CRYSTAL #028303 AT THREE DIFFERENT LOCATIONS ON THE CRYSTAL.

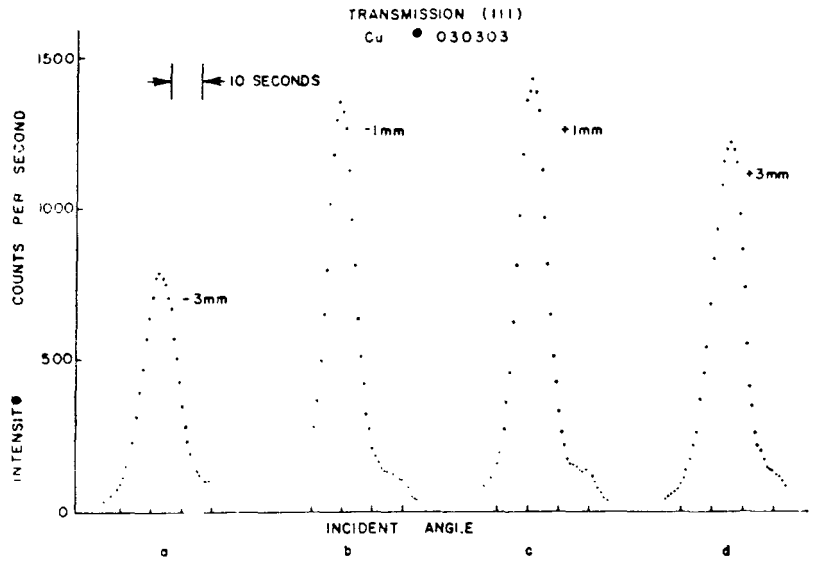

FIGURE 9 DIFFRACTION ROCKING CURVES TAKEN IN THE TRANSMISSION GEOMETRY FOR COPPER CRYSTAL #030303 AT FOUR DIFFERENT LOCATIONS ON THE CRYSTAL.

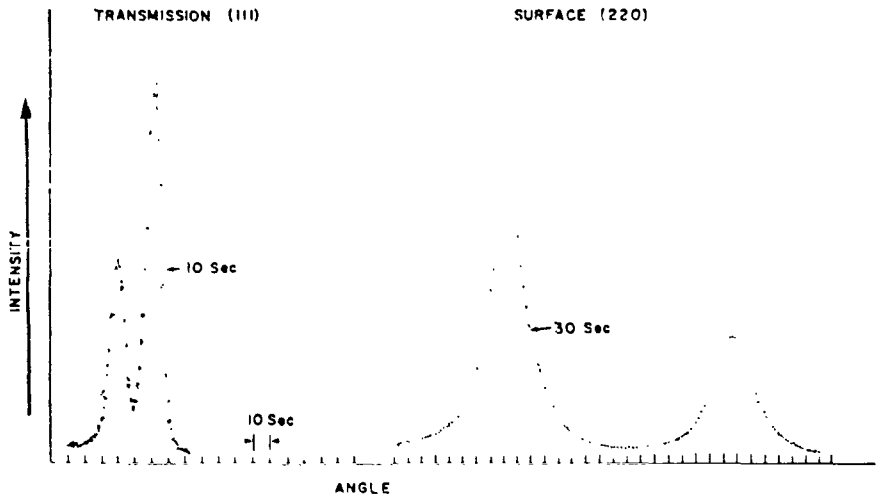

FIGURE 10 DIFFRACTION ROCKING CURVE TAKEN IN BOTH THE SURFACE REFLECTION AND TRANSMISSION GEOMETRY FOR COPPER CRYSTAL #026302 AT ONE LOCATION. FOR THIS ALIGHMENT, BOTH THE COPPER $K\alpha_1$ AND $K\alpha_2$ COMPONENTS ARE PRESENT WITH THE SMALLER PEAK DUE TO THE $K\alpha_2$ COMPONENT.

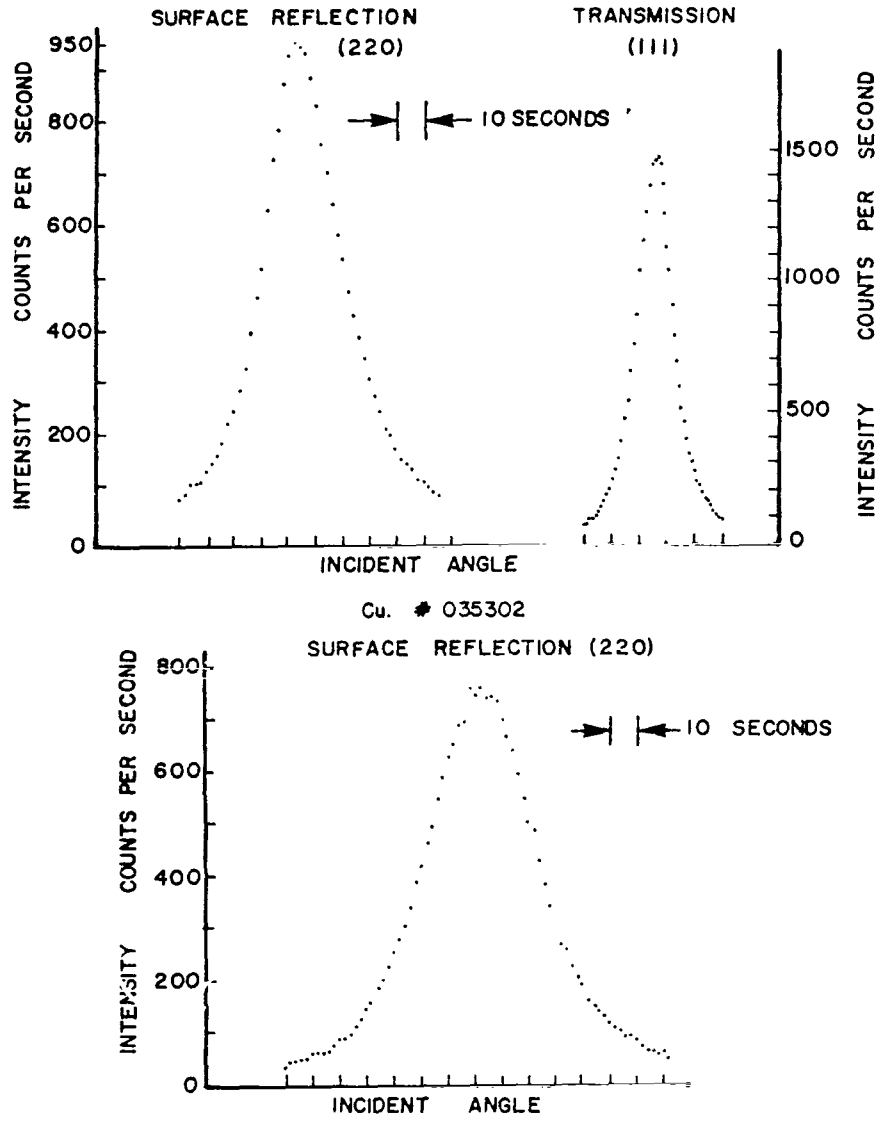

FIGURE 11 DIFFRACTION ROCKING CURVES TAKEN FROM A TYPICALLY GOOD COPPER CRYSTAL (#037303) IN BOTH SURFACE REFLECTION AND TRANSMISSION GEOMETRY AND A TYPICALLY POOR COPPER CRYSTAL (#035302) IN SURFACE REFLECTION.

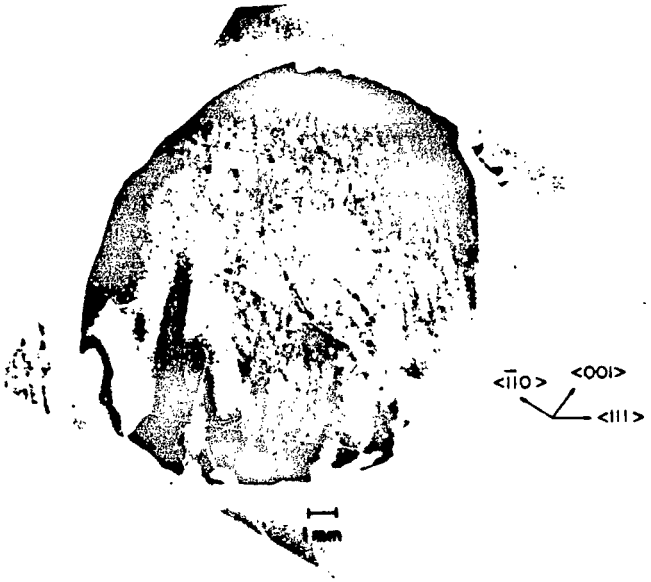

FIGURE 12A ATC X-RAY TOPOGRAPHS OF AS-GROWN COPPER CRYSTAL #028303, GROWTH CONDITION III; (220) SURFACE REFLECTION COMPOSITION TOPOGRAPH

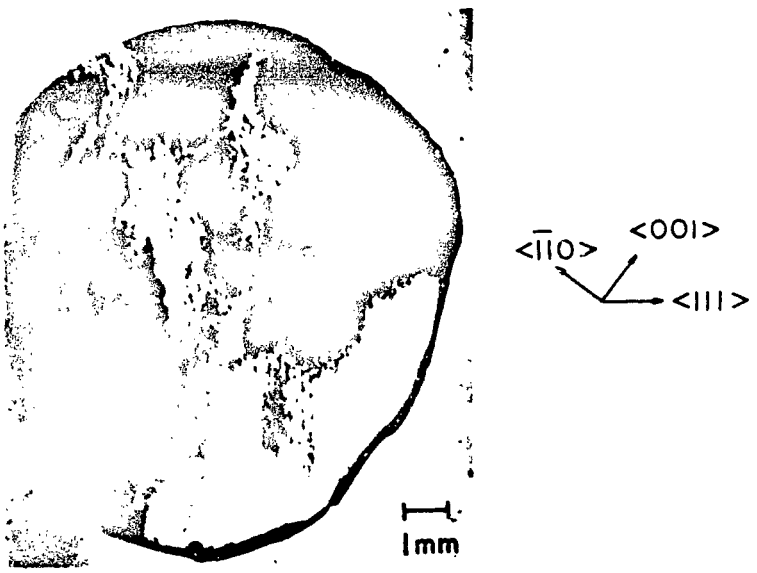

FIGURE 12B ATC X-RAY TOPOGRAPHS OF AS-GROWN COPPER CRYSTAL #028303, GROWTH CONDITION III; (111) TRANSMISSION TOPOGRAPH

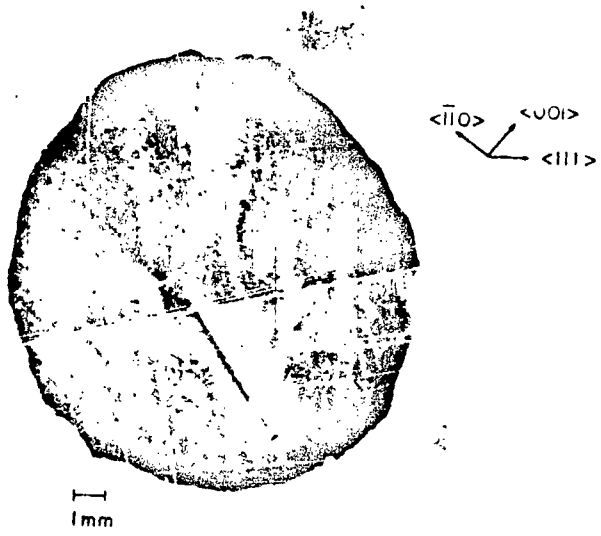

FIGURE 13A ATC X-RAY TOPOGRAPHS OF AS-GROWN COPPER CRYSTAL #037303, GROWTH CONDITION III; (220) SURFACE REFLECTION COMPOSITE TOPOGRAPH

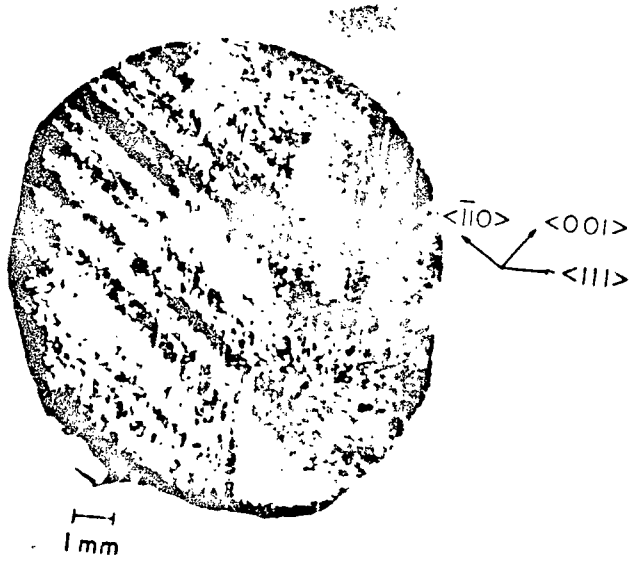

FIGURE 13B ATC X-RAY TOPOGRAPHS OF AS-GROWN COPPER CRYSTAL #037303, GROWTH CONDITION III; (111) TRANSMISSION TOPOGRAPH

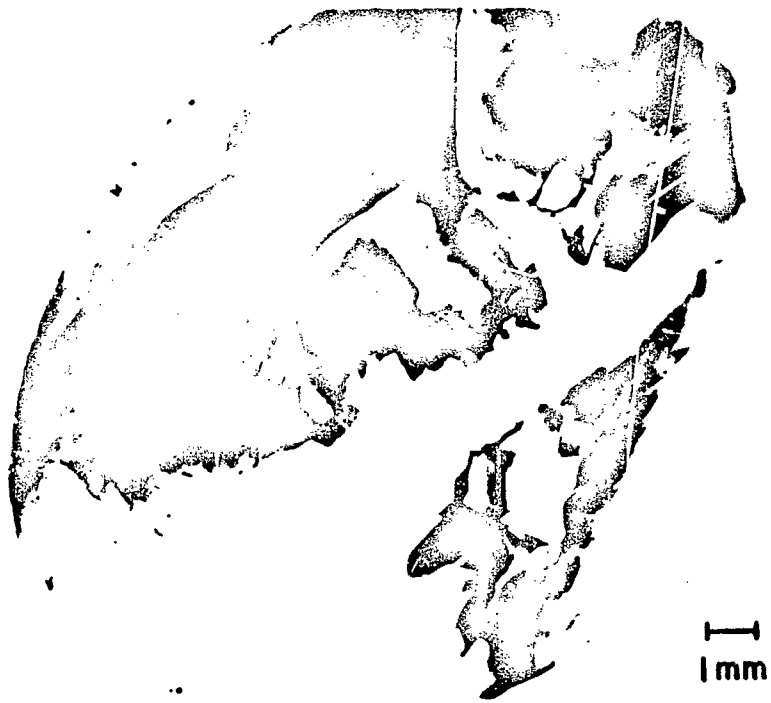

FIGURE 14A ATC X-RAY TOPOGRAPHS OF COPPER CRYSTALS GROWN UNDER GROWTH CONDITION V; (220) SURFACE REFLECTION COMPOSITE TOPOGRAPH OF AS-GROWN COPPER CRYSTAL #034303

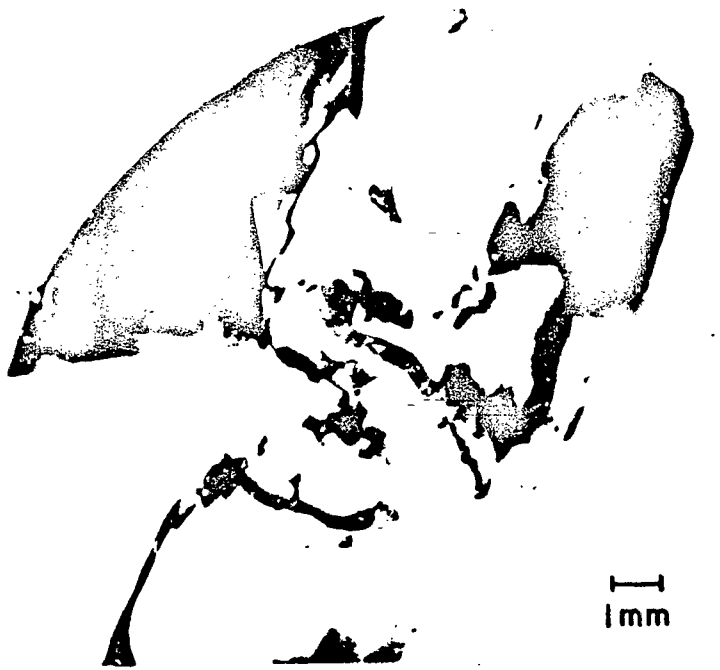

FIGURE 14B ATC X-RAY TOPOGRAPHS OF COPPER CRYSTALS GROWN UNDER GROWTH CONDITION V; (220) SURFACE REFLECTION COMPOSITE TOPOGRAPH OF ANNEALED COPPER CRYSTAL #034301

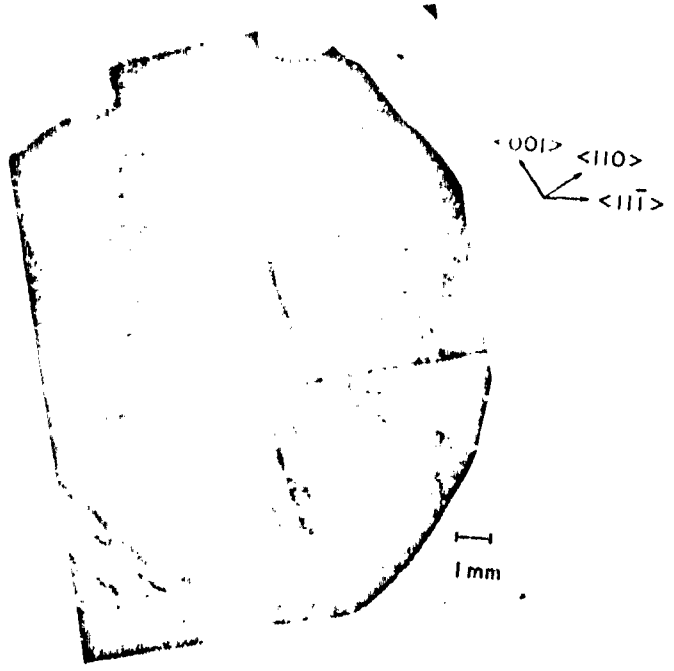

FIGURE 15A ATC X-RAYTTOPOGRAPHS OF ANNEALED COPPER CRYSTAL #025302, GROWTH CONDITION 1; (220) SURFACE REFLECTION COMPOSITE TOPOGRAPH

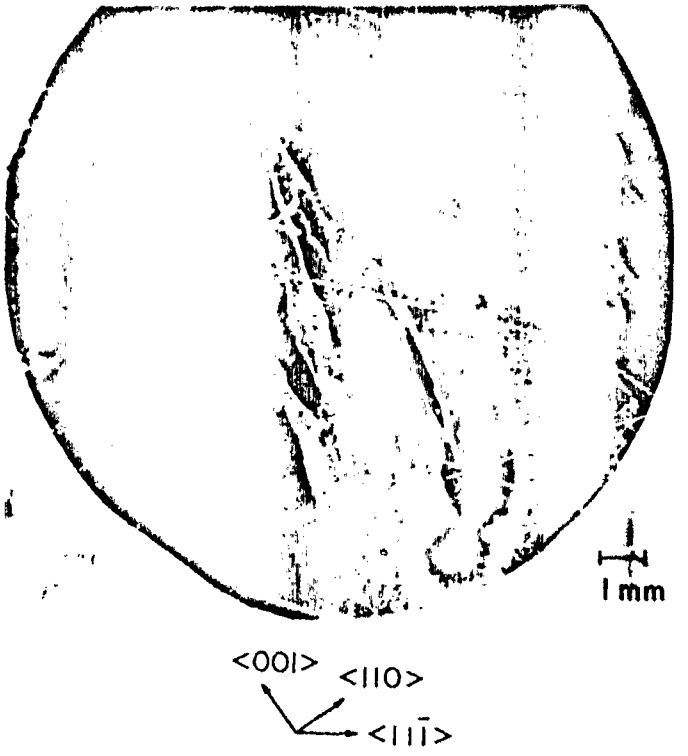

FIGURE 15B ATC X-RAY TOPOGRAPHS OF ANNEALED COPPER CRYSTAL #025302, GROWTH CONDITION 1; (111) TRANSMISSION COMPOSITE TOPOGRAPH

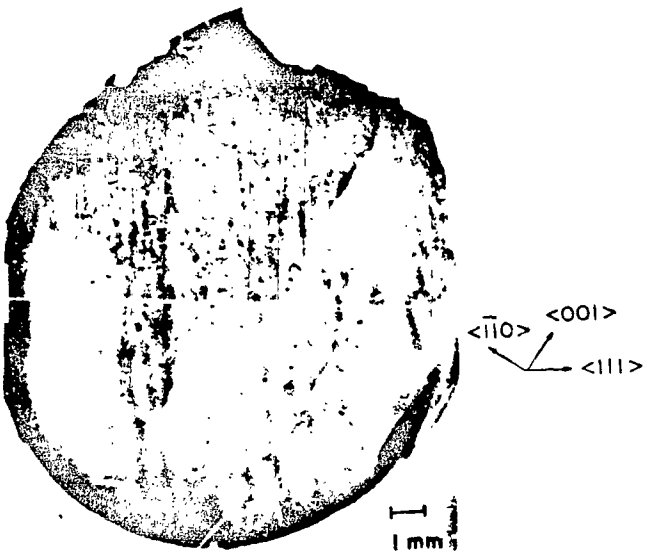

FIGURE 16A ATC X-RAY TOPOGRAPHS OF ANNEALED COPPER CRYSTAL #030303, GROWTH CONDITION III; (220) SURFACE REFLECTION COMPOSITE TOPOGRAPH

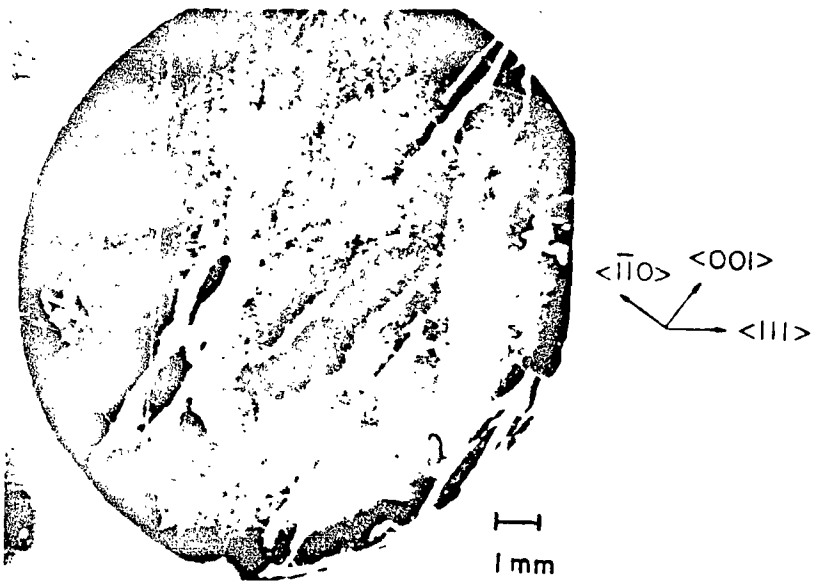

FIGURE 16B ATC X-RAY TOPOGRAPHS OF ANNEALED COPPER CRYSTAL #030303, GROWTH CONDITION III; (111) TRANSMISSION COMPOSITE TOPOGRAPH

FIGURE 17A SCANNING SPECTROMETER TOPOGRAPH OF ANNEALED COPPER CRYSTAL #025302; (220) SURFACE REFLECTION COMPOSITE TOPOGRAPH

FIGURE 17B SCANNING SPECTROMETER TOPOGRAPH OF ANNEALED COPPER CRYSTAL #025302; (111) TRANSMISSION COMPOSITE TOPOGRAPH

FIGURE 18A ENLARGED REGIONS OF SCANNER TOPOGRAPHS; HIGHLY PERFECT REGION

FIGURE 18B ENLARGED REGIONS OF SCANNER TOPOGRAPHS; INTERMEDIATE REGION

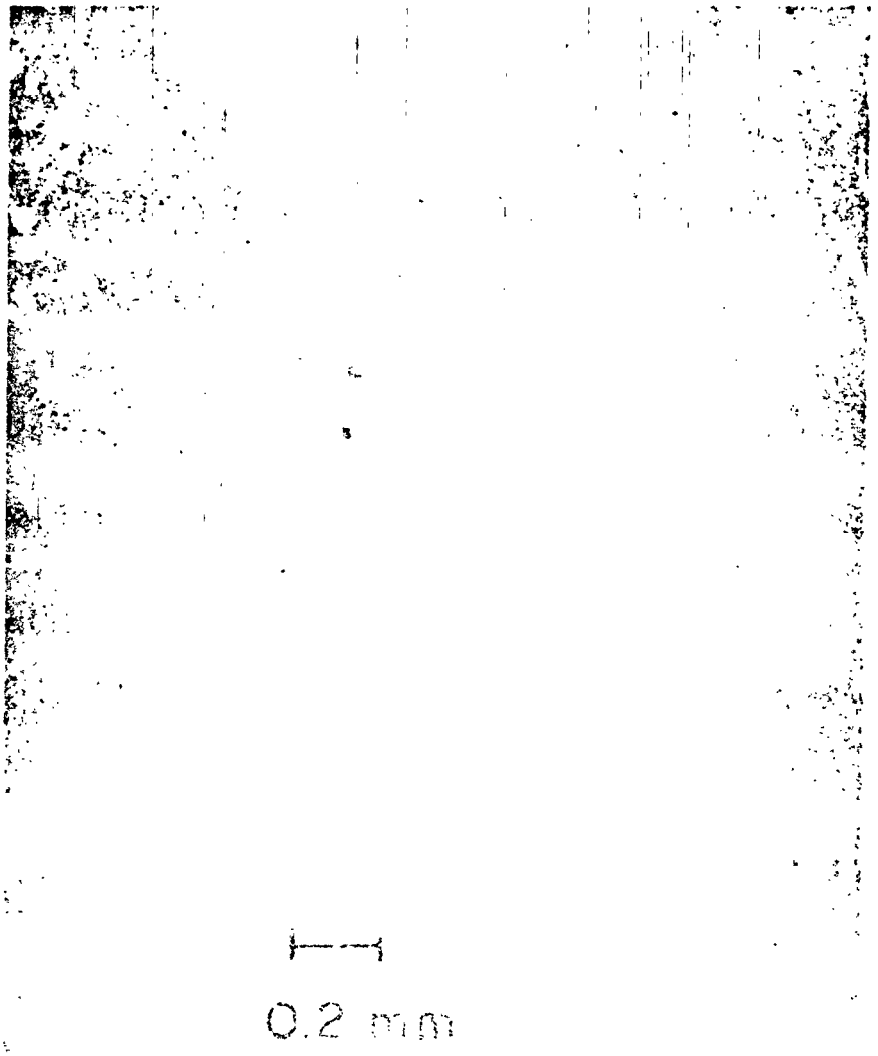

FIGURE 1-[illegible] TOPOGRAPHS;

Task 2 (Acct. No. 179-11-22-01)

EVAPORATIVE PREPARATION OF ULTRAHIGH PURITY MATERIAL*

By

R. C. Paule, J. G. Early and W. J. Boettinger
Institute for Materials Research,
National Bureau of Standards
Washington, D. C. 20234

SUMMARY

A calculational procedure involving the use of complex chemical equilibria has been developed to describe the purification of refractory materials in space. High temperature evaporative purification of refractories is considered under vacuum conditions and under conditions of very low oxidizing or reducing ambient pressures. The calculations show that extensive purification can be obtained and that very low oxidizing or reducing ambient pressures can be used to control the rates of purification. This method could also be used to allow the production of doped materials to pre-selected levels.

Consideration is given to the assumptions affecting the purification calculations, and an experimental program is being developed to check the calculated results. This program involves mass spectrometric measurements on a sessile drop of molten Al_2O_3.

Levitation experiments using R.F. suspension and heating techniques in vacuum have been started on a number of metals including titanium and zirconium.

INTRODUCTION

Hot containers used in the production and purification of refractory materials are themselves a common source of contamination. Space with its zero gravity, high vacuum conditions offers an opportunity for containerless purification of refractories. The heating and distilling out of impurities is a natural means of purification. Evaporative purification of refractories normally involves many complex equilbria since numerous minor impurities are present and since the high temperatures involved allow many "side" reactions. The general formalism for the calculation of complex equilibria has been modified and adapted to describe evaporative purification. Four classes of problems have been investigated. The evaporating gases are described under conditions of (1) constant pressure, (2) constant volume, (3) vacuum, and (4) vacuum but with a low oxidizing or reducing ambient pressure. The latter two conditions (3 and 4) are of particular interest to this project since they allow for greatest isolation of sample and least chance of container contamination.

*Paper presented by R. L. Parker.

CALCULATIONS

There is much work in the literature dealing with the calculation of complex equilibria[1-7]. Available calculations and computer programs, however, do not deal with the problem at hand and would have required extensive modifications. We, therefore, developed our own equations and computer programs. Modifications and adaptations were made to Kandiner and Brinkley's[1] general formalism for the calculation of complex equilibria. Some basic changes were required to properly describe evaporation into vacuum.

The general formalism for the calculations is not particularly difficult, but the actual calculations do get involved and do require the aid of a computer. The calculations, in general terms, can be described as follows:

> One needs to determine the number of moles of all chemical species in a system during purification and to determine the distribution of moles between the condensed phase and the evaporating (gas) phase. For the sake of simplicity one wants to work with the minimum information needed to fully describe the system. This is equivalent to determining a set of independent chemical species. All chemical species are thereby separated into two groups: independent components and dependent constituents. The solution to our problem then deals primarily with the determination of the amount of each independent component. Independent mass balance equations are written for each component. These equations do not directly involve any dependent constituents, and the Newton-Raphson iteration method[8,9] is used to simultaneously solve the mass balance equations.
>
> The dependent constituents are determined from equilibrium constant relationships which only involve the activities and pressures of the independent components. Ideal solution properties are used to describe the condensed phase activities and, for the vacuum evaporation case, the Knudsen equation is used to describe the pressures in terms of the number of moles. A series of sequential solutions are obtained for fixed evaporation times with the condensed phase results from each mathematical solution being used as input feed data in the following problem. It is thus possible to sequentially follow the evaporative purification of a material.

The above general calculational approach is very general and allows for relatively easy and direct modifications to describe a variety of situations of practical interest. A manuscript describing the calculations and examples of their use has been written and NBS approved, and will be submitted for publication.

RESULTS

Our calculations show that good evaporative purification of refractories in vacuum can be obtained, and that the introduction of a low oxidizing or reducing ambient pressure can be used to control rates of vaporization.

Table 1 shows the results for calculations of Al_2O_3 evaporative purification in vacuum at 2400 K, where 10 ppm (mole basis) FeO and SiO_2 impurities are initially present. Row 3 of the table shows that the rate of Al_2O_3 loss is very low, while rows 4 and 5 show that FeO and SiO_2 are rapidly lost from the melt. The FeO and SiO_2 concentrations are approximately halved over a period of only 1.15 seconds. The remaining 12 species in the table, under the heading "Moles of Species Present," represent the moles of gases vaporized during each time interval (0-0.005 seconds, 0.005-0.28 seconds, 0.28-0.46 seconds, etc.). Finally the instantaneous pressures of all species are reported at the bottom of the table. It is evident that the calculations yield considerable information. The computer results, as indicated by this table, are automatically obtained from the solution of each problem.

Calculations showing very high rates of purification (as above) may not be completely accurate in describing the evaporative process. High rates of purification can result in a depletion of impurities at the surface and a concentration gradient can occur. The calculations assume a completely mixed, homogeneous melt. Numerous processes, however, can occur to minimize the concentration gradient. Task 6 (Surface Traction and Other Surface Phenomena), being carried out by A. L. Dragoo, is looking into some of these processes. A general view of the problem would seem to minimize concern regarding surface depletion and concentration gradients since practical purification times can be of the order of 10 minutes rather that the above 0-1.15 seconds. Mixing processes can occur during these longer time periods. Further investigations into this possible problem area are still needed.

Purification rates can be slowed to allow better mixing, or to better control the evaporation process. One should not overlook the possibility of controlled low level doping of materials to pre-selected levels. Slower purification of Al_2O_3 can be obtained by exposing the melt to a low ambient oxygen pressure. Such a pressure can be kept low enough to maintain vacuum (Knudsen) flow conditions and yet be high enough to shift chemical equilibria and slow the vaporization rates. Tables 2 and 3 list results for the evaporative purification of Al_2O_3 containing 10 ppm CaO. Table 2 is for the "pure" vacuum case and Table 3 is for a "vacuum" containing 10^{-5} atm oxygen. The higher oxygen pressures shown in Table 3 result in equilibrium shifts away from the reduced vapor species Ca(g) [$Ca(g)+O(g) \rightarrow CaO(l)$] and this causes slower rates of purification. Figure 1 shows the rate of CaO removal both for the case of "self-developed" oxygen (Table 2) and for the case of P_O equal to 10^{-15} atm (Table 3).

It is clear that many modifications in oxidizing or reducing conditions can be used to achieve desired vaporization (purification) goals.

Some results from this Task and from Task 6 were presented as a talk at the 12th Aerospace Sciences Meeting of the AIAA held January 30 - February 1, 1974 in Washington, D.C. This talk by A. L. Dragoo and R. C. Paule was entitled "Production of Ultrapure Materials: Containerless Evaporation and the Roles of Diffusion and Maragoni Convection."

DISCUSSION

In using the above calculated results one must ask: "How accurate are the calculations?" One can partially answer this question by noting that if the calculational assumptions are correct, then the calculations should be accurate. It appears that we should be able to pick purification conditions of practical interest that will satisfy the assumptions. In general, the method of evaporative purification should be feasible. We must, however, still pick optimum conditions and be able to predict the extent of purification.

Some questions that need to be considered in the evaluation of the accuracy of the calculations are as follows:

Are there significant vapor species other than those used in the calculations?

Are the literature values of the thermodynamic equilibrium constants correct?

Is ideal solution behavior observed? (Because of the low impurity levels considered we would expect Henry's law to be obeyed, but this does not insure that the impurities will obey Raoult's law.)

Is there adequate mixing of the melt to avoid surface depletion and concentration gradients?

Are the evaporation coefficients equal to unity or near unity?

We are now engaged in an experimental program to get an overall check on these and other possible problem areas. We plan to directly observe evaporative purification from Al_2O_3 samples and to be able to check the calculations. If necessary, correction factors could be developed to describe any non-ideal behavior.

CURRENT AND FUTURE EXPERIMENTS

Our current work is in preparation for the experimental measurement of impurity vaporization from Al_2O_3 using the TOF mass spectrometer. Work is centered on improving usable M.S. sensitivity, and on improving quantitative M.S. measurements. A molecular beam chopping system has

been built and a lock-in amplifier added to the system to allow modulated beam detection of species coming from a sessile drop of molten Al_2O_3. Lock-in detection will be particularly important for measuring evaporating species such as O_1 and O_2 since these species are normally present in the M.S. background. The modulated beam system is now operational.

A new calibrated He and Xe leak system has been installed in our M.S. to improve reproducibility. Scales have been added to several instrument potentiometers for better reproducibility. New, more linear electron multiplier strips have been installed on the M.S.

A considerable effort has been devoted to minimizing the M.S. background to increase the usable sensitivity. In addition to extensive leak-checking, we have found it necessary to water cool the walls of the furnace to avoid excessive outgassing. A new smaller water-cooled furnace with a lower heat load is now being built and will replace our current furnace for the heating of the Al_2O_3.

M.S. measurements will be made on evaporating molten Al_2O_3 to determine any non-ideal behavior. This type of experiment should allow for an overall check of the calculations and, if necessary, for the development of correction factors. Other refractory materials may also be tested.

In order to verify the predicted rate of purification and efficiency of purification, containerless purification experiments by levitation melting can be performed on earth using metals. The recent literature reveals that the biggest problem of current levitation techniques is that only one control function is available for controlling levitating force and heat input and thus in general these variables cannot be controlled independently. In order to maintain long time levitation of metals at a selected temperature to allow differential evaporation into a vacuum, one alternative is to levitate without heating using low frequency power and have a separate method of heating the metal and achieving thermal equilibrium.

Some preliminary experiments were carried out in a commercial levitation melting apparatus. Coils of standard cone design were used with a 450 KHz RF power supply in both vacuum and inert gas environments. A variety of metal samples weighing between 5 and 15 grams have been levitated for short periods of time and most have been successfully melted. The samples have included titanium, copper, vanadium, aluminum, chromium, yttrium and zirconium. Initial efforts to control the stability and the temperature of the levitated metal especially in the vacuum environment through the use of the power knob on the RF unit have not been successful with the exception of aluminum where the presence of the oxide skin appears to play a stabilizing role.

Several modifications were made on the levitation unit to improve efficiency and increase the power delivered at the coil. Experiments are underway to investigate the behavior of smaller sized samples of the previously levitated metals.

A levitation coil was designed which greatly improved the lateral stability of the levitated melt. This enabled a pyrometric determination of the temperature. Experiments have been conducted which generally confirm the theoretical predictions of several papers on the effects of sample size, resistivity, density, and coil current. Plans are being made to try to levitate metals with a lower frequency R.F. generator (10 kHz). The use of a He atmosphere enabled the levitation of various metals at a constant (but uncontrollable) temperature for as long as 20 minutes. A literature survey on the evaporative purification of metal-gas systems has been started in order to choose a system for experiments which can be vacuum purified and which can be stably levitation melted.

We have been studying in detail mass spectrometric modulated beam operation and lock-in detection in order to design and build an improved quadrupole mass spectrometric modulated beam system. This will be used to measure impurity species evaporating from oxide samples. Appropriate observations of phase relationships of composite signals associated with modulated beams will allow the separation of information regarding the parent vapor species. In addition to identification of parent species, the relative amounts of each species can be determined.

REFERENCES

1. H.J. Kandiner and S.R. Brinkley, Ind. Eng. Chem., 42, 850 (1950).

2. W.B. White, S.M. Johnson and G.B. Dantzig, Chem. Phys., 28, 751 (1958).

3. S. Gordon and B.J. McBride, NASA, SP-273 (1971).

4. H.F. Feldmann, W.H. Simons and D. Bienstock, U.S. Bur. of Mines, RI-7257 (1969).

5. F.J. Zeleznik and S. Gordon, Ind. Eng. Chem., 60, 27 (1968).

6. F. Van Zeggeren and S.H. Storey, The Computation of Chemical Equilibria, Cambridge University Press, 1970.

7. M. Klein, Physical Chemistry, Vol. 1/Thermodynamics, Chapter 7, edited by Eyring, H.E, Jost, W., and Henderson, D., Academic Press, New York, 1971.

8. H. Margenau and G.M. Murphy, The Mathematics of Physics and Chemistry, 2nd. ed., page 492, D. Van Nostrand Company, Princeton, New Jersey, 1956.

9. F.E. Hildebrand, Advanced Calculus for Engineers, page 353, Prentice-Hall, New York, 1949.

Table 1

Vacuum Evaporation of Al_2O_3 + 10 ppm FeO and SiO_2

Moles of Species Present

Temperature (K)			2400		
Cuml. Time (Sec)	0.005	.28	.46	.81	1.15
Liquids					
Al_2O_3	1.0000E+00	1.0000E+00	1.0000E+00	9.9999E-01	9.9999E-01
FeO	9.9821E-06	9.0607E-06	8.5012E-06	7.4910E-06	6.6129E-06
SiO_2	9.9667E-06	8.3538E-06	7.4416E-06	5.9152E-06	4.7170E-06
Gases					
O	1.8199E-07	6.2370E-06	6.3661E-06	6.0993E-06	5.8593E-06
O_2	6.1007E-09	2.0593E-07	2.0833E-07	1.9652E-07	1.8638E-07
Al	8.9146E-08	3.1734E-06	3.3121E-06	3.2990E-06	3.2725E-06
AlO	1.2000E-08	4.2074E-07	4.3523E-07	4.2682E-07	4.1799E-07
AlO_2	6.6628E-10	2.3009E-08	2.3590E-08	2.2778E-08	2.2022E-08
Al_2O	1.8579E-09	6.6641E-08	6.9864E-08	7.0130E-08	7.0015E-08
Al_2O_2	1.0292E-11	3.6359E-10	3.7780E-10	3.7339E-10	3.6802E-10
Fe	1.7815E-08	5.7128E-07	5.5694E-07	4.8504E-07	4.2203E-07
FeO	8.2998E-11	2.6215E-09	2.5330E-09	2.1720E-09	1.8657E-09
Si	2.2587E-13	6.7909E-12	6.3420E-12	5.0603E-12	4.0287E-12
SiO	3.3262E-08	9.8495E-07	9.1167E-07	7.1622E-07	5.6293E-07
SiO_2	2.0138E-11	5.8734E-10	5.3881E-10	4.1677E-10	3.2340E-10

Pressure of Species Present (Atm)

Gases					
O	3.5140E-06	3.4610E-06	3.4303E-06	3.3774E-06	3.3343E-06
O_2	1.6659E-07	1.6161E-07	1.5875E-07	1.5389E-07	1.5000E-07
Al	2.2352E-06	2.2867E-06	2.3175E-06	2.3721E-06	2.4182E-06
AlO	3.7976E-07	3.8265E-07	3.8437E-07	3.8736E-07	3.8986E-07
AlO_2	2.4700E-08	2.4514E-08	2.4405E-08	2.4216E-08	2.4061E-08
Al_2O	7.5013E-08	7.7327E-08	7.8718E-08	8.1202E-08	8.3313E-08
Al_2O_2	4.6061E-10	4.6766E-10	4.7185E-10	4.7923E-10	4.8542E-10
Fe	6.4267E-07	5.9228E-07	5.6068E-07	5.0180E-07	4.4870E-07
FeO	3.3961E-09	3.0826E-09	2.8923E-09	2.5486E-09	2.2499E-09
Si	5.7788E-12	4.9931E-12	4.5279E-12	3.7127E-12	3.0377E-12
SiO	1.0661E-06	9.0729E-07	8.1546E-07	6.5834E-07	5.3178E-07
SiO_2	7.5356E-10	6.3161E-10	5.6264E-10	4.4724E-10	3.5665E-10

Table 2

Vacuum Evaporation of Al_2O_3 + 10 ppm CaO

Moles of Species Present

Temperature (K)			2400	
Cuml. Time (Sec)	0.005	20.00	40.00	60.00
Liquids				
Al_2O_3	1.0000E+00	9.9975E-01	9.9950E-01	9.9925E-01
CaO	9.9998E-06	9.2986E-06	8.6465E-06	8.0401E-06
Gases				
O	1.6143E-07	6.4560E-04	6.4548E-04	6.4535E-04
O_2	4.8005E-09	1.9197E-05	1.9193E-05	1.9189E-05
Ca	1.8850E-10	7.0120E-07	6.5210E-07	6.0643E-07
Al	1.0670E-07	4.2676E-04	4.2671E-04	4.2665E-04
AlO	1.2741E-08	5.0957E-05	5.0949E-05	5.0941E-05
AlO_2	6.2753E-10	2.5097E-06	2.5092E-06	2.5088E-06
Al_2O	2.3611E-09	9.4435E-06	9.4424E-06	9.4413E-06
Al_2O_2	1.1602E-11	4.6402E-08	4.6396E-08	4.6389E-08

Pressure of Species Present (Atm)

Gases				
O	3.1171E-06	3.1170E-06	3.1169E-06	3.1168E-06
O_2	1.3109E-07	1.3108E-07	1.3107E-07	1.3106E-07
Ca	5.7606E-09	5.3581E-09	4.9838E-09	4.6355E-09
Al	2.6754E-06	2.6756E-06	2.6757E-06	2.6758E-06
AlO	4.0321E-07	4.0322E-07	4.0323E-07	4.0323E-07
AlO_2	2.3264E-08	2.3264E-08	2.3263E-08	2.3263E-08
Al_2O	9.5332E-08	9.5338E-08	9.5343E-08	9.5348E-08
Al_2O_2	5.1926E-10	5.1927E-10	5.1929E-10	5.1930E-10

Table 3

Evaporation of Al_2O_3 + 10 ppm CaO, Vacuum + 10^{-5} Atm Oxygen

Moles of Species Present

Temperature (K)			2400	
Cuml. Time (Sec)	0.005	60.00	120.00	180.00
Liquids				
Al_2O_3	1.0000E+00	9.9984E-01	9.9967E-01	9.9951E-01
CaO	9.9999E-06	9.3413E-06	8.7259E-06	8.1511E-06
Gases				
Ca	5.8757E-11	6.5868E-07	6.1532E-07	5.7482E-07
Al	1.8569E-08	2.2281E-04	2.2278E-04	2.2276E-04
AlO	7.1134E-09	8.5352E-05	8.5343E-05	8.5333E-05
AlO_2	1.1240E-09	1.3486E-05	1.3485E-05	1.3483E-05
Al_2O	2.2941E-10	2.7526E-06	2.7523E-06	2.7520E-06
Al_2O_2	3.6165E-12	4.3393E-08	4.3388E-08	4.3384E-08

Pressure of Species Present (Atm)

Gases				
O	1.0000E-05	1.0000E-05	1.0000E-05	1.0000E-05
O_2	1.3491E-06	1.3491E-06	1.3491E-06	1.3491E-06
Ca	1.7956E-09	1.6776E-09	1.5674E-09	1.4644E-09
Al	4.6560E-07	4.6560E-07	4.6560E-07	4.6560E-07
AlO	2.2512E-07	2.2512E-07	2.2512E-07	2.2512E-07
AlO_2	4.1669E-08	4.1669E-08	4.1669E-08	4.1669E-08
Al_2O	9.2626E-09	9.2626E-09	9.2626E-09	9.2626E-09
Al_2O_2	1.6186E-10	1.6186E-10	1.6186E-10	1.6186E-10

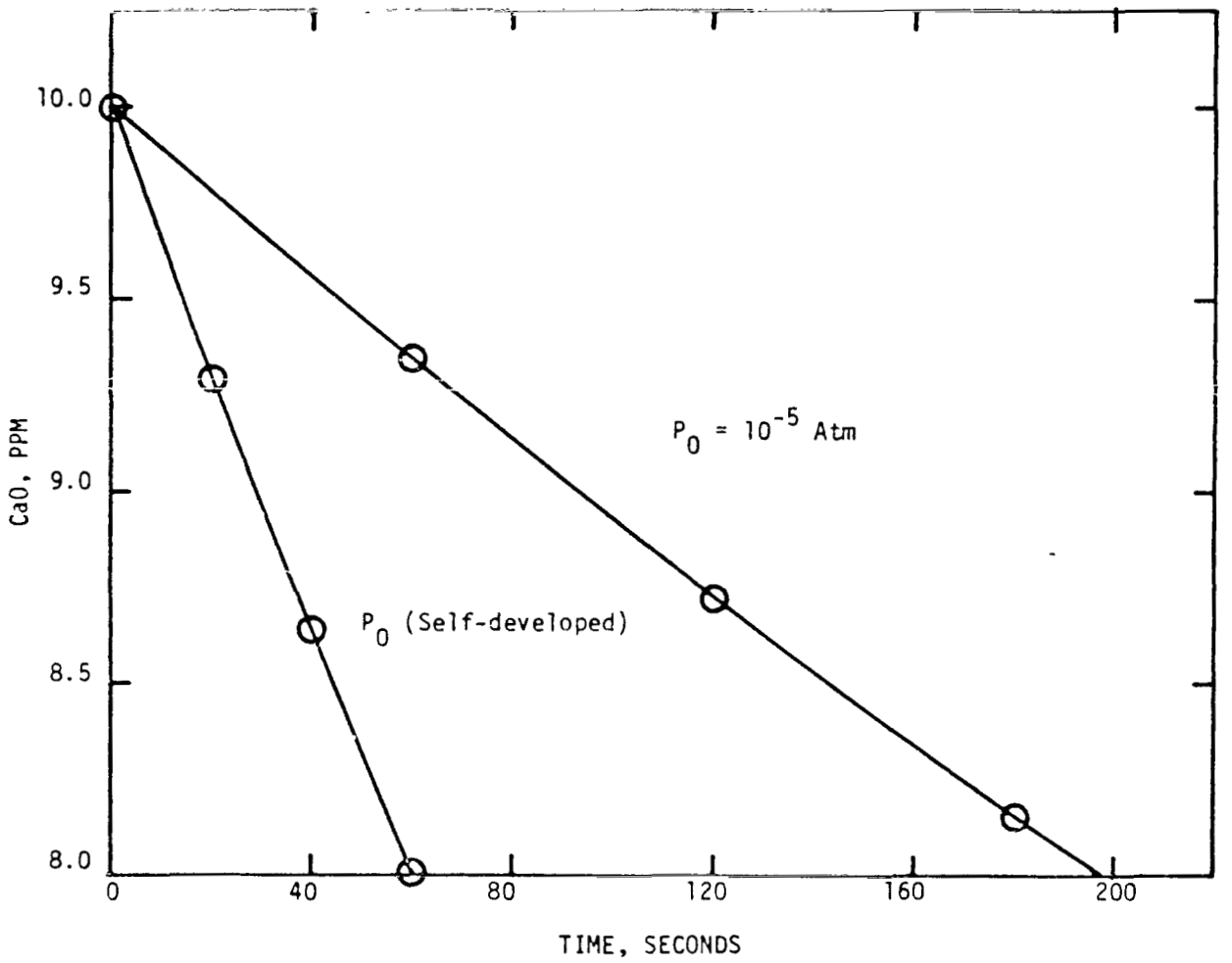

FIGURE 1. CaO VAPORIZATION FROM Al_2O_3 AT 2400 K.

Task 3 (Acct. No. 179-11-31-03)

VACUUM EFFECTS IN THE PREPARATION OF COMPOSITE MATERIALS *

By

H. Yakowitz and D. E. Newbury
Institute for Materials Research,
National Bureau of Standards
Washington, D. C. 20234

SUMMARY

Useful composites usually have strong continuous bonds between matrix and core. Improved bonding might be obtained by improving the final vacuum under which the composite is prepared so as to remove most adsorbed gases from the matrix-core interface. Good bonding can be expected when strains between matrix and core are minimal and coherent. Hence, this exploratory phase of the study was largely devoted to obtaining a means to study the bond both microscopically and with regard to determining strains at or near the bond. For this purpose, the scanning electron microscope was chosen as the primary tool. A means to use electron channelling patterns prepared in the scanning electron microscope to obtain strain data was formulated. The effect of strain, surface coatings and specimen tilt with respect to the primary electron beam was studied. Divergent beam x-ray microdiffraction patterns were also prepared in the scanning electron microscope as a means to obtain strain data at the micrometer level of spatial resolution.

A number of composite test specimens have been received through Marshall from General Dynamics and are currently undergoing SEM examination.

INTRODUCTION

Composite materials are well known entities. Such materials have been used for a long time in an effort to obtain improved material characteristics through combining disimilar constituents such as soft matrices with very hard cores. One of the keys to preparing useful composites is to obtain strong, continuous bonding between the matrix and core. One of the ways improved bonding might be obtained would be to improve the vacuum under which the final composite is prepared. In this case, more adsorbed gases can be removed and better bonding is possible.

The purpose of the work carried out in the first phase was to explore whether or not bonding could be studied by means of electron channelling patterns in the scanning electron microscope. In this first phase, only conventional materials were used in order to establish techniques. One of the main objectives was to correlate channelling patterns with divergent beam (Kossel) x-ray patterns in order to obtain quantitative stress-strain data from the channelling pattern. Such a procedure would allow mapping of the strain field in the vicinity of the matrix-core interface. The lower the strains, the better the bond.

*Paper presented by R. L. Parker.

Divergent Beam (Kossel) Microdiffraction

This method can provide quantitative information about the stress-strain configuration in a material. In particular, the Kossel internal stress-strain analysis yields for the sampled volume:

a. Average Cauchy strains

b. Principal strains and their axes

c. Principal stresses and their axes

d. Maximum shear strain in any (hkl) plane

e. Total stored elastic energy

f. Shear stored elastic energy

However, the time and effort needed to obtain a sufficient amount of data from a given material by the Kossel method is prohibitive[1]. Another problem is the large amount of data required to describe the results of a single point using the Kossel internal stress-strain analysis. More than one-hundred separate measurements are needed to completely describe the point. Hence, using the Kossel method alone represents a nearly impossible situation for carrying out a practical task. Therefore, another means of determining quantitative stress-strain relationships at the micrometer level of spatial resolution was sought for this task. The most appealing method is to use electron channelling patterns prepared with the aid of the scanning electron microscope. This is because the scanning electron microscope itself provides an ideal means to locate and examine regions of interest on the specimen, and electron channelling patterns can usually be obtained rapidly from the region of interest.

Scanning Electron Microscopy

In the scanning electron microscope, an electron beam of 1 to 50KV, having a small diameter, ranging from 100Å to 1μm, is scanned in a square raster on a specimen. The beam interacts with the specimen to produce ($\leq$50eV), x-rays and visible light which can be monitored continuously by appropriate detectors. The detector signal is used to control the brightness of the flying spot of a cathode ray tube (CRT) which is scanned in synchronism with the same raster as the specimen. A one-to-one correspondence is made to exist between points on the specimen and the image on the cathode ray tube. Thus, the micrograph is built up. The scanning electron microscope is useful for surface analysis because of (1) the high spatial resolution which can be achieved, (2) the large depth of focus - about 100 times greater than an optical microscope, and (3) the large variety of contrast mechanisms which result from beam-specimen interactions. For further details see Ref. [2].

Electron Channelling Patterns

Electron channelling contrast arises because electrons can penetrate crystals more easily along certain directions than others (Fig. 1). When the electrons are able to enter open passages (channels) in the crystal lattices, they penetrate deeply, and few escape. By slightly altering the angle the beam makes with the crystal, these channels become difficult to enter, and the electrons interact with the specimen nearer the surface so that more escape. An electron channelling pattern can be obtained by rocking the beam through a range of angles in the form of a cone.

Electron channelling patterns are capable of providing information about the orientation of the crystal as well as its perfection. To date, almost the only quantitative use of electron channelling patterns has been in orientation determination. This is because the relationships by which the state of perfection can be determined contain factors such as the so-called extinction length[3], which are not well known. For example, Schulson[4] has suggested the following:

$$2\omega_g = 2/(\xi_g|\vec{g}|) \tag{1}$$

where $2\omega_g$ is the channelling pattern line width in radians

ξ_g is the extinction distance for the reflection excited

$|\vec{g}|$ is the reciprocal lattice vector translation.

Now $|\vec{g}|$ is equivalent to 1/d where d is the interplanar spacing for a plane of Miller indices (hkl). It has been shown that if $\Delta d/d$ can be measured properly, then the entire stress-strain configuration for the sampled crystal volume can be determined[5].

The use of a few Kossel patterns in order to provide a basis for inferring the needed d values from channelling patterns may, therefore, be attractive. In such a case, one would require a well annealed crystal and the capability of simultaneously preparing the electron channelling pattern and the Kossel pattern in the scanning electron microscope. Accurate d values could be obtained from the Kossel pattern; the corresponding channelling pattern line widths, $2\omega_g$, can be measured. Changes due to strains result in changes in $2\omega_g$; from these Δd values can be obtained through simple manipulation of Eqn. (1). Hence, $\Delta d/d$ can be determined from the channelling information. Hence, the factor $(2/\xi_g)$ in Eqn. (1) could be determined empirically. Then, electron channelling patterns could be used to provide the necessary $\Delta d/d$ values for determining the stress-strain configuration from the sampled volume.

One of the major thrusts of this exploratory project was to see if such a correlation could be carried out. This necessitated devising a means to simultaneously prepare electron channelling patterns and Kossel patterns as well as a means to accurately observe and record electron channelling line profiles in the scanning electron microscope. In particular, we needed to know the effect of applied stresses on electron

channelling patterns. The response of electron channelling patterns to experimental conditions such as specimen tilt had to be investigated as well as effects of surface deposits on the pattern. The former is an experimental response and the latter a material effect.

Investigation of Electron Channelling Line Profiles

A typical electron channelling pattern from a well-annealed single crystal of aluminum is shown in Fig. (2). There are crystallographic bands and lines whose width and intensity depend upon the state of perfection of the crystal and the basic crystal parameters such as the lattice spacing. The sample was electropolished to remove any surface damage after the crystal was held for fifteen hours at 610°C in a purified argon atmosphere. The crystal was normal to the electron beam which was accelerated through 30kV. Aluminum was chosen for study since it is often used as the matrix in composite materials.

The line seen in Fig. (2) shows where the electron beam was made to scan in a single line along the crystal. The profile produced by this line is shown in Fig. (3). This profile was recorded on an oscilloscope screen; the y-intensity is shown as a function of position. The profile can be related to the lines and bands of Fig. (2) in a straightforward manner; features responsible for intensity variations can be identified.

Next, the crystal was cold rolled 5% and electropolished again. Fig. (4) shows the electron channelling pattern after rolling. Clearly, the pattern is diffuse compared to Fig. (2). The corresponding profile (Fig. 5) shows that virtually all details except the major (200) type band have been eliminated. Material deformed up to 10% tensile strain has been successfully studied using electron channelling contrast[8].

The effect of surface layers was studied with a niobium single crystal. Niobium can be used in directionally solidified composite materials. The crystal was chemically polished in a mixture consisting of 70% concentrated HNO_3 and 30% concentrated HF. The electron channelling pattern of the as-polished crystal is shown in Fig. (6); the <012> pole is at the left of the pattern. The profile corresponding to the impressed line is shown in Fig. (7). Next, a 200Å layer of carbon was evaporated onto the surface of the crystal. The thickness was determined with a piezo-electric method said to be accurate to about ±10%. The electron channelling pattern is shown in Fig. (8) and the line profile in Fig. (9). Noticeable changes in the profile have occurred. Increasing the carbon thickness to 450Å resulted in further degradation of the pattern as shown in Figs. (10) and (11). A layer of amorphous carbon 1000Å in thickness caused still more degradation but certainly an identifiable pattern remained as seen in Figs. (12) and (13). The crystal was a deep purple after this much carbon had been evaporated onto it.

These results were both surprising and extremely encouraging because previously it was believed that only a few hundred angstroms carbon deposit would wipe out the electron channelling pattern completely. The fact that this is not the case means that perhaps composites consisting of a metal

matrix and non-metallic core can be studied by depositing a few hundred angstrom layers of carbon onto the surface to make it conducting. Perhaps totally non-metallic materials can be studied in this way as well.

As we shall see, a tightly bound oxide layer gives quite different and less encouraging results. Oxidizing the niobium crystal in a controlled fashion was somewhat difficult. We used a bath devised by Picklesimer[6] to anodize the niobium, with layer thickness determined by color. A layer about 750Å thick as indicated by the gold color produced was grown onto the surface. The clean crystal case is shown in Figs. (14) and (15) while after anodizing, the corresponding results are shown in Figs. (16) and (17). This oxide thickness virtually destroys the channelling pattern. Anodizing until a purple color developed (>1000Å) did destroy the pattern.

The effect of tilting the specimen on the properties of channelling bands and lines was investigated next. This effect is important since surfaces in a true composite will not necessarily be flat and perfectly aligned over long distances. Hence, it will be necessary to separate tilt effects from effects due to internal strains and/or surface layers. For the tilt study, a silicon crystal was chosen; silicon is frequently a component in composite materials.

The results are shown in Figs. (18) - (23). Tilting the crystal with respect to the electron beam causes the contrast to undergo a change in character. For example, the {440} type reflections change from close black/white pairs at normal beam incidence to distinctly black or white lines for tilted specimens, as indicated by the corresponding line traces.

Preparation of Kossel Patterns in the Scanning Electron Microscope

We were able to prepare both reflection and transmission Kossel patterns in the scanning electron microscope. The reflection patterns using a tilted specimen will almost certainly be the ones of most interest in the study of composites; preparing thin (~50μm) sections of composites will be difficult so that transmission work may not be feasible. Hence, the tilted foil electron channelling study was essential in order to establish a basis for attempting to correlate Kossel patterns and electron channelling patterns prepared from composite materials.

Reflection patterns were prepared from an iron crystal; a typical pattern is shown in Fig. (24). Here, the crystal was tilted about 60°. The lines are sharp and have enough contrast to carry out meaningful measurements. Tilted foil electron channelling patterns can be prepared simultaneously using the NBS specimen current amplifier constructed for the scanning electron microscope[7].

Preliminary Study of Conventional Composite Materials

Two types of composite materials were obtained from Sandia and the U.S. Army Research Center (Watertown, Mass.) respectively. The Sandia material consisted of plasma sprayed aluminum onto boron-silicon (borsic) fibers. The fibers were prepared using a thin tungsten wire as a base.

This material, imaged in the scanning electron microscope, is shown in Fig. (25). First attempts to obtain electron channelling patterns from this material failed. The probable causes for this failure were the huge fabrication strains and the extremely fine "grain-size" of the aluminum matrix, as indicated by conventional x-ray diffraction techniques. The grains were probably smaller than the minimum region from which we could obtain an electron channelling pattern, i.e., about ten micrometers.

The Army material consists of carbon fibers in a magnesium matrix. Work will be underway on this material shortly. We also have some directionally solidified eutectic material on hand for study.

CONCLUSIONS

1. Line profiles from electron channelling patterns can be measured with our apparatus so that the $2\omega_g$ term in Eqn. (1) can be determined for a variety of specimen conditions, i.e., strained, coated and tilted.

2. Kossel patterns can be prepared from bulk specimens in the scanning electron microscope with sufficient information to provide satisfactory $|\vec{g}|$ data for Eqn. (1). Then the term $(2/\xi_g)$ in Eqn. (1) can be determined empirically for the specimen of interest. Hence, electron channelling patterns can be used to study strains at the micrometer level of spatial resolution.

3. A reduction of 5% by rolling nearly destroys electron channelling contrast. Hence, highly strained material cannot be investigated by means of electron channelling contrast.

4. Surface layers of oxides and carbon on the order of 1000Å destroy electron channelling contrast.

5. Layers of 200Å affect the line profiles of electron channelling patterns.

6. Electron channelling patterns change characteristically as the specimen is tilted with respect to the electron beam; band contrast decreases and line character changes.

This work virtually completes the preliminary exploratory phase of the study. Next, strains in various materials will be investigated using electron channelling patterns. Then strains at matrix-fiber interfaces will be investigated.

Tungsten, SiC and Al_2O_3 in aluminum based matrices prepared by General Dynamics have been received from Mr. T. C. Yates of Marshall S.F.C., and tests using the SEM are now underway on these materials.

REFERENCES

1. H. Yakowitz, NBS Monograph 130, 75 p (1973).

2. C. Oatley, The Scanning Electron Microscope, Pt. I, The Instrument, Cambridge University Press, Cambridge (1972).

3. P.B. Hirsch, et al. Electron Microscopy of Thin Crystals, Butterworths, London, p. 100-103.

4. E.M. Schulson, Phys. Stat. Sol. (b) 46, 95 (1971).

5. T. Imura, S. Weissman and J.J. Slade, Acta. Cryst. 8, 786 (1962).

6. M.L. Picklesimer, The Microscope 15, 472 (1967).

7. H. Yakowitz, C.E. Fiori and D.E. Newbury, SEM/1973 (Johari, ed.) IITRI, Chicago, Ill. (1973) p. 173.

8. D.C. Joy and D.E. Newbury, SEM/1971 (O. Johari, ed.) IITRI, Chicago, Ill. (1971) p. 113.

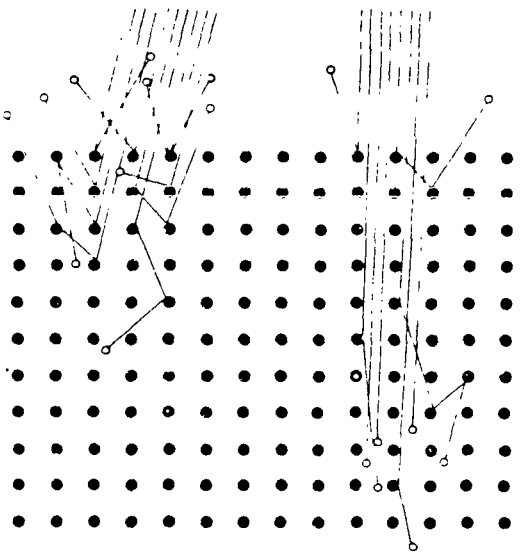

FIGURE 1. ORIGIN OF ELECTRON CHANNELLING PATTERNS; ELECTRONS PENETRATE THE CRYSTALLINE SPECIMEN MORE DEEPLY IN CERTAIN DIRECTIONS THAN IN OTHERS.

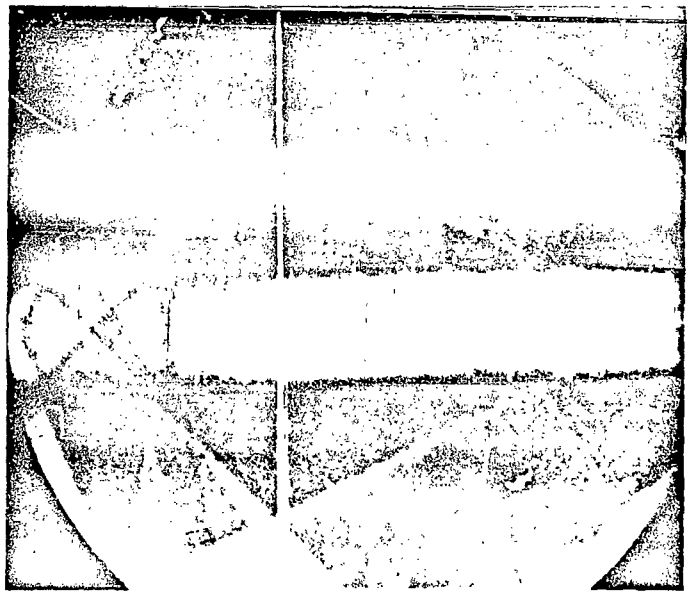

FIGURE 2.

ELECTRON CHANNELLING PATTERN OF ANNEALED, ELECTROPOLISHED ALUMINUM. LINE INDICATES REGION FROM WHICH PROFILE INFORMATION WAS TAKEN.

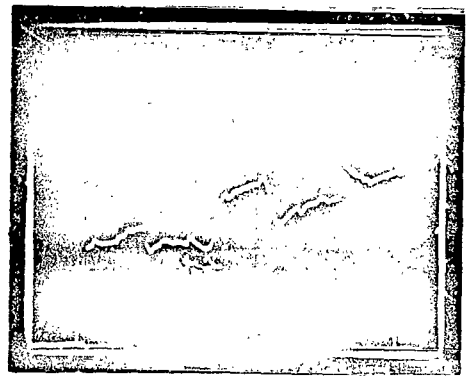

FIGURE 3.

INTENSITY PROFILE ALONG LINE IN FIGURE 2. SCALE: 2 VOLTS/cm.

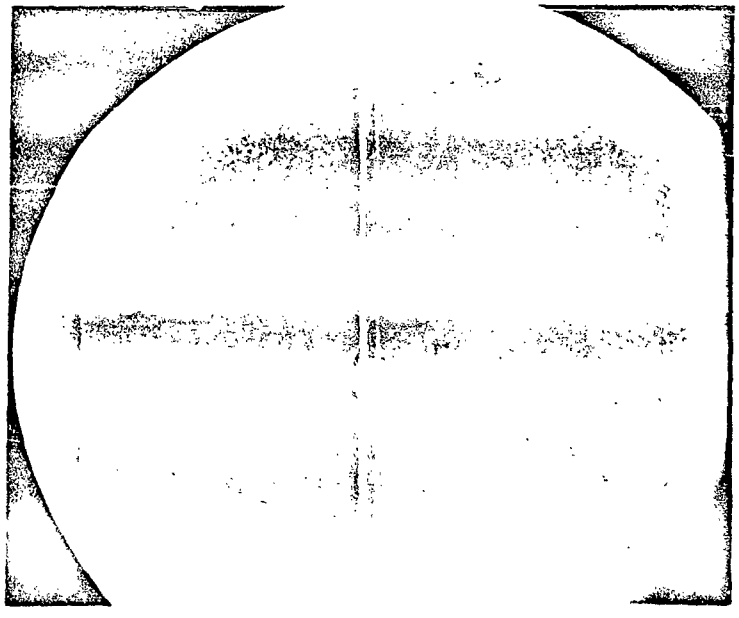

FIGURE 4.

ELECTRON CHANNELLING PATTERN OF ALUMINUM CRYSTAL ROLLED TO 5% REDUCTION AND THEN ELECTROPOLISHED. LINE INDICATES PROFILE TRACE POSITION.

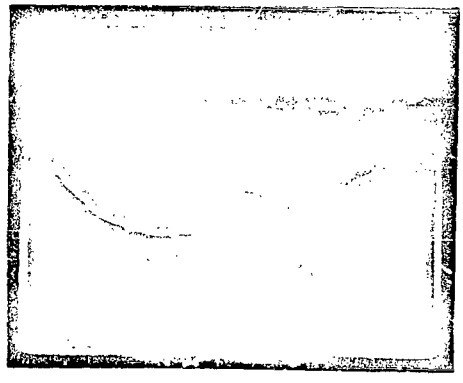

FIGURE 5.

INTENSITY PROFILE ALONG LINE IN FIGURE 4. SCALE: 2 VOLTS/cm. COMPARE WITH FIGURE 3.

FIGURE 6.
ELECTRON CHANNELLING PATTERN FROM CHEMICALLY POLISHED NIOBIUM CRYSTAL. LINE INDICATES PROFILE TRACE POSITION.

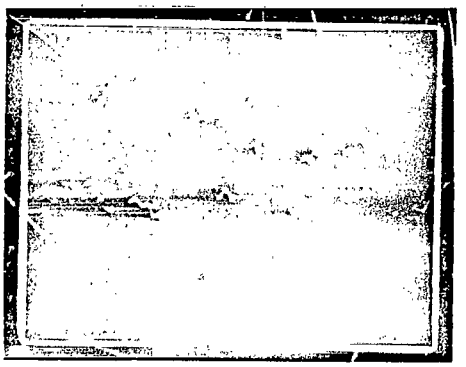

FIGURE 7.
INTENSITY PROFILE ALONG LINE IN FIGURE 6. SCALE: 2 VOLTS/cm.

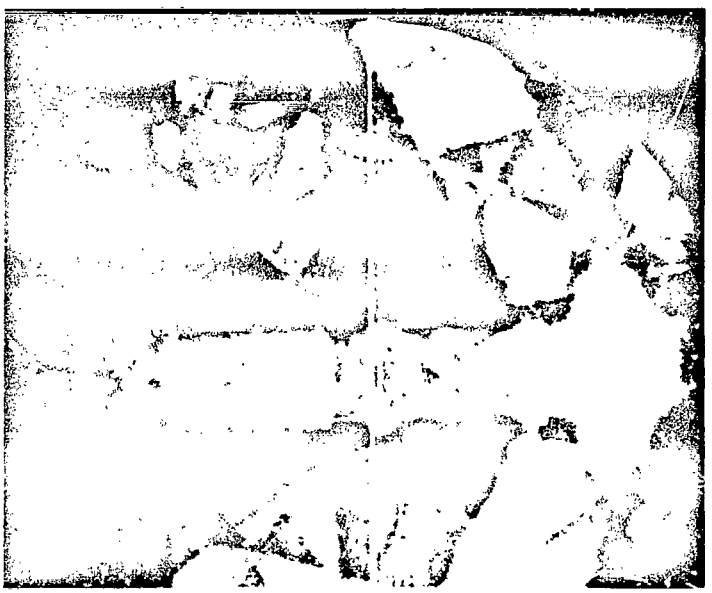

FIGURE 8.
ELECTRON CHANELLING PATTERN FROM NIOBIUM CRYSTAL AFTER EVAPORATION OF 200Å THICK CARBON LAYER ONTO THE SURFACE. LINE INDICATES PROFILE TRACE POSITION.

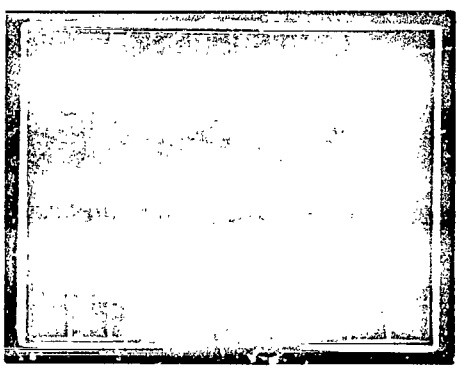

FIGURE 9.
INTENSITY PROFILE ALONG LINE IN FIGURE 8. SCALE: 2 VOLTS/cm. COMPARE WITH FIGURES 7, 11 and 13.

FIGURE 10.
ELECTRON CHANNELLING PATTERN FROM NIOBIUM CRYSTAL AFTER EVAPORATION OF 450Å THICK CARBON LAYER ONTO THE SURFACE. LINE INDICATES PROFILE TRACE POSITION.

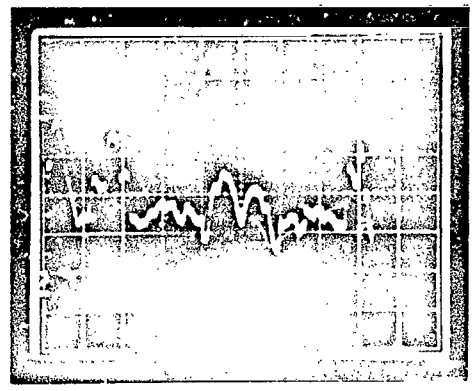

FIGURE 11.
INTENSITY PROFILE ALONG LINE IN FIGURE 10 SCALE: 2 VOLTS/cm. COMPARE WITH FIGURES 7, 9 AND 13.

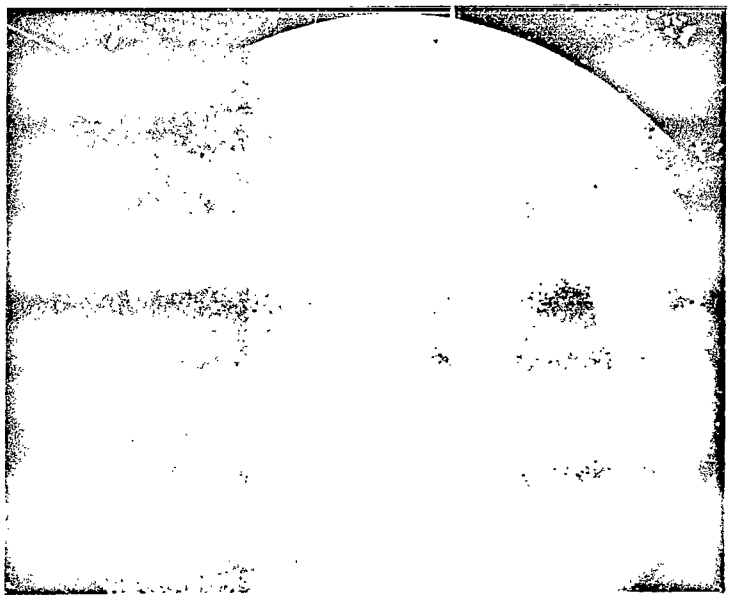

FIGURE 12.
ELECTRON CHANNELLING PATTERN FROM NIOBIUM CRYSTAL AFTER EVAPORATION OF 1000Å THICK CARBON LAYER ONTO THE SURFACE. LINE INDICATES PROFILE TRACE POSITION.

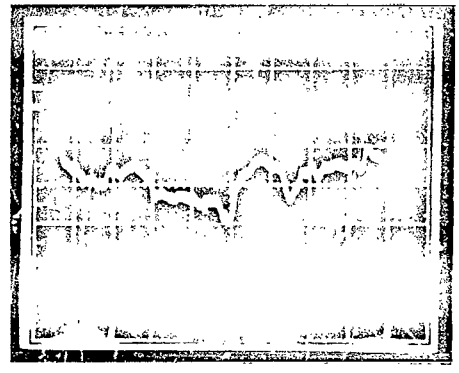

FIGURE 13.
INTENSITY PROFILE ALONG LINE IN FIGURE 1 SCALE: 2 VOLTS/cm. COMPARE WITH FIGURE 7, 9 AND 11.

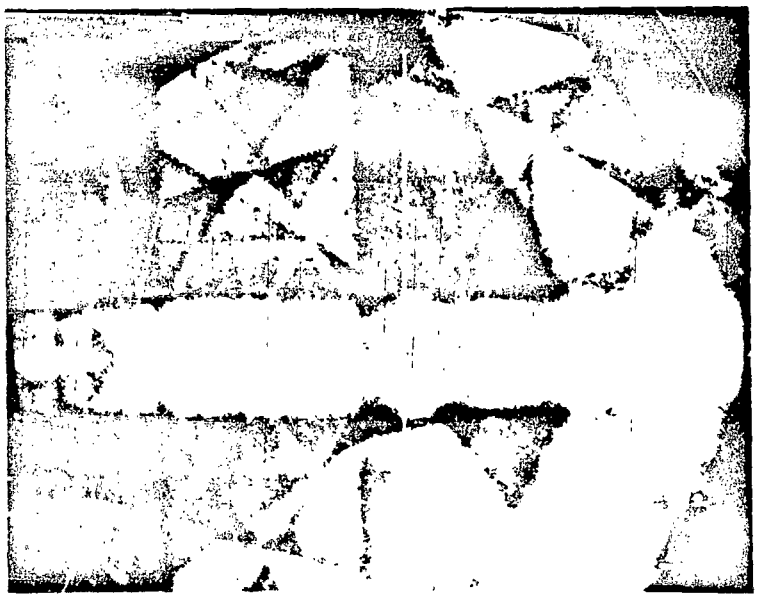

FIGURE 14.
ELECTRON CHANNELLING PATTERN OF CHEMICALLY POLISHED NIOBIUM CRYSTAL. LINE INDICATES PROFILE TRACE POSITION.

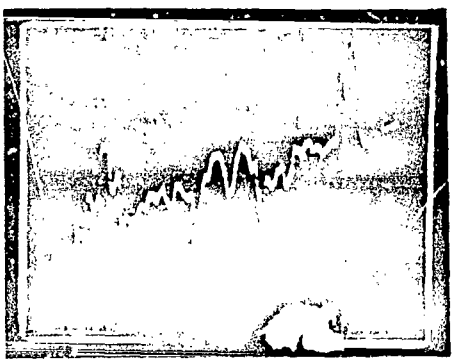

FIGURE 15.
INTENSITY PROFILE ALONG LINE IN FIGURE 14. SCALE: 2 VOLTS/cm.

FIGURE 16.
ELECTRON CHANNELLING PATTERN OF NIOBIUM CRYSTAL AFTER ANODIC OXIDATION YIELDING ABOUT 750_A THICK LAYER AS INDICATED BY COLORATION. LINE INDICATES PROFILE TRACE POSITION.

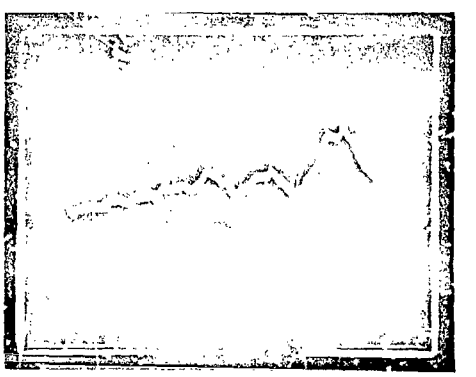

FIGURE 17.
INTENSITY PROFILE ALONG LINE IN FIGURE 16. SCALE: 2 VOLTS/cm. COMPARE WITH FIGURE 15.

FIGURE 18.
ELECTRON CHANELLING PATTERN OF SILICON WITH CRYSTAL NORMAL TO ELECTRON BEAM AXIS. LINE INDICATES PROFILE TRACE POSITION.

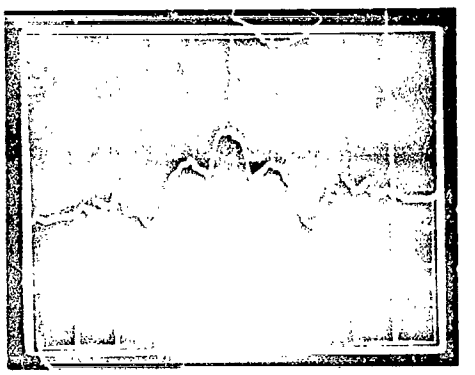

FIGURE 19.
INTENSITY PROFILE ALONG LINE IN FIGURE 18. SCALE: 2 VOLTS/cm.

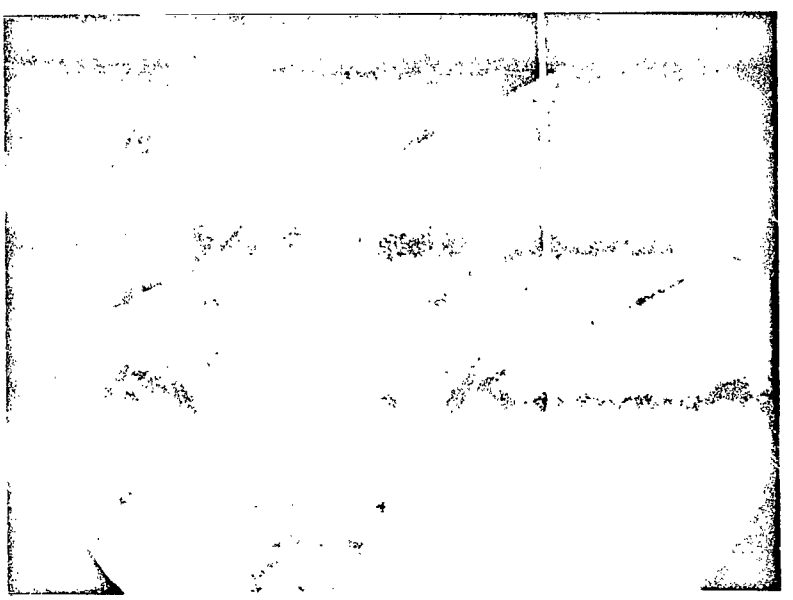

FIGURE 20.
ELECTRON CHANNELLING PATTERN OF SILICON WITH CRYSTAL TILTED 17° WITH RESPECT TO ELECTRON BEAM AXIS. LINE INDICATES PROFILE TRACE POSITION.

FIGURE 21.
INTENSITY PROFILE ALONG LINE IN FIGURE 20. SCALE: 2 VOLTS/cm. COMPARE WITH FIGURES 19 and 23.

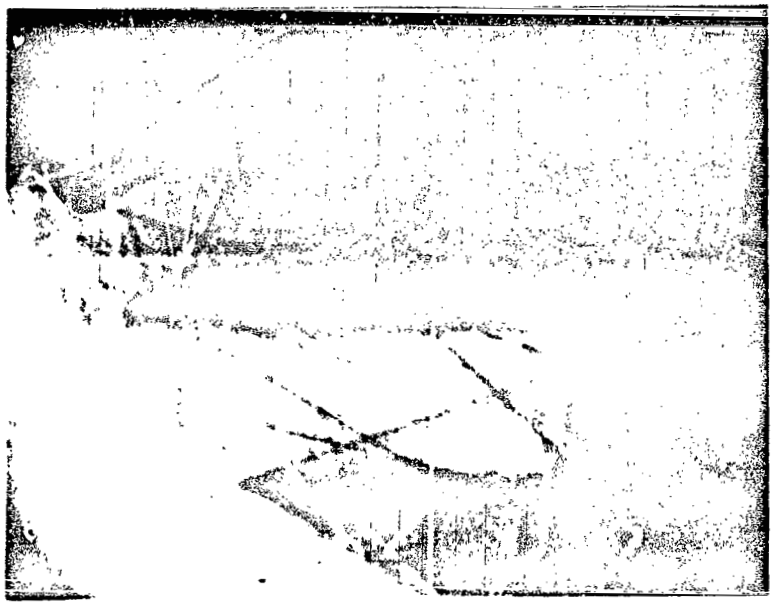

FIGURE 22.
ELECTRON CHANNELLING PATTERN OF SILICON WITH CRYSTAL TILTED 24.6° WITH RESPECT TO ELECTRON BEAM AXIS. LINE INDICATES PROFILE TRACE POSITION.

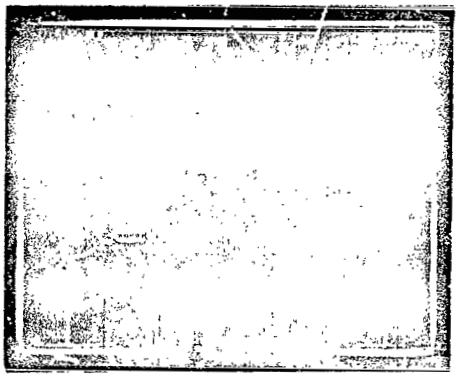

FIGURE 23.
INTENSITY PROFILE ALONG LINE IN FIGURE 22. SCALE: 2 VOLTS/cm. COMPARE WITH FIGURES 19 and 21.

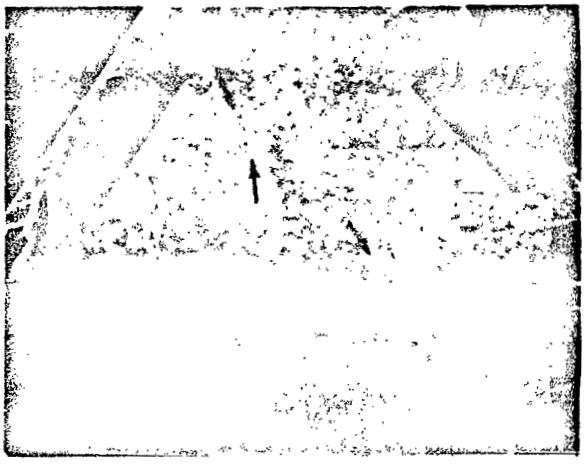

FIGURE 24. REFLECTION KOSSEL PATTERN OF IRON CRYSTAL. LINES (INDICATED BY ARROWS) INCLUDE [220], [211] AND [200] TYPES.

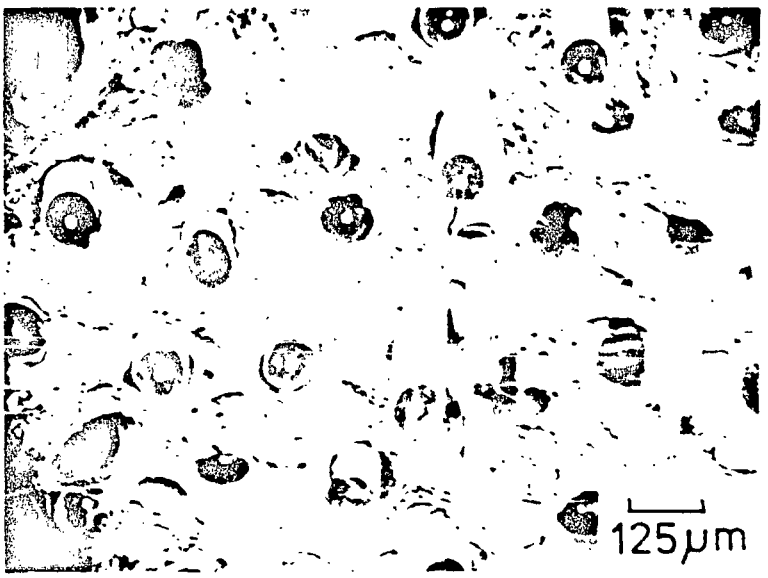

FIGURE 25. SCANNING ELECTRON MICROGRAPH OF PLASMA SPRAYED ALUMINUM MATRIX-BORSIC FIBER COMPOSITE. THE BRIGHT CENTRAL REGION OF THE BORSIC FIBER IS TUNGSTEN WIRE.

Task 4 (Acct. No. 179-12-13-05)

MELT SHAPE IN WEIGHTLESS CRYSTAL GROWTH*

By

S. R. Coriell and S. C. Hardy
Institute for Materials Research,
National Bureau of Standards
Washington, D. C. 20234

SUMMARY

In vertical floating zone melting and during crystal pulling (Czochralski growth), the shape of the liquid-vapor interface depends on the gravitational field. If the liquid zone is too long (or if in crystal pulling the crystal is too far above the melt), the liquid falls away from the solid ending the crystal growth process. Heywang calculated, using certain approximations, the maximum possible zone length during vertical floating zone melting and the maximum height of a crystal above the melt during crystal pulling. We have undertaken the extension of Heywang's calculations to the case of very small gravitational fields, and have begun measurements of contact angles in connection with the proper boundary conditions to be used in the calculation procedures.

INTRODUCTION

During vertical floating zone melting and during crystal pulling (Czochralski growth), the shape of the liquid-vapor interface depends on the gravitational field. If the liquid zone is too long (or if in crystal pulling the crystal is too far above the melt), the liquid falls away from the solid ending the crystal growth process. For the case of a liquid in contact with a different solid, e.g., water on glass, the differential equation for the shape of the liquid-vapor interface in a gravitational field is well known. For example, it has been used to derive meniscus shapes and the shapes of sessile and pendant drops. Heywang[1] used this equation to calculate the maximum possible zone length during vertical floating zone melting and the maximum height of a crystal above the melt during crystal pulling. While a rigorous treatment of the above problem obviously requires consideration of heat and fluid flow during the crystal growth process, Heywang's treatment may be a reasonable approximation. Heywang took account of the crystal growth process by requiring a particular boundary condition at the freezing interface, viz., that the liquid-vapor interface be vertical at the freezing interface. In addition to a few numerical calculations, Heywang gives a number of approximate analytic treatments. These approximations may not be valid in the limit of small gravitational fields (which were not of primary interest to Heywang). Carruthers and Grasso[2-3] have recently made experimental studies of floating liquid zones, suspended between glass tubes, for various effective gravitational fields. They found poor agreement between their experimental results and the theoretical results of Heywang. Some of the disagreement may be due to approximations made by Heywang. However, Heywang used quite

*Paper presented by R. L. Parker.

different boundary conditions than would be appropriate for the experiments of Carruthers and Grasso, i.e., the boundary conditions at a freezing interface may not be the same as those at a solid A-liquid B interface. It would be of great interest to determine either theoretically or experimentally the proper boundary condition.

A study of the literature on the shape of the liquid meniscus during Czochralski crystal growth has indicated the possible occurrence of non-zero liquid-solid contact angles in several opaque systems. This observation is in contradiction to the usual assumption that a liquid perfectly wets its solid phase. As a consequence, we have designed an experiment to observe the meniscus between a pool of water and a cylindrical ice crystal held isothermally at the melting point. The use of a transparent material will permit an observation of the liquid-solid interface in addition to the liquid-air and solid-air interfaces observed in opaque systems. This is important because a curved liquid-solid interface could result in a non-zero contact angle.

Recently Pitts [J. Fluid Mech. 59, 753 (1973)] has studied the stability of a two dimensional pendent liquid drop. Considering small perturbations in the shape of the liquid drop, Pitts calculates the energy to second order in the perturbation. He shows that the drop is stable as long as the height and the area increase together. We have studied in detail the methods used by Pitts in order to attempt to apply similar techniques to the stability of floating zones and crystal pulling.

Observations have been made of the liquid meniscus between a cylindrical single crystal of ice and a pool of water held isothermally at the melting point. The liquid-solid contact angle appeared to be zero in these experiments. However, since the crystal was at its melting point, its surface was covered with a liquid film and a zero contact angle with the melt would be expected. A new apparatus has been constructed which will permit the crystal to be held slightly below the melting point and the pool of water slightly above the melting point. This arrangement will eliminate the surface water film and will thus more nearly duplicate the conditions used in Czochralski growth.

REFERENCES

1. W. Heywang, Z. Naturforsch 11a, 238 (1956).

2. J. R. Carruthers and M. Grasso, J. Crystal Growth 13/14, 611 (1972).

3. J. R. Carruthers and M. Grasso, J. Appl. Phys. 43, 436 (1972).

Task 5 (Acct. No. 179-14-10-13)

VAPOR TRANSPORT SYNTHESIS AND CRYSTAL GROWTH OF OXIDES*

By

H. S. Parker
Institute for Materials Research,
National Bureau of Standards
Washington, D. C. 20234

SUMMARY

The primary objective of this task is the development of advanced techniques for vapor transport synthesis and crystal growth in mixed oxide systems. The ZrO_2-Ta_2O_5 system was chosen for investigation not only because it is a typical mixed oxide system but because successful development could provide a new type of stabilized ZrO_2.

The results of transport experiments using $I_2 + S_2$ and $ZrCl_4$ for transport of ZrO_2 in the 3-7 atmosphere range at average temperatures of about 950-1100°C were largely negative. Simultaneous transport experiments of $ZrO_2 + Ta_2O_5$ using $ZrCl_4$ and $TaCl_5$ resulted in severe attack of the quartz reaction tubes, although alumina tube liners reduced this attack. Minor success was obtained in simultaneous transport using $ZrCl_4 + S_2$ as transport agents. Additional experiments on pure vapor phase growth of $HgCl_2$ seem quite promising.

INTRODUCTION

The objectives of this study are the investigation of advanced techniques for vapor transport synthesis and crystal growth in binary and ternary oxide systems and definition of the limitations imposed by convective effects on the process at high pressures and large temperature gradients.

Crystal growth of binary and ternary chalcogenides by vapor transport reactions has received considerable attention in the past[1,2]. Applications of the technique to the synthesis and growth of oxide crystals have been confined to single oxides in most cases, with the major exceptions being certain spinels and germanates[2]. Emmenegger[3,4] and Emmenegger and Petermann[5] have investigated the transport and crystal growth of ternary metal oxides and transition metal niobates and tantalates. More recently, Bowen and co-workers[6] have described the growth of transition metal oxide solid solutions.

The selection of ordered fluorite structure type phases in oxide systems for initial investigation was motivated by scientific interest in extension of the vapor transport growth technique and potential technological application of materials possessing this structure. The specific material for initial consideration is ZrO_2 in combination with either Ta_2O_5 or Nb_2O_5. Zirconium dioxide is an important refractory material because of its high melting point, chemical inertness and low

*Paper presented by R. L. Parker.

vapor pressure. In the pure form, ZrO_2 undergoes a reversible phase transition from the monoclinic to tetragonal form at about 1000°C which is accompanied by a disruptive volume change of nine percent. In order to avoid this problem, ZrO_2 is commonly stabilized in a cubic form by the use of up to 15 percent of CaO, Y_2O_3 or MgO as an additive.

Work at NBS has indicated that an alternative method of stabilizing ZrO_2 is the formation of ordered fluorite structure type phases (orthorhombic)[7,8,9]. This structure is an anion excess type rather than the oxygen (anion) deficient type obtained with CaO, Y_2O_3 or MgO additives and should have greater stability. Melting points of suitable compounds in the ZrO_2-Ta_2O_5 systems are in excess of 2000°C, thus, a more stable form of ZrO_2 would be of considerable importance. In addition, little is known about the structure, physical and electrical properties of these phases.

The high melting points present a problem in synthesis and growth of single crystals suitable for characterization and investigation. The largest crystals we have been able to obtain from flux or solid state techniques are of the order of 0.5 mm in size[9]. Vapor phase transport techniques offer the potential for obtaining larger sized crystals at temperatures well below the melting points.

The use of closed tube transport techniques for synthesis and crystal growth, together with the criteria for selection of a suitable transport reaction has been described by Schafer[1,10] and Laudise[11]. Basically, an attempt is made to select a suitable transport agent such that the desired phase is the only solid product at the working temperatures, the equilibrium position is not extreme ($\Delta G^\circ \simeq 0$) and, for reasonable transport rates, the ΔH° value for the reaction should be near zero.

The transport of Ta_2O_5 with halogens is well established[1] according to the reaction:

$$Ta_2O_5 + 3TaCl_5 \rightleftarrows 5TaOCl_3$$

at total pressures of 1 atmosphere at temperatures of 750° and 650° with transport rates in excess of 10 mg/hr. However, only one report of the closed tube transport of ZrO_2 was found in the literature. Nitsche[2] reports the use of $I_2 + S_2$ as transporting agents and temperatures of 1050° - 1000°C although no further experimental details were given.

EXPERIMENTAL

Transport studies were carried out in quartz tubes of 8 mm inside diameter and about 15 cm total length. Prior to use, the tubes were cleaned, evacuated and baked out at about 300°C at pressures of about 1×10^{-6} Torr overnight prior to loading. A sorption rough pump and ion diffusion pumping system was used to avoid contamination from oil vapors.

Following bakeout, the tube was charged with an excess of high purity oxide together with the calculated amount of transport agent. The tube was then re-evacuated and sealed off at pressure of 5×10^{-6} Torr or

less. The oxides used were nominally of 99.99% or higher purity. In the case of simultaneous transport experiments, two different types of charge were used. In one case, the ZrO_2 and Ta_2O_5 were added as the unreacted oxides. The alternative method chosen was to first react the two materials at 1500°C to yield a single phase product of the desired composition and subsequently use this material as the charge.

The furnaces used were of the multizone type, with independent control of each zone. By the use of suitable thermal baffles, two isothermal regions (±10°C) of about 15 cm length could be established, separated by a central region of about 1.5 cm over which the ΔT for transport was established. Both vertical and horizontal configurations were used. The transport tubes were placed in the furnace such that the center of the tube coincided with the temperature gradient.

Total pressures for the various transport agents were calculated on the basis of average tube temperature and assumed ideal behavior of the gaseous species. Typical tube loadings were of the order of 4 to 7 mg per cm^3 of tube volume for the pressure ranges chosen, about 3-7 atmospheres.

RESULTS AND DISCUSSION

The results of the transport experiments are summarized in Table 1. Because of the lack of information regarding the transport of ZrO_2, the major effort was devoted to attempting to establish suitable conditions for the transport of reasonable amounts of ZrO_2 alone. All attempts to duplicate the reported transport[2] using $I_2 + S_2$ were largely unsuccessful, up to the temperature and pressure limits of the quartz tubes. At the highest temperatures and pressures, only milligrams amounts of transport were achieved in reasonable times.

Attempts to use $ZrCl_4$ as a transport agent yielded poor results except at the limits of the quartz tube, although crystallinity of the deposit was improved greatly. A more serious problem when transport of $ZrO_2 + Ta_2O_5$ was attempted was the severe attack on the quartz tube in the presence of $ZrCl_4$ and/or $TaCl_5$. The amount of attack was directly related to temperature. This resulted in a large percentage of tube failures during a run. Optical and x-ray diffraction examination of a typical run with $ZrCl_4$ indicated the major reaction product to be low cristobalite with no detectable $ZrSiO_4$ present. Thus, it appears that the devitrification of the fused quartz is enhanced by the presence of $ZrCl_4$ and/or $ZrOCl_2$. This limitation on maximum working temperature, together with the low transport rates observed, suggested that $ZrCl_4$ with or without $TaCl_5$ is not suitable for larger scale crystal growth in a closed quartz tube system.

Attempts to modify the transport reaction by the addition of another component to the system and thus reduce the temperature required as well as increase transport rates are being investigated. Preliminary results using $ZrCl_4$ and sulfur at lower temperatures, 1070°-970°C, have yielded milligrams of transported material with small, well-formed crystals. However, the transport rate must be increased if sizeable amounts of material are to be grown.

In an attempt to reduce corrosive attack and devitrification of the quartz transport tubes, a dense alumina tube, closed at one end, was used as a liner in the high temperature zone. Preliminary heatings suggest that such a liner will reduce the attack of the $ZrCl_4$ transport agent on the quartz tube.

One transport experiment of 95 hours duration was successfully completed. A tube charge of prereacted $6ZrO_2:Ta_2O_5$ was used, with a 2:1 ratio of $ZrCl_4$:S as transport agent. Temperatures of hot and cold zone were 1050°C and 950°C respectively, with a calculated total pressure of 5 atmospheres. Under these conditions, considerable transport occurred. The transported material was largely dendritic in nature although many poorly formed crystallites were observed.

Attempts were made to increase the mass transport rate by varying the $ZrCl_4:S_2$ ratio while maintaining a calculated total pressure of 6 atmospheres and temperatures of 1100° and 1000°. Over a range of 5 $ZrCl_4:S_2$ to 50 $ZrCl_4:S_2$, no discernable effect was noted and the total amount transported in 100 hour runs was less than previously obtained with a 2 $ZrCl_4:S_2$ ratio.

Work has begun on the study of convection and diffusion effects on the growth of Hg_2Cl_2 by the evaporation-condensation technique. In view of the high vapor pressure of Hg_2Cl_2 at temperatures in the 350° - 450°C temperature range, 0.5 to 8 atmospheres, large mass transport rates should be attainable with reasonable temperature gradients. In one run of 68 hours duration, with an average source temperature of 400°C, 54.05 grams of material were transported by using a 100°C temperature gradient. Because the entire charge was transported, the actual time required is unknown. In a second run, with a source temperature of 390°C, 15.15 grams were transported in 48 hours using a 20°C temperature gradient. Both runs were made in 18 mm I.D. quartz tubing, with the tubes placed horizontally.

REFERENCES

1. H. Schafer, Che ical Transport Reactions, Academic Press, New York 1964.

2. R. Nitsche, Crystal Growth, H.S. Peiser, Ed., 215-220, Pergamon Press, London 1967.

3. F. Emmenegger, J. Crystal Growth 2, 109-110 (1968).

4. F. Emmenegger, J. Crystal Growth 3, 4, 135-140 (1968).

5. F. Emmenegger and A. Petermann, J. Crystal Growth 2, 33-39 (1968).

6. H.K. Bowen, W.D. Kingery, M. Kinoshita and C.A. Goodwin, J. Crystal Growth 13, 14, 402-405 (1972).

7. R.S. Roth and L.W. Coughanour, J. Res. Natl. Bur. Stds. 55, 209-213 (1955) R.P. 2621.

8. R.S. Roth, J.L. Waring, W.S. Brower and H.S. Parker, "Proceedings of 5th Materials Research Symposium," R.S. Roth and S.J. Schneider, Jr., Eds., Natl. Bur. Stds., Special Publication 364, GPO Washington 1972.

9. Jean Galy and R.S. Roth, "The Crystal Structure of $Nb_2Zr_6O_{17}$", J. Solid State Chem., 7, 277-285 (1973).

10. H. Schafer, "Preparative Methods in Solid State Chemistry," P. Hagenmuller, Ed., 251-277, Academic Press, New York 1972.

11. R.A. Laudise, "The Growth of Single Crystals," 225-256, Prentice-Hall, Inc., New Jersey 1970.

TABLE 1

Summary of Transport Experiments

Material	Transport Agent	Temperatures	Time	Total Pressure	Results
ZrO_2	$I_2 + S_2$	1025°-910°C	168 hr.	3.5 atm	no transport
ZrO_2	$4I_2 + S_2$	1100°-1000°C	48 hr.	3.5 atm	minor transport
ZrO_2	$4I_2 + S_2$	1175°-1110°C	100 hr.	7 atm	mg transport
ZrO_2	$ZrS_2 + I_2$	1100°-1000°C	200 hr.	5 atm	mg transport
ZrO_2	$ZrCl_4$	900°-800°C	170 hr.	3 atm	no transport
ZrO_2	$ZrCl_4$	1100°-1000°C	168 hr.	5 atm, 6 atm	mg transport, small crystals formed (<0.5 mm)
10 ZrO_2:Ta_2O_5	1.85 $ZrCl_4$:$TaCl_5$	1125°-1025°C	72 hr.	5 atm, 7 atm	tube failure corrosive attack
10 ZrO_2:Ta_2O_5	1.85 $ZrCl_4$:$TaCl_5$	1075°-975°C	<168 hr.	5 atm, 7 atm	tube failure corrosive attack
10 ZrO_2:Ta_2O_5	1.85 $ZrCl_4$:$TaCl_5$	1050°-950°C	<168 hr.	6 atm	tube failure corrosive attack
8 ZrO_2:Ta_2O_5 a/	$4ZrCl_4$:S_2	1070°-970°C	168 hr.	5 atm	mg transport, crystals 0.5 x 0.5 x 3 mm

a/ prereacted material

Task 6 (Acct. No. 179-15-11-03)

SURFACE TRACTION AND OTHER SURFACE PHENOMENA*

By

A. L. Dragoo
Institute for Materials Research,
National Bureau of Standards
Washington, D. C. 20234

SUMMARY

Theoretical analyses of processes occurring in levitated melts during evaporative purification were carried out. The interactions of non-uniform evaporation and of thermal and solutal capillary convection were considered qualitatively. Studies were begun on pure diffusion coupled with non-uniform evaporation. The pattern of thermocapillary convection cells in a drop with an axially symmetric temperature field on the surface was deduced by determining the zero-points i. the velocity field and the streamlines in the liquid drop. Initial work on the derivation of a formula for the circulation time associated with such cells is described.

INTRODUCTION

1. thermal and solutal capillary convection and mass transfer with non-uniform evaporation.

2. thermocapillary convection for a general steady-state temperature field on the surface of a drop.

Thermal capillary, or thermocapillary, convection is convection driven by a surface tension gradient which is generated by a gradient in the superficial temperature. Solutal capillary convection is convection caused by a superficial concentration gradient including a surface tension gradient. Where the meaning is clear, the word "capillary" will be dropped and only the terms "thermal convection" and "solutal convection" will be used.

*Paper presented by R. L. Parker.

Both of these problems are important to the fluid dynamics of levitated melts. Implicit in both is the assumption that any practical heating configuration will produce a non-uniform heating of the surface of the drop which can result in thermal convection and other effects.

The first problem appears when one attempts to describe the evaporative purification of a melt in which convective-diffusion, non-uniform evaporation, thermal capillary convection and solutal capillary convection are present. Qualitative aspects of all four of these phenomena are considered here. Next, progress on a problem involving pure diffusion coupled with non-uniform evaporation is described.

Work on the second problem extends results, given in the May report, of an analysis of the components of the velocity field. The arrangement of convection cells and the location of zero-points in the velocity field for the general axially symmetric case are considered in this report. Current work on a general expression for the circulation time is described.

1. Thermal and Solutal Convection; Diffusion with Non-uniform Evaporation

In a previous report, a simple convective-diffusion-evaporation problem was solved in which the evaporation rate was assumed to be uniform over the surface although the surface temperature was not uniform. The non-uniform superficial temperature was assumed to operate only through the thermocapillary effect. The convective-diffusion equation was solved by splitting the concentration into a spherically symmetric and an angular dependent part. The former part was found to be expressible in terms of a standard solution to the diffusion equation plus a perturbation term. Furthermore, the rate of loss could be expressed in terms of a standard diffusion result evaluated at the surface plus a perturbation term similar to the above. A self-consistent method of solution was outlined. This simplified solution had two weaknesses:

a. the non-isotropic thermal condition was assumed to influence the surface tension but not the evaporation rate constant,

b. an attendent variation of concentration over the surface and its influence on the surface tension was ignored.

a. Qualitative aspects of the more general problem

The more general problem is one in which convection is driven by surface tension gradients arising both from thermal and solutal gradients and in which diffusion is perturbed both by convection and by non-uniform evaporation. Moreover, these various processes interact. For example, diffusion will alter concentration gradients on the surface which were produced by non-uniform evaporation. The change in these gradients will modify the convection which will react back on both the diffusion and the evaporation processes. A more general problem is which heat transfer is coupled to the above processes was not considered; instead, steady-state heat transfer was assumed to persist throughout.

To simplify the further discussion, the drop will be assumed to be heated at one pole and to be cooled at the other. Evaporation will be faster at the hotter pole, so that the concentration of volatile impurities will be lower there than at the colder pole. If normal thermal convection is present, liquid adjacent to the surface will be pulled toward the colder pole, liquid will descend in the colder hemisphere and will rise in the hotter one. The impurity-rich liquid from the interior will tend to replenish the depleted liquid near the hotter region of the surface while surface currents will tend to smooth out concentration differences between hotter and colder surface regions. The net effect of non-uniform evaporation and normal thermal convection is toward homogenization of the surface concentration. Aromalous thermal capillary convection, on the other hand, will tend to enhance the variation in surface concentration brought about by evaporation.

If, in addition to thermal capillary convection, solutal capillary convection is present, not only will interactions take place in terms of concentration but they will also appear in the velocity. If normal solutal convection is assumed to produce movement of surface liquid from regions of high impurity concentration to regions of low concentration, it will tend to oppose the flow due to thermal convection. As an additional contrast to normal thermal convection, it most likely will enhance the disparity in surface concentration because it will bring impurity-rich liquid from the interior to the colder surface region which already would be enriched with respect to the hotter surface by evaporation. However, the resulting surface flow will tend to level out the concentration disparity between the two regions, albeit not as effectively as the transfer of material from the interior.

The expected consequences of the various processes are summarized in Table I. Non-uniform evaporation is assumed to be present in processes "4." through "9" as the means to the concentration gradients needed for solutal convection although it is only cited explicitly in "1.". The second column shows the direction of fluid flow at the surface for each process both in terms of temperatures, e.g. hot → cold, and in terms of concentration, e.g., low → high. The third column gives the departure of surface concentration near the hotter pole from the average for the total surface. The changes in concentration are those for the process, per se, so that the net concentration is obtained by adding the effect of evaporation if it is required to be present.

b. Pure diffusion coupled with non-uniform evaporation

Work was begun on the problem of diffusion with non-uniform evaporation, the evaporation rate constant having the form

$$\alpha = \alpha_0 + \alpha_1 T_1 \cos\theta \qquad (1)$$

Although the solution to the angular-dependent diffusion problem can be performed easily--the form of the solution being suggested by the analogous quantum mechanical problem of the wavefunctions for a three-dimensional square well, the kinetic boundary condition

$$-D(\partial c/\partial r)\big|_R = \alpha c\big|_R \qquad (2)$$

now introduces a major complication because its dependence on cos θ couples successively higher order of the Legendre polynomials of the concentration expression

$$c(r,\theta,t) = c_o - \sum_{\ell=os} \Sigma\, C_{\ell s}\, e^{-\kappa_\ell^2 Dt_{j\ell}}\, (\kappa_{\ell s} r)\, P_\ell\, (\cos\theta). \qquad (3)$$

The functions j_ℓ and P_ℓ are the ℓth order spherical Bessel function and the ℓth order Legendre polynomial, respectively. The index s runs over values of the wavenumber $\kappa_{\ell s}$ satisfying the boundary conditions.

2. Thermocapillary Convection for a General Steady-State Temperature Field on the Surface of a Drop

In the previous report, a mathematical analysis developed by Miller and Scriven[1] for the oscillations of a fluid droplet immersed in a second fluid was applied to the steady-state problem of surface tension induced flow when an arbitrary superficial temperature field is present on the drop. The temperature field was described by a series expansion in spherical harmonics and the velocity components were found for an arbitrary term in the temperature field, say $Y_\ell^m(\theta,\phi)$. To obtain a solution it was necessary to introduce a function $B(\theta,\phi)$ which described small deformations of the surface of the drop. An expression was given for the generalized characteristic speed

$$U_{\ell m} = \frac{\ell(\ell+1)\gamma_0\,\gamma_T\,T_{\ell m}\,R^\ell}{2\mu[(2\ell+1)(\ell+2)\gamma_0 + \gamma_T R L_\ell]} \qquad (4)$$

(the various coefficients are identified at the end of this report). The circulation time $\tilde{\tau}$ for the second-order mode (ℓ=2, m=0) was estimated and compared with the first-order mode (ℓ=1, m=0). It was found that

$$\tilde{\tau}_2/\tilde{\tau}_1 \simeq 20$$

when $(\partial T/\partial R)_{r=R,\theta=0}$ was the same in both cases. This suggests that the first-order mode could be considerably more important than the second-order mode in such processes as mass transfer.

Subsequent work has been carried out on

1. the identification of the zero-points of the flow rate v for a "pure" axially symmetric mode, i.e., one corresponding to a $Y_\ell^o(\theta,\phi)$ term in the temperature expansion,
2. the development of a general solution for $\tilde{\tau}$ for the axially symmetric case.

The rate of flow

$$v = [u_r^2 + u_\theta^2 + u_\phi^2]^{\frac{1}{2}}, \tag{5}$$

where

$$u_r = \sum_{\ell,m}^{1} u_r(\ell,m) \tag{5a}$$

$$u_\theta = \sum_{\ell,m}^{1} u_\theta(\ell,m) \tag{6b}$$

$$u_\phi = \sum_{\ell,m}^{1} u_\phi(\ell,m) \tag{6c}$$

are the components of the velocity field. For the axially symmetric case, $u_\phi = 0$. The determination of the zero-points of v requires a detailed knowledge of the temperature field at the surface of the drop.

For a pure axially symmetric mode resulting from a superficial temperature field

$$T_s(\theta) = T_{\ell 0} R^\ell Y_\ell^0(\theta,\phi) = T_{\ell 0} R^\ell [(2\ell+1)/4\pi]^{\frac{1}{2}} P_\ell(\cos\theta), \tag{7}$$

the rate of flow in reduced form is

$$\tilde{v}_\ell = \frac{(\ell+2)}{\ell(\ell+1)} \tilde{r}^{\ell-1} \{(1-\tilde{r}^2)^2 (P_\ell)^2 + [(\ell+1)-(\ell+3)\tilde{r}^2]^2 (P_\ell^1)^2\}^{\frac{1}{2}} \tag{8}$$

where $\tilde{v}_\ell = v_\ell/U_{\ell 0} [(2\ell+1)/4\pi]^{\frac{1}{2}}$ and $\tilde{r} = r/R$. It is obvious that $\tilde{v}_\ell = 0$ inside the drop where $\tilde{r}^2 = (\ell+1)/(\ell+3)$ and $P_\ell = 0$. Since P_ℓ has ℓ nodes, there must be ℓ of these points. On the surface of the drop (i.e., $\tilde{r} = 1$), $\tilde{v}_\ell = 0$ if $P_\ell^1 = 0$. P_ℓ^1 has $\ell+1$ nodes, including one at each pole, so that $\tilde{v}_\ell = 0$ at $(\ell+1)$ points on the surface. In addition, if $\ell > 1$, $\tilde{v}_\ell = 0$ when $\tilde{r} = 0$ which implies that flow occurs through the center of the drop only if $\ell = 1$. Finally, we must consider the possible occurrence of other internal zero-points. That is, are there other points such that

$$(1-\tilde{r}^2)^2 (P_\ell)^2 + [(\ell+1) - (\ell+3)\tilde{r}^2]^2 (P_\ell')^2 = 0 \ ?$$

The answer is no. Since each term is either positive or zero, and since neither $(1-\tilde{r}^2)$ and $[(\ell+1)-(\ell+3)\tilde{r}^2]$ nor P_ℓ and P_ℓ' vanish at identical values of $\tilde{r}$ and $\cos\theta$, respectively, there are no other internal zeroes for $\tilde{v}$.

Evaluation of the streamlines shows that each of the internal zero-points serves as a focus for a set of streamlines. Thus, the ℓth-order axial-symmetric mode will consist of ℓ convection cells.

The circulation times $\tilde{\tau}$, which are given formally by

$$\tilde{\tau} = \oint dL/V$$

and which are associated with each of the ℓ convection cells, can be evaluated by requiring that the quantity of material circulating about a zero-point in a time $\tilde{\tau}$ equals the quantity of material in the volume containing the streamlines about that zero-point. It is not apparent from work performed to date that the circulation times associated with the various convection cells are necessarily equal. An expression for $\tilde{\tau}_s$, the circulation time associated with the "s" zero-point, has been obtained in terms of the angles θ_s, θ'_{s-1}, and θ'_s, where P_ℓ (cos θ_s) = 0, P'_ℓ (cos θ'_{s-1}) = P'_ℓ (cos θ'_s) = 0 and θ'_{s-1} and θ'_s are the nearest lower and upper bounds of θ_s, respectively. This expression is very complicated and it is hoped that the analyses of the roots of P_ℓ and P'_ℓ, which are now in progress, will help to simplify this expression, in addition to establishing the relationship between all the $\tilde{\tau}'_s$s.

Work continues on the computer program to plot stream functions. Programming was begun on a routine to compute and to plot evaporation rates for diffusion-controlled and for convective diffusion-controlled evaporation from spherical melts.

Symbols Used in this Report

R	radius of the drop
T	temperature
c	concentration
u_r, u_θ, u_ϕ	components of the velocity field
v	rate of flow
R	rate of evaporation
D	diffusion coefficient
α	evaporation coefficient
$\tilde{\tau}$	circulation time
γ_0	surface tension coefficient
γ_T	thermal coefficient of the surface tension, = $(\partial\gamma/\partial T)_{T_o}$
L_ℓ	thermal coefficient for the surface deformation, = $(\partial T/\partial R)_R$

Quantities associated with the (ℓ,m)-mode, i.e., $Y_\ell^m(\theta,\phi)$

$u_r(\ell,m)$,etc.	components of the velocity field
$U_{\ell m}$	characteristic speed
$v_{\ell m}$	rate of flow
$T_{\ell m}$	thermal coefficient of the temperature field expansion

REFERENCES

1. C.A. Miller and L.E. Scriven, J. Fluid Mech. 32, 417 (1968).

Table 1

Interaction of Evaporation, and Thermal and Solutal Convection

Process	Direction of Convective Flow at the Surface	Departure of Concn. at Hot Pole from Average
1. Evaporation, $\partial a/\partial T>0$	--	Decrease
2. Normal thermal conv.	hot → cold (low c → high c)	Increase
3. Anomalous thermal	cold → hot (high → low)	slight increase
4. Normal solutal conv.	high c → low c (cold → hot)	slight increase
5. Anomalous solutal	low → high (hot → cold)	Increase
6. "2." + "4."	tend to cancel	Increase
7. "3." + "5."	tend to cancel	Increase
8. "2." + "5."	hot → cold	strong increase
9. "3." + "4."	cold → hot	slight increase

REPORTS AND PUBLICATIONS

1. NBSIR 73-402 - "NBS Materials Science and Manufacturing in Space Research" by E. Passaglia and R.L. Parker, November 1973. Final report for the period 1 November 72 - 31 October 73. NASA contract W-13,475 #1. Advanced

2. NBS Report 10873 - "Characterization of Thermal Convection and Crystal Perfection in Metals Grown from the Melt" by M. Kuriyama, J.G. Early and H.E. Burdette, June 15, 1972. Final report for the period 30 June 1971 to 30 June 1972. Government Order H-84832A, Marshall SFC.

3. "Ultrapure Materials: Containerless Evaporation and the Roles of Diffusion and Marangoni Convection" by A.L. Dragoo and R.C. Paule (AIAA Paper No. 74-209, 12th Aerospace Sciences Meeting, Washington, D.C., January 30, 1974).

4. "Fluid Flow Effects on Crystalline Perfection" by M. Kuriyama, J.G. Early and H.E. Burdette (AIAA Paper No. 74-204, 12th Aerospace Sciences Meeting, Washington, D.C., January 30, 1974).

STUDIES OF LIQUID FLOATING ZONES ON SL-IV, THE THIRD SKYLAB MISSION

by

J. R. Carruthers
Bell Laboratories
Murray Hill, New Jersey 07974

SUMMARY

The behavior of liquid floating zones in a zero-gravity environment was studied ~~by Dr. E. Gibson~~ on SL-~~IV~~ 4. These experiments were designed from the results of previous work on floating zones in a simulated zero-gravity model. Molten floating zones are used on earth for the crystal growth and zone refining of reactive materials. The Skylab studies give some insight into the problems associated with the development of the technique for the future space processing of materials. Preliminary results are presented ~~in~~ on this paper on the stability of the liquid zone surface under static, rotational and vibrational conditions without gravitational constraints.

I. INTRODUCTION

One of the most unique advantages of a zero-gravity environment for the processing of materials is the elimination of containers in the handling of molten liquids. Many containers react with melts of interest during crystal growth and solidification processes and result in uncontrolled contamination of the crystal or ingot. Three techniques have been developed to perform containerless melting on earth; the electromagnetic levitation of liquid metal drops weighing 5 to 10 gm,[1-3] the use of sessile drops which freeze onto a seed of similar composition as in the Verneuil technique,[4] and the use of molten floating zones suspended between cylindrical rods of the same material and contained by surface tension for heights less than 1 to 1.5 cm.[5-8] These techniques serve as the basis for the development of suitable methods for the handling of molten liquids in zero gravity.

One of the first successful applications of liquid surface tension forces to contain liquid zones under normal gravitational conditions was the use of floating zones to purify and grow single crystals of reactive materials such as silicon and tungsten. More recently, high melting oxide

single crystals have also been grown from floating zones.[9-12] Although levitation forces may be provided by external fields to support conducting liquids away from solid surfaces, the concept of a solid in contact with its own liquid under only surface tension constraints is basically simple and central to the crystal growth process. The removal of gravitational constraints from such floating zones means that the value of the surface tension will not limit the materials which can be prepared by this technique and that normal resistive or radiative heating of the zones can replace the more concentrated but less desirable rf heating sources currently used on earth.

However crystals grown on earth by the floating-zone technique possess some undesirable features which have limited its widespread use:

(1) the radial distribution of solute dopants or nonstoichiometric components is nonuniform due to variations in the diffusion boundary layer thickness at the freezing interface caused by convective flows in the zone. These convective flows arise from thermal convection, the rotation of the solid end members required to provide radial temperature uniformity and the presence of electromagnetic stirring in the case of RF - heated zones.

(2) the dislocation density can be very high becaus of the large temperature gradients required to control the shape and position of the crystal-melt interface.

(3) the crystal-melt interface curvature is quite often convex into the melt so that, for certain orientations in semiconductor crystals, interface facets are allowed to develop which cause abrupt changes in the rate of solute incorporation across the interface of the growing crystal.

Some of these features can be controlled by a modification of the floating zone method called the pedestal technique where the growing crystal and charge feed rod are of unequal diameters and are not axially aligned. These changes allow different heater designs to be used which possess axial as well as radial components to the temperature gradients around the liquid. In addition nonaxial convection appears to produce more radially uniform diffusion boundary layers.

The use of a zero-gravity environment removes some of the constraints imposed on the dimensions of floating zones, eliminates thermal convection and allows more extensive geometrical modifications than permitted on earth. Studies of floating liquid zones have already been performed on earth in a Plateau simulation system where one transparent liquid is suspended inside another with which it is

immiscible but equal in density.[12,13] The following findings were reported:

(1) The maximum stable, ℓ_{max}, of static cylindrical liquid zones in zero-gravity is equal to the circumference. For conical shapes the maximum stable length is $\ell_{max} = 2\pi[R_\ell^2-(R_\ell-R_s)^2]^{1/2}$ where R_ℓ and R_s are the radii of the large and small solid end members respectively.

(2) The maximum stable length of rotating cylindrical liquid zones is less than the circumference by the factor $n[1+\rho R^3\Omega^2/\sigma]^{-1/2}$ where ρ is the density, Ω is the rotation rate, σ is the surface tension and n is an integer which varies with the unstable mode. This factor has been theoretically predicted for axisymmetric instabilities of uniformly rotating cylindrical zones. However in the simulation model, the liquid-liquid interface did not rotate at a uniform angular velocity so that the experimental results varied between $n = 1$ for short zone lengths and $n = 2$ for long zone lengths. The maximum stable lengths for conical and spherical zone shapes in this simulation model were also measured.

(3) The convective flow patterns in the rotating liquid zones of this model are influenced by the differential rotation velocities between the solid end members and the liquid-liquid interface. Under these conditions

and the constraints of the Taylor-Proudman theorem, three basically distinct flow regimes were identified and velocities measured in the rotating liquid zone. These studies have provided the basis on which the present Skylab experiments were designed. However the Plateau simulation model possesses an inherent limitation in its ability to model an actual liquid floating zone in zero-gravity because of the existence of an outer liquid surrounding the zone. This liquid influences the rotational and vibrational instability modes of the zone and also the form of the flow patterns in the zone. Consequently important similarities as well as differences are expected between the behavior of the two systems. Such comparisons would make further earth simulation experiments more meaningful.

The experiments reported in this paper were carried out to examine the stability constraints imposed on the liquid zone in zero-gravity so that crystal growth and purification processing methods may be developed for the preparation of reactive materials in future Space Shuttle Laboratories.

II. EXPERIMENTAL PROCEDURE

The floating zones were deployed in the arrangement shown in Fig. 1 using water as the liquid for most experiments. The apparatus was constructed with on-board equipment and consisted of socket wrench extension rods which were mounted in four camera mounts so that they were free to rotate

smoothly and could be positioned axially. The ends of the socket wrench extensions were covered with 7/8 inch diameter circular aluminum discs by means of double-coated masking tape. The front surfaces of the discs were coated with grey tape which had been previously treated by immersion in acetone so as to reduce the contact angle with water. During the course of the experiments, the outer edges of the discs were coated with Krytox oil to prevent capillary wetting of the water in that region.

Rotation of the zones was performed manually by first winding twine around the socket wrench extensions and then withdrawing at a uniform rate. Equal isorotations and counter-rotations were obtained by attaching the twine ends to a pinch bar and then withdrawing the pinch bar.

The liquid zones were deployed from calibrated syringes so that one-half of the total volume required for each zone length was placed on each disc. The zone volumes for cylindrical zones of constant circular cross-section are shown in Table 1.

Zone Volume (cm^3)	Zone Length (in)
6	5/8
14	1-3/8
20	2

Table 1. Zone Dimensions for a Constant Diameter of 7/8 inch.

The zones were formed by moving the two drops together and then moving the discs apart to the specified distances. The theoretical maximum static zone length for a 7/8 inch diameter is 2-3/4 inch.

The vibration characteristics of the floating zones were investigated in longitudinal modes.

The effects of increased viscosity were studied by using a foam of water, soap solution and air which was made by vigorous shaking of the mixture in the syringe before deployment.

The various experiments were recorded on videotape with a television camera fitted with a close-up zoom lens and a viewing monitor. Measurements were subsequently made on a television monitor using the disc diameter and timing markers on the extension rods for reference purposes. The total frame time was 1/60 sec while the three primary colors were transmitted sequentially at sampling times of 1/20 sec each. Consequently events lasting longer than 16 milliseconds were visible and could be studied on a frame by frame basis.

III EXPERIMENTAL RESULTS

1. Stability of a Static Cylindrical Zone

The maximum stable zone length recorded was 2.90 in. and was thus in excess of the theoretical value (equal to the circumference) for a right circular cylinder. However as can be seen from Fig. 2 the zone shape has changed to that of an unduloid with a concomitant enhancement in stability.

2. Stability of Rotating Zones

It is necessary to have some idea of the transient spin-up time required for the liquid zone to reach steady-state rotation after the discs have started to rotate. Momentum is transferred to the liquid at a speed of $[\nu\Omega]^{1/2}$ cm/sec where ν is the kinematic viscosity and Ω is the rotation rate. Thus, if the zone length is ℓ, the spin-up time is approximately:

$$t \tilde{>} \ell/[\nu\Omega]^{1/2} \text{ sec} \qquad (1)$$

A number of observations were made on isorotated zones using air bubbles and rotation indicators. These results were in agreement with Eq. (1) and range from spin-up times of 3 sec for the 5/8 inch zone to 20 sec for the 2 inch zone at rotation rates close to the maximum stable values. These times correspond to about 20 revolutions of the discs for all three zone lengths. The actual times over which the various rotations were performed ranged from 5 to 15 sec so that the shorter zones reached steady state while the longest zones did not. This will be evident in the rotational stability results to be presented next.

A typical rotational instability is shown in Fig. 3 for a 1-3/8 inch zone subjected to an isorotation of 60 rpm. It can be seen that there are two types of perturbations present; the axisymmetric shape perturbations observed previously in the Plateau simulation experiments[13,14] and

the nonaxisymmetric, C-shaped mode which has not been seen before. The radial deflection, ΔR, of the zone center in the C-mode can be found from a simple force balance to be approximately

$$\Delta R = \frac{2\sigma}{\rho R \ell \Omega^2} \qquad (2)$$

where σ is the surface tension of water (72 dynes/cm), ρ is the density of water, ℓ is the zone length and R is the zone radius. The C-mode was eliminated by increasing the viscosity of the zone by using a soap solution-air emulsion made by vigorous shaking in a syringe. This foam is shown in Fig. 4 at a rotation rate of 43 rpm and a zone length of 1-3/8 inch. This axisymmetric unstable mode is similar to that observed in all previous Plateau simulation experiments[13,14] where a highly viscous zone contained the zone. It should be noted that axial misalignment of the two end discs is important as a source of shape perturbations for the C-mode. However the degree of alignment was the same in the simulation as in the Skylab experiments since both were fixed "by eye". Hence the viscosity of the liquid zone plays an important role in determining which shape perturbations will become unstable. Such a dependence has not been predicted by existing theories[15-19] of the stability of rotating viscous liquid cylindrical zones.

The rotation rate data are compiled in Fig. 5 for various zone lengths. Because of experimental limitations, each rotation velocity used is given as a data point which indicates whether the zone was stable or unstable so that the

true point of instability lies in between. The two solid curves are given by the theoretical instability limits for[15-18]

(a) axisymmetric azimuthal modes:

$$\ell_{max}/R = 2\pi(1+\rho R^3\Omega^2/\sigma)^{-1/2} \qquad (3)$$

(b) nonaxisymmetric planar (C-) modes:

$$\ell_{max}/R = 2\pi(\rho R^3\Omega^2/\sigma)^{-1/2} \qquad (4)$$

It can be seen from Fig. 5 that the isorotation data were in good agreement with case (a) despite the presence of the C-mode. The deviation of the 2 inch zone data is expected because the liquid zones rotation rate have not achieved steady-state values. The data for single and counter-rotation experiments appear to fit case (b) more closely. The reasons for these differences are not understood at present and are being examined further.

The Skylab isorotation data shown in Fig. 5 are in the same general range as the Plateau simulation data (see Fig. 4 in Ref. (14)). Consequently, despite the different boundary conditions on the zone surface, the stability criteria are quite similar in the two cases.

3. Vibration Behavior of Liquid Zones

The response of the cylindrical liquid zone surface to longitudinal vibrations of the end discs is shown in Fig. 6 for a 2 inch zone. The standing waves shown in Fig. 6 occurred when the disc oscillation frequency coincided with a resonant frequency of the surface. When standing waves were produced, there was no transfer of

liquid from one wave region to another inside the zone. The resonant frequencies of such capillary waves have been determined by Lamb[20] to be:

$$f = [2\pi n^3 \sigma / \ell^3 \rho]^{1/2} \qquad (5)$$

These frequencies are shown as solid curves in Fig. 7 together with the experimental observations. It can be seen that agreement with theory is adequate only for small zone lengths and that for zones longer than $\ell = \pi R$, the resonant frequency actually increases with zone length. The reason for this behavior is not presently understood but it may be associated with viscous energy dissipation effects in the larger zones.

IV. IMPLICATIONS FOR THE USE OF FLOATING ZONES IN SPACE PROCESSING

There are a number of requirements imposed upon the shape and stability of liquid floating zones for use in materials processing. The most important considerations are the controls required for the unidirectional freezing of the molten liquid:

(i) the zone volume and meniscus shape at the interfaces must be held constant in order to control the dimensions of the freezing solid as well as to eliminate uncontrolled fluid flow;

(ii) the heater position and temperature profiles must produce the correct solidification interface shape and move it reproducibly and smoothly;

(iii) the zone surface must be stable with respect to surface tension instabilities under both static and rotating conditions. Spills of the zone represent a safety hazard which must be considered;

(iv) the composition of the zone may require control by the introduction of more than one melting solid into the zone or by vapor-melt mass transfer.

The objectives of temperature uniformity, interface shape control and liquid zone mixing can all be achieved through the use of differential rotation of the zone. The rotation conditions for surface stability may be estimated from Fig. 5 and Eq. (3). For most molten materials,[14] $\rho/\sigma \gtrsim 4\times10^{-3}$ sec^2 cm^3, so that when the zone length is of the order of 1.6 πR, then the requirement is $R^3\Omega^2 < 140$ cm^3 sec^{-2}. In any event the C-mode is highly undesirable because very low rotation rates will sustain the mode once it is initiated and also because the decay rates are very long - of the order of 30 to 60 sec.

The vibration behavior of floating zones requires that frequencies of the order of those for resonant capillary waves (1 to 10 Hz) (Eq. (5) and Fig. 7) should be avoided. Although transverse and torsional vibration modes were not investigated here, the resonant oscillation frequencies are of the same order of magnitude. Thus, vibration isolation over the range 1 to 10 Hz would probably be adequate for most conditions.

ACKNOWLEDGMENTS

This work was performed by Dr. E. Gibson, Johnson Spacecraft Center, NASA. Experimental implementation was arranged by Mr. Tommy C. Bunnister of the Marshall Space Flight Center, NASA and Mr. E. S. Daley of the Martin Marietta Corporation. The assistance of all Flight Control personnel at JSC and also Dr. Joseph P. Allen in coordinating the actual work is gratefully acknowledged. Mr. M. Grasso of Bell Laboratories assisted in data reduction.

REFERENCES

1. D. M. Wroughton, E. C. Okress, P. H. Brace, G. Comenetz and J. C. R. Kelly, J. Electrochem. Soc. 99, 205 (1952) and J. Appl. Phys. 23, 545 (1952).
2. G. Comenetz and J. W. Salatka, J. Electrochem. Soc. 105, 673 (1958).
3. W. A. Pfeifer, J. Metals p.487 (1965).
4. See K. Nassau, J. Crys. Growth, 13/14, 12 (1972).
5. P. H. Keck and M. J. E. Golay, Phys. Rev. 89, 1297 (1953).
6. R. Emeis, Z. Naturforsch, 9a, 67 (1954).
7. H. C. Theurer, Trans. AIME 206, 1316 (1956).
8. B. F. Oliver, Trans. AIME 227, 960 (1963) and 230, 1352 (1964).
9. D. B. Gasson and B. Cockayne, J. Mat. Sci. 5, 100 (1970).
10. T. Akashi, K. Matsumi, T. Okada and T. Mizutani, IEEE Trans. Magnetics, MAG-5 285 (1969).
11. M. Takahashi, S. Nanamatsu and M. Kimura, J. Crys. Growth 13/14 681 (1972).
12. P. A. Arsenjev, M. N. Baranov, K. Bienert and E. F. Kustov, Kristall und Technik, 8, 1113 (1973).
13. J. R. Carruthers and M. Grasso, J. Crys. Growth 13/14 611 (1972).
14. J. R. Carruthers and M. Grasso, J. Appl. Phys. 43, 436 (1972).

15. L. M. Hocking and D. H. Michael, Mathematika 6, 25 (1959).

16. L. M. Hocking, Mathematika, 7, 1 (1960).

17. J. Gillis and B. Kaufman, Quart. Appl. Math. 19, 301 (1961).

18. J. Gillis, Proc. Camb. Phil. Soc. 57, 152 (1961).

19. D. K. Ross, Z. Angew. Math & Phys. 21, 137 (1970).

20. H. Lamb, Hydrodynamics, Dover, New York, p.457.

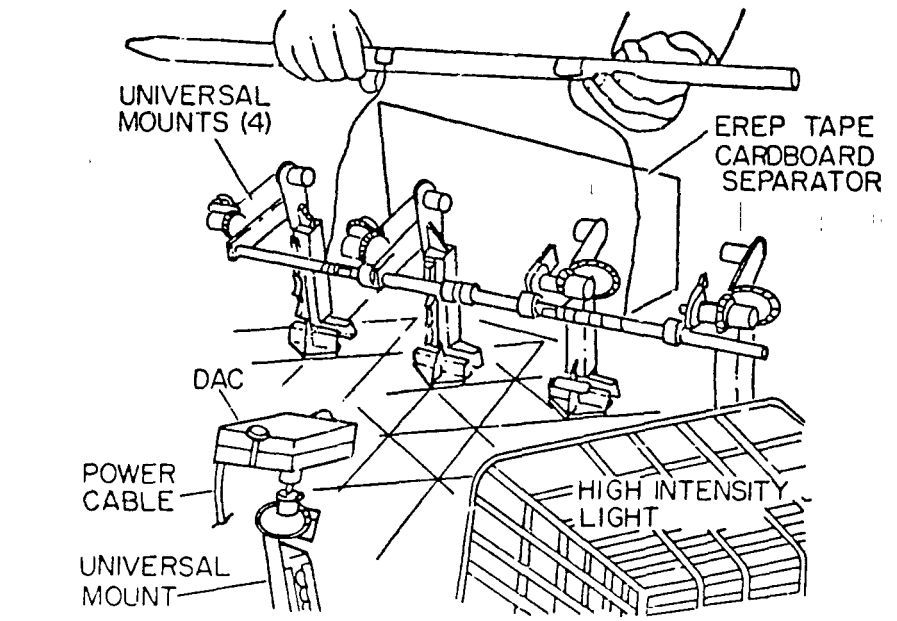

(a)

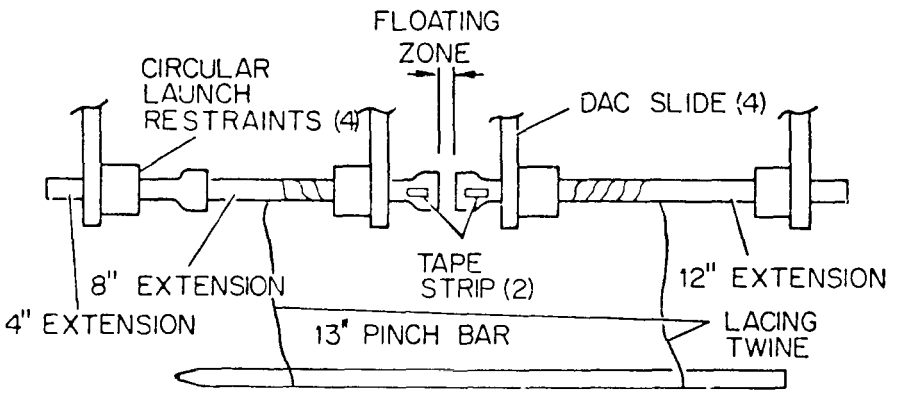

(b)

FIGURE 1. SCHEMATIC ILLUSTRATION OF THE EXPERIMENTAL SET-UP FOR LIQUID FLOATING ZONE STUDIES ON SL-IV (a) PERSPECTIVE VIEW OF APPARATUS AND CAMERA ARRANGEMENT (b) DETAILS SHOWING FLOATING ZONE POSITION AND ROTATION CAPABILITY.

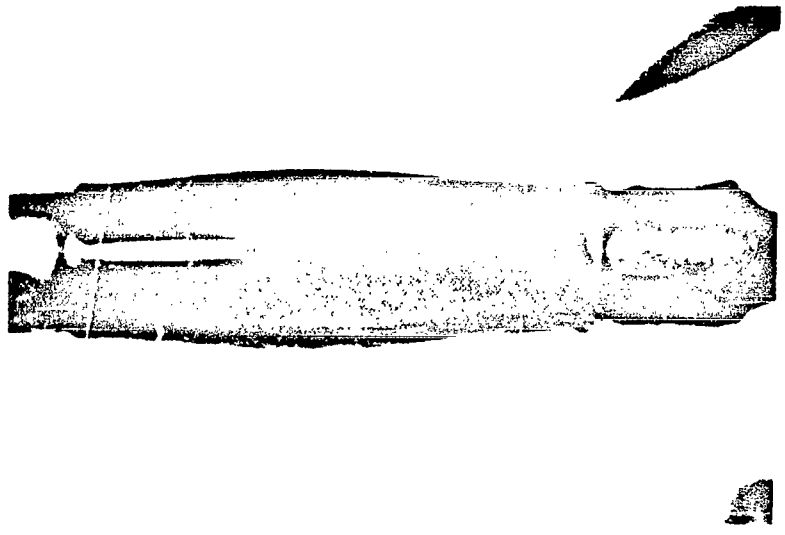

FIGURE 2. UNDULOID ZONE SHAPE CREATED BY EXTENSION OF THE ZONE LENGTH BEYOND A VALUE EQUAL TO THE CIRCULAR CIRCUMFERENCE.

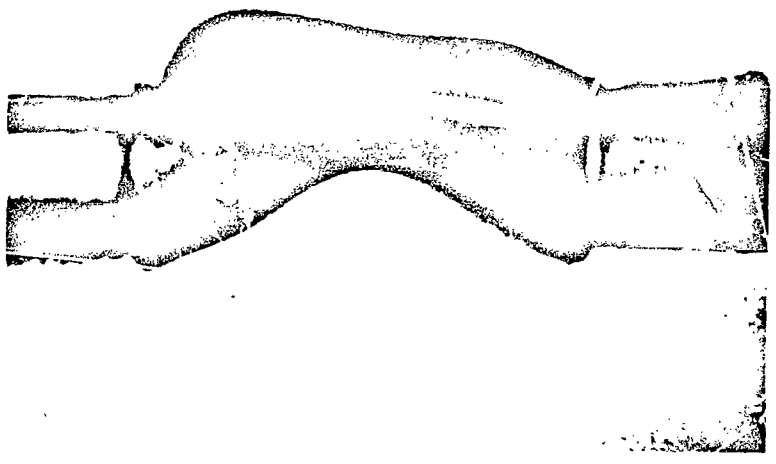

FIGURE 3. NONAXIAL INSTABILITY (C-MODE) OF A ROTATING LIQUID ZONE - ZONE LENGTH 1-3/8 INCHES, ISOROTATION RATE - 60 RPM.

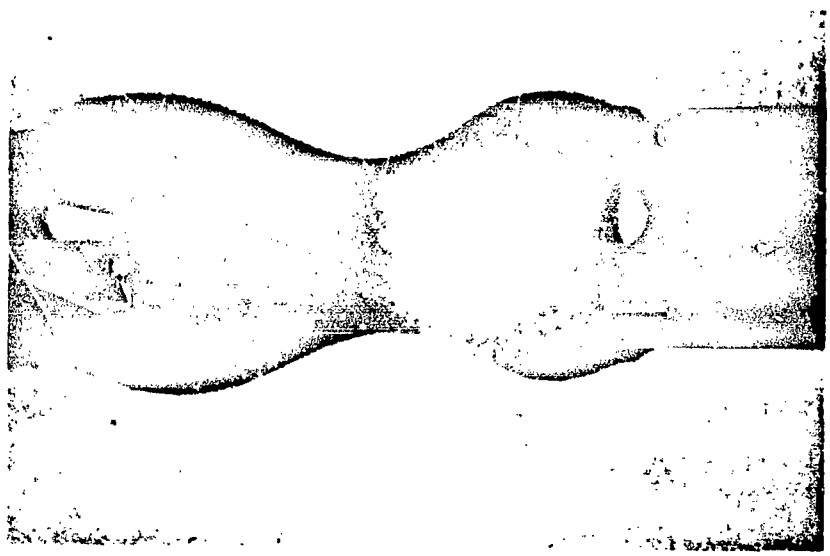

FIGURE 4. AXISYMMETRIC INSTABILITY OF A ROTATING ZONE OF FOAM (AN AIR-SOAP SOLUTION MIXTURE) - ZONE LENGTH 1-3/8 INCHES, ISOROTATION RATE 43 RPM.

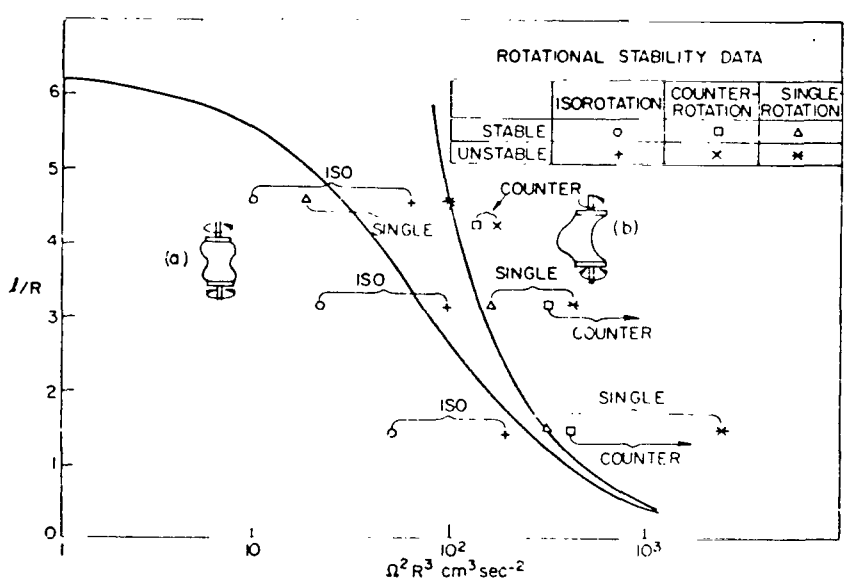

FIGURE 5. ROTATIONAL STABILITY DATA FOR VARIOUS ZONE LENGTHS. SOLID CURVES ARE THE THEORETICAL STABILITY LIMITS FOR (a) AXISYMMETRIC MODES, (b) NONAXIAL MODES.

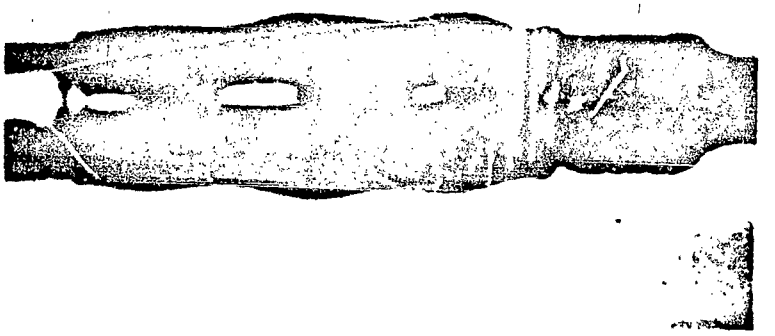

FIGURE 6. VIBRATION BEHAVIOR OF A 2-INCH ZONE SUBJECTED TO LONGITUDINAL OSCILLATIONS OF THE RIGHT-HAND DISC AT A RESONANT FREQUENCY OF THE SURFACE CAPILLARY WAVES.

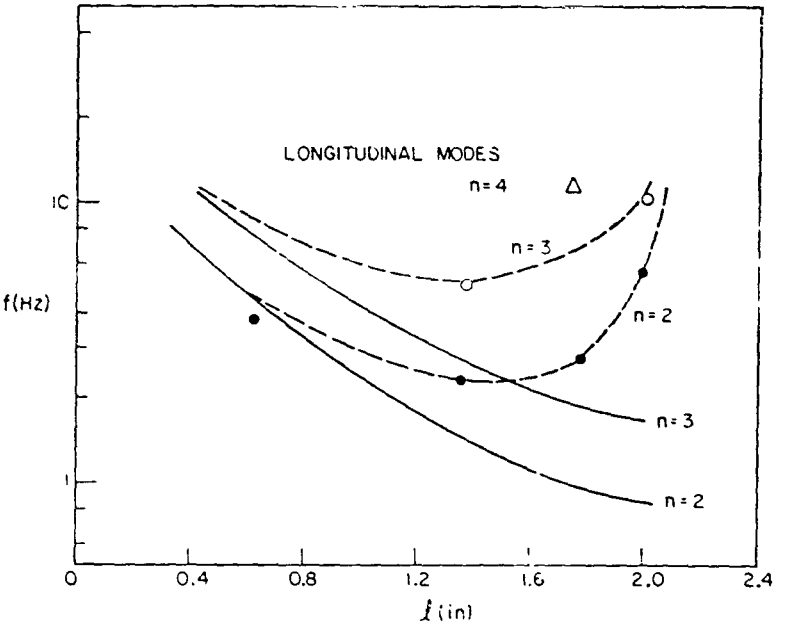

FIGURE 7. RESONANT FREQUENCIES OF VARIOUS ZONE LENGTHS SUBJECTED TO LONGITUDINAL OSCILLATIONS OF AN END DISC. SOLID CURVES ARE THEORETICAL.

LOW-GRAVITY DISPERSION OF SOLIDS IN LIQUID METALS

By

S. Kaye and J. Raat*
General Dynamics/Convair Aerospace Division
San Diego, California 92112

SUMMARY

A number of space processes, particularly the preparation of various types of composite materials, involve mixtures of liquid metals and solid particles. The two predominant problems associated with the attainment of such mixtures are (1) free dispersion of the solids, possible only if they are perfectly "wetted" by the liquid, and (2) mixture stability. The results of related experimental investigations and theoretical studies are the subject of the present paper.

The investigations of the wetting characteristics are based on a new approach, which recognizes that the conventional concept of wetting is valid only in a three-phase system (solid-liquid-gas) and which postulates that most gas-free two-phase systems (solid-liquid) exhibit perfect wetting. Initial experiments indicated that a high-vacuum environment (readily available in space) is not sufficient for the removal of the gases adhering to the solid and liquid surfaces. It was further found that the removal of adsorbed gases is enhanced by thermal surface agitation. This led to the development of a new processing technique capable of a complete removal of gases and other contaminants from the material surfaces, thus generating the conditions for wetting and dispersion in commonly non-wetting materials. The essential features (processing elements) of the technique are (1) a high-vacuum environment, (2) a thermal cycle to a temperature substantially above the melting point and (3) mechanical agitation of the materials. This technique can be considered as a significant advance in liquid-state processing for space as well as terrestrial applications.

Furthermore, an investigation is made of gravity-induced segregation of solid reinforcements in liquid matrices such as molten metals at orbital g-levels. Using dimensional arguments, it is shown that, for a given shape of the solid reinforcements, all segregation results can be correlated in terms of two dimensionless parameters:

* Paper presented by - J. Raat

the Reynolds number and a suitably defined segregation number (N), which consists of known quantities only and includes the gravitational acceleration Thus, correlation curves for different reinforcement shapes can be developed o. the basis of a limited number of selective segregation experiments on earth, using transparent matrices. These curves can in turn be used to predict orbital segregation rates in nontransparent matrices such as liquid metals.

A number of segregation experiments were carried out with slender cylindrical fibers. The results indicated that (1) during segregation the fibers assume a stable horizontal position and (2) the effect of the free end faces on the fiber drag becomes negligible (so that the fibers behave as if they were infinitely long) for slenderness ratios in excess of at least 20, depending on N. Values of N pertaining to orbital segregation in liquid metals might require slenderness ratios as high as 50 for the fibers to be regarded as infinitely long. For those cases where the end effects are indeed negligible, a simple correlation formula is derived, based on the Lamb-Oseen expression for the drag of infinite cylinders. This formula is expected to yield nearly exact predictions of orbital segregation rates for sufficiently slender fibers. The estimates might be somewhat conservative, however, for fibers with slenderness ratios much less than 50.

Finally, an analysis is made of the segregation effect of the centrifugal force on suspended particles in a rotating liquid. Rotary motions may be anticipated in a number of orbital mixing processes. In order to arrive at quantitative results, the particles are considered to be spherical and the liquid matrix motion is represented by a simple solution to the equations of motion governing the time-dependent rotary flow in an infinite circular cylinder at rest. Maximum drifting is found to occur at one-third of the cylinder radius. A criterion is derived at which particle drifting is unimportant on the time scale of decay of the matrix motion, so that the original dispersion remains essentially undisturbed. To first approximation, the results are expected to remain valid for suspended solids of a more general shape. In particular, we may expect the drifting criterion to be useful with regard to fiber dispersions as well.

INTRODUCTION

The stability of liquid-solid mixtures postulated for the zero-gravity environment offers the potential of producing composite materials by liquid-state processing, unfeasible in the one-g environment because even small density differences between the component materials may lead to rapid segregation. Liquid-state processing is of particular interest for metal-matrix composites since metals exhibit an abrupt transition from the solid to the liquid state at the melting point. The absence of a softening range and intermediate viscosity levels, which would permit a segregation-free dispersion of solid reinforcements, limit the preparation of metal-base composites on earth to solid-state techniques with a narrow range of material choices

and product characteristics. Liquid-state processing offers a wider selection of materials and processing conditions, resulting in a greater variety of product capabilities and applications. As is to be expected, the greater number of variables is associated with a greater number of problems. The requirements and problems encountered in the liquid-state processing of composites in a low-gravity environment can be grouped into four major categories:

Material Characteristics

1. Physical material properties
2. Chemical compatibility

Processing Characteristics

3. Joining (Wetting)
4. Dispersion mechanics

The first category is primarily concerned with those properties of matrix and reinforcement materials which determine the capability of the end product, such as strength. It represents the first criterion for the selection of the component materials for a specific composite. The assessment of the individual material properties is based on end-product conditions, integrating all potential effects of the thermal cycle of liquid processing. The chemical compatibility (2) refers to potential reactions between matrix and reinforcement materials during the high-temperature cycle. Chemical reactivity does not necessarily eliminate a pair of materials because a controllable interface reaction may generate a gradual change of properties and, consequently, improved interface bond strength. In both cases, the evaluation of materials employs established theoretical and experimental procedures and data. In contrast, the remaining two categories are unique to liquid-state processing and the zero-g environment, calling for the development of new theoretical concepts and processing techniques.

The condition of free mobility of the solid particles in the liquid exists only if the solids are fully wetted by the liquid, since otherwise the solids tend to agglomerate or are entirely rejected by the liquid. Complete wetting is, therefore, mandatory for liquid-state processing as well as for the generation of a satisfactory bond between reinforcements and matrix upon solidification. Unfortunately, practically all desirable reinforcement materials, such as oxides and carbides, are not wetted by liquid metals. Extensive efforts were, therefore, made to overcome this impasse. Earlier theoretical and experimental work [9] led to the conclusion that the commonly used concept of wetting, in which the wettability is expressed by the contact angle, is valid only for the three-phase (solid-liquid-gas) system; it was further postulated that in a two-phase (solid-liquid) system most materials are mutually wetting. Experimental investigations proved the correctness of this concept. The prime problem in its

practical application was the complete elimination of the gas phase. This cannot be achieved solely by a high vacuum environment, because it is unable to remove completely the gases and other contaminants adhering to the solid surfaces. The successful development of a new technique for the establishment of clean liquid and solid surface conditions and for the achievement of wetting of commonly non-wetting materials is discussed in the section on immersion of fibers in liquid metals.

The ideal structure of the concerned composites is characterized by a uniform dispersion of reinforcements in the matrix. It is, therefore, of fundamental importance to define the conditions necessary for the achievement of a uniform dispersion or, more accurately, to establish relationships and data for the quantitative assessment of the effect of all involved variables upon the behavior of the liquid-solid mixture. The ultimate objective is the determination of the maximum g-level at which a uniform dispersion can be established and maintained for a given set of variables such as density difference of the component materials, matrix viscosity, reinforcement size, reinforcement configuration and processing time. The results of the concerned theoretical studies and the generation of data for the quantitative assessment of the segregation of solids are the subject of the sections on gravity-induced fiber segregation and centrifugal drifting.

IMMERSION OF FIBERS IN LIQUID METALS

This section describes the development of a new technique for the dispersion of high-strength reinforcements in metals to produce composite materials. While developed primarily for space applications, the technique holds considerable promise for terrestrial applications as well.

Theoretical Considerations. Because force fields extend beyond the boundary surface of liquids or solids, extraneous matter tends to become attached to the surface. Examples are the attraction of gases toward solids (adsorption) or liquids and solids toward solids (adhesion). If a solid is left unprotected, its surface usually becomes quickly coated with a film of gas and other contaminants. For example, Giaever [1] simply exposed freshly evaporated aluminum film to air for a few minutes to prepare a 30 Angstrom insulation layer so as to obtain the necessary insulated junction device in his investigations of tunneling phenomena in superconductors.

Although any quantitative treatment of the interfacial forces poses considerable difficulties, a large amount of empirical information has been developed.

The work of adhesion of a liquid to a solid may be calculated as the sum of the work performed in generating one unit area of liquid surface and one unit area of solid surface minus the original liquid-solid interface energy (Figure 1). The result may be expressed by Dupré's equation [2],

$$w_{s\ell} = \gamma_{sv} + \gamma_{\ell v} - \gamma_{s\ell} \qquad (1)$$

where γ_{sv}, $\gamma_{\ell v}$ and $\gamma_{s\ell}$ are the surface tensions at the solid-vapor, liquid-vapor and solid-liquid interfaces, respectively. The difference $\gamma_{sv} - \gamma_{s\ell}$ can in many cases be expressed in measurable quantities by considering a liquid drop resting on the solid (Figure 2). According to Young [3], the equilibrium of the forces acting at the drop periphery requires that,

$$\gamma_{sv} = \gamma_{s\ell} + \gamma_{\ell v} \cos\theta \qquad (2)$$

Eliminating the immeasurable quantities γ_{sv} and $\gamma_{s\ell}$ from Eqs. (1) and (2) we find,

$$w_{s\ell} = \gamma_{\ell v}(1 + \cos\theta) \leq 2\gamma_{\ell v} \qquad (3)$$

The quantity $2\gamma_{\ell v}$ may be set equal to the work of liquid cohesion $w_{\ell\ell}$ (Figure 3). Thus, Eq. (3) shows that the contact angle θ is determined by the relative magnitudes of adhesion of the liquid to the solid ($w_{s\ell}$) and cohesion of the liquid to itself ($w_{\ell\ell}$). The condition for spreading of the liquid on the solid ($\theta = 0$) may then be expressed as,

$$w_{s\ell} - w_{\ell\ell} \geq 0 \qquad (4)$$

the difference on the left-hand side being sometimes referred to as the spreading coefficient of the liquid on the solid.

Apart from the difficulties involved in measuring contact angles, the foregoing relations are strictly valid for clean solid surfaces and uncontaminated liquids. These conditions rarely, if ever, prevail on earth. For instance, when the pure solid-vapor interface, shown in Figure 1, adsorbs a contaminant, its surface energy is lowered such that,

$$\gamma_{sv} = \gamma_{so} - \gamma_c$$

where γ_{so} is the surface energy of the pure solid and γ_c is the spreading energy of the contaminant. It is evident from Eqs. (1) and (4) that by lowering $w_{s\ell}$, the contaminant tends to prevent spreading of the liquid on the solid.[+] Sufficiently high values of γ_c will invalidate inequality (4) or even cause dewetting.

It is of interest to note that the meniscus of mercury in a glass container can be changed from convex to convave through extended boiling [3], baking out [4] or prolonged electrical discharge [5]. Langmuir [6] showed that a one-molecule thick layer of a fatty substance on a glass plate is sufficient to change the contact angle of water on the plate.

A freshly produced surface or an ideally clean surface in vacuum is actually chemically and/or physically reactive to a high degree because it tends to lower its surface energy by adsorbing gases or vapors that satisfy the structure or force field. Adsorption is mono-molecular up to a vapor pressure of about one-fifth the saturated vapor pressure [7], the adsorption layer becoming increasingly thick as the saturated vapor pressure is approached.

The free surface energy of solids ranges from several hundred to a few thousand ergs per cm^2 [8] as shown in Table I.

+With regard to contaminants, the operations of the wetting technique discussed below, justify the assumption of an unchanging value for $\gamma_{\ell v}$.

Table I. Free Surface Energy of Solids in Vacuum

Material	γ_{so} (ergs/cm^2)
Mica	24-5400
Glass	1210
Titanium Carbide (1100° C)	1200
Alumina, Al_2O_3 (1-2000° C)	7-1100
Lime, CaO (0° K)	650-1000
Silver	800
Sodium	170
Sodium Chloride	150-190
Potassium Chloride	160-175
Sodium Bromide	113-175

Generally the higher melting, harder materials (which also tend to have a greater modulus of elasticity) possess the highest free surface energies. These are the kinds of materials which provide reinforcement properties for weaker and softer metals or alloys. It was worthwhile therefore to attempt to produce such reinforced metals by exploiting the surface energy phenomena discussed in the preceding paragraphs. Specifically, the proposed wetting technique involves uncontaminated reinforcement materials with a high free surface energy, so that inequality (4) is satisfied.

Experimental Materials. The criteria for selecting the matrix metal were as follows:

1. Suitable melting temperature
2. Good wetting characteristics
3. Availability
4. Cost
5. Practicality

Earlier experiments such as those prepared for Apollo 14 employed a matrix of a low melting alloy (In-Bi) because it possessed a convenient melting temperature. Iron, nickel or copper metal and alloys have a melting temperature which is rather high for convenient laboratory manipulation. A satisfactory compromise therefore was aluminum and its alloys. These are in common use, have an elevated but not excessive melting point and are inexpensive. The properties of aluminum and its alloys are well known. This feature is valuable for comparative measurements.

The criteria for the selection of reinforcements were:

1. Suitable physical properties
2. Minimum degradation effects
3. Availability
4. Cost

Filaments, whiskers, chopped wires and particles were considered. The materials, which will be described here are pyrolytic graphite fibers (3 mm long), derived from Korean wool, Saphikon chopped sapphire fibers, alumina particles, chopped silicon carbide filaments and chopped tungsten wire. Other materials were considered, tested or rejected for various reasons such as availability, compatibility, cost, reactivity, density, melting point, etc. Crucibles used in the preparation were made of vitreous carbon.

Apparatus. The apparatus is shown in Figure 4. The configuration permits the immersion of the various reinforcements in the aluminum matrix in a high vacuum. The components are a heat-resistant quartz or Vycor vacuum chamber located in the center of an induction heating coil. The aluminum matrix metal in the form of cut wire or sawn pieces of ingot were placed together with the chopped reinforcement material into a vitreous carbon crucible, which also served as a susceptor. Agitation was achieved with a manual stirrer of tungsten wire in a vacuum feed-through fitting. Sample temperatures were measured with an optical pyrometer by viewing directly through the quartz or Vycor tube. Pressures were monitored by a suitable vacuum gage. An additional argon supply system further provided for pre-vacuum flushing and for the establishment of an inert atmosphere, if desired.

Experimental Procedure. The following steps were carried out to obtain the reinforced metal matrix:

1. Cutting the reinforcements to size ($L/D > 10$).
2. Cutting the aluminum matrix to size from wire or ingots.
3. Cleaning the materials in solvent and acid.
4. Placing the combined metal and reinforcements in a vitreous carbon crucible and inserting it into the vacuum apparatus.
5. Exchanging the inner atmosphere of air with argon by evacuating and purging to atmospheric pressure three or more times.

6. Evacuating to a pressure of 10^{-4} to 10^{-6} mm Hg for 1/2 to 3 hours.

7. Heating to the melting point of aluminum and stirring at rising temperature until immersion occurs.

8. Cooling in the inert atmosphere.

9. Sectioning and evaluating the product.

Discussion and Results. The goal in developing the procedure was to achieve a pure two-phase system with no interfacial contaminants from either the metal or the reinforcements. This was accomplished by using all of the following techniques:

1. Cleaning metal matrix and reinforcements.

2. Substituting argon for air.

3. Evacuating to low pressure.

4. Sputtering contaminants from the surface in a glow discharge.

5. Heating

6. Stirring

The first step is not required for bulk material and macroscopic reinforcements because the total surface to volume ratio is small; the contaminants are easily removed by the subsequent steps in the procedure.

Argon, an inert gas, is less readily adsorbed than oxygen on most surfaces. Also, any oxygen present reacts with the aluminum matrix or some of the reinforcements to produce a troublesome amount of an extra phase.

Low pressure is necessary to reduce the equilibrium amount of material adsorbed on the material surfaces. The lower the pressure, the less adsorption occurs. This is also true for chemisorption at aluminum and carbon surfaces at higher temperatures.

Maintaining the system for a period of time in a glow discharge, subjects the surfaces to ion and electron bombardment. This causes a detachment of many adsorbed materials from the surface.

All physical adsorption decreases with temperature. Many oxides also decompose at elevated temperatures. Organic materials decompose and volatilize with other materials of low vapor pressure.

Heat melts the aluminum, increases its mobility, lowers the surface tension and viscosity and thus provides conditions allowing the metal to surround and adhere to the clean surface of the reinforcements.

Stirring is necessary to break up the contaminants and scrub them from the surfaces. It also produces intimate contact between the liquid metal and the reinforcements. Disturbing the surface of the metal disrupts the orientation of atoms at the liquid surface, which may form a network strong enough to prevent any metal evaporation. Observation shows that wetting and immersion of the reinforcements proceeds rapidly only when vapors of aluminum are deposited on the wall of the vacuum chamber. Observations show also that after wetting takes place, there sometimes appears a film of oxide crystals floating on the aluminum. These crystals gradually disappear. It is not certain whether they decompose or are wetted and become immersed in the melt. The distinction between Al_2O_3 and Al by scanning electron microscope techniques is still under study.

Photomicrographs of sections of the products obtained are shown in Figures 5 through 9.

The aluminum-tungsten composite (Figure 5) shows excellent wetting and dispersion. Part of the material is produced by dissolution of the stirrer and the remainder has reacted completely with the aluminum matrix because of the prolonged immersion and overheating. The nature of a reaction zone is shown in Figure 6. Yakowitz* at the National Bureau of Standards has also analyzed these samples and provided additional descriptions of the reaction zones.

The needles, which appear in all the photographs, are tungsten whiskers with an aspect ratio of 30, resulting from the tungsten stirrer. This may imply a useful method for the preparation of aluminum-tungsten whisker composites.

Excellent wetting and dispersion was also obtained in the aluminum-sapphire composite (Figure 7). It should be noted that a drop of aluminum on sapphire usually shows not only a positive contact angle but one exceeding 90 degrees (i.e., no wetting). The harder polished sapphire is elevated over the softer aluminum in this metallurgical section. According to evaluation by NBS*, the interface of the specimen is excellent and the grain boundaries are clean at magnifications to 10,000x.

Wetting and dispersion were also achieved with alumina particles of 15 and 120 microns average diameter. The dispersion of smaller particles was not yet successful due to the large surface area and the large amount of adsorbed/trapped gases.

*private communication

Figure 8 shows the cross section of the aluminum-silicon carbide composite. Good dispersion and wetting is evident. However, a closer analysis showed extensive reaction zones. The tungsten present seemed to have a strong affinity for the silicon carbide. There is also some as yet unidentified material in the matrix grain boundaries.

Figure 9 shows the aluminum-graphite specimen. While wetting is obtained (as also evidenced by the wetting of the carbon crucible), there was extensive reaction between the fibers and the aluminum. This may be a characteristic of the particular carbon material used since there was no evidence of reaction with the carbon crucible even after extensive heating periods.

From the results presented, it is evident that precast reinforced metal composites can be made for space experiments. This may lead to the space processing of materials containing reinforcements capable of providing new and unusual properties. The preparation of the final materials at orbital g-levels would then consist of remelting the pre-casts, followed by agitation to obtain uniform dispersions (guided by the criteria discussed in the sections below.)

Because the developed process involves phenomena of a fundamental nature, it should be applicable to a wide range of composite materials, limited only by the compatibility of the reinforcements with the high processing temperatures.

GRAVITY-INDUCED FIBER SEGREGATION

Calculation of the fluid-dynamical drag of a particle (of arbitrary shape) in uniform motion through a liquid involves the following relevant dimensional quantities: particle drag (F), liquid density (ρ_ℓ), liquid dynamic viscosity (μ), particle velocity (U), and a characteristic dimension of the particle (D). Application of dimensional analysis (Buckingham's pi-theorem) shows that the relationship between the foregoing five dimensional quantities can be expressed in terms of two dimensionless groups,

$$\frac{F}{\rho_\ell U^2 D^2} = \text{function (Re)} \tag{5}$$

where $Re = UD/\nu$ is the Reynolds number of the motion ($\nu = \mu/\rho_\ell$ being the liquid kinematic viscosity).

If the motion is due to gravity, the particle segregation velocity is determined by the exact balance between the drag F and the difference between particle weight and buoyancy force, so that,

$$F \propto (\rho_s - \rho_\ell)\, gD^3 \tag{6}$$

where ρ_s is the particle material density and g is the gravitational acceleration. Eliminating F from Eqs. (5) and (6), we find,

$$\frac{(\rho_s - \rho_\ell)\, gD}{\rho_\ell U^2} = \text{function (Re)}$$

or multiplying both sides by Re^2,

$$\frac{\rho_s - \rho_\ell}{\rho_\ell} \quad \frac{gD^3}{\nu^2} = \text{function (Re)} \tag{7}$$

We define the following segregation number, which consists of known quantities only,

$$N = \frac{\rho_s - \rho_\ell}{\rho_\ell} \quad \frac{gD^3}{\nu^2} \tag{8}$$

It then follows from Eq. (7) for the Reynolds number (which contains the unknown segregation velocity U) that,

$$Re = \text{function } (N) \tag{9}$$

Eq. (9) expresses a similarity law, which, for a given particle shape, permits correlation of all experimental segregation results in terms of the two parameters Re and N only. Correlation curves for different particle shapes can be developed on the basis of a limited number of selective segregation experiments on earth, using transparent liquids. These correlation curves can then be used to predict low-gravity (orbital) segregation in non-transparent matrices such as molten metals.

A number of 1-g segregation experiments were carried out with cylindrical fibers of various materials, diameters and lengths in different liquids [9]. The fiber diameter varied between 125 and 625 microns; the slenderness (length-to-diameter) ratio ranged from 5 to 100; and the liquid dynamic viscosity varied between 1 and 110 times the value for water. Each fiber was released in a horizontal position just below the surface of the liquid. The location of the fiber as it was falling was recorded on 16mm motion picture film. The films were evaluated in a data analyzer and the measurements of location and elapsed time tabulated. From these data the fiber velocities were determined. The fiber position remained horizontal during the motion through the liquid. After any initial inclination from the horizontal, the fibers were observed to assume their stable horizontal position during the subsequent motion.

For slenderness ratios greater than approximately 20, and N on the order of 0.1 to 100, the segregation velocity was generally found to be independent of the slenderness ratio. In that case the effect of the free end faces on the drag becomes negligible so that the cylinders behave as if they were infinitely long. However, in the experiments with highly viscous liquids, involving segregation numbers on the order of 0.001 to 0.01 (which are more characteristic of orbital segregation), slenderness ratios as high as 50 were required for the segregation velocity to become independent of the slenderness ratio. Figure 10 shows typical results in the form of segregation velocity versus slenderness ratio.

As long as end effects are negligible and the Reynolds number is small, the drag force per unit length of the cylinder can be calculated from the Lamb-Oseen formula [10],

$$\frac{F}{\rho_\ell U^2 D} = \frac{4\pi}{Re\,\ell n(7.4/Re)} \tag{10}$$

Eq. (10) becomes exact as $Re \to o$ and yields accurate drag results up to $Re \approx 1$.

The difference between cylinder weight and buoyancy force per unit length of the cylinder is,

$$F = (\rho_s - \rho_\ell)\, g\, \frac{\pi D^2}{4} \tag{11}$$

Eliminating F from Eqs. (10) and (11), we find,

$$N = \frac{16\,Re}{\ell n\,(7.4/Re)} \tag{12}$$

where N is the segregation number defined in Eq. (8), based on the cylinder diameter. Eq. (12) is plotted in Fig. 11 for a range of values of N that includes orbital segregation and is expected to yield nearly exact predictions up to $N \approx 10$ ($Re \approx 1$) for very slender fibers. A simple correlation of the experimental data listed in Table II can be obtained as follows. Experimental drag data [11] for very slender circular cylinders indicate that, within the range $0.1 < Re < 30$, we may write, with good approximation,

$$\ell og\left(\frac{F}{\frac{1}{2}\,\rho_\ell U^2 D}\right) = -0.6\ \ell og\,(Re) + 1.1$$

or,

$$F = 6.3\,\rho_\ell U^2 D\,(Re)^{-0.6} \tag{13}$$

Eliminating F from Eqs. (11) and (13), we find,

Table II. Correlation of Fiber Segregation Velocities in Terms of Reynolds Number (Re) and Segregation Number (N)

Liquid	Fiber	ρ_s	$\frac{\rho_s - \rho_\ell}{\rho_\ell}$	U (cm/sec) L/D $\gtrsim$ 20	Re	N
Water	Boron	2.65	1.65	2.1	2.67	31.2
$\rho_\ell = 1$	Copper	8.9	7.9	9.4	12.0	155
$\mu = 1$	Tungsten	19.3	18.3	13.8	17.5	359
	Nylon	1.12	0.12	0.92	2.34	19.3
Water + 25% Glycerine	Boron	2.65	1.48	1.4	1.0	7.53
$\rho_\ell = 1.07$	Copper	8.9	7.32	7.6	6.0	52.8
$\mu = 1.9$	Tungsten	19.3	17.1	10	7.2	103
Water + 75% Glycerine	Copper	8.9	5.9	2.2	0.122	0.22
$\rho_\ell = 1.2$	Tungsten	19.3	15.1	3.2	0.177	0.565
$\mu = 27.5$						
Fluorolube						
$\rho_\ell = 1.3$	Tungsten	19.3	13.9	2.6	0.116	0.335
$\mu = 37$						

All fibers have a diameter of 0.125 mm, except nylon 0.250 mm.

The liquid density ρ_ℓ, solid density ρ_s, and liquid dynamic viscosity μ are all relative to water.

$$Re = 0.23\, N^{5/7} \qquad (14)$$

Eq. (14) is plotted in Fig. 12 and compared with the experimentally determined segregation rates. The agreement is generally satisfactory, the discrepancies being at least partly due to inaccuracies in the viscosity data.

In actual space processes aimed at producing reinforced metals, the fibers may be expected to have a diameter on the order of 100 microns, i.e., roughly the same size as investigated in the present study (reinforced metals for more delicate applications might require the use of whiskers with a diameter roughly 10 times smaller). The viscosities of liquid metals being within the range of viscosities of the simulation matrices, the principal difference in the numerical value of the segregation number N between earth-bound and orbital processes is due to a reduction of g down to orbital levels (e.g. 10^{-4} times the terrestrial value). The practical interest would probably be primarily in fibers with slenderness ratio roughly between 10 and 50. Thus, the prediction of orbital segregation rates according to Eq. (12) might be somewhat conservative due to the effect of the free end faces (which would augment the fiber drag and therefore decrease the segregation rate), particularly for the shorter fibers.

CENTRIFUGAL DRIFTING

In this section we study the effect of the centrifugal force on suspended particles in a rotating fluid. Segregation will occur whenever there exists a difference in material density between the particles and the fluid (gravity being assumed absent).

For the sake of simplicity we assume the particles to be spherical. Particle concentration, size and relative velocity are considered to be sufficiently small so that we may assume that the basic fluid motion remains essentially unaffected by the presence of the particles.

For the basic fluid motion we consider the time-dependent rotary motion of a viscous incompressible fluid contained in an infinite circular cylinder at rest. It is furthermore assumed that the fluid motion remains confined to planes perpendicular to the cylinder axis. Under these conditions the fluid velocity will be tangential and constant along concentric circles about the axis, i.e., $q = q(r,t)$, where r and t are the radial distance and time, respectively. It can be shown [10] that the equation of motion in tangential direction is satisfied by elementary solutions of the

form*

$$q_n(r,t) = A_n \exp(-\alpha_n^2 \nu t/a^2) \quad J_1(\alpha_n r/a) \tag{15}$$

where $n = 1, 2, 3 \ldots\ldots$ and J_1 is the Bessel function of the first kind of order unity; the α_n's are the zeros of J_1 (the first three zeros being $\alpha_1 = 3.83$, $\alpha_2 = 7.02$, $\alpha_3 = 10.2$). In the present problem, we choose the first mode q_1 (Fig. 13) as a representative basic fluid motion, i.e.

$$q(r,t) = q_m \exp(-\alpha_1^2 \nu t/a^2) \frac{J_1(\alpha_1 r/a)}{J_1(\alpha_1 \bar{r}/a)} \tag{16}$$

where q_m is the maximum initial fluid velocity, located at $\bar{r}/a = 0.47$.

If we define the relaxation time T of the fluid motion (somewhat arbitrarily) as the time required for the velocity distribution to drop off to 10 percent of its initial level, we find, from Eq. (16),

$$\exp(-\alpha_1^2 \nu T/a^2) = 0.1 \tag{17}$$

so that, substituting $\alpha_1 = 3.83$,

$$T = 0.16\, a^2/\nu \tag{18}$$

In fact, the first mode in Eq. (15) exhibits the slowest decay (the coefficient in Eq. (18) being 0.047 and 0.022 for the second and third mode, respectively).

*General solutions, satisfying arbitrary initial conditions, are obtained through linear superposition of the elementary solutions with the coefficients A_n set equal to those of the Fourier-Bessel expansion of the initial velocity distribution.

The centrifugal force on a particle is $F_1 = mq^2/r$ where m is the particle mass. The particle also experiences a Coriolis force of magnitude $F_2 = 2mUq/r$, where U is the velocity of the particle relative to the fluid (F_2 and U, being perpendicular to each other, are both lying in a plane normal to the axis of rotation). However, $F_2/F_1 \sim U/q$ so that the Coriolis force may be disregarded in view of our assumption that the relative motion is slight compared to the basic motion. It is not difficult to show that the particle inertia effect due to the spatial variation of the angular velocity of the fluid (about the axis of rotation) may then also be neglected. Furthermore, the particle inertia force due to the temporal variation of angular velocity will be small compared to the centrifugal force if the time required for one rotation is small compared to the relaxation time of the fluid.

Thus the principal driving force is the centrifugal force and the motion of the particle will be essentially radial. In the following we assume that the relative motion may, with good approximation, be treated in quasi-steady fashion with the viscous resistance set equal to the instantaneous value of the Stokes solution for a sphere [10]: $6\pi\mu UR$, where R is the radius of the sphere. The use of the Stokes formula is permitted as long as the Reynolds number of the relative motion UR/ν is smaller than approximately unity.

The pressure gradient in the fluid is such that it precisely balances the centrifugal force experienced by the fluid particles. Because the suspended sphere is assumed to be small compared to the cylinder radius, the outward force on the particle due the combined action of pressure gradient and centrifugal effect may be written as

$$\frac{4}{3}\pi R^3 (\rho_s - \rho_\ell)\frac{q^2}{r}$$

where ρ_s and ρ_ℓ are the material densities of the sphere and the liquid respectively; q and r are "local" quantities (taken at the center of the sphere).

According to our quasi-steady treatment this outward force is at all times balanced by the viscous Stokes drag, which gives the following result for the instantaneous relative velocity of the sphere

$$U = \frac{2}{9}\frac{R^2}{\nu}\frac{\rho_s - \rho_\ell}{\rho_\ell}\frac{q^2}{r} \tag{19}$$

where q is given by Eq. (16). In order to simplify the subsequent calculations, the radial velocity distribution may, with sufficient accuracy, be approximated by a parabola, i.e.

$$\frac{J_1(\alpha_1 r/a)}{J_1(\alpha_1 \bar{r}/a)} \approx 4\frac{r}{a}\left(1-\frac{r}{a}\right) \tag{20}$$

Using this approximation, substitution of Eq. (16) into Eq. (19) yields the following differential equation for the radial position of the particle,

$$\frac{dz}{d\tau} = 0.12\ \beta\, z(1-z)^2\, e^{-\tau} \tag{21}$$

where

$$z = r/a;\quad \tau = 2\alpha_1^2\,\nu t\,/a^2;\quad \beta = \frac{\rho_s-\rho_\ell}{\rho_\ell}\left(\frac{q_m R}{\nu}\right)^2$$

Eq. (21) can be solved exactly through separation of the variables. However, for the present purposes it suffices to consider only a slight drifting. in which case Eq. (21) may, in the immediate vicinity of the original particle position z_o, be simplified as follows:

$$\frac{dz}{d\tau} = 0.12\ \beta\, z_o(1-z_o)^2\, e^{-\tau}$$

with solution,

$$z-z_o = 0.12\ \beta z_o\,(1-z_o)^2\,(1-e^{-\tau}) \tag{22}$$

Eq. (22) gives the particle drift as a function of original position and time. The function $f(z_o) = z_o(1-z_o)^2$ is sketched in Fig. 14. Maximum drifting occurs at $z_o = 1/3$ (one-third of the cylinder radius) with $f(1/3) = 4/27$. Eq. (22) then gives,

$$(z-z_o)_{max} = 0.018\ \beta\ (1-e^{-\tau}) \tag{23}$$

The importance of particle drifting on the time scale of decay of the basic fluid motion can now be evaluated through substitution of the relaxation time T into Eq. (23). Thus, according to Eq. (17) and the definition of τ, $\exp(-\tau) = 0.01$, so that,

$$[z(T) - z_o]_{max} = 0.018\,\beta \tag{24}$$

The right-hand side of Eq. (24) must be small compared to unity for particle drifting to be unimportant. Otherwise, particle dispersions will certainly be nonuniform with a pronounced concentration near the container wall. If we consider dispersions with nonuniformities in the amount of a few percent of the cylinder radius acceptable, then, on the basis of Eq. (24), we are led to the criterion,

$$\beta = \frac{\rho_s - \rho_\ell}{\rho_\ell} \left(\frac{q_m R}{\nu} \right)^2 \lesssim 1$$

for particle drifting to be negligible. Note that this criterion is independent of the size of the container, $q_m R/\nu$ being simply the maximum initial particle Reynolds number. Furthermore, although the foregoing conclusions were derived for spherical particles, to first approximation they are expected to remain valid for particles of a more general shape. For instance, we may expect the drifting criterion to be useful with regard to fiber dispersions as well.

CONCLUSION

For the successful preparation of composite materials by liquid-state processing in low-g environments, two requirements are of fundamental significance: (1) the achievement of complete wetting between the component materials during the liquid processing cycle and (2) the maintenance of a uniform dispersion.

Based on the previously advanced postulation that most materials are mutually wetting in a gas-free two-phase system (solid-liquid), a new technique was developed which produces complete wetting between commonly non-wetting materials. Wetting is a mandatory prerequisite for particle dispersion and for an effective interface bond upon solidification. The necessary removal of gases and other contaminants from the material surfaces is achieved by a high vacuum environment, a thermal cycle beyond the melting temperature and material agitation. While primarily developed for space processing, the technique may also have significant applications in terrestrial materials production.

Relationships established for gravity-induced and centrifugal segregation provide reliable means for a sufficiently accurate numerical definition of segregation rates or the absolute particle displacement within the liquid-state processing time. The most significant application of the fiber segregation results is the definition of the low-g level required to maintain adequate mixture stability for any set of materials and processing variables. The theoretical results for centrifugal drifting will furthermore be useful in the development of suitable mixing techniques, which at least in some cases are likely to involve rotary motions.

ACKNOWLEDGEMENTS

The authors are greatly indebted to Dr. W. H. Steurer for his valuable contributions and kind advice during the preparation of the manuscript.

This work was partly supported by NASA MSFC under contracts NAS 8-27806 (monitored by Messrs. I.C. Yates, Jr. and F. J. Beyerle) and NAS 8-29620 (monitored by Mr. I. C. Yates, Jr.).

REFERENCES

1. Giaever, I.; Science, 183, p. 1253 (1974).

2. Dupré, A.; Théorie Mécanique de la Chaleur, Gauthier - Illars, Paris, p. 369 (1869).

3. Young, T.; Phil. Trans. Roy. Soc. London, 95, (1805).

4. Schumacher, E. E.; J. Am. Chem. Soc., 45, p. 2255 (1923).

5. Manley, J. J.; Phil Mag., 5, p. 958 (1928).

6. Langmuir, I.; Trans. Farad. Soc., 15, p. 69 (1920).

7. Langmuir, I.; J. Am. Chem. Soc., 40, p. 1361 (1918).

8. Gregg, S. J., "The Surface Chemistry of Solids," Second Edition, Reinhold Publishing Co., New York, p. 140, (1961).

9. Steurer, W. H., and Kaye, S., "Preparation of Composite Materials in Space," Vol. II, Final Technical Report No. GDCA-DBG 73-001 (Contract NAS 8-27806), January 1973.

10. Lamb, H., "Hydrodynamics," Dover Publications, New York, n.d. (reprint from the Sixth Edition).

11. Batchelor, G. K., "An Introduction to Fluid Dynamics," p. 261, Cambridge Univ. Press, 1967.

BIBLIOGRAPHY

Gregg, S. J.; "The Surface Chemistry of Solids", 2nd. Ed., Reinhold Publishing Co., N. Y., 1961.

Adam, N. K.; "The Physics and Chemistry of Surfaces", Dover Publications, Inc., New York, 1968.

Semenchenko, V. K.; "Surface Phenomena in Metals and Alloys", Pergamon Press, New York, 1961.

BIBLIOGRAPHY (cont'd)

"Chemistry and Physics of Interfaces", Sidney Ross Chm, Symposium on Interfaces, American Chemical Society Publication, Washington, D.C., 1965.

Adamson, A. W.; "Physical Chemistry of Surfaces", Interscience Publishers, Inc., New York, 1960.

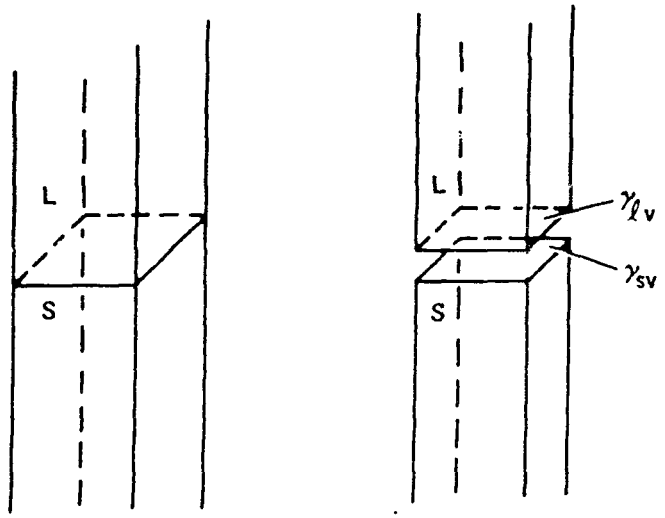

FIGURE 1. WORK OF ADHESION

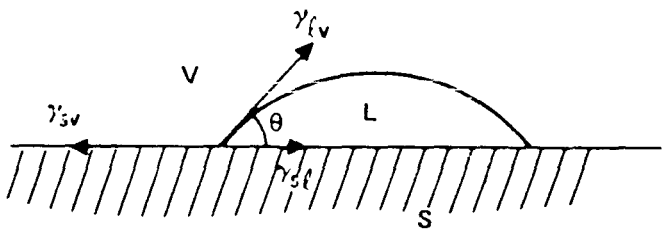

FIGURE 2. FORCES ACTING AT PERIPHERY OF LIQUID DROP ON SOLID SURFACE.

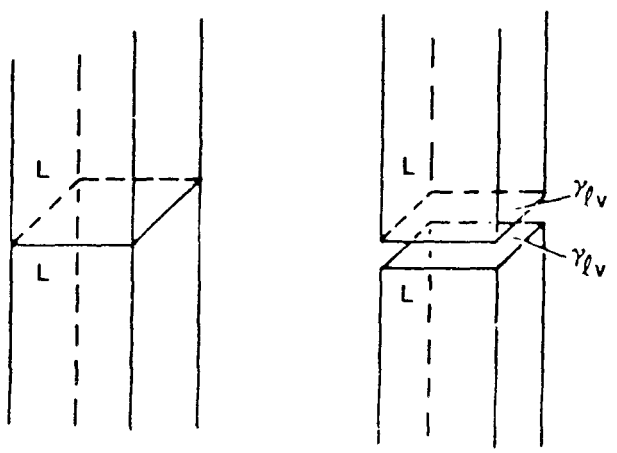

FIGURE 3. WORK OF COHESION.

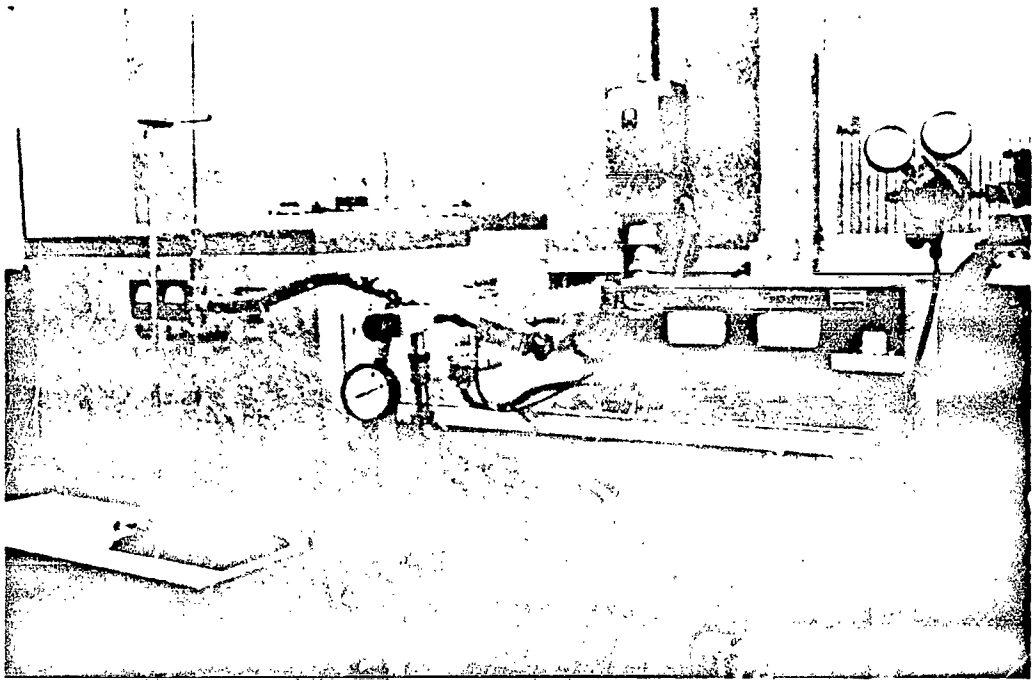

FIGURE 4. APPARATUS FOR PREPARING REINFORCED METAL COMPOSITES.

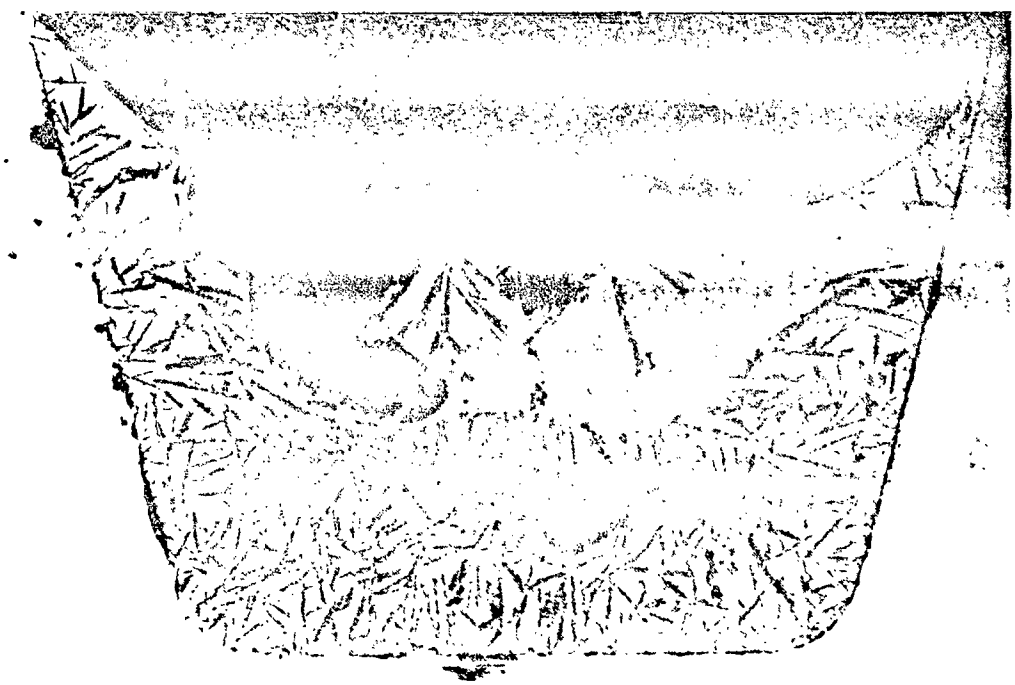

FIGURE 5. ALUMINUM-TUNGSTEN COMPOSITE (10X).

FIGURE 6. ALUMINUM-TUNGSTEN COMPOSITE (500X).

FIGURE 7. ALUMINUM-SAPPHIRE COMPOSITE (100X).

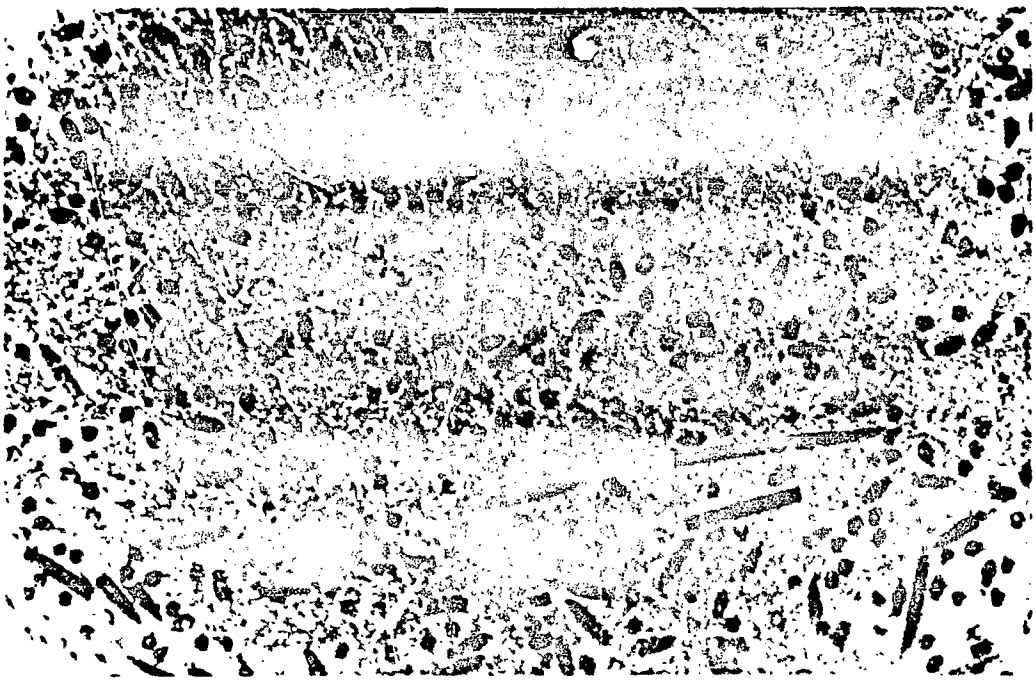

FIGURE 8. ALUMINUM-SILICON CARBINE COMPOSITE (10X).

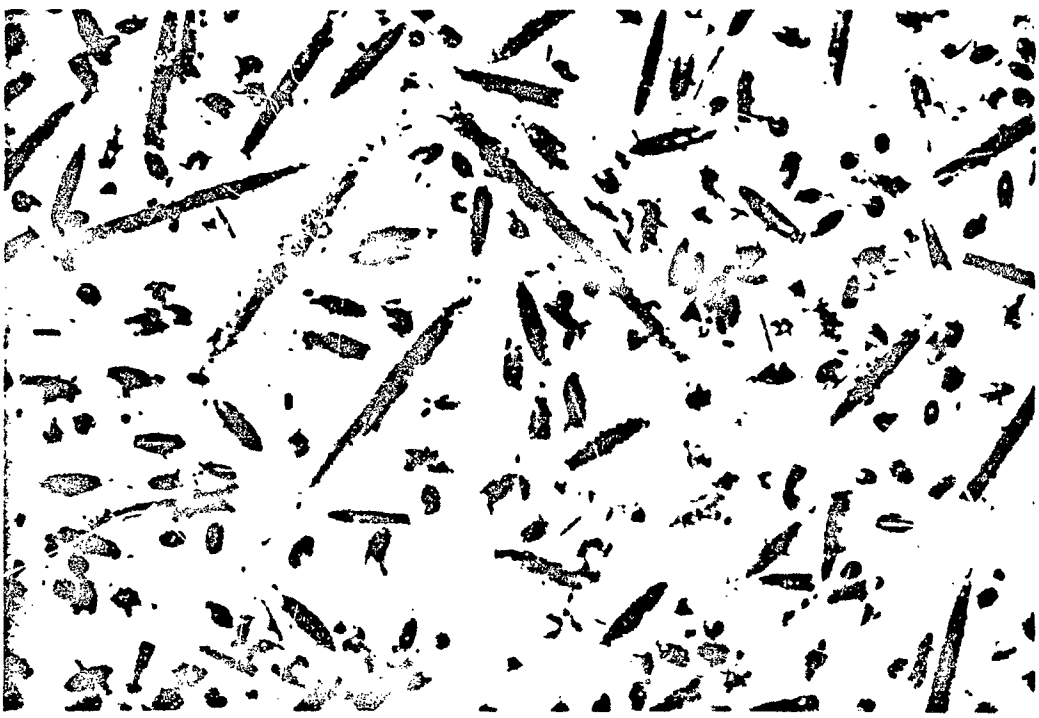

FIGURE 9. ALUMINUM-GRAPHITE COMPOSITE (150X).

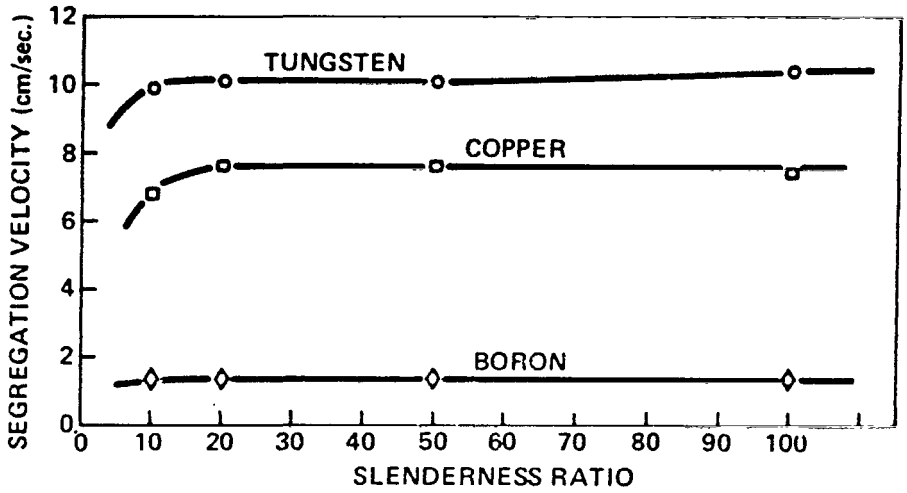

FIGURE 10. SEGREGATION VELOCITIES OF FIBERS (D = 125 MICRONS) IN WATER + 25% GLYCERINE SOLUTION.

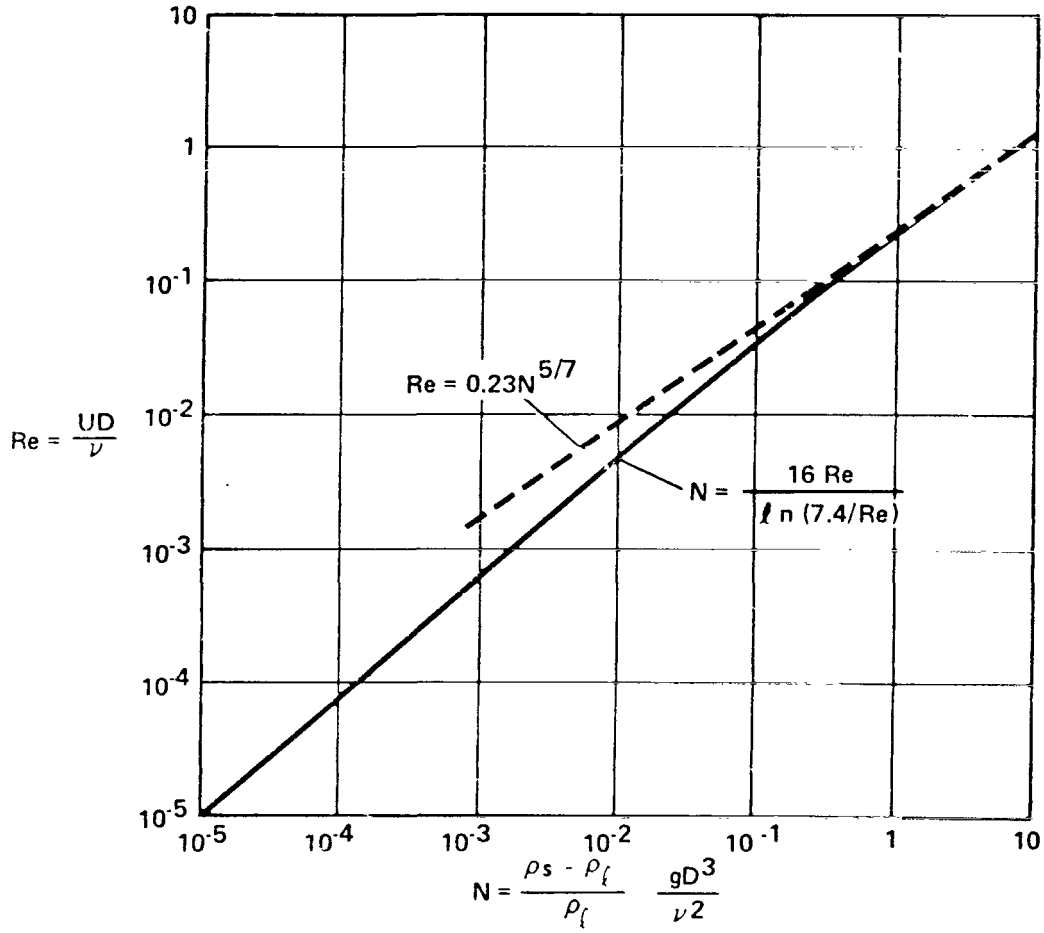

FIGURE 11. REYNOLDS NUMBER VERSUS ORBITAL SEGREGATION NUMBER FOR VERY SLENDER FIBERS.

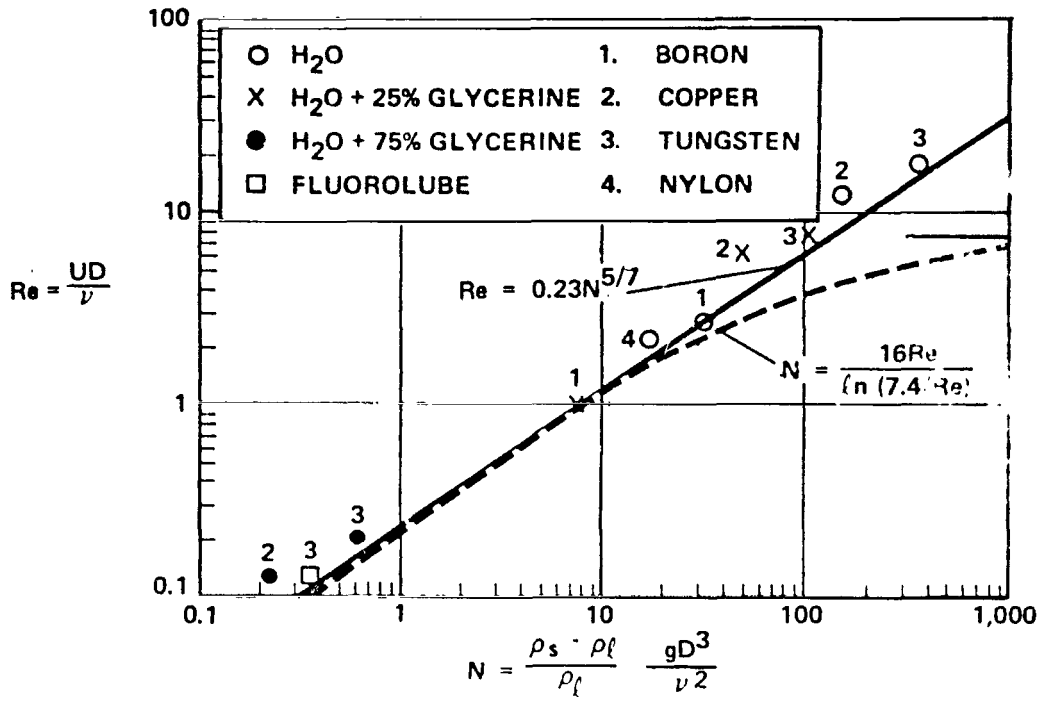

FIGURE 12. CORRELATION OF EXPERIMENTAL SEGREGATION DATA IN TERMS OF Re AND N.

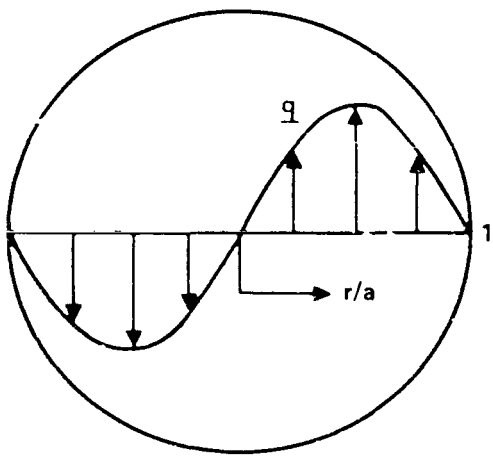

FIGURE 13. ASSUMED LIQUID VELOCITY DISTRIBUTION IN CYLINDRICAL CONTAINER.

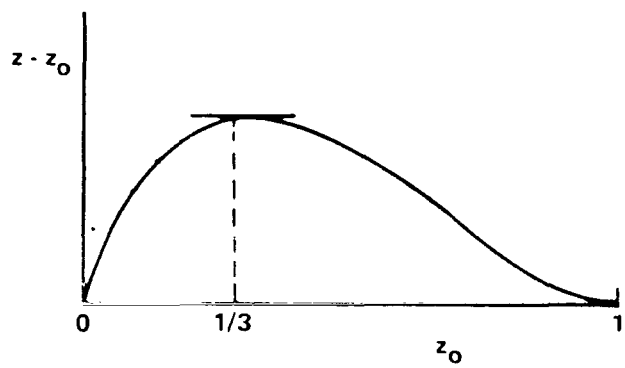

FIGURE 14. PARTICLE DRIFT AS A FUNCTION OF INITIAL POSITION.

N74 29919

OXIDE GLASS PROCESSING IN SPACE

By

R.A. Happe*
Space Division, Rockwell International
Downey, California 90241

and

L.E. Topol
Science Center, Rockwell International
Thousand Oaks, California 91360

SUMMARY

Space melting of potential new glass formers has the advantage that no solid container or mold would be required. The absence of such a mold would remove the possibility of contamination of melts (especially those at high temperature) by the container and, in addition, on cooling would offer no heterogenous nucleation sites for crystallization. New glasses with interesting combinations of optical properties, e.g., index of refraction and dispersion, then might be produced.

An approach to containerless melting in the laboratory has been studied for the past few years. Various oxides and combinations of oxides, not known to be glass formers, were hot pressed into rods of about 1/8-inch (3 mm) diameter. The investigations were limited to oxides since they have predictable properties and are stable in air. The rods were rotated in a high-speed drill motor and a CO_2 laser beam of about 250-watt intensity was focused on the end and face of the spinning rod. The small molten droplets that were spun off were allowed to free-fall cool. Approximately 100 spherules of each of the compositions tested were collected. These ranged from crystalline to clear, smooth glass spherules. Glasses of 100 to 800 microns in diameter were formed from at least 80 weight percent of the oxides Al_2O_3, Ga_2O_3, In_2O_3, La_2O_3, ZrO_2, HfO_2, Nb_2O_5 and Ta_2O_5 with 20 or less weight percent of CaO + SiO_2 and from the pure lanthanide oxides La_2O_3, Sc_2O_3, Y_2O_3, Sm_2O_3, Gd_2O_3, Yb_2O_3, and Lu_2O_3. The pure La_2O_3 glass decomposed rapidly in air but stable glasses were produced from binary La_2O_3 compositions with 25, 50 and 75 weight percent of each of the oxides Y_2O_3, Yb_2O_3, Nb_2O_5 and Ta_2O_5 and from the ternary compositions 40 weight percent La_2O_3 + 20 weight percent CaO + 40 weight percent Al_2O_3 or Ga_2O_3. The indices of refraction of all the glasses and the Abbe numbers of several were measured. Many of the glasses produced had a refractive index greater that 2.0.

To attempt to produce larger glass samples [of 1/4-inch (6 mm) diameter], a second approach is being tried. This consists of the use of a vertical wind tunnel to suspend a sample on an air stream while it is being

*Paper presented by R. A. Happe.

superheated and then cooled. A piece of the base oxide rod is fused to the tip of a 1- to 3-mm-diameter fused silica probe with the laser beam. The base oxide is then melted completely with the laser while suspended in the air stream with the aid of the silica probe. The probe, containing no crystalline matter, does not appear to contribute nucleation sites.

Preliminary work has resulted in crack-free glasses of about 1/4-inch diameter being obtained repeatedly from 80-20 Ga_2O_3 - CaO and on one occasion from 50-50 La_2O_3-Nb_2O_5. Although glasses of the Ga_2O_3 - CaO composition have been reported previously, they were formed only in small sizes (about 1/50 of the present mass) and only through the use of a fast water quench.

INTRODUCTION

The combination of circumstances attending melting in space presents the possiblity of making glasses from substances which to date have been observed only in the crystalline condition. The absence of a need for a solid container during the melting and superheating portion of the manufacturing cycle permits contamination-free melting, the only contact of the melt with its surroundings being a gaseous atmosphere or, if so desired, a vacuum. Thus it is possible to melt without contamination many high melting point materials that heretofore could not be successfully melted because of reaction with the melting crucible material. This advantage alone might permit the preparation of new substances as glasses if their viscosity is sufficiently high to suppress crystal growth on cooling. In addition, space melting permits cooling without requiring the use of a solid mold. Thus, many of the usual crystal nucleation sites are eliminated. Unless a given material can spontaneously nucleate on cooling, and this requires that a nucleation energy barrier be surmounted, super-cooling below the normal melting point will occur. If a sufficient amount of undercooling is obtained (i.e., below the glass transition temperature) and if the undercooling is accompanied by a sufficient increase in viscosity, crystallization will be avoided entirely, and glass will result. The concept of glassmaking in space is particularly intriguing for the following reasons:

1. There is a strong possibility that oxides such as La_2O_3, Ta_2O_5, Al_2O_3, Y_2O_3, and some of the rare earth oxides can be prepared as glasses in commercially useful sized spherical boules through space melting and cooling.

2. Glasses produced from such oxides or combinations of them with other oxide additions should have optical properties not obtainable in the conventional silicate, borate, and phosphate-based glasses.

3. The combination of optical properties projected for such glasses should make them suitable for use in advanced optical systems.

4. The spherical shape of glass boules that would result naturally from space production is quite suitable for the making of lenses and windows.

5. The production of glass, given a well-engineered space facility, should be well within the capabilities of the astronauts after a suitable brief training period, the more technically and/or skill oriented operations being performed terrestrially before and after flight operations.

6. A well-directed research and development program leading to the production of useful space glasses should yield much valuable scientific information on the nature of glass formation, nucleation theory, etc.

It is envisioned that the process described need not be limited to oxide glasses. Perhaps other compounds such as carbides, nitrides, and chalcogenides will ultimately beocme producible as glasses by space processing.

To date studies of space glasses have by choice been confined to oxide glasses only. It is felt that the applications for such glasses are more readily predictable than for the other materials, and that many of the principles that will evolve from a study of oxide glasses, which can be melted in air, permit a more direct approach to non-oxide materials in the future.

The present paper gives the highlights of experimental work conducted over the past three years leading to the production of useful new optical glasses in space.

EXPERIMENTAL WORK

The experimental work performed to date has been aimed at the ultimate production of new oxide glasses for use in optical systems functioning in the visible portion of the spectrum. Initial work utilized a laser spin-melting technique to produce 100- to 800-micron-diameter spherules under free-fall conditions. Many compositions were prepared in this manner and seven promising compositions were selected for scaling to a 1/4-inch (6 mm) size category. Current work employs the CO_2 laser for melting energy in an attempt to prepare 1/4-inch (6 mm) equivalent spherical diameter glass boules which are suspended on a vertical air column during melting and cooling. The work being conducted currently will be summarized as will the earlier screening studies.

RATIONALE

An Abbe diagram, familiar to lens designers, is shown in Figure 1. The index of refraction in sodium D light is plotted on the ordinate and the Abbe number, an inverse measure of dispersion, is plotted on the abscissa. The higher Abbe numbers to the left of the diagram indicate a low dispersion (i.e., a flatter slope of the index vs. wavelength curve), and the lower Abbe numbers to the right of the diagram have high dispersion, or a steeper index vs. wavelength curve. Approximately 100 years ago the flint glasses were developed. This permitted the designing of the first achromatic, or color-corrected multi-element lenses. Responding to the demands for better and better quality lenses, the optical glass industry developed more glasses with properties between those of the crown and flint glasses. More recently glasses have been developed to fill out the area labeled, "commercial glasses",* in Figure 1. The trend has been to push the area up and to the left and many of the glasses have very complex compositions. It should also be noted that because lens design is an iterative process, isolated glasses with unusual combinations of properties are rarely of any value. The lens design process requires that small shifts in optical properties from those initially selected be available.

If glasses could be prepared from oxides beyond the reach of current technology, the area of useful properties could be more than doubled as is shown in the area labled, "potential space produced glasses", in Figure 1. If the promise of space production can be realized by the preparation of simple compositions with properties falling roughly in the circles marked 1, 2, and 3, it should be possible by combining these compositions, to fill in the areas shown in the figure. Thus, efforts to date have been largely devoted to attempts to prepare simple compositions with glass properties falling roughly within the three circles in Figure 1.

*From the catalogue of Schott Glass, Germany.

The candidate base oxides initially selected for study are as follows:

Class*	Base Oxide
1	Al_2O_3, Ga_2O_3, MgO, $MgAl_2O_4$ (spinel)
2	La_2O_3, Y_2O_3, Yb_2O_3, Gd_2O_3, Lu_2O_3, Sc_2O_3, Sm_2O_3, Dy_2O_3, Nd_2O_3, Bi_2O_3, and PbO
3	Nb_2O_5, Ta_2O_5, ZrO_2, HfO_2, TiO_2, ZnO, CeO_2

Note that all of the oxides shown are white in color (should yield clear glasses) and most of them should be chemically stable in air, thus simplifying experimental operations. As can be seen in Table I, most of them have high melting points, which should result in very high ratiation cooling rates to the glass transition temperature, a consideration which should enhance the probabilities of glass formation.

Table I. Properties of Oxides

Oxide	Approx. Melting Point, C	Approx. Boiling Point, C	Remarks
Al_2O_3	2070	2980	
Ga_2O_3	1800	-	
Gd_2O_3	2330	-	Hygroscopic
HfO_2	2900	~5400(?)	
La_2O_3	2310	4200	Hygroscopic
Lu_2O_3	High	-	
MgO	2850	3600	
Nb_2O_5	1490	-	
Sc_2O_3	> 2405	-	
Sm_2O_3	2350	-	
Ta_2O_5	1870	> 2200	
TiO_2	1845	-	Loses O_2 above 1900 C
Y_2O_3	2410	4300	
Yb_2O_3	2250	-	
ZnO	1970	-	
ZrO_2	2690	4300	

Note: All of the oxides are white or colorless

*As defined by the properties within the three circles of Figure 1.

Additionally, there is another important area of application which these glasses might fill. Space production offers an opportunity to prepare new families of glasses free of the usual base oxides, SiO_2, B_2O_3, and P_2O_5. Noncross-bred glasses should open possibilities for the lens designer for correcting "secondary spectrum". References 1 and 2 cover this subject in more detail.

Table II, which has been abstracted from an applications study performed under subcontract by the Perkin-Elmer Corporation, lists some of the specific types of systems where space glasses might find applications. The reader is referred to Appendix I of Reference 3 for a comprehensive treatment of applications for space glasses.

Table II. Potential Applications for Space-Produced Glasses

Non-Imaging
Host materials for 1.06 micron lasers
Raw materials for coatings
Imaging
Multi-element lenses for high numerical aperture systems
Microscope objectives
Low light level lenses
Long focal length lenses
Multi-element lenses (high n)
Anastigmatic photo objectives
Aplanats
Lower curvature lenses
Zoom
Spectrometers
Monochromators
Polarizing microscopes
High speed, large lenses
High numerical aperture systems
Oil immersion microscope objectives
Fiber optics bundles

SCREENING STUDIES

Glass Preparation Techniques

A 250-watt continuous wave CO_2 laser (Model 41, Coherent Radiation Laboratories, Palo Alto, California) operating at a wavelength of 10.6 micrometers* was used as the heat source. In the early experiments, carried out at

*All oxides of interest are opaque to this wavelength.

the Sandia Laboratories, NaCl windows and a KCl lens of 100 mm focal length were utilized. In the more recent runs made with a similar laser at the Space Division of Rockwell International, gallium arsenide lenses of 6.35 or 12.7 cm focal length were used. The beam was focused downward onto the target, the end of a horizontally positioned ceramic rod.

The technique employed by Nelson, Skaggs and Richardson (Reference 4) was used to produce the glass spherules; this involves rotating a ceramic rod at a known speed of 8,000 to 30,000 rpm with a high-speed drill motor. The face and tip of the spinning rod were then introduced into the laser beam and molten droplets were spun off. These varied in size from about 100 μm to 800 μm depending on the material, the speed of rotation, and the laser beam power density. In the present study, a beam power of 200 to 300 watts and spin speed of 20,000 rpm usually gave an optimum yield. Figure 2 is a time exposure showing a ceramic rod in the process of being spun under the laser beam at about 10,000 rpm. The traces of the ejected molten droplets are clearly visible. The spherules were caught in a large funnel-shaped aluminum foil hopper and collected in a stainless steel tray. The spherules were then transferred into small plastic boxes and were examined microscopically.

Material

Compositions tested are listed in Tables III, IV, and V. With the exception of the lanthana-containing compositions of Table V, all of the compositions contained at least 80 weight percent of the base oxide. Each composition of single or mixed oxides of high purity were uniformly blended, then hot pressed and sintered into rods 2.5 to 5 cm long by 0.3 cm diameter by the Haselden Company, San Jose, California.

Table III. Results of Laser Melting Experiments

Major Constituent	Wt % CaO	Wt % SiO_2	Glass Yield, %*	n_D	Abbe Number
Al_2O_3	0	0	0	-	-
	0	5	<1	1.728	33
	0	10	<1	1.720	36
	0	15	<1	1.634	45
	0	20	1-10	1.629	39
	5	0	<1	-	-
	10	0	<1	1.650	50
	15	0	<1	-	-
	20	0	1-10	1.642	38
	5	5	<1	-	-
	10	5	<1	-	-
	5	10	<1	-	-
	10	10	<1	1.632	37

Table III. Results of Laser Melting Experiments (Continued)

Major Constituent	Wt % CaO	Wt % SiO_2	Glass Yield, %*	n_D	Abbe Number
La_2O_3	0	0	~10	2.2±0.1	-
	0	5	< 1	-	-
	0	10	< 1	-	-
	0	20	< 1	-	-
	5	0	< 1	-	-
	10	0	~ 1	>2.1	-
	5	5	< 1	-	-
	10	10	< 1	-	-
	20	0	< 1	-	-
ZrO_2	0	0	0	-	-
	0	5	0	-	-
	0	10	< 1	-	-
	0	20	< 1	-	-
	10	0	0	-	-
	20	0	0	-	-
	10	10	< 1	1.89	-
HfO_2	0	0	0	-	-
	0	5	0	-	-
	5	10	0	-	-
	0	15	0	-	-
	5	0	0	-	-
	10	0	0	-	-
	15	0	< 1	-	-
	0	20	0	-	-
	20	0	0	-	-
	5	5	0	-	-
	5	10	0	-	-
	10	5	0	-	-
	10	10	0	-	-
Nb_2O_5	0	5	< 1	2.19	-
	0	10	< 1	-	-
	0	15	< 1	-	-
	0	20	< 1	2.11	-
	5	0	< 1	-	-
	10	0	< 1	2.23	-
	15	0	30	2.19	30
	20	0	>10	2.13	-
	5	5	0	-	-
	10	5	>10	2.18	-
	5	10	< 1	-	-
	10	10	< 1	2.16	-

Table III. Results of Laser Melting Experiments (Continued)

Major Constituent	Wt % CaO	Wt% SiO_2	Glass Yield, %*	n_D	Abbe Number
Ta_2O_5	0	0	0	-	-
	0	5	< 1	-	-
	0	10	< 1	-	-
	0	15	< 1	2.04	-
	0	20	< 1	-	-
	5	0	< 1	-	-
	10	0	>10	2.12	15
	15	0	< 1	2.05	-
	20	0	< 1	1.95	21-25
	5	5	1-10	2.07	-
	10	5	< 1	2.03	-
	5	10	< 1	2.05	-
	10	10	>10	1.97	-
MgO	0	0	0	-	-
$MgO.Al_2O_3$	0	0	0	-	-
ZnO	0	0	0	-	-
Ga_2O_3	0	0	< 2	1.91	25
	10	0	< 1	1.852	25
	20	0	~10	1.794	25
In_2O_3	20	0	< 5	1.98(2.18)	-
TiO_2	0	0	0	-	-
Ta_2O_5	10	0	0	-	-
	10	0	0	-	-
	20	0	0	-	-
WO_3	0	0	0	-	-

*Average yield for several runs
a. ZnO added instead of CaO
b. BaO added instead of CaO

Table IV. Results of Laser Melting Experiments - Lanthanides

Major Constituent	Wt % CaO	Glass Yield, %	n_D	Abbe Number
Sc_2O_3	-	< 1	1.920	18
Sc_2O_3	10	0	-	-
Sc_2O_3	20	0	-	-
Y_2O_3	-	>10	1.920	25
Y_2O_3	10	>10	1.920(?)	-
Y_2O_3	20	<10	1.920(?)	-
Y_2O_3	10[a]	< 1	1.920(?)	-
Sm_2O_3	-	>10	2.12	-
Sm_2O_3	10	<10	2.04	-
Sm_2O_3	20	< 1	-	-
Gd_2O_3	-	>10	2.09	-
Gd_2O_3	10	<10	2.07	-
Gd_2O_3	20	< 2	-	-
Yb_2O_3	-	>10	1.938	25
Lu_2O_3	-	< 1	1.933	23
Lu_2O_3	10	< 1	1.920	23
Lu_2O_3	20	0	-	-

a. BaO substituted for CaO

Table V. Results of Laser Melting of La_2O_3 With Other Glass Formers

Other Constituents (B)	Wt % B	Glass Yield, %	n_D	Abbe Number
Y_2O_3	25	< 1	2.1	-
Y_2O_3	50	< 1	2.09	-
Y_2O_3	75	< 1	2.10	-
Yb_2O_3	25	<10	2.10	-
Yb_2O_3	50	<10	2.09	-
Yb_2O_3	75	<10	2.07	-
Nb_2O_5	25	<10	2.18	-
Nb_2O_5	50	>10	2.20	-
Nb_2O_5	75	>10	2.18	-
Ta_2O_5	25	<10	2.18	-
Ta_2O_5	50	~50	2.13	-
Ta_2O_5	75	>50	2.16	-
Al_2O_3 + CaO	40 + 20	<10	1.85	50
Ga_2O_3 + CaO	40 + 20	10	1.88	30

Optical Properties

The optical properties shown in Tables IiI, IV, and V were measured, using techniques which were described in detail in References 5, 6, or 7. Abbe numbers could be obtained for only a few compositions and these should be viewed "cum grano salis" because the refractive indices could be measured to no more than two figures to the right of the decimal in such small samples.

Approximately one hundred spherules of each of the compositions tested were collected. A large variety of samples was obtained ranging from those which were obviously crystalline to clear, smooth spherules. The clear, spherical (or ellipsoidal in one system), smooth-surfaced specimens were invariably glass. Clear spherules with a fairly smooth surface having some irregularities generally had a glass interior and a crystalline surface. Translucent spherules were, generally, very finely crystalline and resembled a finely devitrified glass in the microscope. Specimens which had non-spherical, irregular or lumpy surfaces were generally crystalline.

Figures 3 through 6 show four of the compositions that yielded large fractions of glass. Figure 3 is illustrative of the variety of textures obtained with a sample where a large fraction of glass spherules were produced. The textures of the spherules range from clear, smooth glass to milky, translucent micro-crystalline, to opaque white, fine-grained crystalline to relatively coarse-grained, translucent crystalline lumpy spheres. Six of these Ta_2O_5 glass spheres were mounted for microprobe analysis. The compositions were uniform within any given sphere within the precision of the microprobe analysis and the largest difference between spheres was less than 2 percent of the amount of CaO or SiO_2. The Nb_2O_5-CaO system (Figure 4) produced one of the highest yields of good quality glass. The Ga_2O_3 + CaO mixture (Figure 6) is seen to contain numerous bubbles and some ellipsoidal glass forms.

Tables III, IV and V show the experimental results. Many of the spheres were made in at least two separate experiments; others were done once. Separate experiments with a given composition did not always yield the same results, and differences in glass-forming ability shown in the table are not hard and fast. For some compositions, no glass was observed in one experiment and some recovered in another. These were always noted by < 1 percent. Different experimental conditions seemed to lead to different glass forming tendencies. At spin velocities < 25,000 rpm and where > 1 percent glass spherules were produced some where invariably large (i.e., 0.4 - 0.8 mm). Many of the crystalline spherules containing Nb_2O_5 or Ta_2O_5 were colored blue-gray or buff, probably indicating variable valence states. The glasses produced were always water white. The lanthanum oxide and indium oxide formed light brown to orange to colorless crystalline spherules and it is possible that suboxide formation is the cause of the color. Again, the glasses were always colorless. Further, the glassy La_2O_3 spherules between crossed nicols usually showed some microcrystalline phases to be present. The La_2O_3 spherules deteriorated to a powder after several hours in air. X-ray analysis of the white powder showed the presence of hydroxide. Another

interesting point with lanthanum oxide is that the glass yield decreased as CaO was added, in contrast to the effect with virtually all the other oxides where glass-forming ability increased with added CaO.

When BaO or ZnO was substituted for CaO with Ta_2O_5, a good glass-forming oxide, no glass was formed. Specificity or ionic size as well as composition may be important here. The volatility of ZnO and WO_3 makes their use as glass formers under the present conditions very difficult. Mixing these with CaO may aid glass formation. The TiO_2 yielded mainly dark opague material but also some light matter. This suggests that different valence states of Ti are present. Note that TiO_2 starts losing oxygen just above the melting point.

The index of refraction n_D at 589 mu and the Abbe number ν, an inverse measure of the dispersion, of all the glasses measured in this study are also reported in Tables III, IV and V. However, sample yield, stability (for La_2O_3), and time did not permit Abbe number measurements on all of the glasses produced.

The index of refraction of La_2O_3 was uniquely difficult to measure, presumably due to its instability to moisture. The two values found for indium oxide suggest the higher value was due to either a lower-valent indium oxide or some contamination by another system, e.g., Nb_2O_5 + 15% CaO. Similar high values were also found in some samples of Ga_2O_3 + 20% CaO. Emission spectroscopic analysis of a group of about 50 of the Ga_2O_3 glass spheres showed that high Nb_2O_5 concentrations were present. Since the Nb_2O_5-CaO compositions were run just before the In_2O_3-CaO and Ga_2O_3-CaO, cross contamination appears to have occurred.

It should also be noted that it is not possible to superheat* the material during the spin melting operation - the material being ejected as soon as it becomes molten, or partially molten in the case of compositions with a significant freezing range. This suggests the distinct possibility that some compositions that did not show good glass-forming tendencies in the spin melting experiments may still be rendered glass formers under more controlled conditions where superheating can be incorporated in the cycle. Theoretically a superheating temperature of 200 C* above the crystalline melting temperature (liquidus) is desirable in order to insure digestion of residual nuclei from the crystalline starting material. It is hoped that the techniques being developed as described in the following section will permit controlled superheating.

EXPERIMENTS LEADING TO THE PREPARATION OF 1/4-INCH-DIAMETER GLASS SAMPLES

Under contract NAS 8-28991, which was awarded in May 1973, techniques are being developed which, it is hoped, will enable the preparation of glass samples in the 1/4-inch-size class. While the contract is not yet complete, some success has been achieved. The balance of this paper describes the approach taken and the preliminary results achieved to date.

---

*Digestion of nuclei is, of course, time as well as temperature dependent. For fast-cycle operations such as these ground simulated experiments, 200 C seems a reasonable temperature.

Initially, two approaches were considered for the containerless preparation of 1/4-inch-size glass samples. One was to construct a drop tower where a long-focussed CO_2 laser beam would be directed vertically to the top of the tower where the end of a ceramic rod of the desired composition would be melted by the laser beam - the molten drop falling down the beam to superheat it. A light sensing device would trigger a mechanism to remove the vertical-directing mirror. This would start the cooling cycle and provide clearance for the falling drop after which it would descend into a vertical well shaft for the balance of the cooling cycle.

The second approach, which has been investigated actively in the present study, consists essentially of suspending the molten drop of oxide on a vertical column of air, heating being accomplished by directing a focussed CO_2 laser horizontally onto the drop of molten oxide.

Wind Tunnel

A significant portion of the research effort to date has been concerned with the development of a vertical wind tunnel capable of suspending both solids and liquids. The first tunnel built was a simple one constructed according to the description given in Reference 8. The referenced tunnel was used for suspending water drops of 0.9-cm diameter for rain drop studies. The first tunnel contained a small amount of turbulence at the exit but was capable of suspending 1/4-inch-spherical diameter water drops as constructed. Unfortunately, the drops in suspension were in a continual state of motion. Of equal significance, it was impossible to hold solids of any shape in the tunnel (with the exception of a ping pong ball). After numerous attempts to improve matters, it was decided to rebuild the wind tunnel following modern wind tunnel design practices as closely as possible.

The final tunnel is shown in Figure 7. A 2-foot square wooden box which served as a plenum chamber has a shrouded circular hole approximately 14 inches in diameter in the side away from the camera. The squirrel cage blower of the original tunnel was replaced with a 14-inch 4-bladed propeller of maple (made from a pair of 2-bladed model airplane propellers). The propeller is mounted flush in the hole in the box and is driven by a one horsepower d-c motor equipped with a generator/feed back loop to maintain constant speed regardless of line voltage fluctuations. A control head (under one of the writer's hands in the figure) permits the speed of the motor to be varied continuously over a wide range and is equipped with a vernier control to permit fine adjustments.

The air is exhausted from the plenum chamber into a 6-inch-square parallel section about one-foot long. This section contains three tightly stretched pieces of ordinary window screening to smooth the air flow. Above the screens is a flow straightener consisting of a piece of 3/16-cell-size aluminum honeycomb of one-inch thickness. The latter seemed to be necessary to obtain good laminar flow. Immediately above the parallel section is a reduction section which reduces the air column from 6-inch square to 2-inch square, approximately a nine to one area reduction. Above the reduction section is a removable exit section with a 2-degree expending wall taper.

the top of this section holds a shaped screen to provide a velocity well. About 6 inches above the shaped screen is a back pressure plate which proved to be necessary to obtain suspension. A more detailed treatment of the experimental work with the wind tunnel, including the many ideas that were tried before the final configuration was arrived at, will be given in the final report on this program, and is outside the scope of this paper.

The final tunnel provides good laminar flow and is capable, with the back pressure plate, of suspending water drops as large as 9 mm equivalent spherical diameter as shown in Figure 7. Figure 8 shows a close-up of a water drop in suspension and also provides a better view of the shaped screen. Motions of the suspended drop in the X and Y directions are negligible. Fluctuations in the Z direction are normally within about ± 1 drop diameter of the mean position. However, there are also sporadic Z direction motions where the drop "pops" several inches above its mean position and immediately returns to the mean position. Solid shapes still cannot be suspended in the final tunnel. Additional difficulties were encountered when attempting to suspend molten oxide drops. For example, it was found to be very difficult to detach the molten pool in the end of a starting rod in the air stream. It is quite likely that all of the problems encountered are solvable with enough effort. However, a technique was devised for obtaining the desired stability through the use of a probe rod, to be described later, so that further attempts to solve the problems according to the original conception were abandoned for the time being.

Laser

The CO_2 laser being used is mounted below ground in a tunnel on the site of the Electronics Research Division of Rockwell International in Anaheim, California. It presently emits a raw beam about 3-1/2 inches in diameter and 1500 watts intensity. Figure 9 shows the optical components of the laser beam focussing and directing set-up. The raw beam, which emerges from beyond the lower right-hand corner of the photograph, goes through an NaCl beam splitter and then impinges upon a 45-degree plane gold-plated mirror serving as an optical switch directing the beam to a brick on the wall where the energy is dissipated. The beam splitter directs about 8 percent of the beam energy into a calorimeter (not shown) for continuous monitoring of beam power.

When the optical switch is pulled forward on its track, the beam enters a planoconvex NaCl lens with a focus just before a second planoconvex NaCl lens. The combination of lenses gives a long focus, the beam being reflected vertically from a gold-plated plane mirror on the optical bench to a second mirror (at the top of the photograph). The second plane mirror reflects the beam horizontally across the top of the wind tunnel. This mirror can be rotated by means of a long handle that is provided with stops to limit its motion.

Oxide Melting - Mullite

Rather than continuing to attempt to solve the free-suspension problems, a method of "cheating" was devised to provide the necessary stability for melting oxides and at the same time circumvent the problems with detaching liquid drops from the solid starting rods. Mullite was chosen as the oxide for this portion of the study for the following reasons:

1. It is readily available as electrical/thermal insulation tubes.

2. It is relatively inexpensive.

3. It has a similar melting temperature (about 1850 C) to typical oxides of interest.

4. It has a very low viscosity when molten, similar to that of water. Similar low viscosity above the melting temperature is characteristic of the oxides of interest.

5. It can be classed as a poor glass former; to date the glassy state has been achieved by the authors only when laser melted drops were dropped a short distance into water. The drops were close to 1/4-inch diameter, but were invariably full of fractures resulting from thermal shock. Figure 10 shows a number of drops produced in this manner.

Techniques were devised for transferring molten oxide from the end of laser melted mullite rods to the end of a small (1 to 3 mm) fused silica rod. The fused silica rods were chucked on a slow speed motor and the blob of oxide remelted using the laser beam and air suspension to provide a uniform shape. Figure 11 shows the present melting setup. The laser beam, which was positioned to miss the mullite sample for this photograph, has been rendered visible by sprinkling talcum powder in its path. The talc particles are heated to incandescence by the laser beam. A small d-c motor, in the upper part of the photograph, can be turned on to rotate the sample slowly during melting to provide better heat distribution. The wind tunnel propeller speed is adjusted just short of free suspension velocity, the remaining lift being provided by the silica probe. The purpose of the silica probe is primarily to eliminate the vertical motions in the air-suspended drop. Only a minor portion of the lift is provided by wetting of the probe by the oxide drop. With the silica probe alone, only very small (approximately 2-mm diameter) drops can be held.

A slow motion picture (250 frames/second) was made of the melting and cooling of suspended mullite drops of the 1/4-inch size class. Twenty-four cycles were photographed. The mullite invariably crystallized. The film shows very clearly the nucleation starts and the growth of the crystals from the parent liquid. In only one of the 24 cycles did the mullite appear to crystallize starting near the silica probe. This proved that the silica did not participate in causing crystallization and that its use is justified so far as the objectives of the present study are concerned. The mullite under-

cooled an estimated 650 to 850 C before crystallization commenced. In all but one cycle only one to three crystal starts were observed. The remaining cycle contained four to six starts. From the "jiggling" of the liquid, which can be observed in the film, and the rapid rate of crystal growth, it appears that the viscosity of the mullite did not increase noticeably from the molten state at the beginning of the cycle through the undercooled state before and during crystallization.

Oxide Melting - Glass Candidates

Seven oxide compositions were received recently in the form of hot-pressed 1/4-inch-diameter rods. The seven compositions are as follows:

1. 50 w/o Nb_2O_5 - 50 w/o La_2O_3
2. 75 w/o Nb_2O_5 - 25 w/o La_2O_3
3. 40 w/o La_2O_3 - 40 w/o Al_2O_3 - 20 w/o CaO
4. 75 w/o Ta_2O_3 - 25 w/o La_2O_3
5. 90 w/o Ta_2O_5 - 10 w/o CaO
6. 85 w/o Nb_2O_5 - 15 w/o CaO
7. 80 w/o Ga_2O_3 - 20 w/o Cao

We have succeeded to date in preparing glass samples from two of the compositions. A single sample about 3/16-inch diameter has been obtained from the 50 w/o La_2O_3 - 50 w/o Nb_2O_5 composition. The sample, which fractured on cooling because of differential thermal contraction of it and the silica probe, is shown in Figure 12. The glass is a light amber in color and appears to be free of bubbles or other serious flaws. As of this writing, limited attempts have failed to duplicate the earlier result. It is suspected that difficulties in obtaining high enough superheating temperatures are responsible for the inability to duplicate the result.

Very good quality boules of 1/4 inch or slightly larger diameter have been prepared from the 80 w/o Ga_2O_3 - 20 w/o CaO composition. One such boule is shown in Figure 13. The glass is clear, free of bubbles and cracks, and is light-greenish or bluish-grey in color. The cause of the colors of these two glasses has not been clearly explained as of this writing. They were produced too recently to permit other than visual inspection. Jeevaratnam and Glasser, Reference 9, reported glass formation in the Ga_2O_3 - 20 w/o CaO composition in 1961. However, their samples (20-40 mg) were about 1/50 the mass of the present samples and water quenching was used to obtain the glassy state; air cooling produced crystalline material.

CONCLUSIONS AND FUTURE WORK

The experimental work performed thus far has resulted in the preparation of new glass compositions not reported heretofore in the open literature. Recent experiments which have resulted in the formation of 1/4-inch-diameter glass samples from two compositions, suggest that containerless melting and cooling as envisioned for space operations is of real technological significance.

Future efforts under the present contract will be concerned primarily with attempting to prepare 1/4-inch-diameter glass samples of good quality from the remaining compositions. Techniques will be refined in order to achieve higher temperatures. A spherical reflector has been constructed for reducing radiation losses from the samples and the laser unit is being modified at this writing to provide about 3 to 3-1/2 times the present beam power level. Either or both of these should be helpful for studying the remaining compositions. Toward the end of the contract period it is planned to obtain precision measurements of the Abbe numbers and refractive indices of the best glass-forming compositions.

The compositions being studied are all very simple in terms of traditional glass practices, none of them containing more than three major constituents. Future efforts should be concerned with more complex compositions, both to cover a broader range of optical properties and to enhance glass-forming tendencies.

ACKNOWLEDGEMENTS

The writers wish to acknowledge the support given in the past by the Rockwell International Corporation under its Interdivisional Technology Program (ITP-7). More recent work was supported by the NASA Marshall Space Flight Center under contracts NAS 8-28014 and NAS 8-28991.

The contributions of Dr. Milton Blander, formerly of the Rockwell International Science Center, are gratefully acknowledged. Dr. Blander and Dr. Topol performed most of the earlier experimental work assisted by Dennis Hengstenberg of the Science Center.

The concept of laser spin-melting was developed by Dr. Lloyd Nelson of the Sandia Corporation, Albuquerque, New Mexico. Some of the earlier work was performed in his laboratory with his help. The melting at the Space Division was performed by Floyd Yerian.

An applications study, the findings which are summarized in Table II, was performed under subcontract by the Perkin-Elmer Corporation, Norwalk, Connecticut, under the direction of Walter Augustyn.

The current work employed the tunnel laser unit located at the Electronics Research Division, Rockwell International, Anaheim, California. Melting operations have been performed by R.A. Happe. The wind tunnel was constructed at the Science Center by Bob Sullivan of the Atomics International Division of Rockwell International. The assistance of Mr. Bain Dayman, Jet Propulsion Laboratory, Pasadena, California and Dr. N. Malmuth of the Rockwell International Science Center, in the design of the wind tunnel is gratefully acknowledged.

REFERENCES

1. Happe, R.A. "Implications of Zero Gravity for Producing New Glasses in Space" J. Non-Crystalline Solids 3, 4 (1970) 375.

2. Brewster, G.F., J. R. Hensler, J. L. Rood and R.A. Weidel."Partial Dispersion Ratios of Some New Borate and Phosphate Glasses" Appl. Opt. 5 (1966) 1891.

3. Happe, R.A., Principal Investigator. Final Report, Contract NAS8-38014, "Study of the Preparation of Unique New Glasses" SD72-SA-0083.

4. Nelson, L.S., S.R. Skaggs, and N.L. Richardson."Spheroidization of Refractory Oxides with a Carbon Dioxide Laser" J. Am. Ceram. Soc. 53, (1970) 115.

5. Topol, L.E., et al. "Formation of New Oxide Glasses by Laser Spin Melting and Free Fall Cooling" J. Non-Crystalline Solids, 12 (1973) 377.

6. Topol, L.E. and R.A. Happe. "Formation of New Lanthanide Oxide Glasses by Laser Spin-Melting and Free Fall Cooling" J. Non-Crystalline Solids (to be published).

7. Happe, R.A. and L.E. Topol. "Experiments Leading to the Production of New Glasses in Space" AIAA Paper No. 74-159, presented at the AIAA 12th Aerospace Sciences Meeting, Feb. 1, 1974.

8. Blanchard, D.C. "Experiments with Water Drops and the Interaction Between Them at Terminal Velocity in Air" General Electric Research Laboratory Occasional Report Number 17, Project Cirrus, RL-285, 15 December 1949.

9. Jeevaratnam, J. and F.P. Glasser."The System $CaO-Ga_2O_3$" J. Am. Ceram. Soc. 44 (1961) 564.

SELECTED BIBLIOGRAPHY

SPACE GLASSES

Happe, R.A. "Possibilities for Producing New Glasses in Space" Space Processing and Manufacturing. ME 69-1 NASA/MSFC (p. 146) Oct. 21, 1969.

Deeg, E.W. "Glass Preparation in Space" Space Processing and Manufacturing. ME 69-1 NASA/MSFC (p. 41) Oct. 21, 1969.

Frost, R.T. "Weightless, Containerless Melting and Solidification of Potential New Metal and Ceramic Products." Space Processing and Manufacturing. ME 69-1 NASA/MSFC (p. 115) Oct. 21, 1969.

Happe, R.A. "Possibilities for Producing New Glasses in Space" Technical Report SD 69-394, Space Division, North American Rockwell.

Happe, R.A. "Implications of Zero Gravity for Producing New Glasses in Space" J. Non-Crystalline Solids 3, 4 (1970) 375.

Happe, R.A., Principal Investigator. Final Report, Contract NAS8-38014, "Study of the Preparation of Unique New Glasses". SD72-SA-0083.

Topol, L.E., et al. "Formation of New Oxide Glasses by Laser Spin Melting and Free Fall Cooling" J. Non-Crystalline Solids, 12 (1973) 377.

Topol, L.E. and R.A. Happe. "Formation of New Lanthanide Oxide Glasses by Laser Spin-Melting and Free Fall Cooling" J. Non-Crystalline Solids (to be published).

Happe, R.A. and L.E. Topol. "Experiments Leading to the Production of New Glasses in Space" AIAA Paper No. 74-159, presented at the AIAA 12th Aerospace Sciences Meeting, Feb. 1, 1974.

Topol, L.E. and R.A. Happe. "Preparation of New Oxide Glasses by Laser Melting." Technical Report SD74-SA-0022, Space Division, Rockwell International Corp.

GLASS FORMATION AND NUCLEATION THEORY

Happe, R.A. "The Glass Formation Regions of Oxide Mixtures Based on the Oxides of Aluminum, Cerium, Lanthanum, Magnesium, Niobium, Tantalum, Titanium, Zinc, and Zirconium (Hafnium)." Technical Report SD74-SA-0021, Space Division, Rockwell International. (This is a literature search compiled in early 1971 and contains listings of glass formation regions for the above oxide systems from the open literature with emphasis on the period 1965-1970. The Japanese literature was searched for the period 1960-1970. There are 121 references cited.)

Rawson, H. Inorganic Glass Forming Systems. Academic Press 1967. Weyl and Marboe. The Constitution of Glasses - Vol. II, Part 1, Interscience 1964.

Jeevaratnam, J. and F.P. Glasser "The System CaO-Ga_2O_3" J. Am. Ceram. Soc. 44 (1961) 564.

Turnbull, D. "Under What Conditions Can a Glass be Formed?" Contemp. Phys. 10, 5 (1969) 473.

Katz, J.L., Saltzburg, H. and Reiss, H. "Nucleation in Associated Vapors," Jnl. Colloidal Interface Science 21 (1966) 560.

Katz, J.L. and Ostermier, B.J. "Diffusion Cloud-Chamber Investigation of Homogeneous Nucleation." Jnl. Chem. Phys. 47, (1967) 478.

Shand, E.B. Glass Engineering Handbook McGraw-Hill 1958

Dietz, E.D. "The Glassy State." International Science and Technology Conover-Mast (Nov. 1968).

Worrall, A.J. "Materials for Infrared Optics." Infrared Physics, Vol. 8 Pergamon (London) 1968 p. 49.

Hilton, A.R. "Nonoxide Chalcogenide Glasses as Infrared Optical Materials." Appl. Opt. 5 (1966) 1877.

Duwez. P. "Structure and Properties of Alloys Rapidly Quenched from the Liquid State." Trans. of the ASM 60 (1967) 606.

Neely, J.E. and F.M. Ernsberger. "Absence of Devitrification at Bubble Surfaces in Soda-Lime Glasses." Jnl. Am. Ceram. Soc. 49 (1966) 396.

Levine, H.S. "Formation of Vapor Nuclei in High Temperature Melts." Jnl. Phys. Chem. 76 (1972) 2609.

Levine, H.S. "On the Initiation Mechanicam for Explosion During Combustion of Metal Droplets." High Temp. Sc. 3 (1971) 237.

Levine, H.S. "Homogeneous Nucleation of CO Bubbles in Fe-C-O Melts." Met. Trans 4 (1973) 779.

OPTICAL PROPERTIES

Dietz, E.D. "The Glassy State." International Science and Technology, Conover-Mast (Nov. 1968).

Dana, Systems of Mineralogy, 7th Ed. Wiley 1944.

Hass, G. and E. Ritter. Jnl. Vac. Sc. Tech. 4 (1967) 71.

Loc, V., A. Anthony, and R. Bouaziz. Compte Rendus, Academy of Science of Paris 262 Ser. b (1966).

Smakula, A. "Physical Properties of Optical Crystals with Special Reference to the Infrared." Office of Technology Services, U.S. Dept. of Commerce (Oct. 1952).

Matovilov, O.A. "Optical Properties of Sputtered Multilayer Dielectric Mirrors." Soviet Jnl. Opt. Tech. 34, 5 (1967) 595.

Larsen, E.S. and H. Berman. The Microscopic Determination of Nonopaque Materials. 2nd Ed. U.S. Dept. of Interior Bull. 848 (1944).

Brewster, G.F., J.R. Hensler, J.L. Rood and R.A. Weidel, "Partial Dispersion Ratios of Some New Borate and Phosphate Glasses" Appl. Opt. 5 (1966) 1891.

AIR SUSPENSION

Blanchard, D.C. "Experiments with Water Drops and the Interaction Between Them at Terminal Velocity in Air" General Electric Research Laboratory Occasional Report Number 17, Project Cirrus, RL-285, 15 December 1949.

Blanchard, D.C. "The Behavior of Water Drops at Terminal Velocity in Air." Trans. Am. Geophys. Union 31 (1950) 836.

Cotton, W.R. and N.R. Gokhale. "Collision, Coalescence, and Breakup of Large Water Drops in a Vertical Wind Tunnel." Jnl. Geophys. Res. 72 (1967) 4041.

Pruppacher, H.R. and K.V. Beard. "A Wind Tunnel Investigation of the Internal Circulation and Shape of Water Drops Falling at Terminal Velocity in Air." Quart. J.R. Met. Soc. 96 (1970) 247.

Garner, F.H. and D.A. Lihou. "Mass Transfer to and from Drops in Gaseous Streams." Dechema-Monographien 55 (1964) 955.

Garner, F.H. and P. Kendrick. "Mass Transfer to Drops of Liquid Suspended in a Gas Stream--Part T - A Wind Tunnel for the Study of Individual Liquid Drops." Trans. Instn. Chem. Engrs. 37 (1959).

Maybank, J. and G.K. Briosi. "A Vertical Wind Tunnel" Suffield Technical Paper No. 202 (December 18, 1961).

Blanchard, D.C. Artificial Simulation of Rain. edited by H. Weickmann and W. Smith, Pergamon Press, N.Y. (1955) 233.

Livesey, J.L. and E.M. Laws. "Flow Through Non-uniform Gauze Screens." J. Fluid Mech. 59, pt. 4 (1973) 737.

RELATED SUBJECTS

Nelson, L.S., M. Blander, S.R. Skaggs, and K. Keil. "Use of a CO_2 Laser to Prepare Chondrule-Like Spherules from Supercooled Molten Oxide and Silicate Droplets." Earth and Planetary Science Letters 14 (1972) 338.

Nelson, L.S. "Extreme Temperature Studies with Droplets of Molten Refractory Materials." High Temperature Technology, Proceedings of the 3rd International Symposium (1967) 565.

Nelson, L.S., S.R. Skaggs, and N.L. Richardson, "Spheroidization of Refractory Oxides with a Carbon Dioxide Laser." J. Am. Ceram. Soc. 53, 2 (1970) 115.

Nelson, L.S., N.L. Richardson, K. Keil, and S.R. Skaggs. "Effects of Oxygen and Argon Atmospheres on Pendant Drops of Aluminum Oxide Melted with Carbon Dioxide Laser Radiation." High Temp. Sc. 5 (1973) 138.

Nelson, L.S. "CO_2 Laser Enhances Study of Materials." Ceramic Age (Nov. 1970).

Nelson, L.S. and H.S. Levine. "Correlation Between Conservation of Metal and Luminosity of a Zirconium Droplet During Free-Fall Combustion in Oxygen." High Temp. Sc. 1, 2 (1969) 163.

Nelson, L.S., H.S. Levine, D.E. Rosner, and S.C. Kurzius. "The Combustion of Zirconium Droplets in Oxygen/Rare Gas Mixtures." High Temp. Sc. 2, 4 (1970) 343.

Keil, K., Prinz, M. Planner, H.N., Skaggs, S.R., Dowty, E., Nelson, L.S., Richardson, N.L., and Blander, M. "A Qualitative Comparison of Textures in Lunar Chrondrules and CO_2 Laser-Formed Synthetic Chrondrule-Like Spherules." Special Publ. No. 7, University of New Mexico Institute of Meteoritics (1973).

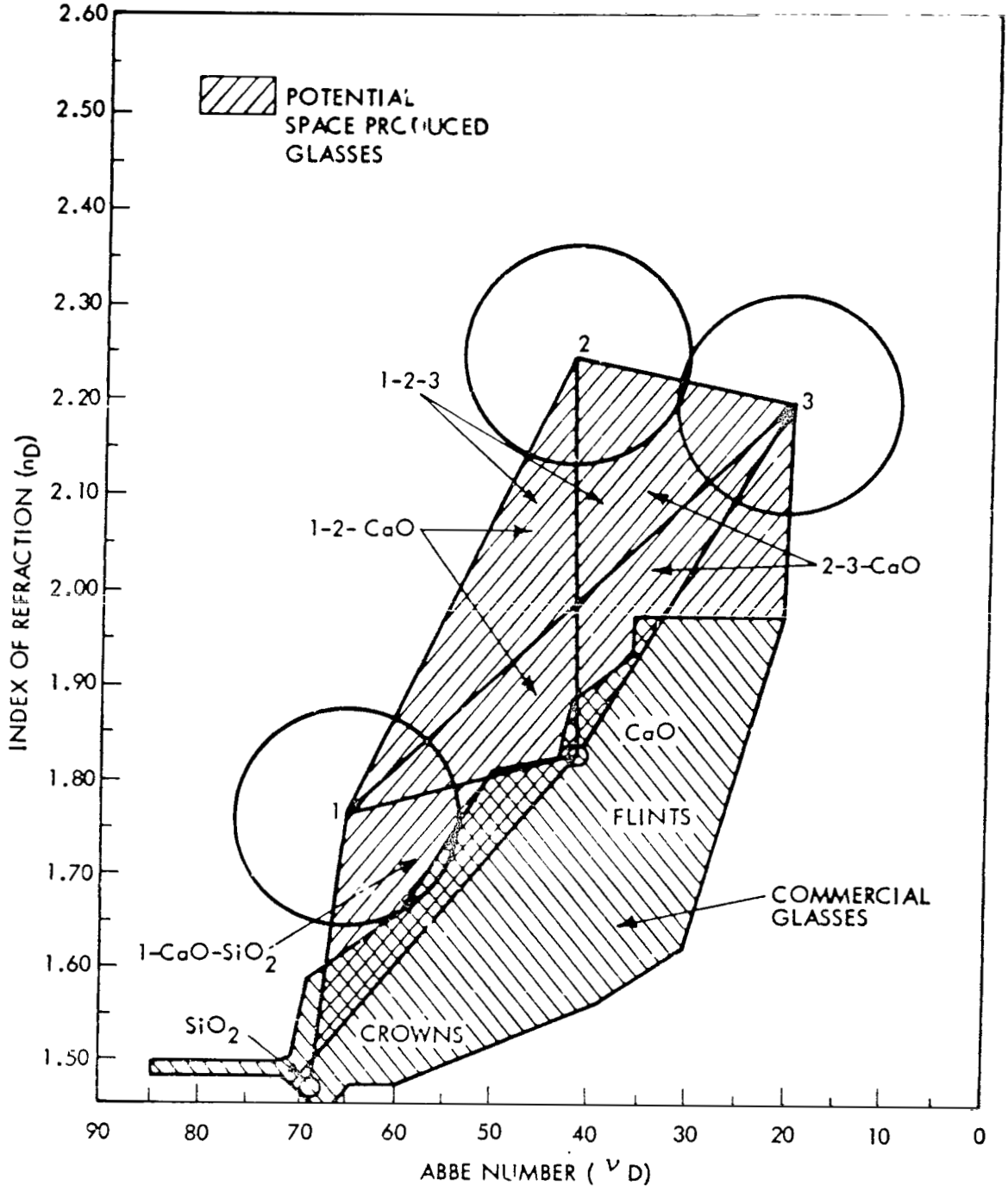

FIG. 1 POTENTIAL SPACE-PRODUCED GLASSES

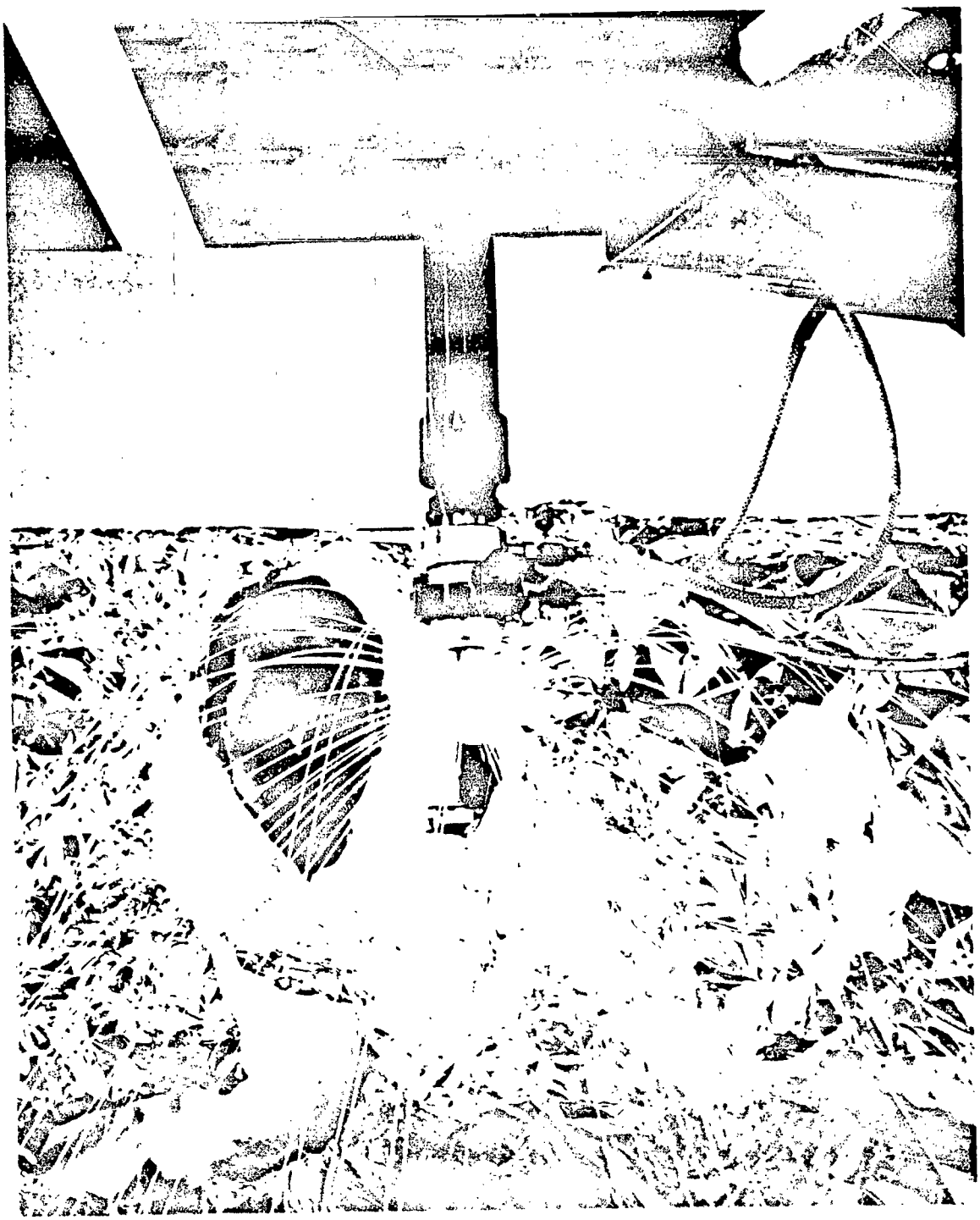

FIG. 2 CERAMIC ROD BEING SPUN MELTED

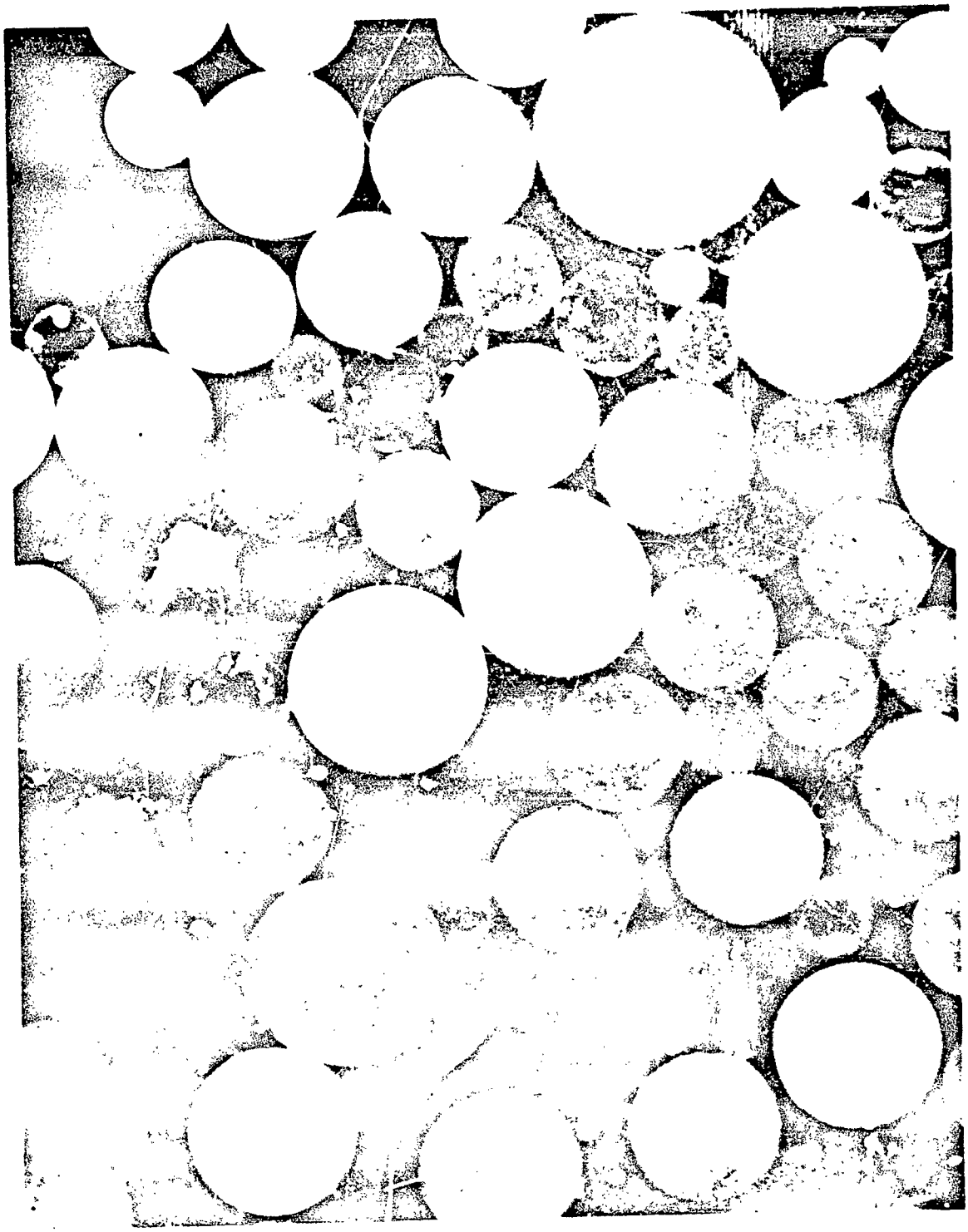

FIG. 3 [illegible] SiO_2 SPHERULES

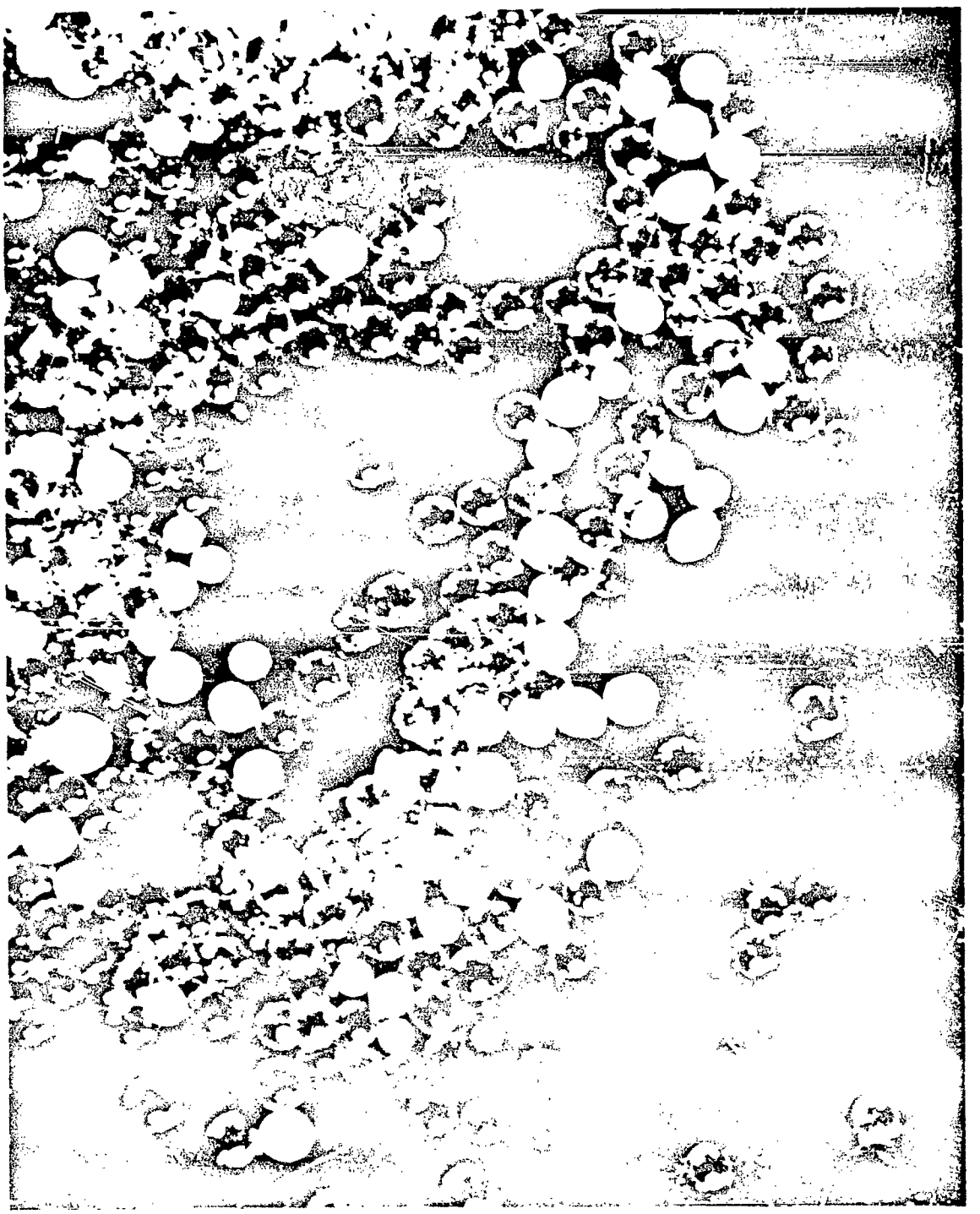

FIG. 4

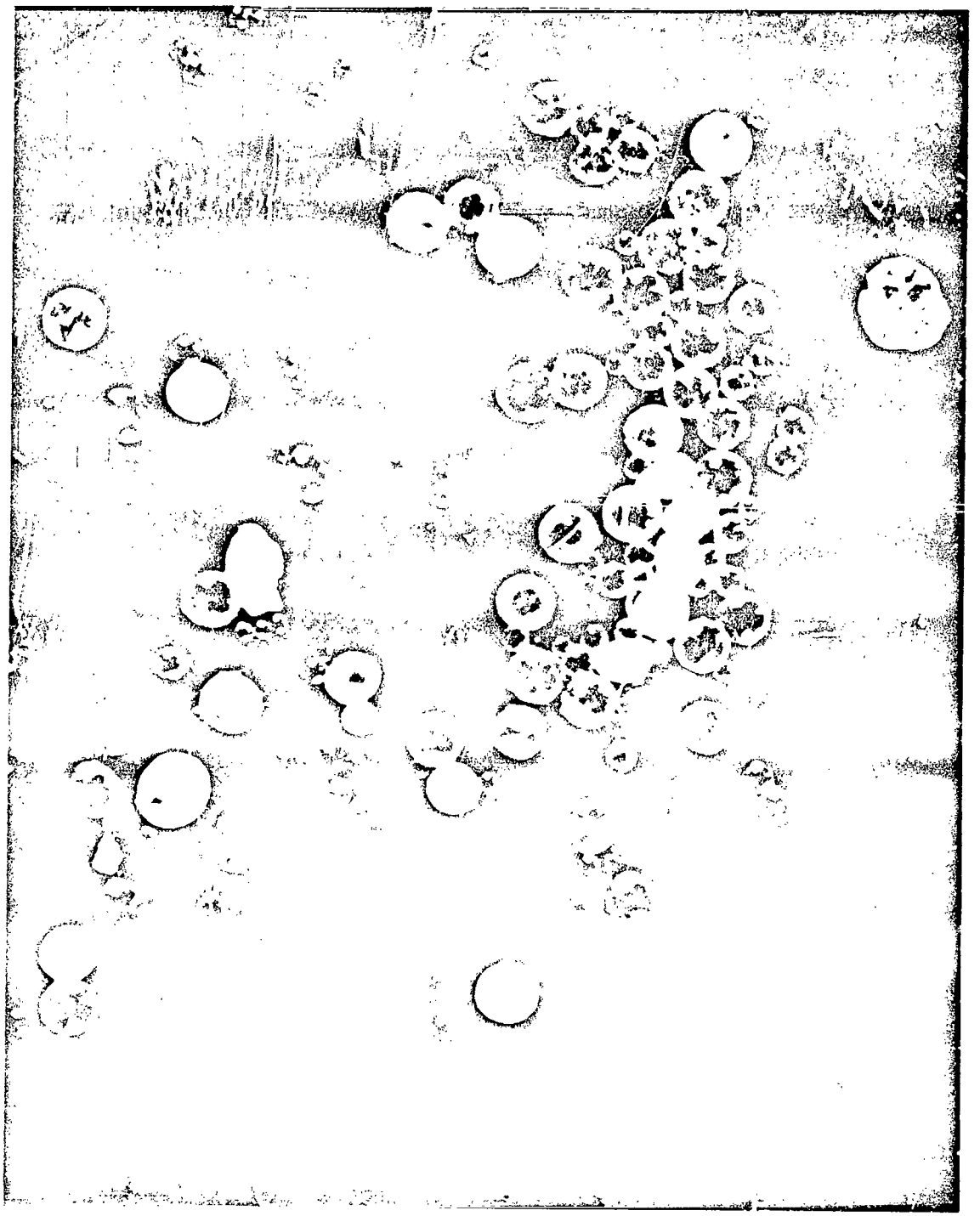

FIG. 5 Fe_2O_3 SPHERULES

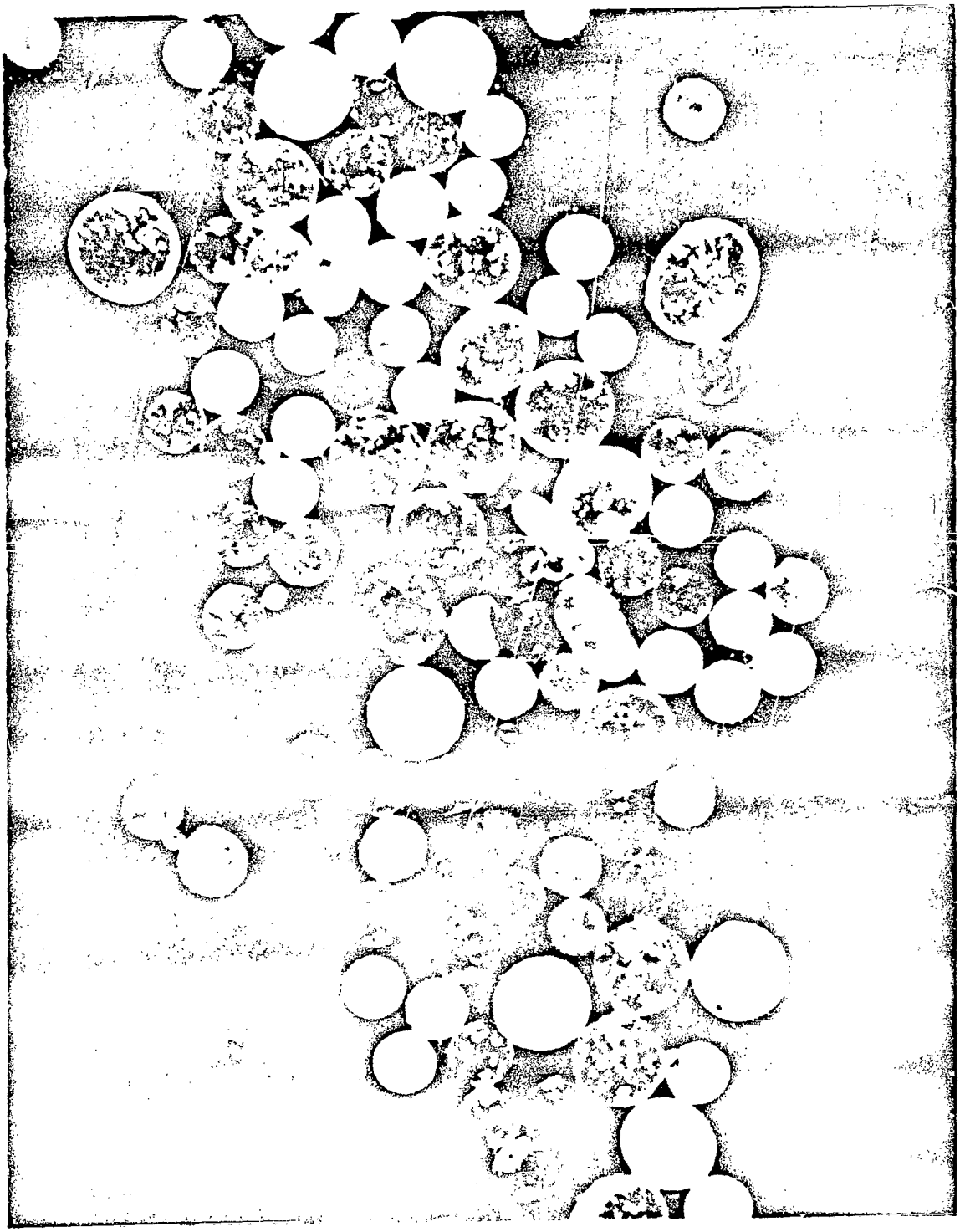

FIG. 6 Ga_2O_3 + 20 Wt % CaO SPHERULES

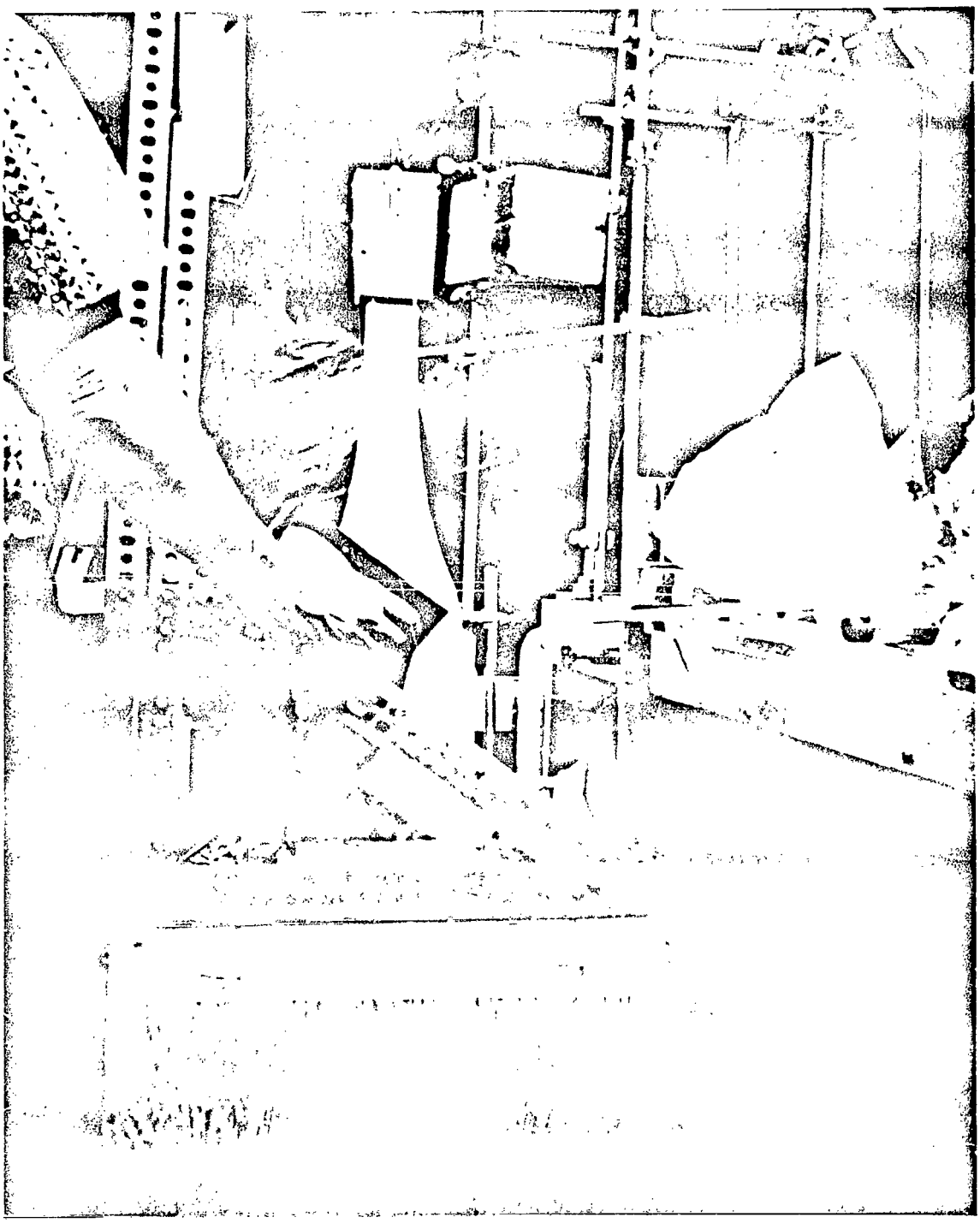

FIG. 7 VERTICAL WIND TUNNEL

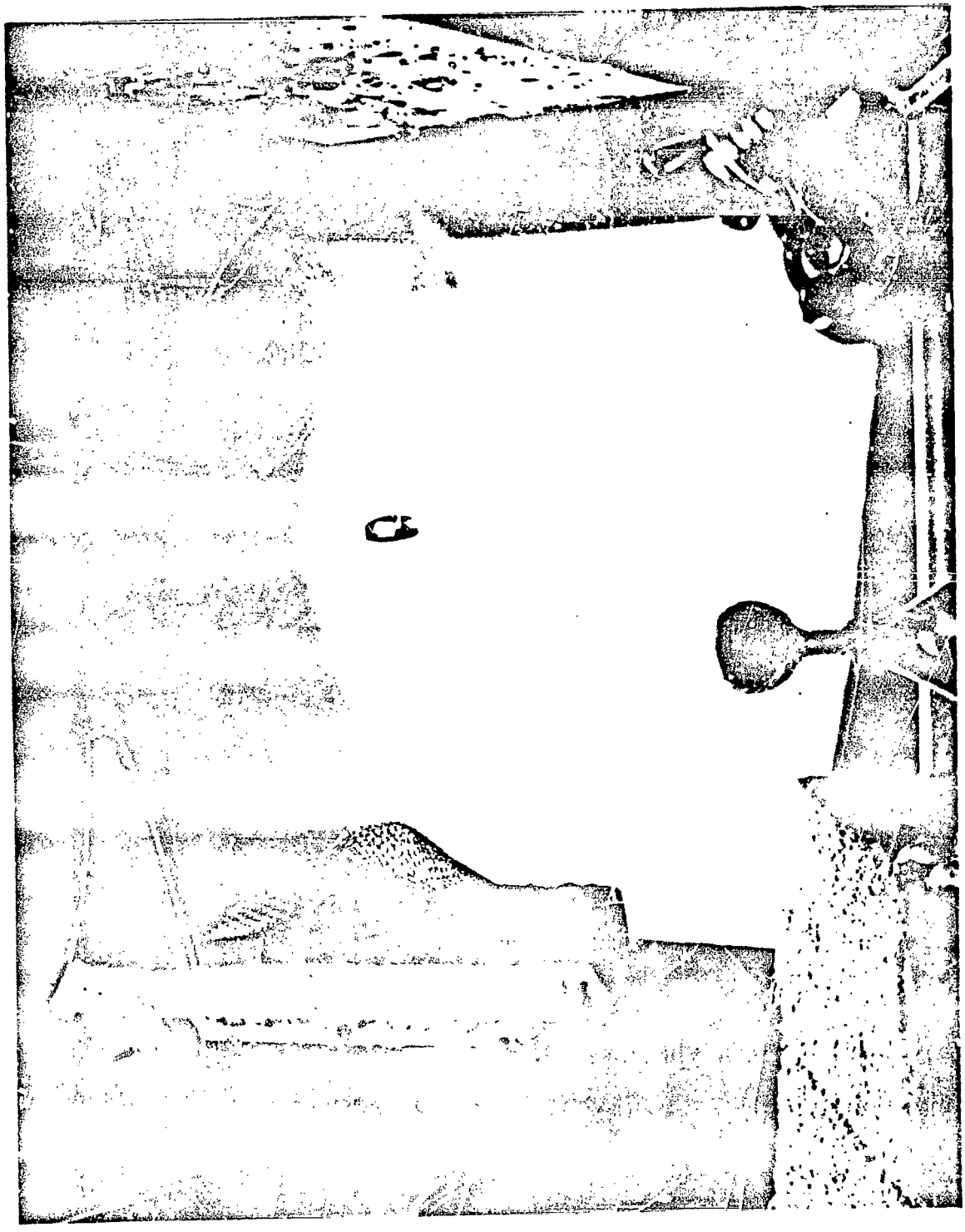

FIG. 8 WATER DROP IN SUSPENSION

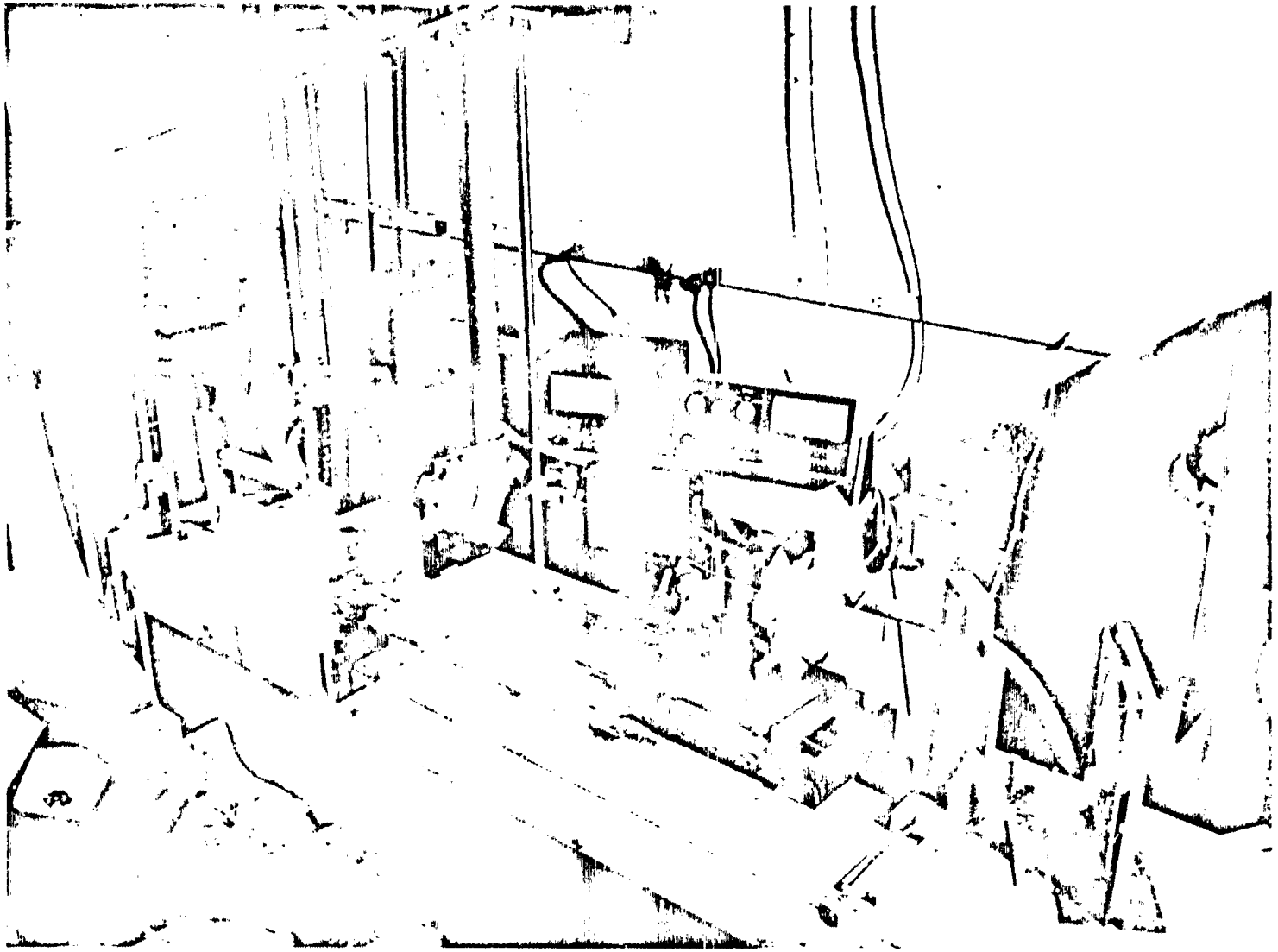

FIG. 9 OPTICAL BENCH FOR FOCUSING AND DIRECTING LASER BEAM

FIG. 10 MULLITE GLASS SAMPLES

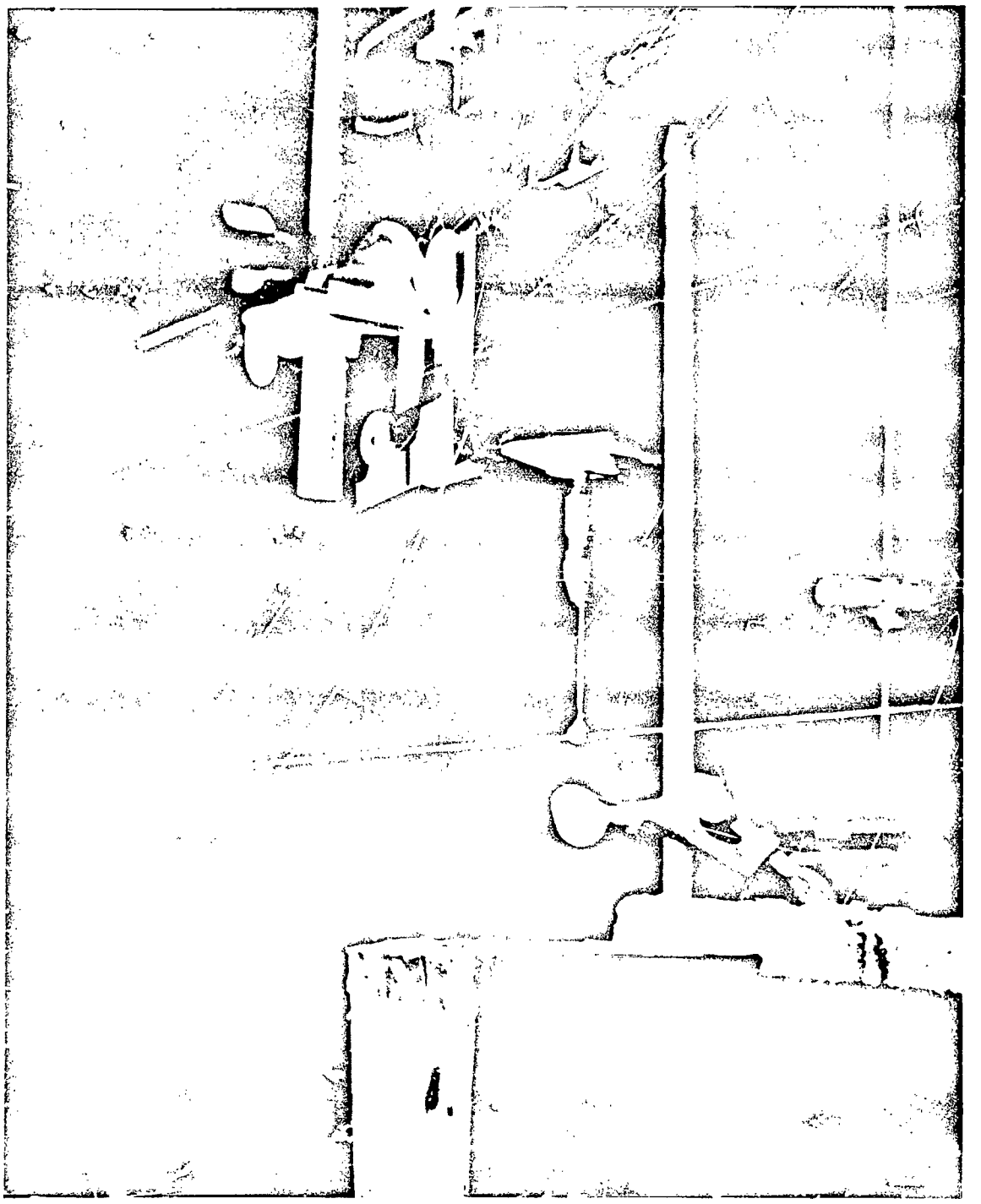

FIG. 11 SETUP FOR MELTING OXIDES

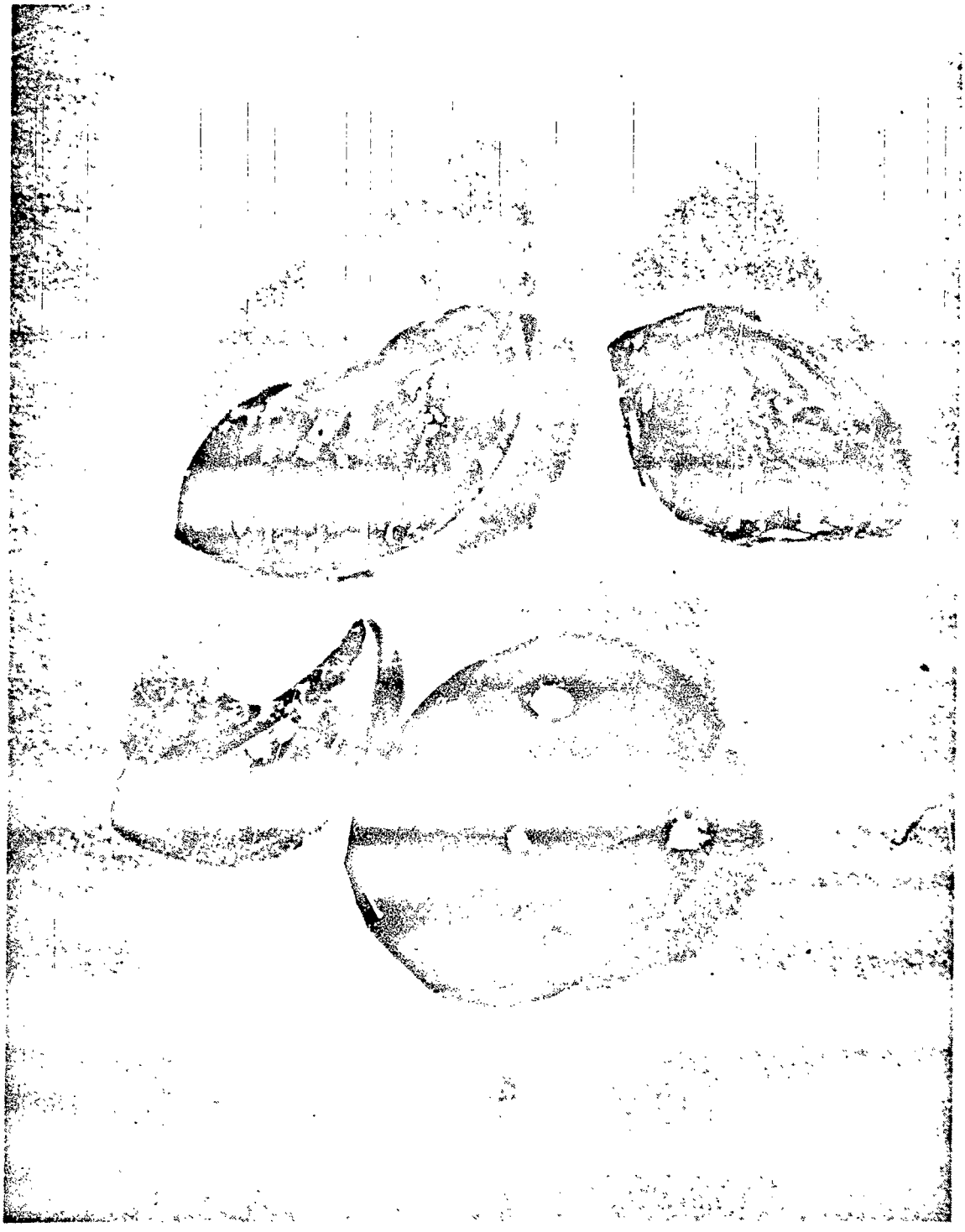

FIG. 12 50 W/O La_2O_3 - 50 W/O Nb_2O_5 GLASS SAMPLE

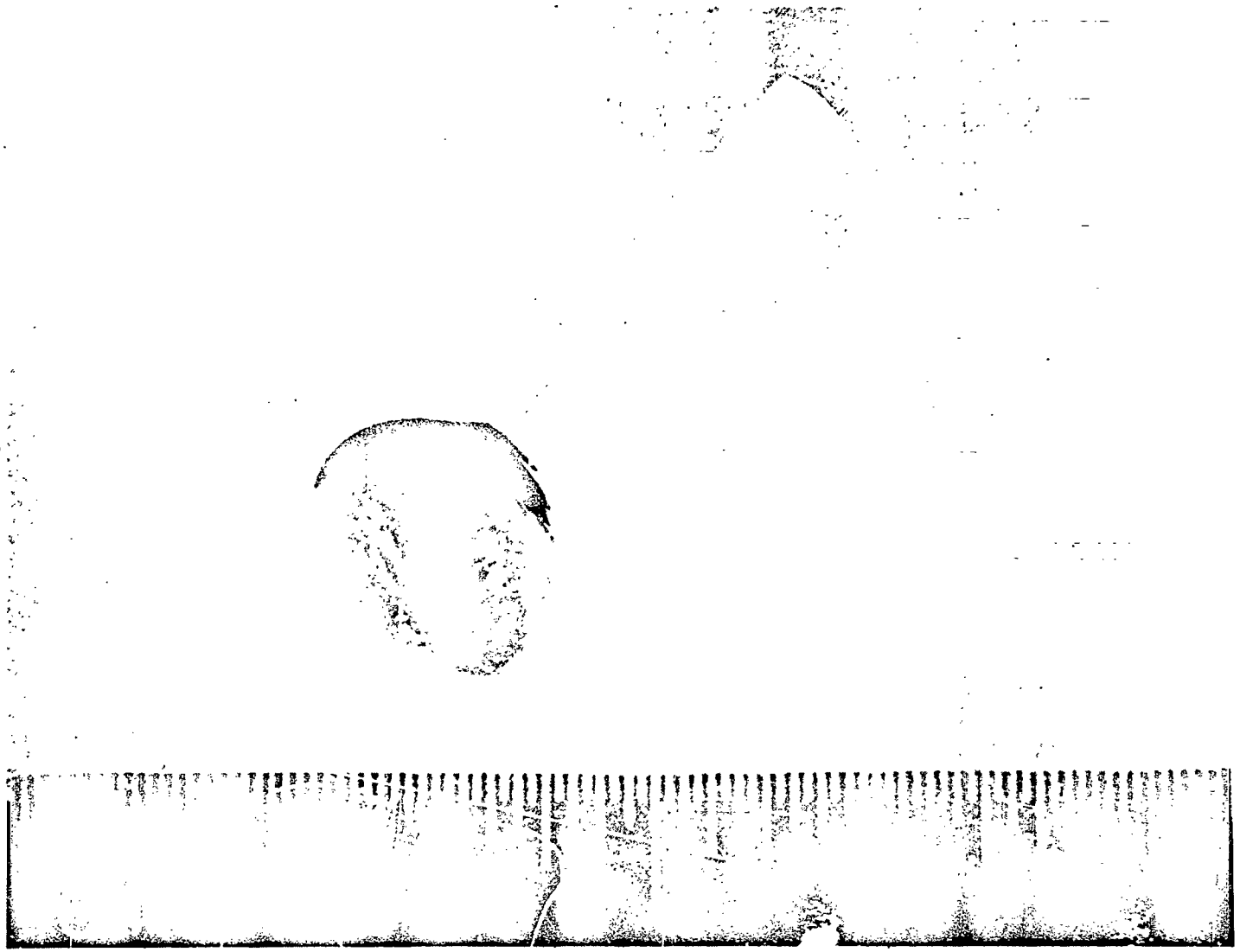

FIG. 13 80 W/O Ca_2O_3 - 20 W/O CaO GLASS SAMPLE

SPACE PROCESSING OF CHALCOGENIDE GLASSES

N74 29920

By

D. C. Larsen, M. A. Ali, W. B. Crandall*
IIT Research Institute
Chicago, Illinois 60616

SUMMARY

Manufacture of chalcogenide glasses in space will eliminate many of the causes of optical non-homogeneity and contamination that are inherent in earth-bound manufacture. A program is outlined to demonstrate the feasibility of various techniques and processes that will be utilized to manufacture chalcogenide glasses in space. Amorphous character, purity, and homogeneity parameters are being investigated at various stages of the glass forming process. These parameters in merit index form will serve to provide guidelines for the design of the actual melting experiment in space, and for the optimization of the exact chalcogenide composition to be included in the space experiments.

INTRODUCTION

Chalcogenide glasses have been found to be relatively good infrared transmitters and to possess good strength, corrosion resistance, and scale-up potential as compared to competing systems. The present disadvantages of earth manufactured chalcogenide systems have to do with optical non-homogeneity and environmental and container contamination.

It is recognized that glass making in the environment of an in-space earth orbital vehicle has the potential for eliminating the causes of optical non-homogeneity and contamination in chalcogenide systems. Specifically, space manufacture provides for containerless melting in a near weightless environment. Manufacture in space should thus eliminate (1) dissimilar optical areas in the chilled glass caused by separation due to

*Paper presentation by - W. B. Crandall

a 1-G earth manufacture environment, (2) contamination from earth melting crucible by oxygen and other elements deleterious to infrared transmission, and (3) heterogeneous nucleation at earth melting crucible/glass interface producing crystallization of certain melt compositions.

By overcoming these features through space manufacture, it will be possible to produce a large optical quality IR transmitting glass demonstrating features unequaled in earth manufacture today. The value added to the glass product regarding improved IR transmission characteristics, precise dimensional control of intricate shapes formed during melting, and the size scale up potential is predicted to more than justify the costs incurred in space manufacture.

This paper outlines a program designed to demonstrate the feasibility of various techniques, processes, and equipment that will be utilized to manufacture chalcogenide glasses in space. Optimum methods, techniques and equipment are being defined through evaluation of amorphous character, purity, and homogeneity parameters at various stages of the glass forming process (i.e., from the raw material stage through the melt-quenching stage). However, only the high temperature process involved in glass forming, supercooling from a homogeneous molten condition, must be carried out in space to take advantage of containerlessness and weightlessness. The preparation for melting and the final treatment of the material for an optical element can be done on earth without reducing the quality of the space-melted material.

The program outlined herein will not only determine optimum preparation techniques, but will also serve to provide guidelines for the design of the actual melting experiment in space, and for the optimization of the exact chalcogenide composition to be included in the space experiments. The glasses prepared on earth during this study will eventually be compared to space produced glasses (transmission characteristics, etc.), providing a direct measurement of the value of

space processing. The current IITRI program therefore represents the initial phase of an overall systematic effort to insure a high probability of success for the space experiment.

TEXT

The essential elements of IITRI's chalcogenide glass space processing program are illustrated in Figure 1, and are detailed in the following sections.

SAMPLE PREPARATION - EVALUATION OF TECHNIQUES

Two of the causes of optical inhomgeneity in earth-manufactured chalcogenide glasses, the 1-G field and the presence of a crucible, are not present in space manufacture. Even these two improvements in space manufacture, however, cannot overcome certain deficiencies that might exist in the precursor sample before melting in space. Therefore, the major emphasis of the IITRI program is to develop/evaluate compounding and mixing techniques that will yield the highest degree of purity and homogeneity in the earth melting experiments. In this manner the actual space-melting experiments will have a very high probability of demonstrating the major overall objective of this program, i.e. that space manufacture provides for a degree of optical quality that is unattainable in earth manufacture.

Accordingly, very pure materials are being prepared by thorough mixing methods. Chemical vapor deposition (gas methods) and slurry techniques (liquid methods) are being combined with clean chamber techniques (mechanical mixing in a dry box) to prepare samples for melting. To insure the success of the program, evaluation of purity and homogeneity is being made prior to melting, and after melting by the techniques described below. The optimum batch preparation technique will thus be determined by the resulting purity and homogeneity evaluations.

Our initial evaluations are being conducted for the As-S binary system. Standard techniques of dry powder mixing and melting in a sealed silica container are being performed first for the purpose of generating baseline information about the materials and processes. More elaborate techniques for more complex systems such as Si-As-Te-Sb will be employed to improve the levels of homogeneity, purity, and amorphous character farther downstream. For instance, compounding high melting intermetallic materials such as $SiAs_2$ and $SiTe_2$ by a cold stage vapor deposition technique will minimize evaporation losses and smooth melting point disparities between the various elements constituting the batch composition. Also, improvements in batch homogeneity may be attained by employing a liquid slurry technique to promote more uniform dispersion of raw batch particles.

Final batch compositions will have to eventually meet the additional constraint that they must be transported to the earth-orbital laboratory. Final compositions will therefore have to be formed into pellets which must be able to withstand, without crumbling, the "g" forces associated with space vessel acceleration during lift-off. The compositions will therefore be shaped into cylindrical pellets (1 cm dia, 1 cm long) by hot-pressing in a dry box up to 6000 psi at very low temperature (150°C). This should be enough (in the presence of Te and As) to start some degree of sintering without causing any contamination. The pressing die will be graphite or graphite lined (oxygen getter). If the need arises, silicon shot blasting of external surfaces will be performed to remove any possible contamination from the graphite pressing die.

MELTING EXPERIMENTS (TERRESTRIAL)

The purpose of the earth-bound melting experiments is twofold. One purpose is to determine the experimental parameters of time, temperature, vapor pressure, forming method, etc. to be designed into the space experiments. The second is to manufacture the best possible quality earth bound glass samples for comparison with the space manufactured samples.

Accordingly, three glass melting methods are being investigated: (1) a conventional silica ampoule method, used to provide "reference data," (2) a hanging support method, used to investigate the effect of "crucible"/glass contact area during melting, and (3) levitation melting. Heating and cooling rate, contact extent, firing time, fining time, and other important melting/quenching parameters are being evaluated using the hanging support method. Levitation melting simulates the actual space melting configuration in all but one respect. Containerless melting will be performed, but the 1-G gravitational field will still be present.

The conventional silica ampoule melting method entails containment of the glass batch constituents in a sealed, "oxygen free," thick-walled silica container. The sealed ampoule is then heated above the fusion temperature either in a wire wound radiant heating tube furnace, or within an inductively heated susceptor. During melting the ampoule is either rotated or rocked in a cyclic manner to promote homogenization. The ampoule is then either withdrawn from the furnace chamber for cooling or cooled in place to form the glass.

The hanging support method of melting is being performed to evaluate glass quality as a function of the amount of container present during melting. This experiment will thus provide data on techniques and equipment that are directly applicable to the space melting package. The hanging support method is illustrated in Figure 2. The specimen to be melted by radiant heating is contained in a vacuum/inert gas capsule, being supported in a tungsten cup that hangs down into the furnace hot zone. Extent of glass-container contact is controlled by the cup geometry. The capsule will be quartz, with and without an O_2 getter material. Methods of controlling the equilibrium vapor pressure in the heated capsule are being investigated. After melting, the glass is formed by either in-place radiation cooling, or by a drop/quench method.

Levitation melting is illustrated in Figure 3. The molten sample is suspended by acoustic forces generated by the levitator. This method completely eliminates container contamination and possible heterogeneous nucleation sites, thus providing direct prediction of the levels of purity and amorphousness attainable in space. However, in earth-bound levitation melting the 1-G gravitational field is still present. Therefore the homogeneity of terrestrially melted chalcogenides will mainly be a function of the homogeneity of the starting materials (raw batch). This investigation is being conducted through a NASA funded cooperative effort between IITRI and Intersonics.*

EVALUATION AND COMPARISON OF METHODS OF BLENDING AND MELTING

A major objective of the earth melting experiments is to develop techniques and methods of mixing and melting that will insure a high probability of success in the subsequent space melting experiments. This can be accomplished by applying some pertinent form of merit index to the results of the earth melting experiments, and extrapolating to conditions of space manufacture. IITRI is employing a so-called "ACH" factor for this purpose; i.e. degrees of Amorphousness, Contamination, and Homogeneity. Utilizing the results of the various melting techniques, the ACH factor will be related to "degree of containerlessness." This analysis will then be extrapolated to the degree of containerlessness expected in the space melting experiments (i.e. stinger-glass contact), as illustrated in Figure 4. The extrapolated ACH factor will thus represent the expected quality of the space manufactured glass, as measured by parameters describing homogeneity, contamination, and lack of crystallization. In this manner, the prediction of the success of the space manufacture mission, as measured by improved quality glass, may be possible.

*R. R. Whymark, Intersonics, Inc., Chicago, IL

The evaluation stage of IITRI's research is being conducted at various distinct points, both after batch compositions have been prepared and after the earth melting experiments. Emphasis is placed on techniques indicating optical quality, contaminants, inhomogeneities, crystallization, and strength. "Standard" earth manufactured chalcogenide glasses, such as Texas Instruments Corp. glass TI #1173, are being employed to establish "benchmark data." These same evaluation techniques can be subsequently used to compare space-and-earth-manufactured chalcogenide glasses as an indicator of the success of the overall NASA program.

Optical quality will be studied by analyzing transmission characteristics and absorption characteristics. The transmission characteristics will be measured using an infrared spectrophotometer. The absorption measurements will be made by measuring the energy absorbed by the glasses being irradiated with a 10.6μ CO_2 laser.

Low level impurities causing absorption bands (primarily O_2 and other interstitials N_2, C, H) are being detected by Charged Particle Activation Analysis (CPAA) and Charged Particle X-ray Spectroscopy (CPXS). These techniques employ a van de Graaff accelerator and were developed at IITRI. Both techniques possess characteristics ideally suited for trace impurity detection in chalcogenide glasses, generally in concentrations in the parts per million range or below. This technique has been employed to generate baseline data on oxygen impurity concentrations in our initial chalcogenide compositions. Figure 5 illustrates oxygen peaks obtained by CPAA for TI #1173 (5 ppm O_2) and a chalcogenide prepared by IITRI using as yet non-improved preparation techniques. Measurements on relatively impure chalcogenides provide the necessary bracketing data required for the CPAA technique.

Striae and inhomogeneities are observed using optical microscopy and scanning electron microscopy (SEM). Polished specimens are optically examined under low magnification. Micro-inhomogeneities are determined using the electron microscope. This technique is being used to determine the homogeneity of a mixed powder batch prior to melting, as well as the homogeneity of the melted-quenched product.

For evaluation of amorphous character, x-ray diffraction and electron microscopy techniques are utilized to determine the possible extent of crystalline inclusions in the glass samples.

SPACE MELTING EXPERIMENTS

Throughout the IITRI program cognizance of the requirements of the actual in-space melting experiments is being maintained. For instance, there are several heating methods that are presently being considered for installation on earth-orbital vehicles; electron beam melting, induction heating, and radiation heating in an electric wire-wound furnace. The IITRI program employs radiation heating. However, the basic techniques of mixing, sample preparation, support, and handling that are being developed will be applicable to any of the heating modes under consideration.

Awareness is also being maintained regarding the methods of sample support and containment that are envisioned for the actual in-space experiments. IITRI's work is amenable to the stinger methods and acoustic manipulator support methods being considered.

The success of the overall NASA program depends upon how well the requirements of the space melting experiments can be established in the present earth bound experiments. When the correct parameters are established in the IITRI program, there will be a high degree of confidence that the subsequent in-space experiment will produce high quality optical glass with scale-up potential. Judgement of the quality of space manufactured glass will be made by comparison

of properties with corresponding properties of glass prepared during the current program by best possible earth manufacturing methods.

CONCLUSION

A non-oxide chalcogenide glass is being evaluated in IITRI's program to demonstrate two potentials of space manufacture: 1) technical improvements (improved infrared transmission) through space manufacture where there is no need for a melting crucible and there are very low gravitational forces, and 2) the monetary value added to this improved glass due to the technical improvement (i.e. good amorphous character, very low contamination, and a highly homogeneous chilled form with size scale-up potential.)

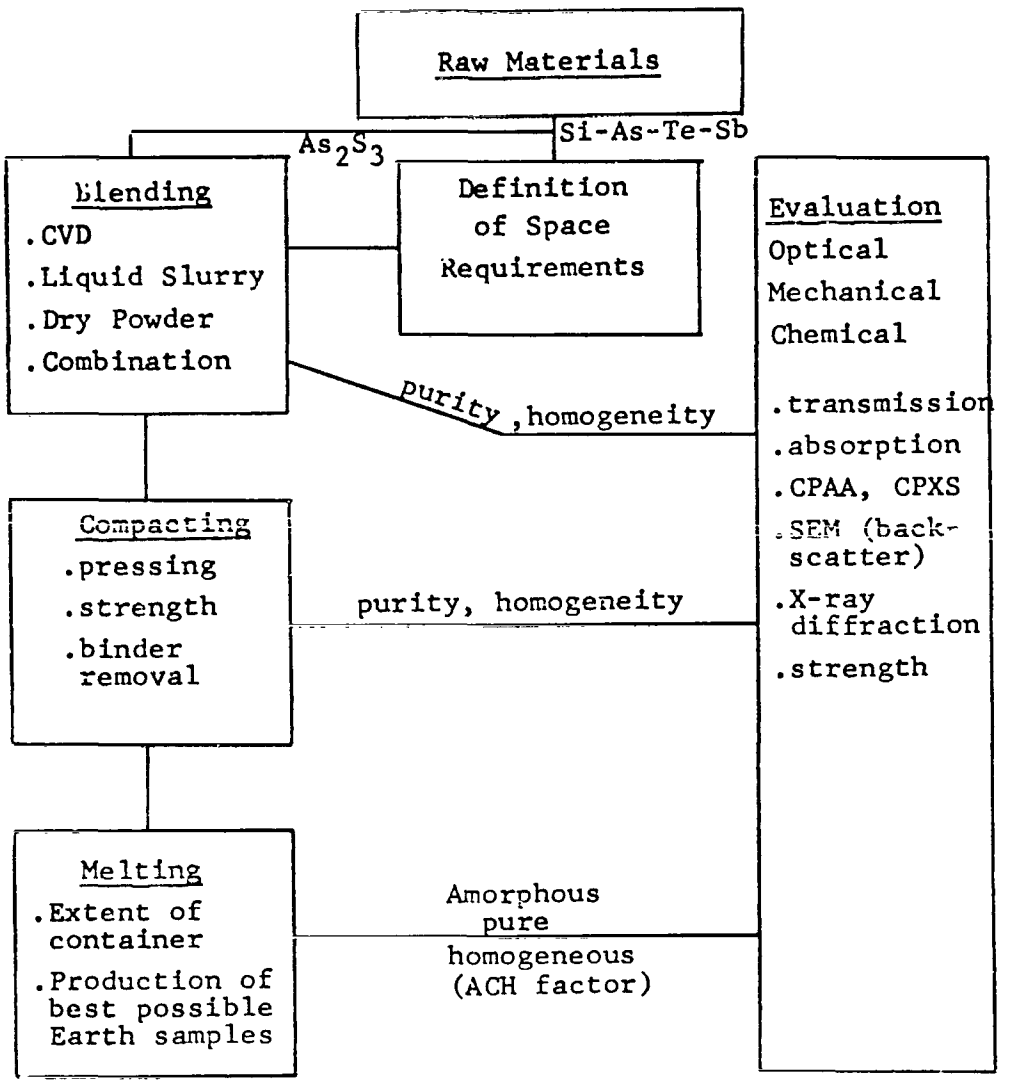

FIGURE 1 FLOW CHART OF IITRI PROGRAM

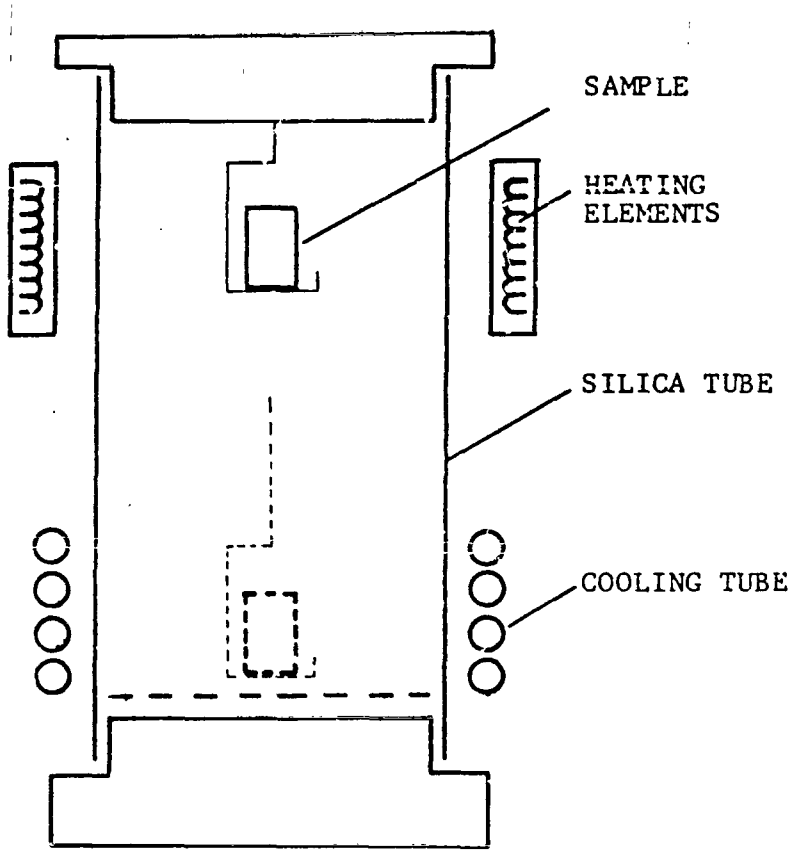

FIGURE 2 HANGING SUPPORT MELTING

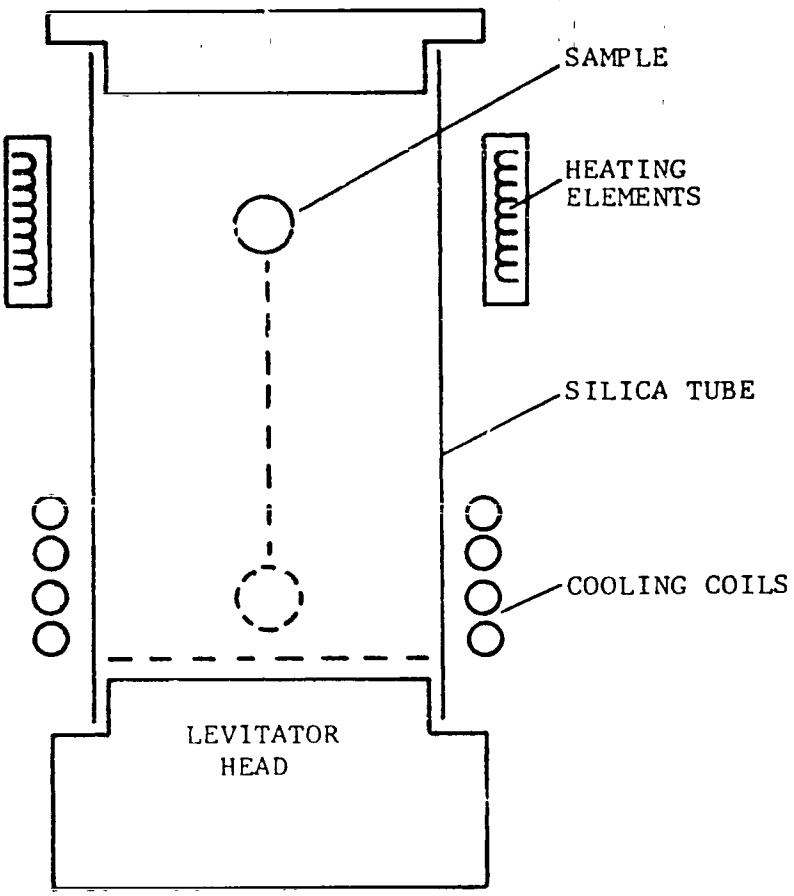

FIGURE 3 LEVITATION MELTING

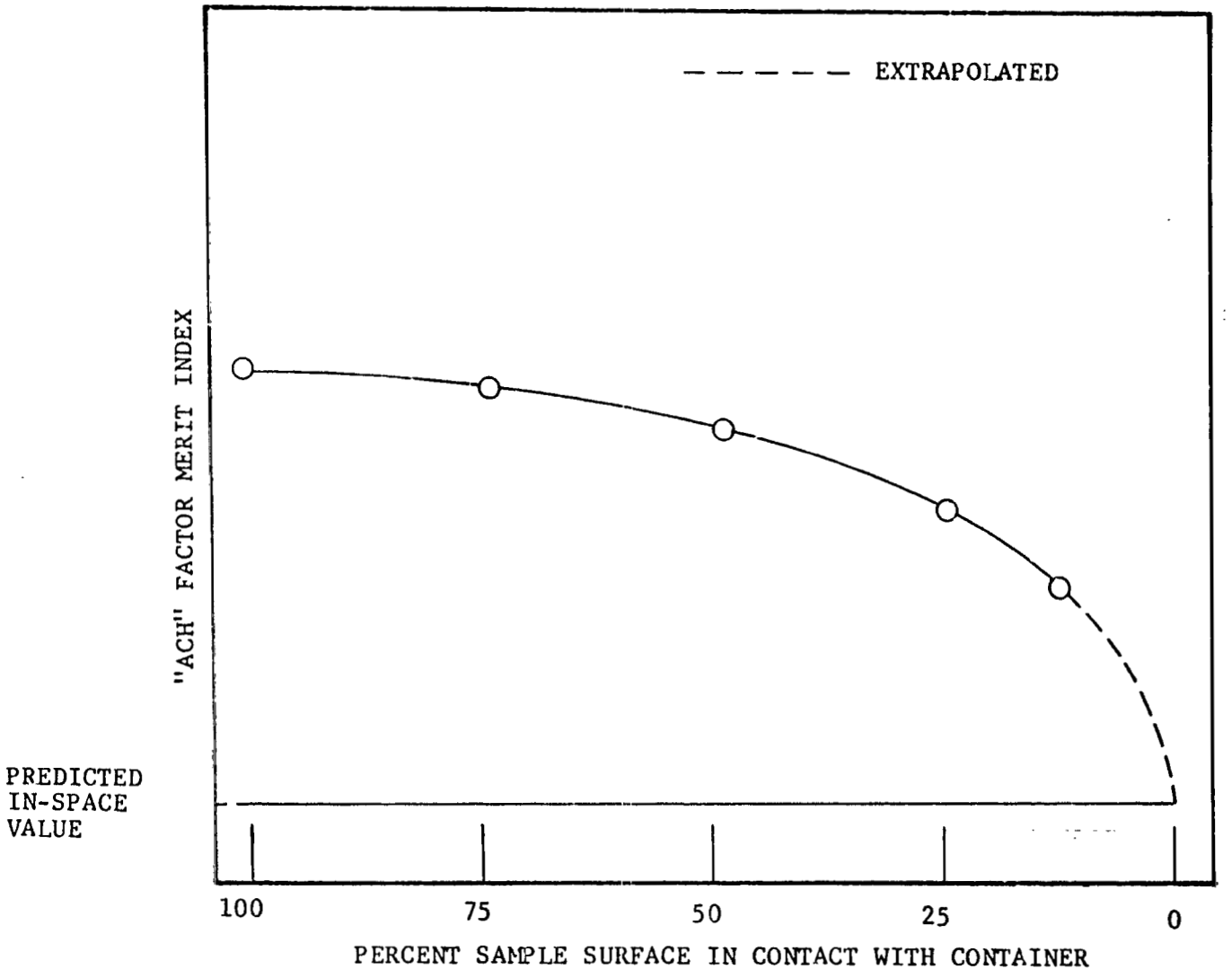

FIGURE 4 "ACH" FACTOR CONCEPT

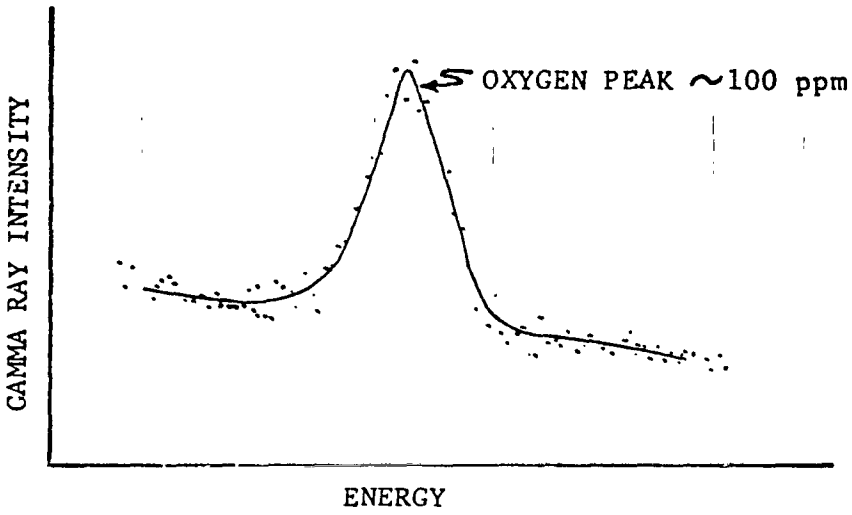

FIGURE 5a CPAA RESULTS: INITIAL IITRI CHALCOGENIDE

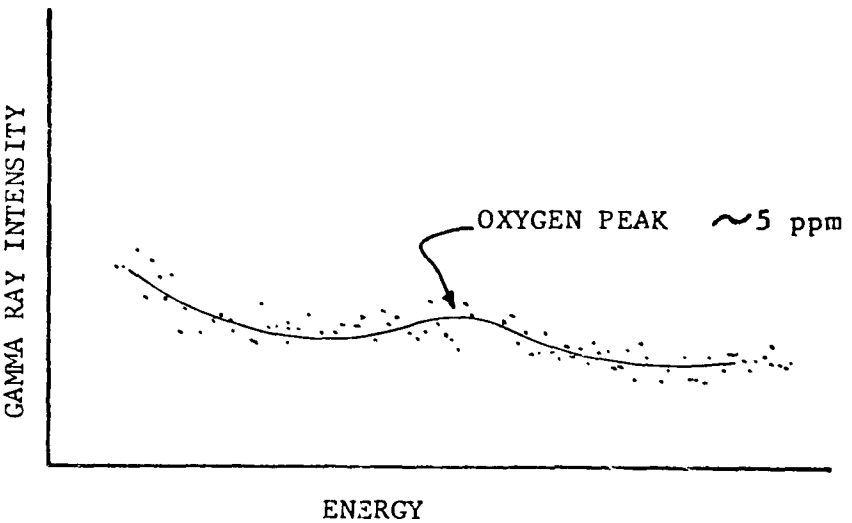

FIGURE 5b CPAA RESULTS: TI #1173 CHALCOGENIDE

EUTECTIC SOLIDIFICATION

by

F. C. Douglas* and F. S. Galasso
United Aircraft Research Laboratories
East Hartford, Connecticut 06108

SUMMARY

Directional solidification processes have been applied to a wide variety of eutectic compositions resulting in materials with interesting mechanical, optical, electronic and magnetic properties. The results of such investigations have led to improvements in the mechanical properties in high temperature alloy systems. These studies have applied the directional solidification technique to off-eutectic compositions to obtain a greater latitude in composition.

The unique, but less intensively studied, nonstructural properties have awaited the development of improved techniques of solidification which are capable of providing better microstructures upon which a widespread use of eutectic compositions with directionally aligned structure depends.

The possibilities of using the low-gravity space environment for the processing of directionally solidified materials in order to remove the limitations imposed by the 1-g earth environment have led to a careful evaluation of the directional solidification process and the results commonly obtained. Defects in the regularity of the microstructure have been identified as one of the most important areas where present processing technology needs to be improved. One-g environment material processing must also be carefully characterized before it can be determined if zero-g processing will produce significant benefits in eutectic and off-eutectic solidification.

It is suggested in this paper that a combination of experimental and analytical thermal studies will be required to optimize the solidification process in order to minimize the structural defects which occur due to present processing techniques.

*Paper presented by F. C. Douglas

INTRODUCTION

Eutectics can be unidirectionally solidified to form composite structures which contain rods of one phase in another or alternating plates of the two phases. It has been shown that it is also possible to vary the relative amounts of the two phases by the controlled solidification of off-eutectic compositions (Ref. 1).

The natural, aligned composites which result from the unidirectional solidification of eutectics have been found to have exceptional strength and are stable at elevated temperatures. The directionality of their structures, whether rod- or plate-like, produces anisotropic properties which can be used to advantage in a variety of applications.

Improvements in the mechanical properties obtained by directional solidification of eutectic compositions have led to investigations of a wide variety of eutectic as well as off-eutectic compositions in which an aligned microstructure could be obtained. Such investigations have been largely generated by the need for improved high strength, high temperature materials for use in gas turbines. In addition, a number of studies have been performed on materials which have exhibited interesting optical, electronic or magnetic behavior.

As the results from a number of different compositions subjected to directional solidification and subsequent evaluation have grown, it has become increasingly clear that a significant effort must be made in the area of process control. Obtaining high quality, low defect, continuous microstructure appears to be the key to producing high quality materials. Coupling this requirement with the production of complex shapes makes the problem of process control even more difficult and this difficulty is compounded in some cases by the necessity of operating at temperatures up to 1500°C for superalloy turbine blade casting, or higher in the case of ceramic systems.

The entire process of solidification and process control has come under scrutiny by virtue of the eutectic solidification experiments performed in preparation for and in the orbiting space laboratory. In particular, the study of defect structures and the parameters which control them have been investigated. The low-gravity environment of a space laboratory provided a unique opportunity to process materials without some of the hindrances of a 1-g environment.

DIRECTIONAL SOLIDIFICATION

Solidification Techniques

The typical procedure used to directionally solidify a material has been to place the material in a suitable crucible, melt it in a furnace, and then withdraw the crucible of molten material from the furnace at a constant rate. Various arrangements of power input and cooling have been used to provide desired conditions at the solid-liquid interface, such as maintaining a high thermal gradient in the liquid at the solid-liquid interface position. Figure 1 illustrates a system used for high melting point alloys which produces a high thermal gradient in the melt. It consists of an induction heating system with variable spacing between the coil elements to concentrate the power input, and a flowing water quench system for heat extraction. Resistance-heated furnaces with similar arrangements are also used, but generally lack the power input capability of the induction system. Thermal fluctuations at the solidifying interface must be eliminated in order to obtain good microstructure. This generally necessitates the use of a thermal monitoring and feedback control system to achieve good results.

The microstructure of a directionally solidified eutectic alloy from such a furnace is illustrated in Fig. 2.

Directional microstructure can also be obtained using a system which traverses a molten zone through the ingot. Different methods of producing molten zones are illustrated in Figs. 3, 4, 5, 6 and 7. A traveling zone has the advantage that only a small portion of the total material is molten at any one time. This shortens the time that the molten material is in contact with a crucible. Thermal gradients can be achieved which are high enough to study off-eutectic solidification, as illustrated in Fig. 8, which shows the thermal profile obtained in a lead-tin eutectic melt using the zone furnace system shown in Fig. 7.

An interesting method which lends itself to production of shaped pieces is the edge-defined film-fed growth process developed at Tyco Laboratories, Inc. This is illustrated in Fig. 9. The shape of the solid is determined by the outside dimensions of a die which feeds the solidifying form by capillary action. In order that capillary feeding will occur, the molten material must wet the die material.

Many laboratories are engaged in the study of directionally solidified materials. A recent compilation (Ref. 2) provides a directory which was current in October 1973.

Materials Studies

The widespread interest which has developed in the area of composite structures as produced by directional solidification has naturally led to the investigation of many alloy compositions. A list of the eutectic compositions which have been studied is contained in Refs. 2 and 3. Reference 3 provides excellent reviews of the physical properties of composite materials. The mechanical behavior of unidirectionally solidified composites have been given, the nonstructural applications are reviewed, and the status of the theoretical understanding of the solidification process is presented.

An example of a structural material based on a directionally solidified pseudo-binary eutectic is the Ni-Al-Cb system. The Ni_3Al-Ni_3Cb eutectic was used as a starting point and the amounts of Ni, Al and Cb were varied with the addition of Cr to optimize the desirable properties such as high strength and corrosion resistance at high temperatures. These were achieved while maintaining an aligned composite microstructure. In addition, as pointed out in Ref. 3, the limitations imposed by the material, the composition, and the crystallography can be surpassed because of the versatility of the directional solidification technique. One can, in fact, obtain complex in situ grown composites having any number of elements in order to get a material possessing a set of properties chosen in advance.

The review papers in Ref. 3 also discuss the nonstructural uses of directionally solidified eutectics. A magnetoresistive material has been made by directionally solidifying the pseudo-binary eutectic InSb-NiSb. In this material, the eutectic microstructure consists of NiSb conductive rods in a matrix of InSb. When the flow of current through the material, the direction of the rods, and an applied magnetic field are all at right angles, a maximum magnetoresistive effect appears, caused by the short-circuiting of the induced Hall voltage by the NiSb rods. This material also makes an effective infrared polarizer.

An example of an optical application is the formation of birefringent materials from isotropic materials by directional solidification. The system NaCl-NaF has been used to form a uniaxial material from phases which by themselves are isotropic. The advantage realized is that the wavelength region where the material is effective can be selected because of the control over the size of the separated phase elements through the rate of solidification. Thus, quarter-wave plates and polarizers can be constructed for regions of the spectrum where no natural materials are available.

A final example of the versatility of solidification is the creation of filters of uniform porosity and passage size by solidification of a monotectic system. In such a system, a homogeneous liquid transforms to a liquid plus a solid phase, from which the liquid can then be removed, leaving a porous structure. Such filters are now made under the tradename of Nuclepore.

Orbiting Space Laboratory Studies

Some preliminary solidification studies have been performed on the copper-aluminum eutectic using the materials processing facility on board the presently orbiting space laboratory. Because of the nature of the experiments, these studies have not been conclusive in determining if low gravity produces any gross effects in the microstructure which consists of alternating parallel plates of Al and $CuAl_2$. It is known that such factors as changing growth rate and solid-liquid interface curvature predominate in effecting the defects in the microstructure. Other factors such as gravity-driven convection may be second-order effects as far as affecting the microstructure is concerned. For this reason, a high degree of control over the solidification process must be exercised first before the advantages which zero-g processing could provide can be evaluated. It should be noted that in off-eutectic solidification the effect of convection may be more important because of a need for an undisturbed boundary layer at the solid-liquid interface.

To investigate the nature of the control which must be exercised to eliminate such problems as nonconstant growth rate and nonplanar solid-liquid interface shape in composite microstructural materials, a series of experiments has been performed on rod- and plate-forming eutectics under NASA Contract NAS8-29669 at the United Aircraft Research Laboratories. The objective of these experiments was to evaluate the feasibility of using the space environment for producing eutectics of unique characteristics of value on earth. The experiments have investigated the nature of the microstructure obtained under processing such as simple solidification of cylindrical rod specimens, solidification by passing a molten zone through a rod, formation of thin sheets of material, solidification around obstacles, and an attempt to evaluate the effect of crucible wall thickness. In addition to working with eutectic compositions, off-eutectic solidification studies have been performed.

One result stands out which seems to be a common problem to almost all solidification systems in which a molten ingot is withdrawn from a furnace into a region where it solidifies. This is that the rate of solidification is continually changing, which is a known cause of defects. For long ingots, it becomes nearly constant during part of the operation, but not over periods long enough to produce regions of highly perfect microstructure.

A second common problem being studied analytically and experimentally results from the finite heat conduction into and out of materials subjected to the solidification process. The problem is the curvature of the solid-liquid interface. The direction of growth of the phases making up the microstructure is perpendicular to the solid-liquid interface. If this is not planar, then new phase units must be initiated or, conversely, some must disappear, depending on the curvature, with the result that a significant volume of defect structure appears.

The changing of the rate of solidification appears to be significantly decreased, and may be eliminated, by use of a traveling molten zone. This technique also enables one to generate high thermal gradients which are needed to obtain an

aligned composite structure in off-eutectic compositions, and which may contribute to providing a plane solid-liquid interface. The effect of the sagging in the molten zone due to gravity still has not been determined.

Eutectic microstructure seems to be able to maintain integrity to a large extent when forced to grow around an obstacle, provided that the rate of change of direction is not too high. Again, the success which can be achieved in this type of experiment depends on the degree to which the flow of heat can be controlled through the solidifying ingot.

The effect of container thicknesses on the microstructure of a directionally solidified ingot is also being investigated. It is of interest due to the control it exerts over the heat transfer into and out of the ingot. In addition, for heavy materials, the container thickness must be great enough to support the weight of the molten material, and usually acts as a very good insulator. In a zero-gravity environment, the container could be very thin. In order to determine whether a thin container in fact is desirable requires that the container be treated as a thermal transfer device and optimized for the production of the desired structure of the ingot it contains.

In support of the experimental program to investigate the effects on eutectic microstructure of various processing operations, a program to coordinate experimental investigations and analytical descriptions generated by solutions to the heat-flow equations has been started. The present effort in this area is to obtain an operational, 3-dimensional numerical program to solve the heat-flow equations, and to also obtain an accurate thermal description of the experimental systems in which the materials are directionally solidified.

CONCLUSIONS

Significant progress has been made in producing controlled microstructures in a wide variety of compositions, starting from the binary metal alloys. Materials in which a controlled, directional microstructure has been obtained include ceramics, multicomponent metals, semiconducting systems, superconductors, and noneutectic compositions. Mechanical, electrical, magnetic and optical properties have been demonstrated which are a function of the controlled microstructure in the material.

Areas where further effort appears to be needed are concerned with processing technology, where a combination of analytical and experimental efforts is suggested as the most rapid way to make progress in obtaining the desired fabricated shapes with the appropriate microstructure. The mechanisms by which defects are introduced into the microstructure and the means to eliminate them appear to be a fertile area for progress.

In order to improve the processing technology, supporting programs in which the thermal properties of the material being processed are required. In particular, the determination of the thermal properties of compositions when molten are now unavailable. This type of data forms the input for the analytical portion of a solidification optimization.

REFERENCES

1. Mollard, F. R. and M. C. Flemings: Growth of Composites from the Melt. Trans. Met. Soc. AIME 239, 1534 (1967).

2. AGARD-R-609: Directory of Research Activities on In Situ Composites. Compiled by Battelle Columbus Laboratories, Metals and Ceramics Information Center. Published in October 1973.

3. Proceedings of the Conference on In Situ Composites, September 5-8, 1972, Lakeville, Connecticut, USA. Reported by the National Materials Advisory Board, published as NMAB 308-I, 308-II, 308-III in January 1973.

BIBLIOGRAPHY

1. Galasso, F. S.: High Modulus Fibers and Composites. Gordon and Breach, 1969. See esp. Ch. 5 and Appendix.

2. Hogan, L. M., R. W. Kraft and F. D. Lemkey: Eutectic Grains. Published in Advances in Materials Research, Vol. 5, Wiley-Interscience, 1971 (Ed. H. Herman).

3. Steurer, W. H., et al: Preparation of Composite Materials in Space. Final Report NASA-CR-124172, General Dynamics/Convair, January 1973.

4. Douglas, F. C. and F. S. Galasso: Materials Processing in Space. United Aircraft Research Laboratories report under NASA Contract NAS8-28724.

5. Douglas, F. C. and S. F. Galasso: Processing Eutectics in Space. United Aircraft Research Laboratories report under NASA Contract NAS8-29669.

6. Hulse, C. O. and J. A. Batt: Effect of Eutectic Microstructure on the Properties of Ceramic Oxides. United Aircraft Research Laboratories report under ONR Contract N00014-69-C-0073, Project No. NR 032-516/9-11/68.

7. Davis, K. G. and P. Fryzuk: Growth of Off-Eutectic Composites by Zone Melting. Can. Met. Quarterly 10, No. 4, 273 (1971).

8. Proceedings of Space Processing and Manufacturing Meeting, Marshall Space Flight Center, Alabama, October 21-22, 1969.

9. Thompson, E. R., F. H. Kraft and F. D. George: Investigation to Develop a High Strength Eutectic for Aircraft Engine Use. United Aircraft Research Laboratories report under Naval Air Systems Command Contract N00019-71-C-0096.

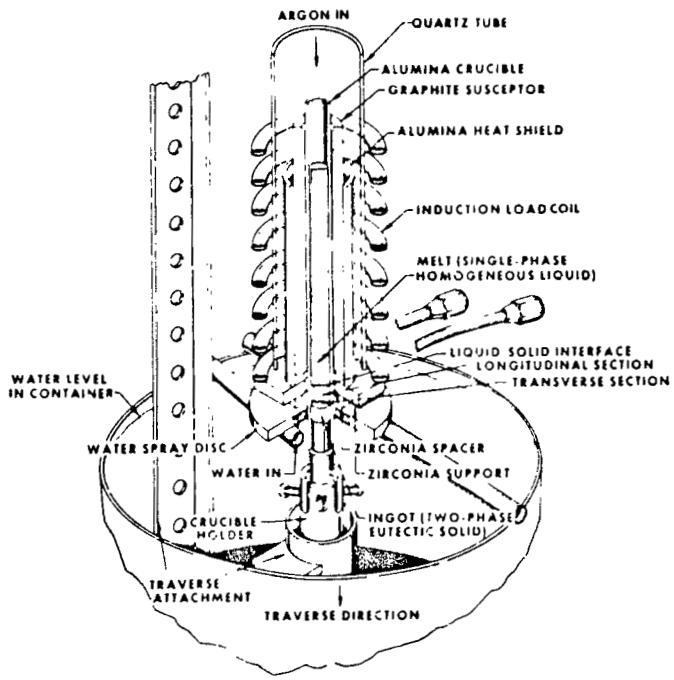

FIGURE 1. HIGH THERMAL GRADIENT DIRECTIONAL SOLIDIFICATION APPARATUS.

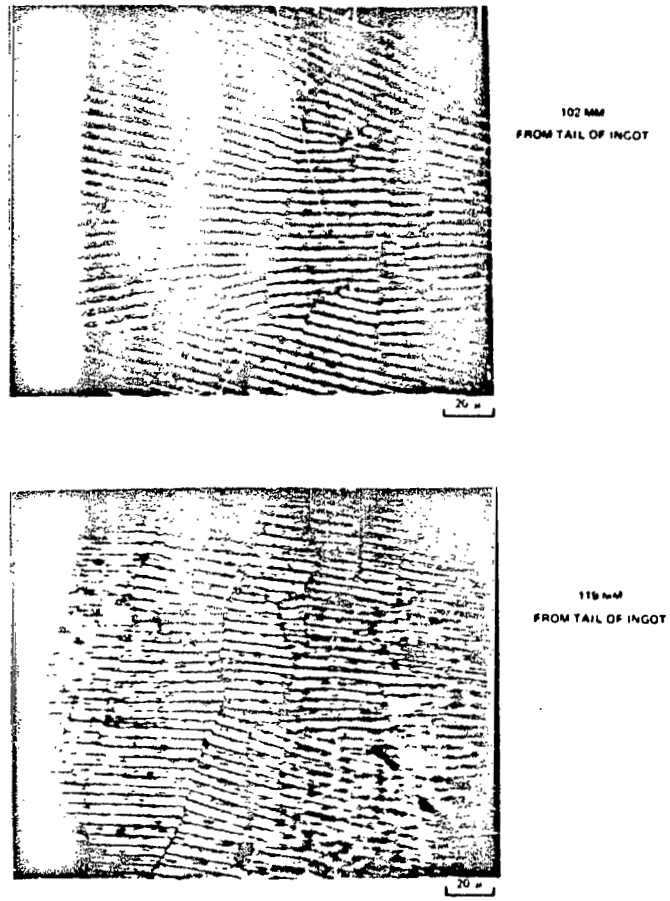

FIGURE 2. TRANSVERSE SECTION OF INGOT A72-1121 DIRECTIONALLY SOLIDIFIED IN INDUCTION-HEATED FURNACE.

FIGURE 3. SCHEMATIC OF DIRECTIONAL SOLIDIFICATION EQUIPMENT FOR CERAMIC OXIDE EUTECTICS.

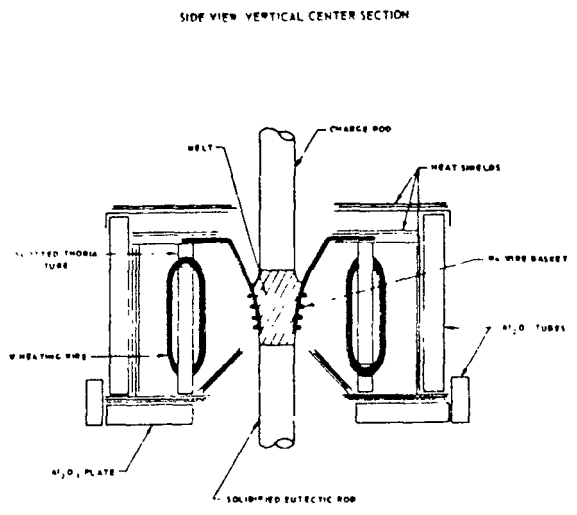

FIGURE 4. TUNGSTON HEATER FOR ZONE MELTING OF EUTECTIC RODS.

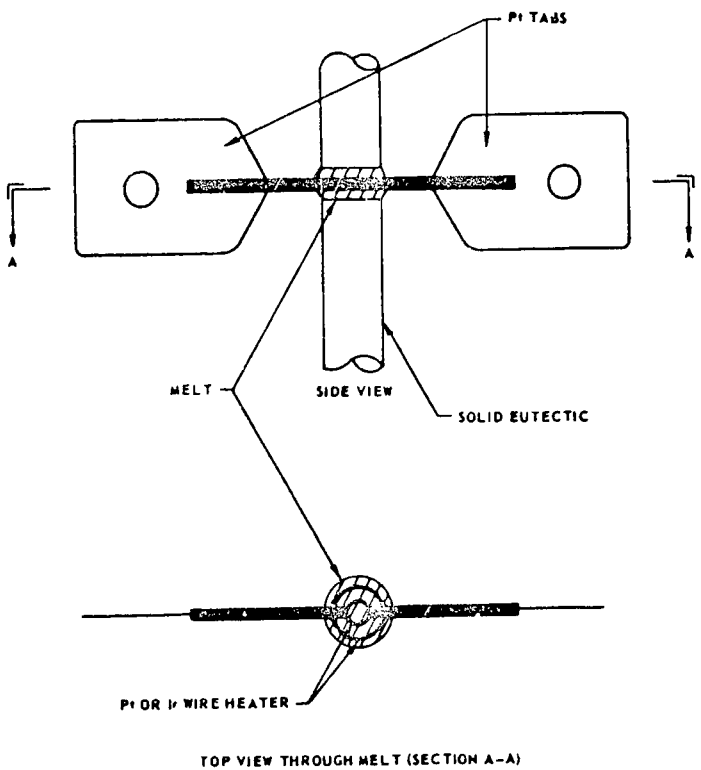

FIGURE 5. WIRE IMMERSION HEATER FOR FLOAT ZONE EUTECTICS

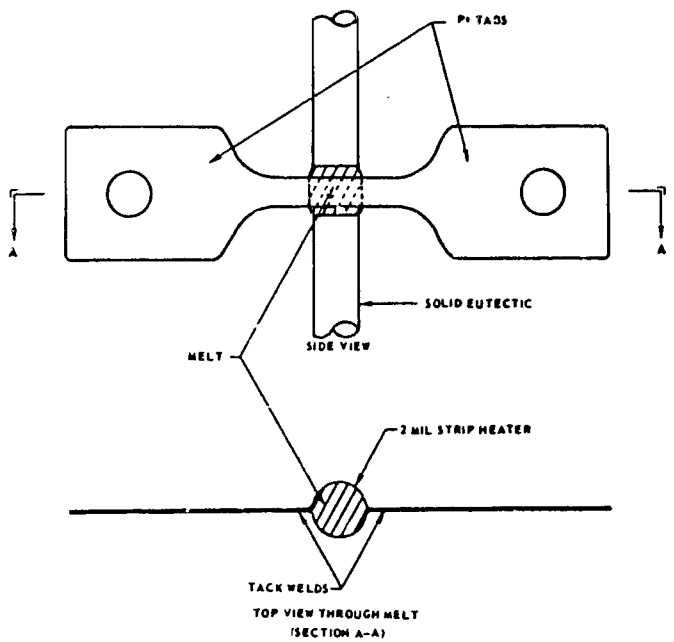

FIGURE 6. PLATINUM OR Ir STRIP HEATER FOR FLOAT ZONE EUTECTICS.

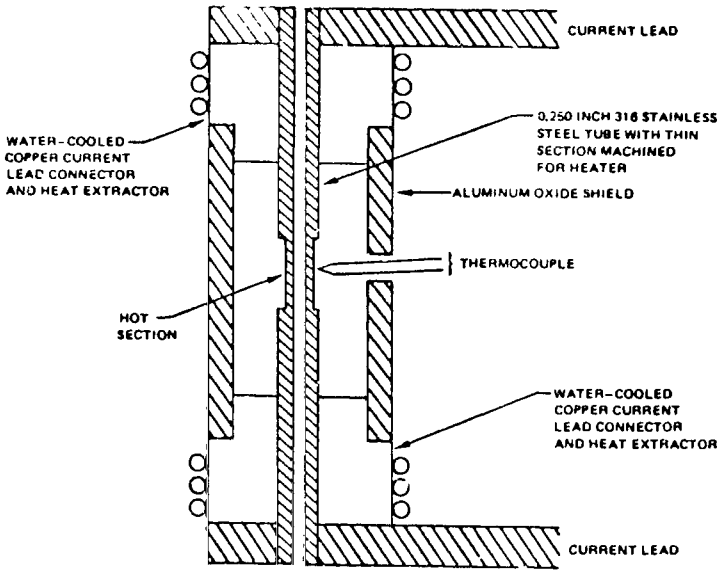

FIGURE 7. HIGH THERMAL GRADIENT ZONE FURNACE.

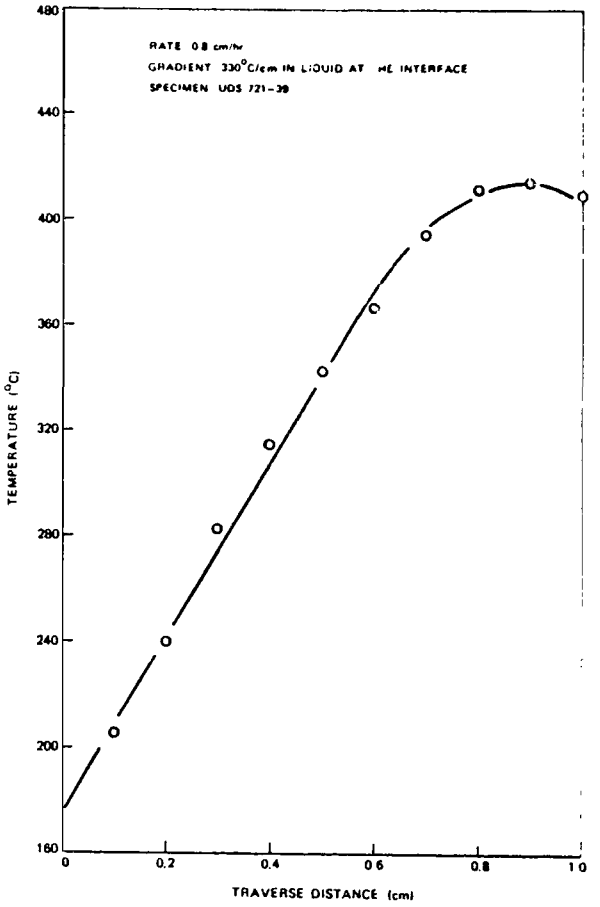

FIGURE 8. THERMAL PROFILE MEASURED IN A Pb-Sn ALLOY USING A ZONE-MELTING FURNACE

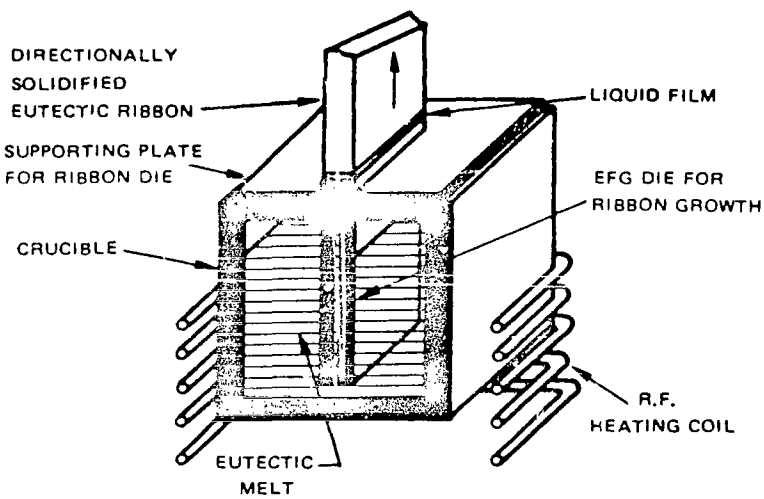

FIGURE 9. EDGE-DEFINED FILM FED GROWTH SYSTEM.

CONCENTRATION CHANGES DURING EUTECTIC SOLIDIFICATION

By

Biliyar N. Bhat
Process Engineering Laboratory
George C. Marshall Space Flight Center
Marshall Space Flight Center, Alabama 35812

SUMMARY

Thermotransport (or thermal diffusion, Soret effect) is shown to cause significant amount of segregation during the directional solidification of aluminum-copper eutectic. The concentration changes are predicted quantitatively and they are a function of temperature gradient, rate of melting and solidification and the time of soaking. There is a fair agreement between the experiments and calculations. A process is suggested where these concentration changes may be minimized.

INTRODUCTION

Eutectic solidification experiment (M566) consists essentially in (1) partially melting a single grain Al_2Cu-Al eutectic alloy, (2) holding it in the temperature gradient for one hour (soaking) and (3) directionally solidifying it at a predetermined rate. The objective of this experiment is to determine the effect of zero gravity conditions of the Skylab on the growth of lamellar eutectic. This is done by comparing the eutectic structures grown under 1-G conditions on ground and 0-G conditions in the Skylab (SL-3 and SL-4)

It is well known that good lamellar structures can be obtained by use of large temperature gradients (G) and slow rates of solidification (R) (1,2). However, under these conditions thermotransport also becomes significant (3,4). Thermotransport is a phenomenon where atoms migrate in the presence of a temperature gradient. This can lead to segregation effects which may be significant in zero gravity conditions where convective mixing is nearly absent. Temperature gradients present in M566 experiment are rather large and hence significant amount of thermotransport may be expected. In Al-Cu

system, copper atoms are known to migrate to the colder regions (5) and affect the structure of directionally solidified Al-Al_2Cu eutectic (4). This paper presents a study of concentration changes in M566 experiment due to thermotransport. A method is suggested by which these concentration changes can be corrected.

EXPERIMENTAL

The aluminum-copper eutectic specimens were housed in cartridges and positioned in the multipurpose electric furnace. (Details of the cartridges and the furnace may be found in reference (6). It took approximately two and a half hours to heat up and melt and two hours to solidify it completely with an in between soak period of one hour. Only about 6.5 cm length of the sample was remelted and directionally solidified. The thermal analysis of the experimental package showed that the temperature gradient in liquid metal ahead of the interface was 45°C per cm (6). After the experiment, the cartridges were brought back to earth and X-rayed. Each sample was examined and the composition along the length of the sample was determined by use of X-ray fluorescence technique. (This was done by Georgia Tech).

Skylab experiments were also performed on earth in the laboratory to provide a comparison with the Skylab results. A few special experiments were performed to determine the variation of temperature at the solid-liquid interface during the soaking period. This was accomplished by introducing a thermocouple through the threaded end of the sample and positioning it in such a way that the tip of the thermocouple coincided with the solid-liquid interface. Experiments were run in the usual manner and the thermocouple readings were recorded during the soak period. These data are presented in the next section. After the run, the samples were examined metallographically.

RESULTS AND DISCUSSION

X-ray radiographs indicated that there was some segregation of copper at the remelt interface. Optical microscopy revealed that this region of segregation was 0.01 to 0.03 cm thick. The structure of the interface is shown in figures 1a and 1b. It consists mostly of θ phase, The remainder being α phase. The structure is columnar in the interface region but is lamellar on either side of it.

Figure 2 shows the variation in the temperature at the remelt interface during the soak period. It is observed that the temperature of the remelt interface actually rises during the soak period, but slowly. The rate of rise and the amount of variation in the temperature is different for different samples and it varied by a factor of two or three. There seems to be a correlation between the variation of temperature in the heat leveller of the furnace (reference 6) and that of the remelt interface. A larger variation in temperature

leads to a wider interface region and vice versa.

The above observations can be explained quantitatively on the basis of thermotransport in the liquid aluminum-copper eutectic alloy during melting and soaking. From reference 4, the thermal diffusion coefficient of copper in this alloy is

$$D' = 6.21 \times 10^{-8} \ cm^2/sec\text{-}^\circ C \qquad (1)$$

and the flux due to thermotransport is

$$J_1 = -D' \zeta \ x_1 \ x_2 \ G \qquad (2)$$

where ζ is the density, x_1, x_2 are the atom fractions of copper and aluminum respectively. The relative importance of thermotransport in the solidification of aluminum-copper eutectic alloy is given by the expression

$$\eta = \frac{\text{Thermal diffusion flux}}{\text{Rate of Solidification (R)}} = \frac{D' x_2 \ G}{R} \qquad (3)$$

Figure 3 shows the dependence of this ratio on the rate of solidification. The effect of thermal diffusion is negligible for large values of R ($> 2 \times 10^{-4}$ cm/sec) It becomes appreciable for lower rates of R. For $R = 2.15 \times 10^{-6}$ cm/sec, thermal diffusion is so high that solid θ will form during solidification. For intermediate values of R, the contribution from thermal diffusion is such that the solid formed will be richer in copper and columnar grains of θ phase are obtained and the inter-columnar space is filled by α phase. This appears to be the case with the Skylab samples.

The rate of solidification (or melting) can be calculated from the following expression,

$$R = \frac{dZ}{dt} = \frac{dT/dt}{dT/dZ} = \frac{dT/dt}{G} \qquad (4)$$

where Z is the direction of solidification, T is the temperature and τ is the time. Since G is known to be 45°C cm, R can be determined from the plot of T vs τ (Figure 2). It may be observed that T-t curve does not reach a plateau during the soak period. The rate of heating is higher in the early part of soak period and falls to lower values toward the end of the soak period (Figure 2).

An average rate of melting is $\simeq 1.15 \times 10^{-5}$ cm/sec. This occurs for a period of approximately 40 minutes. Hence, the total movement of interface (which corresponds to the thickness of the interface region) is 0.028 cm (or 4.2 cm at 150 X). This value is in good agreement with the experimental values of interface thickness which are 4.0 cm for SL-3 sample and 4.7 cm for the ground base sample respectively.

Referring to Figure 3, the contribution due to thermotransport is approximately 20% when the melting rate is 10^{-5} cm/sec. Hence, the solid formed at the remelt interface will have 21 atom percent copper which corresponds to 38.5 wt. % copper (or 63% θ phase). Actual concentration of copper will be higher since some segregation is already present before the soak period.

This segregation is also caused by thermotransport which occurs during the melting process when the solid-liquid interface moves from the heat leveller to its final position. (This takes approximately 80 minutes).

It is interesting to note that the interface is melting slowly during the soak period. Since thermotransport tends to enrich the cold end with copper, the liquid next to the solid-liquid interface is getting richer in copper during the soak period. Under these conditions θ phase will be stable with respect to small super heating, but α phase is not (5). Hence, α phase is preferentially dissolved and the excess copper is deposited on the existing θ lamellae, making them thicker. If the rate of melting is sufficiently low, it is possible to obtain a solid θ phase at the remelt interface. This is nearly the case with the Skylab samples towards the end of soak period.

It is also possible to estimate the variation in composition in the liquid away from the interface. In the absence of convection, the segregation due to thermotransport is given by (4)

$$\frac{X_c\,(1-X_h)}{X_h\,(1-X_c)} \cong \left| + \frac{2\,D'\,\Delta T\,t}{a^2} \right| , \quad t \ll \frac{a^2}{\pi^2 D} \qquad (5)$$

where c and h refer to the cold and hot ends respectively, a, length of the column of metal under the temperature gradient ΔT. In this case $a \simeq 5$ cm $\Delta T = 250$ C and $t = 6 \times 10^3$ sec. (time of soak + half the time of melting). Hence, from equation (5)

$$X_c - X_h \cong 4.6 \times 10^{-3} \text{ atom fraction of copper} \qquad (6)$$

$$= 0.7 \text{ weight percent copper.}$$

This value is small and it is difficult to verify experimentally. At sufficiently large values of G/R, however, $\chi_c - \chi_h$ will become appreciable.

From the above discussion it is evident that thermotransport is important in space processing. Interestingly, it can be controlled by choosing the correct G/R ratio. A constant G/R is necessary for growing fault-free eutectic grains. Since the temperature gradient is always present this will result in some macro-segregation from one end to the other, leading to defects in the structure. Such segregation can be eliminated by use of the following procedure.

Since thermotransport makes the cold end richer in copper - this can be compensated for by starting out with a material which is slightly deficient in copper at the cold end. This can be accomplished by holding the liquid alloy in a temperature gradient for a predetermined period of time. This procedure will introduce a concentration gradient as given by equation (5). This sample is then directionally solidified (or quenched) to preserve the concentration profile. The sample is then inverted and the crystal is grown in the usual manner. It may be necessary to use a seed to start the grain in the proper orientation. The original concentration gradient is now in a direction opposite to the gradient which would be created during the growth. These tend to cancel each other and one can obtain a more uniform composition and hence a better structure.

CONCLUSIONS

(1) Significant changes in concentration occur during the solidification of aluminum-copper eutectic alloy under zero-gravity conditions.

(2) These concentration changes can be controlled by modifying the process of crystal growth.

ACKNOWLEDGEMENTS

This work was accomplished while the author held an NRC Resident Research Associateship. Mr. Donald J. Tucker of the Research and Process Technology Division of the Process Engineering Laboratory assisted in conducting the ground base tests.

REFERENCES

(1) F. R. Mollard and M. C. Flemings, "Growth of Composites from Melt", Part II: Transactions of the Metallurgical Society of AIME, Volume 239, October 1967, pp 1534 - 1546.

(2) R. M. Jordan and J. D. Hunt, "The Growth of Lamellar Eutectic Structures in the Pb-Sn and Al-$CuAl_2$ Systems", Metallurgical Transactions, Volume 2, December 1971, pp 3401 - 3410.

(3) J. D. Verhoeven, J. C. Warner and E. D. Gibson, "Effect of Thermotransport Upon Off-Eutectic Composite Growth in Sn-Pb Alloys", Metallurgical Transactions, Volume 3, June 1972, pp 1437 - 41.

(4) B. N. Bhat, "Effect of Thermotransport on Directionally Solidified Aluminum-Copper Eutectic", Process Engineering Laboratory, NASA-MSFC, To be Published (1974).

(5) B. N. Bhat, "Thermotransport in Liquid Aluminum-Copper Alloys", NASA TR R-415, Marshall Space Flight Center, Alabama 35812, September 1973.

(6) "Data Package for Cartridges for the Multipurpose Electric Furnace System, M518", WANL-TME-2831, Volume II, November 1972, Westinghouse Astronuclear Laboratory, P. O. Box 10864, Pittsburgh, Pennsylvania 15236, (Contract NAS8-28271).

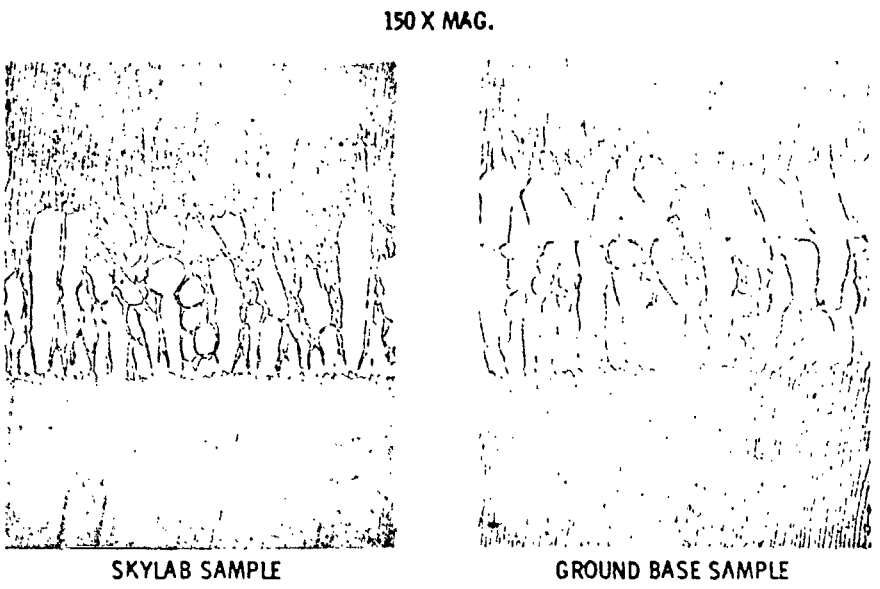

FIGURE 1. PHOTOMICROGRAPHS OF THE REMELT INTERFACE OF (a) SKYLAB-3 SAMPLE AND (b) GROUND BASE SAMPLE. NOTE: GROUND BASE SAMPLE HAD CRACKED AT THE INTERFACE.

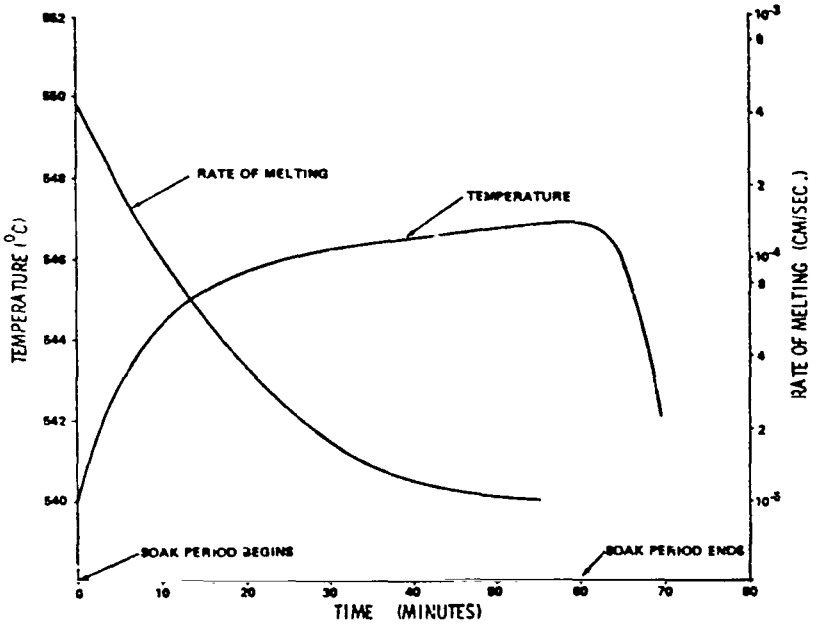

FIGURE 2. PLOT OF THE TEMPERATURE AND THE RATE OF MELTING OF THE INTERFACE DURING THE SOAK PERIOD.

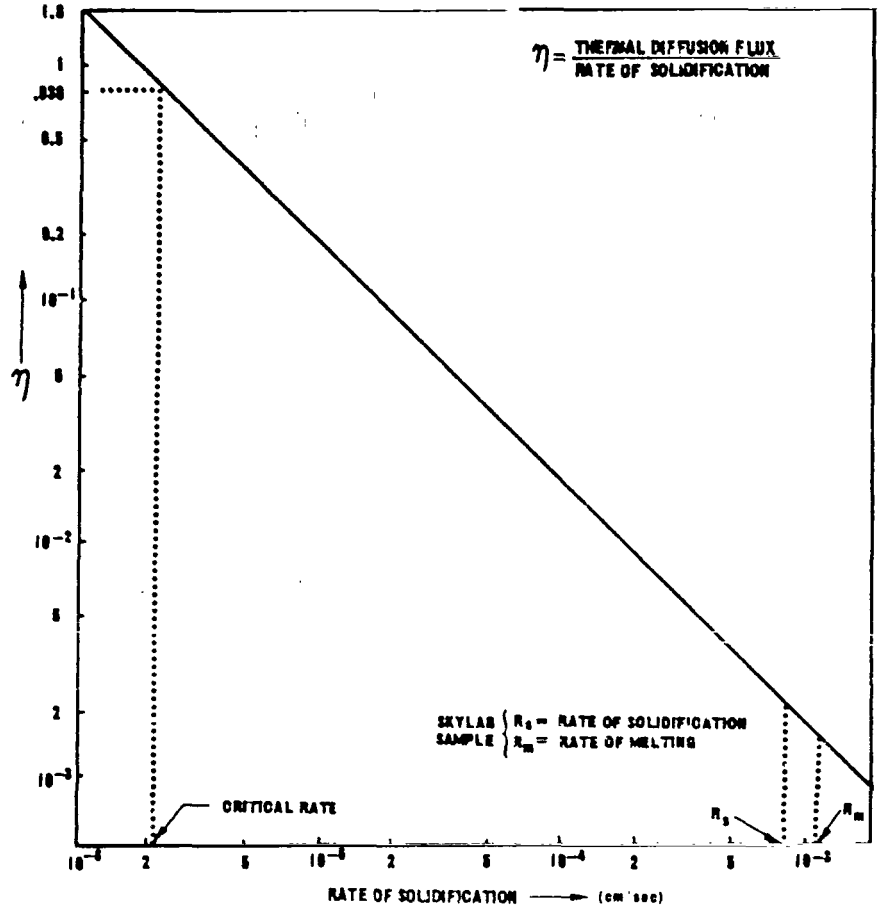

FIGURE 3. RELATIVE CONTRIBUTION OF THERMOTRANSPORT AS A FUNCTION OF RATE OF SOLIDIFICATION (OR MELTING).

EFFECT OF GRAVITY ON LIQUID PHASE SINTERING

By

T. Mookherji*, W. B. McAnelly
Teledyne Brown Engineering
Huntsville, Alabama 35807

and

E. C. McKannan, S&E-ASTN-MM
George C. Marshall Space Flight Center
Huntsville, Alabama 35807

SUMMARY

The objective of the present work is to study the utilization of the unique conditions offered by the Earth orbital environment in material processing involving both solid and liquid phases -- such as liquid phase sintering.

To achieve this, an experimental development program involving both test and theoretical work was initiated. Experimental work using material combinations selected such that maximum information about the effect of gravity can be derived has been conducted. Wetting of the solid phase by the liquid during sintering is an important phenomenon in liquid phase sintering, and gravity has influence on both capillary phenomenon and density segregation; hence, material combinations were selected such that these two effects can be suitably studies. The experimental work is meant to form the basis for similar comparative work done under low-g conditions.

The part of the model dealing with the capillary phenomenon, as related to liquid phase sintering and the effect of gravity on it, suggest that gravity will have negligible effect on the Bond number and that the cohesive force is dependent on both the amount of liquid phase and the angle of contact.

The experimental results support this part of the model.

*Paper presented by -- T. Mookherji

INTRODUCTION

The weightless conditions in an orbiting spacecraft offer some unique advantages for work on materials and processes that can yield valuable returns. One of the main advantages of this weightless condition foreseen for achieving such a result is the elimination of gravity-driven forces. This has been very clearly demonstrated through the low-gravity solidification of immiscibles, where segregation effects due to density differences make bulk sample production [1] and numerous other experiments [2] practically impossible on Earth.

It appears that this unique condition can be very profitably utilized in material processes which simultaneously involve solid and liquid phases, such as liquid phase sintering (LPS). This is a processing technique where a mass of small particles of different components is heated above the melting temperature of one of the components so that all the particles become bonded into a solid mass on cooling.

Sintering is a complex process consisting of a series of closely related physicochemical phenomena. It should be regarded as a thermodynamic process in which the system tends to attain a state with minimal free energy. From the work of numerous investigators, it seems clear that certain minimum requirements regarding the wetting of the solid phase by the liquid during sintering must be met in order to successfully sinter with a liquid phase. It is of importance then to consider the wetting

phenomenon and its relation to LPS. In an otherwise non-wetting system, wetting can be achieved by decreasing the solid-liquid interfacial energy through preferential adsorption of one of the constituents in the liquid phase on the surface of the solid phase and/or by diffusion fluxes.

The necessary interface condition of wetting is effected by both gravity and the environment. It has been pointed out in a theoretical study [3] that the adsorption of the residual gases of the space environment, which contains a high percentage of O and O_2, will affect the specific surface energy of both the solid and liquid phases. It was also shown that both vacancy concentration and thermal faceting are functions of surface energy.

The present paper deals with that part of the theoretical model which deals with the capillary phenomenon, as related to LPS and the effect of gravity on it, and some experimental results that corroborate with this part of the model. Modeling for the trapped gas bubble and segregation and their influence on LPS will be reported in the future.

FUNDAMENTAL CONCEPTS FOR LIQUID PHASE SINTERING MODEL

During various stages of the sintering process a simple LPS can be viewed as a trinary system. Figure 1 shows schematically the microstructure of an LPS during the various stages of sintering. In the green state, after the work piece has been compacted, the individual particles, according to Goetzel [4], are held together by interatomic forces (i.e., surface adhesion and cold welding) and mechanical interlocking. In this state the LPS compact is a solid/solid/void or, more correctly, a solid/solid/gas system. The void fraction depends on the plasticity of the base materials, the particle sizes and shapes, compacting pressure, and other factors. During the sintering process the compacted material goes from a solid/solid/gas to solid/liquid/gas, and back to a solid/solid/gas system.

Letting f_s, f_{ls}, f_v represent the volume fractions of the higher melting point solid, the lower melting point solid, and the void, respectively, it is obvious that for this simple LPS compact,

$$f_s + f_{ls} + f_v = 1 \quad . \tag{1}$$

Maximum densification of the final product occurs when $f_v \rightarrow 0$.

During the process of sintering, the void fraction changes, due to various processes, from its initial value to a final value; the difference accounts for the shrinkage.

From the viewpoint of fluid flow, an LPS compact in the green state consists of many capillary tubes. During the sintering process, as the temperature is raised, several changes occur. At a temperature well below the melting point, the lower melting component becomes very plastic and the bonding forces between adjacent particles is reduced. Shrinkage of the compact can occur during this phase because the plasticity of the lower melting component allows the particles to move into closer packing.

As the temperature is raised above the point where the lower melting component becomes liquidus, the liquid, driven by capillary forces, flows among the solid particles. Simultaneously, the surface tension forces, produced as the liquid fills the voids, moves the solid particles.

For a liquid melt which is highly non-wetting with respect to the solid particles (i.e., $\theta > 90°$ where θ is the liquid/solid contact angle), the liquid tends to form into a sphere (Figure 1) because of the influence of surface tension and the minimum energy principle. Under these conditions the liquid surface tension forces tend to separate the solid particles.

For a liquid melt which is highly wetting (i.e., $\theta \approx 0°$) the liquid tends to flow along the surfaces of the solid material (Figure 1). Under these conditions the surface tension forces tend to pull the solid particles together.

As the liquid flows through the circuitous capillary tube system, represented by the spaces between the solid particles, gas bubbles can be trapped. These trapped gas bubbles become the voids when the compact is resolidified.

Another factor which influences the final state of the sintered compact is the segregation of material according to density. Depending upon the degree of compaction and the particle size and shape, the void fraction can vary from 0.25 to 0.5. According to Lenel [5], the fraction of liquid must be at least 0.25 in order to fill all the voids. For spherical particles, theoretical calculations [6] indicate that a liquid fraction of 0.35 is required to fill all of the voids. Under conditions where the density of the solid is significantly different from that of the liquid, and/or where the

Naidich, et al [8] studied the same problem, except that gravitational effects were ignored.

Their derivation produced equations identical to Equations 24, 25, and 26. Packing of particles is a debatable point in any theoretical colloid or particle problem. For the simple problem, where the body is formed of spherical particles, the maximum and minimum pore space is obtained when the packing is cubic and rhombohedral, respectively. The orientation of the packed spheres is shown in Figure 7. The density of a packed mass is related to the densities of the solids and the pore space and, therefore, to the volume of the pore space.

As can be seen in Figure 7, for cubic packing each central sphere has six neighors, and for rhombohedral packing each central sphere has twelve neighbors. By passing tangent planes between adjacent spheres at the nearest points and perpendicular to a line between the centers, it can be seen that the total space occupied by each sphere and and its pore space is a cube for cubic packing and a rhombic dodecahedron for the rhombohedral packing (Figure 7). Assuming the spheres to be a uniform distance (ℓ) apart at the nearest point and letting R be the spherical radius (same as that used in Figure 4), the total volume occupied by each sphere and its pore space can be derived and gives:

$$\text{cubic packing} \qquad V_t = 8(R + \ell/2)^3 \quad ; \tag{27}$$

$$\text{rhombohedral packing,} \qquad V_t = \frac{8}{\sqrt{2}} (R + \ell/2)^3 \quad . \tag{28}$$

Letting the spheres represent the solid particles of an LPS, we see that

$$f_s = \frac{V_s}{V_t} \tag{29}$$

and

$$f_{LS} = \frac{n V_\ell}{V_t} \tag{30}$$

where V_S is the volume of the solid. Then, from Equation 1

$$f_v = 1 - (f_S + f_{\ell v}) = 1 - \frac{V_S + n V_\ell}{V_t} \tag{31}$$

where n is the number of surfaces in contact (i.e., n = 6 for a cube and n = 12 for a rhombic dodecahedron). For cubic packing, Equations 29, 30, and 31 give

$$(f_s)_{cp} = \frac{\pi}{6} \cdot \frac{R^3}{(R + \ell/2)^3} \tag{32}$$

$$(f_{\ell s})_{cp} = \frac{2/3\ V_\ell}{(R + \ell/2)^3} \tag{33}$$

$$(f_v)_{cp} = 1 - \frac{4/3\ \pi\ R^3 + 6\ V_\ell}{8(R + \ell/2)^3} \quad . \tag{34}$$

For rhombohedral packing, Equations 29, 30, and 31 give

$$(f_s)_{rp} = \frac{\sqrt{2}\ \pi}{6} \frac{R^3}{(R + \ell/2)^3} \tag{35}$$

$$(f_{\ell s})_{rp} = \frac{\sqrt{2}}{8} \frac{12\ V_\ell}{(R + \ell/2)^3} \tag{36}$$

$$(f_v)_{rp} = 1 - \frac{\sqrt{2}\ (4/3\ \pi\ R^3 + 12\ V_\ell)}{8(R + \ell/2)^3} \quad . \tag{37}$$

For close packing, i.e., $\ell = 0$ and for no liquid, Equations 34 and 37 give maximum and minimum void fractions of

$$(f_v)_{cp} = 0.4764 \tag{38}$$

and

$$(f_v)_{rp} = 0.2595 \quad . \tag{39}$$

From these results it is easy to deduce that the amount of liquid required to just fill all the voids of the compact must be between 25.95 and 47.64% by volume.

Figures 8, 9, and 10 show how the surface tension-induced, adhesive forces vary with the contact angle, distance between particles, and liquid fraction.

amount of liquid is much greater than the minimum amount required to fill the void space, the solid and liquid components can segregate themselves according to density. The forces controlling the segregation are buoyancy forces with respect to the gravitational vector. Surface tension and adhesion can also force some of the liquid through the outer pores of the compact.

The previous discussion suggests that at least three simple phenomenological models are necessary for describing the fluid aspects of liquid phase sintering. These three models of the problem are shown in Figures 2 and 3.

MODELING OF SURFACE TENSION FORCES ACTING DURING SINTERING

Depicting the compact ideally as many spheres, with adjacent spheres connected at their nearest points by a small amount of liquid (Figure 2), can explain some of the forces acting during the sintering process. Adjacent spheres are attracted or repelled because of the capillary-like forces which are produced by the intervening liquid. For a wetting liquid the forces are attractive, therefore, an interior particle, as depicted in Figure 2, is subject to attraction in all directions by neighboring particles. Particles on the surfaces are attracted inwards and to the sides by neighboring particles, but there is no outward attraction to balance the inward pull. Hence, every surface particle is subject to inward attraction more or less perpendicular to the surface. For conditions where no other forces act to prevent inward movement the exterior particles tend to move inward causing omnidirectional shrinkage. It is possible to model the capillary forces by considering two spheres with an intervening liquid as shown in Figure 4. In the general case the liquid-vapor interface shape varies as depicted in Figure 4. Because of hydrostatic forces the radii of curvature are assumed to vary with the angles α and β. Later it will be shown that constant radii of curvature is a very safe assumption for LPS.

For a wetting liquid the pressure (P_ℓ) on the liquid side of the liquid-vapor interface is less than the pressure (P_v) on the vapor side. Therefore, the spheres are subjected to a compressive force given by

$$dF_1 = (P_v - P_\ell)\, dA_{\alpha, z} \qquad (2)$$

where

dF_1 - hydrostatic force acting to attract the spheres (note that when $dF_1 < 0$, the force is repulsive)

$dA_{\alpha, z}$ - projection of the wetted area on the α, z plane.

A surface tension component opposite to the σ vector shown in Figure 4 is also acting to pull the spheres together. A differential surface tension force is given by

$$dF_2 = \sigma_{\ell v} \cos [90 - (\phi_0 + \theta)] \, dS \qquad (3)$$

where

dF_2 - surface tension force acting to attract the spheres (note that when $dF_2 < 0$, the surface tension force is repulsive)

$\sigma_{\ell v}$ - liquid-vapor surface tension

dS - liquid-solid wetted perimeter increment

ϕ_0 - angle between the sphere centerlines and the wetted perimeter

θ - liquid, solid contact angle.

Letting

$$dA_{\alpha, z} = R \sin \phi \, d\alpha \cdot d(R \sin \phi) \qquad (4)$$

$$dS = R \sin \phi \, d\alpha \, . \qquad (5)$$

Then the resultant force is given by

$$dF = dF_1 + dF$$

$$= (P_v - P_\ell) R \sin \phi \, d(R \sin \phi) \, d\alpha$$

$$+ \sigma_{\ell v} \sin (\phi_0 + \theta) R \sin \phi_0 \, d\alpha \, . \qquad (6)$$

The integration of Equation 6 requires a complete definition of the interface shape and the hydrostatic forces. The hydrostatic forces can be related to the surface tension through Laplace's first law, giving

$$P_v - P_i = \sigma_{lv}\left(\frac{1}{r_2} - \frac{1}{r_1}\right) . \quad (7)$$

where r_1 and r_2 are the principal radii of curvature at any point on the liquid-vapor surface (α, x, z). Assuming an acceleration vector (g) to be aligned with the z axis the hydrostatic pressure on the liquid side of the liquid-vapor interface is given by

$$P_l = P_{lo} + P_l\left(\frac{g}{g_0}\right)(z_0 - z) \quad (8)$$

where

P_{lo} - hydrostatic pressure at the interface where $\alpha = 0$, $x = 0$, $z = z_0 = r_{10}$ (i.e., top, center of the interface)

P_l - liquid density

g_0 - sea level gravitational constant.

Since $z = r_1 \cos\alpha$, Equation 8 can be written as

$$P_l = P_{lo} + P_l\left(\frac{g}{g_0}\right)(r_{10} - r_1 \cos\alpha) , \quad (9)$$

Then, Equation 7 becomes

$$(P_v - P_l) = P_v - P_{lo} - P_l\left(\frac{g}{g_0}\right)(r_{10} - r_1 \cos\alpha)$$

$$= \sigma_{lv}\left(\frac{1}{r_2} - \frac{1}{r_1}\right) . \quad (10)$$

At the point $\alpha = 0$, $z = 0$, $z = z_0$, Equation 7 gives

$$P_v - P_{lo} = \sigma_{lv}\left(\frac{1}{r_{20}} - \frac{1}{r_{10}}\right) . \quad (11)$$

Then, defining a mean radius of curvature as

$$\frac{2}{r_m} = \left(\frac{1}{r_2} - \frac{1}{r_1}\right) \quad (12)$$

and

$$\frac{2}{r_{mo}} = \left(\frac{1}{r_{20}} - \frac{1}{r_{10}}\right) \tag{13}$$

Equation 10 gives

$$\frac{(P_v - P_\ell)}{\sigma_{\ell v}} = \frac{2}{r_{mo}} - \frac{P_\ell}{\sigma_{\ell v}}\left(\frac{g}{g_0}\right)(r_{10} - r_1 \cos\alpha) = \frac{2}{r_m} \quad . \tag{14}$$

Equation 14 can be rearranged to give

$$\frac{r_{mo}}{\sigma_{\ell v}} (P_b - P_\ell) = 2 - B_o\left(\frac{r_{10} - r_1 \cos\alpha}{r_{mo}}\right) \tag{15}$$

where B_o is the Bond number given by

$$B_o = \frac{\rho(g/g_0)\, r_{mo}^2}{\sigma_{\ell v}} \quad . \tag{16}$$

From Equation 15, the simple relation obtained is

$$\frac{r_{mo}}{r_m} = 1 - \frac{1}{2} B_o\left(\frac{r_{10} - r_1 \cos\alpha}{r_{mo}}\right) \quad . \tag{17}$$

Equation 17 can be viewed as a measure of the eccentricity of the vapor-liquid interface. Table I lists the density and surface tension of several common LPS liquid phase materials in addition to those of water.

TABLE I. LPS LIQUID PROPERTIES

MATERIAL	SP. GR.	$\sigma_{\ell v}$ (dyne/cm)	$\rho/\sigma_{\ell v}$ [gm/(dyne cm^2)]
Cu	8.9	1270	0.007
Ag	10.5	940	0.01117
Pb	11.3	455	0.02484
CaO	3.3	820	0.00402
MgO	3.6	1090	0.0033
H_2O	1.0	75	0.01333

Letting the mean radius of curvature r_{mo} in Equation 16 be equal to the radius of the sphere of Figure 4, the effects of gravity, particle radius, and the liquid density-surface tension ratio can be evaluated. From Table I it is seen that most of the common LPS liquids have density to surface tension ratios of the order of $0.001 < (\rho)/(\sigma_{\ell_v}) < 0.01$. For particle-sizes ranging from 10 μ to 1000 μ, the Bond numbers for various (g/g_0) levels have been computed and are shown in Figure 5. In most liquid phase sintering, particle sizes of the order of 10μ to 100μ are generally used. From Figure 5 it is seen that the Bond number for a one (g/g_0) environment is on the order of 10^{-3} and less. For the same size particles in a 10^{-4} (g/g_0), the Bond number is 10^{-7} and less. Therefore, because the particle sizes in LPS are so small, the Bond number is significantly less than unity.

An understanding of how the Bond number affects the liquid-vapor interface shape can be obtained by considering the results derived by Hastings [7]. Using the principle of minimum energy, Hastings computed the liquid-vapor interface shape of a liquid confined in an axis-symmetric container as a function of Bond number. Dimensionless interface shapes for Bond numbers varying between 0 and ∞ are shown in Figure 6. Normally, in low-gravity fluid mechanics problems, the Bond number changes from a large number under one-g conditions to a very small number as gravity approaches zero. For example, a one-foot-diameter container of water has a Bond number of approximately $B_o = 3000$ at one g, which reduces to $B_o = 0.3$ at $g/g_0 = 10^{-4}$. As can be seen in Figure 6, this causes the interface to change from a flat shape at one g to a nearly spherical shape at 10^{-4} g/g_0.

In liquid phase sintering, however, the particle sizes are so small that the Bond number is nearly zero even under one-g conditions. Reducing the Bond number further by reducing the gravitational component has a negligible effect on the interface shape. Therefore, Equation 17 gives

$$\lim_{B_o \to 0} \left(\frac{r_{mo}}{r_m} \right) = 1 \quad .$$

Thus, it is seen that as the Bond number tends to zero for whatever cause, the mean radius of curvature becomes a constant with respect to the variables α and β (see Figure 4). Equations 12 and 13 then give

$$\frac{2}{r_m} = \frac{2}{r_{mo}} = \left(\frac{1}{r_2} - \frac{1}{r_1} \right) = \left(\frac{1}{r_{20}} - \frac{1}{r_{10}} \right)$$

$$= \text{constant} \quad . \qquad (19)$$

Equation 10 then gives

$$(P_v - P_l) = \frac{2\sigma_{lv}}{r_{mo}} \quad . \tag{20}$$

Equation 6 can then be written as

$$dF = \frac{2\sigma_{lv}}{r_{mo}} R \sin\phi \, d(R \sin\phi) \, d\alpha + \sigma_{lv} \sin(\phi_0 + \theta) R \sin\phi_0 \, d\alpha \quad . \tag{21}$$

Then since $r_m = r_{mo}$ = constant, and ϕ is not a function of α for $[1/r_{20}) - (1/r_{10})]$ = constant, Equation 21 can be integrated to give

$$F = \int_0^{R \sin\phi_0} \int_{\alpha=0}^{2\pi} \frac{2\sigma_{lv}}{r_{mo}} R \sin\phi \, d(R \sin\phi) \, d\alpha + \int_{\alpha=0}^{2\pi} \sigma_{lv} \sin(\phi_0 + \theta) R \sin\phi_0 \, d\alpha \tag{22}$$

$$F = (2\pi)\left(\frac{\sigma_{lv}}{r_{mo}}\right)\frac{(R \sin\phi)^2}{2} + 2\pi \sigma_{lv} \sin(\phi_0 + \theta) R \sin\phi_0 \tag{23}$$

or

$$F = \sigma_{lv}\left[\pi R^2 \sin^2\phi_0 \left(\frac{1}{r_{20}} - \frac{1}{r_{10}}\right) + 2\pi R \sin\phi_0 \sin(\phi_0 + \theta)\right]. \tag{24}$$

Letting l be the distance between spheres gives

$$r_{10} = R \sin\phi_0 - \left[R(1 - \cos\phi_0) + \frac{l}{2}\right] \frac{1 - \sin(\phi + \theta)}{\cos(\phi + \theta)} \tag{25}$$

$$r_{20} = \frac{R(1 - \cos\phi) + \frac{l}{2}}{\cos(\phi + \theta)} \tag{26}$$

From Figure 8 it can be seen that the cohesive force decreases as the contract angle increases. The force is also seen to decrease as the angle ϕ increases. For any contact angle less than 90 degrees, it can be seen that the force becomes repulsive as the angle ϕ is increased from the critical value where the force is zero.

Figure 9 shows how the cohesive force varies with distance between particles for $\phi = 30°$. For highly wetting liquids (i.e., for θ near zero) the force is highest when the particles are touching and decreases as the distance between particles increases. For liquids where the contact angle approaches 90 degrees, the force is reduced as the distance between particles decreases. For $75° < \theta < 90°$ the forces are repulsive for distances between particles of $\ell/R < 0.2$. Referring to Figure 8 it is seen that as ϕ increases the contact angle at which the forces become repulsive decreases. This suggests a tendency of the particles to trap bubbles as shrinkage occurs.

Figure 10 shows how the cohesive force varies as the contact angle and liquid fraction are varied for the idealized rhombohedral packing with $\ell = 0$. This figure shows that the cohesive force varies only slightly as more liquid is added but decreases significantly as the contact angle is increased.

These results suggest that conditions can exist which cause the particles to tend to trap bubbles. This tendency is somewhat supported by the studies of liquid between cylinders carried out by Princen [9]. One of Princen's conclusions is shown schematically in Figure 11. As seen in Figure 11, when cylinders are moved together the entrapped liquid tends to separate into columns, leaving a void in the center. As the distance between cylinders was increased bubbles became trapped.

Bubble entrapment and material segregation according to density are much more strongly influenced by changes in gravity. The forces acting on the particles or bubbles are related to buoyancy according to

$$F_b = V_b \cdot (\rho_\ell - \rho_v) \left(\frac{g}{g_0}\right) . \qquad (40)$$

As gravity is reduced from the one-g condition to the low-g condition of orbit, the buoyancy force tends to zero. The latter is anticipated to produce unique distribution conditions in the LPS. Models of bubble entrapment and material segregation will be developed in the following phases of this study.

MATERIAL AND PROCEDURE

The formation of a powder metallurgical body during liquid-phase sintering occurs in a system consisting of solid, liquid, and gaseous phases. Since the particle size of the solid phase is usually small, the green body to be sintered is a capillary system. The behavior of such a system with highly developed surfaces, the distribution of phases within it, and, consequently, the properties of the body itself, will depend to a considerable extent on the properties of the boundaries between the phases within the system. That is, it will depend on the wetting of the solid phase by the liquid phase. Moreover, the two phases of this process tend to segregate due to considerable difference in density.

Gravity has influence on both capillary phenomena and this type of segregation. Since liquid state is present, both Marangoni and Rayleigh convection phenomena will take place.

Based on the above arguments, emphasis was placed on wetting characteristics and density difference and the following material combinations were selected:

(a) 30 vol % Ag and Al_2O_3
(b) 40 vol % Cu and W
(c) 40 vol % Cu and Fe.

The relevant properties of these materials are given in Table II.

TABLE II. RELEVANT PROPERTIES

MATERIAL	MELTING POINT °C	DENSITY	SURFACE TENSION		CONTACT ANGLE AT 1100°C
			σ_{SV} erg/cm^2	σ_{LV} erg/cm^2	
Ag	960.8	10.5		940	83°
Al_2O_3	2050	3.5	905		
W	3370	19.3	>2300		35°
Cu	1083	8.92		1270	0°
Fe	1535	7.86	2039		

The combinations were thoroughly blended in a laboratory blender and compacted in an isostatic pressuring unit. The pressures used for Ag-Al_2O_3, Cu-W, and Cu-Fe were 30.000, 15,000, and 7,000 psi, respectively. The compacted, cylindrical samples were about 4.5 centimeters in diameter and 4.0 centimeters in length. Both Cu-Fe and Cu-W powders were reduced in a hydrogen furnace before compacting.

The compacts were sintered in a vacuum furnace with a protective atmosphere of pure argon. Steel containers with molybdenum lining were used. The samples were put in the containers with their cylindrical axis vertical and kept in the vacuum furnace for about 16 hours under a vacuum of 10^{-5} torr. Then the temperature of the furnace was raised to about 300°C under dynamic vacuum and held for about 4 hours. Pure argon was then introduced into the furnace without breaking the vacuum. The furnace was then brought to 1,100°C and held at this temperature for 1 hour. A safety valve kept the pressure in the furnace around atmosphere during the heating cycle. Typical heating time was about 2 hours and the cool-down time was about 10 to 12 hours.

Densities of both green and sintered samples were determined and the samples were cut along the cylinder axis and polished. Metallographic picture and scanning electron microscopy was done on the polished surface. Electrical resistivity mapping of the polished surface was done with a four-point resistivity probe. The variation in the concentration of the liquid phase along lengths parallel to the cylinder axis was determined using atomic absorption spectroscopy.

The experimental work is meant to form the basis for similar reproducible comparative work done under low-g conditions.

RESULT AND DISCUSSION

The results of the measurement of density are shown in Table III. The theoretical density is also tabulated for comparison.

TABLE III. RESULTS ON MEASUREMENT OF DENSITY

SYSTEM	THEORETICAL DENSITY	GREEN DENSITY	SINTERED DENSITY
Cu-W	13.184	8.839	8.259
Cu-Fe	8.252	4.357	7.711
Ag-Al_2O_3	4.875	3.281	

The Ag-Al_2O_3 system could not be sintered properly under the present experimental conditions. It was possible, though, to compact it properly without any plasticizer, and the green density achieved was 67.3 percent of theoretical density. Such high theoretical density, in general, should give good densification upon sintering.

Observation shows that the sintered part consists of spherical droplets of Ag, of various sizes, scattered around in the matrix of Al_2O_3 (Figure 12). and the bottom part of the sample is stronger than the top part. The problem in this case is that molten Ag does not wet Al_2O_3 at a contact angle of 83 degrees. Each individual molten particle of the metal thus flows down under the influence of gravity, since Ag is heavier than Al_2O_3 (Table II), joins with other molten particles, and forms a big droplet. This process continues throughout the entire sample until the droplets are so large that they cannot flow any further between the particles of Al_2O_3.

This decreases the concentration of silver in the top part of the sample and the Al_2O_3 particles no longer have any bonding, making the top structure lose its strength. Moreover, the non-wetting characteristics, according to our model, should give a repelling force between the Al_2O_3 particles. This means that, after sintering, there should be a swelling, instead of shrinkage, of the sample. This, however, could not be verified, in this case, because the structure could not retain its compacted shape. According to the model, the cohesive force is dependent on both the angle of contact and the quantity of the liquid phase. For the same angle of contact the cohesive force decreases with the increase of the quantity of the liquid phase. This phenomenon is true for spherical particles but may be entirely different for particles of other shapes.

The Ag-Al_2O_3 sample represents a classical case of density segregation in a non-wetting system. In a low gravity, the segregation effect is not expected. The individual molten particles of silver will not bond with Al_2O_3, but are expected to stay well dispersed without forming large, spherical droplets. It is expected, according to the model, that the repelling forces will be present and that the sintered density may be lower than the green density.

The Cu-W system could be sintered under the present experimental conditions; however, it was found that all 40 percent by volume of Cu could not be retained in the sintered body. Only about 38 percent by volume of the liquid phase was retained and the rest extruded. The extruded liquid phase suggests that the angle of contact is not 35 degrees

under the present experimental conditions. According to the theoretical model, in systems with a large angle of contact the particles are, in general, repelled and there is no shrinkage after sintering. As indicated before, the cohesive force is also dependent on the amount of liquid phase. This postulation of the model is verified through the density measurement. The measured sintered density is lower than the green density (Table III). The green density is 67 percent of the theoretical density, whereas the sintered density is only 61.7 percent of the theoretical density.

From the metallographic pictures (Figures 13 and 14), it is clear that there is migration of the two phases along the gravity direction during sintering. The distribution of the two phases in the green sample (Figures 13a, b, c) is much more uniform as compared to the sintered sample (Figures 13d, e, f). This is further verified through resistivity (Figure 17) and copper concentration mapping. The segregation effect is probably evident because the wetting of the solid phase by the liquid phase is poor and there is a considerable difference between their densities (Table II).

The Cu-Fe system turned out to be the best after sintering. This was expected since liquid copper has a contact angle of 0 degrees with iron. The sintered density is 7.711 i.e., 94 percent of the theoretical density as compared to 53 percent for the green. This is in accordance with the model. The model predicts a high attractive force with a contact angle of 0 degree.

From the metallographic pictures (Figures 15 and 16), it is evident that the distribution of the two phase is quite uniform along the gravity direction of the sample after sintering. This distribution does not seem to be different from the distribution in the green sample. There is considerable grain growth after sintering. This is further verified through resistivity (Figure 18) and copper concentration mapping. The segregation effect is not present because the densities of the two phases are almost equal (Table II).

It can be concluded that the capillary forces acting on the solid particles are dependent on contact angle and the quantity of the liquid phase. Even for moderate angles of contact the cohesive force can be converted to repulsive force by varying the quantity of the liquid phase. The capillary force acting on the particles under "one-g" conditions are negligibly different from those which will exist under "zero-g" conditions.

REFERENCES

1. J. L. Reger, "AIAA 12th Aerospace Sciences Meeting", Paper No. 74-207

2. M. L. Yaffee, Aviation Week of Space Technology, February 25, 1974, p. 40

3. R. Fabiniak, T. Fabiniak, E. C. McKannan, and R. Abbott, "Space Processing and Manufacturing", ME-59-1, 448, October 21, 1969

4. C. G. Goetzel, Treatise on Powder Metallurgy, Vol. 1, p. 259, Interscience Publisher, New York, 1969

5. F. V. Lanel, The Physics of Powder Metallurgy, McGraw-Hill, New York, 1951

6. W. D. Kingery, J. Appl. Phys., 30, 301, 1959

7. L. J. Hastings, "Low Gravity Liquid-Vapor Interface Shapes in Axisymmetric Containers", M.S. Thesis, University of Alabama, Huntsville, Alabama, 1968

8. Yu. V. Naidich, J. A. Lavrinenko, and V. N. Eremenko, International Jour. Powder Met., 1, 41, 1965

9. H. M. Princen, J. Colloid Interface Sci., 34, 1971, 1970

BIBLIOGRAPHY

N. K. Adam, "Physics and Chemistry of Surfaces"

D. P. Woodruff, The Solid-Liquid Interface, Cambridge University Press, 1973

J. T. Davies and E. K. Rideal, Interfacial Phenomena, Academic Press, New York, 1963

V. K. Semenchenko, Surface Phenomena in Metals and Alloys, Pergamon Press, New York, 1961

F. V. Lenel, Trans. AIME, 175, 878, 1948

T. J. Whalen and M. Humenik, Jr., Trans. AIME, 218, 952, 1960

W. D. Kingery, J. Am. Ceramic Soc., 37, 42, 1954

D. Moskowitz and M. Humenik, Jr., 1965 International Powder Metallurgy Conference, New York, June 17,

W. D. Kingery, J. Appl. Phys., 30, 301, 1959

T. J. Walen and M. Humenik, Jr., Progress in Powder Metallurgy, 18, 85, 1962

W. D. Kingery, E. Niki, and M. D. Narasimhan, J. Am. Ceramic. Soc., 44, 29, 1961

W. D. Kingery and M. D. Narasimhan, J. Appl. Phys., 30, 307, 1959

L. H. VanVleck, J. Metals, 3, 251, 1951

Ed. W. D. Kingery, Kinetics of High Temperature Processes, John Wiley and Sons, Inc., 1959

A. L. Prill, H. W. Hayden, and J. H. Brophy, Trans. AIME, 233, 960, 1965

G. C. Kuczynski, J. Metals, 1, 159, 1949

M. Humenik, Jr. and N. M. Parikh, J. Am. Ceramic Soc., 39, 60, 1956; ibid. 40, 316, 1957

G. W. Greenwood, Acta Met., 4, 243, 1956

Y. Okamoto, J. Japan Soc. Powder Metallurgy, 9, 4, 1962

L. H. VanVleck and O. K. Riegger, Trans. AIME, 224, 957, 1962

O. K. Riegger, G. I. Madden, and L. H. VanVleck, Trans. AIME, 227, 971, 1963

C. Herring, J. Appl. Phys., 21, 301, 1950

J. T. Smith and C. W. Spencer, Trans. AIME, 227, 783, 1963

B. Jackson, W. F. Ford, and J. White, Trans. Brit. Ceramic Soc., 62, 577, 1963

P. Schwartakopf and R. Kieffer, Refractory Hard Metals, Macmillan, New York, 1953

N. J. Anathanarayanan and J. E. Gibsch, J. Metals, 5, 78, 1953

R. K. Geggs, J. Metals, 3, 860, 1951

A. Bondi, Chem. Rev., 52, 417, 1953

N. Cabrera, Trans. AIME, 188, 668, 1950

B. Cech, J. Powder Met., 1, 112, 1963

P. Duwez and H. Martens, J. Metals, 1, 571, 1949

J. Gurland and J. T. Norton, J. Metals, 4, 1040, 1952

J. Gurland, Trans. AIME, 215, 601, 1959

J. Graham, J. H. Weymouth, and L. S. Williams, J. Austral. Inst. Met., 8, 280, 1963

C. Kawashima, S. Saito, and T. Hanazawa, J. Ceram. Assoc. Japan, 66, 191, 1958

W. D. Kingery and M. Breg, J. Appl. Phys., 26, 1205, 1955

N. S. Kothari and J. Waring, Powder Metallurgy, 7, 13, 1964

E. Niki, S. Konara, and K. Tatsuzawa, J. Ceram. Assoc. Japan, 70, 313, 1962

H. R. Peiffer, Trans. AIME, 218, 755, 1960

W. J. O'Brien and C. J. Ryge, J. Am. Ceram. Soc., 47, 5, 1964

J. W. Taylor, Prog. Nuclear Energy, Series 5, Vol. 2, 398, 1959

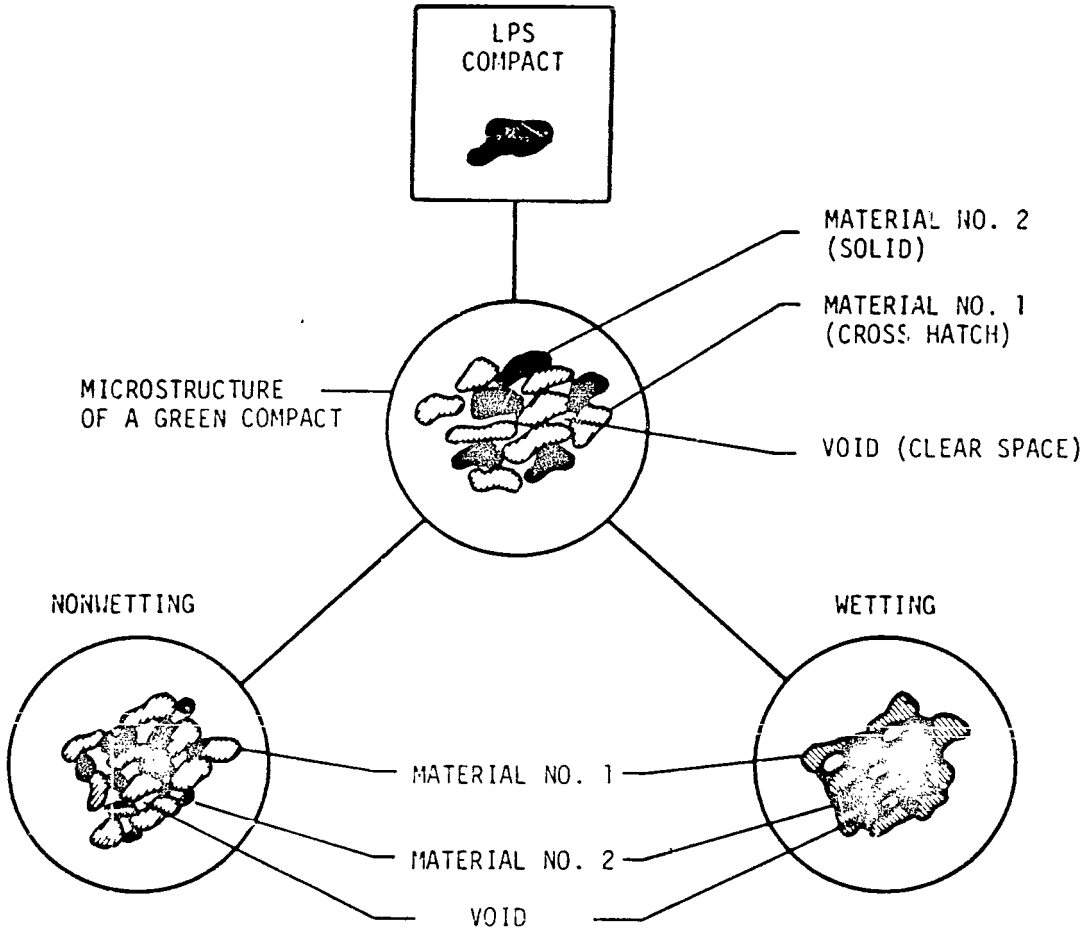

LIQUIDUS/SOLIDUS MICROSTRUCTURE

FIGURE 1. LPS MICROSTRUCTURE DURING VARIOUS PHASES OF SINTERING

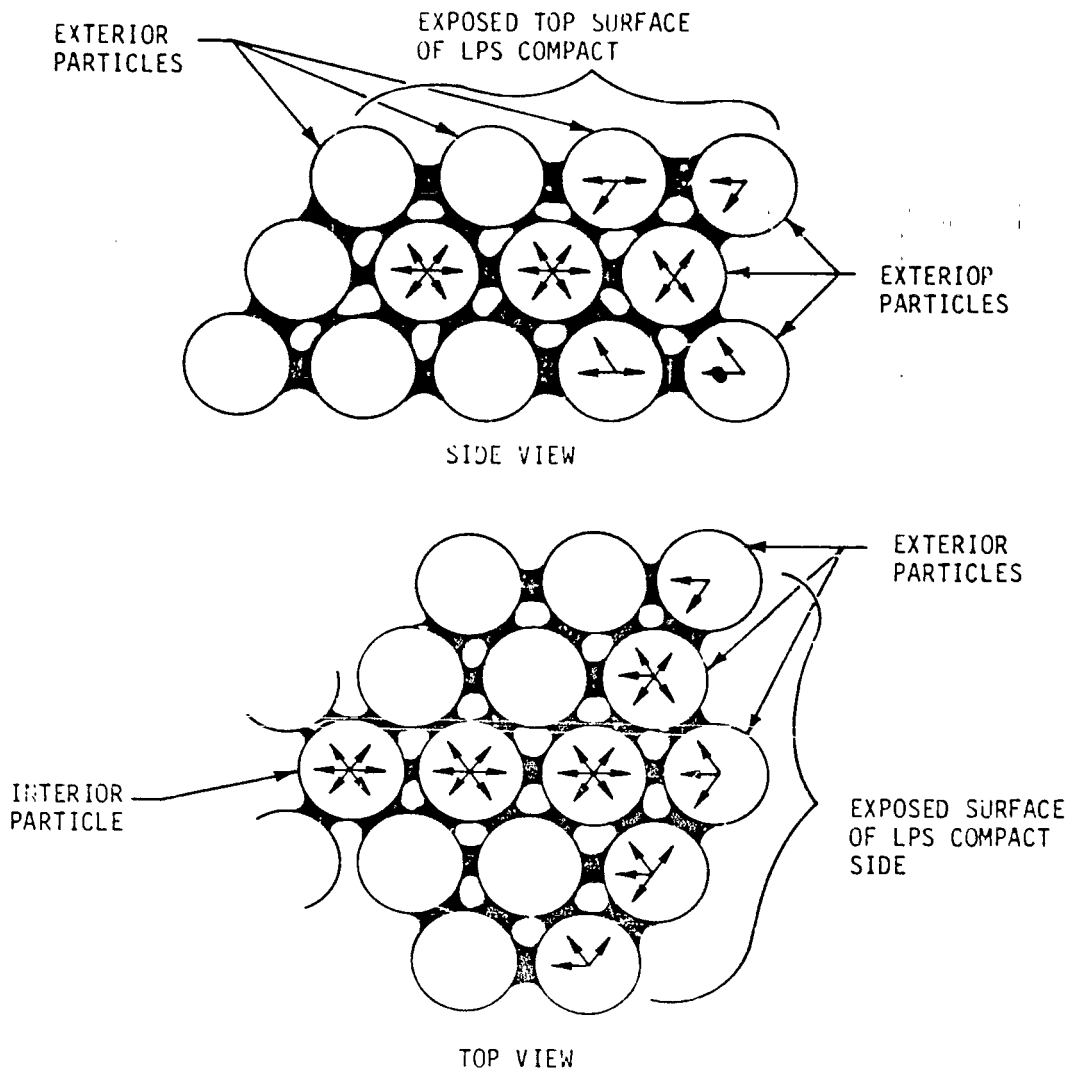

FIGURE 2. SOLID/LIQUID SURFACE TENSION MODEL

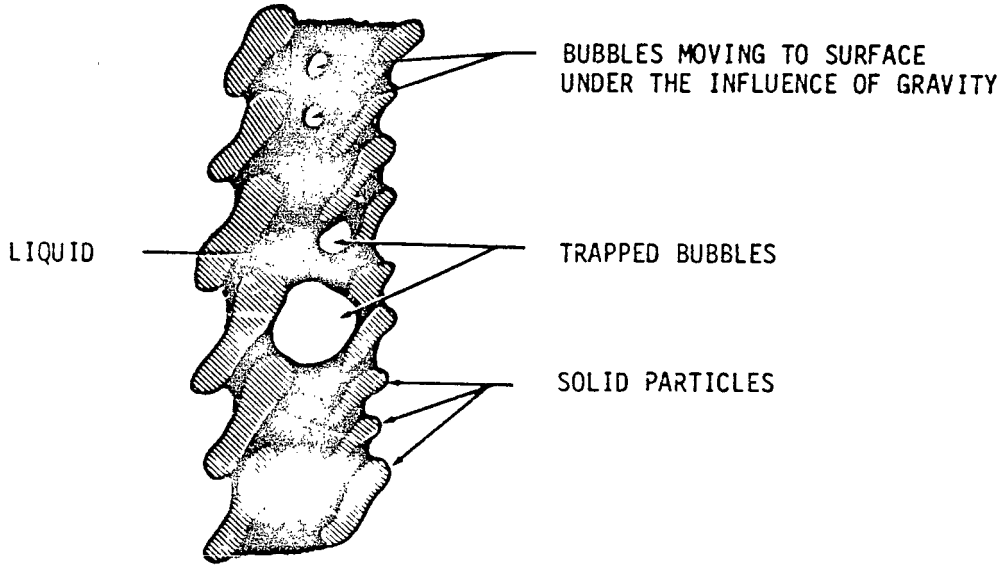

a. Trapped and Moving Bubbles in LPS

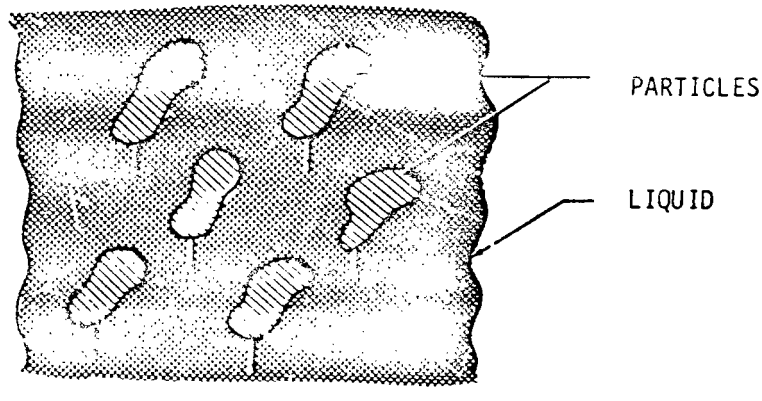

b. Particle Segregation

FIGURE 3. TRAPPED BUBBLE AND SEGREGATION MODEL

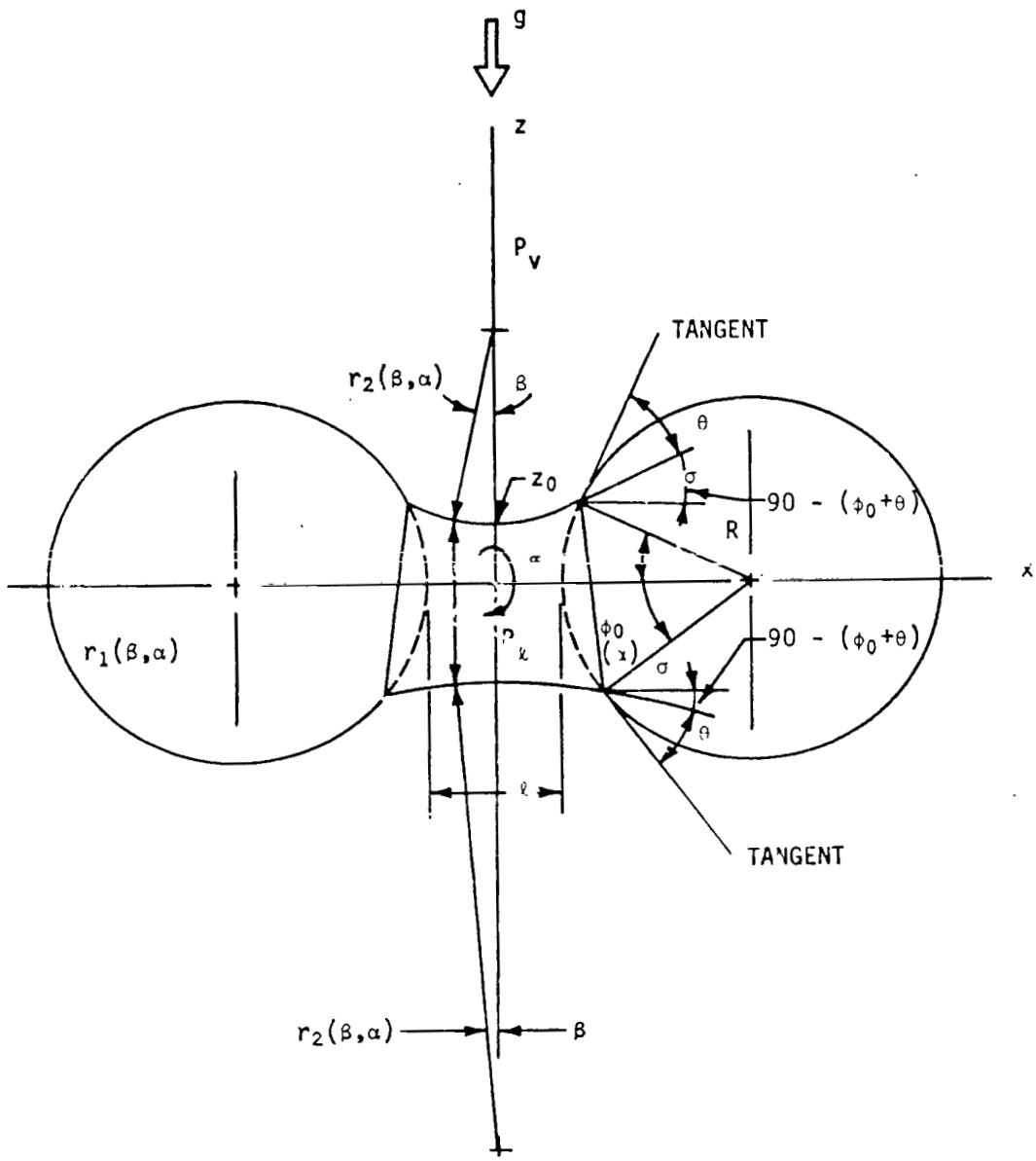

FIGURE 4. TWO-SPHERE SURFACE TENSION MODEL

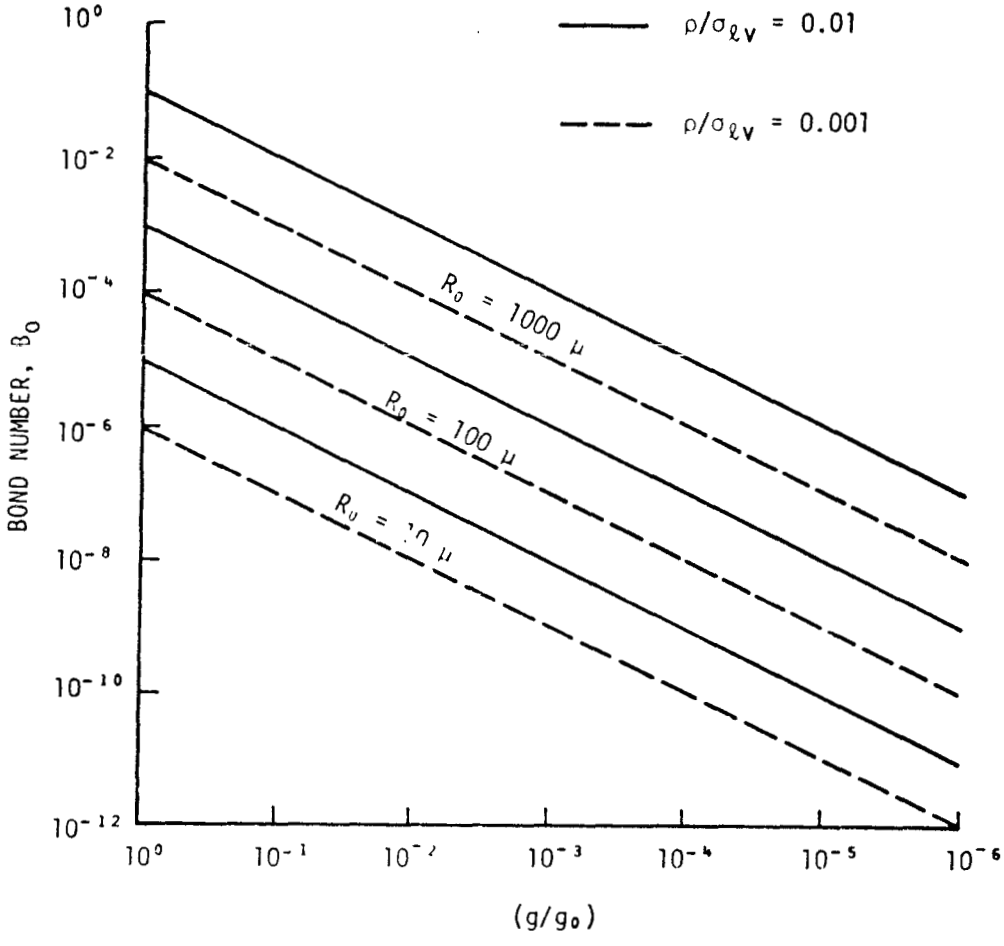

FIGURE 5. BOND NUMBER AS A FUNCTION OF GRAVITY FOR VARIOUS PARTICLE SIZES

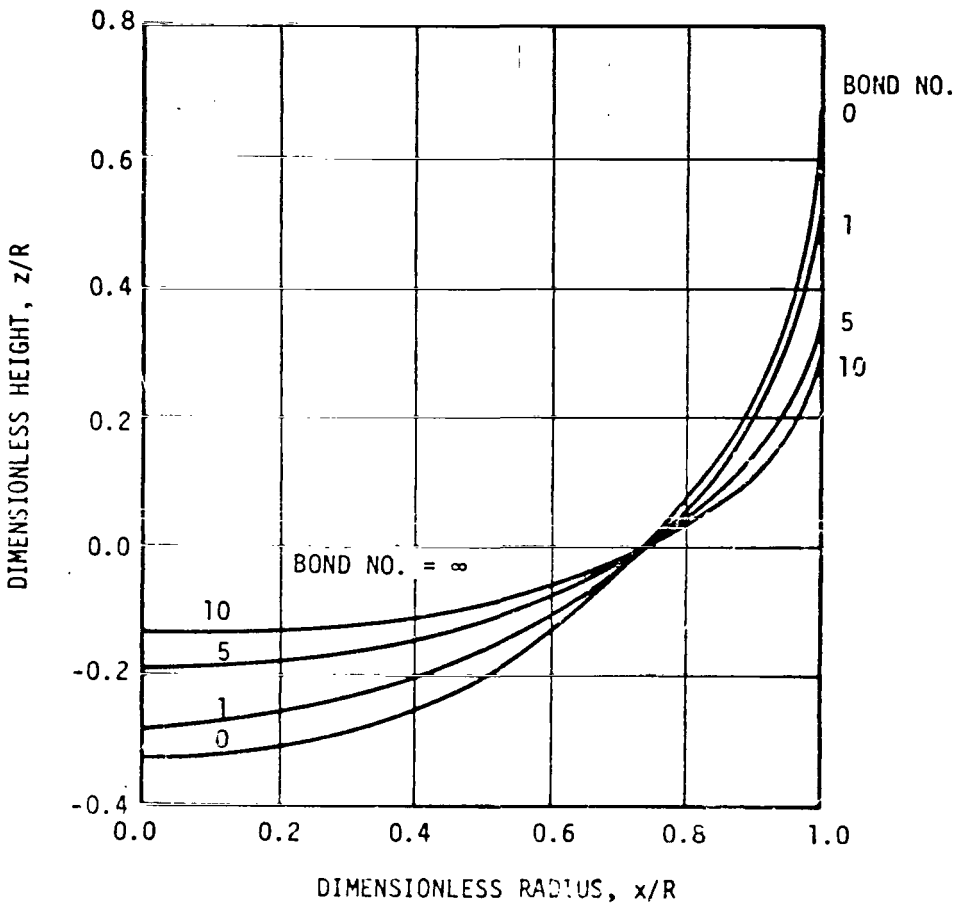

FIGURE 6. LOW GRAVITY ZERO CONTACT ANGLE INTERFACE SHAPES IN CYLINDRICAL CONTAINERS

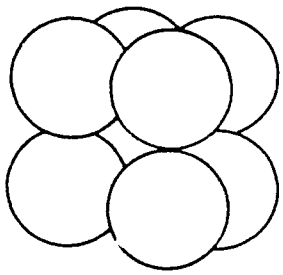

CUBIC PACKING

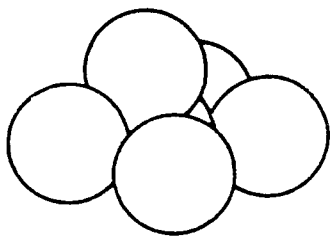

RHOMBOHEDRAL PACKING

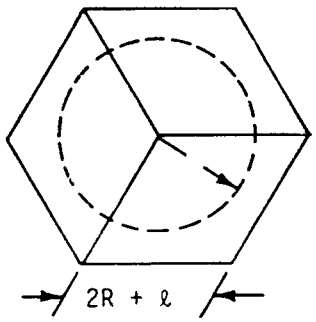

CUBE

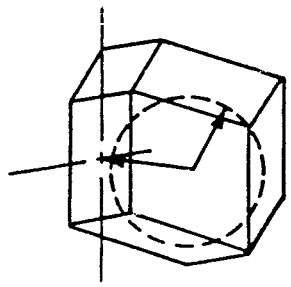

RHOMBIC DODECAHEDRON

FIGURE 7. CUBIC AND RHOMBOHEDRAL PACKING

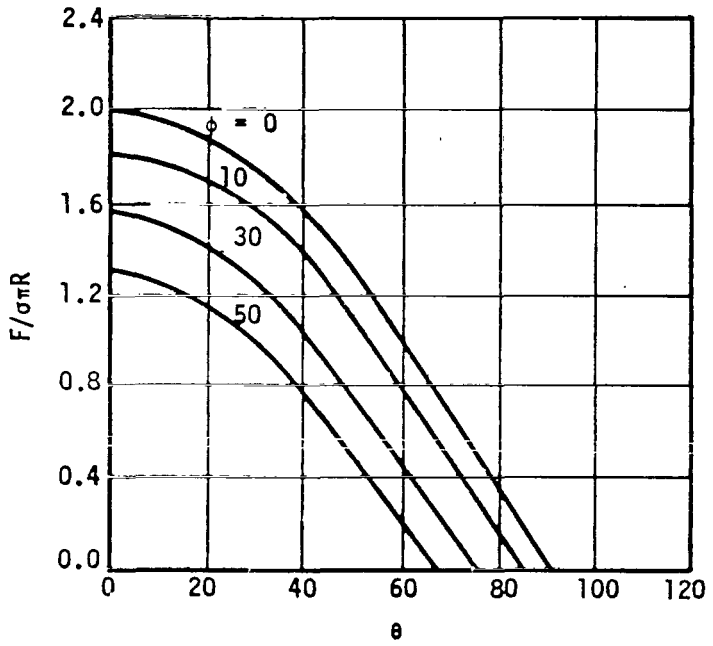

FIGURE 8. VARIATION OF COHESIVE FORCE WITH CONTACT ANGLE AND AMOUNT OF LIQUID PHASE

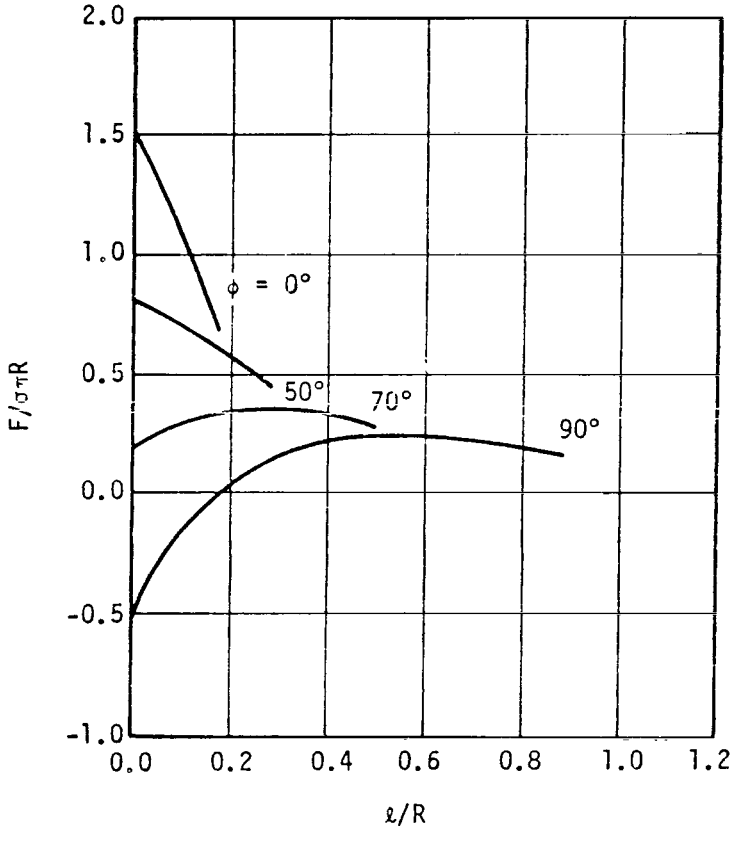

FIGURE 9. VARIATION OF COHESIVE FORCE WITH DISTANCE BETWEEN SPHERES FOR VARIOUS CONTACT ANGLES

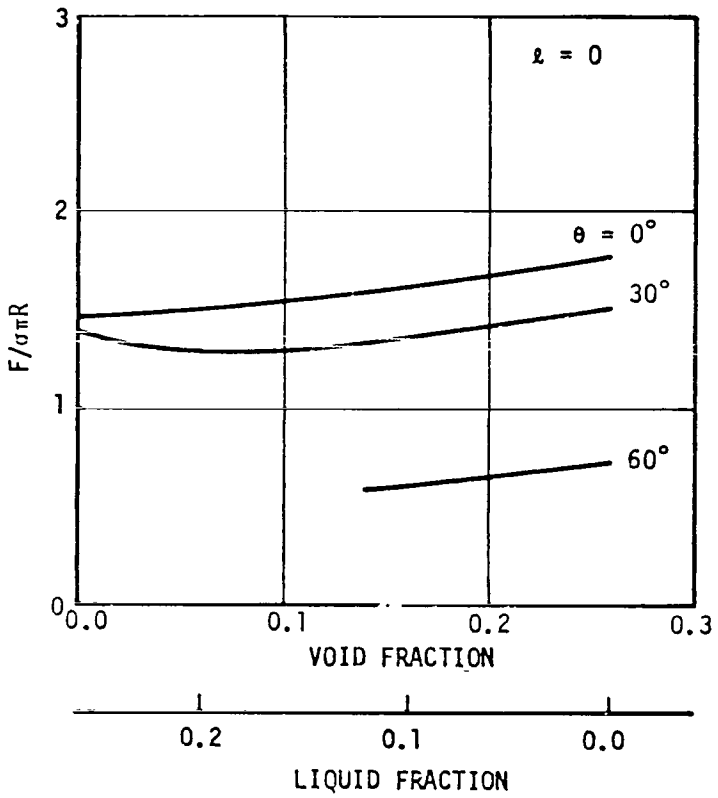

FIGURE 10. VARIATION OF COHESIVE FORCE WITH VOID FRACTION FOR DIFFERENT ANGLES OF CONTACT

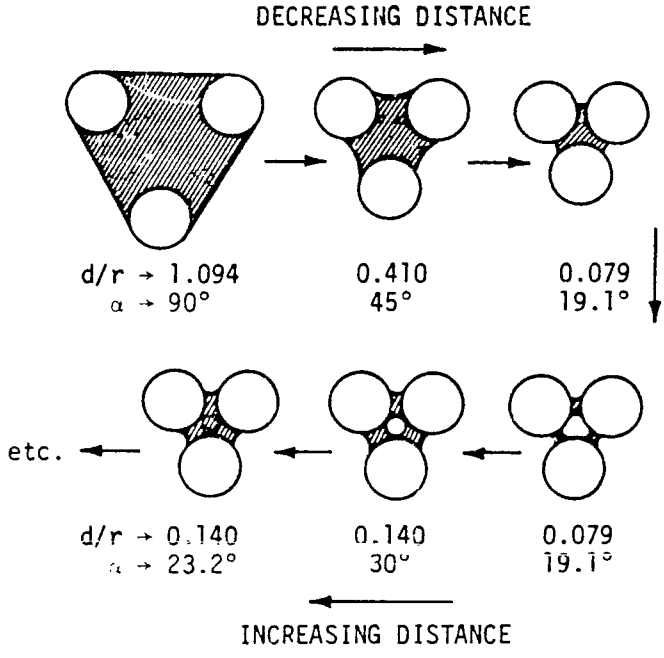

FIGURE 11. CYLINDERS WITH ENTRAPPED LIQUID

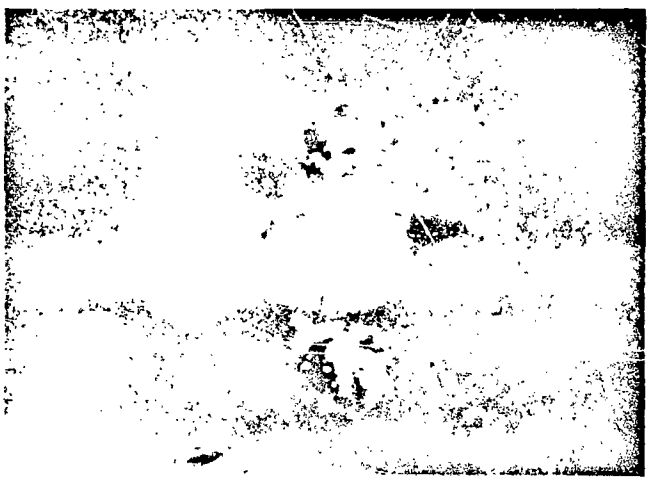

FIGURE 12. PHOTOMICROGRAPH OF SINTERED Ag-Al_2O_3

(a) TYPICAL DISTRIBUTION, 200x MAGNIFICATION

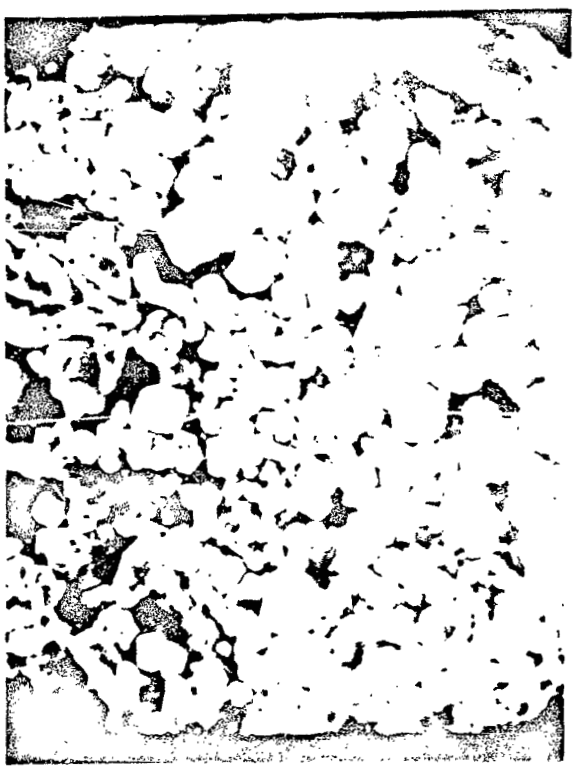

(b) TOP PART OF SAMPLE, 2000x MAGNIFICATION

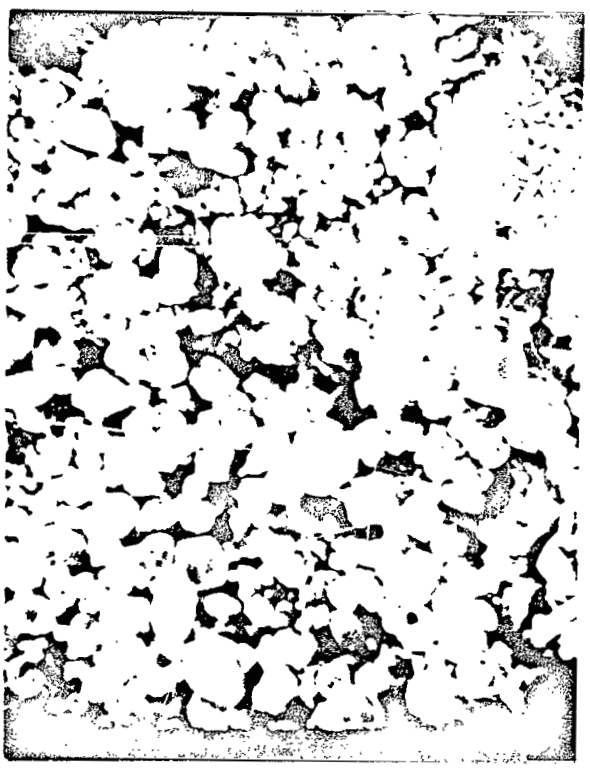

(c) BOTTOM PART OF SAMPLE, 2000x MAGNIFICATION

FIGURE 13. PHOTOMICROGRAPH OF Cu-W IN THE GREEN STATE

(a) TYPICAL DISTRIBUTION, 200x MAGNIFICATION

(b) TOP PART OF SAMPLE, 2000x MAGNIFICATION

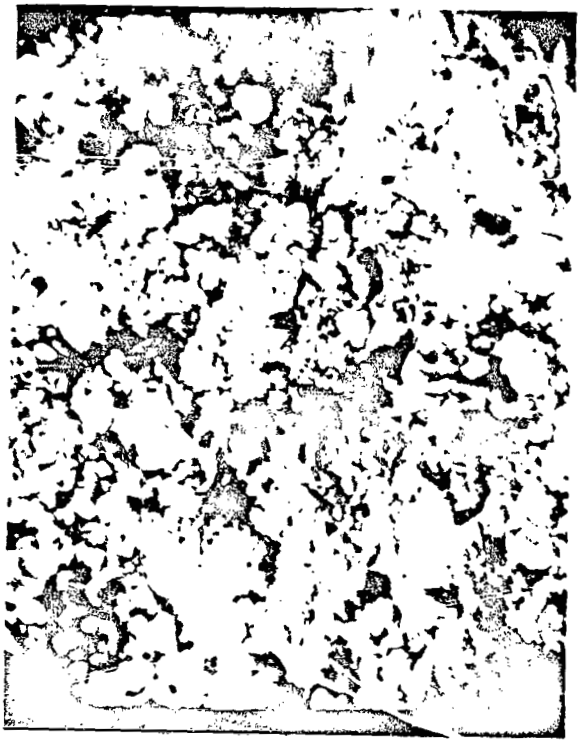

(c) BOTTOM PART OF SAMPLE, 2000x MAGNIFICATION

FIGURE 14. PHOTOMICROGRAPH OF SINTERED Cu-W

(a) TYPICAL DISTRIBUTION, 200x MAGNIFICATION

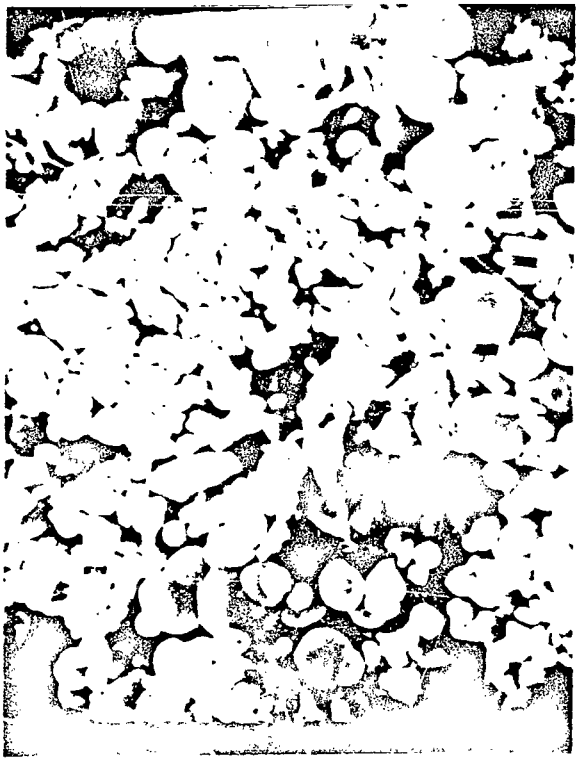

(b) TOP PART OF SAMPLE, 2000x MAGNIFICATION

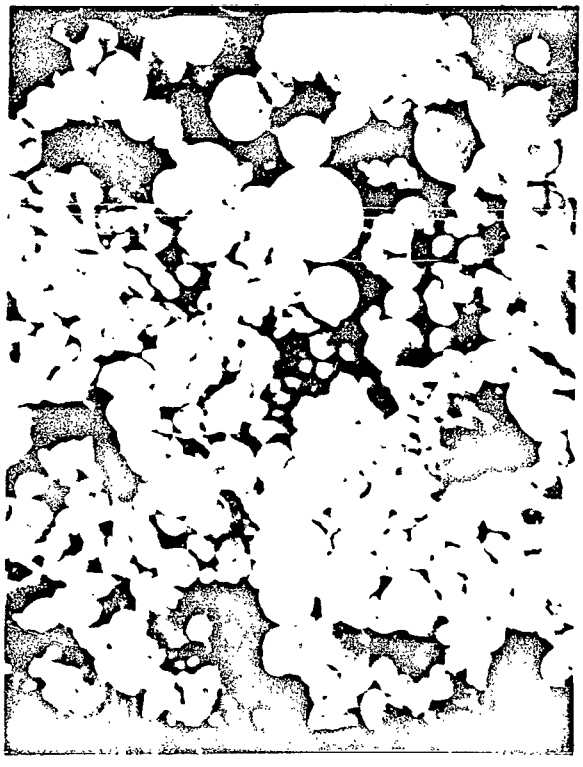

(c) BOTTOM PART OF SAMPLE, 2000x MAGNIFICATION

FIGURE 15. PHOTOMICROGRAPH OF Cu-Fe IN THE GREEN STATE

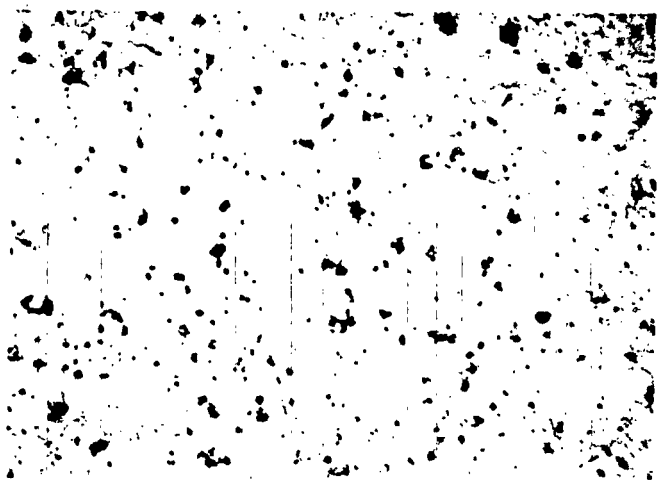

(a) TYPICAL DISTRIBUTION, 200x MAGNIFICATION

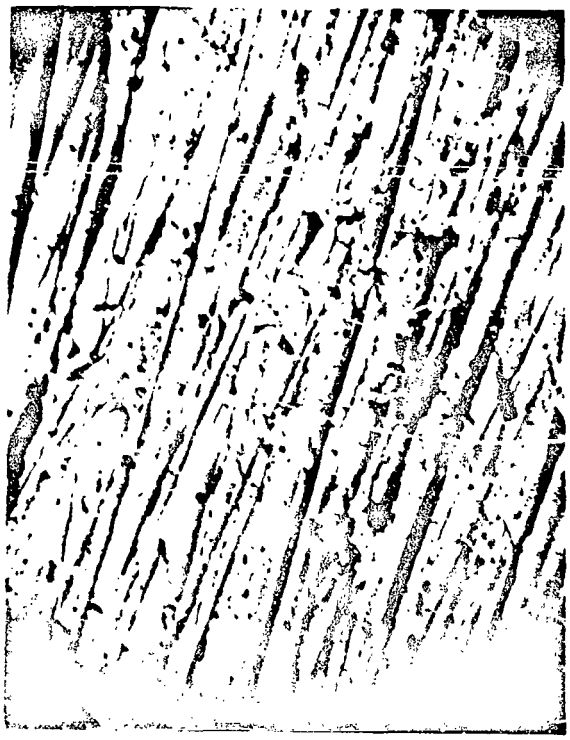

(b) TOP PART OF SAMPLE, 2000x MAGNIFICATION

(c) BOTTOM PART OF SAMPLE, 2000x MAGNIFICATION

FIGURE 16. PHOTOMICROGRAPH OF SINTERED Cu-Fe

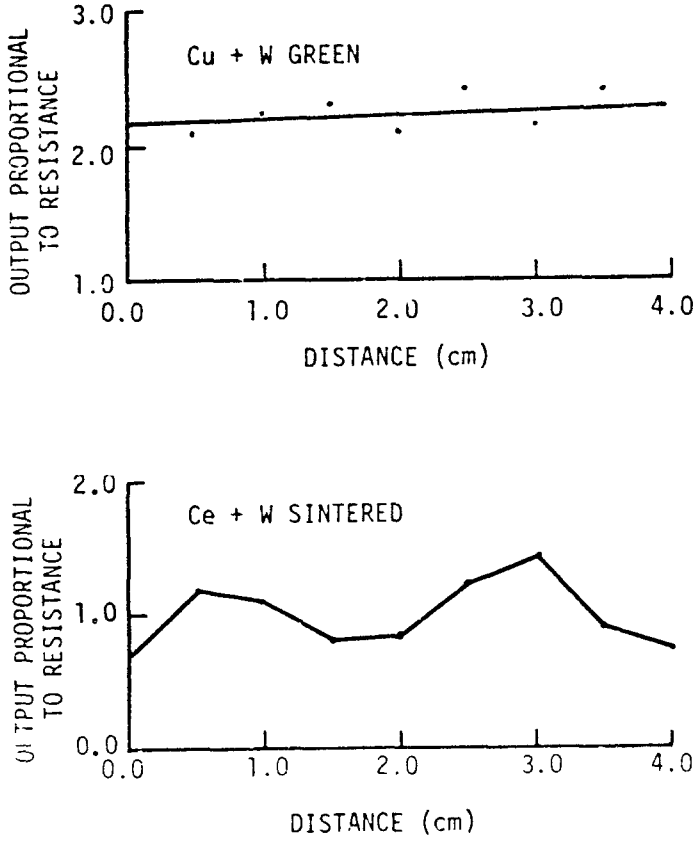

FIGURE 17. VARIATION OF RESISTIVITY WITH DISTANCE

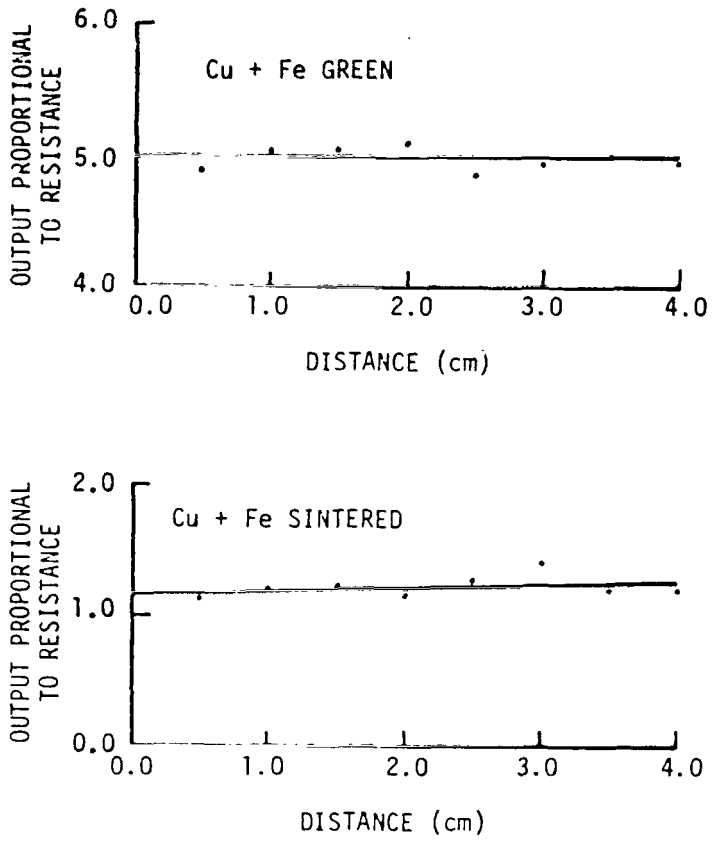

FIGURE 18. VARIATION OF RESISTIVITY WITH DISTANCE

IMMISCIBLE MATERIALS AND ALLOYS

By

A. J. Markworth, S. H. Gelles*, J. J. Duga
Battelle
Columbus Laboratories
Columbus, Ohio 43201

and

W. Oldfield
Materials Research and Computer Simulation
Westerville, Ohio 43081

SUMMARY

Only immiscible materials which involve a fluid phase have a potential advantage when considered for space processing. Processing of such systems at low gravity can lead to a material which is very homogeneous and contains a finely dispersed mixture of phases. Materials with such structures may exhibit potentially useful properties for such applications as superconductors, dispersion-strengthened materials, superplastic materials, permanent magnets, etc.

These conclusions have resulted from review of past efforts in the field of low-g processing of materials containing a liquid phase miscibility gap and from present efforts at Battelle's Columbus Laboratory dealing with such systems. These latter studies have concentrated on precipitation of liquid droplets in a host liquid during cooling through the miscibility gap. The major objective of this effort has been to study the agglomeration of the droplets both experimentally and through computer simulation in order to understand the mechanisms involved and to deduce the effect of gravity on the droplet distribution and resulting structure of the solidified material. The agglomeration mechanisms treated in detail are those due to diffusional growth and collision processes caused by Stokes or convection current-induced droplet migration. The collision processes are considered to be the major agglomeration mechanisms operative and the ones most sensitive to the presence of gravitational forces. These agglomeration processes are essentially eliminated at low-g thus leading to materials with finer structures.

INTRODUCTION

There has been considerable interest generated in the possibility that processing of immiscible materials under low-gravity conditions would lead to products with unique structures and properties. Although there has been some effort to look into this possibility, the results produced thus far are rather limited. There have, however, been some

---

* Paper presented by S. H. Gelles.

experimental results that have shown some unusual features and potential benefit of processing immiscible materials at low g. Also much progress has been made in understanding the mechanisms controlling the structure and properties produced by the 0-g verses 1-g processing of these materials.

It is the purpose of this paper to review past activities in this field, to describe current research in this area at Battelle Columbus Laboratories, and to explore potentially useful immiscible systems which might benefit from being processed at near 0-g.

IMMISCIBLE SYSTEMS--DESCRIPTION

Before detailing our research activities, it is meaningful to define what is meant by an immiscible material. In the most general terms, an immiscible material consists of a mixture of phases having limited mutual solubility. Such materials can be formed in a number of different ways as shown in Figure 1. They can be produced by simply mixing phases of limited mutual solubility together as is done in some composite materials (Figure 1a). Processing of such materials can be performed by having one of the materials (a solid reinforcement) infiltrated by a liquid phase (matrix). Alternatively, entirely solid-state techniques may be used. In these, powders of matrix material are mixed with the reinforcement (either in particulate or fiber form) and consolidated into a dense structure by pressing and/or sintering processes. An example of another solid-state technique for producing composites involves the roll-bonding of filamentary reinforcements between thin foils of the matrix. Examples of composite materials produced by some of these techniques are boron in aluminum, silcon carbide in silver, or aluminum oxide in aluminum. The reinforcement can be particulate or be made up of short or continuous fibers.

One of the more common ways of forming mixtures of solid phases is through reactions which are very familiar to the metallurgist and physical chemist. One such group starts with a homogeneous liquid which is allowed to cool to a temperature at which the reaction occurs. In the case of a eutectic reaction (Figure 1b) the homogeneous liquid, L, of composition, C_E, decomposes at temperature T_E according to the reaction

$$L \rightarrow A + B$$

to a mixture of the Phases A and B. Often this mixture has a plate or rod morphology similar to the composites described above (Figure 1a). Structures of this form are being studied for turbine blade applications.(1) The reinforcement improves creep properties.

A similar decomposition reaction is found in the so-called monotectic systems. In this case a liquid, L_1, having the composition C_m (See Figure 1d) decomposes at temperature T_m into a solid phase and a liquid, L_2, of a different composition according to the reaction

$$L_1 \rightarrow A \text{ (Solid)} + L_2 \quad .$$

The morphology of the resulting mixture can be similar to that achievable in eutectic systems.(2) However, there has been relatively little work performed with these systems.

Another common type of transformation involving a liquid is the so-called peritectic reaction in which a liquid and solid phase react to form another solid phase, C, according to the reaction

$$A + L \rightarrow C \quad .$$

This reaction is somewhat different from the eutectic and monotectic reactions in that during cooling from the homogeneous liquid range a solid, A, is first precipitated. At temperature, T_p, the solid A reacts with the remaining liquid to form the C phase.

Precipitation of solid phases prior to decomposition of the liquid can also occur in both eutectic and monotectic systems if the liquid composition does not correspond exactly to the eutectic or monotectic composition. In the case of the monotectic system, either liquid or solid droplets may precipitate, depending on the composition of the decomposing liquid.

Materials containing mixtures of phases can also be produced by solid-state reactions involving the decomposition of homogeneous solid phases either by the precipitation of a second phase from a super-saturated solid solution or by eutectoid or peritectoid reactions. The latter are solid-state reactions analogous to the eutectic or peritectic transformations involving liquid phases. These solid-state reactions are of little interest to space processing.

SPACE PROCESSING OF IMMISCIBLE MATERIALS

Only materials and reactions that involve fluid phases (liquids or gases) have a special role in space processing. It is only in these that the effects of gravity would be pronounced. The more obvious mechanisms influenced by gravity are

- Segregation in a single phase, liquid or gas, due to density differences arising from local variations in composition or temperature
- Segregation in a multiphase system due to density differences between droplet and host phases (Stokes Migration)
- Convection currents in both single-phase fluids and those containing liquid or solid droplets due to temperature gradient-induced or composition-induced density variations in the liquid phase
- Segregation of a liquid phase in a porous solid host phase. This mechanism may be applicable to segregation in castings or in liquid-phase sintered compacts.

What is not obvious from the above discussion and a factor which will be shown later in this paper is that gravity can affect the fineness of the structure resulting from the processing of multiphase materials in which a fluid phase is involved. All other conditions being equivalent, it is anticipated that finer structures are achievable by processing at 0-g because of the absence of agglomeration-producing collision mechanisms.

Our work at Battelle Columbus Laboratories in the area of immiscible systems has concentrated on those systems containing a liquid phase miscibility gap, i.e. a two-phase field consisting of two liquids ($L_1 + L_2$ in Figure 1d) which at sufficiently high temperature becomes a homogeneous single-phase liquid. Our efforts in this area have been concerned with the potential usefulness of such materials, the relationship between their microstructure and properties, the evolution of these microstructures at 1-g and at 0-g, and the role of space processing in developing unique properties and microstructures in these materials.

In the remainder of this paper, we will review the past pertinent work on systems with miscibility gaps, discuss their potential usefulness in terms of properties and microstructural features, describe a computer-simulation study aimed at understanding the development of the microstructure in such systems at 1- and 0-g and discuss the potential of space processing of such systems.

PAST WORK ON SYSTEMS WITH A MISCIBILITY GAP

The past work concerning experiments on processing materials with liquid-phase miscibility gaps at low-g have recently been summarized by Reger and Yates.(3) Their review starts with the Appollo 14 experiments on the system paraffin-sodium acetate trihydrate with and without additions of argon or solid tungsten microspheres. It also describes the TRW low-g experiments conducted in the MSFC drop tower on Bi--50 atomic percent gallium and lead--50 atomic percent zinc alloys and those conducted in KC-135 research aircraft on gold--40 atomic percent germanium (hypereutectic composition in a simple eutectic system), copper--50 atomic percent lead and chromium--55 atomic percent copper alloys. Lastly, Reger and Yates described the skylab experiments on gold--23.1 weight percent germanium, lead--45.1 weight percent zinc--9.9 weight percent antimony, and lead--14.8 weight percent tin--15.0 weight percent indium alloys.

The following observations were made:

Segregation--In general the low-g processed material was less segregated than the terrestrially processed samples.

Microstructure--The dispersed phase was generally more finely distributed in the low-g processed samples than in those processed at 1-g.

Additional Phases--In the case of the gold-germanium alloys and lead-zinc-antimony alloys, unidentified X-ray diffraction lines were obtained from the 0-gravity processed samples and not from the samples processed at 1-g.

Unusual Properties--The electrical properties of the Bi-Ga alloys processed by Reger in the MSFC drop-tower were studied by Lacy and Otto[4]. These authors demonstrated that the finely dispersed structures present in some of the low-gravity processed samples produced manifestations of semiconducting behavior, while only metallic behavior was observed in the coarser earth-processed alloy.

There has been little analysis done of the differences to be expected in structure and properties when systems containing a miscibility gap are processed at 0-g. Certainly the minimization of segregation effects is expected. The observation of the fine microstructure obtained by 0-g processing is not as obvious. However, our computer-simulation studies have clearly demonstrated that it also is to be expected as a result of the removal of gravity-driven collision processes which cause droplet coalescence during cooling through, or holding in, a miscibility gap.

No explanations have been put forth dealing with the unexpected presence of unidentified phases in the 0-g processed materials or the unusual electrical properties observed. Further analysis and experimentation is much needed in this area.

Reger and Yates[4] have expressed cautious optimism that some space-processed immiscible systems will have potentially useful properties as superconductors, permanent magnets, catalysts, etc. A list of systems containing known and suspected miscibility gaps has been compiled by Reger[5] as part of a NASA contract. These have been organized into rather broad categories according to their potentially useful properties. The list has become a starting point for the Battelle Columbus Laboratories analysis into space processing of potentially useful immiscible systems.

POTENTIAL OF SPACE PROCESSING MATERIALS WITH A MISCIBILITY GAP

As concluded from a recent NASA study,[6] there are three principal resources that may prove valuable for future space work in materials science and technology:

- The condition of virtual weightlessness
- The infinite vacuum sink provided by space
- Unattenuated solar radiation.

With regard to space processing of materials in general and materials with a miscibility gap in particular, the weightless condition is the most important and the factor that can lead to unique material structures and properties. The other two factors can be reproduced on earth but might have a significant influence on the economics of a potential space process.

As previously discussed, low-g processing of materials with a miscibility gap can lead to products with decidedly less segregation and a much finer structure. It is these factors that must be looked to for any unique products produced by space processing of materials with a miscibility gap. There are, of course, the possibilities that there are other factors which are presently unrecognized that might produce unique structures and properties in these systems. Such, for example, may be the situation in the case where phases having different crystallographic structures were found present in 0-g processed material but not in 1-g processed material. Accordingly, it is necessary to carry out experimental programs aimed at uncovering such effects and, once uncovered, to confirm that the origin is the low gravity. It is then necessary to understand the mechanisms leading to the effect in order to take full advantage of it. However, from the standpoint of predicting which systems with a miscibility gap have potentially useful properties when processed under low-gravity conditions, we can only rely on the known or reasoned effects of low gravity, namely the potential advantage of a highly homogeneous material consisting of a fine distribution of phases with limited mutual solubility.

There are still two basic questions which must be addressed:

- What are the relations between the potentially useful properties and the fine homogeneous structures that can be produced by space processing?

- How do the economics of space processing determine which systems with a miscibility are potentially attractive?

With regard to the latter question, it may be somewhat premature to consider the economics of this situation since too little of the necessary experimental and analytical work has been done and since an insufficient appreciation of the technology of space processing has as yet been obtained.

We have not devoted much of our attention to the economic aspects of this question, preferring to initially investigate a larger range of systems rather than limit our attention prematurely. However, there are certain economic ground-rules that should be kept in mind during consideration of potential systems for space processing.

Space processing must produce either 1) a unique product that cannot be produced on earth and be of sufficient value to cover the costs

of manufacturing and transportation, 2) a product that can be produced more efficiently in space so as to cover the additional costs of transportation, or 3) a product having sufficient improvement in properties and performance to merit the additional expenses required in transportation.

These guidelines are, of course, applicable to any product which might be manufactured in space.

The key basic question that we are currently addressing is that concerned with the circumstances under which a homogeneous finely distributed structure processed from a system with a miscibility gap might produce a material with unusual and valuable properties. Fundamental knowledge (in some cases missing) of the basic relations between the structure and properties of such systems is needed to answer this question. We need to know what the properties of the individual phases making up the material need to be and how the phases should be distributed to produce, for example, a superconductor with an increased transition temperature or a superior bearing material or superplastic material.

Our analysis has begun with the TRW listing[5] of systems containing a miscibility gap and the potentially useful properties some of these systems might display. The categories of applications suggested by Reger are

Catalysts
Fine particle superconductors
Fine particle permanent magnets
Breeder reactor fuel
Nuclear reactor structural materials
Electrical contact materials
Nuclear reactor control rods
Bearing alloys
Dispersion-strengthened alloys
Jewelry
Solid lubricants
III-V Semiconductors
Extrinsic semiconductors.

We are also planning to consider other categories, such as superplastic materials.

Since this aspect of the work is still incomplete, our discussion will deal only with the approach to defining potentially useful systems having a miscibility gap. The conclusions and recommendations must await further work. It should also be mentioned that the outlined approach can be used to categorize other systems such as eutectics (stoichiometric or off-stoichiometric), peritectics, or monotectics, etc.

Our mode of operation consists first of selecting a potentially useful property, e.g. superplasticity and defining where possible the structural features (type and distribution of the phase mixture) that lead to enhancement of the selected property. In the case of superplasticity, the melting temperatures of the individual phases and the fineness and intimacy of the phase mixture are important.

The next step is to list the systems that would meet the defined criteria. It would then be necessary to weigh the choice of the selected system on the basis of the defined property, the probability of achieving the desired effect, the usefulness of the product, the competition from earth processing, and an estimate of the economics of the situation. From such a listing of systems and applications, it will be possible to define space-processing experiments which could potentially lead to space-manufacturing processes.

COMPUTER-SIMULATION STUDY

Introduction

A computer-simulation study of a given physical process is comprised of essentially two ingredients: 1) a physical model, which incorporates a description of the major kinetic phenomena giving rise to the process, and 2) an appropriate numerical interpretation of the physical model, which can be used, via the computer, to generate a quantitative description of the manner in which the process under consideration evolves with time for given input conditions. Computer-simulation methods are finding ever-widening applications in the materials-science area. This stems partly from the fact that, on the one hand, kinetic processes occurring in materials are generally of an extremely complex nature, whereas on the other hand, increasingly sophisticated technological applications of materials require as complete an understanding of materials behavior as possible. Among the advantages offered by computer-simulation methods are the following:

(1) One is freed from requirements of analytical tractability in the development of theoretical models. The physical model one uses as the basis for his simulation is limited only by the bounds of current knowledge and the time and funds allotted to prepare and execute the program.

(2) Phenomena difficult to reproduce within the laboratory can often be more efficiently carried out by simulation techniques.

(3) It is a relatively simple and inexpensive matter to alter processing and physical parameters, in a given computer "experiment", then repeat the "experiment" to observe resulting changes.

(4) Laboratory experimentation can be minimized when computer-simulation methods are used and the simulations themselves represent a valuable supplement to corresponding laboratory experiments.

Space-production processes, in particular, because of the unique processing conditions, cannot be tested completely in terrestrial experiments. This fact provides the incentive for the use of computer-simulation methods, which can be related to partially relevant experiments to predict, as accurately as possible, the results to be expected in the zero-gravity environment. Such simulations take account of the best available theoretical results, and employ laboratory experiments to test the predictions as far as possible.

The research described herein constitutes a computer-simulation study of transformation processes occurring in liquid immiscible systems, the emphasis being placed upon behavior to be expected in zero gravity. The two principal stages which comprise this research are the following: (1) formation and subsequent evolution of the distribution of second-phase droplets formed when an initially single-phase liquid is cooled from a temperature above the miscibility gap to one within the gap; (2) solidification of the resultant two-phase system. We are presently well into the development of the first stage and have not yet attacked the second stage. Consequently, we shall summarize here the work which has been done to date and then qualitatively describe the work yet to be accomplished.

Transformation Processes in Liquid Immiscible Systems

Basically, the approach of a liquid immiscible system toward thermodynamic equilibrium involves a series of kinetic processes, including the following:

(1) Nucleation of second-phase droplets within the supersaturated host phase

(2) Growth of the droplets by long-range diffusion of solute within the host phase, with consequent approach of the supersaturation level toward zero

(3) Coalescence of droplets by any of the following processes:

  (a) Direct impingement of growing droplets

  (b) Impingement resulting from Brownian-motion migration

  (c) Impingement resulting from Stokes flow, in which droplet velocity (within a gravitational field) is a function of its radius

  (d) Impingement resulting from velocity gradients within host-fluid flow field

(e) Impingement resulting from temperature-gradient-induced variation in interfacial energy (the Marangoni effect)[7];

(f) Ostwald ripening, or growth of larger droplets at the expense of smaller ones.[8]

Droplet nucleation results from fluctuations in solute concentration within the host phase, and the resultant competition between the decrease of Gibbs free energy associated with droplet formation and the increase of interfacial energy. Droplets which attain a certain critical size are stable, and their growth continues as the Gibbs free energy of the system decreases toward its equilibrium value. The various coalescence processes which subsequently occur are driven by the reduction in overall interfacial energy, which occurs as particles collide and merge. In addition, Stokes migration serves to reduce the overall gravitational energy of the system. It should be noted that droplet migration can be affected by the magnitude of the interfacial energy between the host phase and second phase, with a relatively low energy resulting in reduced migration velocities.[9] Also, certain factors may affect droplet coalescence, including the following: (1) the probability that two migrating droplets approaching one another will actually coalesce may be reduced by effects of the fluid-flow fields in their neighborhood; and (2) a finite time is required to drain the liquid film separating two droplets in close proximity (see Turkdogan's discussion of these phenomena).[10]

The development of a quantitative physical model to describe the separation kinetics of an immiscible system can best be carried out in terms of a continuous function $f(\bar{r},R,t)$, which describes the size distribution of droplets. To this end, we define this function such that the number dN of droplets (assumed spherical), at time t, having radii within incremental range dR measured about R and lying within volume element $d\bar{r}$ of space measured at position vector $\bar{r}$, relative to the origin of coordinates, is given by

$$dN = f(\bar{r},R,t)d\bar{r}dR \quad .$$

This function is, of itself, not of primary physical interest, although properties that are of interest (e.g., droplet concentration $n(\bar{r},t)$, means radius $\langle R \rangle$, volume fraction $f_v(\bar{r},t)$) can be expressed in terms of algebraic moments of the distribution function, the ℓ^{th} moment being given by

$$\mu_\ell(\bar{r},t) \equiv \int_0^\infty R^\ell f(\bar{r},R,t)dR \quad .$$

According to this definition,

$$n(\bar{r},t) = \mu_0(\bar{r},t) \quad ,$$

$$\langle R \rangle = \mu_1(\bar{r},t)/\mu_0(\bar{r},t) \quad ,$$

$$f_v(\bar{r},t) = 4\pi\mu_3(\bar{r},t)/3 \quad .$$

If, on the average, the distribution function is independent of spatial coordinates, then, of course, the moments and the associated properties of the second-phase distribution are functions only of time.

One can easily demonstrate that the distribution function must satisfy a continuity relation having the following form:

$$\frac{\partial f}{\partial t} + \mathrm{div}(\bar{v}f) + \frac{\partial}{\partial R}(vf) = \sum_i \psi_i \quad , \tag{1}$$

where $\bar{v}$ is the velocity of a droplet through coordinate space, v is its rate of growth (i.e., its "velocity" in radius space) and the various "source" functions ψ_i describe the rates at which droplets of given size are created and annihilated such as through nucleation and collision processes. Clearly, this expression is analogous to the familiar Boltzmann integrodifferential equation which describes the distribution function for molecules of a gas.[11]

The source functions for droplet-collision effects, resulting from droplet migration, are well known.[12-14] Consider, for example, the hypothetical case for which the instantaneous concentration of droplets having radii R_1 and R_2 are n_1 and n_2, respectively. Then the rate at which these droplets are colliding is just $n_1 n_2 \pi (R_1 + R_2)^2 (\bar{v}_1 - \bar{v}_2)$, where $\bar{v}_1$ and $\bar{v}_2$ are the respective velocities of particles of types 1 and 2. (We are ignoring, at this time, possible spatial variations of droplet velocities.) Of course, these velocities can have contributions arising from both Stokes migration and from velocity-gradients.[14] Generalizing this concept to a size distribution of droplets, and defining

$$Q(R',R'') \equiv \pi (R' + R'')^2 |\bar{v}' - \bar{v}''| \quad , \tag{2}$$

the source function ψ_c describing the creation of droplets of radius R is simply

$$\psi_c = 1/2 \int_0^\infty dR' \int_0^\infty dR'' \delta (R - (R'^3 - R''^3)^{1/3}) Q(R',R'') f(R',t) f(R'',t) \quad ,$$

where δ is the Dirac delta function. Integration over R" yields

$$\psi_c = \frac{R^2 R}{2} \int_0^\infty \frac{dR'}{(R^3 - R'^3)^{2/3}} Q(R', (R^3 - R'^3)^{1/3}) f(R',t)$$

$$f((R^3 - R'^3)^{1/3}, t) \quad . \tag{3}$$

Likewise, the source function, ψ_a describing the annihilation of droplets of radius R is

$$\psi_a = -f(R,t) \int_0^\infty dR' Q(R,R') f(R',t) \quad . \tag{4}$$

Another source function can also be written, in principle at least, for droplet nucleation. This function may depend largely upon empirical nucleation data for want of an adequate nucleation theory. Source functions for creation and annihilation of droplets by direct impingement, as growth occurs, can also be developed.

The growth velocity in droplet-radius space, v, depends upon such factors as cooling rate, kinetic data (e.g., solute diffusivity within the host fluid), droplet concentration, and phase-diagram data describing the miscibility gap at the temperatures in question. An adequate expression for v can generally be derived, at least under appropriate simplifying assumptions.

We thus have the essence of the physical model describing the breakdown of a liquid immiscible system. It should be noted that the various kinetic processes are likely to occur under different time scales, so that at any given instant, one or another or some combination of these processes may actually be dominating the overall kinetics. In a given situation, one or another of the processes may never contribute to an appreciable degree; for instance, if the system of second-phase droplets is very disperse, direct impingement of growing droplets may occur only to a negligible extent.

In general, the integrodifferential equation describing the temporal evolution of the distribution function cannot be integrated analytically. It is at this point that the computer must be brought in, and solutions generated numerically.

Kinetics of Droplet Growth

The Equilibrium Configuration. Consider a hypothetical liquid immiscible system, for which a portion of the phase diagram is illustrated in Figure 2. The system contains two types of atoms, which we denote by A and B. Let us analyze the growth kinetics of second-phase droplets when the system is cooled from temperature T_1 above the miscibility gap, down to temperature T_2 within the gap at atomic fraction f of B atoms, where

$$f = \frac{N_B}{N_A + N_B} \quad , \tag{5}$$

with N_A and N_B being the respective numbers of atoms of types A and B in the system. (Extensive quantities, such as numbers of atoms, may be considered as referred to unit volume.) At temperature T_2, the equilibrium

configurations of the system consists of a host phase and second phase characterized by atomic fractions f_1 and f_2 of B atoms, respectively, with

$$f_1 = \frac{N_{B1}}{N_{A1} + N_{B1}} \quad , \tag{6}$$

$$f_2 = \frac{N_{B2}}{N_{A2} + N_{B2}} \quad , \tag{7}$$

where N_{A1} and N_{B1} are the respective numbers of A and B atoms in the host phase and N_{A2} and N_{B2} are the numbers of A and B atoms in the second phase. Clearly, we must require that

$$N_A = N_{A1} + N_{A2} \quad , \tag{8}$$

$$N_B = N_{B1} + N_{B2} \quad . \tag{9}$$

One can use Equations (5) through (9) to derive the familiar "lever rule", i.e., that the equilibrium fractions F_1 and F_2 of all atoms within the host phase and second phase, respectively, are given by

$$F_1 = \frac{f_2 - f}{f_2 - f_1} \quad , \tag{10a}$$

$$F_2 = \frac{f - f_1}{f_2 - f_1} \quad . \tag{10b}$$

Obviously, this discussion of equilibrium compositions says nothing about the equilibrium morphology of the second phase. The computer-simulation study is devoted to evaluating the temporal evolution of the morphology of the second phase as thermodynamic equilibrium is approached.

Approach to Equilibrium. Clearly, a computer-simulation study deals with the nonequilibrium situation in the sense of using an appropriate physical model to describe the kinetic of the approach of a system to its equilibrium configuration. In our case, we consider the growth of a system of second-phase droplets under the following simplifying assumptions:

(1) The system is cooled to a temperature T_2 within the miscibility gap, but outside the spinodal, such that diffusion coefficients remain positive.[15]

(2) Nucleation occurs very rapidly and all nuclei are formed at essentially time $t = 0$.

(3) Growing second-phase droplets are situated at random positions throughout the volume of the host phase, and at any given instant during the stage at which the host phase is decomposing, all droplets have the same size at any given instant. (Thus, for example, effects due to collisions and subsequent coalescence of adjacent growing droplets are not included in the present treatment.)

(4) The growth stage occurs rapidly enough such that effects of droplet migration through the liquid need not be considered while growth is taking place.

(5) The second phase consists of droplets having composition f_2, and all growing droplets maintain this constant equilibrium concentration throughout the period of growth.

(6) Droplet growth occurs via the long-range diffusion of A and B atoms through the host phase, the diffusion of one of these atomic species being taken to be significantly slower than the other and, hence, rate-controlling when atomic diffusion is the process governing droplet growth. In addition, the concentration field of diffusing atoms around each growing droplet is taken to be spherically symmetric with an otherwise uniform field of solute existing within the host phase.

(7) The composition of the host phase at the interphase boundaries is maintained at the equilibrium value (i.e., fraction f_1 of B atoms).

(8) The average atomic volume occupied by A and B atoms, denoted by Ω_A and Ω_B, respectively, does not change, to a first approximation, through the range of relative compositions within the given system.

Obviously, the validity of assumptions such as these must be tested both through comparison with experimental data and through demonstrated self-consistency within the physical model.

In simulating the approach of the system to thermodynamic equilibrium, upon cooling to temperatures within the miscibility gap, two limiting cases can be considered: (1) cooling rate occurring very rapidly relative to the rate at which atoms can diffuse to droplets, and conversely (2) cooling rate occurring very slowly relative to the rates of diffusive influx to droplets. In the former situation, decomposition of the host phase does not begin until cooling is virtually finished; in the latter, cooling occurs so slowly that the system is always in virtual equilibrium as defined by the phase diagram. Of course, cooling can also occur at intermediate rates, such that no process is rate controlling, but we shall not consider this significantly more complex problem at this time.

Very Rapid Cooling. Consider, first, diffusion-controlled growth kinetics. The system is rapidly cooled to temperature T_2 (after Figure 2) upon which n droplets nucleate from solution and begin to grow. We assume an initially homogeneous system, and also take the diffusion of B atoms to be rate-controlling. Now let N'_{A2} and N'_{B2} be the instantaneous numbers of A and B atoms, respectively, in the second phase, and likewise, let N'_{A1} and N'_{B1} be the instantaneous numbers of A and B atoms in the host phase. Clearly,

$$N_A = N'_{A1} + N'_{A2} \quad , \tag{11}$$

$$N_B = N'_{B1} + N'_{B2} \quad , \tag{12}$$

and from assumption (5),

$$f_2 = \frac{N'_{B2}}{N'_{A2} + N'_{B2}} \quad , \tag{13}$$

and we define as f'_1, the instantaneous fraction of B atoms contained within the host phase, i.e.,

$$f'_1 = \frac{N'_{B1}}{N'_{A1} + N'_{B1}} \quad . \tag{14}$$

It is evident that f'_1 is equal to f initially and approaches f_1 as decomposition of the host phase approaches completion.

Let us assume the diffusion kinetics to be quasistationary, implying that the diffusion of B atoms to droplets can be described to a good approximation, using the time-independent diffusion equation (this will yield an underestimate of the instantaneous rate of influx of B atoms to droplets). One thus obtains the following expression for the rate at which N'_{B2} changes with time, t:

$$\frac{dN'_{B2}}{dt} = 4\pi n D_B (C'_{B1} - C^e_{B1}) + 4\pi n R^2 C^e_{B1} \frac{dR}{dt} \quad , \tag{15}$$

where D_B is the diffusion coefficient for B atoms in the host phase, C'_{B1} is the concentration of B atoms within the host phase at distances far from any droplets, C^e_{B1} is the equilibrium concentration of B atoms in the host phase at temperature T_2 and R is the instantaneous droplet radius. The first term on the right-hand side of Equation (15) represents

the net rate of diffusive influx of B atoms into droplets and the second term represents the rate at which B atoms already present in the host phase, at the interface, are collected into droplets.

Now one can use Equations (5) to (14) to show that

$$C'_{B1} = \frac{f'_1}{(1 - f'_1)\Omega_A + f'_1\Omega_B} \quad , \tag{16}$$

$$C^e_{B1} = \frac{f_1}{(1 - f_1)\Omega_A + f_1\Omega_B} \quad , \tag{17}$$

$$N'_{B2} = \frac{N_B f_2}{f}\left(\frac{f - f'_1}{f_2 - f'_1}\right) \quad . \tag{18}$$

In addition, the instantaneous total volume occupied by the second-phase droplets is just

$$\frac{4\pi n R^3}{3} = N'_{A2}\Omega_A + N'_{B2}\Omega_B \quad . \tag{19}$$

Combining Equations (13) and (19),

$$\frac{4\pi n R^3}{3} = \frac{N'_{B2}}{f_2}[(1 - f_2)\Omega_A + f_2\Omega_B] \quad , \tag{20}$$

from which we obtain

$$4\pi n R^2 \frac{dR}{dt} = \frac{1}{f_2}[(1 - f_2)\Omega_A + f_2\Omega_B]\frac{dN'_{B2}}{dt} \quad . \tag{21}$$

Differentiating Equation (18) with respect to time and substituting the result, together with Equations (16), (17), and (21) into (15), we obtain

$$\frac{df'_1}{dt} = -\lambda(f_2 - f'_1)^{5/3}(f - f'_1)^{1/3}\left[\frac{f'_i}{(1 - f'_1)\Omega_A + f'_1\Omega_B}\right.$$

$$\left. - \frac{f_i}{(1 - f_1)\Omega_A + f_1\Omega_B}\right] \quad , \tag{22}$$

where

$$\lambda \equiv \frac{3^{1/3} D_B}{f_2(f_2 - f)\alpha} \left(\frac{4\pi n f}{N_B}\right)^{2/3} [(1 - f_2)\Omega_A + f_2\Omega_B]^{1/3} \quad ,$$

with

$$\alpha \equiv 1 - \frac{f_1}{f_2}\left[\frac{(1 - f_2)\Omega_A + f_2\Omega_B}{(1 - f_1)\Omega_A + f_1\Omega_B}\right] \quad .$$

Integration of Equation (22), by some appropriate method, will yield the explicit variation of f_1' with time.

Also, one can combine Equations (18) and (20) to obtain

$$\frac{4\pi n R^3}{3} = \frac{N_B}{f}\left(\frac{f - f_1'}{f_2 - f_1'}\right)[(1 - f_2)\Omega_A + f_2\Omega_B] \quad . \tag{23}$$

Equation (23) is a direct relation between the total volume of droplets (or volume fraction, if we refer n and N_B to unit volume) and the parameter f_1'.

We have solved Equation (22) numerically using a fourth-order Runge-Kutta method and using the following representative numerical values:

$$f_1 = 0.3, \; f = 0.4, \; f_2 = 0.7 \quad ,$$

$$\Omega_A = \Omega_B = 3 \times 10^{-23} \text{ cm}^3 \quad ,$$

$$N_B = (4/3) \times 10^{22} \text{cm}^{-3} \quad ,$$

$$D_B = (4/7) \times 10^{-5} \text{cm}^2/\text{sec} \quad .$$

The results are plotted in Figure 3 for three different droplet concentrations. Note that growth proceeds faster as the droplet concentration increases. This is what one would expect, since higher droplet concentrations mean that solute atoms have smaller distances, on the average, to diffuse in order to reach droplets. The times predicted here for growth to take place (of the order of a tenth of a second or less for these particular cases) are roughly consistent with the predictions of Lindborg and Torssell[14] and of Turkdogan[10] for the growth of deoxidation products from a liquid metal. One can show, by substituting appropriate numerical values into Equation (23), that the net volume fraction occupied by second-phase droplets at the conclusion of growth is 2% volume percent for all three cases (noting that $f_1' = f_1$ when growth is completed.

Very Slow Cooling. At the opposite extreme of the limiting case discussed above is that corresponding to a cooling rate so slow that the distribution of atoms between host phase and second phase always remains in quasiequilibrium, relative to the phase diagram, as the temperature is lowered into the miscibility gap. The instantaneous volume occupied by the droplets is still given by an expression analogous to Equation (23), i.e.,

$$\frac{4\pi nR^3}{3} = \frac{N_B}{f}\left(\frac{f - f_1'}{f_2' - f_1'}\right)[(1 - f_2')\Omega_A + f_2'\Omega_B] \quad , \tag{24}$$

where now f_1' and f_2' represent the atomic fraction of B atoms at the lower and upper compositional limits of the miscibility gap corresponding to the instantaneous temperature T. As T is slowly lowered to its final value T_2 (see Figure 2), f_1' and f_2' follow the miscibility-gap limits and finally reach values f_1 and f_2 respectively, at the final temperature T_2.

Equation (24) can be differentiated with respect to time, noting that

$$\frac{df_i'}{dt} = \dot{T}\frac{df_i'}{dT} \quad ,$$

where $\dot{T}$ is the cooling rate and where i = 1,2 with the derivative df_i'/dT being the local slope measured along the locus of points defining the limit of the miscibility gap. One thus obtains,

$$4\pi nR^2\frac{dR}{dt} = \frac{N_B|\dot{T}|}{f(f_2' - f_1')^2}\{(f - f_1')[(1 - f_1')\Omega_A + f_1'\Omega_B]\frac{df_2'}{dT}$$

$$+ (f_2' - f)[(1 - f_2')\Omega_A + f_2'\Omega_B]\frac{df_2'}{dT}\} \quad . \tag{25}$$

We see, from Equation (25), that the geometry of the miscibility gap (in composition-temperature space) becomes an important factor in determining droplet growth kinetics at very slow cooling rates.

Droplet Coalescence

Once the growth of liquid droplets from the host phase is completed, the structure of the two-phase system can undergo continued changes resulting from droplet coalescence. Coalescence can potentially occur by any of the several processes previously described, although it is likely that not all of these processes contribute significantly under a given set of conditions. Except for the direct overlap of growing droplets, coalescence processes generally occur on a larger time scale compared to nucleation and growth processes and, if such is the case, can be assumed

to occur, to a significant extent, only after the separation of the system into its two component phases has been virtually completed. Let us assume here (1) that coalescence is indeed important only after growth is completed, (2) that coalescence occurs principally by the collision of moving droplets, and (3) that the size distribution of droplets is, on the average, independent of spatial coordinates. In this case, Equation (1) reduces to

$$\frac{\partial f}{\partial t} = \psi_c + \psi_a \quad , \tag{26}$$

where ψ_c and ψ_a are given by Equations (3) and (4), respectively. Equation (26) can be integrated numerically once appropriate velocity functions are selected to describe the droplet-migration kinetics (see Equation (2)).

Our computer-simulation study of droplet-collision kinetics consists essentially of an integration of Equation (26) using a form of the Gaussian quadrature procedure. To permit the accuracy of the integration to be altered in a convenient way, a five-term quadrature was modified to include a variable integration interval. To obtain higher accuracy, the integration interval was subdivided into a set of smaller intervals. The accuracy of the procedure could be tested by computing the total volume of droplets which should be invariant in time.

The result of a sample calculation (carried out using data of Lindberg and Torssell and including effects of Stokes rise and fluid-velocity gradients on droplet migration) is shown in Figure 4 on computer-drawn curves. It can be seen that, at least for the times shown, the principal effects of droplet migration and collisions is to cause the magnitude of the distribution function to become reduced at smaller radii and increased at larger radii. This is to be expected, of course, since smaller droplets are being "lost" from the distribution as collisions occur, and larger droplets are consequently being formed.

FUTURE PLANS

Future work in the area of immiscible materials and alloys will continue the exploration of systems with a liquid phase miscibility gap.

Computer-simulation studies in this area will initially concentrate on the terrestrial behavior of such systems. Experiments conducted under various cooling conditions on Al-In alloys will provide experimental data on droplet-size distributions for testing the self consistency of the computer simulation.

Once, the simulation is found to correlate well with the terrestrial data, attention will be focussed upon behavior to be expected in space. Processes which contribute terrestrially only to second order (e.g., Ostwald

ripening) effects can be expected to play a more dominant role in space, once the removal of first-order gravitational effects is achieved. Initial application of the computer simulation to studies of droplet-coalescence kinetics in zero gravity will be made to a Science Demonstration Experiment conducted on Skylab. The experiment deals with the separation of an initially well-mixed oil-water mixture.

Simulation studies will also be made of the solidification kinetics of two-phase liquid-metal systems and effects of zero gravity are also likely to be felt here as well as in the kinetics of second-phase coalescence.

In addition, experiments will be repeated at low-g on the Al-In alloy system to provide additional comparative data on the particle-size distribution at low-g verses 1-g.

Finally, select systems containing miscibility gaps will be experimentally screened by measuring specific properties of potential interest. This will be done on alloys which have been very rapidly cooled to produce structures which might simulate those obtained by 0-g processing. This experimental work will be in addition to the analytical efforts underway for evaluating the potential of these systems.

REFERENCES

1. F. D. Lemkey and E. R. Thompson, "Nickel and Cobalt Eutectic Alloys Reinforced by Refractory Metal Carbides", Met. Trans., 2 (1971) 1537.

2. J. D. Livingstone and H. E. Cline, "Monotectic Solidification of Cu-Pb Alloys", Trans. Met. Soc. AIME, 245 (1969) 351.

3. J. L. Reger and I. C. Yates, Jr., "Preparation and Metallurgical Properties of Low Gravity Processed Immiscible Materials", AIAA Paper No. 74-207, Presented at AIAA 12th Aerospace Sciences Meeting, Washington, D.C., Jan. 30-Feb. 1, 1974.

4. L. L. Lacy and G. H. Otto, "The Electrical Properties of Zero-Gravity Processed Immiscibles", AIAA Paper 74-208, Presented at AIAA 12th Aerospace Sciences Meeting, Washington, D.C., Jan. 30-Feb. 1, 1974.

5. J. L. Reger, "Study on Processing Immiscible Materials at Zero Gravity", Interim Report to NASA-MSFC, Contract NAS8-28267, May, 1973.

6. Final Report of the Space Shuttle Payload Planning Working Groups. Materials Processing and Space Manufacturing, NASA-GSFC, May, 1973.

7. D.B.R. Kenning, "Two-Phase Flow with Nonuniform Surface Tension", Appl. Mech. Rev., 21 (1968) 1101.

8. A. J. Markworth, "The Kinetic Behavior of Precipitate Particles Under Ostwald Ripening Conditions", Metallography, 3 (1970) 197.

9. C. Bodsworth and H. B. Bell, Physical Chemistry of Iron and Steel Manufacture (Second Edition), Longman Group Limited, London (1972), Section 13.6: "Formation and Removal of the Deoxidation Products", 418-427.

10. E. T. Turkdogan, "Deoxidation of Steel", in Chemical Metallurgy of Iron and Steel, Iron and Steel Institute, London (1973), 153-170; also in J. Iron Steel Inst., 210 (1972) 21.

11. R. D. Present, Kinetic Theory of Gases, McGraw-Hill Book Co., Inc., New York (1958), Section 11-3: "The Boltzmann Integrodifferential Equation", 224-232.

12. E. M. Baroody, "Calculations on the Collisional Coalescence of Gas Bubbles in Solids", J. Appl. Phys., 38 (1967) 4893.

13. R. L. Drake, "Processes Influencing Evolution of Droplet or Aerosol Spectrum", in Precipitation Scavenging (1970), Coordinated by R. J. Engelmann and W.G.N. Slinn, USAEC Report CONF-700601 (December, 1970) 385.

14. U. Lindborg and K. Torssell, "A Collision Model for the Growth and Separation of Deoxidation Products", Trans. Metall. Soc. AIME, 242 (1968) 94.

15. J. L. Meijering, "Precipitation", J. Less-Common Metals, 28 (1972) 419.

BIBLIOGRAPHY

on

SECOND-PHASE FORMATION PERTINENT TO IMMISCIBLE SYSTEMS

C. Bodsworth and H. B. Bell, Physical Chemistry of Iron and Steel Manufacture, Longman Group Limited (Second Edition, London, 1972), Section 13.6: "Formation and Removal of the Deoxidation Products", 418.

H. A. Davies, "On the Excess Volume of Mixing of Liquid Alloys", J. Mater. Sci., 9 (1974) 160.

P.E.J. Flewitt, "Phase Transformations in Niobium 16 to 40% Zirconium Alloys Above the Monotectoid Temperature -- I and II", Acta Met., 22 (1974) 47 and 65.

C. Gatellier and M. Olette, "Kinetic Study of Deoxidation of Liquid Steel", Chemical Metallurgy of Iron and Steel, The Iron and Steel Institute (London, 1973) 153.

P. Haasen, "Mechanical, Magnetic, and Superconductor Hardening by Precipitates", Mater. Sci. Eng., 9 (1972) 191.

R. W. Haskell, "Introduction to the Thermodynamics of Spinodal Decomposition", J. Amer. Ceram. Soc., 56 (1973) 355.

R. B. Heady and J. W. Cahn, "Experimental Test of Classical Nucleation Theory in a Liquid-Liquid Miscibility Gap System", J. Chem. Phys., 58 (1973) 896.

J. Higgins, R. B. Nicholson, and P. Wilkes, "Precipitation in the Iron-Beryllium System", Acta Met., 22 (1974) 201.

J. S. Langer, "Theory of Spinodal Decomposition in Alloys", Annals of Physics, 65 (1971) 53.

J. S. Langer and M. Bar-on, "Theory of Early-Stage Spinodal Decomposition", Annals of Physics, 78 (1973) 421.

J. S. Langer, "Statistical Methods in the Theory of Spinodal Decomposition", Acta Met., 21 (1973) 1649.

U. Lindborg and K. Torssell, "A Collision Model for the Growth and Separation of Deoxidation Products", Trans. Metall. Soc. AIME, 242 (1968) 94.

J. D. Livingston, "Growth of Duplex Crystals", Mater. Sci. Eng., 7 (1971) 61.

S. Lungu, I. L. Beleuță, D. Apostol, and O. Rădulescu, "Some Theoretical Aspects in the Spinodal Decomposition and Crystallization of Silicate Melts. Experimental Results for the UO_2-SiO_2 System", J. Nucl. Mater., 48 (1973) 165.

J. L. Meijering, "Precipitation", J. Less-Common Metals, 28 (1972) 419.

D. E. Mikkola and K. B. Rundman, "The Kinetics of Ordering and Antiphase Domain Growth vs. the Kinetics of Spinodal Decomposition and Coarsening", Scripta. Met., 6 (1972) 1095.

A. E. Nielsen and S. Sarig, "Homogeneous Nucleation of Droplets and Interfacial Tension in the Liquid System Methanol-Water-Tribromomethane", J. Crystal Growth, 8 (1971) 1.

R. Roberge and H. Herman, "Precipitation in Liquid-Quenched Al-Base Ag Alloys", J. Mater. Sci., 8 (1973) 1482.

D. Robertson and G. M. Pound, "Numerical Simulation of Heterogeneous Nucleation and Growth", J. Crystal Growth, 19 (1973) 269.

E. Rudy, "Boundary Phase Stability and Critical Phenomena in Higher Order Solid Solution Systems", J. Less-Common Metals, 33 (1973) 43.

D. Stroud, "Theory of Phase Separation in Liquid-Metal Alloys: Li_xNa_{1-x}", Phys. Rev. B, 7 (1973) 4405.

D. Stroud, "Simple Mean-Field Approach to Phase Separation in Liquid-Metal Alloys", Phys. Rev. B, 8 (1973) 1308.

D. Stroud, "Theory of Phase Separation in Liquid-Metal Alloys", unpublished manuscript (Dept. of Physics, The Ohio State University, Columbus, Ohio 43210).

R. A. Swalin, Thermodynamics of Solids, John Wiley & Sons, Inc. (New York, 1962), Chapter 11: "Free Energy of Binary Systems", 156.

J. L. Tomlinson, "Spinodal Decomposition in an Electric Field as a Mechanism for Switching in Amorphous Semiconductors", NWCCL TP 899.

E. T. Turkdogan, "Deoxidation of Steel", Chemical Metallurgy of Iron and Steel, The Iron and Steel Institute (London, 1973) 173, and J. Iron Steel Inst., 210 (1972) 21.

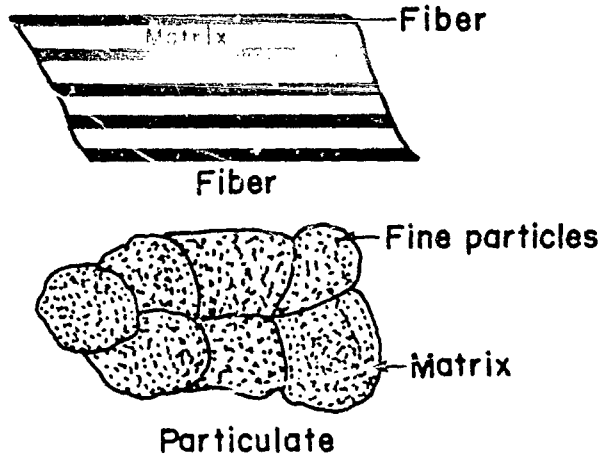

COMPOSITES

(a)

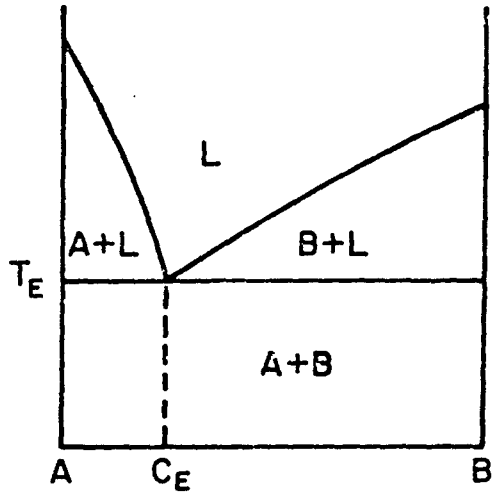

$L \rightarrow A+B$

EUTECTIC

(b)

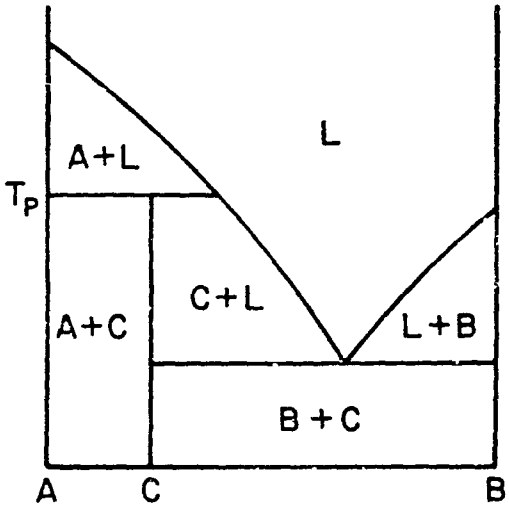

$A+L \rightarrow C$

PERITECTIC

(c)

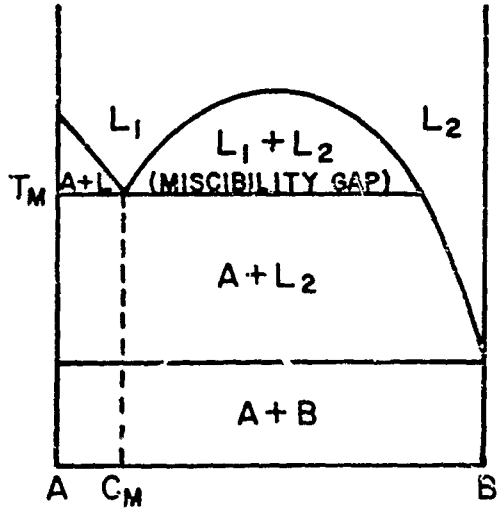

$L_1 \rightarrow A+L_2$

MONOTECTIC

(d)

FIGURE 1. VARIOUS TYPES OF IMMISCIBLE SYSTEMS.

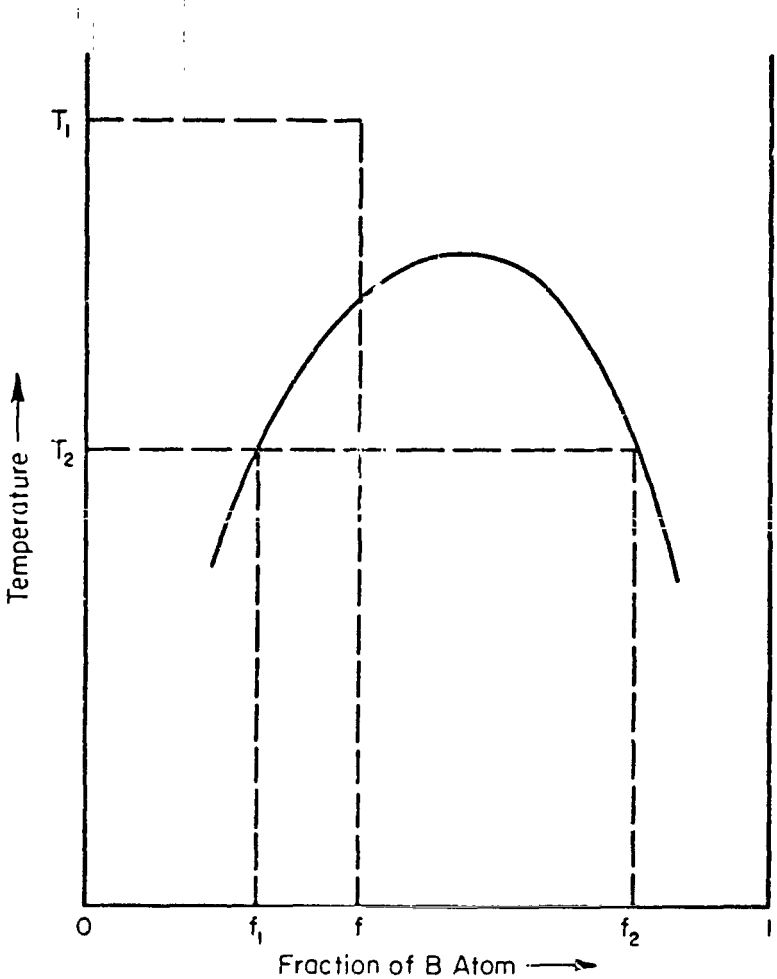

FIGURE 2. HYPOTHETICAL MISCIBILITY GAP, SHOWING EQUILIBRIUM COMPOSITIONS OF HOST PHASE AND SECOND PHASE (f_1 AND f_2, RESPECTIVELY) UPON COOLING FROM T_1 TO T_2 AT COMPOSITION f

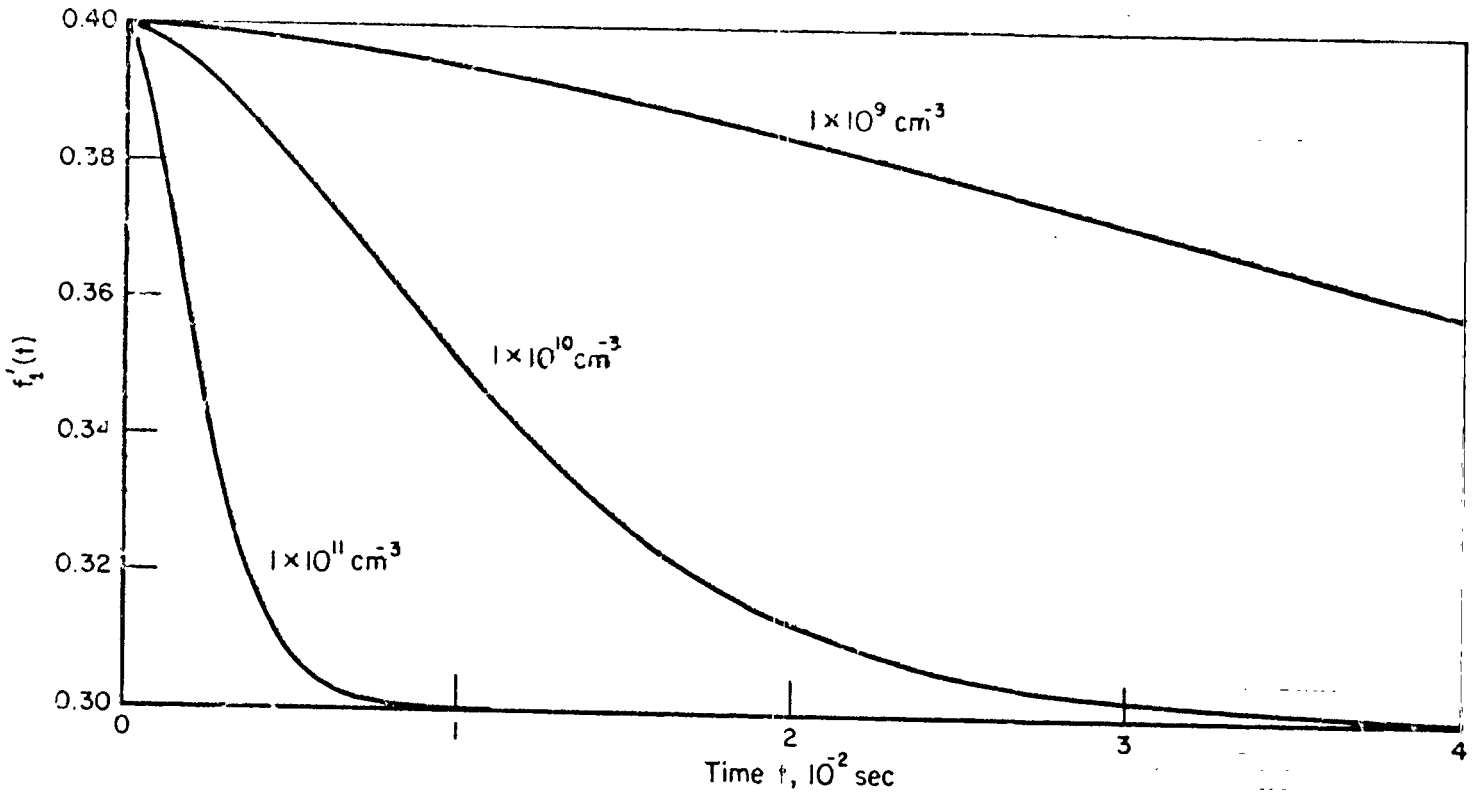

FIGURE 3. VARIATION OF f_1', WITH TIME, DURING DROPLET GROWTH, FOR THREE DIFFERENT DROPLET CONCENTRATIONS

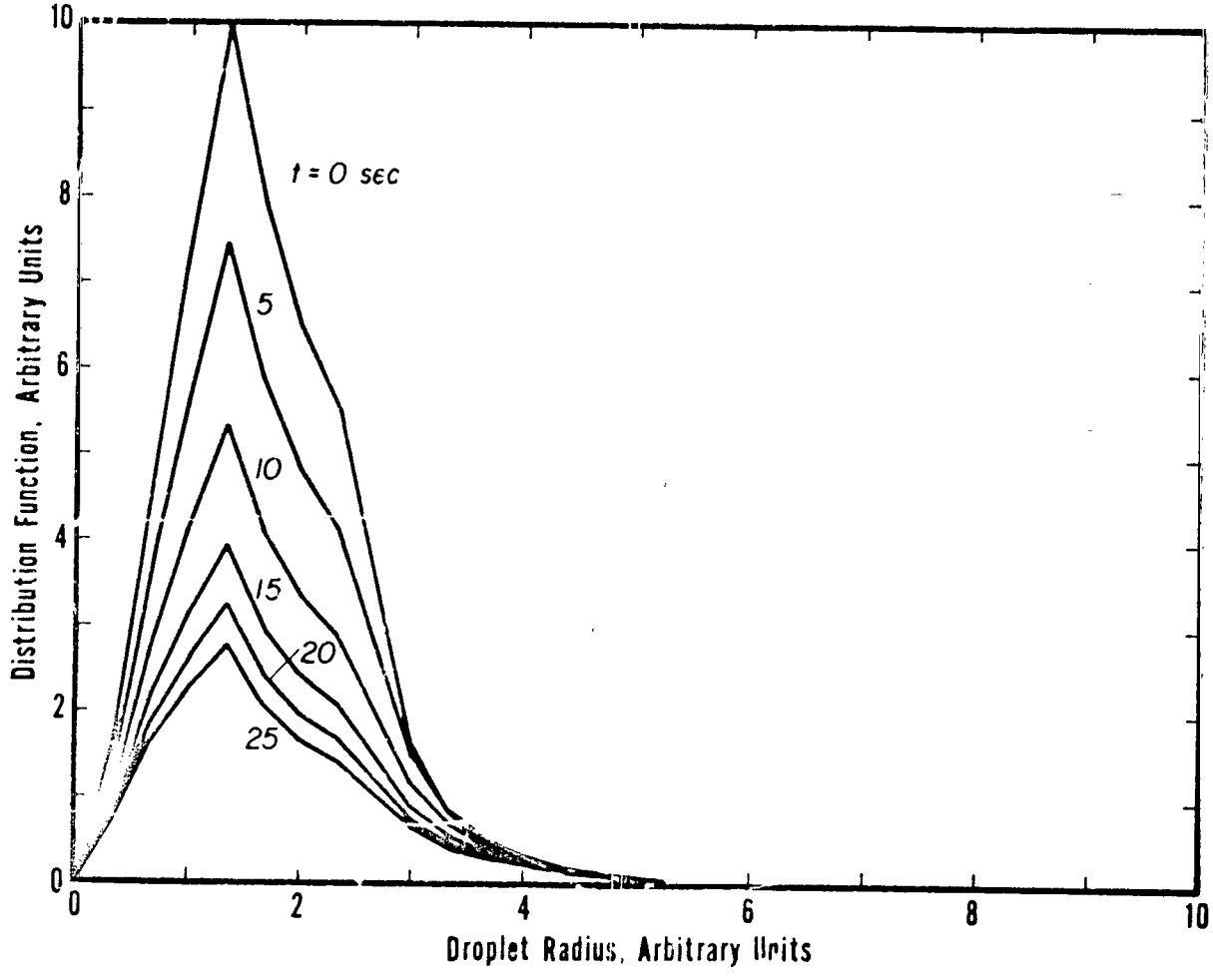

FIGURE 4. COMPUTER PLOTTED SIZE DISTRIBUTION FUNCTIONS SHOWING THE COALESCENCE OF DEOXIDATION PRODUCTS. RAW DATA FROM LINDBORG AND TORSSELL[14]

THE ELECTRICAL PROPERTIES OF LOW-G PROCESSED IMMISCIBLE ALLOYS

By

G. H. Otto*
Physics Department
University of Alabama in Huntsville
Huntsville, Alabama 35807

and

L. L. Lacy
Space Sciences Laboratory
NASA/Marshall Space Flight Center, Alabama 35812

SUMMARY

When dispersed or mixed immiscibles are solidified on earth, a large amount of separation of the constituents takes place due to differences in densities. However, when the immiscibles are dispersed and solidified in zero-gravity, density separation does not occur, and unique composite solids can be formed with many new and promising electrical properties. By measuring the electrical resistivity and superconducting critical temperature, T_c, of zero-g processed Ga-Bi samples, it has been found that the electrical properties of such materials are entirely different from the basic constituents and the ground control samples. The finest dispersions are obtained only in a low-gravity environment. The degree of dispersion critically controls the temperature dependence of the electrical resistivity. Our results indicate that space-processed immiscible materials may form an entirely new class of electronic materials.

This paper will also briefly review the interesting electrical properties of directionally solidified Al-Cu eutectic, a two-component alloy consisting of Al and Al_2Cu which was processed on Skylab (M566). The electrical resistivity of directionally solidified eutectics with a lamellar structure are highly anisotropic and have been studied both experimentally and theoretically. The local resistivity of the space-processed samples are compared to a ground control sample and to the expected theoretical results.

I. INTRODUCTION

Immiscible alloys may be defined as two or more component materials which are mutually insoluble when intimately mixed at a given temperature and pressure. Each of the components of the complex may be either a gas (G), a liquid (L), or a solid (S). A few of the following examples will illustrate some of the possible binary combinations. Perhaps the most common of the immiscible substances is the liquid-liquid (L,L) system (i.e., water/oil emulsions). Also widely known is the liquid-solid (L,S) system such as sols (i.e., ink) and the liquid-gas system such as foams.

*Paper presented by G. H. Otto.

An important economic class of immiscible materials is the solid-solid group of which some solidified alloys are the best examples. By the above definition, solidified eutectics would be in the (S,S) system.

Since the two components of a complex usually have different densities, the dispersion of one of the components (G, L, or S) into a liquid matrix will result in the separation of the two phases when the operation is performed on earth. The main technique for overcoming density segregation in emulsions is to reduce the size of the dispersed particles to the submicron range such that the Brownian motion prevents settling and to keep the mixtures dilute such that the rate of coalescence is small. If the dispersion is performed in zero-gravity, particles (either G, L, or S) of any size and density can be uniformly mixed within a liquid matrix and subsequently solidified. In the low gravitational field levels (10^{-4} to 10^{-6} g) experienced in earth orbit, only the small adhesive and cohesive forces and the mixing technique control the uniformity of the particle distribution. Even in zero-gravity, a question remains of whether or not a (L,L) dispersion tends to separate by coalescence for long solidification times. It has been demonstrated in this respect on Skylab 4 that a dispersion of oil and water will not visibly change and separate by coalescence within a period of 10 hrs[1]. Such a time interval is sufficient for most solidification rates.

The absence of density segregation in zero-gravity allows processing and solidification of immiscible alloys and new metal systems which cannot be made on earth. In this paper, we will consider both theoretically and experimentally the electrical properties of such binary material systems, an account of which has been presented earlier[2]. Of particular interest to us are the expected properties of zero-g solidified emulsions (L,L) and sols (L,S). In the next section, we will theoretically consider some of the parameters expected to influence the electrical properties of such materials. Sections III and IV deal with the electrical and superconducting properties experimentally observed for low-g processed samples of Ga-Bi (L,L system). In Section V, we will report on the results of measurements of the electrical resistivity in directionally solidified samples of Al-Cu eutectic processed on Skylab 3 and 4.

II. THEORETICAL CONCEPTS

The electrical components of a solidified immiscible system can be divided into four classes: insulators, semiconductors, conductors, and superconductors. This classification of the components has been schematically illustrated in Figure 1 along with typical values of the relative resistivity ρ and a common example in each class. The overlapping area represents those few materials in each class which may take the properties of two different classes depending on temperature, pressure, and impurity conditions. The superconductors are considered as a subclass of conductors, since they are normal conductors above some critical temperature, T_c, which is typically below about 20K. What is important for our discussion here is that the properties of a given material generally fall in only one of the above classes; there are very few materials which fall into the overlapping areas. With zero-gravity dispersion and solidification of

immiscibles, we are suddenly faced with the possibility of obtaining entirely new electronic materials whose properties have been crossbred from the above components.

Since either the matrix or the dispersed phase may have any one of the above properties, 16 different permutations are possible. Indeed, many interesting and useful combinations could be produced. For example, if one dispersed a small amount of particulate insulator (i.e., oxides) in a superconducting matrix, the resulting composite could carry a larger critical current than the basic superconductor because of an increase in magnetic flux pinning. The immiscible used in the above example would, however, behave quite differently if superconducting particles were dispersed in an insulating matrix. The only difference between the two examples is the relative volume fraction of each phase used. The electrical resistance of the two immiscibles would differ by many orders of magnitude; one would be a good superconductor with a resistivity ρ of less than 10^{-20} $\mu\Omega$-cm, and the other would be a low temperature diamagnetic insulator of $\rho \sim 10^{15}$ $\mu\Omega$-cm. The behavior of such an immiscible system (i.e., Pb-PbO) would change greatly with small changes in the volume fractions of the two phases. Other interesting combinations would include semiconductors-superconductors and superconductors-conductors.

If one also includes the magnetic properties of the materials (i.e., ferromagnetic, diamagnetic, or magnetoresistive), the number of combinations becomes very large, and synergistic material properties may appear. For example, if one should disperse ferromagnetic particles of low retentivity (e.g., Fe) into a magnetoresistive matrix (e.g., Bi), the resulting composite should have greatly enhanced magnetoresistive properties. Such immiscibles could act as magnetic switches or solid state relays with fast switching times. This immiscible system might also be useful as a magnetic detector with enhanced sensitivity.

Another important concept concerning the electrical properties of space-solidified immiscibles is that these properties will depend on size and interface effects. When the size of the dispersed phase becomes smaller than some critical distance, the electronic properties of the composite will undergo large changes. This critical size depends on the particular property of interest, but in many cases may be comparable to the electron mean-free-path, which is typically 10^{-8} to 10^{-6} m. Simultaneously, with the decreasing size of the dispersant, the amount of interface area increases leading to increased electron scattering. For spherical particles of radius R, dispersed in a continuous matrix, the total surface area S of the dispersed phase per unit volume is

$$S = 3v/R \quad , \tag{1}$$

where v is the volume fraction of the dispersed phase. Thus, as will be shown in the next section, a decrease in R will lead to an increase in S with a subsequent increase in electron scattering and interface effects. For materials with $R \lesssim 10^{-6}$ m, the dispersed phase may achieve thin film properties, and the matrix phase is expected to be strongly influenced by these surface effects.

In summary, the electrical or magnetic properties of space-processed immiscibles would depend on the nature of each phase (i.e., insulator or conductor), the volume fraction of each phase, and the size of the dispersed particles.

III. ELECTRICAL RESISTIVITY OF Ga-Bi

A simple method for obtaining a liquid dispersion of two metals without having to mechanically mix is to make use of the miscibility gap, occuring in numerous metallic constitution diagrams[3]. Samples of Ga-Bi were processed during 3.5 sec of free fall in the MSFC drop tower[4]. In this time span, a single-phase metallic liquid was cooled through the liquid miscibility gap to form two liquid phases which were subsequently solidified. A ground control sample was processed under otherwise identical conditions except that the sample was not dropped. The Ga-Bi samples were processed in tantalum containers using metals with at least 99.999 percent purity and a concentration of 50 a/o of each element. Details of the processing procedure are given by Reger and Yates[5].

Photomicrographs of the samples can be seen in Figure 2, where the light-colored areas represent the Bi matrix and the darker, circular areas are the Ga. As expected, the low-g processing led to a finer and more uniform dispersion of Ga particles in a Bi matrix.

The temperature dependence of the electrical resistivity $\rho(T)$ was measured on two dropped samples (A and B) and one ground control sample (C) by the conventional four-contact technique. A constant current of 10 mA was passed through a thin slice of the material by means of fine-spring-loaded-copper wires contacted to the sample bases by silver conductive paint. The voltage drop was measured on two separate potential leads and could be recorded as a function of temperature. The sample temperature was measured with a calibrated platinum resistance thermometer to 20K and below this temperature with a calibrated Ge resistance thermometer.

The results of the resistivity measurements $\rho(T)$ are given in Figure 3. Each letter refers to the same samples as identified in Figure 2. The results clearly show that the resistivity of the zero-gravity samples (A and B) is quite different from the ground control sample (C). For comparison, the resistivities for pure Bi (curve D) and pure Ga (curve E)[6] have also been included. The room temperature (295K) value for all samples is approximately the same as for the pure Bi. An absolute determination of ρ for all samples is limited by the small sample geometry to within 8 percent, indicated by the room temperature error bar. However, the relative values of ρ for a given curve are accurate to within 1 percent. What is of interest here is that the changes in resistivity as a function of temperature for the three samples are quite different.

The slope ($d\rho/dT$) of the curves (C), (D), and (E) are all positive which is typical of normal conductors. Note that the coarse dispersion of the ground control sample (C) has given a material with the same

electrical characteristics as for pure Bi. However, when the dimensions or diameter of the dispersed Ga particles in sample (B) become small (3-10 μm), the electrical characteristics of the Bi matrix have changed (i.e., $d\rho/dT \approx 0$). For even smaller dispersions ($d \lesssim 1$ μm) as seen in the zero-g sample (A), the conductivity of the matrix has completely changed such that $d\rho/dT < 0$, and a broad maximum occurs at 100K. The high temperature resistivity of sample (A) behaves similar to an intrinsic semiconductor. As indicated by Equation (1), the resistivity of the samples depends strongly on the particle size R even for the same volume fraction v.

In the low temperature region between 25 and 4.2K, all samples show typical metallic behavior. The temperature-dependent resistivity may be expressed as the sum of a temperature-independent term, ρ_o, and a temperature-dependent term, $\rho_i(T) = CT^n$, in accordance with Matthiessen's rule[7],

$$\rho = \rho_o + CT^n \quad . \tag{2}$$

The value of ρ_o can be associated with electron scattering from impurities, defects, or interfaces and is indeed very high for sample (A), having the finest dispersion. From Figure 3, it can be seen that ρ_o increases as the particle size becomes smaller, indicating that ρ_o is proportional to the surface area S in Equation (1). The temperature-dependent term for all samples can be expressed with n varying between 2 for pure bismith and 4 for pure gallium.

Similar resistivity peaks have been reported by Thompson[8] for Bi samples doped with Pb, Sn, and Ge. It should be noted, however, that our results are not expected to be influenced by impurity effects, since very pure materials were used and the resistivity peak does not occur for the ground control sample.

In summary, our results show that the electrical properties of the Bi matrix are drastically changed by zero-g processing. The finer the dispersion, the more pronounced is the change in the properties of the composite as expected from Equation (1).

IV. SUPERCONDUCTIVITY OF Ga-Bi

In many instances, the superconducting properties of a material can be used as a complementary means of analyzing its conditions of state. Although bismuth in its bulk form is not superconducting[9] above a temperature of 0.5K, gallium should show a transition to the superconducting state[10] at 1.08K.

Whereas the resistance measurements indicate the formation of superconducting paths in the material, the inductance measurements reveal the amount of magnetic flux excluded from the material as it becomes superconducting. Typical results of the inductaace measurements, where the sample is located inside a coil, are shown in Figure 4. In Figure 4, the relative change in inductance, $\Delta L/L$, is plotted against temperature. The sharp change in inductance at 7.9K reveals a superconducting phase with a broad transition extending until 6.0K. Using a calibration sample of

known superconducting volume, the signal amplitude can be used to determine the volume fraction of the superconducting phase in the Ga-Bi samples. All samples contained between 1.5 to 3.0 volume percent of the superconducting phase.

Since it is found that all samples, including the ground control samples, contain a small fraction of the superconducting phase, then the superconductivity cannot be entirely associated with the dispersed Ga particles or the Bi matrix. Annealing of the samples up to 100°C for 40 min, which is 70°C above the melting temperature of Ga, leaves the amount of the superconducting phase nearly unchanged.

Although part of the samples becomes superconducting, the resistivity does not drop to zero at temperatures below 7.9K as may be seen from Figure 3. In fact, the resistance at this particular temperature did not drop by more than 1 percent, which is the relative accuracy of the resistance measurement. This observation indicates that the superconducting phase consists of isolated regions.

The fact that portions of the samples become superconducting above the usual T_c of either component cannot be attributed to processing in zero-g, since the ground control sample shows the same effect. The behavior must be attributed to a change in state of some of the gallium or bismuth. Both materials are known to produce phase changes, some of which are listed in Table I, when put under sufficiently high pressure[11] or when fabricated in thin films[12, 13]. The transition temperature changes accordingly and can be as high as 8.55K for Bi under a pressure of 90 kbar or 8.4K, respectively, for thin film gallium. There is a strong possibility that either of these phases may exist in our samples.

Table I. Transition temperature and superconducting volume of various Ga, Bi, and Ga-Bi samples

Sample	T_c (K)	Superconducting Volume (percent)
(A)	8.01	1.7
(B)	7.96	1.6
(C)	7.95	3.0
Ga	1.08	-
Ga (β)	6.2	-
Ga (γ)	7.62	-
Ga (thin film)	8.4	-
Bi	< 0.5	-
Bi IV (43 kbar)	7.0	-
Bi V (68 kbar)	6.7	-
Bi VI (90 kbar)	8.55	-

V. RESISTIVITY OF SKYLAB 3 AND 4 SOLIDIFIED Al-Cu EUTECTIC (M566)

The solidification of an eutectic involves the decomposition of a single liquid phase into two solid phases. The Al-Cu eutectic directionally solidified on Skylab consists of alternating layers or lamellae of Al and Al_2Cu with a typical lamellar thickness varying between 3.4 and 4.1 μm. For a detailed description of the experiment and for typical photomicrographs of the lamellar structure, see the paper presented by Hasemeyer[14] or the final report on the M566 Experiment[15].

The electrical properties of single-phase metals are relatively well understood[7], whereas the electrical properties of two-phase alloys, such as directionally solidified eutectics, have only recently received attention[16,17,18]. The final report on the M566 Experiment will show that the electrical resistivities, ρ, of directionally solidified eutectics with a lamellar structure are highly anisotropic and can be completely specified if four parameters are known. These parameters are the electrical resistivity of the two individual components (i.e., ρ_1 and ρ_2), the volume ratio v of the phases, and a lamellar orientation angle θ which is defined herein. With the first three parameters, one may calculate the resistivity, $\rho_\perp$, perpendicular to and, $\rho_\parallel$, parallel to the lamellar structure. That is, it will be shown that

$$\rho_\parallel = \rho_1 \, r(1 + v)/(r + v) \tag{3}$$

and

$$\rho_\perp = \rho_1 \, (1 + rv)/(1 + v) \quad , \tag{4}$$

where r is the resistivity ratio ρ_2/ρ_1. The volume ratio, $v \equiv V_2/V_1$, may be calculated from precise density measurements or determined from measurements of the lamellar spacing:

$$v = \lambda_2/\lambda_1 \quad , \tag{5}$$

where λ_1 is the lamellar thickness of the first phase and λ_2 is the thickness of the second phase.

The resistivity for any arbitrary direction can then be shown to be

$$\rho(\theta) = \rho_\perp \cos^2 \theta + \rho_\parallel \sin^2 \theta \quad , \tag{6}$$

where θ is the angle between a specified direction in the material and a vector normal to the lamellar structure.

Directionally solidified samples of Al-Cu eutectic consist of alternating layers of Al_2Cu and Al doped with less than 1 percent Cu. Our density measurements indicate that the samples have only a slightly higher volume fraction of Al (51 percent) than Al_2Cu. The resistivity of Al-Cu eutectic and components can, thus, be characterized by the data in Table II. In Table II, the resistivity value for Al_2Cu is a measured bulk value, and

the value for Al is for pure Al. The resistivity values for the eutectics are calculated from Equations (3) through (6).

Table II. Electrical resistivity characterization of Al-Cu eutectic

Material	Resistivity [μΩ-cm]
Al	2.74
Al_2Cu	6.27
Eutectic	
$\rho_\perp = \rho(0°)$	4.47
$\rho_\parallel = \rho(90°)$	3.78
$\rho(45°)$	4.12

Because the resistivity in these eutectic samples is relatively low and the sample diameters are relatively large (6.1 mm), conventional techniques for measuring resistivity are not sufficiently accurate. Therefore, it became necessary to develop a better technique which extends the accuracy of the measurements from about 5 percent to about 0.4 percent. In this new technique, we measured the decay of eddy currents in a manner similar to the systems as first described by Bean[19].

In the eddy-current-decay technique, a rapidly decreasing axial magnetic field generates eddy currents which flow around the cylindrical sample and decay in a characteristic time which depends on the local resistivity of the sample. It will be shown in the final report that the eddy currents average out the angular dependence of $\rho(\theta)$ as given by Equation (6) to yield

$$\rho(EC) = (\rho_\perp + \rho_\parallel)/2 = \rho(45°) \qquad (7)$$

where $\rho(EC)$ represents the measured ρ by the eddy current technique. The expected value of $\rho(45°)$ is also given in Table II.

A typical result indicating the resistivity variation in the samples as a function of length is shown in Figure 5, where the local resistivity of a zero-g sample melted on Skylab 4 (sample M566-8) is compared to a 1-g melted sample (M566-12). The error bar represents a typical reproducibility of the measurement. The drawing at the top of the graph shows the relative position of the sample (M566-8) and important identifying features such as the remelt line. The dashed line in Figure 5 represents the theoretical value for a perfect sample as given in Table II.

Note that the resistivity value of the hot end of both samples is about the same and agrees with the theoretical value. Likewise, $\rho(EC)$ agrees for both samples in the unmelted positions of the material. What is indeed surprising is that the local resistivities are quite different

in the center part of the melted samples, with a peak occurring in the flight material.

Since the peak in the resistivity occurs near the surface deformation of the flight sample, it was suspected that the two are closely related. To determine if there is any correlation between the peak and the deformation, the cross sectional areas of the samples were measured. The results of the cross sectional area measurements indicated that there is a close correlation between the resistivity values and the surface deformation, but these deformations are not severe enough to account for the total height of the peak. It is expected that part of the increase in resistivity is associated with a disturbance of the lamellar structure.

The interpretation of the results of the peak in resistivity will require further study. We will attempt to correlate the resistivity data with photomicrographs supplied by the metallurgical investigators. It should be noted that the peak effect occurs in all flight samples at the same location, including those processed on Skylab 3. Additional physical properties of the sample, such as resistivity ratios $\Gamma \equiv \rho(300K)/\rho(4.2K)$ and densities can be found in References [15] or [18].

VI. CONCLUSIONS

When immiscible materials are dispersed and subsequently solidified in a low-gravity environment, unique composite solids can be formed. The electronic properties of such materials can be quite different from the properties of the basic constituents and will depend on the amount of dispersion. There are a wide variety of possible material combinations which can lead to numerous electrical or electronic applications. The initial experiments on zero-g processed Ga-Bi samples indicate semiconducting, normal conducting, and superconducting type properties in the same sample. As described in the section on Theoretical Concepts, such a range of electrical properties cannot occur in single-phase alloys. Some of the electrical properties can be qualitatively correlated with photomicrographs. An even finer dispersion of Ga in Bi below 1 μm particle size should increase the peak in resistivity. The high T_c observed in our samples cannot be correlated with zero-g processing but may be related to some high pressure or thin film modifications in the bulk material.

The electrical resistivity of directionally solidified Al-Cu eutectic is anisotropic and can be well characterized by Equations (3) through (7) and the data of Table II. The local resistivity as a function of length along the samples differed between the Skylab and ground-processed samples, with the Skylab samples always exhibiting a peak in resistivity near the surface deformation. The peak in resistivity is not yet well understood but is believed to be associated with changes in the lamellar structure.

ACKNOWLEDGEMENTS

We would like to express our appreciation for the contributions of M. Haworth and D. Homesley in the development of our eddy-current-decay technique. We would also like to acknowledge useful discussions and

collaboration with I. Yates and J. Reger. The M566 Skylab samples were kindly supplied by E. Hasemeyer.

REFERENCES

1. L. L. Lacy and G. H. Otto: Quick-Look Report on Skylab 4 Science Demonstration TV102: Immiscible Liquids. Space Sciences Laboratory, Marshall Space Flight Center, March 1974.

2. L. L. Lacy and G. H. Otto: The Electrical Properties of Zero-Gravity Processed Immiscibles. Paper No. 74-208, AIAA 12th Aerospace Sciences Meeting, Washington, DC, February 1, 1974.

3. See for example M. Hansen: Constitution of Binary Alloys. McGraw-Hill, New York, NY, 1958.

4. J. L. Reger: Experimental Development of Processes to Produce Homogenized Alloys of Immiscible Metals. Final Report on NASA Contract NAS8-27805, TRW Systems Group Report No. 18677-6019-RU-00, January 1973.

5. J. L. Reger and I. C. Yates: Preparation and Metallurgical Properties of Low-Gravity Processed Immiscible Materials. Paper No. 74-207, AIAA 12th Aerospace Sciences Meeting, Washington, DC, February 1, 1974.

6. Amer. Inst. of Physics Handbook. 3rd Edition, McGraw-Hill, New York, NY, 1972.

7. See for example A. H. Wilson: The Theory of Metals. 2nd Edition, Cambridge University Press, New York, NY, 1965.

8. N. Thompson: Proc. Roy. Soc. A, 155, 1936, p. 111.

9. N. Kürti and F. Simon: Proc. Roy. Soc. 151, 1935, p. 6.

10. N. E. Phillips: Phys. Rev. 134, 1964, p. A385.

11. M. A. Il'ina and E. S. Itskevich: JETP Lett. 11, 1970, p. 218.

12. W. Buckel and W. Gey: Z. Physik 176, 1963, p. 336.

13. A. Eichler and J. Wittig: Z. Angew. Phys. 25, 1968, p. 319.

14. E. A. Hasemeyer: M566 Eutectic Alloy Growth. Third Space Processing Symposium--Skylab Results, Huntsville, AL, April 30, 1974.

15. E. A. Hasemeyer, et al.: Final Report on Skylab Experiment M566 Al-Cu Eutectic. To be published.

16. W. G. Watson: Morphological Characterization of Aligned Fibrosis Eutectic by Electrical Analog Melting. Ph.D. dissertation, Lehigh University, Bethlehem, PA, 1972.

17. F. S. Galasso, F. C. Douglas, and J. Batt: J. of Metals 22, 1970, p. 40.

18. L. L. Lacy: Preliminary Report on the Physical Properties of Al-Cu Eutectic Samples Processed on Skylab 4. Report No. MISC-SSL-74-2, Space Sciences Laboratory, Marshall Space Flight Center, AL, April 1974.

19. C. B. Bean, R. W. Deblois, and L. B. Nesbitt: J. of Appl. Physics 30, 1959, p. 1976.

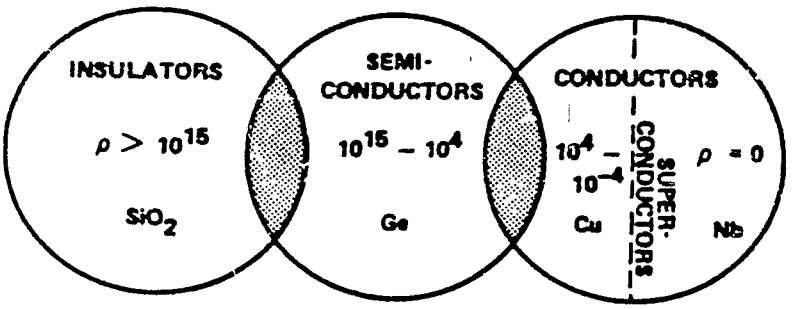

FIGURE 1. A CLASSIFICATION OF THE POSSIBLE ELECTRONIC COMPONENTS OF AN IMMISCIBLE SYSTEM.

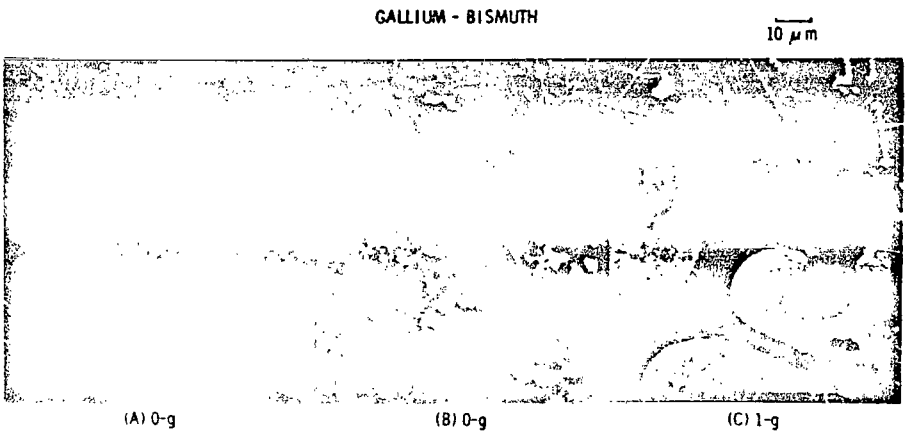

FIGURE 2. PHOTOMICROGRAPHS, REPRODUCED FROM REFERENCE [4], OF TYPICAL SAMPLES OF THE IMMISCIBLE SYSTEM Ga-Bi.

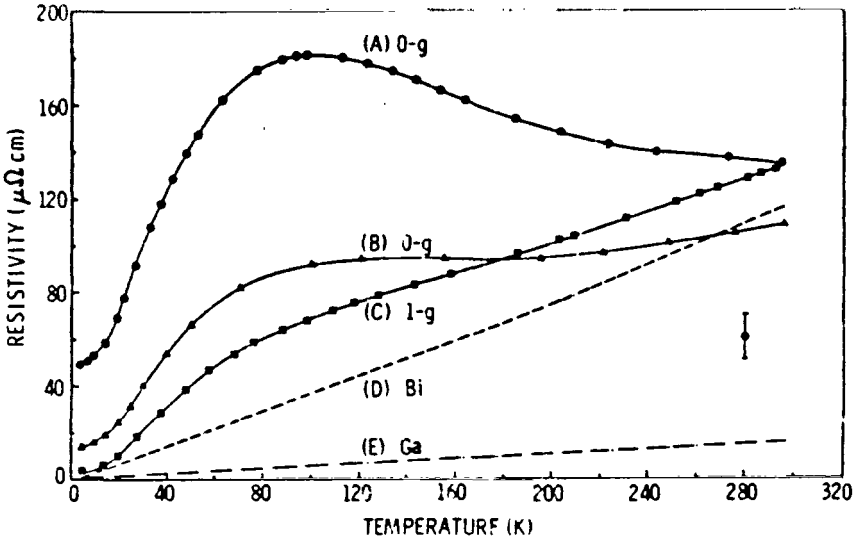

FIGURE 3. THE TEMPERATURE DEPENDENCE OF THE ELECTRICAL RESISTIVITY OF BOTH LOW-g AND 1-g SOLIDIFIED SAMPLES OF Ga-Bi.

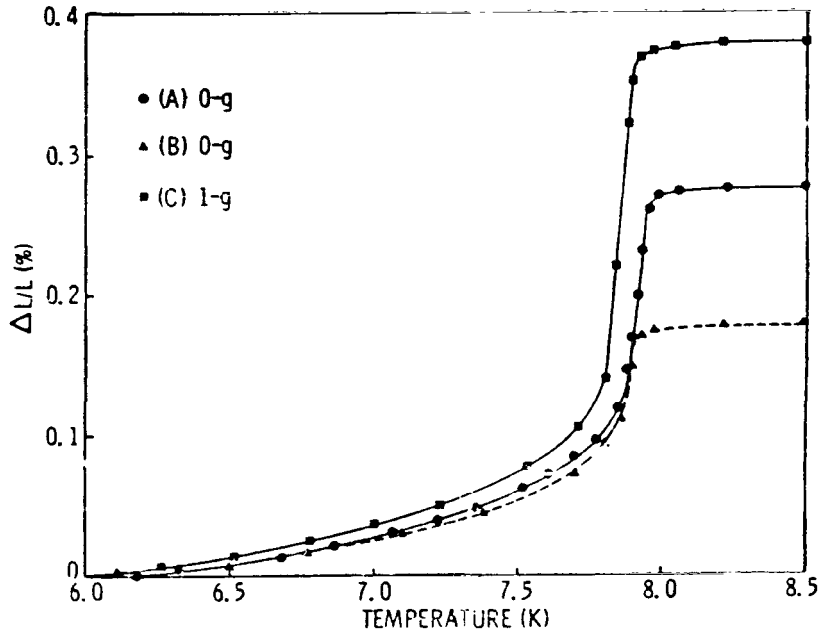

FIGURE 4. INDUCTIVELY MEASURED SUPERCONDUCTING TRANSISTIONS OF Ga-Bi SAMPLES.

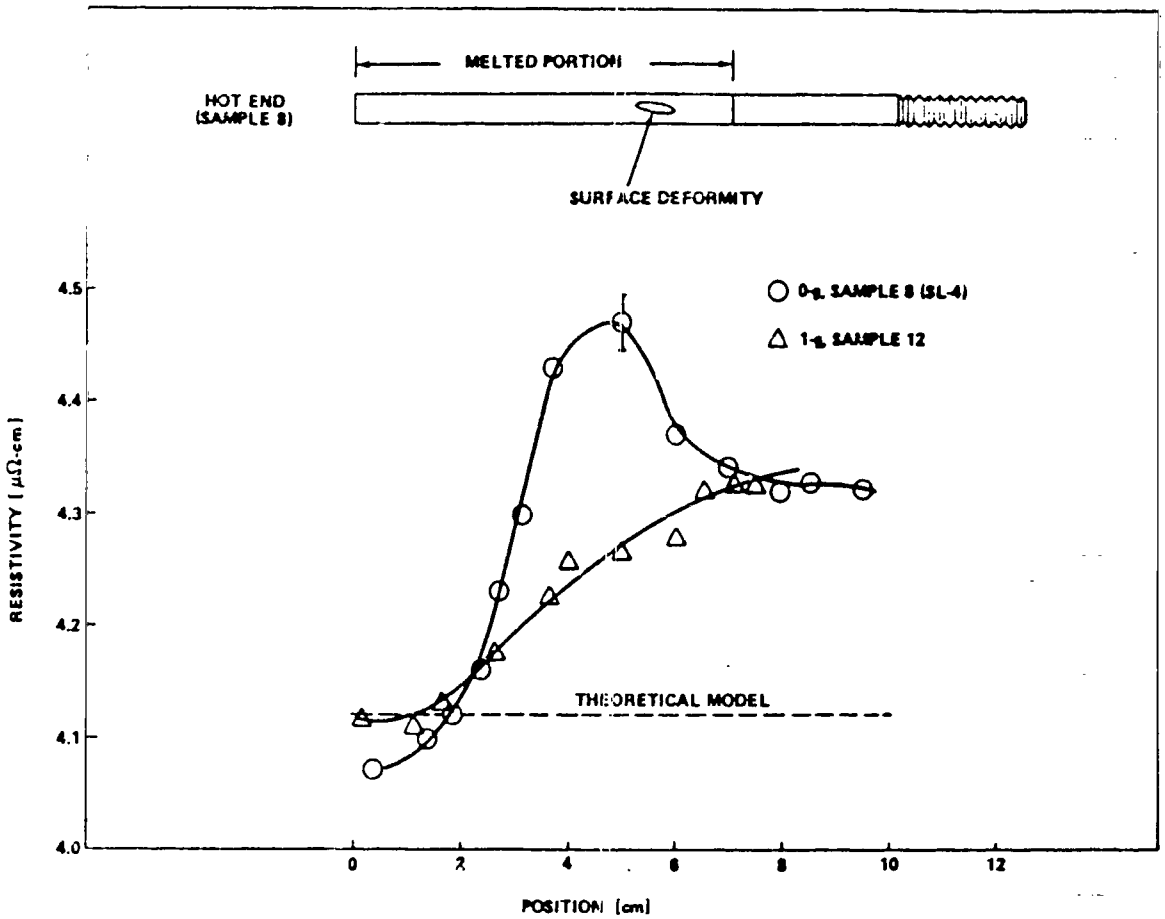

FIGURE 5. LOCAL RESISTIVITY MEASURED BY THE EDDY-CURRENT-DECAY TECHNIQUE FOR A SKYLAB AND A GROUND CONTROL SAMPLE OF Al-Cu EUTECTIC ALLOY.

PROJECTED FUTURE SPACE PROCESSING ACTIVITIES

By

Dr. James H. Bredt
NASA Office of Applications
Washington, D.C. 20546

The purpose of this concluding paper of the Third NASA Space Processing Symposium is to review where the space processing program stands with respect to its long range objectives and what plans have been made to pursue them in the next several years. Very briefly, these objectives can be summed up in the statement that we are trying to make a permanent place for space processing as an integral part of the world's materials technology, and from this broad viewpoint there are two things that are clearly necessary to reach the program's goal. One of them is a space flight system large enough to support materials research and development work on a significant scale and eventually support manufacturing operations as well if these develop. The other is a group of materials scientists and engineers large enough to do space research and development on a scale that can impact materials science and technology and eventually develop manufacturing as well as research applications of space processing.

We can be reasonably certain that the Space Shuttle and Spacelab will provide suitable flight capabilities for space processing when they become operational, and in fact the point of the payload planning studies described by K. R. Taylor at this Symposium has been to ensure their suitability. To date we believe that the right design choices have been made in both systems from the space processing viewpoint; the next steps that are planned in the Shuttle/Spacelab payload area will be discussed below.

On the other hand, the development of a group of users for the Shuttle and Spacelab systems calls for a kind of engineering that is very different from what one does for payload planning and development. The space processing program's development plans in this area are discussed in the following two sections, which detail what we have done and plan to do to ensure that the space processing community will be ready to make full use of the resources that will become available to them in 1980.

SKYLAB AND ASTP EXPERIMENT PROGRAMS

Since the middle of 1971 we have regarded the space processing experiment program on Skylab in part as a user development project, and the successful completion of the flight experiments has brought this aspect of the effort approximately to its halfway point. The other half of the project consists of thoroughly understanding the results of the

experiments and informing the scientific and industrial community about what they mean. There is no formal schedule for this part of the effort, and although the program obviously cannot afford to be dilatory we should like to make sure that the investigators work as long as they need to and have whatever help is required to achieve a full understanding of their results. We also wish each of them to publish complete details of their work in the permanent open literature of their respective scientific and engineering disciplines. The latter is important in order to show scientists and engineers who have never considered using space capabilities in their work that some of their colleagues have used space and made discoveries that would not have come about otherwise.

I believe that this last function of the Skylab experiment program is the really vital one it has to perform, because its effects in initiating action by other investigators will be felt long after the experiments themselves have become of purely historical interest. It is very encouraging that the presentations at this Symposium have indicated that the publications from the Skylab program will evidently be of great interest to the people we wish to reach, and it is also gratifying that the ASTP program will continue the activity begun on Skylab and multiply its effects. These two programs should have the effect of producing a fairly steady flow of publications at least through 1977, which will be of a considerable value in preparing for Shuttle and Spacelab activities. In addition, we hope to make good use of the advice of experienced Skylab and ASTP investigators in our planning activities henceforth.

SOUNDING ROCKET EXPERIMENT PROGRAM

Assuming that we do succeed in interesting a wider community in space processing, the next thing that is needed is a way for them to give practical effect to their interests by trying out what space can do for them. However, a complete payload has already been selected for the ASTP mission, which is the last manned flight scheduled before the Shuttle/Spacelab program begins. The only other alternative seems to be to conduct our own flight program, and it is because of this that the Office of Applications has decided to initiate a series of sounding rocket experiments flights in FY 1975, as Mr. Mathews announced in his keynote speech. Mr. Wuenscher has given an elegant justification for sounding rocket experiments in his presentation, but from the mundane standpoint of a program manager I have to admit that the decision was made mostly because such experiments promise to be reasonably useful for a fairly wide range of topics and they were the best that we could afford.

We believe that a satisfactory capability for sounding rocket experiments involving weightlessness will soon be demonstrated. During the month of May, the Goddard Space Flight Center has scheduled two rocket flights carrying a system designed to limit payload accelerations to 10^{-5}g in free flight. Concurrently with these tests, we intend to prepare an Announcement of Flight Opportunity for space processing experiments with a target date of May 31 for signature if GSFC meets its schedule and if the system works as designed. The mechanics of production

and distribution for Announcements of Flight Opportunity are such that addressees should receive their copies in the mail by about July 1 if we meet our planned signature date.

Our baseline plan for the sounding rocket program calls for flying a total of about 750 lb. of experimental apparatus (about equal to the experiment payload of the ASTP mission) in the first year of flight operations and building up to a steady rate about twice as large during the next year or two. Thereafter, the program is intended to run at that rate until the Shuttle becomes available. We hope to complete the first series of flights by the end of FY 1975 for reasons related to the NASA budget cycle, so that the first participants in the rocket program will involve themselves in the kind of high pressure development effort that had to be staged for the Skylab Multipurpose Furnace experiments. Since the flight program will be continuous over a period of years, however, the initial proposal selection can cover experiments with a broad spectrum of development times, and we can fly the ones with shorter lead times first.

The more interesting aspect of the rocket program is the use we can make of it when it is in steady state operation. The Announcement of Flight Opportunity for the program will be open and international in scope like the Skylab announcements, and like them it will express NASA's continuing interest in negotiating cooperative agreements with private organizations that wish to invest in experiment activities and secure proprietary rights in data that are commensurate with the amount of their investment. Unlike the Skylab announcements, however, rocket announcements will be issued with yearly revisions and remain open for proposals until we decide to begin closing down the program.

Therefore, in about a year we expect to be running an experiment program that has many analogies to the Shuttle program itself. Experiment selection can be continuous within the constraints imposed by financial cycles, and flight opportunities will be available whenever an investigator with a legitimate reason for a series of experiments can be ready to start. In addition, unlike the Skylab and ASTP programs, the rocket program can be expanded above its baseline level if this seems to be warranted by the degree of user interest and the value of the experiment results it produces.

By running the program in this way, we hope to build up a much larger group of experienced space processing experimenters than Skylab and ASTP could provide, and also to create a general consciousness of the utility of space methods in the several materials communities whose interests are affected. If all goes well, we may also be able to develop the kinds of policies and administrative precedents that are needed for commercial participation in the Shuttle experiment program.

To summarize, we think that we can reasonably expect to conduct experiment operations through the rest of the 1970's on a scale and in

a way that will enable the space processing user community to make a fairly smooth transition into the Shuttle/Spacelab program when it begins. In the remainder of this paper, I wish to turn to the question of planning and developing Shuttle and Spacelab payloads.

SHUTTLE/SPACELAB PAYLOAD PROGRAM

In the payload area, as in relations with potential users, the space processing program's assignment for the 1970's is to cope with the startup problems presented by an experiment program much larger than anything that will have been done before it begins. During the payload studies that Mr. Taylor has described, we have tried to estimate the requirements of a fully developed space processing experiment program so as to support the design of the Shuttle and Spacelab systems. In the process, we have found that it will be possible to fly tons of equipment on the Shuttle, provide between 10 and 20 kw of electric power if required, and prepare literally hundreds of samples on a single seven day mission. On the other hand, since the design features of these large flight systems are quite insensitive to most details of individual experiments, most of our work to date has been done with very general and approximate estimates of requirements.

The Space Shuttle's basic design is now quite well defined, and all of the major design choices for the Spacelab system will be made by the time of the Preliminary Design Review which is to be held early next year. Most of the data that will represent the space processing program's influence on these design choices have already been prepared, and the rest of what needs to be done involves specialized engineering topics that need not be discussed here.

The next payload problem to be faced is that of designing and building the equipment that must be ready when Shuttle and Spacelab operations begin, and I believe that the results presented at this Symposium have made it virtually certain that space processing will be one of the disciplines that actually builds payloads for the early Shuttle flights. Building these payloads will be much the largest project that the space processing program has undertaken, and the first step in the process must be to define what our equipment requirements will be in 1980-82 as far as we can foresee them, both for experiments we can plan now and for ones that may be proposed after another five years of progress. These requirements are sure to be quite different from the approximations that were appropriate during the Shuttle and Spacelab design phases.

The business of defining requirements for our early Shuttle and Spacelab payloads will call upon us to use all of the information that can be brought to bear from the Skylab program and other available sources. We are now in the process of planning how to do this, and most of the details remain to be settled, but the broad outlines are sufficiently clear so that they can be sketched here.

The medium we plan to use to assemble preliminary requirements is an Announcement of Planning Opportunity to be issued at the end of this summer, calling for proposals to participate in a consulting panel activity to begin definition of payloads for early Shuttle experiment operations. From various contacts we have had since the Skylab-3 mission landed, I believe that the response to this announcement is likely to be quite lively, and that we can assemble a strong group to assist us.

The planning panel to be set up in this way will need to compile a fairly comprehensive set of preliminary requirements by the end of the year, because we wish to begin Phase A engineering studies of our payloads early next year after the Spacelab design solidifies. The engineering contractors will be expected to combine the data that will then be available on spacecraft interfaces and constraints with the requirements generated by the planning panel to derive design envelopes and conceptual designs for equipment that meets the requirements and uses the resources of the vehicles efficiently. During the course of the studies the engineering work will be reviewed periodically with the planning panel, and we expect that the panel's thinking will evolve significantly as the engineering implications of their recommendations become visible. We therefore intend to keep the planning panel active throughout the Phase A period and to call for several revisions of their recommendations. The Phase A activity will conclude with a Preliminary Requirements Review in the first quarter of 1976.

The results of the Phase A activity will be used to portray the prospective space processing capabilities of the Shuttle and Spacelab in an Announcement of Flight Opportunity and to construct a Statement of Work for a Phase B payload definition study. A group of intending experimenters will be selected from among the respondents to the announcement and will function during Phase B as the planning panel did in Phase A; that is, they will provide requirements data to the engineering contractor on their general disciplines as well as on the specific experiments which they are under contract to implement. The engineering contractor will be charged with assembling detailed specifications for a sufficient initial complement of general purpose payload equipment, beginning with the items that have the longest lead times. We expect that the first approved specifications will be released in the spring of 1977 and that the first contracts for design and construction of equipment to fly in 1980 will be let in the second half of 1977.

The Announcement of Flight Opportunity will be renewed and new experimenters selected yearly after 1976, so as to build up an experiment program that will fill the available Shuttle/Spacelab resources when the flight program begins. The experimenters will be kept directly involved in all stages of equipment definition, design and development, and work on new equipment items will be initiated at least yearly after 1976 in response to requirements raised by the yearly selection of new experiments. We expect that payload development will pass through a period of peak effort in the two years before Shuttle operations begin

and then slacken to a lower steady-state level when the inventory of available equipment becomes large enough to meet most ordinary experimental needs.

Finally, I feel that it is possible to venture only one prediction regarding what will happen when the Shuttle/Spacelab experiment program begins, but I think that this prediction has a solid basis in the data reviewed for us at the present Symposium. We have learned in the past two days that about a third of the space processing activities performed on the Skylab missions have produced results whose implications reach well beyond what anyone expected beforehand. If this proportion is maintained in the Shuttle era when we shall be performing hundreds of experiments per year, I am confident that the first few years of operations will be a period of explosive, revolutionary growth in space processing, and that they will lead to developments in materials science and technology which will surpass the boldest ideas we can conceive today.

LIST OF ATTENDEES

INDUSTRIES AND RESEARCH

Mr. M. Adamson
General Dynamics Convair
Aerospace Division
P.O. Box 80877
San Diego, CA 92138

Dr. Choh-Yi Ang
Northrop Corporation
Research and Technology Center
3401 West Broadway
Hawthorne, CA 90250

Mr. William M. Aubin
Grumman Aerospace Corporation
Bethpage, NY 11714

Mr. Harold L. Bloom
General Electric Company
Space Division
P.O. Box 8555
Philadelphia, PA 19101

Dr. John K. Boah
General Electric Company
Auburn, NY 13021

Dr. Sidney V. Bourgeois
Lockheed Missiles & Space Co.
P.O. Box 1103
Huntsville, AL 35807

Mr. David N. Braski
Union Carbide
Oak Ridge, TN 37830

Mr. Buford L. Brock
Eastern Airlines, Inc.
Miami, FL 33148

Mr. Stephen H. Buzzard
Martin Marietta Corporation
P.O. Box 179
Denver, CO 80201

Dr. John R. Carruthers
Bell Laboratories
Murray Hill, NJ 07974

Mr. George D. Case
IBM
150 Sparkman Drive
Huntsville, AL 35805

Dr. I. Cheng
Roy C. Ingersoll Research Center
Borg-Warner Corporation
Wolf & Algonquin Roads
Des Plaines, IL 60018

Mr. James P. Christoffel
IBM
150 Sparkman Drive
Huntsville, AL 35805

Mr. William R. Clayton
IBM
150 Sparkman Drive
Huntsville, AL 35805

Dr. E. W. Collings
Battelle Memorial Institute
505 King Avenue
Columbus, OH 43201

Mr. Walter E. Crosmer
Bendix Aerospace
Ann Arbor, MI 48107

Mr. W. B. Crandall
IIT Research Institute
10 West 35th Street
Chicago, IL 60616

Mr. Gilbert C. Dodson
General Electric Company
P.O. Box 8555
Philadelphia, PA 19101

LIST OF ATTENDEES (Continued)

INDUSTRIES AND RESEARCH (Continued)

Dr. Frank C. Douglas
United Aircraft Research Labs
Silver Lane
East Hartford, CT 06108

Mr. Benton A. Durley
Intersonics, Inc.
450 E. Ohio Street
Chicago, IL 60611

Mr. Jon T. Eliason
Sperry Rand
716 Arcadia Circle
Huntsville, AL 35805

Dr. Robert J. Fawcett
The B. F. Goodrich
Research and Development
Brecksville, OH 44141

Mr. Jerome M. Feret
Westinghouse Astronuclear Lab
P.O. Box 10864
Pittsburgh, PA 15236

Dr. Robert M. Fisher
U.S. Steel Corporation Research Lab
125 Jamison Lane
Pittsburgh, PA 15146

Dr. L. Michael Foster
IBM
P.O. Box 128
Yorktown Heights, NY 10598

Mr. Theodore K. Freeman
Space Systems Division
P.O. Box 3999
Seattle, WA 98124

Dr. Robert T. Frost
General Electric Company
P.O. Box 8555
Philadelphia, PA 19101

Dr. Francis S. Galasso
United Aircraft Research Labs
East Hartford, CT 06108

Mr. Stanley H. Gelles
Battelle Columbus Labs
505 King Avenue
Columbus, OH 43201

Dr. Gerald L. Glen
Owens-Illinois
Toledo, OH 43666

Mr. Robert E. Gordon
IBM
150 Sparkman Drive
Huntsville, AL 35805

Dr. Richard N. Griffin
General Electric Company
P.O. Box 8555
Philadelphia, PA 19101

Dr. Philomena G. Grodzka
Lockheed Missiles & Space Co
P.O. Box 1103
Huntsville, AL 35807

Mr. Robert L. Hammel
TRW Systems, Space Park
Redondo Beach, CA 90278

Mr. Ralph A. Happe
Rockwell International, Space Division
12214 Lakewood Blvd
Downey, CA 9024'

Mr. Al Haraway
The Boeing Company
P.O. Box 1470
Huntsville, AL 35807

Dr. Ronald B. Heady
Shell Development Co.
P.O. Box 481
Houston, TX 77001

LIST OF ATTENDEES (Continued)

INDUSTRIES AND RESEARCH (Continued)

Dr. Robert T. Howard
IBM
150 Sparkman Drive
Huntsville, AL 35805

Mr. Robert E. Hueschen
General Electric Company
Milwaukee, WI 53201

Mr. Lee B. James
The Boeing Company
P. O. Box 1470
Huntsville, AL 35807

Dr. Samuel Kaye
General Dynamics Convair Aerospace
P.O. Box 80847
San Diego, CA 92138

Mr. David W. Keller
General Electric Company
P.O. Box 8555
Philadelphia, PA 19101

Dr. Michael Kestigian
Sperry Research Center
100 North Road
Sudbury, MA 01776

Dr. Arye Kidron
Hayes International Corp
Huntsville, AL 35807

Mr. Edward H. Kobisk
Union Carbide
Oak Ridge, TN 37830

Dr. Gerald R. Kotler
NL Industries, Inc.
Doehler-Jarvis Division
P.O. Box 902
Toledo, OH 43691

Mr. Jack L. Kracke
IBM
150 Sprakman Drive
Huntsville, AL 35805

Dr. D. J. Larson
Grumman Aerospace Corporation
Bethpage, NY 11714

Mr. Almon E. Leach
Bell Aerospace Company
P.O. Box 1
Buffalo, NY 14240

Mr. Lynn R. Lewis
Bendix Aerospace
3300 Plymouth
Ann Arbor, MI 48107

Dr. Chou H. Li
Grumman Aerospace Corporation
Bethpage, NY 11714

Dr. M. David Lind
Rockwel. International Science Center
P.O. Box 1085
Thousand Oaks, CA 91360

Mr. John B. Little
IBM
P.O. Box 218
Yorktown Heights, NY 10598

Mr. Thomas P. Long
Western Electric Co., Inc.
Princeton, NJ 08540

Mr. Jerald F. Lowry
Westinghouse Research Labs
Pittsburgh, PA 15235

Dr. Elbert M. Mahla
E.I. du Pont de Nemours & Co., Inc
Wilmington, DE 19898

LIST OF ATTENDEES (Continued)

INDUSTRIES AND RESEARCH (Continued)

Mr. Robert G. Mapes
Battelle Columbus Labs
P.O. Box 4107
Huntsville, AL 35802

Mr. William J. Marks
General Electric Company
P.O. Box 8555
Philadelphia, PA 19101

Mr. Dave Marshall
Battelle Columbus Labs
Columbus, OH 43201

Mr. William R. Marx
McDonnell Douglas - East
P.O. Box 516
St. Louis, MO 63166

Dr. Robert Mazelsky
Westinghouse Research Labs
Beulah Road
Pittsburgh, P A 15235

Mr. William B. McAnelly
Teledyne Brown Engineering
Huntsville, AL 35801

Mr. Louis R. McCreight
General Electric Company
P.O. Box 8555
Philadelphia, PA 19101

Dr. John H. McDermit
Lockheed Missiles & Space
Huntsville, AL 35807

Mr. Jack R. McDowell
Battelle Columbus Labs
Columbus, OH 43201

Dr. Thomas R. McGuire
IBM
P.O. Box 218
Yorktown Heights, NY 10598

Mr. Ron Miller
The Boeing Company
P.O. Box 1470
Huntsville, AL 35807

Dr. Abraham I. Mlavsky
Tyco Laboratories, Inc.
16 Hickory Drive
Waltham, MA 02154

Dr. Herbert R. Moeller
Union Carbide Corporation
Tarrytown, NY 10591

Dr. Tripty K. Mookherji
Teledyne Brown Engineering
Huntsville, AL 35807

Mr. Larry J. Murphy
IBM
150 Sparkman Drive
Huntsville, AL 35805

Mr. Roger D. Nichols
McDonnell Douglas
3322 Memorial Parkway S
Huntsville, AL 35801

Mr. Robert P. Olsen
Rockwell International
Downey, CA 90241

Mr. Buzz N. Ordonio
General Electric Company
3322 Memorial Parkway S
Huntsville, AL 35801

Mr. Fred Ordway
4118 Shelby Avenue
Huntsville, AL 35801

Mr. Russell J. Page
ARTCOR
17821-h Sky Park Circle
Irvine, CA 92707

LIST OF ATTENDEES (Continued)

INDUSTRIES AND RESEARCH (Continued)

Dr. Martin Tobin
Westinghouse Astronuclear
P.O. Box 10864
Pittsburgh, PA 15236

Dr. Donald R. Ulrich
General Electric Space Sciences
P.O. Box 8555
Philadelphia, PA 19355

Dr. Michael C. Weinberg
Owens-Illinois
Toledo, OH 43666

Mr. Sanford A. White
White Ind.
306 Spring Valley Ct
Huntsville, AL 35802

Mr. Bennett Whiteson
McDonnell Douglas Corporation
St. Louis, MO 63166

Mr. Fraser K. Williams
IBM
150 Sparkman Drive
Huntsville, AL 35805

Mr. Roy R. Whymark
Intersonics, Inc.
450 E. Ohio Street
Chicago, IL 60611

Dr. Gary Workman
PDR Electronics
Athens, AL

Mr. Gerald Wouch
General Electric Company
P.O. Box 8555
Philadelphia, PA 19101

Dr. John T. Yue
Texas Instruments, Inc.
P.O. Box 5936
Dallas, TX 75222

Mr. Seymour Zeenkov
General Dynamics Convair Aerospace
P.O. Box 80847
San Diego, CA 92138

LIST OF ATTENDEES (Continued)

INDUSTRIES AND RESEARCH (Continued)

Dr. John A. Peterson
Armco Steel Corporation
Research & Technology
Middletown, OH 45042

Dr. Richard W. Porter
General Electric Company
570 Lexington Avenue
New York, N.Y. 10022

Mr. William Prince
PDR Electronics, Inc.
Athens, AL

Dr. Jan Raat
General Dynamics Convair Aerospace
P.O. Box 80847
San Diego, CA 92138

Dr. Richard E. Reed
Union Carbide Corporation
Oak Ridge, TN 37830

Dr. Eberhard Rees
3917 Panorama Drive SE
Huntsville, AL 35801

Mr. Jo L. Reger
TRW Systems Group
1 Space Park
Redondo Beach, CA 92078

Dr. Leonard Reiffel
Interand Company
450 East Ohio Street
Chicago, IL 60611

Dr. David Richman
RCA Laboratories
Princeton, NJ 08540

Mr. Abb L. Scarbrough
NL Industries, Inc.
P.O. Box 420
Highstown, NJ 08520

Dr. Raymond G. Seidensticker
Westinghouse Research Labs
Beulah Road
Pittsburgh, PA 15235

Mr. Donald S. Slater
Bendix Corporation
2796 S. Federal Blvd
Denver, CO 80236

Dr. Elias Snitzer
American Optical Corporation
Framingham, MA 01701

Mr. Ralph J. Starks
Eagle-Picher Industries, Inc.
Miami, OK 74354

Dr. Lee Steg
General Electric Company
P.O. Box 8555
Philadelphia, PA 19101

Mr. Allen Strickler
Beckman Instruments, Inc.
1630 S. State College Blvd
Anaheim, CA 92806

Dr John M. Svoboda
American Foundrymen's Society
Cast Metals Institute
Golf & Wolf Rds
Des Plaines, IL 60016

Mr. Charles H. Tarrant
IBM
150 Sparkman Drive
Huntsville, AL 35805

Mr. Dewey A. Thiessen
Fairchild Industries
Germantown, MD 20767

LIST OF ATTENDEES (Continued)

UNIVERSITIES

Professor C. M. Adams, Jr.
University of Wisconsin
4078N Richland Ct
Milwaukee, WI 53211

Mr. John L. Brown
Georgia Institute of Technology
Engineering Experiment Station
Atlanta, GA 30332

Dr. Ray K. Brown
Wayne State University School
of Medicine
Department of Biochemistry
540 E. Canfield
Detroit, MI 48201

Professor Rointan F. Bunshah
University of California at LA
6532 Boelter Hall
Los Angeles, CA 90024

Dr. J. G. Castle
University of Alabama in Huntsville
Huntsville, AL 35807

Dr. Alan T. Chapman
Georgia Institute of Technology
Atlanta, GA 30332

Mr. David L. Christensen
University Research Institution
Huntsville, AL 35810

Dr. Stuart W. Churchill
University of Pennsylvania
Philadelphia, PA 19174

Dr. Dale S. Cowgill
Weber State College
3750 Harrison Blvd
Ogden, UT 84403

Dr. Moran Coxon
University of Arizona
Aerospace and Mech. Engrg Dept
Tucson, AZ 85721

Dr. Jack H. Davis
University of Alabama in Huntsville
Huntsville, AL 35807

Dr. George W. Farwell
University of Washington
Seattle, WA 98195

Dr. Carl W. Hale
Auburn University
Auburn, AL 36830

Dr. Essie F. Helms
University of Alabama
University, AL 35486

Mr. Harold A. Helms, Jr.
University of Alabama
University, AL 35486

Mr. James L. Hubbard
Georgia Institute of Technology
Atlanta, GA 30332

Dr. R. J. Hung
University of Alabama in Huntsville
Huntsville, AL 35807

Professor Alex Ignatiev
University of Houston
Houston, TX 77004

Dr. Alan A. Johnson
Washington State University
Pullman, WA 99163

LIST OF ATTENDEES (Continued)

UNIVERSITIES (Continued)

Dr. Theo Z. Kattamis
University of Connecticut
Storrs, CT 06268

Dr. Norbert J. Kreidl
University of Missouri
Rolla, MO 65401

Dr. A. R. Kuhlthau
University of Virginia
P.O. Box 5127
Charlottesville, VA 22903

Dr. Allen W. Lacy
Auburn University
Auburn, AL 36830

Dr. Ravi B. Lal
Paine College
Augusta, GA 30904

Professor Henry Leidheiser
Lehigh University
Sinclair Laboratory
Bethlehem, PA 18015

Dr. Esther M. Leise
Georgetown University
37th & O St NW
Washington, DC 20007

Professor Manereo Lichtensteiger
Massachusetts Institute of Technology
Cambridge, MA 02139

Professor Ralph A. Lowry
University of Virginia
Charlottesville, VA 22901

Mr. Alan G. McDevitt
Auburn University
Gentilly #269
Auburn, AL 36109

Professor Simon Ostrach
Case Western Reserve University
Cleveland, OH 44106

Professor Guenther H. Otto
University of Alabama in Huntsville
Huntsville, AL 35807

Dr. Donald L. Parker
Texas A&M University
College Station, TX 77843

Professor Robert B. Pond, Sr.
The Johns Hopkins University
Baltimore, MD 21218

Dr. Wilbur A. Porter
Texas A&M University
College Station, TX 77843

Dr. Francis H. Raven
University of Notre Dame
Notre Dame, IN 46556

Professor Guy E. Rindone
The Pennsylvania State University
University Park, PA 16802

Professor Shao L. Soo
University of Illinois
Urbana, IL 61801

Dr. Carl D. Spear
Utah State University
Logan, UT 84321

Professor Donald R. Uhlmann
Massachusetts Institute of Technology
Cambridge, MA 02139

Dr. Anthony O. Ukanwa
Howard University
Washington, DC 20001

LIST OF ATTENDEES (Continued)

UNIVERSITIES (Continued)

Professor Carel J. van Oss
State University of New York
at Buffalo
School of Medicine
Buffalo, NY 14214

Professor J. Bruce Wagner
Northwestern University
Evanston, IL 60201

Dr. Hans U. Walter
University of Alabama in Huntsville
Huntsville, AL 35802

Mr. Micheal Watson
Georgia Institute of Technology
Atlanta, GA 30332

Dr. Heribert Wiedemeier
Rensselaer Polytechnic Institute
Troy, NY 12181

Dr. Roy C. Wilcox
Auburn University
Auburn, AL 36830

Professor William R. Wilcox
University of Southern California
Los Angeles, CA 90007

Professor August F. Witt
Massachusetts Institute of Technology
Cambridge, MD 02139

Dr. Deloris R. Wright
Auburn University
Auburn, AL 36830

Dr. S. T. Wu
University of Alabama in Huntsville
Huntsville, AL 35807

Professor Alfred S. Yue
University of California
Los Angeles, CA 90024

Dr. Jay Zemel
University of Pennsylvania
Philadelphia, PA 19172

LIST OF ATTENDEES (Continued)

OUT OF COUNTRY

Professor Etienne Aeronoudt
Departement Metaalkunde
G. de Croylaan 2
Heverlee, Belgium 3030

Professor H. Ahlborn
European Space Research Organization
Neuilly sur Seine, France 92

Dr. A. B. Bewersdorff
European Space Research Organization
Neuilly sur Seine, France 92

Mr. Winfried Dewes
Gesellschaft fur Weltraumforschung
505 Porz-Wahn, Germany

Mr. Burkhard Franke
ERNO
Bremen, Germany

Dr. Sennousuke Takahashi
National Research Institute for Metals
Tokyo, Japan 153

Dr. Alfred F. W. Tegtmeier
ERNO
Bremen, Germany 28

PRESS

Mr. Barry J. Casebolt
Huntsville Times
Huntsville, AL 35801

Mr. Michael L. Yaffee
Aviation Week
1221 Avenue of the Americas
New York, NY 10020

LIST OF ATTENDEES (Continued)

NASA HEADQUARTERS

Dr. James H. Bredt
Mr. Larry P. Chamber
Mr. Thomas E. Hanes
Dr. Harvey W. Herring
Mr. Charles W. Matthews
Mr. William F. Moore
Mr. Francis L. Williams

OTHER NASA

Dr. John J. Park, GSFC
Mr. Martin H. Leipold, JPL
Dr. Melvin M. Saffren, JPL
Mr. Charles H. Savage, JPL
Dr. T. Wang, JPL
Mr. Buster Keton, JSC
Mr. John Howard Kimzey, JSC
Mr. Edward K. Svrcer, JSC
Capt. Paul J. Weitz, JSC
Mr. Gordon L. Harris, KSC
Mr. William D. Klopp, Lewis

LIST OF ATTENDEES (Continued)

MSFC

Mr. William R. Adams
Mr. Bill R. Aldrich
Dr. Robert E. Allen
Mr. Gary M. Arnett
Mr. Tommy C. Bannister
Mr. L. H. Berge
Mr. Cecil A. Best
Mr. James R. Bishop
Mr. J. Blumrich
Mr. Arthur Boese
Mr. John P. Boggess
Mr. Donald R. Bowden
Mr. James B. Bramlet
Ms. Judy E. Braun
Mr. E. L. Brown
Dr. George Bucher
Mr. James C. Bush
Mr. William T. Carey
Mr. Joseph M. Carlton
Mr. Otto F. Cerny
Mr. Roger P. Chassay
Mr. Warren G. Coiner
Mr. Ron G. Crawford
Mr. Mirt Davidson
Mr. Carmine E. DeSanctis
Mr. Glenn A. Dill, Jr.
Ms. Bo Facemire
Mr. Eugene H. Fikes
Mr. L. E. Fikes
Mr. Henry B. Floyd
Mr. Jack A. Freedman
Mr. Carl G. Fritz
Mr. B. J. Gaines
Mr. Arthur W. Galzerano
Mr. Herman P. Gierow
Mr. Frank M. Graham
Mr. Lloyd V. Gray
Mr. C. C. Gregg
Ms. Carolyn S. Griner
Dr. Walter Haeussermann
Mr. James D. Hankins
Mr. Earl A. Hasemeyer
Mr. B. C. Hughes
Mr. Rein Ise
Dr. William G. Johnson
Mr. Kenneth D. Johnston
Dr. Mary H. Johnston
Mr. William L. Kimmons
Dr. Roger L. Kroes
Dr. Lewis L. Lacy
Mr. Robert E. Lake
Mr. Charles V. Lovoy
Dr. W. R. Lucas
Dr. Charles A. Lundquist
Mr. Carl H. Maroney
Mr. E. Marshall
Ms. Debora A. Massa
Mr. James C. McCaig
Mr. Eugene C. McKannan
Mr. Brian O. Montgomery
Mr. Fletcher Brooks Moore
Mr. James T. Murphy
Mr. Ralph W. Murphy
Mr. Max E. Nein
Mr. Ron Nichols
Mr. Rabon P. Page
Mr. Richard A. Parr
Dr. Rocco A. Petrone
Mr. James W. Poe
Mr. Richard Poorman
Mr. Clifford E. Price
Mr. Allen M. Priester
Mr. John B. Rendall
Mr. Rudolph C. Ruff

MSFC

Mr. Byron Schrick
Mr. Paul H. Schuerer
Ms. Frances E. Scott
Dr. Mathias P. Siebel
Mr. Jerry W. Smelser
Mr. Richard G. Smith
Mr. William C. Snoddy
Dr. Robert S. Snyder
Mr. Alvin Steinberg
Mr. Charles D. Stocks
Dr. Ernst S. Stuhlinger
Mr. Leland K. Swaim
Mr. Kenneth R. Taylor
Mr. Roy A. Taylor
Mr. Otha H. Vaughan
Mr. Jesco H. von Puttkamer
Ms. Ruth G. Von Saurma
Mr. Thomas M. Wade
Mr. J. H. Waite
Mr. William A. Wall
Mr. James T. Watkins
Mr. Willie E. Weaver
Mr. Gerald A. Wheeler
Mr. Tyree H. Wilkinson
Mr. James R. Williams
Mr. Carl E. Winkler
Mr. Hans F. Wuenscher
Mr. Iva C. Yates, Jr.
Mr. Vaughn H. Yost

LIST OF ATTENDEES (Continued)

OTHER GOVERNMENT

Dr. Biliyar N. Bhat
Research Associate
National Research Council
NASA MSFC (S&E-PE-MX)
Huntsville, AL 35812

Mr. William E. Blades
US Army Missile Command
Redstone Arsenal, AL 35809

Dr. Robert Kahal
Deputy for Space Programs
Office of Assistant Secretary for R&D
Department of the Air Force
Washington, DC 20330

Dr. William B. McLean
Naval Undersea Center
Technical Director
San Diego, CA 92132

Mr. Harry S. Parker
National Bureau of Standards
Washington, DC 20234

Dr. Robert L. Parker
National Bureau of Standards
Washington, DC 20234

Dr. Elio Passaglia
National Bureau of Standards
Washington, DC 20234

Mr. Edwin S. Tankins
Naval Air Development Center
Warminster, PA 18974

☆ U.S. GOVERNMENT PRINTING OFFICE 1974 – 640 444/1 REGION NO. 4